Advances in Underground Mine Backfill

Lead Guest Editor: Lijie Guo
Guest Editors: Tingting Zhang, Qianqian Wang, and Qi Jia

Advances in Underground Mine Backfill

Advances in Underground Mine Backfill

Lead Guest Editor: Lijie Guo
Guest Editors: Tingting Zhang, Qianqian Wang, and Qi Jia

Chayut Ngamkhanong (iD), Thailand
Trung Ngo, Australia
Tengfei Nian, China
Mehdi Nikoo (iD), Canada
Youjun Ning (iD), China
Olugbenga Timo Oladinrin (iD), United
Kingdom
Oladimeji Benedict Olalusi, South Africa
Timothy O. Olawumi (iD), Hong Kong
Alejandro Orfila (iD), Spain
Maurizio Orlando (iD), Italy
Siti Aminah Osman, Malaysia
Walid Oueslati (iD), Tunisia
SUVASH PAUL (iD), Bangladesh
John-Paris Pantouvakis (iD), Greece
Fabrizio Paolacci (iD), Italy
Giuseppina Pappalardo (iD), Italy
Fulvio Parisi (iD), Italy
Dimitrios G. Pavlou (iD), Norway
Daniele Pellegrini (iD), Italy
Gatheeshgar Perampalam (iD), United
Kingdom
Daniele Perrone (iD), Italy
Giuseppe Piccardo (iD), Italy
Vagelis Plevris (iD), Qatar
Andrea Pranno (iD), Italy
Adolfo Preciado (iD), Mexico
Chongchong Qi (iD), China
Yu Qian, USA
Ying Qin (iD), China
Giuseppe Quaranta (iD), Italy
Krishanu ROY (iD), New Zealand
Vlastimir Radonjanin, Serbia
Carlo Rainieri (iD), Italy
Rahul V. Ralegaonkar, India
Raizal Saifulnaz Muhammad Rashid,
Malaysia
Alessandro Rasulo (iD), Italy
Chonghong Ren (iD), China
Qing-Xin Ren, China
Dimitris Rizos (iD), USA
Geoffrey W. Rodgers (iD), New Zealand
Pier Paolo Rossi, Italy
Nicola Ruggieri (iD), Italy
JUNLONG SHANG, Singapore

Nikhil Saboo, India
Anna Saetta, Italy
Juan Sagaseta (iD), United Kingdom
Timo Saksala, Finland
Mostafa Salari, Canada
Ginevra Salerno (iD), Italy
Evangelos J. Sapountzakis (iD), Greece
Vassilis Sarhosis (iD), United Kingdom
Navaratnarajah Sathiparan (iD), Sri Lanka
Fabrizio Scozzese (iD), Italy
Halil Sezen (iD), USA
Payam Shafigh (iD), Malaysia
M. Shahria Alam, Canada
Yi Shan, China
Hussein Sharaf, Iraq
Mostafa Sharifzadeh, Australia
Sanjay Kumar Shukla, Australia
Amir Si Larbi (iD), France
Okan Sirin (iD), Qatar
Piotr Smarzewski (iD), Poland
Francesca Sollecito (iD), Italy
Rui Song (iD), China
Tian-Yi Song, Australia
Flavio Stochino (iD), Italy
Mayank Sukhija (iD), USA
Piti Sukontasukkul (iD), Thailand
Jianping Sun, Singapore
Xiao Sun (iD), China
T. Tafsirojjaman (iD), Australia
Fujiao Tang (iD), China
Patrick W.C. Tang (iD), Australia
Zhi Cheng Tang (iD), China
Weerachart Tangchirapat (iD), Thailand
Xiaxin Tao, China
Piergiorgio Tataranni (iD), Italy
Elisabete Teixeira (iD), Portugal
Jorge Iván Tobón (iD), Colombia
Jing-Zhong Tong, China
Francesco Trentadue (iD), Italy
Antonello Troncone, Italy
Majbah Uddin (iD), USA
Tariq Umar (iD), United Kingdom
Muahmmad Usman, United Kingdom
Muhammad Usman (iD), Pakistan
Mucteba Uysal (iD), Turkey

Ilaria Venanzi , Italy
Castorina S. Vieira , Portugal
Valeria Vignali , Italy
Claudia Vitone , Italy
Liwei WEN , China
Chunfeng Wan , China
Hua-Ping Wan, China
Roman Wan-Wendner , Austria
Chaohui Wang , China
Hao Wang , USA
Shiming Wang , China
Wayne Yu Wang , United Kingdom
Wen-Da Wang, China
Xing Wang , China
Xiuling Wang , China
Zhenjun Wang , China
Xin-Jiang Wei , China
Tao Wen , China
Weiping Wen , China
Lei Weng , China
Chao Wu , United Kingdom
Jiangyu Wu, China
Wangjie Wu , China
Wenbing Wu , China
Zhixing Xiao, China
Gang Xu, China
Jian Xu , China
Panpan , China
Rongchao Xu , China
HE YONGLIANG, China
Michael Yam, Hong Kong
Hailu Yang , China
Xu-Xu Yang , China
Hui Yao , China
Xinyu Ye , China
Zhoujing Ye , China
Gürol Yildirim , Turkey
Dawei Yin , China
Doo-Yeol Yoo , Republic of Korea
Zhanping You , USA
Afshar A. Yousefi , Iran
Xinbao Yu , USA
Dongdong Yuan , China
Geun Y. Yun , Republic of Korea

Hyun-Do Yun , Republic of Korea
Cemal YİĞİT , Turkey
Paolo Zampieri, Italy
Giulio Zani , Italy
Mariano Angelo Zanini , Italy
Zhixiong Zeng , Hong Kong
Mustafa Zeybek, Turkey
Henglong Zhang , China
Jiupeng Zhang, China
Tingting Zhang , China
Zengping Zhang, China
Zetian Zhang , China
Zhigang Zhang , China
Zhipeng Zhao , Japan
Jun Zhao , China
Annan Zhou , Australia
Jia-wen Zhou , China
Hai-Tao Zhu , China
Peng Zhu , China
QuanJie Zhu , China
Wenjun Zhu , China
Marco Zucca, Italy
Haoran Zuo, Australia
Junqing Zuo , China
Robert Černý , Czech Republic
Süleyman İpek , Turkey

Contents

Contents

Research Article

Study on the Relationship between the Fluidity of Paste in Stope and the Rheological Properties of Paste

Liang Wang,[1,2] **DengPan Qiao** ⬤,[1] **JinCheng Xie** ⬤,[1] **Jun Wang,**[1] **and Fei Huang**[1]

[1]*Kunming University of Science and Technology, Kunming 650000, Yunnan, China*
[2]*Sinosteel Maanshan General Institute of Mining Research Co, Ltd., Xuancheng, Anhui, China*

Correspondence should be addressed to DengPan Qiao; danielshak@163.com

Paste should be kept in homogeneous state without segregation or weak segregation during pipeline transportation, which can reduce the occurrence of pipe blockage accidents in engineering application. Only when the paste is homogeneous can the paste have good stope fluidity, and the stope fluidity is also restricted by the geometric size of the stope and other factors. Therefore, it is very important to study the homogeneity of paste and analyze the influence of paste rheological characteristics on stope fluidity. In this paper, it is pointed out that the vertical settling velocity of solid phase materials in paste in the liquid-phase dense medium is the main factor affecting the homogeneity of paste. Increasing the plastic viscosity and yield stress of the liquid-phase dense medium is beneficial to increase the drag force of aggregate and then reduce the settling speed of aggregate in the liquid-phase dense medium. On this basis, the homogeneity of paste can be judged. In the simplified paste flow field, using Cauchy stress equation and flow boundary conditions, the relationship between paste stope flow performance and paste rheological properties was analyzed, and the relationship model between the slope angle of paste flow formation and paste rheological properties was established. Compared with the experimental results, the error of the model results is small, and the slope angle of paste flow can be well predicted.

1. Introduction

For the study of flow capacity of filling slurry in stope: Shi et al. [1] have carried out a similar simulation test of filling slurry flow and mechanical strength test of in situ filling in stope. The results show that the final slope of filling slurry flow tends to be normal distribution when cutting at a single point. During the flowing process, the filling slurry produced segregation and delamination, which mainly showed that the particle size of filling material increased first and then decreased along the flowing direction of slurry. The research results of Lu et al. [2] show that the trajectory curve of filling slurry along the flow direction tends to be normal distribution, and the strength of filling body along the flow direction of filling slurry shows an inverted S-shaped distribution of decreasing-increasing-decreasing. The results of theoretical analysis by Tang and Xiao [3] show that after the filling slurry enters the stope, it flows to the periphery,

and the shape of the pile surface obeys the normal distribution law. The size of the mean square deviation reflects the smoothness or steepness of the surface formed after the slurry flows, and its value mainly depends on the filling material and mixture ratio. Hui et al. [4] tested the fluidity of paste under different concentrations and ratios by loop experiment and finally determined the best paste filling concentration, the best lime sand, and the corresponding resistance along the way. Xue et al. [5] carried out the slurry slump test aiming at the influence of different pumping agent content on filling slurry in a mine. The results show that pumping agent has a nonlinear gradient effect on slump, and with the increasing amount of pumping agent, the influence ability of pumping agent with the same dose on slump gradually weakens; the yield stress and plastic viscosity decrease with the increase of pumping agent content. When the pumping agent content exceeds 3%, the yield stress decreases obviously. For plastic viscosity, when the

pumping agent content exceeds 2%, the decrease begins to slow down obviously. Tao et al. [6], aiming at the problems of poor rheological stability, delamination in slurry and pipe blockage caused by coarse aggregate settlement in long-distance filling slurry of pumped large double line in coal mine filling mining, measured the fluidity value and fluidity loss with time of four groups of filling slurry by using the fluidity loss experiment method. On the basis of diffusion theory, Li [7] deduced the vertical distribution formula of coarse aggregate filling slurry concentration, considering the factors of solid particle size, particle shape and density, slurry density, and yield stress. Xue et al. [8] aimed at naphthalene series water-reducing agent and BF high-efficiency water-reducing agent, studied the role of water-reducing agent in filling slurry flow process by analyzing the influence of adding ways and types of water reducing agent on slurry rheological properties. The test results show that the fluidity of slurry prepared by adding water-reducing agent by the postmixing method is relatively good, and the fluidity of graded tailings slurry after adding water-reducing agent is significantly improved. Under the same conditions, the yield stress and apparent viscosity of slurry decrease. Niu and Peng [9] carried out experimental research on the fluidity and studied the workability of slurry with different concentrations and lime-sand ratio aggregates by using slump bucket and L-tube, and finally obtained the rheological parameters of this kind of tailings. Gao et al. [10] studied the influence of polycarboxylate and naphthalene superplasticizer on the fluidity of phosphorus tailings filling slurry by expansion method, fluidity method, and L-tube method. The results show that polycarboxylate superplasticizer is superior to naphthalene superplasticizer. At the same time, polycarboxylate superplasticizer has a strong dispersing effect on phosphorus tailings filling slurry, which can change the flocculation structure of cement and improve the fluidity of filling slurry. Xie et al. [11] gave a new definition of ultrafine particles in filling slurry and analyzed the influence of ultrafine particles on rheological properties of slurry.

As mentioned above, many scholars have analyzed the influencing factors of filling slurry fluidity by means of experiments and theoretical research, and established some qualitative analysis models. However, most of the analysis is based on the pipeline transportation capacity of slurry, and there is no in-depth discussion on the free flow and leveling of slurry in the open area. It cannot directly solve the problem of slurry flowing ability in stope. In this paper, the relationship between rheological properties of filling slurry and stope fluidity is studied by constructing a direct physical and mechanical model of filling slurry rheological properties and stope fluidity.

2. Theoretical Study

2.1. Influence of Rheological Properties of Heavy Medium on Slurry Homogeneity.
Filling slurry can be regarded as a suspension system formed by the aggregate and liquid-phase heavy medium, so the rheological properties of the liquid-phase heavy medium and the basic physical and mechanical parameters of aggregate will affect the movement of aggregate in slurry, thus affecting the homogeneity of slurry.

The slurry meeting the condition of critical flow state concentration is paste, and the paste should have enough antisegregation ability. Insufficient antisegregation ability often leads to the separation of aggregate in the process of slurry flow, and the coarse aggregate settles and accumulates in the process of pipeline transportation, forming embolism and causing pipeline blockage; or the uneven accumulation in stope makes the filling layer form a weak surface, which is extremely unfavorable to the control of backfill strength. Therefore, it is very important to analyze the stress of aggregate in slurry, so as to establish the quantitative characterization of the critical flow concentration condition in the slurry and judge whether the slurry belongs to the paste.

It is assumed that there is no relative movement between aggregate and liquid heavy medium in horizontal direction. In the vertical direction, the aggregate is balanced by its own gravity, buoyancy, and viscous resistance in the liquid-phase heavy medium (as shown in Figure 1):

$$F_v = g\Delta\rho V. \tag{1}$$

In the above formula, F_v represents viscous resistance, $\Delta\rho$ represents density difference between liquid heavy medium and aggregate, and V represents volume of aggregate.

It is noted that the viscous resistance in the liquid-phase heavy medium is

$$F_v = C_D\rho_S\frac{v^2}{2}\pi r^2. \tag{2}$$

C_D represents drag coefficient, v represents vertical velocity of coarse aggregate, and ρ_S is apparent density of the liquid-phase heavy medium.

Therefore, the relative movement speed v of aggregate relative to the liquid-phase heavy medium is equal to

$$v = \frac{8g\Delta\rho r}{3C_D\rho_S}. \tag{3}$$

When Reynolds number is low, the drag coefficient of C_D can be expressed as

$$C_D = f(R_e). \tag{4}$$

Equation (4) can be expressed by Reynolds number; that is, the relative movement speed of aggregate in the vertical direction in the liquid-phase medium can be expressed by Reynolds number of slurry flow.

However, the Reynolds number exists only for Newtonian fluid. As the filling slurry is a Bingham fluid in non-Newtonian fluid, compared with Newtonian fluid, it has a yield stress τ_0; that is, the shear stress needs to overcome τ_0 before the fluid can flow. Therefore, the Reynolds number formula of Newtonian fluid is not applicable and needs to be replaced by the generalized Reynolds number of Bingham fluid [12].

The generalized Reynolds number R_e of slurry as Bingham fluid is

$$R_e = \frac{2\rho_P r v}{\eta + \tau_0 r/3v}, \tag{5}$$
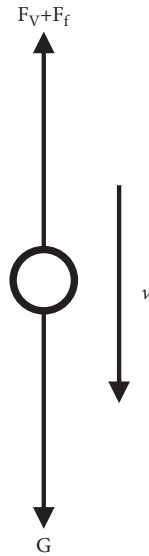
FIGURE 1: Stress analysis of aggregate.

FIGURE 2: Schematic diagram of slurry segregation.

where η represents the viscosity of slurry, τ_0 represents the yield stress of slurry, ρ_P represents the apparent density of slurry, and r represents the pipe radius of slurry in the process of pipe flow.

Equation (5) gives the speed expression of relative movement of coarse aggregate in the liquid-phase heavy medium. From (2), it can be seen that the relative movement speed of aggregate in the liquid-phase heavy medium is the result of plastic viscosity and yield stress of the liquid-phase medium, which is different from Newtonian fluid only affected by viscosity. In fact, when the plastic viscosity and yield stress are small, the speed of aggregate relative to slurry will increase; that is, the settlement will accelerate, causing the segregation of slurry in the flow process; when the plastic viscosity increases and the yield stress remains unchanged, if the vertical velocity of the aggregate relative to the liquid dense medium decreases, the slurry can still remain homogeneous in the flow process and yield stress will also cause the decrease of relative movement speed of aggregate. Therefore, the homogeneity of slurry depends not only on the plastic viscosity of liquid heavy medium, but also on the yield stress.

A large number of documents [13–17] show that the slump spread test can well characterize the segregation state of slurry movement.

In fact, the aggregate and the surface-covered liquid-phase heavy medium can be considered as a unit (as shown in Figure 2). When the aggregate particles move, the surface-covered liquid-phase medium and aggregate move evenly together. If the relative movement distance exceeds the thickness of the unit, it means that the slurry is separated during the movement. Generally, the test time of slump spread is $T_i \approx 5s$.

From this, the judgment formula of slurry segregation is obtained:

$$\int_0^{T_i} v d_t \le \left(\frac{1}{\lambda} - 1\right) \cdot r. \tag{6}$$
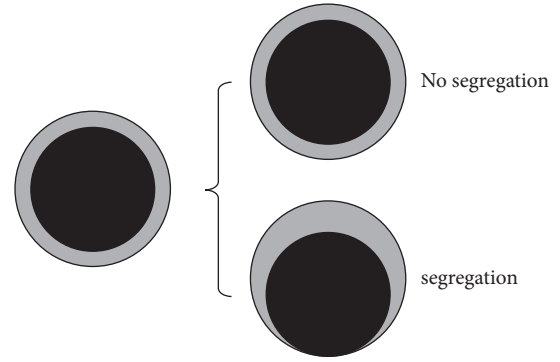
Equation (6) is the discriminant of slurry homogeneity without segregation, where λ refers to the ratio of aggregate particle size in slurry to the particle size of globules composed of the liquid medium. It is noted that there is a distribution range of aggregate particle size, so r in the above formula refers to the average radius of aggregate particle in mathematical sense.

It can be seen from the above formula that the homogeneity of slurry is affected by the yield stress and viscosity of the liquid medium, and it is also related to the gradation of aggregate (λ is the comprehensive reflection of gradation and content). If the slurry does not meet the above inequality, it means that segregation will occur in the process of natural flow and pipeline transportation, or if it does not meet the critical flow state concentration condition, it is not a paste.

2.2. Influence of Rheological Properties of Paste on Stope Fluidity. An important index of paste filling performance is its flow performance in the stope. The paste with good fluidity has the characteristics of long-distance self-leveling, and the slope angle formed by paste from the feeding point to the farthest end of stope is small. For the case of requiring top connection, under the condition of ensuring the roof rate of stope, it can effectively reduce the number of roof connection and ensure the quality of filling body; when the filling body is used as the working platform for equipment operation, the thickness uniformity of the working platform can be ensured, and the damage of the filling body caused by insufficient thickness can be reduced.

The flow of paste in stope is shown in Figure 3: the paste is affected by conveying pressure, gravity, and yield stress. When the sum of conveying pressure and gravity is greater than yield stress, the paste starts to flow. With the flow of paste, the stacking height of paste decreases, and the pressure generated by its own gravity decreases. When the pressure is less than the yield stress, the paste stops flowing; then, a slope of accumulation is formed. For the paste which produces the stacking slope at the stop, its flow form can be simplified as the free flow of a certain volume of fluid in a horizontal infinite space.

The shear stress required by the paste flow is provided by the pressure in the paste, and the shear stress of paste obtained from Cauchy stress equation is
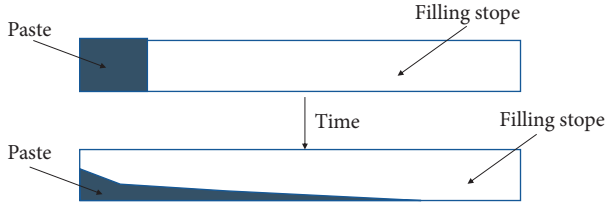
FIGURE 3: Schematic diagram of paste flowing in stope.

$$\tau = \frac{\Delta p y}{2L}, \tag{7}$$

in which Δp is the resistance loss of paste flow.

From the relationship between the rheological model of paste and shear stress,

$$-\tau = -\frac{\Delta p y}{2L}$$
$$= \tau_0 + \eta \frac{du}{dy}. \tag{8}$$

The integral of the above formula is

$$u = \frac{1}{\eta} \times \left[-\frac{\Delta p y^2}{4L} - \tau_0 y - c \right]. \tag{9}$$

It is noted that there is a part with shear stress less than τ_0 at the top of the paste (as shown in Figure 4), which means that the paste in this part will not move, so the speed $u = 0$ at this time; then, bring it into the above formula:

$$u = \frac{1}{\eta} \times \left[\frac{\Delta p}{2L} \left(H \times \left(H - \frac{\tau_0}{\rho g} \right) - Hy \right. \right.$$
$$\left. \left. + \frac{1}{2} \left(y^2 - \left(H - \frac{\tau_0}{\rho g} \right)^2 \right) \right) - \tau_0 \left(\frac{H}{2} - \frac{\tau_0}{\rho g} \right) \right]. \tag{10}$$

Let the average speed be v, and the expression of the average speed is

$$v = \frac{1}{H - \tau_0/\rho g} \int_0^{H - \tau_0/\rho g} u_x dy. \tag{11}$$

The relationship between the average velocity of paste on AB plane and the resistance loss Δp can be obtained. It is noted that the paste has velocity distribution along Y direction, and the velocity decreases with the increase of Y, but the velocity of paste is consistent in horizontal X direction, which means that in order to maintain the velocity, the resistance loss is increasing along X positive direction:

$$\Delta p = \frac{6v\eta L}{(H - \tau_0/\rho g)^2} + \frac{3\tau_0 L}{(H - \tau_0/\rho g)}. \tag{12}$$

It can be seen from the above formula that Δp is related to the average velocity, the height H of paste flowing, and the flowing distance L. It is noted that when the paste stops flowing, $V = 0$, and the pressure $\rho g h_2 = \Delta p$ provided by the paste at this time; therefore, it is obtained:
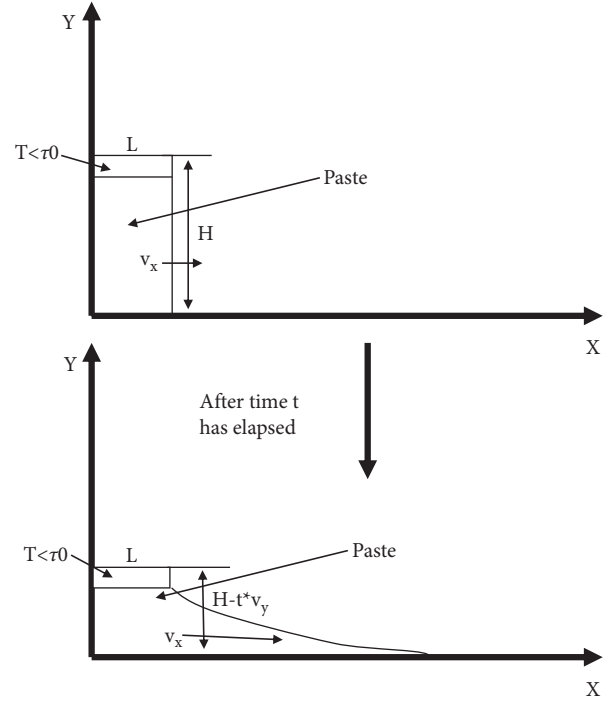
FIGURE 4: Simplified flow diagram of paste stope.

$$\rho g h_2 = \frac{3\tau_0 L}{(H - \tau_0/\rho g)}. \tag{13}$$

Then, the flow angle of paste is obtained:

$$\tan\alpha = \frac{3\tau_0}{(H - \tau_0/\rho g)\rho g}. \tag{14}$$

The above formula illustrates the relationship between the leveling angle of a certain volume of paste and its physical properties and can be used to judge the flowing distance and angle of a certain volume of paste. In fact, when the rheological properties of paste are determined, the angle of paste flow is only related to the height.

As shown in Figure 5, the higher the paste height means that the paste has greater potential energy and can provide greater pressure. Under the condition of constant paste resistance loss, the greater the paste pressure, the farther the paste can flow, and the smaller its flow angle.

Under the same flow height, the flow distance of different pastes is related to their yield stress (as shown in Figure 6); that is, the yield stress is inversely proportional to the flow distance, and the greater the yield stress, the smaller the flow distance, whereas the smaller the yield stress, the farther the flow distance. This is the same trend as the relationship between paste expansion and yield stress in slump test. In fact, the farther the flowing distance is, the smaller the angle formed by the paste after stopping flowing, and the smaller the stacking angle is, the more favorable it is for the top connection of paste and the leveling of working face, and the safety of mining activities and the operation of large-scale equipment.
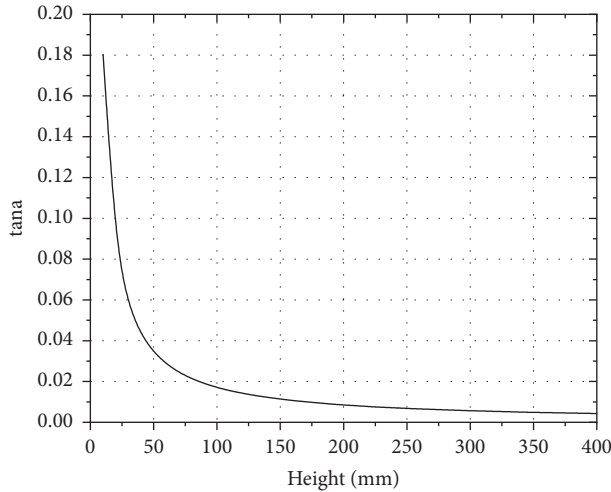
FIGURE 5: Relationship between leveling angle and height of paste.
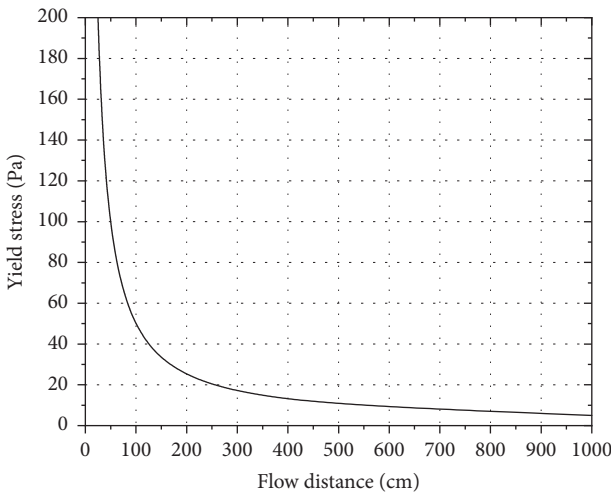
FIGURE 6: Relationship between flow distance and yield stress.

3. Experimental Study

3.1. Test Material.
The fine aggregate used in the test is desert sand and river sand, and the coarse aggregate is waste rock. The basic physical parameters and gradation are shown in Table 1.

It can be seen from Table 1 that the apparent density gap of the three kinds of filling aggregate is not large. The difference of packing compactness between waste rock and desert sand is small, and that of river sand is the largest, which means that river sand has smaller packing volume and the highest packing compactness in natural loose state.

Table 2 shows the mineral composition analysis, and it can be seen that the main components of the tailings are calcite and mica. The chemical properties of the tailings are relatively stable, and there is no chemical reaction with water.

As fine aggregate, the biggest difference between river sand and desert sand is the difference of gradation between them. The negative cumulative distribution of gradation of three aggregates is shown in Figure 7.

The following can be seen from Figure 7:

TABLE 1: Basic physical parameters of filling aggregate.

Category	Apparent density (kg/m³)	Moisture content (%)	Packing compactness (%)
Waste rock	2625	1.255	59.6
River sand	2610	0.757	62.2
Desert sand	2570	0.219	59.1

TABLE 2: Analysis results of mineral composition.

Mineral name	Mineral content of waste rock (%)	Mineral content of river sand (%)	Mineral content of desert sand (%)
Calcite	40–50	50–55	25–30
Mica	25–35	20–30	25–30
Fluorite	5–10	1–5	5–10
Dolomite	5–10	1–5	5–10
Amphibole	1–5	1–5	5–10

(1) The grading range of wind sand is below 1.18 mm. Generally speaking, 99% of the wind sand is within 0.6 mm; the median particle size and average particle size of negative cumulative distribution of wind and sand are 0.23 mm and 0.3 mm, respectively.

(2) The grading range of river sand is below 9.5 mm. Generally speaking, 90% of river sand particles are below 4.75 mm; the median particle size of negative cumulative distribution of river sand is 0.89 mm; average particle size is 1.82 mm.

(3) The grading range of waste rock is below 10 mm, and generally speaking, 90% of waste rock particles are below 9.5 mm; the median particle size of negative cumulative distribution of waste rock is 3.56 mm; average particle size is 4.81 mm.

3.2. Homogeneity Test of Slurry.
Homogeneity of slurry is a necessary condition to evaluate whether it belongs to paste or not. Homogeneous slurry can flow smoothly and reduce segregation in the flow process. According to the theoretical research, whether the slurry segregates or not depends on the formula (6), which essentially depends on the ratio of the central particle size to the spherical particle size of aggregate, the yield stress of the liquid-phase heavy medium, the plastic viscosity, and the average particle size of coarse aggregate.

The test scheme of slurry homogeneity is based on the paste with the ratio of waste rock to tailings of 7 : 3. The rheological properties of the liquid-phase heavy medium in slurry are adjusted by adjusting the mass concentration or cement content. The test scheme is shown in Table 3.

The following can be seen from equation (6): the necessary condition to judge whether the slurry is segregated or not is the rheological properties of the liquid medium in coarse aggregate slurry, including plastic viscosity and yield stress. Therefore, it is necessary to use rheometer to test the rheological properties of the liquid medium. It can be seen from the
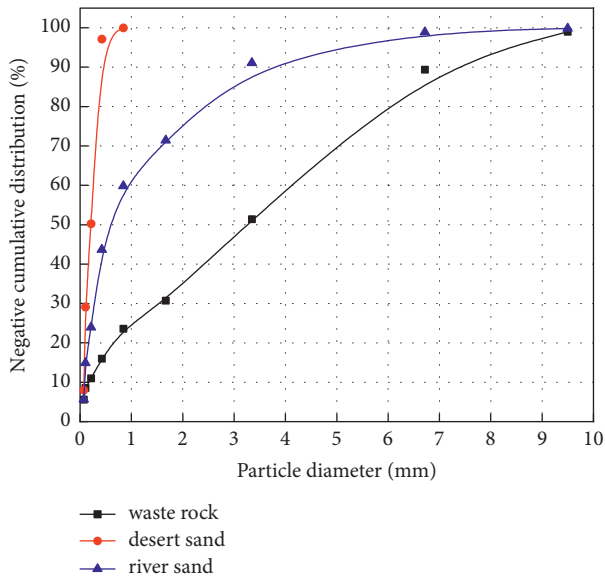
Figure 7: Gradation of Jinchuan filling aggregate.

Table 3: Homogeneity test of slurry.

Type of aggregate	Ratio of coarse aggregate to fine aggregate (mass ratio)	Cement content (kg/m³)	Mass concentration (%)
Waste rock-desert sand	7 : 3	310	80–84
Waste rock-desert sand	7 : 3	280	80–84
Waste rock-desert sand	7 : 3	260	80–84

test scheme in Table 2 that the coarse aggregate is waste stone and the fine aggregate is desert sand. Therefore, it is necessary to test the rheological properties of desert sand slurry with different concentrations. Test scheme is shown in Table 4.

3.2.1. Results of Slurry Homogeneity Test.
According to the test scheme in Table 4, the rheological properties of the liquid medium are tested, and the test results are shown in Table 5.

The following can be seen from Table 4: with the same cement content, the plastic viscosity of the liquid medium will increase with the increase of mass concentration, and the yield stress follows the same rule. At the same concentration, with the decrease of cement content, the plastic viscosity of the liquid-phase medium decreases, which is caused by the decrease of fine particle content in the liquid-phase medium.

According to the test scheme in Table 3, the homogeneity of slurry was tested, and the segregation results were obtained by observing the segregation conditions of slurry, and compared with the predicted results of formula (6) (in the formula, the flow rate is 2.41 m/s and the pipe diameter is 0.138 m according to the actual parameters of Jinchuan No. 2 Mining Area).

Table 4: Rheological test of the liquid medium.

Type of aggregate	Ratio of coarse aggregate to fine aggregate (mass ratio)	Cement content (kg/m³) (%)	Rheological property
Desert sand	310	75–79	τ_0, η
Desert sand	280	75–79	τ_0, η
Desert sand	260	75–79	τ_0, η

As shown in Table 6, there is almost no difference between the predicted results and the actual results, and the slurry begins to show no segregation at 82%, reaching the critical flow state concentration, indicating that the homogeneity is better at this concentration. However, it is noted that the predicted results are different from the actual results when the cement content is 280 kg/m and the mass concentration is 82%, and the measured results are no segregation, but the predicted results show segregation, which is caused by the difference between the yield stress and viscosity test results. In fact, prediction formula (6) should be stricter, and the judgment of segregation will be more conservative.

3.3. Fluidity Test of Paste Stope.
In order to verify the theoretical research results, a similar simulation test was carried out on the fluidity of paste stope, and the test scheme is shown in Table 7.

In the test, a filling stope model with a length of 4 m, a width of 0.7 m, and a height of 0.6 m was constructed with wooden boards (Figure 8). Paste with the above ratio was injected from one end of the device to keep the device closed. When the filling paste stopped flowing, the height of the filling body was measured and the maximum slope angle of the filling body was calculated. In addition, it is compared with the slope angle calculated by formula (13).

3.3.1. Results of Stope Fluidity Test.
According to the stope fluidity test scheme, the stope fluidity test was carried out for pastes with different proportions and concentrations, and the process is as Figure 9.

The following can be seen form Figure 9: during the experiment, a rectangular groove with a length of 4 meters, a width of 0.7 m meters, and a height of 0.6 meters was built with wooden boards. Inject the prepared paste from one end of the rectangular groove. Because the top of the rectangular groove is not closed, the flow process of paste can be clearly seen. There was no segregation of paste during the experiment. After the paste is solidified and molded, measure the maximum slope angle of the paste and compare it with the predicted result.

According to the results of the stope fluidity test, Table 8 is drawn.

According to the contents shown in Table 8 and Figure 10 under the condition of the same material and gradation, the maximum slope angle increases with the increase of mass concentration, because the plastic viscosity and yield stress of paste increase with the increase of mass concentration, which leads to the increase of shear stress to be overcome in the flow process, which leads to the increase of maximum slope angle.

TABLE 5: Rheological test results of the liquid medium.

Type of aggregate	Cement content (kg/m³)	Mass concentration (%)	Plastic viscosity (Pa∗s)	Yield stress (Pa)
Desert sand	310	75	0.19	1.734
Desert sand	310	76	0.23	2.007
Desert sand	310	77	0.28	2.331
Desert sand	310	78	0.35	2.715
Desert sand	310	79	0.44	3.174
Desert sand	280	75	0.18	1.811
Desert sand	280	76	0.21	2.094
Desert sand	280	77	0.26	2.427
Desert sand	280	78	0.32	2.821
Desert sand	280	79	0.40	3.289
Desert sand	260	75	0.17	1.882
Desert sand	260	76	0.20	2.173
Desert sand	260	77	0.24	2.516
Desert sand	260	78	0.30	2.920
Desert sand	260	79	0.38	3.400

TABLE 6: Homogeneity judgment of slurry.

Mass concentration (%)	Cement content (kg/m³)	Measured results	Calculation result
80	310	Segregated	Segregated
81	310	Segregated	Segregated
82	310	Nonsegregation	Nonsegregation
83	310	Nonsegregation	Nonsegregation
84	310	Nonsegregation	Nonsegregation
80	280	Segregated	Segregated
81	280	Segregated	Segregated
82	280	Nonsegregation	Segregated
83	280	Nonsegregation	Nonsegregation
84	280	Nonsegregation	Nonsegregation
80	260	Segregated	Segregated
81	260	Segregated	Segregated
82	260	Nonsegregation	Nonsegregation
83	260	Nonsegregation	Nonsegregation
84	260	Nonsegregation	Nonsegregation

TABLE 7: The scheme of the paste stope fluidity test.

Type of aggregate	Ratio of coarse aggregate to fine aggregate (mass ratio)	Cement content (kg/m³)	Mass concentration (%)	Test content (°)
Waste rock-desert sand	7 : 3	310	82	Slope angle
Waste rock-desert sand	7 : 3	310	83	Slope angle
Waste rock-desert sand	7 : 3	310	84	Slope angle
Waste rock-desert sand	7 : 3	280	82	Slope angle
Waste rock-desert sand	7 : 3	280	83	Slope angle
Waste rock-desert sand	7 : 3	280	84	Slope angle
Waste rock-desert sand	7 : 3	260	82	Slope angle
Waste rock-desert sand	7 : 3	260	83	Slope angle
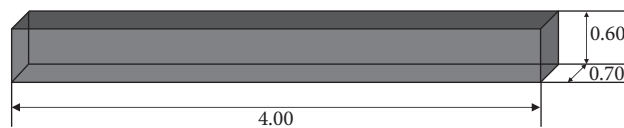
FIGURE 8: Paste fluidity test device.

(a)   (b)

FIGURE 9: Paste fluidity test.

TABLE 8: Results of the paste fluidity test.

Type of aggregate	Ratio of coarse aggregate to fine aggregate (mass ratio)	Cement content (kg/m³)	Mass concentration (%)	Slope angle (°)	Predicted slope angle (°)	Error (%)
Waste rock-desert sand	7 : 3	310	82	1.14	1.27	11.40
Waste rock-desert sand	7 : 3	310	83	1.19	1.25	5.04
Waste rock-desert sand	7 : 3	310	84	1.25	1.29	3.20
Waste rock-desert sand	7 : 3	280	82	1.09	1.21	11.01
Waste rock-desert sand	7 : 3	280	83	1.12	1.23	9.82
Waste rock-desert sand	7 : 3	280	84	1.17	1.26	7.69
Waste rock-desert sand	7 : 3	260	82	1.05	1.12	6.67
Waste rock-desert sand	7 : 3	260	83	1.09	1.16	6.42
Waste rock-desert sand	7 : 3	260	84	1.15	1.20	4.35

The predicted slope angle has the same change trend as the actual measured maximum slope angle, but the predicted value is too large because the predicted slope angle does not take into account the influence of paste kinetic energy on the final flow situation in the process of paste flow. However, the predicted slope angle is effective as a basis for measuring paste flow in stope, which is equivalent to adding a safety factor to paste flow state. If the predicted degree angle of paste cannot meet the flow requirements in stope, its actual flow state will naturally not meet the demand of stope.

Generally speaking, the predicted value is close to the actual value, and the error is between 3% and 11%. Under the same filling material, the higher the concentration, the smaller the error. This is because the higher the concentration, the better the average property of the slurry, which means that the slurry is more stable, and the possibility of its yield stress changing in the flow process is reduced, thus reducing the error. The lower the slurry concentration, the greater the possibility of shear thinning, which leads to the increase of error.
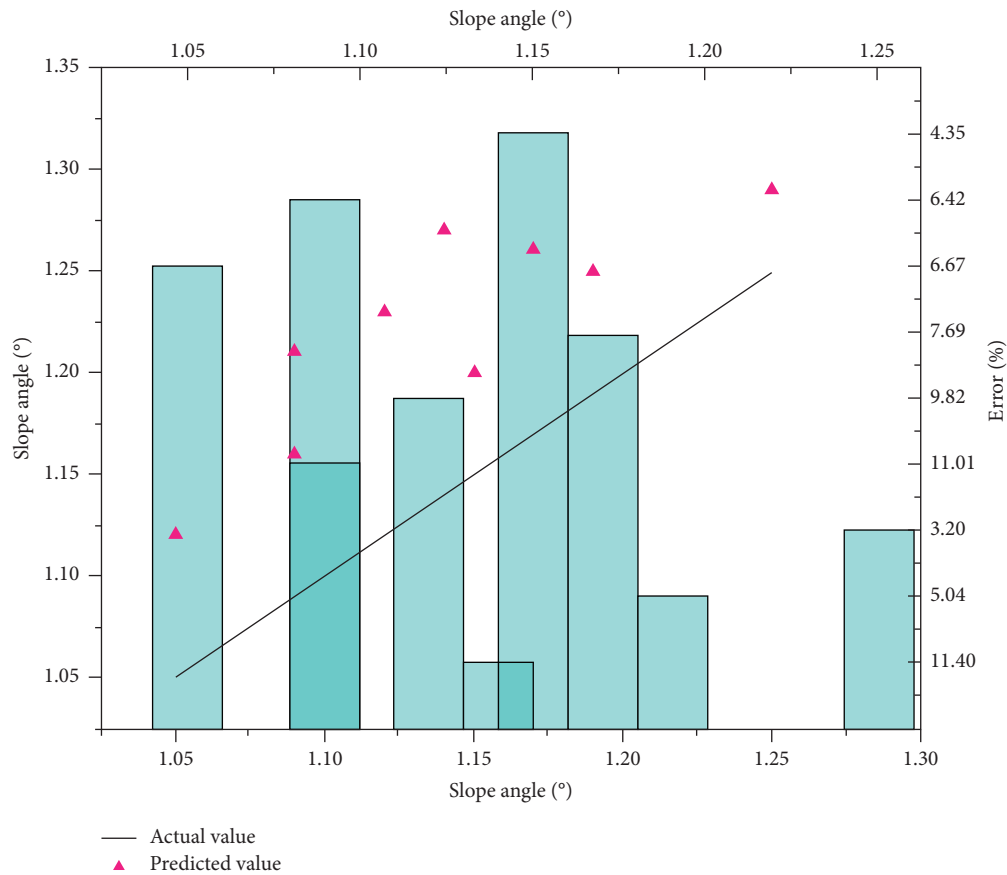
Figure 10: Test result.

4. Conclusion

In this paper, the force analysis of solid materials in the dense medium of paste liquid is carried out, and the judgment model of paste homogeneity is established. The model is verified by experiments. Based on Cauchy stress equation, the prediction model of paste profile angle is established by simplifying the flow behavior of paste in the mining field. The prediction model is verified by a similar simulation test. The results show that there is little difference between the prediction model and the actual results, and the prediction error is less than 11%. The prediction model has a greater safety factor. The above two models provide a theoretical basis for the design and optimization of paste and stope structure.

Data Availability

The data used to support the findings of this study are included within the article.

Conflicts of Interest

The authors declare that they have no conflicts of interest.

References

[1] C. Shi, L. Guo, and X. Chen, "Experimental study on the flow and segregation law of stope filling slurry," *Gold Science and Technology*, vol. 26, no. 4, pp. 520–527, 2018.

[2] H. Lu, P. Liang, S. Nan, A. Song, and H. Yajun, "Research on the flow trajectory of stope filling slurry and analysis of filling body characteristics," *Metal Mine*, vol. 2016, no. 10, pp. 31–34, 2016.

[3] L. Tang and W. Xiao, "Study on the flow law of filling slurry in stope," *Mining Research and Development*, vol. 2005, no. 2, pp. 7–9, 2005.

[4] L. Hui, B. Xu, N Wang, H. Jiao, X. Chen, and L. Yang, "Fluidity test of paste filling slurry in Chambishi copper mine," *Metal Mine*, vol. 2021, no. 6, pp. 127–130, 2021.

[5] Z. Xue, Y. Zhang, D. Gan, X. Zhang, and S. Hu, "Effect of pumping agent content on fluidity and mechanical properties of filling slurry," *Metal Mine*, vol. 2020, no. 11, pp. 25–30, 2020.

[6] L. Tao, B. Xianhao, Z. Yuxi et al., "Thoracic aortic computed tomography angiography in swine: establishment of a baseline for endovascular evaluation of the ascending aorta," *Interactive Cardiovascular and Thoracic Surgery*, vol. 31, no. 2, pp. 248–253, 2020.

[7] L. Li, *Study on Segregation Mechanism and Control Technology of Jinchuan Coarse Aggregate Filling Slurry*, University of Science and Technology Beijing, Beijing, China.

[8] S. Xue, L. Guo, and W khaw boon, "Analysis of the influence of water reducer on the fluidity of filling slurry," *China Mining Industry*, vol. 27, no. S1, pp. 382–386, 2018.

[9] Z. Niu and L. Peng, "Study on fluidity of tailings filling slurry in Shenkeng Iron Mine," *Mining Technology*, vol. 19, no. 3, pp. 32–35, 2019.

[10] H. Gao, Y. L. Huang, Y. Qiu, and O. Pg, "Study on the influence of water reducing agent on the conveying fluidity of

cement filling slurry of phosphorus tailings," *Mining and Metallurgy Engineering*, vol. 38, no. 1, pp. 30–34, 2018.

[11] J. Xie, D. Qiao, R. Han, T. Deng, J. Wang, and T. Zhang, "New definition of ultrafine particles in mine paste and its relationship with rheological properties," *Advances in Civil Engineering*, vol. 2021, pp. 1–11, Article ID 5560899, 2021.

[12] S. Yang and H. Cui, *Non-Newtonian Fluid Mechanics of Petroleum Engineering*, Petroleum Industry Press, Houston, TX, USA, 2013.

[13] Z. Li, "State of workability design technology for fresh concrete in Japan," *Cement and Concrete Research*, vol. 37, no. 9, pp. 1308–1320, 2007.

[14] Y. Guo, H. Chen, and Y. Li, "Experimental study on rheological slump and yield stress of tailings paste," *Mining Machinery*, vol. 2016, no. 4, pp. 81–85, 2016.

[15] Y. Guo and D. Xu, "Test method of rheological parameters of tailings paste," *Journal of Taiyuan university of Science and Technology*, vol. 36, no. 5, pp. 396–401, 2015.

[16] X. Liu, A. Wu, H. Wang, and Y. M. Wang, "Influence mechanism and calculation model of paste rheological parameters," *Journal of Engineering Science*, vol. 39, no. 2, pp. 190–195, 2017.

[17] Q. Zhang, W. Liu, and X. Wang, "Optimized prediction model of rheological parameters of filling paste," *Journal of Central South University*, vol. 2018, no. 1, pp. 124–130, 2018.

Research Article

Stiffness Determination of Backfill-Rock Interface to Numerically Investigate Backfill Stress Distributions in Mine Stopes

Guangsheng Liu [iD],[1,2] **Xiaocong Yang**,[1,2] **and Lijie Guo** [iD][1,2]

[1]*BGRIMM Technology Group, Building 23, Zone 18 of ABP, No. 188, South 4th Ring Road West, Beijing 100160, China*
[2]*National Center for International Research on Green Metal Mining, No. 22, Beixing Road East, Daxing District, Beijing 102628, China*

Correspondence should be addressed to Lijie Guo; guolijie@bgrimm.com

Numerical modeling is an effective and efficient method to investigate the stress distributions of backfill in stopes, which should be well understood in underground mining. Interface elements between backfill and rock in simulated stopes had been proved to be essential components, for which the stiffness parameters need to be assessed and assigned. However, few reports have revealed the effects of interface stiffness on backfill stress distributions, and there is not yet a clear solution to determine the interface stiffness to simulate stresses in backfilled stopes, except an empirical method for simply applying a high value suggested in FLAC manual. In this study, a new solution is first proposed to determine the normal stiffness and shear stiffness of interface elements, respectively, in numerical modeling of backfill stresses. The applicability of the solution has been verified by investigating backfill stress distributions in mine stopes of two widely used mining methods with variable stiffness values. The results show that the newly proposed method leads to totally the same backfill stress distributions with models applying the interface stiffness by the method in FLAC manual based on a "rule-of-thumb" but will save at least 20%–30% calculation time to improve modeling efficiency under the same simulation conditions and will carry much clear physical meanings corresponding to the interaction between backfill and rock walls in mine stopes. In addition, the vertical and horizontal stresses show good agreements with the analytical stresses predicted by the Marston equation under the at-rest state, which validates the reliability of the proposed solution for interface stiffness. Moreover, the plotting methods of stress distributions and the coefficient of lateral earth pressure of backfill in simulated stopes with proposed interface stiffness were discussed to further clarify the reasonable methods to investigate the backfill stresses in mine stopes, especially after considering the effects of the convergence from rock walls, which is a very significant and common phenomenon in practical mining engineering.

1. Introduction

Mining with backfill is used to extract valuable minerals as much and safe as possible by filling underground voids with mine wastes (tailings, waste rocks) and/or binders. The backfill in stopes can provide steady working platform, increase ore recovery, and improve ground conditions in mining processes [1–3]. The consumption of the mine wastes for backfill is also beneficial for the environmental protection of mine communities, which has accelerated the development and utilization of the mining methods world widely [4–6].

Open stoping with subsequent backfill and upward cut and fill are the most widely used mining methods with backfill in metal mines. The first method is designed with large stopes for mass mining, leading to high efficiency and safe working environment. Backfill slurry is poured into the mined voids to build vertical pillars for the following extraction of adjacent stopes. It is the most efficient mining method with backfill, which is usually employed in excavating thick ore bodies (e.g. copper, iron). The second method is commonly used in mining of midthick to narrow and/or irregularly shaped ore bodies, which often host high-value minerals (e.g. gold, silver). Normally, after cutting two layers of an upward height (about 4~6m) in stopes, backfill slurry is poured about half height (2~3 m) of the mined void to construct a platform for next upward cut. By looping

through the process, the stopes are mined out with a high recovery ratio because it can make flexible decisions to excavate one area in every cut layer after identifying the minerals contents within the boundaries of the ore veins.

To successfully implement the desired functions of backfill in different mine stopes, backfill stress distributions should be well understood and evaluated, which will further construct the basis for required strength design and stability analysis of backfill in the above mining methods [7–11]. Arching theory [12, 13] has been used to develop some analytical solutions to calculate backfill stresses in vertical or inclined stopes [14–17]. Some physical tests were carried out to validate the analytical results of backfill stresses [18, 19]. In addition, numerical simulations typically with FLAC [20] and other programs are proved to be effective and efficient to investigate the stresses in backfilled stopes with sensitive analysis of influential factors, including stope dimensions and backfill strength properties. [21–26]. The convergence of rock walls in a stope can have variable effects on backfill stress distributions due to different interaction mechanism of backfill-rock contact surfaces in above two mining processes.

It is known that the backfill cured with tailings and/or binders is a soft material compared with the hard rock in mine stopes. The contacting surfaces should be simulated by interface elements to represent the particular behaviors of sliding, rotating, or separating the backfill from the rock walls. Recently, it had been proved that backfill stress distributions were dominated by physical (e.g. roughness) and mechanical (e.g. cohesion, internal friction angle) parameters of the contacting interfaces between backfill and rock walls rather than by shear strength properties of backfill [27, 28], if the interface shear strength is lower than that of backfills. Direct shear tests further demonstrated that the shear strength parameters along the backfill-rock interfaces are proportional to those of the backfill [29–31]. Therefore, it is very necessary to consider the interface elements between backfill and rock walls when numerically simulating stress distributions of backfill in mine stopes.

Apart from the shear strength parameters of interfaces, the numerical models built with FLAC (or other programs) also require stiffness parameters. In the FLAC manual [20], the elastic stiffness of slip and/or separation interfaces are not considered as important, and it is suggested to use an apparent stiffness recommended for glued interfaces based on a "*rule of thumb*." The physical meanings of the suggested empirical equation are unclear neither. A method of stiffness determination for backfill-rock interface with clear physical meanings is desired, while there are very few published reports in current literatures.

Kong et al. [32] analyzed interface stiffness between mudstone and concrete piles by the back-analyses method based on field measured shear stresses and displacements of the piles. A sufficiently high value for interface stiffness was suggested to match the field dilation effect of installed piles into the mudstone. A similar approach with a high value for interface stiffness had been adopted by Pirapakaran [33] to numerically analyze vertical stress and displacement of filling materials. In the study by Sivakugan et al. [34], interface

stiffness were determined by following the recommended empirical equations from the FLAC manual to compare backfill stresses in different positions of stopes. In other numerical simulations with self-developed programs [22, 35], the determination of interface stiffness was not presented in detail. These works indicate that the stiffness along the contact interfaces between backfill and wall is significant in numerical models but all using very large values based on empirical methods. A definition of interface stiffness with clear physical meanings is needed to be proposed.

In this study, the empirical solution suggested in the FLAC manual to determine the apparent stiffness of interface elements will be firstly discussed. And then, new expressions with practical physical meanings for normal and shear stiffness of interface elements are proposed. To validate the reliability of the proposed method for interface stiffness, the vertical and horizontal stresses of the backfill in mine stopes of the two mining methods are simulated by FLAC3D after applying different interface stiffness values. In addition, the simulated backfill stresses with the proposed interface stiffness will then be verified against the analytical stresses with the Marston equation [12]. Furthermore, different plotting methods for backfill stresses and the coefficient of lateral earth pressure in simulated backfilled stopes of two mining methods with different interface stiffness values will be further discussed. The advantages of newly proposed solutions for interface stiffness in numerical modeling will be summarized at the end of the article.

2. Interface Stiffness in Numerical Models

2.1. Suggested Empirical Method in FLAC. When interface elements are applied in numerical models with FLAC program [20], the normal stiffness (k_n) and shear stiffness (k_s) have to be assigned based on Mohr–Coulomb constitutive model, as shown in Figure 1.

Three types of interface elements are defined in the FLAC manual [20], including glued interface (artificial component to connect subgrids together), slip and/or separation interface (real interface that is stiff and can slip and/or open under anticipated loading), and interface containing fill material (real interface that is soft to affect the system, such as a geological fault or joint with soft clay).

Without any doubt, the second type should be applied to the contacting interfaces between backfill and rock walls in mine stopes. For such type of interfaces, the FLAC manual [20] states that the strength properties of the interfaces are important, but the stiffness properties are not important. It further suggests using the stiffness solution recommended for glued interfaces based on a "rule of thumb,":

$$k_n = k_s = 10 \times k_{\text{neib. max}} = 10 \times \max \frac{(K + 4G/3)}{\Delta z_{\min}}, \quad (1)$$

where $k_{\text{neib.max}}$ is the equivalent stiffness of the stiffest neighboring zone, K (Pa) is the bulk modulus of the backfill, G (Pa) is the shear modulus of the backfill, and $\Delta z_{\min}$ (m) is the size of the smallest backfill element at the contact zones of the interface.
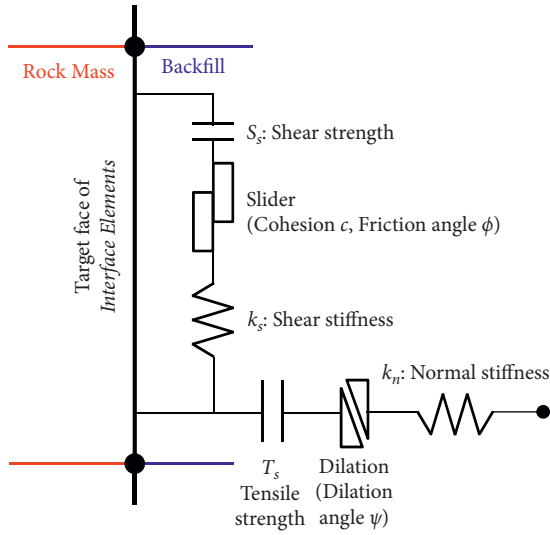
FIGURE 1: Schematic diagram for interface elements between backfill and rock in stopes.

Clearly, equation (1) shows that the normal (k_n) and shear (k_s) stiffness have a unit of "Pa/m." However, it is unclear whether the suggested utilization of an extremely large value for interface stiffness is just to ensure stable numerical results, and whether it can reflect the physical response of backfill-rock interaction in stopes or not. Besides, there is still no explanation why the manual argues that the stiffness properties of the interface elements are not important. So far there have been no reasonable explanations for these doubts.

To better understand this issue, one considers the classical definition of the stiffness k in the field of material mechanics. In the SI system (International System of Units) [36], stiffness is the resistance of an elastic body to deflection or deformation by an applied force, which can be detailed expressed as a ratio between the applied force and the corresponding displacement. Thus, the stiffness k can be expressed as follows:

$$k = \frac{\Delta F}{\Delta L} = \frac{\Delta F}{A} \times \frac{A}{L} \times \frac{L}{\Delta L} = \Delta\sigma \times \frac{A}{L} \times \frac{1}{\varepsilon} = \frac{\Delta\sigma}{\varepsilon} \times \frac{A}{L}, \quad (2)$$

where ΔF (N) is the variation of an applied force on an area A (m^2), which leads to a length variation ΔL (m) for the material, $\Delta\sigma$ (Pa) is the variation of induced stress, and ε is elastic strain (relative deformation, dimensionless) of the material with an original length L (m).

From equation (2), it is found that the stiffness k should have a unit of "N/m" or "Pa·m," which is different from the unit of "Pa/m" of the normal (k_n) and shear (k_s) stiffness in manual of FLAC [20]. The updated solutions of apparent stiffness should be consistent with methods in the manual about the stiffness unit to meet the requirements in following numerical simulations by the FLAC program.

2.2. Newly Proposed Solution. Based on the comparison of definitions for interface stiffness, one can find the physical meanings of the normal stiffness k_n characterizing the ratio

of normal stress to displacement perpendicular to the interface elements and the shear stiffness k_s characterizing the ratio of shear stress to displacement parallel to the interface elements, near the contacting surface between the backfill and rock walls in mine stopes, as shown in equations (3) and (4).

$$k_n = \frac{\Delta\sigma}{\Delta L} = \frac{\Delta\sigma}{L} \times \frac{L}{\Delta L} = \frac{\Delta\sigma}{L} \times \frac{1}{\varepsilon} = \frac{\Delta\sigma}{\varepsilon} \times \frac{1}{L} = \frac{K}{L}, \quad (3)$$

$$k_s = \frac{\Delta\tau}{\Delta L} = \frac{\Delta\tau}{L} \times \frac{L}{\Delta L} = \frac{\Delta\tau}{L} \times \frac{1}{\varepsilon} = \frac{\Delta\tau}{\varepsilon} \times \frac{1}{L} = \frac{G}{L}. \quad (4)$$

Then, the normal stiffness k_n and the shear stiffness k_s of the stiffest neighboring zone along backfill-rock interface can be approximately defined as equations (5) and (6):

$$k_n = \frac{K}{\Delta z_{\min}}, \quad (5)$$

$$k_s = \frac{G}{\Delta z_{\min}}, \quad (6)$$

where K (Pa) is the bulk modulus of the backfill, G (Pa) is the shear modulus of the backfill, and $\Delta z_{\min}$ (m) is the size of the smallest backfill element at the contact of the interface.

Equations (5) and (6) construct the newly proposed expression for determining the apparent normal and shear stiffness of the interface elements between backfill and rock walls in simulated backfilled stopes.

The reliability of the proposed solutions and the induced influences on backfill stress distributions will then be compared with the cases using different interface stiffness values including those suggested parameters of FLAC manual [20] from the viewpoints of stably computational accuracy and efficiency. The simulated stresses will also be validated with the analytical results by the Marston equation [12].

3. Numerical Simulations and Results Analysis

3.1. Numerical Models and Cases. To validate the proposed solution for apparent interface stiffness and investigate their influences on backfill stress distributions in stopes of two most widely used mining methods, numerical models were built with FLAC3D, which is a finite difference program using an explicit Lagrangian calculation scheme and a mixed discretization zoning technique. It is a well-adapted tool for handling geomechanical problems, including excavation and backfilling of mine stopes [3, 8, 9, 15, 19, 25–28].

Figure 2(a) shows a vertical backfilled stope with a width of B. The mined void of the stope is filled with two programs to a height of H to simulate the open stoping with subsequent backfill mining and the upward cut and fill mining methods.

For the first filling program, the whole height H of the stope is mined out with one excavating step, which simulates mass mining of open stoping with deep blasting holes. The energy release and closure deformation of surrounding rock walls caused by excavation are assumed to be fully completed before the backfilling, as it practically takes months to muck
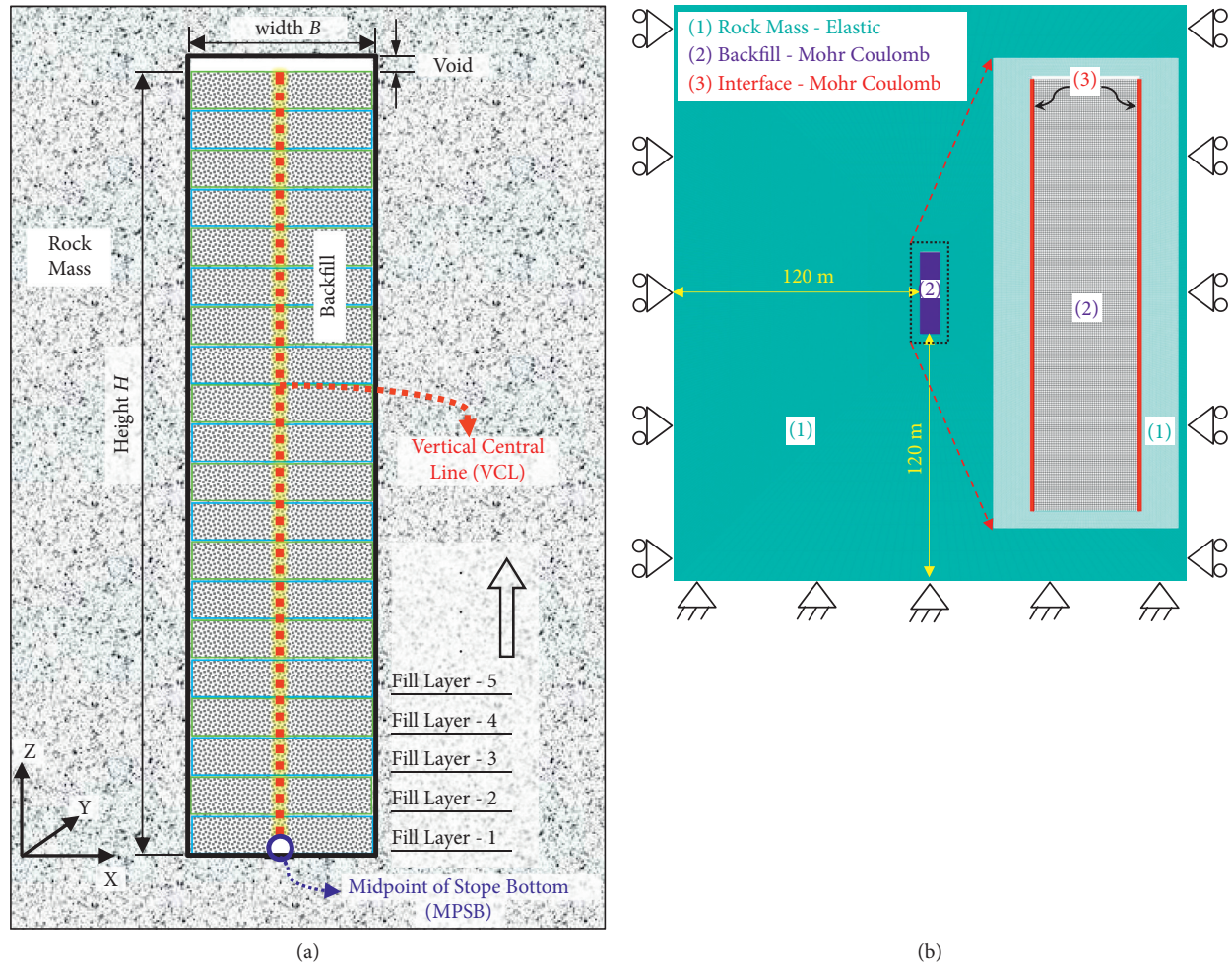
Figure 2: Typical backfilled stope. (a) Physical model. (b) Numerical model built in FLAC3D.

out the blasted ores and then return to fill the mined void. In this program, an equivalent multistep loading for the whole height of the backfill was simulated with 10 layers [28, 37] to obtain a stably static numerical solution based on a series of sensitivity analyses (not shown here) about the effects of filling layers on simulated backfill stresses, which revealed that the backfill stresses became numerically stable and insensitive to the further increase the filling layers after reaching 10. Besides, a space of 0.5 m in height was left at the top part of the backfilled stope, to simulate the practical difficulty of roof-contact filling due to drainage and settling of backfill slurry, or in some occasions, the space is designedly left to be a platform for continuous mining of upper stope.

For the second filling program, the ore rocks in the stope are excavated from bottom to top and layer by layer following the practical cut and fill process. In detail, after cutting the first and second layers (2 m per layer in height) starting from stope bottom, a backfill of 2 m in height will then be loaded to the first layer void. Then the third layer will be excavated on the backfill platform of the first layer. By looping through the process, a stope of 40 m in height will be mined out with 20 layers' cutting and filling respectively,

which also meets the requirements of using more than 10 filling layers for numerically stable results. The simulations of every cutting and filling were solved to reach the same equilibrium state in FLAC. In this program, the convergence of rock walls induced by one layer cut might be applied to the previous layers of backfill. The stress distributions of backfill will then be affected by its self-weight and the closing pressure of rock walls which is transferred from the interfaces between backfill and rock mass.

Figure 2(b) shows a typical numerical model constructed with FLAC3D corresponding to the physical model. The bottom boundary is fixed in all directions, and the two lateral boundaries are only fixed in horizontal direction. All elements of the model are fixed in Y-direction (perpendicular to paper plane) to simulate plane strain conditions. After a series of domain and mesh sensitivity analyses, the external boundaries are determined at 120 m from stope boundaries, and the optimal mesh size for the backfill is set to 0.2 m.

The rock mass is considered homogeneous, isotropic, and linearly elastic, characterized by $\gamma_r = 27$ kN/m^3 (unit weight), $E_r = 30$ GPa (Young's modulus) and $\mu_r = 0.25$ (Poisson's ratio). The values were selected based on typical values given in the literature [38, 39]. The backfill is modeled

as an elastoplastic material obeying the Mohr–Coulomb criterion. It is characterized by $\gamma = 18\,\text{kN/m}^3$ (unit weight), $E = 300\,\text{MPa}$ (Young's modulus), $\mu = 0.3$ (Poisson's ratio), $c = 0\,\text{kPa}$ (cohesion), $\phi = 35°$ (internal friction angle), and $\psi = 0°$ (dilation angle). The stope width B is fixed at 10m, and the final backfill height H is fixed at 40m. The values were selected based on typical values given in the literature [1, 18, 19, 40–43] and partly on authors' experience gained from mining projects with backfill.

The mechanical properties of the interfaces between backfill and rock walls are characterized by the cohesion $c_i = 0\,\text{kPa}$ and internal frictional angle $\delta = 0.6\phi = 21°$, which are based on the published shear tests of interfaces [29–31]. The normal (k_n) stiffness and shear (k_s) stiffness of interfaces are also key inputs for the numerical models.

Table 1 shows the fixed parameters of rock mass, backfill, and interfaces in all models. It needs to be emphasized that the effects of backfill compaction and density-dependent stiffness of the backfill along the height of mine stopes were not considered in the numerical models here. The physical and mechanical parameters of the backfill were uniformly distributed and kept as constant in the simulated stopes shown in Table 1.

Table 2 presents numerical programs to simulate and investigate the backfill stresses varying with key influential factors, which are emphasized on the normal (k_n) and shear (k_s) stiffness of interface elements. The backfill stresses in stopes of two typical mining methods and the stress plotting methods were also critical factors that should be discussed. The influence of a given parameter on the backfill stress distributions in mine stopes is analyzed by varying its value and keeping other parameters unchanged. Besides, what should be mentioned here is that the normal and shear stiffness for the interfaces between backfill and rock walls are kept unchangeable along the height of the backfilled stopes, which was inherited from the conventional hypothesis used in the FLAC manual [20] and relevant published articles [21, 28, 32–34] without considering the cumulative effects of interface variability with filling depth in mine stopes.

Based on the above numerical models and backfill properties, one can have backfill bulk modulus $K = 250\,\text{MPa}$ and shear modulus $G = 115\,\text{MPa}$ calculated with backfill Young's modulus $E = 300\,\text{MPa}$ and Poisson's ratio $\mu = 0.3$ and the smallest backfill element size $\Delta z_{\min} = 0.2\,\text{m}$ at the contacting surface to the interfaces.

With the empirical solution given in FLAC manual [20], the normal stiffness (k_n) and shear stiffness (k_s) of the interfaces are $k_n = k_s = 20.2\,\text{GPa/m} = 2.02 \times 10^{10}\,\text{Pa/m}$ after applying (1).

With the newly proposed solution here, the normal stiffness (k_n) and shear stiffness (k_s) of the interfaces are $k_n = 1.25\,\text{GPa/m} = 1.25 \times 10^9\,\text{Pa/m}$, $k_s = 0.58\,\text{GPa/m} = 5.8 \times 10^8\,\text{Pa/m}$ after applying equations (5) and (6), respectively.

3.2. Effect of Interface Stiffness on Backfill Stress in Open Stoping with Subsequent Backfill.
Figure 3 illustrates vertical (σ_v) and horizontal (σ_h) stresses along vertical central line (VCL) with different normal stiffness k_n and fixed shear

stiffness k_s of the interfaces in the open stoping with subsequent backfill mining method. The numerical results presented in Figure 3 shows that the normal stiffness (k_n) of the interface elements can significantly affect the backfill stresses along the VCL of the stope.

The horizontal stress increases slightly with the increase in the interface normal stiffness, but the vertical stress decreases obviously when the interface normal stiffness increases from 2 to 200 MPa/m. When the normal stiffness is above 200 MPa/m, the vertical stress becomes almost insensitive to its further increase. What should be emphasized is that when $k_n = 2.02 \times 10^{10}\,\text{Pa/m}$ is set for interface normal stiffness after applying equation (1) of the empirical solution suggested in FLAC manual [20], the vertical and horizontal stresses follow the same distributions with the case using the interface normal stiffness of the newly proposed method here ($k_n = 1.25 \times 10^9\,\text{Pa/m}$, $k_s = 5.8 \times 10^8\,\text{Pa/m}$).

However, it is not computationally efficient to increase interface stiffness to higher values because the running time to reach the same equilibrium state will become undesirably higher under the same calculation conditions. In the numerical model with only one backfilled stope shown in Figure 2, the required running time to complete the calculation with the interface stiffness by the newly proposed method can be statistically 20%–30% less than the simulating backfill stress using interface stiffness of the solution suggested in FLAC manual. This computationally efficient effect will be exponentially highlighted if a lot of backfilled stopes are simulated in a model with interface elements between backfill and rock walls.

Therefore, it can be preliminarily concluded that the newly proposed equations to determine the interface stiffness carry more advantages in calculating efficiency of numerical simulation to obtain the same backfill stresses than the empirical solution suggested in FLAC manual; meanwhile, there have been clearer physical meanings corresponding to the interaction between backfill and rock walls in mine stopes.

Figure 4 illustrates vertical (σ_v) and horizontal (σ_h) stresses along vertical central line (VCL) of stopes with different shear stiffness k_s and fixed normal stiffness k_n of interfaces in open stoping with subsequent mining method.

Figure 4 shows that the vertical and horizontal stresses in the backfilled stopes are less sensitive to the variation of shear stiffness k_s comparing with the normal stiffness k_n shown in Figure 3. However, it presents the vertical stress decreases with the increase in shear stiffness of interfaces from the model of $k_s = 2.02 \times 10^6\,\text{Pa/m}$ to model of $k_s = 2.02 \times 10^8\,\text{Pa/m}$, whereas the horizontal stress only presents a slight decrease. Besides, the same distributions about the vertical and horizontal stresses are shown for the models after applying the shear stiffness of $k_s = 2.02 \times 10^{10}\,\text{Pa/m}$ by equation (1) suggested by FLAC manual and the models applying the interface stiffness by the newly proposed method of equations (5) and (6).

The variations of the vertical and horizontal stresses in backfilled stopes calculated with different normal and shear stiffness values shown in Figures 3 and 4 demonstrate the good reliability to determine reasonable interface stiffness

TABLE 1: A summarize of fixed parameters in all numerical models.

Items	Unit weight (kN/m^3)	Young's modulus (Pa)	Poisson's ratio	Cohesion (Pa)	Internal friction angle (°)	Dilation angle (°)
Rock mass	27	3×10^{10}	0.25	—	—	—
Backfill	18	3×10^{8}	0.3	0	35	0
Interface	—	—	—	0	21	—

TABLE 2: Numerical simulation programs for stresses analyses in backfilled stopes.

Cases	Mining methods	Interface stiffness		Stress plotting methods	Filling layers
		Normal stiffness k_n (Pa/m)	Shear stiffness k_s (Pa/m)		
Case 1-0	Open stoping with subsequent backfill	2.02×10^{10}	2.02×10^{10}	*Method1*: Plot stresses along vertical central line (VCL) after filling whole stope height	10
Case 1-1		*VAR*	2.02×10^{10}		
Case 1-2		2.02×10^{10}	VAR		
Case 1-3 (*Proposed*)		1.25×10^{9}	5.8×10^{8}		
Case 2-0	Upward cut and fill mining	2.02×10^{10}	2.02×10^{10}	*Method2*: Monitor stresses at midpoint of stope bottom (MPSB) after filling each layer	20
Case 2-1		*VAR*	2.02×10^{10}		
Case 2-2		2.02×10^{10}	VAR		
Case 2-3 (*Proposed*)		1.25×10^{9}	5.8×10^{8}		

Note. VAR means variable values.
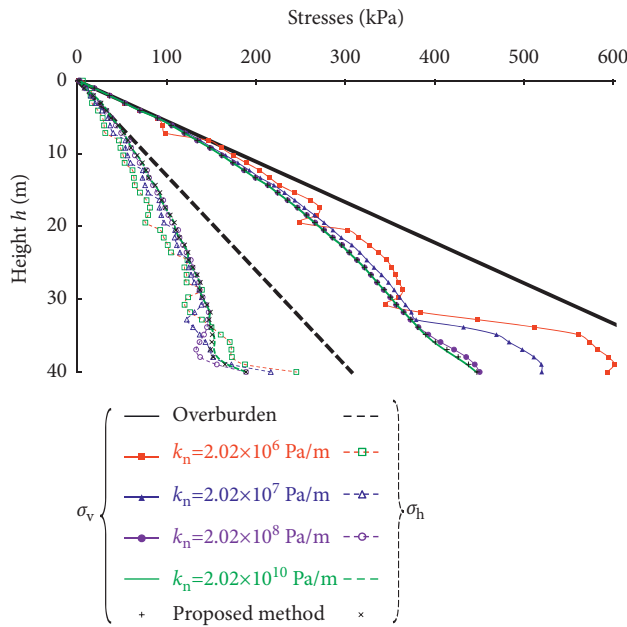
FIGURE 3: Vertical (σ_v) and horizontal (σ_h) stresses plotted along VCL of stopes with different normal stiffness (k)$_n$ of interfaces in open stoping with subsequent backfill mining.

FIGURE 4: Vertical (σ_v) and horizontal (σ_h) stresses plotted along VCL of stopes with different shear stiffness (k)$_s$ of interfaces in open stoping with subsequent backfill mining.

parameters to obtain numerically stable stresses of backfilled stopes in open stoping with subsequent backfill mining method.

3.3. Effect of Interface Stiffness on Backfill Stress in Upward Cut and Fill. To further investigate the effects of varying interface stiffness values on numerical stress distributions of
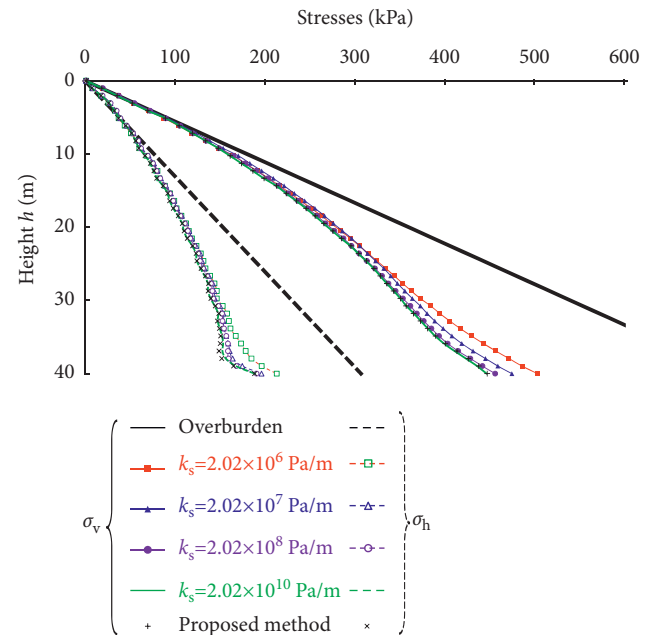
the backfill in mines stopes and to comprehensively validate the applicability of the newly proposed solution for interface stiffness determination, the simulated vertical (σ_v) and horizontal (σ_h) stresses plotted along vertical central line (VCL) of backfilled stopes with different normal (k_n) and shear (k_s) stiffness of interfaces in the upward cut and fill mining method are shown in Figure 5 and 6.
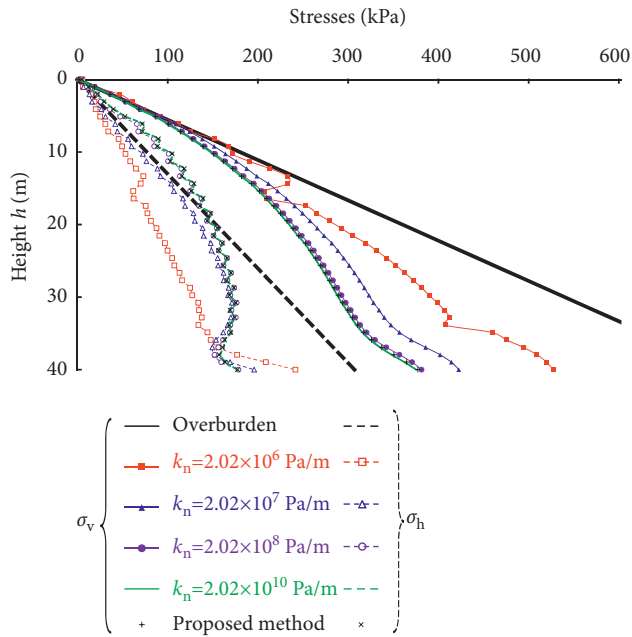
FIGURE 5: Vertical (σ_v) and horizontal (σ_h) stresses plotted along VCL of stopes with different normal stiffness $(k)_n$ of interfaces in upward cut and fill mining.
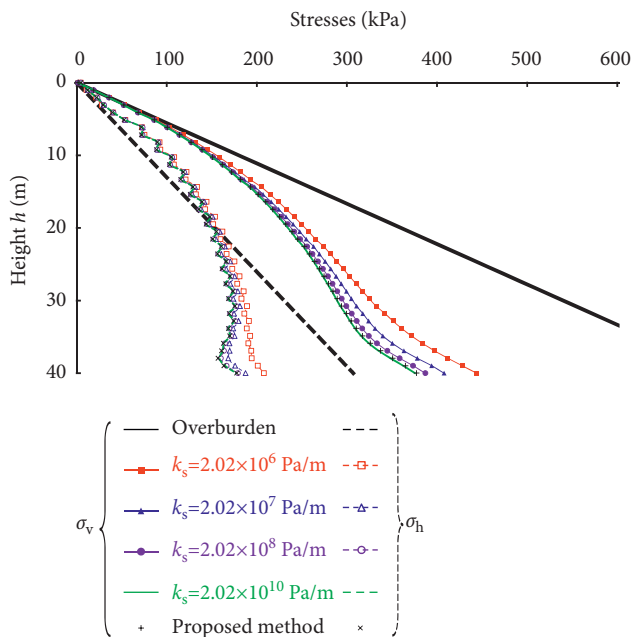
FIGURE 6: Vertical (σ_v) and horizontal (σ_h) stresses plotted along VCL of stopes with different shear stiffness $(k)_s$ of interfaces in upward cut and fill mining.

Figure 5 shows that the vertical stress reduces significantly with the normal stiffness of interface increasing from $k_n = 2.02 \times 10^6$ Pa/m to $k_n = 2.02 \times 10^8$ Pa/m, whereas the horizontal stress has an obvious trend of enlargement. However, the vertical and horizontal stresses become almost insensitive to the variation of the normal stiffness k_n of interface when its value is above 2.02×10^8 Pa/m, even though the stresses in the model of

$k_n = 2.02 \times 10^8$ Pa/m still have a bit difference with the stresses distributions in the model of $k_n = 2.02 \times 10^{10}$ Pa/m. It is worth mentioned that both vertical and horizontal stresses after applying interface stiffness by the newly proposed method ($k_n = 1.25 \times 10^9$ Pa/m, $k_s = 5.8 \times 10^8$ Pa/m) have the same numerically stable stress distributions with the model of $k_n = 2.02 \times 10^{10}$ Pa/m by the suggested empirical method in FLAC manual, but the newly proposed method took much less computation time (i.e., higher efficiency for simulation).

Figure 6 illustrates the similar trends of vertical and horizontal stresses with the variations of shear stiffness k_s compared with Figure 4. In details, the vertical stress along vertical central line (VCL) of backfilled stopes decreases gradually with the increase in the shear stiffness of interface from $k_s = 2.02 \times 10^6$ Pa/m to $k_s = 2.02 \times 10^{10}$ Pa/m, whereas the horizontal stress reduces slightly under these variations of shear stiffness. In addition, the stresses in the backfill model with interface shear stiffness calculated by suggested empirical method of FLAC manual show again the same and stable distributions with the backfill model of applying interface stiffness determined by the newly proposed method.

The vertical and horizontal stresses varied with different normal and shear stiffness values shown in Figures 5 and 6 demonstrate again the good reliability to determine reasonable interface stiffness parameters to achieve numerically stable results on stresses of backfilled stopes in upward cut and fill mining method. The numerical modeling about the stresses in backfilled stopes considering interfaces with stiffness values determined by the newly proposed solution has better calculating efficiency and clearer physical meanings to simulate the interaction between backfill and rock walls, compared with the numerical models of using interface stiffness by empirical solution suggested in the FLAC manual.

3.4. Comparison of Simulated Stresses with Analytical Results of the Marston Model.

The sensitive analyses about the simulated stress distributions in backfilled stopes with variable stiffness values of interface elements between backfill and rock walls shown in Figures 3–6 have demonstrated the strong reliability and stable accuracy of the newly proposed methods to determine the interface stiffness, together with much better calculating efficiency than the empirical solution suggested in FLAC manual. To further validate the newly proposed solution, the numerical results about backfill stresses in mine stopes of two typical mining methods will be compared with the analytical results obtained by the Marston solution [12, 13], which is a classical theory to evaluate the backfill stresses under arching effect in mine stopes [14–17].

Figure 7 presents the numerically simulated vertical (σ_v) and horizontal (σ_h) stresses of the backfill along the vertical central line (VCL) of stopes in the open stoping with subsequent backfill mining method and the upward cut and fill mining method, respectively. In these numerical models, the normal (k_n) and shear (k_s) stiffness of interfaces were set up after applying the proposed solution (equations (5) and
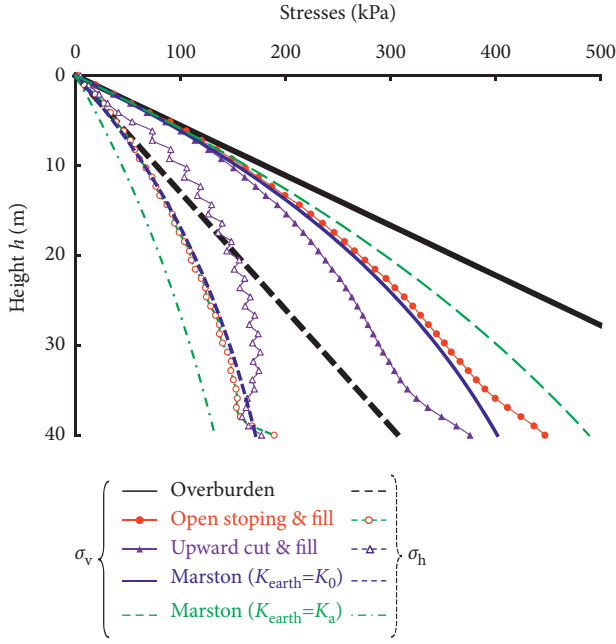
FIGURE 7: Comparisons of vertical (σ_v) and horizontal (σ_h) stresses plotted along VCL of simulated stopes in two mining methods with analytical results of the Marston equation.

(6)), and the other parameters were referred to the values shown in Table 1.

The analytical results with the Marston theory [12, 13] by applying equations (7) and (8) to calculate the vertical and horizontal stresses are also plotted in Figure 7 for verifying the simulated stresses. In addition, the stress distributions based on the overburden solution are added in Figure 7 for comparison which has no consideration of arching effect for the backfill in stopes. The overburden backfill stresses can be assessed by $\sigma_v = \gamma \times h$, $\sigma_h = K_0 \times \sigma_v$, where h (m) is the depth from the top surface of the backfill, $K_0 = 1 - \sin\phi$ is the at-rest coefficient of lateral earth pressure, and ϕ is the internal friction angle of backfill.

$$\sigma_v = \frac{\gamma B}{K_{earth}} \times \frac{1 - \exp\left(-2K_{earth}h/B \tan\delta\right)}{2\tan\delta}, \quad (7)$$

$$\sigma_h = K_{earth} \times \sigma_v, \quad (8)$$

where γ ($= 18 \text{ kN/m}^3$) is unit weight of backfill, $B = (10 \text{ m})$ is the width of backfilled stope, δ ($= 0.6 \times \phi = 21°$) is internal friction angle along interfaces between backfill and rock walls in stopes, K_{earth} is coefficient of lateral earth pressure of backfill that can be set to active state $K_{earth} = K_a = (1 - \sin\phi)/(1 + \sin\phi)$ or at-rest state $K_{earth} = K_0 = 1 - \sin\phi$.

It can be seen from Figure 7 that for the backfilled stopes in the open stoping with subsequent backfill mining method (red dots), the vertical and horizontal stresses along the vertical central line (VCL) of the backfill are much lower than the overburden stresses (black lines), which indicates the occurrence of arching effect, and these stress distributions show good agreements with the analytical stresses predicted by the Marston solution (blue lines) under the at-

rest state ($K_{earth} = K_0$). Based on the comparisons, it validates again the good reliability of the newly proposed methods to determine the interface stiffness values for numerically simulating backfill stresses in practical mining methods.

In addition, Figure 7 illustrates that for the backfilled stopes in the upward cut and fill mining method (purple triangles), the vertical stress is much lower, and the horizontal stress is much larger than the analytical stresses by the Marston solution (equations (7) and (8)). Furthermore, the simulated horizontal stress at the height of $h = 0–20$ m of the backfilled stope in the upward cut and fill mining method is even much larger than the overburden stress. These differences mean a much stronger arching effect for the backfill stresses in the stopes of the upward cut and fill mining method. It can be preliminarily speculated that this phenomenon is mainly caused by the lateral convergent displacements of rock walls acting on the previous backfill layers during the later cutting and filling process. To further explain it, Figure 8 illustrates the horizontal convergent displacements along the rock walls in the stopes of the two mining methods.

From Figure 8, it can be seen that the convergent displacements along the right rock wall of the stope (Figure 2, the same results can be obtained to plot along the left rock wall) in open stoping with subsequent backfill mining method are only slightly larger than zero (0–0.1 mm), which indicates a positive displacement going forward along the X-axis. This is because the whole height of the stope was excavated at once step in the mining method, and the closure deformation of rock walls had finished before backfilling the stope void. The self-weight of the subsequent backfill will lead to a pushing pressure on the rock walls to make a slight increment of rock walls' extending displacement. The highest positive displacement is closing to the bottom part (height 30 m) of the stope and then gradually decreasing to zero at the top and bottom surfaces of the backfill.

However, Figure 8 shows that the convergent displacements along the right rock wall of the stope in the upward cut and fill mining method are much lower than zero ($-0.4 \sim -1.3$ mm), showing an approximately semicircular distribution with a diameter of stope height H (highest closure deformation near the midheight of stope and gradually decreasing towards the top and bottom surfaces). What is more interesting is that the convergent displacements are all negative values, indicating obvious convergence of rock walls leading to closure pressure on every backfill layer. This gives a good explanation of the much stronger arching effect (shown in Figure 7) in the backfilled stope of the upward cut and fill mining method and the nonagreement with the analytical stresses based on the Marston method.

Combined with the results in Figures 7 and 8, it not only further verifies the reliability of the newly proposed methods for interface stiffness determination to numerically simulate backfill stresses in mine stopes but also reveals that the backfill stress distributions are affected obviously by different levels of rock walls convergence based on the excavating and filling processes in different mining methods, which forms a practical factor to modify the arching theory originally from the field of soil mechanics [12, 13].
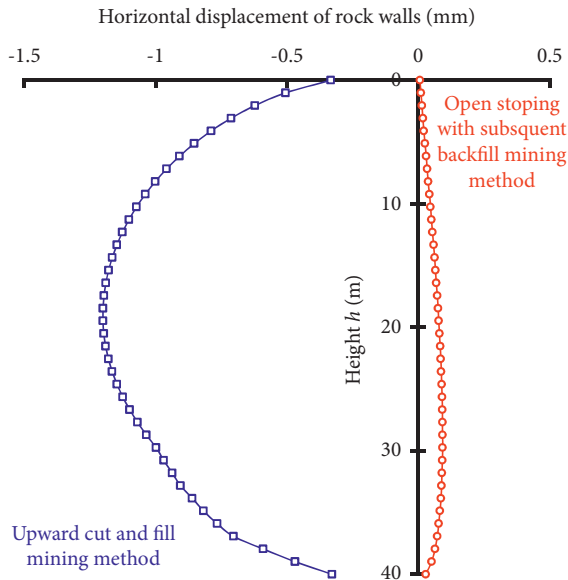
FIGURE 8: Convergent displacements along stope rock walls in two mining methods.

4. Discussions

4.1. Plotting and Monitoring Methods for Backfill Stresses. A good understanding of the stress distributions in mine stopes is essential for underground mining design with backfill, but it is more important to reasonably evaluate the vertical and/or horizontal stresses in backfill to meet their practical usages in specific engineering conditions. For numerical modeling of stress distributions in backfilled stopes, there are currently two typical methods to plot and/or monitor the backfill stresses (see details in Figure 2(a) and Table 2). The first method is to plot stresses along vertical central line (VCL) after filling the whole height of excavated stope void, which mainly illustrates the stress variations along with backfill height. Also, the second method is to monitor stresses at the midpoint of stope bottom (MPSB) after filling each layer in stopes, which usually presents the stress or pressure at stope bottom varying with the increasing process of backfill height.

Similar discussions on the plotting and monitoring methods were reported by Sivakugan et al. [34] but only for the vertical stress analysis without considering horizontal stress. Based on its final conclusions [34], the second method was preferable to monitor the vertical loadings on the preburied conduits at the bottom of trenches with subsequent filling by granular materials. The preferable second method of monitoring the vertical stress in numerical models was also employed to compare with the laboratory physical tests of the vertical stress in dry granular fills [18, 19, 44], to investigate arching effects of sands behind retaining walls, fills in trenches, and hydraulic backfills in stopes.

However, in the practical engineering conditions of underground mining with backfill, not only the vertical stress but also the horizontal stress of backfill should be well evaluated. In most conditions, the horizontal stress

distributions are relatively more important. For example, in order to assess the lateral pressure on adjacent structures, including the cemented backfill in adjacent primary stopes [3] or the man-made barricades in access drifts throughout the backfilling process [45], it is the horizontal stress that should be paid more attention, which will be transferred to horizontal pressure to affect the stability of these structures.

To illustrate the differences of the two methods to plot and monitor stresses, Figure 9 shows the contrastive results about the vertical and horizontal stress distributions plotted along vertical central line (VCL) and monitored at the idpoint of stope bottom (MPSB) with different normal stiffness k_n of interfaces between backfill and rock walls in open stoping with subsequent backfill mining method.

It can be seen from Figure 9 that there are obvious differences about the backfill stress distributions between plotted along VCL and monitored at MPSB under the same numerical models. What is more interesting is that only at the top and the bottom surfaces of the backfilled stopes are the stress values that are same for the two plotting methods. Both the vertical stress and the horizontal stress plotted along VCL are lower than the stresses monitored at MPSB in the same backfilled stope condition. In addition, a peculiar phenomenon can be seen from Figure 9 (also in Figure 3–6) that there are some sudden increases near the stope bottom about the horizontal and vertical stresses of the backfill plotted along VCL. This is mainly caused by the restricted movement of the backfill layers near the stope bottom by the base rock to limit the mobilization and arching development of the backfill layers. However, this phenomenon has not happened for the monitored stresses at MPSB shown in Figure 9 because these stresses were collected at the fixed midpoint of the backfill bottom surface as shown in Figure 2a, which cannot illustrate the stress distributions along the height of the backfilled stope.

Besides, with the above two different stress plotting methods, both the vertical and horizontal stress distributions are not numerically stable at the interface normal stiffness of $k_n = 2.02 \times 10^6$ Pa/m, but the numerical results will no longer change when the normal stiffness k_n reaches the values determined by the newly proposed method (equations (5) and (6)). It can be further explained that the stresses will not change with the variations of interface shear stiffness k_s any more (not shown here) after using values by the proposed solution under the two plotting methods. These comparisons further demonstrate the good reliability and adaptability of the proposed solution to determine the interface stiffness in different stress plotting methods within different mining processes with backfill.

However, in order to further reveal the different influences of the two plotting methods about backfill stresses to clarify their applicable conditions, the vertical (σ_v) and horizontal (σ_h) stresses monitored at MPSB of simulated stopes in the open stoping with subsequent backfill mining method and the upward cut and fill mining method have been shown in Figure 10. The analytical stresses with the Marston theory [12, 13] by applying equation (7) and (8) have also added in Figure 10 for comparison.
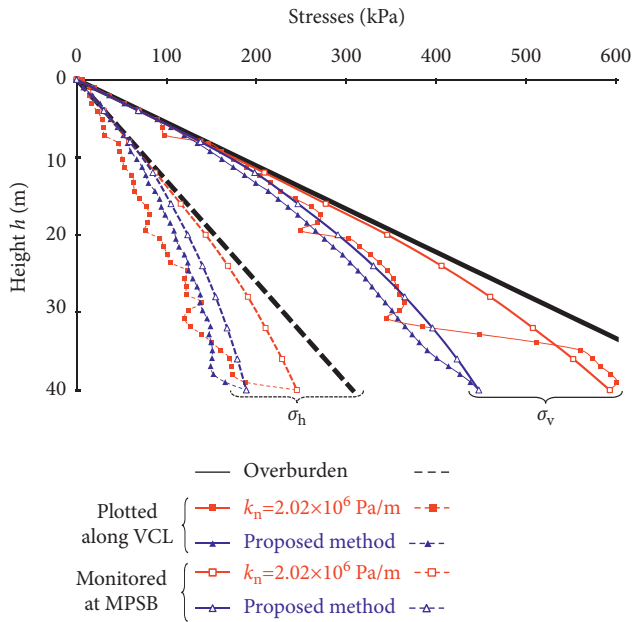
FIGURE 9: Vertical (σ_v) and horizontal (σ_h) stresses plotted along VCL and monitored at MPSB with different normal stiffness (k)$_n$ of interfaces.
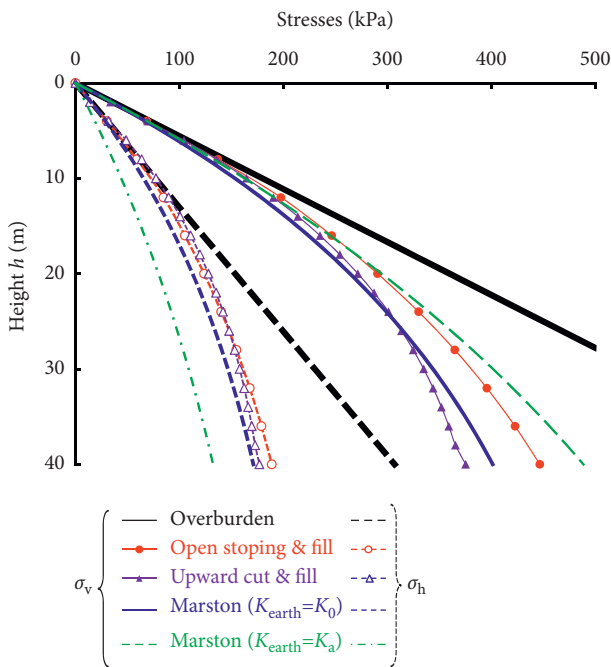
FIGURE 10: Comparison of vertical (σ_v) and horizontal (σ_h) stresses monitored at MPSB of simulated stopes in two mining methods with analytical results of the Marston equation.

It can be seen from Figure 10, when using the stress monitoring method at MPSB, the horizontal stresses of the backfill in stopes of open stoping with subsequent backfill mining and upward cut and fill mining show almost the same distributions, which cannot present the significant differences in the convergent displacements by the closure deformation of stope rock walls, as shown in Figures 7

and 8. Therefore, the effects of the mining-induced convergence of rock walls on backfill stresses can only be presented by plotting along VCL, whereas the stress monitoring at MPSB is not adaptable to rightly illustrate stress distributions of backfill in underground stopes after considering the mining closure, which is a very significant and common phenomenon in practical mining engineering [46–49].

4.2. Coefficient of Lateral Earth Pressure for Backfilled Stopes.

To further verify the reliability of the proposed solution for interface stiffness determination to simulate backfill stresses and to clearly distinguish the applicable conditions of two stress plotting methods, the coefficient of lateral earth pressure K_{earth} under different interface normal stiffness k_n in open stoping with subsequent backfill mining method has been shown in Figure 11. According to the definition in soil mechanics, the coefficient of lateral earth pressure K_{earth} is a ratio of the horizontal stress over the vertical stress at different positions in soils, sands, fills, or other granular materials. It can be used to conveniently illustrate the stress state of filled materials. It is also an important input to do analytical calculations about backfill stresses [12–17] and strength requirements [3, 7, 8].

It can be seen from Figure 11(a) that with the increase of interface normal stiffness k_n, the coefficient of lateral earth pressure K_{earth} along with the whole height of backfilled stopes gradually decreases to numerically stable states and keeps constant after reaching the stiffness values by the newly proposed method, and the values of K_{earth} generally are close to the at-rest state ($K_{earth} = K_0$).

However, Figure 11(b) shows that when the interface normal stiffness k_n increases from around 2 MPa/m to 2000 MPa/m, the coefficients of lateral earth pressure K_{earth} calculated with stresses by monitoring midpoint of stope bottom (MPSB) after filling each layer in stope are almost insensitive to the stiffness variations. Therefore, if the investigations on the effects of variable interface stiffness values on backfill stresses in the two mining methods shown in Figure 3–6 were presented by the monitored stresses at MPSB, there would be no clear and right illustrations, which means the stress monitoring method at MPSB has the applicable limitations, and this is under the conditions of nonconsidering the convergence of rock walls acting on backfill in practical mine stopes.

Therefore, in the discussed conditions of considering different interface stiffness and the closure effects of stope walls, the stress plotting along the vertical central line (VCL) of the stope is a preferable method than monitoring the stresses at the midpoint of stope bottom (MPSB) after filling each layer in stopes.

It is worth further clarification that the presented earth pressure distributions with depth shown in Figure 11 were obtained in plane strain numerical models of mine stopes to simulate the backfill stresses under 2D arching effect. The variations of coefficient of lateral earth pressure in the context of 3D soil arching will be further investigated in the future by the authors and their collaborations.
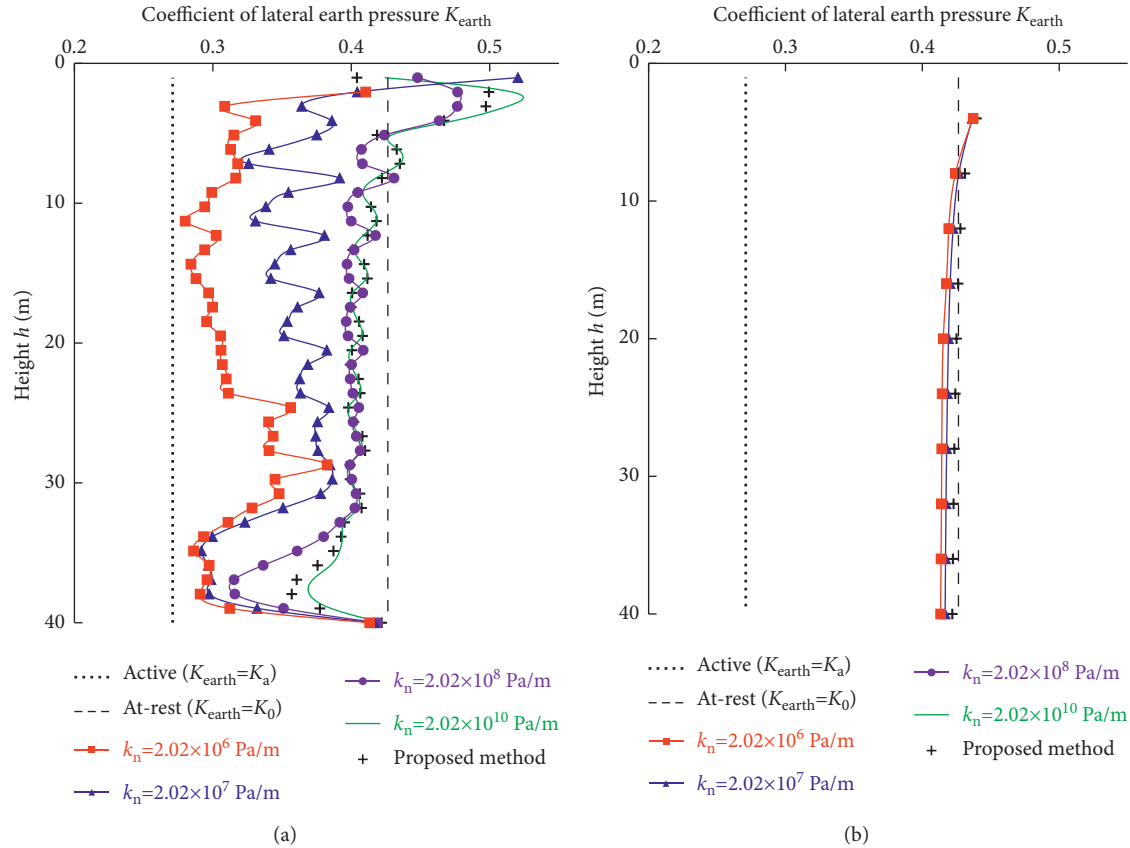
FIGURE 11: Coefficient of lateral earth pressure calculated by stresses (a) plotted along VCL and (b) monitored at MPSB with different normal stiffness $(k)_n$ of interfaces.

5. Conclusions

To better understand stress distributions of backfill in mine stopes of two most widely used mining methods with backfill (i.e. open stoping with subsequent backfill, upward cut and fill mining), numerical simulations with FLAC3D were employed to do the calculations after inserting the necessary interface elements between backfill and rock walls. Analyses about the interface stiffness determination had been firstly carried out to propose a new reasonable solution to calculate the normal and shear stiffness, respectively. The effects of interface stiffness on stress distributions of backfilled stope under different excavating and filling processes in mining methods with backfill had been comprehensively investigated considering the accuracy and efficiency of the numerical simulations. Some key conclusions have been obtained as follows:

(1) The proposed expressions to determine the apparent normal k_n and shear k_s stiffness of the interface elements between backfill and rock walls in simulated backfilled stopes can be suggested as $k_n = K/\Delta z_{min}$ and $k_s = G/\Delta z_{min}$. The new validated solution will lead to totally the same backfill stress distributions with the results in numerical models applying the interface stiffness values by the empirical method in FLAC manual but will save at least 20%–30%

calculation time to improve modeling efficiency under the same simulation conditions and will carry much clear physical meanings corresponding to the interaction between backfill and rock walls in mine stopes.

(2) With the proposed solution to determine interface stiffness in numerical models, the vertical and horizontal stresses along the vertical central line (VCL) of backfill in stopes of open stoping with subsequent backfill mining method show good agreements with the analytical stresses predicted by the Marston solution under the at-rest state ($K_{earth} = K_0$). For the backfilled stopes in the upward cut and fill mining method, the vertical stress is much smaller and the horizontal stress is much larger than the analytical stresses by the Marston solution, which means a much stronger arching effect. The obvious differences of backfill stress distributions in mine stopes of two mining methods are mainly induced by different pressure of convergent displacements from rock walls.

(3) The numerically calculated stress distributions with the proposed solution for interface stiffness plotted along vertical central line (VCL) after filling the whole stope height are significantly different with the values by monitoring stresses at the midpoint of

stope bottom (MPSB) after filling each layer. Only at the top and the bottom surfaces of the backfilled stopes are the stress values the same for the two plotting methods. Both the vertical stress and the horizontal stress plotted along VCL are lower than the stresses monitored at MPSB in the same backfilled stope condition.

(4) The effects of the mining-induced convergence of rock walls on backfill stress distributions and on the coefficient of lateral earth pressure K_{earth} can only be presented by the plotted stresses along VCL, whereas the monitored stresses at MPSB is almost insensitive and not applicable to rightly illustrate stress distributions of backfill in underground stopes after considering the mining closure, which is a very significant and common phenomenon in practical mining engineering.

Data Availability

The data used to support the findings of this study are available from the corresponding author upon request.

Conflicts of Interest

There are no conflicts of interest regarding the publication of this paper.

Acknowledgments

References

[1] F. Hassani and J. Archibald, *Mine Backfill*, Canadian Institute of Mine, Metallurgy and Petroleum, Montreal, Canada, 1998.

[2] P. Darling, *SME Mining Engineering Handbook*, Society for Mining, Metallurgy, and Exploration (SME), Englewood, CO, USA, 3rd edition, 2011.

[3] G. Liu, N. A. Li, X. Yang, and L. Guo, "Required strength estimation of a cemented backfill with the front wall exposed and back wall pressured," *International Journal of Mining and Mineral Engineering*, vol. 9, no. 1, pp. 1–20, 2018.

[4] M. Aubertin, B. Bussière, and L. Bernier, *Environment and Mine Wastes Management*, Presses Internationales Polytechnique, Montreal, Canada, 2002.

[5] Y. Potvin, E. Thomas, and A. Fourie, *Handbook on Mine Fill. Australian Centre of Geomechanics*, University of Western Australia, Nedlands, Australia, 2005.

[6] X. C. Yang and L. J. Guo, *Comprehensive Utilization Techniques of Mine Tailings and Waste Rocks*, Chemical Industry Press, Beijing, China, 2018.

[7] R. J. Mitchell, R. S. Olsen, and J. D. Smith, "Model studies on cemented tailings used in mine backfill," *Canadian Geotechnical Journal*, vol. 19, no. 1, pp. 14–28, 1982.

[8] L. Li, "Generalized solution for mining backfill design," *International Journal of Geomechanics*, vol. 14, no. 3, pp. 1–11, 2014.

[9] G. Liu, L. Li, X. Yang, and L. Guo, "Stability analyses of vertically exposed cemented backfill: a revisit to Mitchell's physical model tests," *International Journal of Mining Science and Technology*, vol. 26, no. 6, pp. 1135–1144, 2016.

[10] K. Ekanayake and C. Ekanayake, "Suitability of the overhand cut-and-fill mining method for narrow vein graphite extraction-a case study," in *Proceedings of the International Seminar on Design Methods in Underground Mining*, pp. 307–313, Australian Centre for Geomechanics, Perth, Australia, November 2015.

[11] B. Sirait, R. K. Wattimena, and N. P. Widodo, "Rockburst prediction of a cut and fill mine by using energy balance and induced stress," *Procedia Earth and Planetary Science*, vol. 6, pp. 426–434, 2013.

[12] A. Marston, *The Theory of External Loads on Closed Conduits in the Light of Latest Experiments* Iowa Engineering Experiment Station, Ames, Lowa, 1930.

[13] K. Terzaghi, *Theoretical Soil Mechanics*, Wiley, New York, NW, USA, 1943.

[14] L. Li, M. Aubertin, and T. Belem, "Formulation of a three dimensional analytical solution to evaluate stresses in backfilled vertical narrow openings," *Canadian Geotechnical Journal*, vol. 42, no. 6, pp. 1705–1717, 2005.

[15] L. Li and M. Aubertin, "An improved analytical solution to estimate the stress state in subvertical backfilled stopes," *Canadian Geotechnical Journal*, vol. 45, no. 10, pp. 1487–1496, 2008.

[16] C. H. Ting, N. Sivakugan, W. Read, and S. K. Shukla, "Analytical expression for vertical stress within an inclined mine stope with non-parallel walls," *Geotechnical & Geological Engineering*, vol. 32, no. 2, pp. 577–586, 2014.

[17] A. Jahanbakhshzadeh, M. Aubertin, and L. Li, "A new analytical solution for the stress state in inclined backfilled mine stopes," *Geotechnical & Geological Engineering*, vol. 35, no. 3, pp. 1151–1167, 2017.

[18] K. Pirapakaran and N. Sivakugan, "A laboratory model to study arching within a hydraulic fill stope," *Geotechnical Testing Journal*, vol. 30, no. 6, pp. 1–8, 2007.

[19] C. H. Ting, N. Sivakugan, and S. K. Shukla, "Laboratory simulation of the stresses within inclined stopes," *Geotechnical Testing Journal*, vol. 35, no. 2, pp. 1–15, 2012.

[20] Itasca, *FLAC3D-Fast Lagrangian Analysis of Continua, User's Guide*, Itasca Consulting Group, Minneapolis, Minnestoa, 2012.

[21] K. Pirapakaran and N. Sivakugan, "Arching within hydraulic fill stopes," *Geotechnical & Geological Engineering*, vol. 25, no. 1, pp. 25–35, 2007.

[22] M. Fahey, M. Helinski, and A. Fourie, "Some aspects of the mechanics of arching in backfilled stopes," *Canadian Geotechnical Journal*, vol. 46, no. 11, pp. 1322–1336, 2009.

[23] L. Li, M. Aubertin, and A. Shirazi, "Implementation and application of a new elastoplastic model based on a multiaxial criterion to assess the stress state near underground openings," *International Journal of Geomechanics*, vol. 10, no. 1, pp. 13–21, 2010.

[24] M. A. Sobhi, L. Li, and M. Aubertin, "Numerical investigation of earth pressure coefficient along central line of backfilled

stopes," *Canadian Geotechnical Journal*, vol. 54, no. 1, pp. 138–145, 2017.

[25] P. Yang, L. Li, and M. Aubertin, "Stress ratios in entire mine stopes with cohesionless backfill: a numerical study," *Minerals*, vol. 7, no. 10, p. 201, 2017.

[26] P. Yang, L. Li, and M. Aubertin, "Theoretical and numerical analyses of earth pressure coefficient along the centerline of vertical openings with granular fills," *Applied Sciences*, vol. 8, no. 10, p. 1721, 2018.

[27] G. Liu, L. Li, X. Yang, and L. Guo, "Numerical analysis of stress distribution in backfilled stopes considering interfaces between the backfill and rock walls," *International Journal of Geomechanics*, vol. 17, no. 2, Article ID 06016014, 2017.

[28] G. Liu, L. Li, X. Yang, and L. Guo, "A numerical analysis of the stress distribution in backfilled stopes considering nonplanar interfaces between the backfill and rock walls," *International Journal of Geotechnical Engineering*, vol. 10, no. 3, pp. 271–282, 2016.

[29] M. Fall and O. Nasir, "Mechanical behaviour of the interface between cemented tailings backfill and retaining structures under shear loads," *Geotechnical & Geological Engineering*, vol. 28, no. 6, pp. 779–790, 2010.

[30] N. J. F. Koupouli, T. Belem, P. Rivard, H. Effenguet, and H. Effenguet, "Direct shear tests on cemented paste backfill-rock wall and cemented paste backfill-backfill interfaces," *Journal of Rock Mechanics and Geotechnical Engineering*, vol. 8, no. 4, pp. 472–479, 2016.

[31] G. Liu, W. Wu, L. Guo, X. Yang, and Z. Zhang, "Experimental investigation on shear strength properties of interface between backfill and rock, Minefill 2020-2021," in *Proceedings of the 13th International Symposium on Mining with Backfill*, F. Hassani, J. Palarski, V. Sokoła-Szewioła, and G. Strozik, Eds., pp. 80–89pp. 80–, Katowice, Poland, May 2021.

[32] K. Ho Kong, J. Kodikara, and A. Haque, "Numerical modelling of the side resistance development of piles in mudstone with direct use of sidewall roughness," *International Journal of Rock Mechanics and Mining Sciences*, vol. 43, no. 6, pp. 987–995, 2006.

[33] K. Pirapakaran, *Load-deformation Characteristics of Minefills with Particular Reference to Arching and Stress Developments*, Ph.D. thesis, James Cook University, Townsville City, Australia, 2008.

[34] N. Sivakugan, S. Widisinghe, and V. Z. Wang, "Vertical stress determination within backfilled mine stopes," *International Journal of Geomechanics*, vol. 14, no. 5, Article ID 06014011, 2014.

[35] M. Helinski, M. Fahey, and A. Fourie, "Coupled two-dimensional finite element modelling of mine backfilling with cemented tailings," *Canadian Geotechnical Journal*, vol. 47, no. 11, pp. 1187–1200, 2010.

[36] Engineering Tool Box. *Stiffness*, https://www.engineeringtoolbox.com/stiffness-d_1396.html, 2008.

[37] L. Li and M. Aubertin, "Numerical investigation of the stress state in inclined backfilled stopes," *International Journal of Geomechanics*, vol. 9, no. 2, pp. 52–62, 2009.

[38] E. Hoek, "Rock mass properties for underground mines," in *Underground Mining Methods: Engineering Fundamentals and International Case Studies*, W. A. Hustrulid and R. L. Bullock, Eds., Society for Mining, Metallurgy, and Exploration, Englewood, Colorado, 2001.

[39] B. H. G. Brady and E. T. Brown, *Rock Mechanics for Underground Mining*, Springer Science & Business Media, Dordrecht, Netherlands, 3rd edition, 2004.

[40] M. Fall, T. Belem, S. Samb, and M. Benzaazoua, "Experimental characterization of the stress-strain behaviour of cemented paste backfill in compression," *Journal of Materials Science*, vol. 42, no. 11, pp. 3914–3922, 2007.

[41] K. le Roux, W. F. Bawden, and M. F. Grabinsky, "Field properties of cemented paste backfill at the Golden Giant mine," *Mining Technology*, vol. 114, no. 2, pp. 65–80, 2005.

[42] S. Yin, A. Wu, K. Hu, Y. Wang, and Y. Zhang, "The effect of solid components on the rheological and mechanical properties of cemented paste backfill," *Minerals Engineering*, vol. 35, pp. 61–66, 2012.

[43] G. Liu, L. Li, M. Yao et al., "An investigation of the uniaxial compressive strength of a cemented hydraulic backfill made of alluvial sand," *Minerals*, vol. 7, no. 1, p. 4, 2017.

[44] N. Sivakugan and S. Widisinghe, "Stresses within granular materials contained between vertical walls," *Indian Geotechnical Journal*, vol. 43, no. 1, pp. 30–38, 2013.

[45] B. D. Thompson, W. F. Bawden, and M. W. Grabinsky, "In situ measurements of cemented paste backfill at the Cayeli Mine," *Canadian Geotechnical Journal*, vol. 49, no. 7, pp. 755–772, 2012.

[46] N. Falaknaz, M. Aubertin, and L. Li, "Numerical investigation of the geomechanical response of adjacent backfilled stopes," *Canadian Geotechnical Journal*, vol. 52, no. 10, pp. 1507–1525, 2015.

[47] D. R. Tesarik, J. B. Seymour, and T. R. Yanske, "Long-term stability of a backfilled room-and-pillar test section at the Buick Mine, Missouri, USA," *International Journal of Rock Mechanics and Mining Sciences*, vol. 46, no. 7, pp. 1182–1196, 2009.

[48] G. S. Liu, X. C. Yang, and L. J. Guo, "Optimization research on backfill strength requirement of open stoping with subsequent backfill mining based on excavating and filling sequences," *Nonferrous Metals Engineering*, vol. 9, no. 10, pp. 85–94, 2019.

[49] P. Marlow and P. A. Mikula, "Shotcrete ribs and cemented rock fill ground control methods for stoping in weak squeezing rock at Wattle Dam Gold Mine," in *Proceedings of the Seventh International Symposium on Ground Support in Mining and Underground Construction*, pp. 133–147, Australian Centre for Geomechanics, perth, Australia, 2013.

Research Article

Workability and Compressive Strength Behavior of a Cemented High-Porosity Backfill Material

W. H. Cao [1,2] **X. F. Wang** [1,3,4] **D. S. Zhang,**[1] **X. J. Ji** [2] **X. Z. Chen,**[2] **A. Zhang,**[2] **and F. X. Zhu**[2]

[1]*State Key Laboratory of Coal Resources and Safe Mining, China University of Mining & Technology, Xuzhou, China*
[2]*School of Civil Engineering, Nanyang Institute of Technology, Nanyang, China*
[3]*Laboratory of Mine Earthquake Monitoring and Prevention, China University of Mining & Technology, Xuzhou, China*
[4]*School of Mines, China University of Mining & Technology, Xuzhou, China*

Correspondence should be addressed to X. F. Wang; wangxufeng@cumt.edu.cn

A full understanding of the workability and unconfined compressive strength (UCS) of the cemented high-porosity (CHPB) material, made of surface sand, widely distributed in the western mining area, foam, and cementing materials, is important for applying in ecologically fragile mining areas of western China. In this article, the influence of solid content, density grade, sand/binder ratio, and silica fume dosage in binder on workability and strength development of CHPB samples in different curing ages is studied. Test results show that the fresh CHPB mix has good workability, due to the existence of a large number of bubbles. With the increase of density grade, the UCS of the CHPB sample increases exponentially. Workability of fresh CHPB samples significantly decreases with increasing solid content due to the reduction of interparticle distance. For a given mix proportion, the optimal solid content of CHPB samples is 83.7%. The variation of the sand/binder ratio from 3 to 4.5 results in a slight increase of workability and a significant increase of the UCS. Silica fume demonstrates improvement on workability and strength behavior, and the optimal dosage in the binder should not exceed 10%.

1. Introduction

Underground mining leads to a series of mining damage and environmental problems, such as the destruction of aquifer resources, surface subsidence damage to ground buildings, and surface vegetation death caused by ecological environmental damage [1, 2], which will become more prominent, with the development of coal resources gradually shifting its focus to arid and semiarid areas in western China [3]. As the most effective method to control surface subsidence and realize green mining, the filling and mining technology plays an essential role in the process of coal resource mining for its unique mining technique [4].

Filling material is the decisive factor and the bottleneck of the development of the filling mining. Over the past few decades, scholars have been looking for filling materials with sufficient raw materials, low cost, stable mechanical properties, and good fluidity. Due to the large amount of solid wastes such as waste rock, coal gangue, and tailings, the reasonable use of solid wastes to prepare composite cemented filling materials not only reduces the environmental pollution and surface waste treatment costs but also effectively reduces the cost of filling mining [5–8].

At present, with the development of cemented filling technology, remarkable achievements have been made in the preparation and properties of different solid waste cement filling materials. The particle size of gangue has a significant effect on the strength of CRF, which is also known as consolidated rockfill [9]. Cemented paste backfill (CPB) and cemented tailings backfill (CTB) are widely used in underground metal mining [10]; fly ash, blast furnace slag (slag), silica fume, pozzolanic ash, and alkali-activated materials were used as binder instead of ordinary Portland cement to reduce the cost of CPB mix [11–14]. At the same time, the properties and ratio of different types of new cementing materials, such as soil paste filling material [15],

gangue-waste concrete cemented paste backfill [16], and coal gangue backfill [17], are studied. These studies have greatly enriched the content of cemented filling materials in underground mine.

However, the main raw materials of cement paste materials, such as coal gangue, tailings, and other solid wastes, are still far less than the mining space, so it is difficult to meet the needs of filling in large-volume goaf, especially in the urgent need of green mining in mining areas of western China.

It is exciting that the western mining area is rich in surface sand. The author uses the surface sand of the mining area as the main raw material, mixes it with cementitious material into slurry, and adds foam to form the cemented high-porosity backfill (CHPB) material, which has the advantages of light weight and low cost [18]. The fresh (workability index) and hardened (unconfined compressive strength-UCS) are two main factors when designing an effective, lucrative, and sustainable CHPB matrix for underground structures [19, 20]. The main applications of CHPB in the underground mining industry are roof-contacted filling [21], small pit goaf filling [22], fire prevention, and plugging air leakage in goaf [23]. The effects of the raw material ratio and foam expansion rate on curing time and compressive strength of CHPB were studied [24], and the UCS prediction model for foam-cemented paste backfill was proposed. These studies have important reference to the research of this paper.

The objectives of this study are to therefore experimentally investigate the impacts of a number of parameters such as solid content, density grade, sand/binder ratio, and silica fume dosage on workability and strength properties of the CHPB matrix.

2. Experimental Program

2.1. Materials

2.1.1. Binder. Ordinary Portland cement (OPC) is the most common binder agent used in backfill operations due to its versatility. However, the optimization of filling material performance and the reduction of backfill cost lead to the extensive use of some pozzolanic materials, such as fly ash (FA) and blast furnace slag (slag) [19, 20].

OPC was used as binder and blended with silica fume at different replacement ratios in this study. The principal binder used is OPC (Type P.O 42.5 R, from Xuzhou, Jiangsu Province, China, based on Chinese standard GB175-2007 common Portland cement). Silica fume (from Chengdu City, Sichuan Province, China) is mainly composed of silica with a particle size of about 0.15 μm; hence, silica fume is often used as an active mineral admixture. The chemical composition of OPC and silica fume is presented in Table 1, which was measured by the X-ray fluorescence spectrometer (XRF).

2.1.2. Surface Sand. Sand used in the study was taken from the surface of Menkeqing coal mine, Ordos City, Shendong mining area, Inner Mongolia Region of China, where is rich

in surface sand. Particle size distribution of the sample was determined using a laser particle size analyzer, as shown in Figure 1. The sampled surface sand has a relatively poor particle size distribution with a uniformity coefficient (Cu) of 2.5 and with particles over 0.1 mm accounted for 82.15% (over 75%), which belongs to fine sand. Meanwhile, the sample had an initial water content of around 5% and bulk density of $1.704 \, g/cm^3$. Moreover, the crystalline components in tailings were identified using X-ray diffraction (XRD). XRD patterns displayed in Figure 2 show that the crystalline phases are predominantly quartz, albite, and potassium feldspar, which are all inert substances.

2.1.3. Foaming Agent and Water. HTQ-1 compound foaming agent developed by Huatai Building Materials Company, Henan province, China, was used in this study, of which the main raw materials are nonpolluting animal protein oil and vegetable oil and will not produce any side effects to producers, users, and the environment. Meanwhile, the foaming agent can be used under the low temperature environment. The foaming agent adopts the physical method for foaming (Figure 3(a)), which has high foaming multiple and good stability. At the same time, the bubbles are independent of each other and evenly distributed in the cement slurry, which can form a large number of closed pores (Figure 3(b)).

Tap water was used to mix the binders and fine aggregate and used for foaming solution, with a pH of 6.8.

2.2. Sample Preparation and Mix Proportion. CHPB samples with different solid contents, surface sand/binder (S/B) ratios, density grade, and silica fume in binder were prepared. First, prepare the raw materials according to the experimental project. Second, the mixture slurry was prepared by using a blender, and after diluting the foaming agent 30 times, stable foam was formed through the foaming mechanism. Then, the foam was added to the mixture slurry and stirred well to produce the desired CHPB mixture (Figure 4). The produced backfill mixtures were cast into $100 \times 100 \times 100$ mm cubic molds. Demoulded after 24 hours, the manufactured cubes were cured in the environmental chambers (Figure 5) at specific curing temperatures for periods of 7, 28, and 90 days. The relative humidity and the temperature were kept constant at %95 ± 1 and 20°C ± 2, respectively. The detailed testing protocols of the CHPB mixtures are summarized in Table 2.

It should be noted that the weight of samples of the same density grade should not exceed ±50 g from the design value due to the different degree of damage of the foam in the stirring process.

2.3. Experimental Testing

2.3.1. Workability Tests. The workability of the fresh CHPB mix was evaluated by measuring the spread flow using a slump cone with the following dimensions: top diameter, 100 mm; bottom diameter, 200 mm; height, 300 mm. The

TABLE 1: Chemical composition of OPC and silica fume (wt. (%)).

Composition	Al_2O_3	CaO	SiO_2	Fe_2O_3	MgO	SO_3	K_2O	Na_2O	P_2O_5
OPC	4.88	64.38	19.29	3.68	2.98	3.44	1.15	0.06	0.04
Silica fume	3.5	0.6	91.5	0.9	0.3	0.5	-	0.6	-
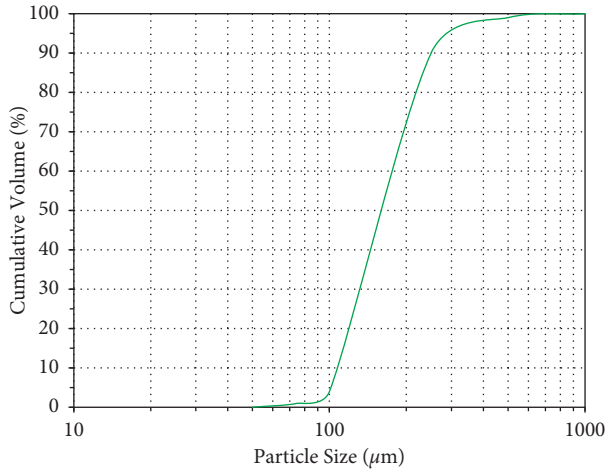
FIGURE 1: Particle-size distribution curves of surface sand.
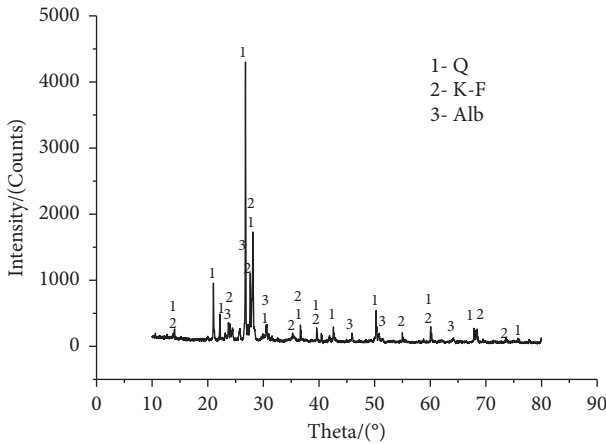
FIGURE 2: XRD pattern of surface sand.

final spread is measured on two perpendicular diameters 2 minutes after cone lifting. Lab tests were carried out in accordance with the Chinese standard test method for performance of ordinary concrete mixtures GB50080-2016. The estimated spread value was then calculated as the average of the two measurements (Figure 6).

At the same time, the bleeding rate of the fresh CHPB mix with different density grades was tested to reflect the water retention performance of the slurry. Under laboratory conditions, a measuring cylinder (mass m_0) was used to test the bleeding rate of slurry. The evenly stirred slurry was first added into the measuring cup to test the total weight M of the measuring cup and slurry. After standing for 3 hours, the water (mass m_1) on its surface was sucked by pipette, and the bleeding rate W was calculated:

$$W = \frac{m_1}{(M - m_0)(1 - C_m)}, \tag{1}$$

where C_m is the solid content.

2.3.2. Unconfined Compressive Strength Tests. At the predetermined curing periods (7, 28, and 90 days), unconfined compressive tests were performed on the cubic samples with a computer-controlled loading machine (Figure 7). The UCS tests were carried out at a constant deformation rate of 0.5 mm/min. Before conducting the UCS tests, the end surfaces of samples were polished to make sure that they are flat and parallel. All the measurements were carried out in triplicate, and the average values were presented in the results. The individual strengths of three specimens, molded with the same characteristics, should not deviate by more than 15% from the mean compressive strength; otherwise, an additional set of specimens needs to be prepared and tested again.

2.3.3. Microstructural Tests. Additional tests, including thermal analyses and specimen microstructure measurement, were carried out to better assess and interpret the results of the UCS tests. The phase compositions of the binder hydration products were determined by using thermal analyses (thermogravimetry (TG) and differential thermogravimetry (DTG)). TG/DTG analyses were performed on specimens at 7 d, 28 d, and 90 d for quantitative analysis of hydration products in different curing time with a PerkinElmer TGA-8000 (Figure 8) in a dynamic N_2 atmosphere at a heating rate of 10 C/min. SEM studies were done with a Quanta TM 250 operated at an accelerating voltage of 15 kV on some CHPB samples. After being soaked in anhydrous ethanol to terminate the hydration process, the specimens were taken out, dried for gold spray treatment, and put into SEM for microstructure analysis.

3. Result and Discussions

3.1. Effect of Density Grade. The overall morphology and the microstructure of specific hydration products of the CHPB specimen at 83.7% solid content cured for 28 days were scanned by the scanning electron microscope. The internal structure of the specimen is similar to honeycomb, which is mainly composed of closed pores with uniform distribution and irregular shape (Figure 9(a)). The dense structure formed by the binder wrapping surface sand is the part outside the pores (Figure 9(b)). The bonding interface of surface sand is filled with hydration products, which mainly consisted of flocculent calcium silicate gel, a certain amount of fine needle-like ettringite, and hexagonal flake calcium hydroxide crystals (Figure 9(c)).
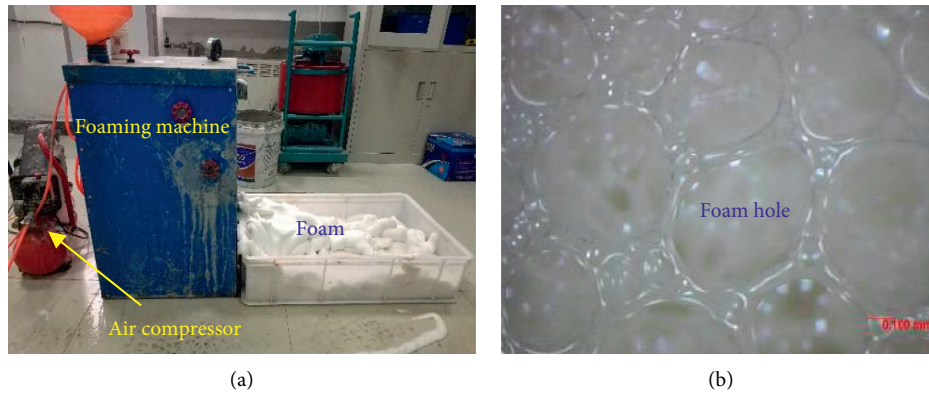
FIGURE 3: Foams were prepared by the physical method (a) and foam microstructure (b).
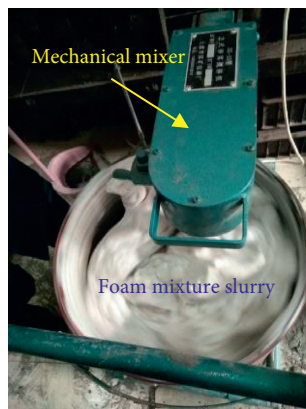
FIGURE 4: Mixing slurry.

FIGURE 5: Curing CHPB samples.

The Group D of fresh CHPB samples were prepared to investigate the influence of density grade on workability and strength development. The effect of density grade ranging from $600 \, \text{kg/m}^3$ to $1600 \, \text{kg/m}^3$ for CHPB mixtures (solid content of 83.7%, surface sand/binder of 3.5, and silica fume in binder of 10%) is illustrated in Figure 10. It is clear that density grade has a significant effect on the workability and strength of the sample when other ratios are constant.

As shown in Figure 10(a), when increasing density grade from $600 \, \text{kg/m}^3$ to $1600 \, \text{kg/m}^3$, the corresponding spread decreases by 11.5%, 9.2%, 8.2%, 5.5%, and 4.3% and the decreasing range of spread gradually slows down. At the same time, the bleeding rate of the fresh mix was 4.5%, 5.1%, 4.8%, 5.2%, 4.1%, and 3.9%, respectively. It indicates that the density grade has little effect on the bleeding rate and the mix slurry with solid content of 83.7% and surface sand/binder of 3.5, and silica fume in binder of 10% has good cohesion.

The sample strength curve with different curing times (i.e., 7 days, 28 days, and 90 days) are approximately an exponential function shown in Figure 10(b). The UCS of CHPB with 28 days curing time from $600 \, \text{kg/m}^3$ to $1600 \, \text{kg/m}^3$ were 0.62 MPa, 1.00 MPa, 1.57 MPa, 3.23 MPa, 8.63 MPa, and 12.00 MPa, respectively. The results shown in Figure 10(b) underline that the curing time has a significant positive role in UCS and its development of CHPB samples.

For example, the UCS of CHPB samples with density grade of $1200 \, \text{kg/m}^3$ increased from 1.95 MPa and 3.25 MPa to 3.88 MPa with increasing curing time from 7, 28, to 90 days. This increase in hydration products with curing time in the result of the TG/DTG analysis performed on 7, 28, and 90 days CHPB samples is shown in Figure 11. The DTG curves show a mass loss at 90–120°C, 440–460°C, and 720–730°C, which denote the evaporation of water along with dehydration of calcium silicate hydrate (C-S-H) and ettringite, dehydroxylation of portlandite (calcium hydroxide (C-H)), and decomposition of calcium carbonate, respectively [25]. A comparison of the DTG curves of the 7, 28, and 90 days CHPB samples shows that the peak or weight loss at around 440–460°C is higher for the latter sample. This indicates that the amount of hydration products increases with curing time since the amount of portlandite is an indication of the degree of hydration.

3.2. Effect of Solid Content. The group A of CHPB samples was prepared with different solid contents (i.e., 82.1%, 83.7%, 85.3%, and 87.0%) at density grade of $1000 \, \text{kg/m}^3$, surface sand/binder of 3.5, and silica fume in binder of 10%. The effect of solid content on workability and strength development of CHPB samples is illustrated by Figure 12. As

TABLE 2: Summary of the mixture composition of the samples.

| Group | Sample | Solid content (wt. (%)) | Solid content proportions | | Density class (kg·m⁻³) | Silica fume in binder (wt. (%)) |
			Binder (%)	Surface sand (%)		
A	1	82.1	22.2	77.8	1000	10
	2	83.7	22.2	77.8	1000	10
	3	85.3	22.2	77.8	1000	10
	4	87.0	22.2	77.8	1000	10
B	5	83.7	25	75	1000	10
	6	83.7	22.2	77.8	1000	10
	7	83.7	20	80	1000	10
	8	83.7	18.2	81.8	1000	10
C	9	83.7	22.2	77.8	1000	0
	10	83.7	22.2	77.8	1000	5
	11	83.7	22.2	77.8	1000	10
	12	83.7	22.2	77.8	1000	15
D	13	83.7	22.2	77.8	600	10
	14	83.7	22.2	77.8	800	10
	15	83.7	22.2	77.8	1000	10
	16	83.7	22.2	77.8	1200	10
	17	83.7	22.2	77.8	1400	10
	18	83.7	22.2	77.8	1600	10

FIGURE 6: Spread flow test.
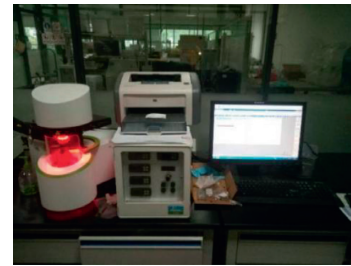
FIGURE 8: Thermogravimetric analyzer.

FIGURE 7: Loading machine.

decreasing, respectively, with higher solid content and then resulting in denser structure and higher strength [28]. When the solid content is higher than 83.7%, the strength of CHPB samples shows a trend of negative growth with solid content increasing. This can be due to the excessively high solid content which means that the water-cement ratio is too low, resulting in insufficient hydration reaction and reducing in hydration products.

In addition, Figure 12(b) also illustrates that the UCS of CHPB increases with the elapsing of curing age regardless of solid content.

expected, the workability of fresh CHPB samples obviously decreases as the solid content rises (Figure 12(a)).

This decrease in workability with a higher solid content (lower water content) is due to the reduction in interparticle distance, thus making it easier for the solid particles to slide past one another during shearing [26, 27].

The results presented in Figure 12(b) indicate that all of the samples show a similar tendency in the time-dependent changes of the UCS. It can be noticed that when the solid content is less than 83.7%, the strength gain of CHPB samples increases with increasing solid content. This can be attributed to the content of calcium silicate hydrate (C-S-H) gel and total porosity within CHPB increasing and

3.3. Effect of Sand/Binder Ratios. The effects of sand/binder ratios on the workability and strength of the CHPB specimens as a function of curing time are summarized in Figure 13 In this test, four different sand/binder ratios (3.0, 3.5, 4.0, and 4.5) were prepared, while other parameters such as the density grade, solid content, and silica fume in binder were maintained constant at $1000 \, kg/m^3$, 83.7%, and 10%, respectively. It can be observed from Figure 13(a) that the spread of fresh CHPB increases slightly with an increase in the S/B ratio. That is because with the increase of the S/B ratio, the amount of sand gradually increases and the content of cementing material decreases. Due to the constant water
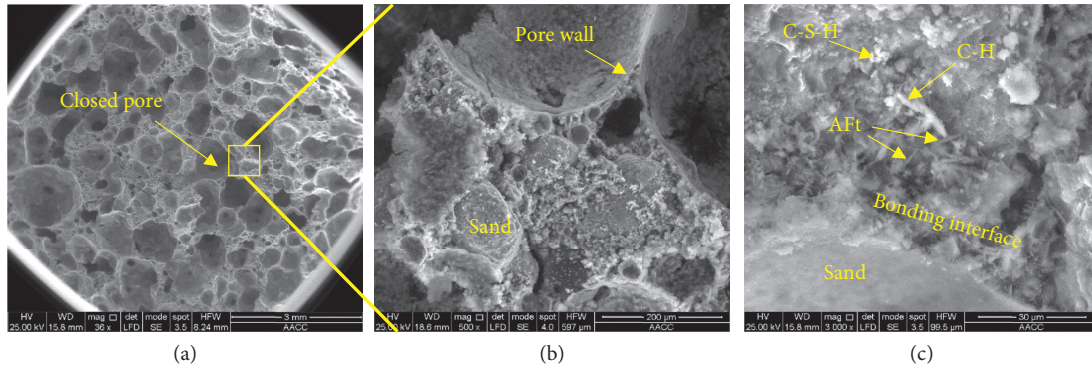
FIGURE 9: SEM diagram of the specimen at 83.7% solid content 28 days. (a) ×36; (b) ×500; (c) ×3000.

(a)

(b)
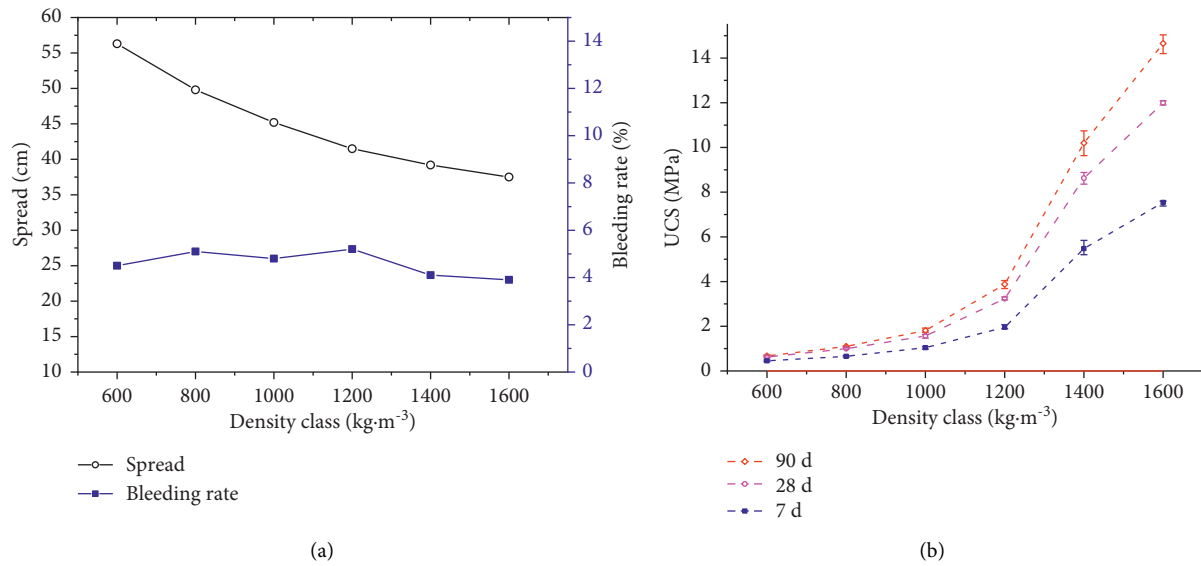
FIGURE 10: Effect of density grade on the (a) flow and strength of CHPB samples.
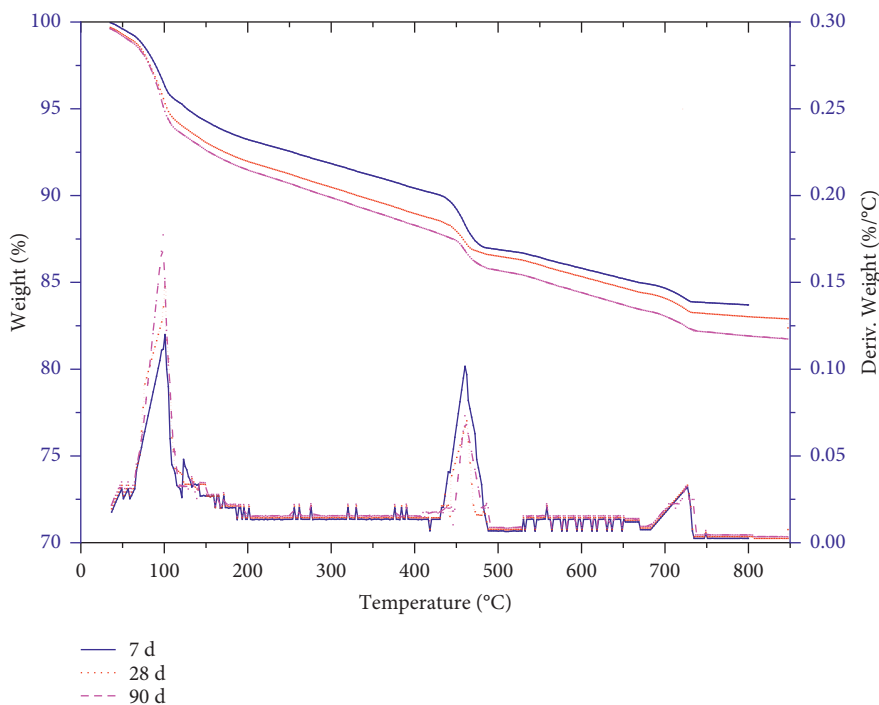
FIGURE 11: TG/DTG diagrams for the CHPB specimen at the density grade of 1200 kg/m^3 cured for 7, 28, and 90 days.

(a)

(b)
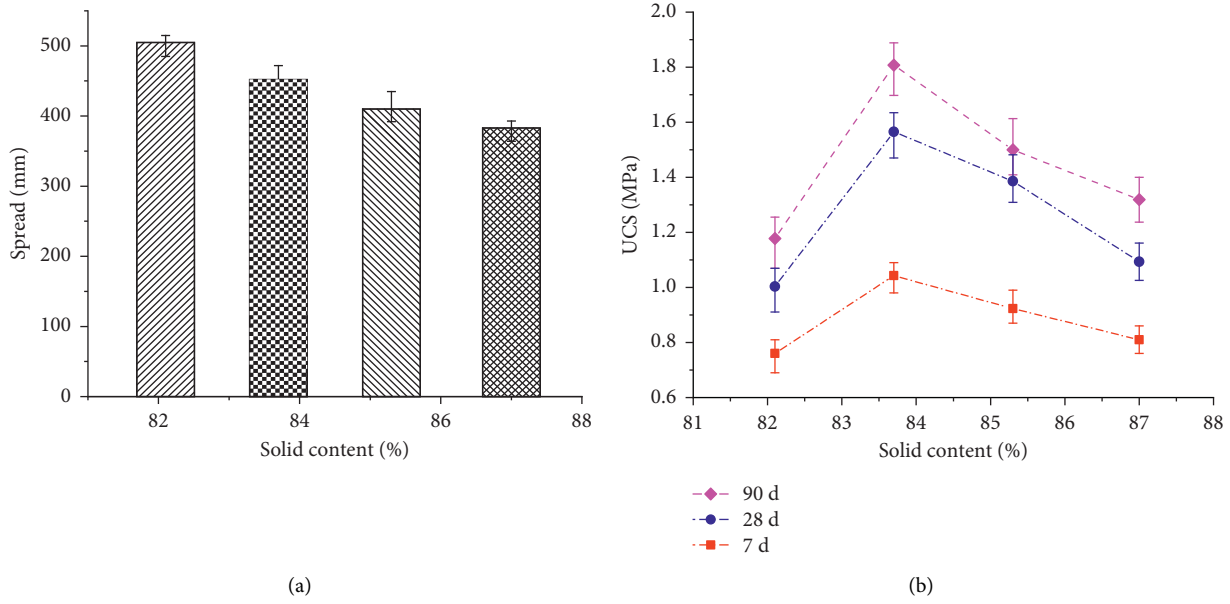
FIGURE 12: (a) Workability and (b) strength of CHPB samples with different solid content.

(a)

(b)
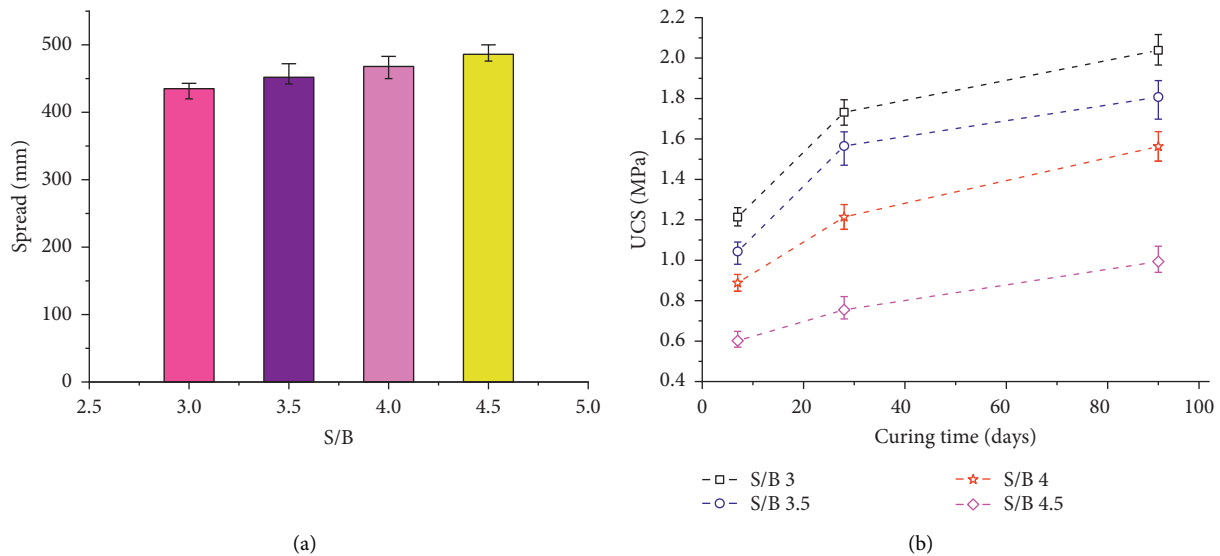
FIGURE 13: Influence of sand/binder ratios on the (a) workability and (b) strength of CHPB samples.

content, on the one hand, the corresponding water-binder ratio increases, and on the other hand, the encapsulation of cementing materials to sand decreases.

From Figure 13(b), it is obvious that the variation of the S/B ratio from 3 to 4.5 results in a decrease of the strength of CHPB. It is mainly due to the reduction of the relative content of cementing materials, resulting in the reduction of hydration products and the encapsulation force of mortar. At the same time, the increase of the water-binder ratio also reduces the compactness of structure. The results presented in Figure 13(b) indicate that all of the samples have a rapid increase in the UCS until 28 days and then a steady increase.

This is due to the fact that cementitious materials develop strength with continual hydration. The rate of strength gain is faster at the early ages but reduced with curing time [29].

3.4. Effect of Silica Fume in Binder. Figure 14 demonstrates the strength development of CHPB samples produced by using a silica fume in binder of 0–15 wt%. The laboratory tests were conducted at a fixed solid content of 83.7%, a sand/binder ratio of 3.5, and a density grade of 1000 kg/m^3. From Figure 14(a), it is fairly obvious that the spread of fresh CHPB is slightly improved with an increase in silica fume

(a)

(b)
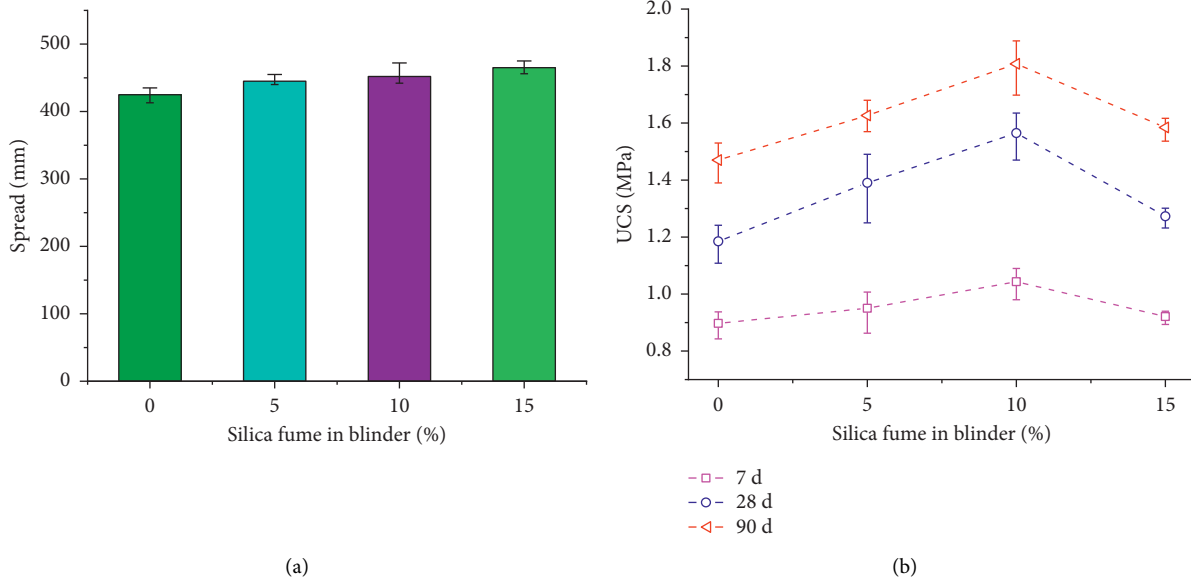
FIGURE 14: (a) Workability and (b) strength of CHPB samples with various silica fume in binder.

dosage in binder. An explanation for this behavior is that higher replacement of processing silica fume results in a reduction of friction between particles [30].

The results presented in Figure 14(b) underline that silica fume dosage in binder has a significant impact on the strength of CHPB. The UCS increases with the dosage up to 10% and then starts to decrease with higher dosage. The optimum dosage that produces the highest compressive strength of the CHPB appears to be about 10%. This can be explained by the following: (i) silica can react with calcium hydroxide (C-H) to form calcium silicate gel. At low dosage, an increase in silica fume leads to more amount of hydration products. (ii) The particle size of silica fume is smaller than that of cement, which can increase the compactness of the internal structure.

Subsequently, this strength is observed to deteriorate gradually as the dosage increase from 10% to 15%.

The reasons for the contrasting trend could be due to excessive silica powder which will reduce the amount of water involved in the hydration reaction, resulting in a decrease in the amount of early hydration products, unable to generate sufficient amount of C-H. At the same time, the agglomeration phenomenon occurs, which reduces the compactness of the material and causes its strength to decrease.

4. Conclusions

In this paper, a comprehensive laboratory test work has been conducted to study the influences of four parameters (i.e., solid content, sand/binder ratios, density grade, and silica fume dosage in binder) on workability and strength development of CHPB samples. For given CHPB samples with different density grades (i.e., 600 kg/m^3, 800 kg/m^3, 1000 kg/m^3, 1200 kg/m^3, 1400 kg/m^3, and 1600 kg/m^3), sand/binder ratio (i.e., 3, 3.5, 4, and 4.5), solid content (i.e., 82.1%, 83.7%,

85.3%, and 87.0%), and silica fume dosage in binder (i.e., 0%, 5%, 10%, and 15%) were prepared to obtain the workability and UCS at different curing times (i.e., 7 d, 28 d, and 90 d). Based on the results of the experimental tests performed, the following conclusions can be drawn:

(1) The internal structure of the CHPB sample contains a large number of closed pores. With the increase of the density grade, the number of pores decreases, and the UCS of the sample increases exponentially. On the contrary, the workability of the samples decreases significantly.

(2) Workability of fresh CHPB samples significantly decreases with increasing solid content due to the reduction of interparticle distance. The UCS increases with increasing solid content from 82.1% to 83.7% through a denser structure. However, a decrease trend in UCS is observed as the solid content exceeds 83.7%.

(3) The variation of the sand/binder ratio from 3 to 4.5 results in a slight increase of workability and a significant increase of the strength. It is mainly due to the reduction of the relative content of cementing materials, resulting in the reduction of hydration products. At the same time, the increase of the water-binder ratio also reduces the compactness of the structure.

(4) Adding silica fume poses a positive effect of silica fume dosage on workability behavior and UCS of CHPB samples. The optimum dosage in binder that produces the highest compressive strength of the CHPB appears to be about 10%.

Data Availability

The data used to support the findings of this study are available from the corresponding author upon request.

Conflicts of Interest

Acknowledgments

References

[1] M. Fall, J. C. Célestin, M. Pokharel, and M. Touré, "A contribution to understanding the effects of curing temperature on the mechanical properties of mine cemented tailings backfill," *Engineering Geology*, vol. 114, no. 3, pp. 397–413, 2010.

[2] W. Yu, B. Pan, F. Zhang, S. Yao, and F. Liu, "Deformation characteristics and determination of optimum supporting time of alteration rock mass in deep mine," *KSCE Journal of Civil Engineering*, vol. 23, no. 11, pp. 4921–4932, 2019.

[3] D. S. Zhang, W. P. Li, X. P. Lai, G. W. Fan, and W. Q. Liu, "Development on basic theory of water protection during coal mining in northwest of China," *China Coal Society*, vol. 42, no. 1, pp. 36–43, 2017.

[4] M. G. Qian and X. X. Miao, "Research on green mining of coal resources in China: current S tatus and future prospects," *Journal of Mining & Safety Engineering*, vol. 26, no. 1, pp. 1–14, 2009.

[5] A. A. Hammond, "Mining and quarrying wastes: a critical review," *Engineering Geology*, vol. 25, no. 1, pp. 17–31, 1988.

[6] Q. Chen, Y. Tao, Y. Feng, Q. Zhang, and Y. Liu, "Utilization of modified copper slag activated by Na2SO4 and CaO for unclassified lead/zinc mine tailings based cemented paste backfill," *Journal of Environmental Management*, vol. 290, Article ID 112608, 2021.

[7] H. Jiang, M. Fall, and L. Cui, "Freezing behaviour of cemented paste backfill material in column experiments," *Construction and Building Materials*, vol. 147, pp. 837–846, 2017.

[8] W. Sun, K. Hou, Z. Yang, and Y. Wen, "X-ray CT three-dimensional reconstruction and discrete element analysis of the cement paste backfill pore structure under uniaxial compression," *Construction and Building Materials*, vol. 138, pp. 69–78, 2017.

[9] H. Jiang, M. Fall, Y. li, and J. Han, "An experimental study on compressive behaviour of cemented rockfill," *Construction and Building Materials*, vol. 213, pp. 10–19, 2019.

[10] J. S. Chen, B. Zhao, X. M. Wang, Q. L. Zhang, and L. Wang, "Cemented backfilling performance of yellow phosphorus slag," *International Journal of Minerals, Metallurgy, and Materials*, vol. 17, no. 1, pp. 121–126, 2010.

[11] Y. Wang, M. Fall, and A. Wu, "Initial temperature-dependence of strength development and self-desiccation in cemented paste backfill that contains sodium silicate," *Cement and Concrete Composites*, vol. 67, pp. 101–110, 2016.

[12] Q. L. Zhang, Y. T. Li, Q. S. Chen, Y. K. Liu, Y. Feng, and D. L. Wang, "Effects of temperatures and pH values on rheological properties of cemented paste backfill," *Journal of Central South University*, vol. 28, no. 6, pp. 1707–1723, 2021.

[13] D. L. Wang, Q. L. Zhang, Q. S. Chen, C. C. Qi, Y. Feng, and C. C. Xiao, "Temperature variation characteristics in flocculation settlement of tailings and its mechanism," *International Journal of Minerals, Metallurgy and Materials*, vol. 27, no. 11, pp. 1438–1448, 2020.

[14] H. Jiang, Z. Qi, E. Yilmaz, J. Han, J. Qiu, and C. Dong, "Effectiveness of alkali-activated slag as alternative binder on workability and early age compressive strength of cemented paste backfills," *Construction and Building Materials*, vol. 218, pp. 689–700, 2019.

[15] Z. Wang, W. J. Yu, and F. F. Liu, "The materialization characteristics and ratio of a new soil paste filling material," *Advances in Civil Engineering*, vol. 2020, Article ID 6645494, 8 pages, 2020.

[16] G. R. Feng, X. Q. Jiang, Y. X. Guo, and T. Qi, "Study on mixture ratio of gangue-waste concrete cemented paste backfill," *Journal of Mining & Safety Engineering*, vol. 33, no. 6, pp. 1072–1079, 2016.

[17] D. Wu, Y. Hou, T. Deng, Y. Chen, and X. Zhao, "Thermal, hydraulic and mechanical performances of cemented coal gangue-fly ash backfill," *International Journal of Mineral Processing*, vol. 162, pp. 12–18, 2017.

[18] X. F. Wang, W. H. Cao, and D. S. Zhang, "Mechanism study on influence of particle size and content of gangue on strength of high-sand and high-foam cement-based filling material," *Journal of Mining & Safety Engineering*, vol. 37, no. 2, pp. 2376–2384, 2020.

[19] D. Ouattara, T. Belem, M. Mbonimpa, and A. Yahia, "Effect of superplasticizers on the consistency and unconfined compressive strength of cemented paste backfills," *Construction and Building Materials*, vol. 181, pp. 59–72, 2018.

[20] E. Yilmaz, T. Belem, B. Bussière, and M. Mamert, "Curing time effect on consolidation behaviour of cemented paste backfill containing different cement types and contents," *Construction and Building Materials*, vol. 75, pp. 99–111, 2015.

[21] J. P. Cui, Z. B. Guo, L. Li, S. Zhang, Y. Zhao, and Z. Ma, "A hybrid artificial intelligence model for predicting the strength of foam-cemented paste backfill," *IEEE Access*, vol. 8, Article ID 84569, 2020.

[22] W. Y. Cai, Z. C. Chang, D. S. Zhang, X. Wang, W. Cao, and Y. Zhou, "Roof filling control technology and application to mine roadway damage in small pit goaf," *International Journal of Mining Science and Technology*, vol. 29, pp. 477–482, 2019.

[23] H. Wen, D. Zhang, Z. J. Yu, X. Zheng, S. Fan, and B. Laiwang, "Experimental study and application of inorganic solidified foam filling material for coal mines," *Advances in Materials Science and Engineering*, vol. 2017, Article ID 3419801, 13 pages, 2017.

[24] Q. P. Wang, H. Wang, and F. F. Min, "Effect of raw material ratio on properties of foam paste backfilling materials," *Materials Review*, vol. 29, pp. 135–139, 2015.

[25] N. Lemonis, P. E. Tsakiridis, N. S. Katsiotis et al., "Hydration study of ternary blended cements containing ferronickel slag and natural pozzolan," *Construction and Building Materials*, vol. 81, no. 11, pp. 130–139, 2015.

[26] D. Simon and M. Grabinsky, "Apparent yield stress measurement in cemented paste backfill," *International Journal of Mining, Reclamation and Environment*, vol. 27, no. 4, pp. 231–256, 2013.

[27] H. Q. Jiang, M. Fall, and C. Liang, "Yield stress of cemented paste backfill in sub-zero environments: experimental results," *Minerals Engineering*, vol. 92, pp. 141–150, 2016.

[28] M. Fall, M. Benzaazoua, and E. G. Saa, "Mix proportioning of underground cemented tailings backfill," *Tunnelling and Underground Space Technology*, vol. 23, no. 1, pp. 80–90, 2008.

[29] A. M. Neville, *Properties of Concrete*, Prentice-Hall, London, England, 2000.

[30] A. Sathonsaowaphak, P. Chindaprasirt, and K. Pimraksa, "Workability and strength of lignite bottom ash geopolymer mortar," *Journal of Hazardous Materials*, vol. 168, no. 1, pp. 44–50, 2009.

Research Article

Analysis of the Control Effect and Parameter Optimisation of Urban Surface Deformation in Underground Coal Mining with Solid Backfilling

Jiaqi Wang ⓘ,[1] **Jixiong Zhang** ⓘ,[2] **Qiang Zhang** ⓘ,[2] **Zhongya Wu**,[1] **Qi Zhang** ⓘ,[1] **Yunbo Wang**,[1] **and Difa Gao**[1]

[1]*State Key Laboratory of Coal Resources and Safe Mining, School of Mines, China University of Mining and Technology, Xuzhou, Jiangsu Province 22116, China*
[2]*School of Mines, China University of Mining and Technology, Xuzhou, Jiangsu Province 22116, China*

Correspondence should be addressed to Jixiong Zhang; zjxiong@163.com and Qiang Zhang; leafkky@163.com

To solve the problems of surface deformation and destruction of buildings caused by urban mining and realise the coordinated development of mining cities, the solid backfilling method was used to extract coal resources beneath the buildings of Tangshan. Based on surface deformation monitoring data of the continuously operating reference station (CORS) system for the past 5 years, the surface deformation process caused by solid backfilling was analysed. The final results revealed a maximum surface subsidence of 66 mm in the *T* zone coal area and 31 mm in the *F* zone area. Furthermore, the surface control effects of the caving method and the solid backfilling method were compared and analysed, and it was shown that solid backfilling could meet the surface building setup requirements. Moreover, based on the probability integral method, the effects on surface deformation due to the surface length of the *F* zone, compression ratio, and coal pillar width were analysed, and the effects on the prediction results due to the subsidence factor, tangent of the major effective angle, and offset distance of the inflection point were studied. The results showed that the compression ratio is the main factor controlling the surface deformation and that it should be kept above 80% for solid backfilling of urban mines. The subsidence factor should be 0.82, and the tangent of the major effective angle should be 2.15 when the surface subsidence of solid backfilling is to be predicted. This paper provides a technical reference for the realisation of urban mining with solid backfilling.

1. Introduction

In recent years, the rapid development of China's economy has increased the demand for coal resources. In 2019 alone, China's coal production reached 3.85 billion tons, a year-on-year increase of 4% [1, 2]. Such large-scale coal resource development has brought exhaustion of conventional coal resources, and some mines have had to explore coal resources beneath buildings, railways, and water bodies, which directly affects and restricts the harmonious development of ecology and society around the mining area. China's production of coal resources from beneath buildings, railways, and water bodies under unified allocation alone has reached 140 billion tons, with the amount of coal resources under

buildings accounting for 70% of the total amount [3, 4]. When such coal resources are mined, the surface deformation causes buildings to be stretched, compressed, and bent, thus causing various degrees of damage and collapse hazards to the buildings. Mining is also accompanied by the discharge of a large amount of solid waste gangue, which pollutes the environment and encroaches on the land. All of these problems cause serious conflicts in the development of a mining city.

The coal industry has been actively exploring ways to coordinate the development of coal mining and mining cities and has done considerable research and practical work. Solid backfill mining [5, 6], which uses backfill to control rock movement and surface subsidence, has become the

main technology to solve the conflicts between the development of the mine and the city. This technology has existed for some time and has been applied in more than 20 mines in China, effectively solving the problem of redundant resource extraction. However, the long-term practice has shown that even the solid backfill mining method can cause large-scale movement and deformation of the ground surface. Current research on this problem has focused mainly on how the fill body controls rock movement, monitoring of surface movement and deformation, and analysis of disasters caused by surface deformation.

Many scholars have researched these problems. Miao et al. [7–9], Zhang et al. [10–12], and Qiang et al. [13, 14] have advanced the equivalent mining height theory, key layer control theory, main roof control theory, and immediate roof control theory. These studies concluded that solid backfill mining can be regarded as extremely thin coal seam mining, allowing the surface subsidence to be controlled. The control targets for solid backfilling in the rock are the key layer, the main roof, and the immediate roof, with the first being the most difficult target and the last being the most precise target. Guo et al. [15–17], Cha et al. [18, 19], and Yao et al. [20, 21] proposed the use of the probability integral method to describe patterns of surface deformation, established a prediction model parameter system for surface subsidence with solid backfilling, and actually measured surface subsidence results using an electronic total station. Fei et al. [22] and Niu et al. [23] further analysed surface deformation characteristics using the analytic hierarchy process evaluation model and evaluation system.

The methods of surface deformation monitoring used in the aforementioned studies are not continuous and cannot show the surface deformation process caused by solid backfill mining because only the control effect of solid backfilling on the overlying rock layer was investigated. In this paper, taking the Tangshan mine as an example, 5 years of continuous surface subsidence data monitored by the continuously operating reference station (CORS) system were used to study the surface subsidence control effect of solid backfill mining. The effects on surface deformation due to surface length, compression ratio, and working surface arrangement were analysed. The effects of the subsidence factor, the tangent of a major effective angle, and offset distance of the inflection point on the prediction results were also studied. Finally, the ranges of the compression ratio control index and the surface subsidence prediction parameters for solid backfill mining in urban mines were obtained.

2. Research Area and Methods

2.1. Mining Geological Conditions.
Tangshan mine, with a field area of $37.28\,km^2$ and a mining area of $55\,km^2$, is located in Lu'nan District, Tangshan City, Hebei Province. It is the only state-owned mega coal mine in China located in a city centre with convenient transportation access. Tangshan mine uses the progressive mining area development method of inclined shafts. At present, there are 7 vertical shafts, which divide the mine into 10 production areas. There are no large-scale faults in the Tangshan minefield, and the main coal seams are 5th, 8th, 9th, and 12th, with average thicknesses of 2.4, 3.7, 3.5, and 6.4 m, respectively. Among these, the 5th coal seam has an immediate roof consisting of 4.8 m thick fine sandstone and a bottom plate of 0.9 m thick mudstone, whereas the 9th coal seam has an immediate roof consisting of 0.7 m thick mudstone and a bottom plate of 1.0 m thick sandy mudstone. The geographical location and working face distribution of the Tangshan mine are shown in Figure 1.

As shown in Figure 2, the production area of Tangshan mine is located beneath the city. The main coal areas are the T zone and the F zone. The T zone has an area of $2.01\,km^2$ and 30.366 million tons of coal, of which 1.427 million tons have been mined to date. There are 67 community and office buildings on the surface. The F zone has an area of $1.27\,km^2$ and 34.413 million tons of coal, of which 34.26 million tons have been mined. Production and living facilities of the mine itself and a park exist at the surface. Figure 2 shows a comparison between the surface and subsurface structures. Figure 3 shows the arrangement of surface deformation observation points.

As examples, the T_3292 working face and the F5001 working face of the Tangshan mine are shown schematically in Figure 4. The T_3292 working face has a length of 90 m, is elevated at an angle, and was in operation from 1 March 2013 to 1 April 2017. The F5001 working face has a length of 66 m, is also elevated at an angle, and was in operation from 1 January 2016 to 1 September 2017.

The T_3292 working face has two surface observation lines, that is, lines A and L (Figure 5), with 22 points online A and 8 points online L. The F5001 working face has one surface observation line, line F, with a total of 22 points. The F5002 working face has four surface observation lines, N, S, W, and E.

The test used the surface subsidence monitoring data obtained from 1 January 2015 to 1 December 2019 as a reference to analyse the surface subsidence after mining on the T_3292 working face, F5001 working face, and F5002 working face. The monitoring data span more than 5 years and so can reflect the long-term surface deformation after solid backfill mining.

2.2. Solid Backfilling Control Method.
The solid backfill mining method, which is carried out through integrated mechanised mining operations on working faces, is used for mining under urban buildings. In the solid backfill coal mining system, the gangue is transported from the surface feeding well and underground separation chamber to the working faces, is then filled into the goaf using key equipment such as the multihole bottom dump conveyor and hydraulic support system for solid backfilling, and is finally compacted by the ramming mechanism behind the hydraulic support system. From 2015 to 2019, the surface feeding well accumulated 604,600 tons of gangue, and the underground separation system accumulated 421,100 tons of gangue. The backfilling system, shown in the basic concept in Figure 4, is running well.
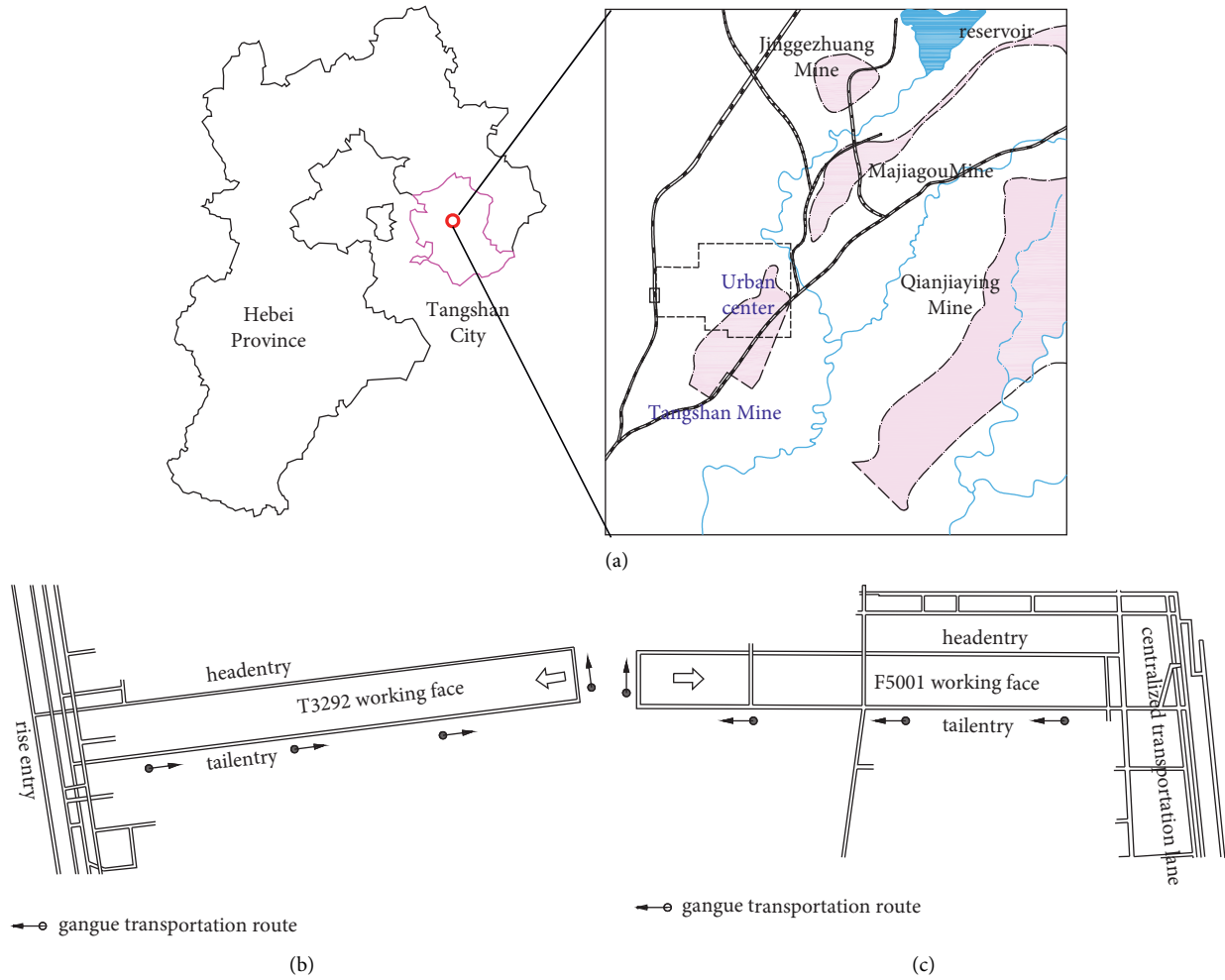
FIGURE 1: Geographical location and working face distribution of Tangshan mine: (a) location of Tangshan mine, (b) layout of T3292 working face, and (c) layout of F5001 working face.

FIGURE 2: Tangshan mine surface-subsurface comparison.

Inspection results of the surface buildings show that the main structures of the surface buildings above Tangshan mine are brick–concrete, brick–wood, and steel structures, which meet the national requirements for Class II–III protection. When mining the coal resources beneath the city, the buildings must be kept below the Class I damage level after mining, that is, horizontal deformation less than 2.0 mm/m, curvature less than 0.2 mm/m^2, and inclination less than 3.0 mm/m.

2.3. Analysis Method of Surface Deformation

2.3.1. Monitoring Method. Monitoring the subsidence and deformation of the surface, buildings, and other structures is
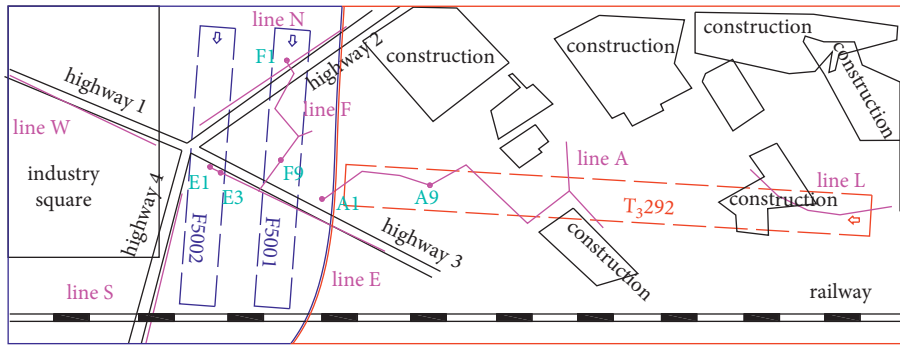
FIGURE 3: Arrangement of surface deformation observation points on solid backfill mining faces.
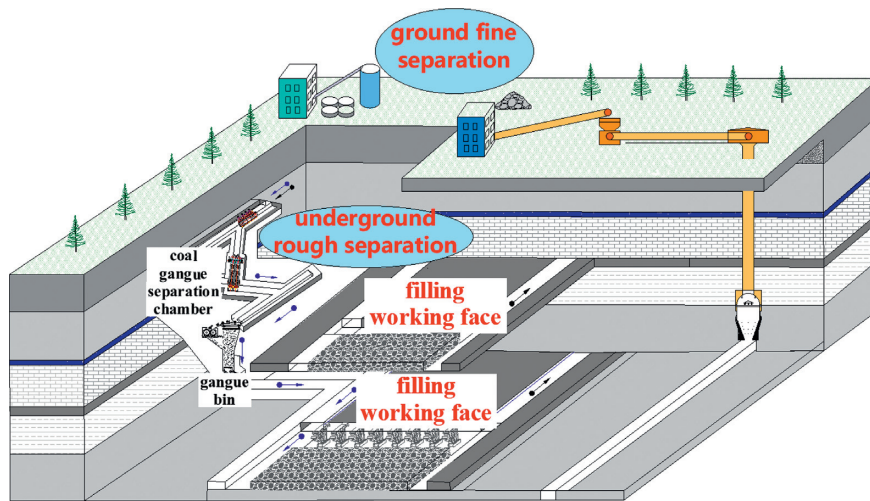
FIGURE 4: Basic concept of solid fill mining.

(a)

(b)
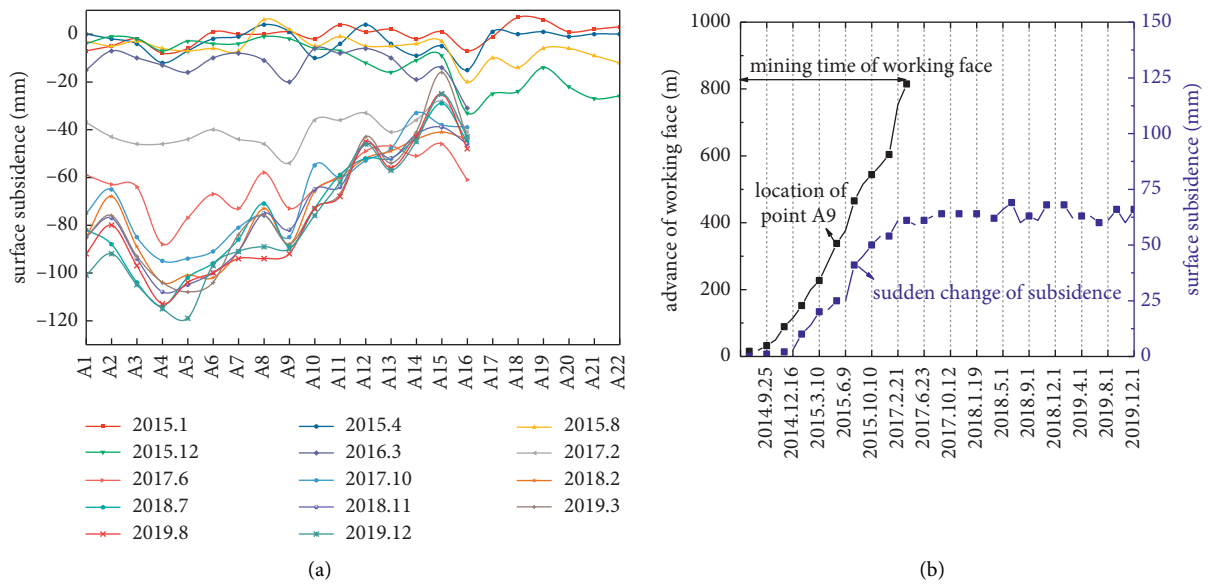
FIGURE 5: Surface subsidence values (a) on line A for each time period and (b) for each time period at measuring point $A9$.

an important task in the process of mining beneath a city. The conventional monitoring methods used for the Tangshan mine include mainly theodolite tracking, total station monitoring, and water level monitoring. The main problems faced in the monitoring process are addressed below. The accuracy of the conventional monitoring methods is not very high. Moreover, the detection process is easily affected by rain, snow, and the mutual obstruction of the surface buildings. In addition, conventional monitoring systems are not capable of continuous monitoring.

The CORS system for intelligent monitoring of surface subsidence can carry out continuous and uninterrupted observation and achieve real-time collection, transmission, calculation, and analysis of data within the subsidence range. The CORS system applied in the Tangshan mine is equipped with China's Beidou Satellite Navigation System, which is compatible with the United States' GPS system and Russia's GLONASS system, to improve the accuracy of surface subsidence deformation measurement. The CORS system basically consists of a data centre, a reference station, a data communication subsystem, and a user application subsystem. It achieves all-weather, fully automatic, and precise positioning through satellite positioning technology, the reference station, and the Internet. The base station and Class I and II measuring points of the Tangshan mine are shown in Figure 6.

2.3.2. Prediction Method.

The probability integral method is used to estimate the surface movement and deformation. Its calculation principle is as follows.

The calculation of subsidence value at any point on the surface is shown in equation (1). The calculation of the inclination deformation value of any point on the surface is shown in equation (2). The calculation of curvature deformation value of any point on the surface is shown in equation (3). The calculation of horizontal movement value of any point on the surface is shown in equation (4). The calculation of horizontal deformation at any point on the surface is shown in equation (5).

$$W(x) = \frac{W_0}{2}\left[\mathrm{erf}\left(\frac{\sqrt{\pi}}{r}x\right) + 1\right], \quad (1)$$

$$i(x) = \frac{W_0}{r}e^{\left(-\pi\left(x^2/r^2\right)\right)}, \quad (2)$$

$$k(x) = -2\pi\frac{W_0}{r^3}xe^{-\left(\pi\left(x^2/r^2\right)\right)}, \quad (3)$$

$$U(x) = bW_0e^{-\left(\pi\left(x^2/r^2\right)\right)}, \quad (4)$$

$$\varepsilon(x) = -2\pi b\frac{W_0}{r^2}xe^{\left(-\pi\left(x^2/r^2\right)\right)}, \quad (5)$$

where $W_0 = M_e q \cdot \cos\alpha$ and $r = H/\tan\beta$. M_e is the equivalent mining height of solid dense filling mining; q is the surface subsidence coefficient of solid dense filling mining; b is the horizontal moving coefficient; $\tan\beta$ is the tangent of the main influence angle; and α is the dip angle of mining seam.

2.3.3. Test Scheme for the Cause of Surface Subsidence.

Taking the F zone as an example, under the mining geological conditions of the Tangshan mine, it is considered that the surface subsidence above the F zone was influenced by the face length, the compression ratio of the working face, and the width of the coal pillar in the section. To analyse the causes of surface subsidence, 15 sets of test plans were designed, as shown in Table 1. Tests 1–5 analysed the effect of face length on surface deformation parameters, tests 6–10 analysed the effect of compression ratio on surface deformation parameters, and tests 11–15 analysed the effect of coal pillar width on surface deformation parameters.

The surface deformation prediction uses the probability integral method based on equivalent mining height. Due to the presence of a large number of primary fissures, joints, and strata in the subsiding rock, it is feasible to predict surface movement and deformation by the probability integral method of the random medium.

In comparison with the caving method, when the probability integral method is used to predict surface subsidence for solid backfill mining, prediction parameters such as the subsidence factor, tangent of a major effective angle, and offset distance of the inflection point change greatly. Therefore, these prediction parameters are considered to have a relatively large influence on the prediction results. Using a compression ratio of 0.8, 15 sets of test plans were designed to analyse the prediction results of surface deformation, and the plans are shown in Table 2. Tests 1–5 analysed the influence of the subsidence factor on the projected results, tests 6–10 analysed the influence of the tangent of the major effective angle on the prediction results, and tests 11–15 analysed the influence of the offset distance of the inflection point on the surface deformation parameters.

3. Results and Interpretation

3.1. Monitoring and Analysis of Filling Surface Deformation

3.1.1. Surface Monitoring Results in Area T.

The T_3292 working face was put into production in March 2013 and stopped being used in April 2017. Line A, measuring surface subsidence in the T zone, crosses the middle of the T_3292 working face, and the projected positions of the selected measuring points below the working face are located at a distance of 340 m from the open-off cut of the working face. The surface subsidence data of each measuring point online A were obtained by processing the monitoring data, as shown in Figure 5(a). The surface subsidence data of each time period at the $A9$ measuring point are shown in Figure 5(b).

As shown in Figure 5(b), the surface subsidence increased slowly from the start of mining on the working face to June 2015, with the subsidence value lower than 25 mm. Between June 2017 and August 2017, after the working face was pushed 90 m beyond measuring point $A9$, the surface subsidence value increased significantly, with its maximum value reaching 41 mm at measuring point $F16$. In April 2017, the working face had been mined completely. By

FIGURE 6: CORS base station and measuring points at Tangshan mine.

TABLE 1: Description of test plans.

Factor	Face length	Compression ratio	Coal pillar width
Test 1	40	0.8	5
Test 2	50	0.8	5
Test 3	60	0.8	5
Test 4	70	0.8	5
Test 5	80	0.8	5
Test 6	60	0.3	5
Test 7	60	0.6	5
Test 8	60	0.7	5
Test 9	60	0.8	5
Test 10	60	0.9	5
Test 11	60	0.8	0
Test 12	60	0.8	5
Test 13	60	0.8	10
Test 14	60	0.8	15
Test 15	60	0.8	20

TABLE 2: Description of test plans.

Factor	Subsidence factor	Tangent of major effective angle	Offset distance of the inflection point
Test 1	0.78	2.15	0.086
Test 2	0.80	2.15	0.086
Test 3	0.82	2.15	0.086
Test 4	0.84	2.15	0.086
Test 5	0.86	2.15	0.086
Test 6	0.82	1.75	0.086
Test 7	0.82	1.95	0.086
Test 8	0.82	2.15	0.086
Test 9	0.82	2.35	0.086
Test 10	0.82	2.55	0.086
Test 11	0.82	2.15	0.006
Test 12	0.82	2.15	0.046
Test 13	0.82	2.15	0.086
Test 14	0.82	2.15	0.126
Test 15	0.82	2.15	0.166

December 2019, the T_3292 working face had reached full mining impact, and its maximum subsidence had increased to 66 mm. From the time of sudden subsidence to full mining impact, the subsidence value increased by approximately 37.8%.

The CORS monitoring system indicated a final maximum surface tilt deformation of 0.76 mm/m, a maximum curvature deformation of 0.064 mm/m^2, and a maximum horizontal deformation of 50.6 mm, or 1.53 mm/m, which meets the surface building protection requirements.

3.1.2. Surface Monitoring Results in Area F

(1) F5001 Working Face. The F5001 working face was put into production in October 2016 and stopped being used in September 2017. Line F, measuring surface subsidence in the F zone, crosses the middle of the F5001 working face, and the projected positions of the selected measuring points under the working face are located at 400 m from the open-off cut of the working face. The monitoring data were processed to obtain the surface subsidence data of each measuring point online F, as shown in Figure 7(a). The surface subsidence data of each time period of measuring point F9 are shown in Figure 7(b).

As shown in Figure 7(b), the surface subsidence increased slowly, with subsidence values lower than 10 mm, from the start of the mining on the working face to May 2017. Between June 2017 and July 2017, after the working face had pushed through 66 m from measuring point F9, the surface subsidence increased significantly, with a maximum value of 19 mm at measuring point F16. In November 2017, the working face was mined completely, and by April 2018, the F5001 working face had reached full mining impact, and its maximum subsidence had increased to 31 mm. From sudden subsidence to full mining impact, the time elapsed was approximately 8 months, and the subsidence value had increased by approximately 38.7%.

The CORS monitoring system indicated a final maximum surface tilt deformation of 1.65 mm/m, a maximum curvature deformation of 0.094 mm/m^2, and a maximum horizontal deformation of 16.1 mm, or 1.25 mm/m, which meets the surface building protection requirements.

(2) F5002 Working Face. The F5002 working face was put into production in November 2017 and stopped being used in December 2018. Line E, measuring surface subsidence in the F zone, crosses the middle of the F5002 working face, and the projected positions of the selected measuring points below the working face are located at 400 m from the open-off cut of the working face. The monitoring data were processed to obtain the surface subsidence data of each measuring point online E, as shown in Figure 8(a). The surface subsidence data of each time period of measuring point E3 are shown in Figure 8(b). There was almost no increase in surface subsidence from the start of mining on the working face to September 2018. Mining on the working face was fully stopped in December 2018, and by July 2019, the surface subsidence of the F5002 working face had reached 17 mm. By December 2019, the full mining impact had been reached, and the maximum increase in subsidence was 25 mm. From sudden subsidence to full mining impact, the time elapsed was approximately 5 months, and there was an increase in subsidence value of approximately 47.1%.

The CORS monitoring system indicated a final maximum surface tilt deformation of 0.29 mm/m, a maximum curvature deformation of 0.012 mm/m^2, and a maximum horizontal deformation of 7.84 mm, or 0.81 mm/m, which meets the surface building protection requirements.

3.2. Analysis of Surface Deformation Monitoring by Caving Method.
Observation of the surface movement and deformation caused by mining on the F5009 working face started in February 2018, and a total of 27 observations were made until August 2020. Line N, measuring the surface subsidence in the caving area, crosses the middle of the F5009 working face, and the projected positions of the selected measurement points below the working face are located 400 m from the open-off cut of the working face. The surface subsidence data of each measurement point online N are shown in Figure 9(a). The surface subsidence data of each time period of measuring point n4 are shown in Figure 9(b).

As shown in Figure 9(b), in comparison with solid backfill mining, the initial value of surface subsidence of the caving method was larger, reaching 60 mm. As mining on the working face continued, the value of surface subsidence increased gradually without any sudden increase. The maximum value of subsidence of measuring point n4 reached 210 mm by August 2020, when all of the mining operations on the working face had been completed.

The CORS monitoring system indicated a final maximum surface tilt deformation of 6.65 mm/m, a maximum curvature deformation of 0.59 mm/m^2, and a maximum horizontal deformation of 168.1 mm, or 4.25 mm/m, which does not meet the surface building protection requirements.

3.3. Comparative Analysis on Control Effect of Different Mining Methods.
A comparison of surface deformation parameters between the solid backfill mining method and the caving method is shown in Table 3.

In addition, the relationship between surface subsidence values and monitoring time was analysed for T$_3$292, F5001, and F5002. The monitoring data were acquired at the time points of the goaf square period, end of mining, 3 months after mining, 1 year after mining, and 2 years after mining. The analysis results showed that the surface subsidence of backfill mining was significantly affected by monitoring time. Although the surface did not show large subsidence during the mining, surface subsidence increased significantly from 3 months to 1 year after mining. The time of 2 years after backfill mining can be regarded as the time when mining was completed, and the surface subsidence above the working face did not increase further at this time.

3.4. Determination of Surface Prediction Parameters in Tangshan Mine.
According to the surface subsidence monitoring results of the Tangshan mine of previous years, the subsidence factor of the Tangshan mine with the caving method was determined to be between 0.55 and 0.85; the tangent of the major effective angle was between 1.92 and 2.40; and the offset distance of the inflection point was 0. Through parameter inversion of the surface subsidence in the F zone, the subsidence factor of backfill mining was determined to be 0.028, and the tangent of the major effective angle was 1.20, as shown in Table 4.

(a)

(b)
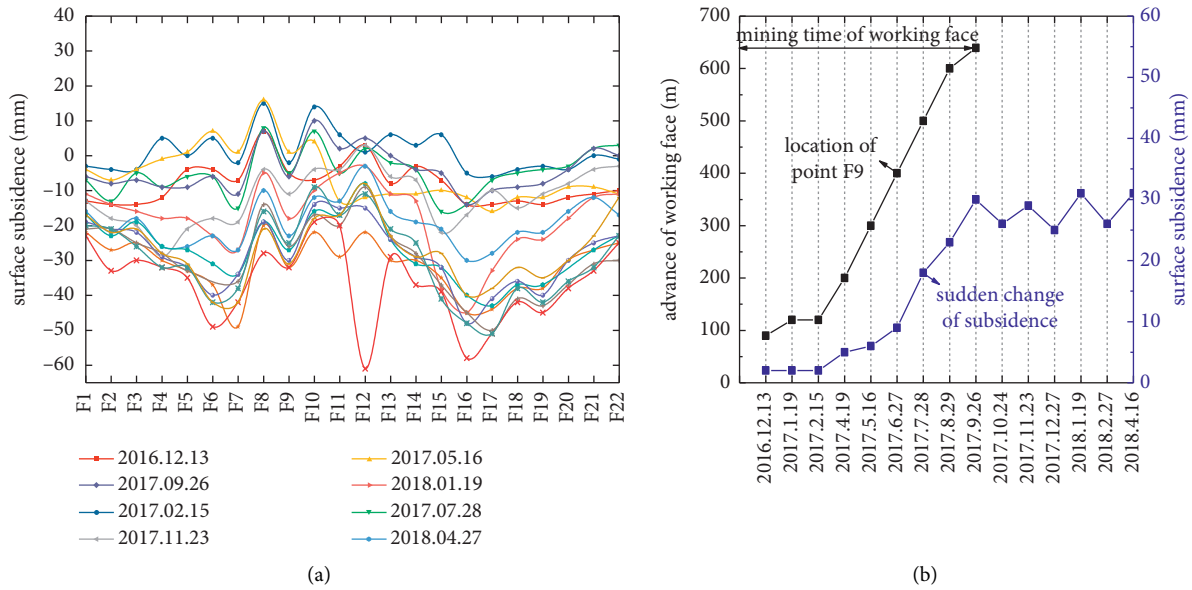
FIGURE 7: Surface subsidence values (a) on line F for each time period and (b) for each time period at measuring point *F9*.

(a)

(b)
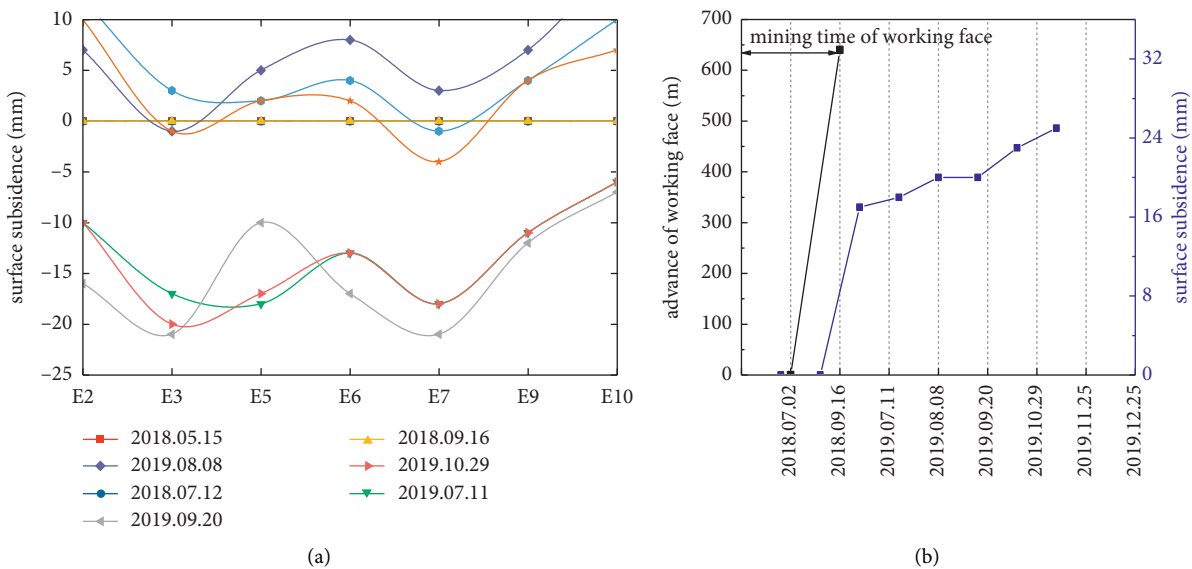
FIGURE 8: Surface subsidence values (a) at line E for each time period and (b) for each time period at measuring point *E3*.

As shown in Table 4, the surface subsidence prediction parameters currently obtained from monitoring one to two working faces are not accurate, as the subsidence factor is extremely low. The prediction with these parameters is thus not representative of the surface subsidence after mining in the area. Therefore, by comparing the predicted results of surface subsidence, considering multiple factors in the *F* zone, the subsidence factor appropriate for the predicted subsidence with solid backfill mining of underground coal in the Tangshan mine was determined to be 0.82, and the tangent of the major effective angle is 2.15. At this time, the predicted result of surface subsidence is 152 mm, which can be regarded as the final amount of surface subsidence after the end of mining in the *F* zone.

4. Discussion

Surface subsidence is greatly affected by mining areas; it is necessary to analyse the influencing factors of surface subsidence. At the same time, the parameters of surface subsidence prediction will change accordingly. An analysis software was used for coal mining subsidence prediction, and the results are shown in Table 5. The surface subsidence, horizontal deformation, curvature, and tilt deformation under different influencing factors were analysed and compared. The test results obtained are shown in Figure 10.

As shown by the analysis in Figure 10, the subsidence, horizontal deformation, curvature, and tilt deformation increase gradually as the face length increases gradually. The

(a)

(b)
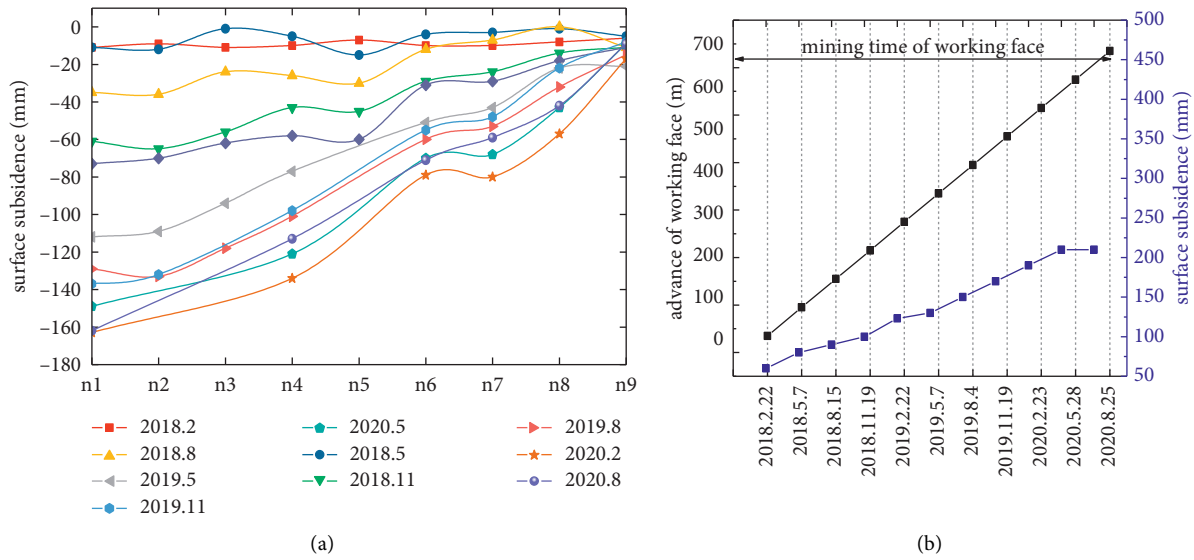
FIGURE 9: Surface subsidence values (a) on line N for each time period and (b) for each time period at measuring point $n4$.

TABLE 3: Comparison of surface deformation parameters between infill mining and collapse mining.

Mining method	Working face	Maximum subsidence (mm)	Maximum tilt deformation (mm/m)	Maximum curvature deformation (mm/m^2)	Maximum horizontal deformation value (mm)	Maximum horizontal deformation (mm/m)
Backfill method	T3292	66	0.76	0.064	50.6	1.53
	F5001	31	1.65	0.094	16.1	1.25
	F5002	25	0.29	0.012	7.84	0.81
Caving method	F5009	210	6.65	0.59	168.1	4.25

TABLE 4: Calibration of projected surface parameters for the Tangshan mine.

Item	Subsidence factor	Tangent of major effective angle	Offset distance of the inflection point	Horizontal movement coefficient	Mining impact propagation angle
Caving method	0.55–0.85	1.92–2.4	0	0.33	82
Backfilling method (experience)	0.85–0.89	1.62–2.20	0.05–0.240	0.33	82
Backfilling method (measured)	0.028	1.20	0	0.33	82
Backfilling method (simulated)	0.82	2.15	0	0.33	82

subsidence, horizontal deformation, curvature, and tilt deformation decrease gradually as the compression ratio increases gradually, and the subsidence, horizontal deformation, curvature, and tilt deformation do not change much with an increase in coal pillar width.

In particular, when the compression ratio is 0.3, that is, the caving method is used to deal with the hollow area, the surface deformation exceeds the set damage level; thus, the compression ratio is the main influencing factor of surface deformation. From the predictive analysis of surface deformation, it is apparent that the compression ratio should be 0.6 or more to ensure the safety of surface buildings. In consideration of the influence due to early subsidence of the roof of the mining area, the compression ratio should be at least 0.8 in an actual backfilling operation.

An analysis software was used for coal mining subsidence prediction, and the results are shown in Table 6. The surface subsidence, horizontal deformation, curvature, and tilt deformation under different influencing factors were analysed and compared. The test results obtained are shown in Figure 11.

From the analysis shown in Figure 11, as the subsidence factor increases gradually, the subsidence increases gradually while the horizontal deformation, curvature, and tilt deformation tend to stabilise. As the tangent of the major effective angle increases, the subsidence, horizontal

TABLE 5: Predicted results.

Test	Subsidence	Horizontal deformation	Curvature	Tilt
1	108	−0.7	−0.01	±0.5
2	131	−0.9	−0.01	±0.6
3	152	−1.0	−0.01	±0.7
4	173	−1.1	0	±0.8
5	194	−1.2	−0.01	0.9
6	533	−3.4	−0.03	2.5
7	304	−2.0	−0.02	1.5
8	228	−1.5	±0.01	1.1
9	152	−1.0	−0.01	±0.7
10	76	−0.5	0	0.4
11	153	−1.0	−0.01	±0.7
12	152	−1.0	−0.01	±0.7
13	152	−1.0	−0.01	±0.7
14	151	−1.0	−0.01	±0.7
15	150	−0.9	−0.01	±0.7
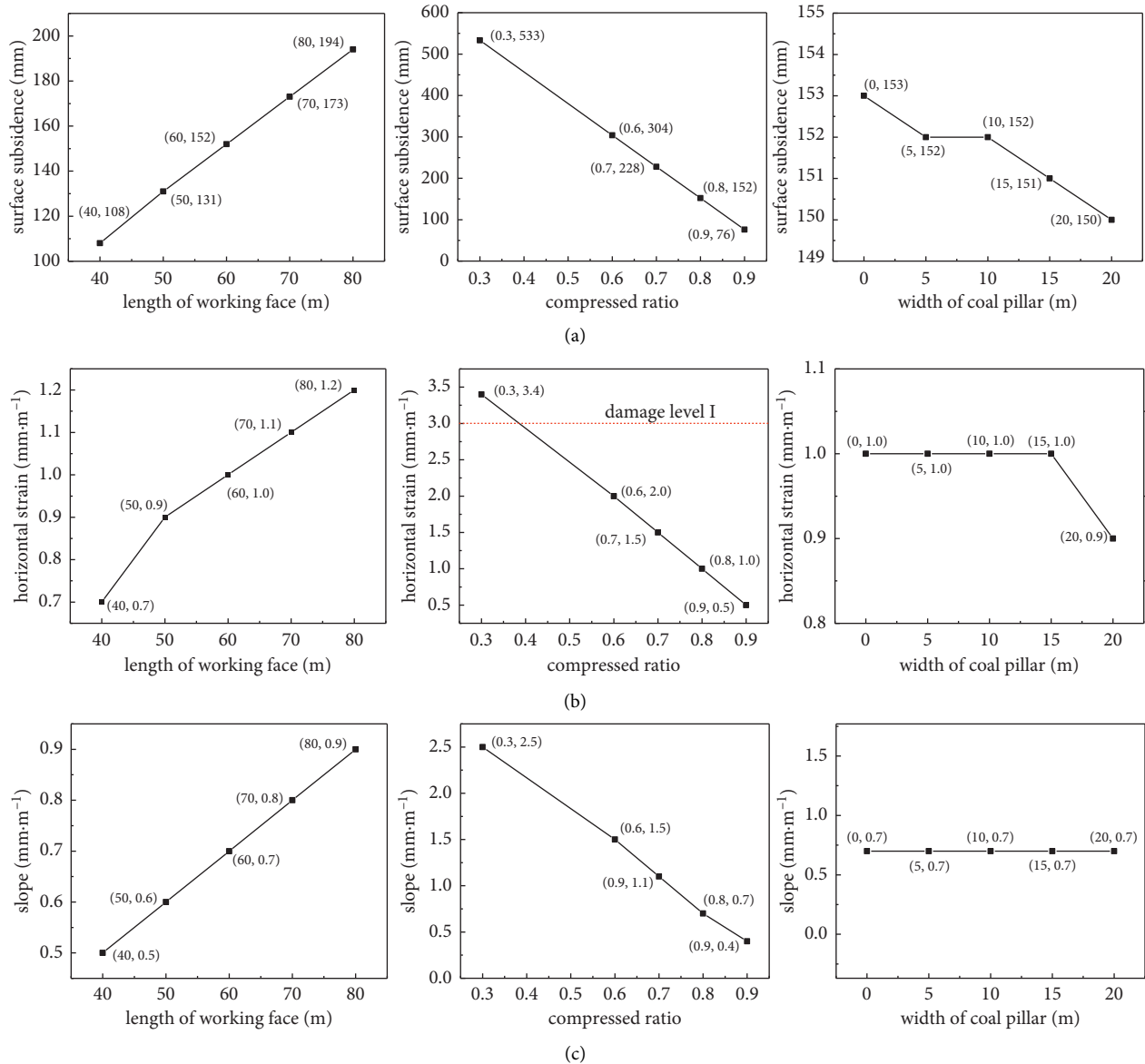
FIGURE 10: Experimental results: (a) surface subsidence values, (b) horizontal deformation, and (c) tilt.

TABLE 6: Predicted results.

Test	Subsidence	Horizontal deformation	Curvature	Tilt
1	145	−0.9	−0.01	±0.7
2	148	−1.0	−0.01	±0.7
3	152	−1.0	−0.01	±0.7
4	156	−1.0	−0.01	±0.7
5	159	−1.0	−0.01	0.8
6	121	−0.6	0	0.5
7	137	−0.8	−0.01	±0.6
8	152	−1.0	−0.01	±0.7
9	167	−1.2	−0.01	0.9
10	181	−1.3	±0.01	±1.0
11	152	−1.0	−0.01	±0.7
12	152	−1.0	−0.01	±0.7
13	152	−1.0	−0.01	±0.7
14	152	−1.0	−0.01	±0.7
15	152	−1.0	−0.01	±0.7
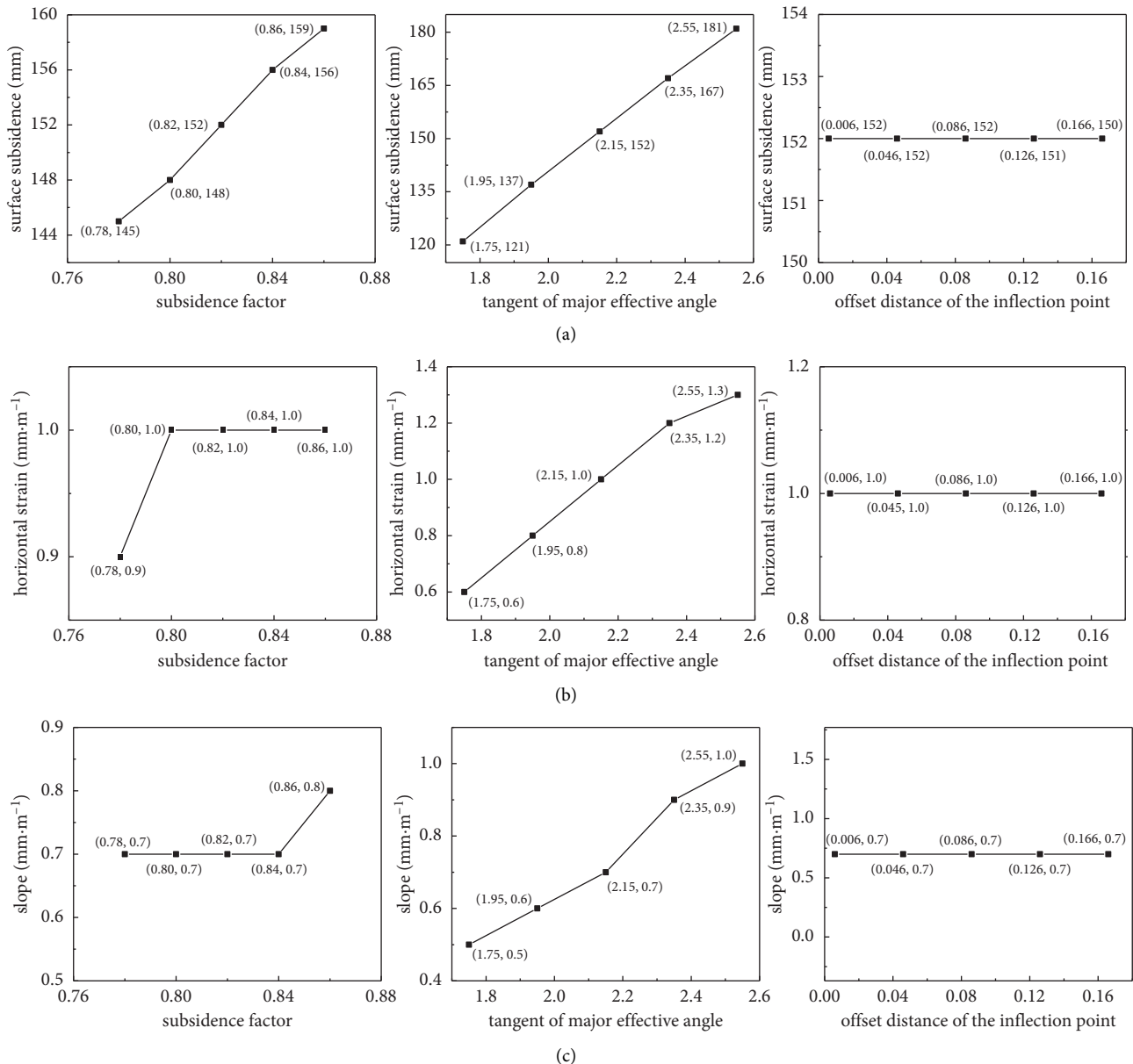
FIGURE 11: Predicted results: (a) surface subsidence values, (b) horizontal deformation, and (c) tilt.

deformation, curvature, and tilt deformation increase gradually. As the offset distance of the inflection point increases, the subsidence, horizontal deformation, curvature, and tilt deformation do not change.

It can be seen that the subsidence factor is the main influencing factor of the surface subsidence prediction results and that the tangent of the major effective angle is the main factor affecting the prediction results of surface horizontal deformation and tilt.

5. Conclusion

(1) The CORS system was used to monitor the surface subsidence of coal mining under Tangshan city, which spanned more than 5 years and covered the T zone and the F zone, corresponding to a mining area of $150,000 \, m^2$. The monitoring results showed that the surface protection requirements of urban mining were met by solid backfill mining, which had gentler surface deformation than caving mining. The maximum subsidence in the T zone after 32 months of working face mining was 66 mm, and the maximum subsidence in the F zone after 6 months of working face mining was 31 mm.

(2) Through the multifactor surface subsidence prediction based on the probability integral method, it was concluded that surface subsidence is strongly influenced by the working face length and the compression ratio. The surface deformation increases gradually as the face length increases and the compression ratio decreases. To ensure the safety of surface buildings, the compression ratio must be at least 0.8.

(3) By comparing the actual measurement data in the field with the quality simulation data, the subsidence factor suitable for the Tangshan mine was finally determined to be 0.82, and the tangent of major effective angle was determined to be 2.15, at which time the predicted results are close to the subsidence results after extensive backfill mining in the mining area.

Data Availability

The data used to support the findings of this study are included within the article.

Disclosure

This manuscript was presented as a preprint in research square (https://www.researchsquare.com/article/rs-221271/v1).

Conflicts of Interest

The authors declare that there are no conflicts of interest.

Authors' Contributions

All authors contributed equally to this research.

References

[1] H. Xie, G. Feng, J. U. Yang, and S. University, "Research and development of rock mechanics in deep ground engineering," *Chinese Journal of Rock Mechanics and Engineering*, vol. 11, pp. 2161–2178, 2015.

[2] H. P. Xie, F. Gao, Y. Ju, M. Z. Gao, R. Zhang, and Y. N. Gao, "Quantitative definition and investigation of deep mining," *Journal of China Coal Society*, vol. 40, no. 1, pp. 1–10, 2015.

[3] H. P. Xie, H. W. Zhou, D. J. Xue, H. W. Wang, R. Zhang, and F. Gao, "Research and consideration on deep coal mining and critical mining depth," *Journal of China Coal Society*, vol. 37, no. 37, pp. 535–542, 2012.

[4] L. Yuan, "Thoughts and suggestions on cracking major scientific and technological problems in deep coal mining," *Science and Technology Review*, vol. 34, no. 2, p. 1, 2016.

[5] J. Zhang, N. Zhou, Y. Huang, and Q. Zhang, "Impact law of the bulk ratio of backfilling body to overlying strata movement in fully mechanized backfilling mining," *Journal of Mining Science*, vol. 47, no. 1, pp. 73–84, 2011.

[6] Z. Qiang, Z. Jixiong, H. Yanli, and J. Feng, "Backfilling technology and strata behaviors in fully mechanized coal mining working face," *International Journal of Mining Science and Technology*, vol. 22, no. 2, pp. 151–157, 2012.

[7] D. Zhou, K. Wu, X. Miao, and L. Li, "Combined prediction model for mining subsidence in coal mining areas covered with thick alluvial soil layer," *Bulletin of Engineering Geology and the Environment*, vol. 77, no. 1, pp. 283–304, 2018.

[8] J. Zhang, Q. Zhang, A. J. S. Spearing, X. Miao, S. Guo, and Q. Sun, "Green coal mining technique integrating mining-dressing-gas draining-backfilling-mining," *International Journal of Mining Science and Technology*, vol. 27, no. 1, pp. 17–27, 2017.

[9] W. Yin, X. Miao, J. Zhang, and S. Zhong, "Mechanical analysis of effective pressure relief protection range of upper protective seam mining," *International Journal of Mining Science and Technology*, vol. 27, no. 3, 2017.

[10] H. Yan, J. Zhang, N. Zhou, S. Zhang, and X. Dong, "Shaft failure characteristics and the control effects of backfill body compression ratio at ultra-contiguous coal seams mining," *Environmental Earth Sciences*, vol. 77, no. 12, p. 458, 2018.

[11] J. Zhang, Q. Sun, A. Fourie, F. Ju, and X. Dong, "Risk assessment and prevention of surface subsidence in deep multiple coal seam mining under dense above-ground buildings: case study," *Human and Ecological Risk Assessment*, vol. 25, no. 4, pp. 1–15, 2018.

[12] Y. Hao, Z. Jixiong, Z. Sheng, and Z. Nan, "Physical modeling of the controlled shaft deformation law during the solid backfill mining of ultra-close coal seams," *Bulletin of Engineering Geology and the Environment*, vol. 78, no. 5, pp. 3741–3754, 2019.

[13] S. Qiang, Z. Jixiong, Z. Qiang, and Y. Hao, "A case study of mining induced impacts on the stability of multi-tunnels with the backfill mining method and controlling strategies," *Environmental Earth Sciences*, vol. 77, no. 6, pp. 1–13, 2018.

[14] Z. Qiang, Z. Ji-Xiong, Q. I. Wen-Yue, Z. Nan, and T. Yang, "Structure optimal design research on backfill hydraulic support," *Journal of Central South University*, vol. 24, no. 7, pp. 1637–1646, 2017.

[15] H. Li, J. Zha, G. Guo, N. Zheng, and Y. Gong, "Improvement of resource recovery rate for underground coal gasification through the gasifier size management," *Journal of Cleaner Production*, vol. 259, Article ID 120911, 2020.

[16] X. Liu, G. Guo, and H. Li, "Thermo-mechanical coupling numerical simulation method under high temperature heterogeneous rock and application in underground coal gasification," *Energy Exploration and Exploitation*, vol. 4, Article ID 014459871988898, 2020.

[17] G. Zhang, Y. Lv, G. Guo, and C. Yu, "Monitoring deep mining similarity material model of super-thick and weak cementation overburden by digital photography," *IOP Conference Series: Materials Science and Engineering*, vol. 782, Article ID 022028, 2020.

[18] W. Qi-Chun, G. Guang-Li, Z. Jian-Feng, and X. Yong, "Study on surface ground movement law of coal rejects backfill mining under thick and loose overburden strata," *Coal Science and Technology*, vol. 41, 2013.

[19] H. Li, G. Guo, and N. Zheng, "Influence of coal types on overlying strata movement and deformation in underground coal gasification without shaft and prediction method of surface subsidence," *Process Safety and Environmental Protection*, vol. 120, pp. 302–312, 2018.

[20] Q.-l. Yao, Z. Xia, C.-j. Tang et al., "Characteristics of heavy metal ion adsorption by silty mudstones in coal mine goafs," *Geofluids*, vol. 2020, no. 4, 17 pages, Article ID 8560151, 2020.

[21] Z. Chong, Q. Yao, X. Li, and K. Shivakumar, "Acoustic emission investigation on scale effect and anisotropy of jointed rock mass by the discrete element method," *Arabian Journal of Geosciences*, vol. 13, no. 9, pp. 1–14, 2020.

[22] J. Fei, L. I. Xiangdong, W. Bing, and L. I. Qiang, "Influence analysis of strata movement in subsequent cemented filling of panel second-step stopes," *Mining Research and Development*, vol. 36, no. 10, pp. 94–98, 2016.

[23] D. X. Niu, P. Wang, Q. Wang, F. Y. Hua, F. Wang, and Z. H. Cai, "Analysis of the power plant security management capability based on the ISM and AHP," *Advanced Materials Research*, vol. 960-961, pp. 1477–1482, 2014.

Research Article

Mechanical Transformation of Fly Ash toward Its Utilization in Cemented Paste Backfill

Haijun Wang [1,2] **and Yun Duan**[1]

[1]*BGRIMM Technology Group, Beijing 100160, China*
[2]*School of Resource and Civil Engineering, Northeastern University, Shenyang 110819, China*

Correspondence should be addressed to Haijun Wang; wang_hj@bgrimm.com

Fly ash (FA) showed low reactivity when being used to prepare the binder for cemented paste backfill (CPB). In the present work, wet-grinding treatment was used to increase the pozzolanic reactivity of FA and promote its sustainable utilization. The results showed that wet-grinding could be a suitable and efficient technology for FA pretreatment. Wet-grinding strongly modified the structure of FA by decreasing the crystalline phase content and the binding energy of Si 2p and Al 2p, contributing to the increase in pozzolanic reactivity of FA. The performance of CPB samples prepared by wet-ground FA was then optimized. This was reflected by the acceleration in the sample setting and increase in the strength development. The compressive strength of the CPB samples prepared by wet-ground FA for 120 min was increased by around 40% after curing for 28 d compared with the control samples.

1. Introduction

Coal is the most abundant natural mineral resources on the earth, and it is also one of the main energy sources used by all countries [1–3]. One of the main uses of coal is to burn coal to generate electricity, which accounted for 72% of China's total power generation in 2015 [2]. Fly ash (FA) is the solid waste produced by coal-fired power plants [4–6]. It is the fine ash collected from the flue gas of coal combustion. FA can cause great harm to ecological environment and human health [7, 8]. On the one hand, a large number of FA particles collected by electrostatic precipitators are stored in the open air, occupying a large amount of land. On the other hand, the FA contains V, Cr, Ni, Cd, Pb, As, Zn, Mo and Cu and other heavy metals, which could cause serious pollution to the land, water, and air environment and then endangers human health [9–11]. Besides, fine FA particles are difficult to be captured by the dust collector and directly discharged into the atmosphere, becoming one of the main sources of atmospheric pollution. The fine FA submicron particles have a large concentration and usually contain a large number of

toxic metal substances, which stay in the atmosphere for a long time. Once inhaled by the human body, it can penetrate deeply into the human alveoli, causing serious harm to human health. As a result, resource utilization of FA could alleviate its harm to environment and human body and balance the relationship between resources and environment.

FA has a wide range of applications. At present, its main technologies include manufacturing building materials (including cement [12], concrete [13], geopolymer [14, 15], road materials [16, 17], and engineering backfill materials [18, 19], soil improvement [20], synthesis of porous materials [21, 22], and extraction of valuable metals [23]. Considering the potential pozzolanic reactivity of FA, utilization of fly ash as pozzolanic material to replace part of cement has been proved to be an efficient way of FA disposal [24]. The addition of FA could modify the rheological properties of the fresh slurry due to the "ball effect" resulting from the spherical shape of the fly ash particles [25]. Besides, the finer particles of FA can fill the voids among cement grains and then increase the packing density and mechanical strength

[26]. Durability of FA cement pastes and mortars in aggressive conditions has also been reported. The resistance of high volume FA cement pastes and mortars has been monitored when attacked by HCl, Na_2SO_4 solution, and sea water [24]. The FA cement binder showed satisfactory resistance to the aggressive solutions comparing to a commercially available sulfate resistant cement reference [24].

Although some benefits from the utilization of FA as cement additives have been reported, some negative effects, such as delay of the setting time, have also been reported resulting from the poor reactivity of FA [27, 28], although the influence of FA is highly dependent on its characteristics. As reported by Zeng et al. [27], the FA reaction extent is still at a low level even after three months. Besides, negative effect of FA on the strength development (especially at early ages) and durability of FA cement was also reported. Obvious reduction in the compressive strength before 28 d was noticed even with low FA replacement [29]. The mechanical and physical properties of mortars with and without fly ash addition were investigated after being attacked by NaCl and $MgSO_4$ solutions by Yildirim and Sümer [30]. The results indicated that the increase in the FA content seemed to have a negative effect on the mortar specimens. For example, flexural and compressive strength of 20% FA replaced mortar specimens cured in water, NaCl and $MgSO_4$ solutions were higher compared with 50% FA replaced the mortar specimens. For this regard, the replacement level of FA in concrete is typically limited in the range of 15–25% [31], which restricts the large scale utilization of FA. Therefore, it is generally believed that reducing the particle size of fly ash and improving the reactivity can promote the recycling of FA in cementitious materials.

Cemented paste backfill (CPB) is one of the strategies for the comprehensive utilization of industrial wastes [32]. During the process of CPB, ordinary Portland cement (OPC) is the main cementitious materials, accounting for approximately 70% of the total cost of CPB [33]. The high cost of OPC clearly increases the total cost of mine production. On the other hand, OPC production is considered as an energy-intensive process with the large power consumption, resulting in the emission of large amount of CO_2, which accounts for approximately 5–8% of the total CO_2 emissions in the world [34, 35]. Thus, it is necessary to prepare alternative binders with lower cost and CO_2 emissions. Using supplementary cementitious materials seems to be one of the commonly used methods to lower the OPC utilization.

FA has been reported to be used in CPB. Liu et al. [36] studied the consequences of temperature on the physical and mechanical properties and microstructure of CGFB when using FA in CPB at a mass ratio of cement: coal gangue: fly ash of 1 : 2 : 5. The increase of curing temperature promotes the early appearance of pozzolanic effect of fly ash. Higher curing temperatures made early compressive strength of CPB specimens increase, but later compressive strength decreased due to the decrease of the bonding of the internal structure due to the thermal damage [36]. Cavusoglu et al. [18] studied the effect of sodium silicate as an accelerator on early age mechanical and microstructure properties of

cemented coal fly ash backfill (CCB). Sodium silicate was found to accelerate setting time and strength of CCB. In another study [37], the effect of water-reducing admixtures on properties of CCB was studied. Admixtures enhanced short- and long-term CCB strengths up to 33% and decreased the porosity. However, to the best of our knowledge, there are few studies focusing on the effect of pretreated FA on the properties of CPB samples. Mechanical refinement is one of the most effective treatment technologies for industrial solid waste disposal [38]. After mechanical activation, the reactivity of the mineral particles is increased due to the physical and chemical alterations [39]. Mechanical activation could decrease the particle size and increase the specific surface area and then increase the contact area between the reactive substances [40]. Therefore, in the present work, wet-grinding was used to pretreat FA with the aim of increase its pozzolanic reactivity. The effect of wet-grinding was evaluated via physical structure, mineralogical modification, and dissolution behavior. The wet-ground FA was used in CPB. The reaction kinetic, setting time, compressive strength development, and pore structure of the CPB samples were then investigated.

2. Materials and Methods

2.1. Materials.
Two types of fly ash (FA) studied in the present work were collected from Liaoning and Hebei, China, respectively. The received FA was dried in an oven under 105°C for 24 h. Ordinary Portland cement (42.5R) produced by CR Cement Co. Ltd was used in the present work. The chemical compositions of the cement are listed in Table 1, measured via X-ray fluorescence (XRF). The specific surface area of the cement was 334 m^2/kg, measured using the Blaine method.

2.2. Experiments

2.2.1. Mechanical Treatment of Fly Ash.
The mechanical treatment of FA was conducted using a wet-grinding method by a vertical stirred mill. Zirconia ball was used as grinding medium with a weight ratio of 10 mm : 8 mm : 6 mm : 2 mm = 1 : 4 : 6 : 2. Zirconia balls, FA, polycarboxylate-based superplasticizers (PCE), and water were poured into the mill after separately weighted with the ratio of water/FA = 0.5, FA/grinding media = 0.5, PCE/FA = 0.3%. The FA was then ground for 10, 30, 60, and 120 min using the motor speed of 450 rpm. After reaching the designed grinding duration, the balls were separated. The FA slurry was then used for the following tests with no need to be dried. FA was wet-milled for 10, 30, 60, and 120 min and was labeled as FA10, FA30, FA60, and FA120, respectively. The raw FA without mechanical treatment was named as FA0.

2.2.2. Dissolution Behavior.
The ground dried FA samples were placed into NaOH solution (0.10 mol/L) at a liquid/solid ratio of 100 ml/g and stirred for 36 hours. The solution was then filtered via a preweighed 0.2 μm nylon syringe filter

TABLE 1: Chemical compositions of the cement (wt.%).

CaO	Al$_2$O$_3$	SiO$_2$	MgO	Fe$_x$O	Na$_2$O	K$_2$O	SO$_3$	MnO$_2$	P$_2$O$_5$
58.23	6.84	25.65	5.29	2.77	0.19	0.16	0.79	0.05	0.03

at designed time intervals. The dissolved tailings can be calculated as follows:

$$\text{dissolved mass percentage} = \frac{1 - m}{1} \times 100\%, \qquad (1)$$

where m is the weight of undissolved solid particles.

2.2.3. Pozzolanic Reaction. The method used in [41, 42] was conducted to investigate the pozzolanic reactivity of FA. First, FA, limestone, and portlandite were dry-mixed before NaOH solution being poured into the mixture. The H$_2$O/binder ratio of 0.5 was used in this work. After mixing for 2 min, the paste was poured into 20 mL centrifuge tubes and cured at 20°C until the targeted ages. Table 2 shows the mix proportion.

2.2.4. Utilization of Wet-Ground Fly Ash in Cemented Paste Backfill. To prepare the CPB samples, OPC was replaced by FA of 40 wt%. The OPC, FA, and tailings were dry-mixed for 1 min before adding water. In the present work, the binder/tailings ratio was 1/6, and the solid content was 72 wt%. The mixture was then poured into cylindrical plastic molds with a dimension of 50 mm in diameter and 100 mm in height after blended for another 2 min. The samples were then sealed and cured at 20°C/95% R.H. for one day. After that, the samples were demolded and cured at 20°C/95% R.H. until designated curing ages. To study the reaction kinetic, the paste without tailings addition was used, and similar preparation procedure like the preparation of CPB samples illustrated above was conducted.

2.3. Characterization Methods. The particle size distribution of FA was tested via a Malvern Mastersizer 2000 in a range from 0.02 μm to 2000 μm using alcohol as dispersion medium.

X-ray diffractometry (XRD) was used to identify the phase assembles of the samples via a Shimadzu XRD-7000. For the hydrated samples, the hardened samples were crushed to <74 μm. After that, they were rinsed with isopropanol (A.R., 99.7%) and stirred for 1 h for the reaction stopping. Next, they were filtered and used for XRD analysis after dried for 24 h under vacuum condition. The samples were scanned in the range between 5° and 50° with a rate of 2° per minute.

Thermogravimetric tests were carried out using a thermogravimetry (TG)/differential thermal analysis system (STA409PC). The heating temperature ranged from room temperature to 1000°C using a heating rate of 15°C/min. The tests were conducted under an atmosphere of high-purity nitrogen.

Microstructure of the samples was observed with a scanning electron microscopy system (Zeiss Gemini 300). For the unhydrated FA samples, FA particles were uniformly

TABLE 2: Mix proportion of the system for pozzolanic reactivity tests (wt.%).

FA	Portlandite	Limestone	NaOH	H$_2$O/binder
50	38	10	2	0.5

dispersed on a double-sided adhesive tape and coated with a gold film to increase electrical conductivity. The microscope was operated in the high vacuum mode, with an accelerating voltage of 20 kV.

X-ray photoelectron spectroscopy (XPS) analysis was conducted using a Thermo ESCALAB 250XI XPS system with a monochromatic Al Kα X-ray beam ($hv = 1486.68$ eV) having a diameter of 500 μm.

A TAM Air isothermal calorimeter (TA/TAM AIR-8) was used to test the heat release during the hydration. The method for slurry preparation was similar to that illustrated in Section 2.2. After preparation, the slurry was immediately transferred to the isothermal calorimeter for testing. The recording duration was about 72 h at 20°C.

The setting time of the composites was measured by the depth of penetration of the Vicat needle into the composites following the method in [43]. The compressive strength of the composites was measured using the standard method ASTM C39. Before testing, the top and bottom surfaces of the cylindrical samples were ground flat for good contact with the probe. The ultimate data was derived from the average values of at least three samples.

The pore structure was analyzed by mercury intrusion porosimetry (MIP, Autopore IV 9500). Crushed samples with a size of 1-2 mm were used. Before testing, the crushed samples were rinsed with isopropanol (A.R., 99.7%) as illustrated previously.

A Brookfield RSR-SST rheometer was used to measure the rheological parameters (i.e., yield stress and plastic viscosity) of fresh CPB mixtures. The rotator was a four-bladed vane type with a diameter and length of 20 and 40 mm, respectively. Rheological testing was performed after pouring the prepared fresh CPB into the test cup following the rheology protocol shown in Figure 1. First, the fresh CPB slurry was homogenized via a preshear phase at 100 s^{-1} lasting 60 s. This was followed by a ramp-up (0 ⟶ 100 s^{-1}) and ramp-down (100 ⟶ 0 s^{-1}) process conducted within 120 s after resting for 15 s. The data were collected from the descending stage.

3. Results and Discussion

3.1. Characterization of the Raw Fly Ash. The chemical composition of the two studied FA is shown in Table 3. It was clearly that the main compositions of both the two FA were Al$_2$O$_3$ and SiO$_2$, accounting for more than 80% of the total content. This was in line with previous reports [44, 45].
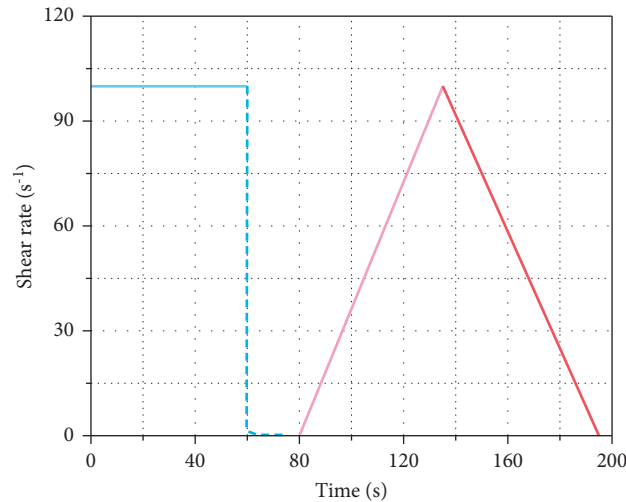
FIGURE 1: Schematic representation of the applied rheology protocol.

However, FA1 clearly contained more Al_2O_3 compared with FA2, which contained higher amount of SiO_2. More CaO was detected in FA1, while FA1 contained more MgO. The differences in the chemical composition could lead to the various behavior when being used to prepared binders.

Figure 2 shows the microstructure of the two FA. The shape of FA1 was irregular and mainly consisted of spongy hollow vitreous particles with loose structure as shown in Figure 2(a). FA2 was dominated by spherical particles. The shape of the particles was reported to highly influence the rheological properties of the slurry.

3.2. Mechanical Transformation of Fly Ash

3.2.1. Particle Size Distribution.
The particle size distribution of FA before and after mechanical activated for 10 min, 30 min, 60 min, and 120 min is presented in Figure 3. Wet-grinding strongly modified the particle size distribution. As shown from Figures 3(a) and 3(b), only one main peak was noticed in the particle size distribution curves of both FA1 and FA2, no matter the grinding duration. This was different from our previous work about the particle size distribution of mechanical activated coal gangue, where a typical bimodal distribution was observed [38]. Besides, the peak of the particle size distribution got narrower with the increase of the grinding duration, indicating a more uniform particles [46]. Figures 3(c) and 3(d) shows that the d10, d50, and d90 values of the two FA decreased with the increase of grinding duration. These values did not show significant changes after grinding for 60 min. At the same time, the specific surface area (SSA) obtained from the particle size analysis data gradually increased with the grinding duration: increase from $1137 \, m^2/g$ to $2614 \, m^2/g$ for FA1, and $1331 \, m^2/g$ to $2608 \, m^2/g$ for FA2, respectively.

3.2.2. X-Ray Diffraction and X-Ray Photoelectron Spectroscopy Analysis.
The mineralogical structure changes of FA resulting from wet-grinding are shown in Figure 4.

The XRD results showed that the main crystalline phases were mullite and quartz. No new phases were identified after wet-grinding, even after grinding for 120 min. However, the intensity for quartz and mullite decreased after wet-grinding. This was mainly caused by the sheer force and friction between grains and grinding media, leading to plastic deformation of the particles and collapse of the crystalline structure [47]. The reason why FA presented lower reactivity under attacking of alkaline species was the high crystalline content; thus, the reduction of quartz and mullite intensity could then favor the enhancement of the reactivity of FA.

X-ray photoelectron spectroscopy (XPS) analysis was used to investigate the surface characteristics of FA after wet-grinding, and the results are shown in Figure 5. It was found that the binding energy of both Si 2p and Al 2p in the two FA decreased with the grinding time. A similar phenomenon was reported elsewhere [46, 47]. The reduction in the binding energy of Si and Al is beneficial to the increase in the pozzolanic reactivity as it witnessed an easy breakage of chemical bonds during reaction [46].

3.2.3. Dissolution Behavior of the Mechanically Treated Fly Ash in Alkaline Solution.
The reaction of FA under alkali activation started from the dissolution of solid particles, which is considered as the crucial procedure for the conversion of the solid particles into available source material [48]. The dissolution behavior also controlled the reaction and properties of OPC/FA composites [38]. Thus, it is necessary to make sense of the dissolution behavior of the FA after mechanical activation. The dissolution behavior of FA under alkaline environment was shown in Figure 6. The testing results showed a parabolic trend, where the dissolved FA increased with the dissolution time until around 20 h at far-from-equilibrium conditions. After that, the dissolution reached equilibrium with only minor amounts dissolved. This was in line with previous reports about the dissolution behavior of other mineral particles [48, 49]. One difference was that more time was needed to reach dissolution equilibrium in this experiment. This could be attributed to the

TABLE 3: Chemical compositions of the raw FA.

Raw materials	CaO	Al_2O_3	SiO_2	MgO	Fe_xO	Na_2O	K_2O	SO_3	MnO_2	P_2O_5	SrO	TiO_2	ZrO_2	LOI
FA1	3.82	47.93	38.73	0.31	5.91	0.25	0.26	0.33	0.26	0.64	0.03	1.5	0.03	0.92
FA2	1.55	25.52	62.31	1.4	6.52	0.47	0.54	0.27	0.31	0.15	0.02	0.85	0.09	1.26
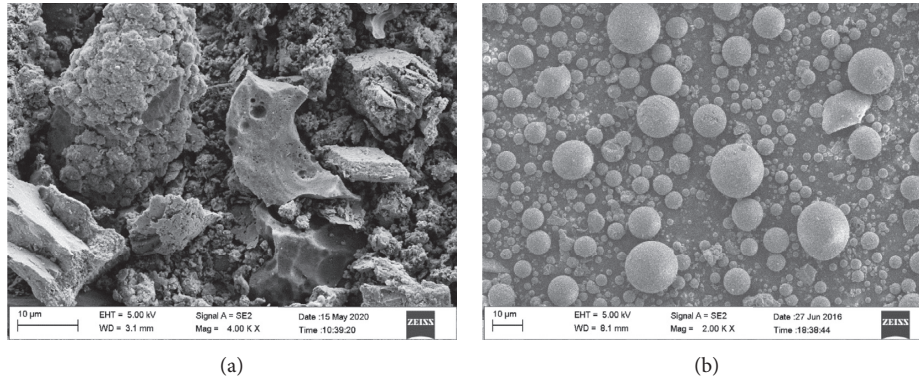
FIGURE 2: Microstructure of the FA: (a) FA1 and (b) FA2.

lower reactivity of FA compared with the materials used elsewhere, such as calcined clay [48]. Both FA1 and FA2 showed an increased trend in the dissolution rate after wet-grinding. The faster dissolution confirms the enhanced reactivity of FA after wet-grinding. On the other hand, FA2 clearly showed higher dissolution rate than that of FA1.

3.2.4. Pozzolanic Performance. Figure 7 shows the calorimetry test results of the pozzolanic test. The heat release during the pozzolanic was caused by the dissolution of FA in alkaline environment with the formation of hydration gels. The heat flow curves, as shown in Figures 7(a) and 7(b), were different from that of the cement-based binders, mainly resulting from the low reaction rate during the alkali activation process. Generally, wet-grinding increased the heat release rate in both FA1 and FA2, indicating that the pozzolanic reactivity increased with the wet-grinding time. This was in line with the dissolution tests' results, which showed that the dissolved FA increased with the mechanical grinding duration. Besides, FA2 presented higher heat flow rate than that of the FA1, suggesting a higher pozzolanic reactivity.

Figures 7(c) and 7(d) show the total heat flow during the pozzolanic reaction, and the cumulative heat flow increased with the wet-grinding time. The raw FA presented lower reactivity and witnessed a low total heat release, reaching around only 23.19 J/g and 39.04 J/g for FA1 and FA2, respectively. After wet-grinding for 120 min, the total heat release increased dramatically, reaching 76.77 J/g and 117.51 J/g for FA1 and FA2, respectively. This directly proves the effect of the wet-milling process, where the pozzolanic reactivity of FA was enhanced after wet-grinding. This could lead to more FA dissolving (Figure 7) and taking part in the pozzolanic reaction, contributing to more hydration heat release.

Thermogravimetry (TG) analysis was used to investigate the constituent parts of the hydration products of the pozzolanic reaction, and the results are shown in Figure 8. The peak located between 50°C and 200°C was caused by the decomposition of the C-S-H. This implied that mechanical grinding did not modify the phase assembles of the hydration products. Besides, it was clear that the intensity of this peak increased with the grinding duration. This phenomenon suggested that more FA participated into the pozzolanic reaction, in line with the results of dissolution tests. On the other hand, FA2 presented higher intensity of this peak than that of the FA1, indicating that FA2 showed higher pozzolanic reactivity than FA1.

3.3. Utilization of the Mechanically Treated Fly Ash in Cemented Paste Backfill

3.3.1. Reaction Kinetics of the Pastes. The early reaction kinetics of the binders used for CPB was studied by isothermal calorimetric analysis. Figure 9 shows the calorimetry test results of the paste binders of FA-OPC used for cemented paste backfill. Generally, four stages were noticed in all the heat flow rate curves (Figures 9(a) and 9(b)), that is, the initial, induction, acceleration, and deceleration stages. Wet-grinding clearly promoted the binders hydration, which was reflected by shortening the induction period and the heat flow rate at the main peak. Table 4 summarizes the kinetic data for the all the binders. For FA1, the ending time of the induction period (t_1) decreased from 8.22 h to 7.68 h, 7.32 h, 7.04 h, and 6.86 h when wet-grinding for 10 min, 30 min, 60 min, and 120 min, respectively. This was accompanied by the advance of the occurrence of the main hydration peak, from 19.29 h to 17.93 h, 16.84 h, 15.76 h, and 14.58 h, after wet-grinding for 10 min, 30 min, 60 min, and 120 min, respectively. At the same time, the maximum heat

(a)

(b)

(c)

(d)
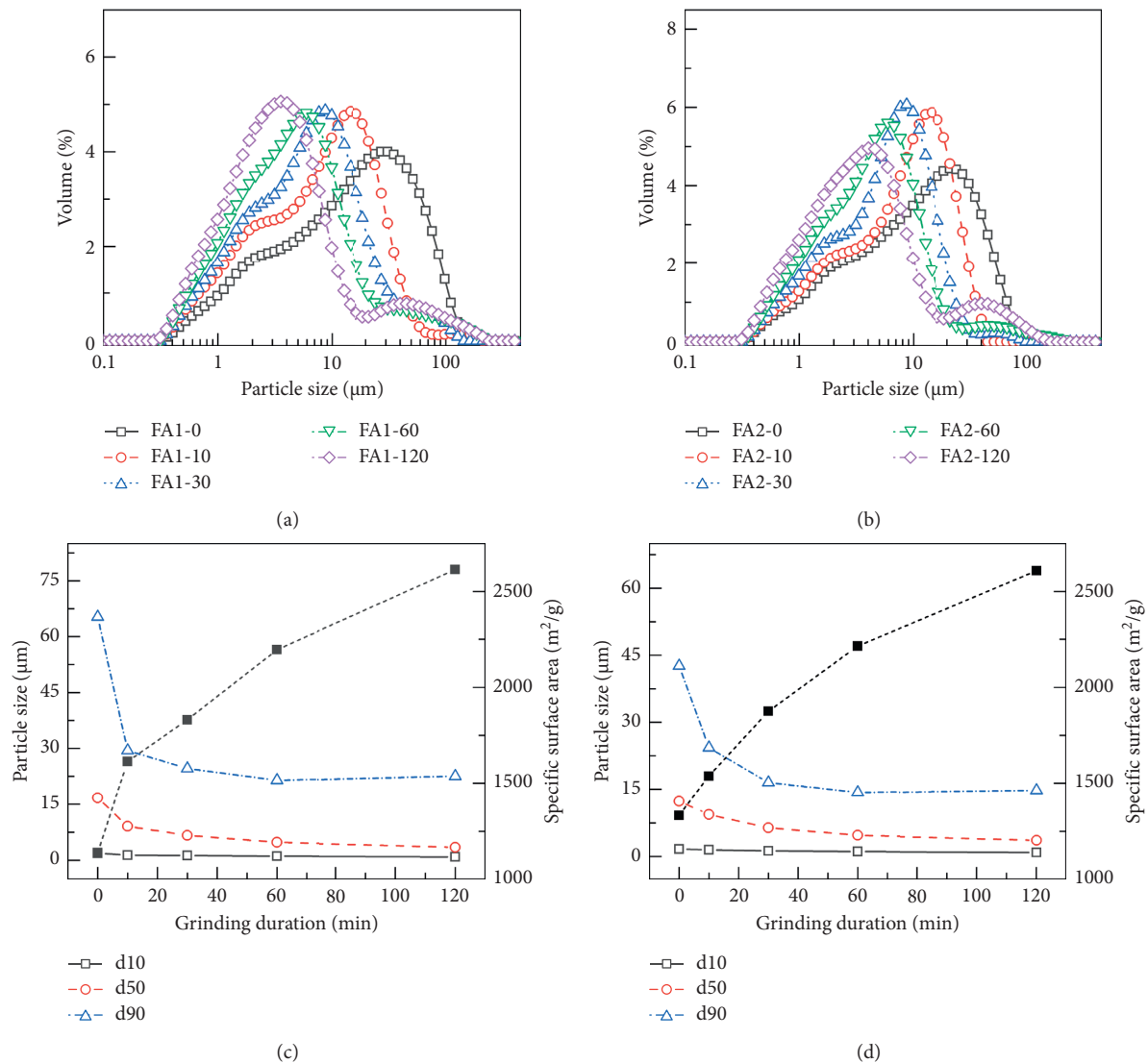
Figure 3: Particle size distribution of (a) FA1 and (b) FA2; characteristic particle parameters (c) FA1 and (d) FA2.

release rate increased by around 10.89%, 12.50%, 5.56%, and 6.02%, for FA1-10, FA1-30, FA1-60, and FA1-120, respectively. All these suggested that the acceleration of cement hydration. Similar trend happens in the FA2 samples. Figures 9(c) and 9(d) show the cumulative heat release during the binders' hydration for 72 h. It was clear that mechanical grinding increased the total heat release in both FA1 and FA2, as listed in Table 4.

The acceleration was attributed to two factors. For one thing, the pozzolanic reactivity of FA was increased as illustrated in Section 3.2.4 after mechanical activation. More FA would participate into the reaction under the activation of portlandite from the cement hydration. For another, the fine particles of FA could act as crystal nucleus to reduce the induction period and accelerate the hydration process, which is known as the "nucleus effect" [50]. This was consistent with previous reports, which indicated that the application of superfine additives could accelerate the cement hydration, including synthesized C-S-H [51–53],

ferrihydrite nanoparticle [54], and SiO_2, TiO_2, and Fe_2O_3 nanoparticles [55]. The "nucleus effect" clearly increased with the increase of grinding duration as more fine FA particles would be produced under the mechanical milling, as shown in Figure 3. This led to a more obvious effect on the acceleration of the hydration process.

3.3.2. Rheological Properties. Rheological properties were the important performance of fresh CPB [56], which affected the pumping efficiency and mine production [57]. Thus, the rheological properties of the fresh cemented paste backfill were tested, and the results are shown in Figure 10. As shown in Figure 10(a), the yield stress increased with the wet-grinding duration, suggesting that higher threshold amount of stress is required to initiate flow. Comparing with the controlled samples, after wet-grinding for 10 min, 30 min, 60 min, and 120 min, the yield stress increased by 48.01%, 38.94%, 26.91%, and 4.49%, respectively. This negative effect of mechanical
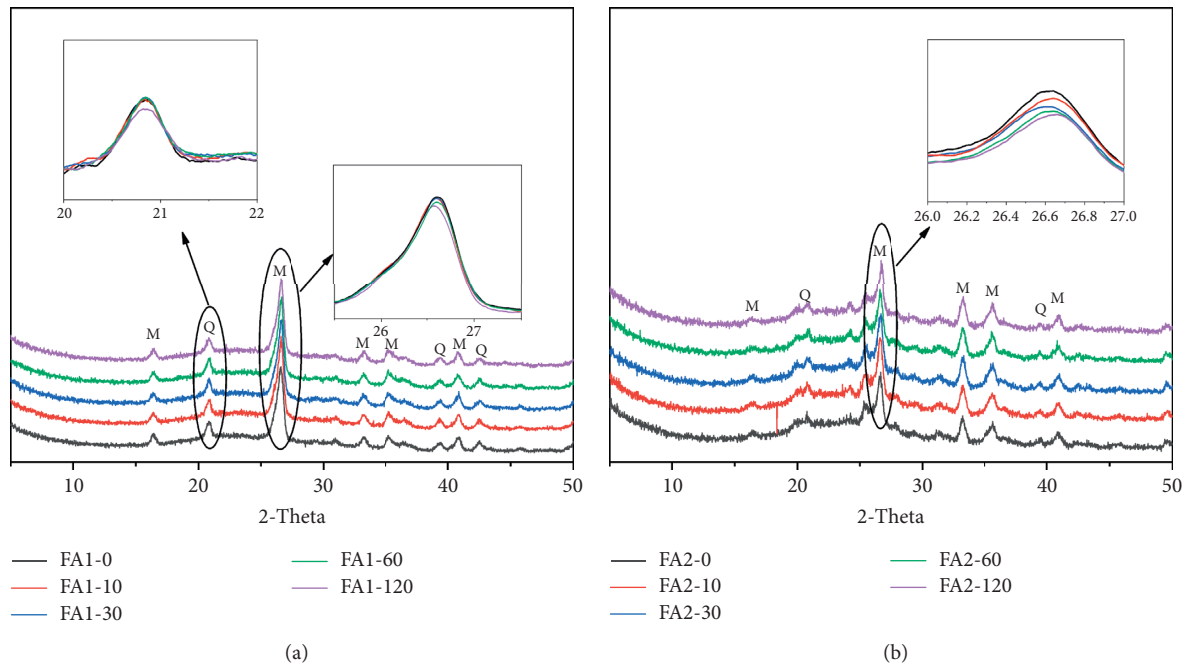
FIGURE 4: Phase assembles of FA: (a) FA1 and (b) FA2 (M: mullite; Q: quartz).

grinding on the yield stress can be attributed to the combined effect of the following mechanisms: the coupling effect of particle packing density and specific surface area is the key to the yield stress and plastic viscosity of CPB. On the one hand, the increase of the packing density will increase the extra water amount to form the water film; on the other hand, the increase of the specific surface area will decrease the thickness of the water film. Therefore, although the packing density of the granular system increases due to the filling effect of fine grains, the specific surface area also increases, and the net effect of these two factors leads to the phenomenon in this paper; the pozzolanic reactivity was increased after mechanical activation, as shown in Section 3.2.4. This led to promoted hydration process with the formation of more hydration gels in a shorter time compared with the controlled sample, resulting in increased yield stress. This could be confirmed by the promoted hydration rate in the calorimetry test results, as shown in Figure 9. Indeed, an increase in hydration products and a reduction in free water enhances the interfrictional resistance of the particle assembly of the CPB, which in turn increases the yield stress [58].

The flowability of the fresh CPB is shown in Figure 10(b), and it was clear that the flowability of both the samples prepared with FA1 and FA2 decreased with the grinding duration. For the samples with raw FA1 addition, the flowability of the fresh CPB was around 25.6 cm. After wet-grinding for 10 min, 30 min, 60 min, and 120 min, the flowability decreased to about 23.7 cm, 22.1 cm, 20.2 cm, and 18.2 cm, respectively. The reduction in the flowability was caused by the increased yield stress, as shown in Figure 10(a). In general, to fulfill the requirement of transportation to stopes by pumping or self-flowing, the flowability of the fresh CPB slurry should be 19–27 cm [59]. The flowability of the slurry was slightly below the minimum

requirement for CPB when adding FA1 after wet-ground for 120 min.

As shown in Figure 2, FA2 was dominated by spherical particles. The "ball effect" of FA2 particles contributes to higher flowability. Although FA2 showed higher pozzolanic reactivity, which can form more hydration gels in a shorter time than FA1 and decrease the flowability, it is obvious this factor has a minor effect. Thus, the physical properties of FA showed a higher impact on the flowability of binders than the chemical properties.

3.3.3. Setting Time and Compressive Strength. The setting time and compressive strength, which determine the mining process and safety, are another two factors influencing the practical applications of the cementitious binders in CPB [60–62]. The initial setting time and compressive strength after curing for 28 d are shown in Figures 11(a) and 11(b). The CPB samples using raw FA1 and FA2 showed a relatively long initial setting time, reaching around 10.2 h and 8.1 h, respectively (Figure 11(a)). Wet-grinding significantly promoted the initial setting of the CPB samples. The reduction of the initial setting time was approximately 39.2% and 33.3% when the FA was ground for 120 h. This phenomenon was in line with the calorimetry test results, where the reaction was promoted by the wet-grinding, leading to faster formation of hydration gels. This would then promote the samples setting. FA2 showed faster setting than FA1, resulting from its higher pozzolanic reactivity, as illustrated in Section 3.2.4.

Figure 11(b) shows the compressive strength of the CPB samples after curing for 28 d. The compressive strength of the CPB samples was low when using the raw FA, reaching around 0.87 MPa and 0.98 MPa, respectively, after curing for 28 d. This
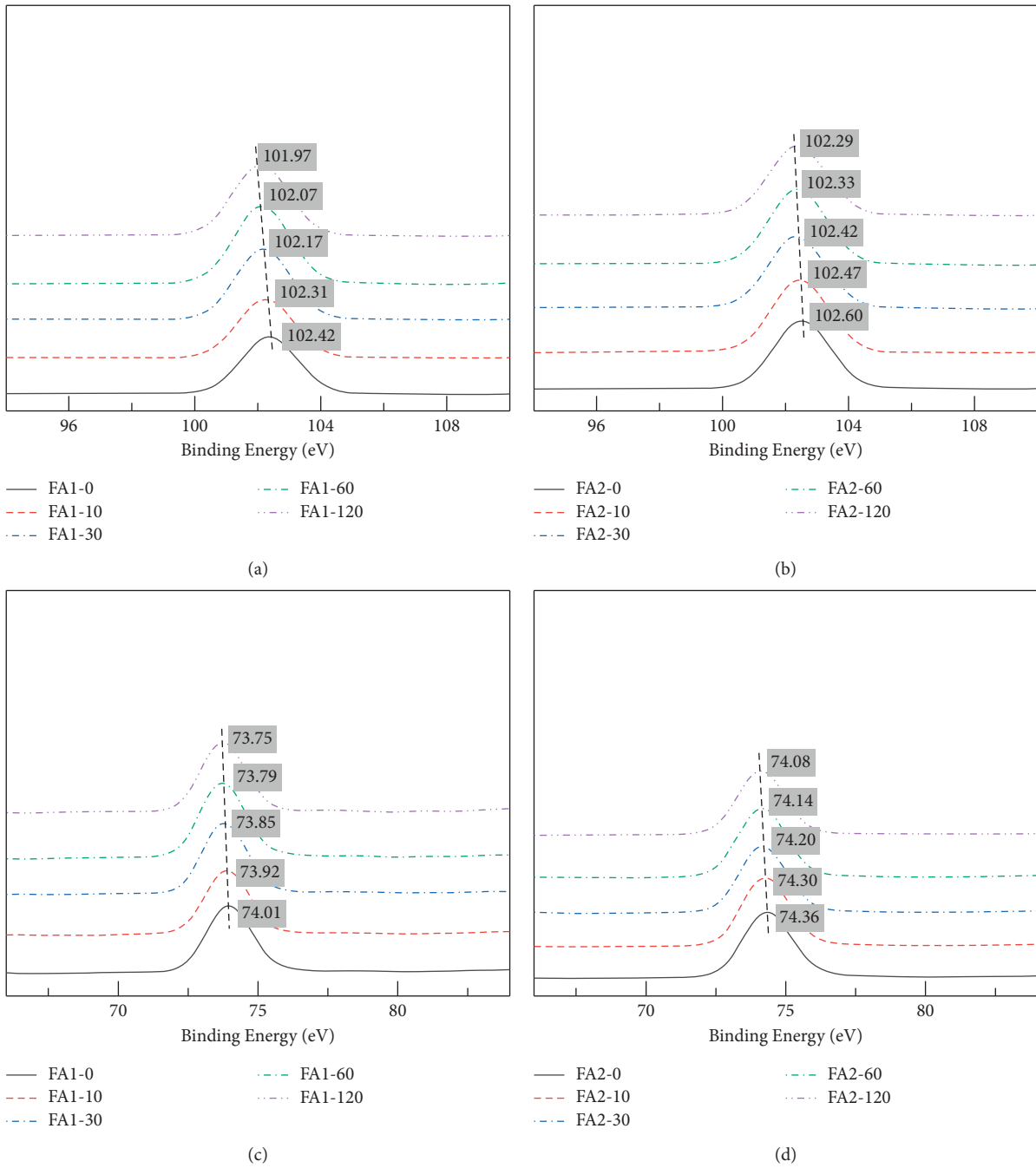
Figure 5: XPS analysis results: (a, b) Si 2p and (c, d) Al 2p.

was attributed to the relatively lower pozzolanic reactivity of the raw FA, in line with previous reports about the FA-doped cement [63]. After wet-grinding, the compressive strength increased with the grinding time, reaching around 1.21 MPa and 1.36 MPa for FA1 and FA2, respectively, after grinding for 120 min. As illustrated in Section 3.2.6, the pozzolanic reactivity increased after mechanical grinding, leading to more FA participating in the reaction. Besides, more fine particles were produced after grinding, which contributed to the reaction process due to the more "nucleation sites." Furthermore, the finer particle could fill the voids during the hardening of the cement, leading to more compact matrix. All these could favor the strength development of the samples. During the reaction of FA-cement, FA will dissolve under the alkali activation of portlandite. FA2 clearly showed higher dissolution rate, as shown in Figure 6. This will then contribute to the formation of more hydration gels, favoring the strength development.

3.3.4. Pore Structure. The pore structure of the hardened CPB samples after curing for 28 d is shown in Figure 12. According to a previous report [64], the pores in the

(a)

(b)
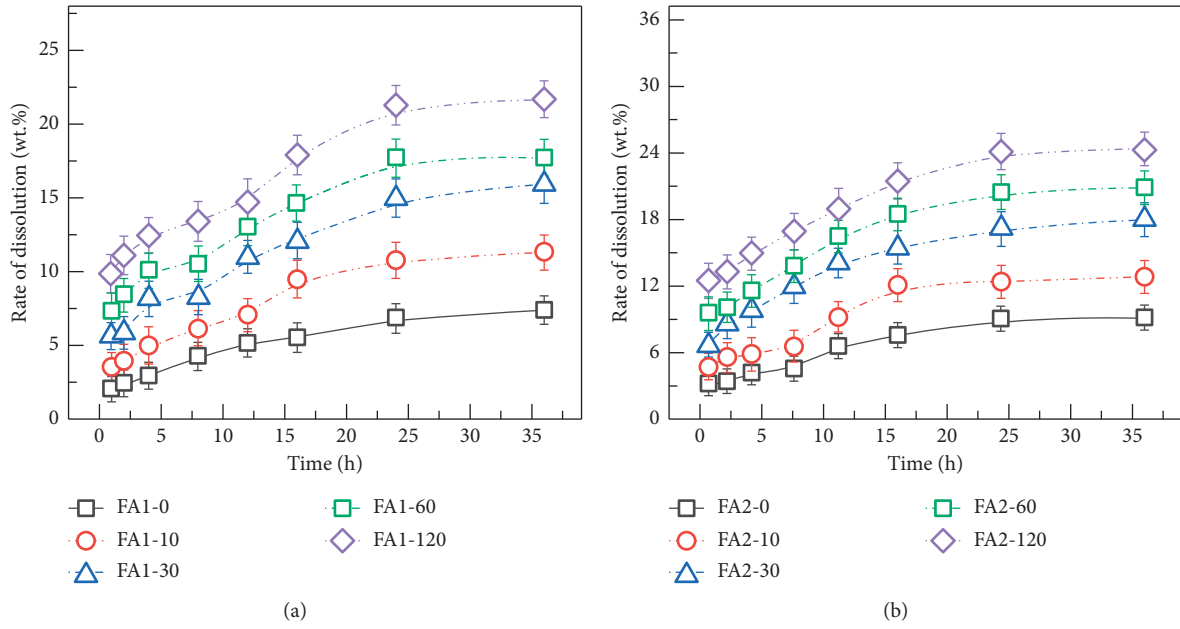
FIGURE 6: Dissolution characteristics of the fly ash: (a) FA1 and (b) FA2.

(a)

(b)
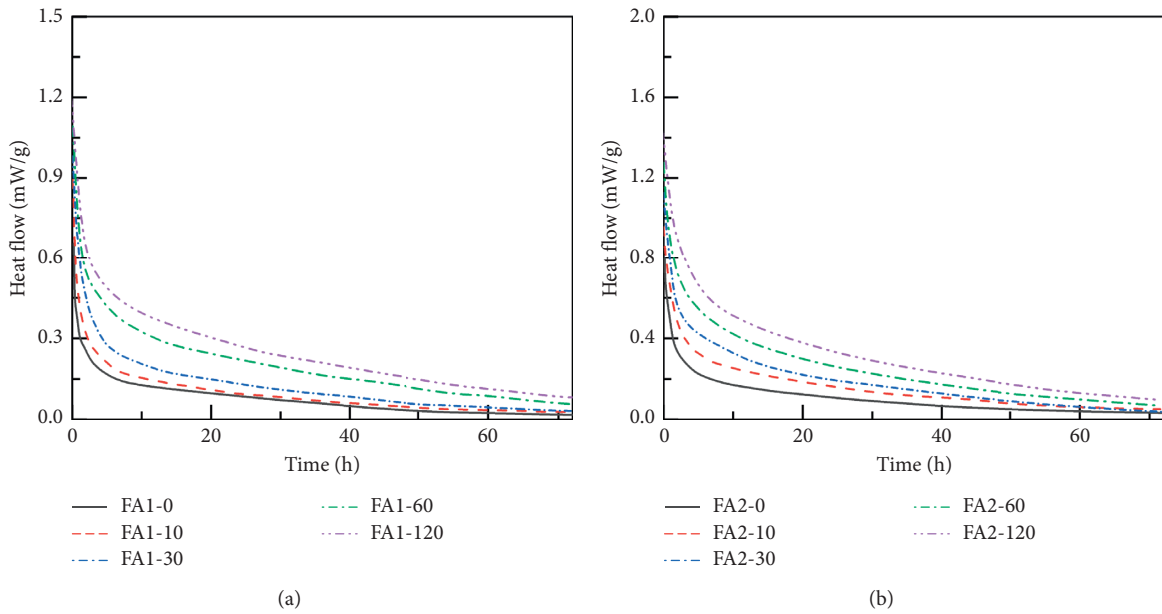
FIGURE 7: Continued.
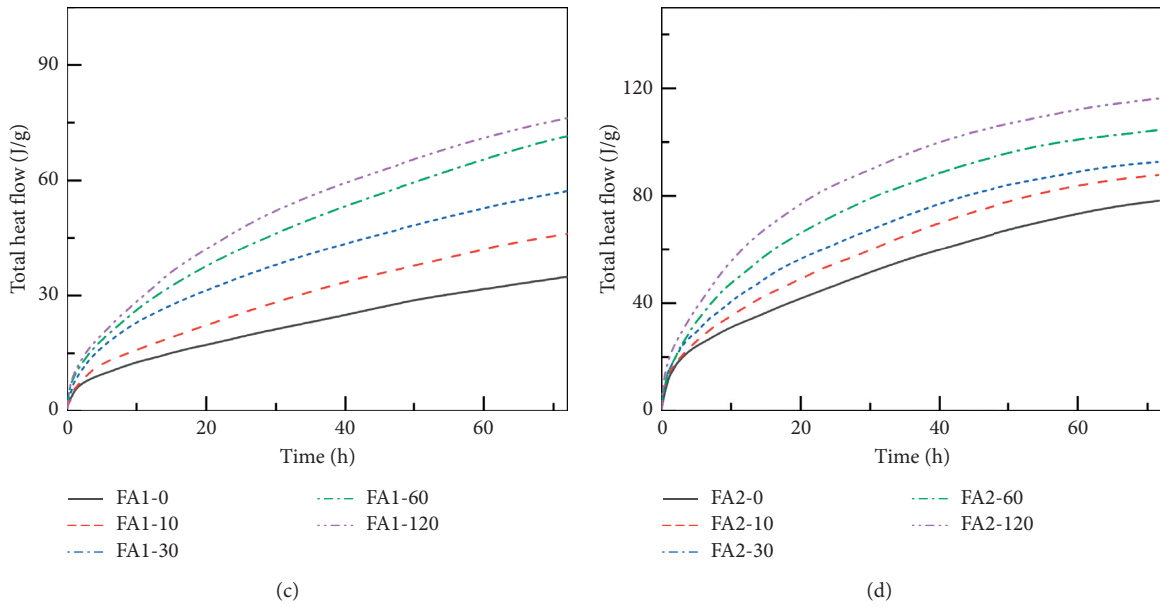
FIGURE 7: Calorimetry test results: (a, b) heat flow rate and (c, d) cumulative heat release.
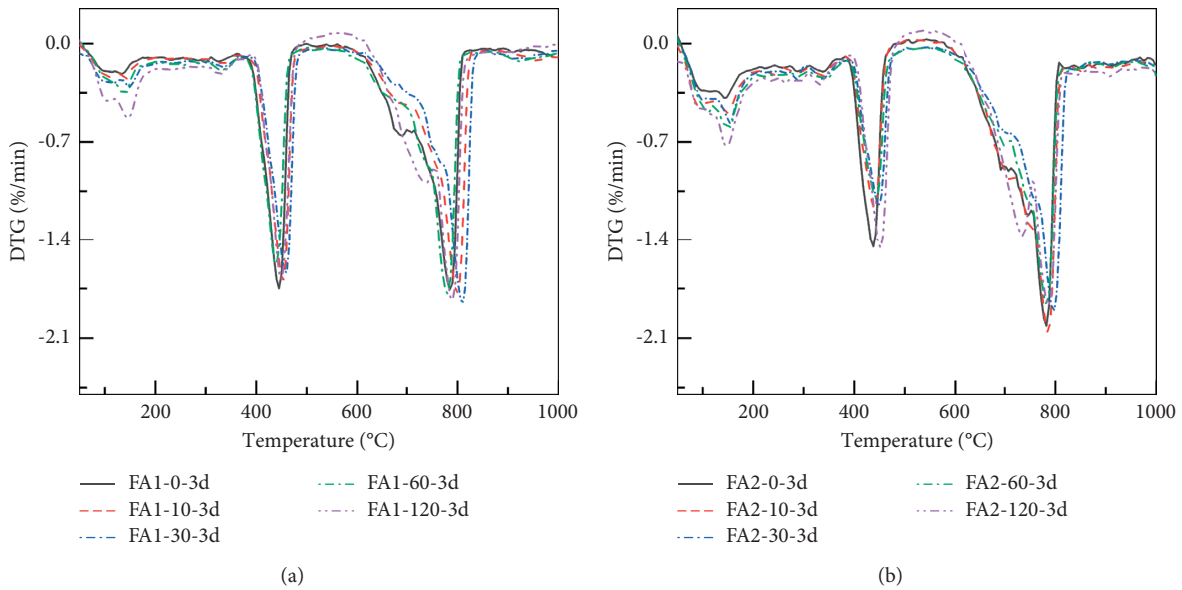
FIGURE 8: DTG analysis results of the hydrated samples after three days: (a) FA1 and (b) FA2.

hardened CPB samples could be divided into micropores (<20 nm), mesopores (20–500 nm), and macropores (>500 nm) [65]. Mesopores were the dominant pores in all the investigated samples. Besides, the mesopores and macropores decreased with the wet-grinding time, accompanied by the increase in the micropores. This led to the decrease in the total porosity. Generally, hydration gels from the cement reaction fill interparticle voids, leading to decreased porosity. The raw FA showed less reactivity, leading to a lower content of hydration gels,

and thus higher porosity [66, 67]. This is one of the reasons why the control presented the lowest strength. The effects of wet-grinding can be ternary: finer FA particles can fill the gaps of cement grains. This could then refine the pore characteristics of the hardened matrix. Second, the mechanically treated FA presented higher reactivity, contributing to the generation of much smaller hydration gels. Besides, the superfine particles can also act as hydration nucleation sites, promoting the cement reaction.
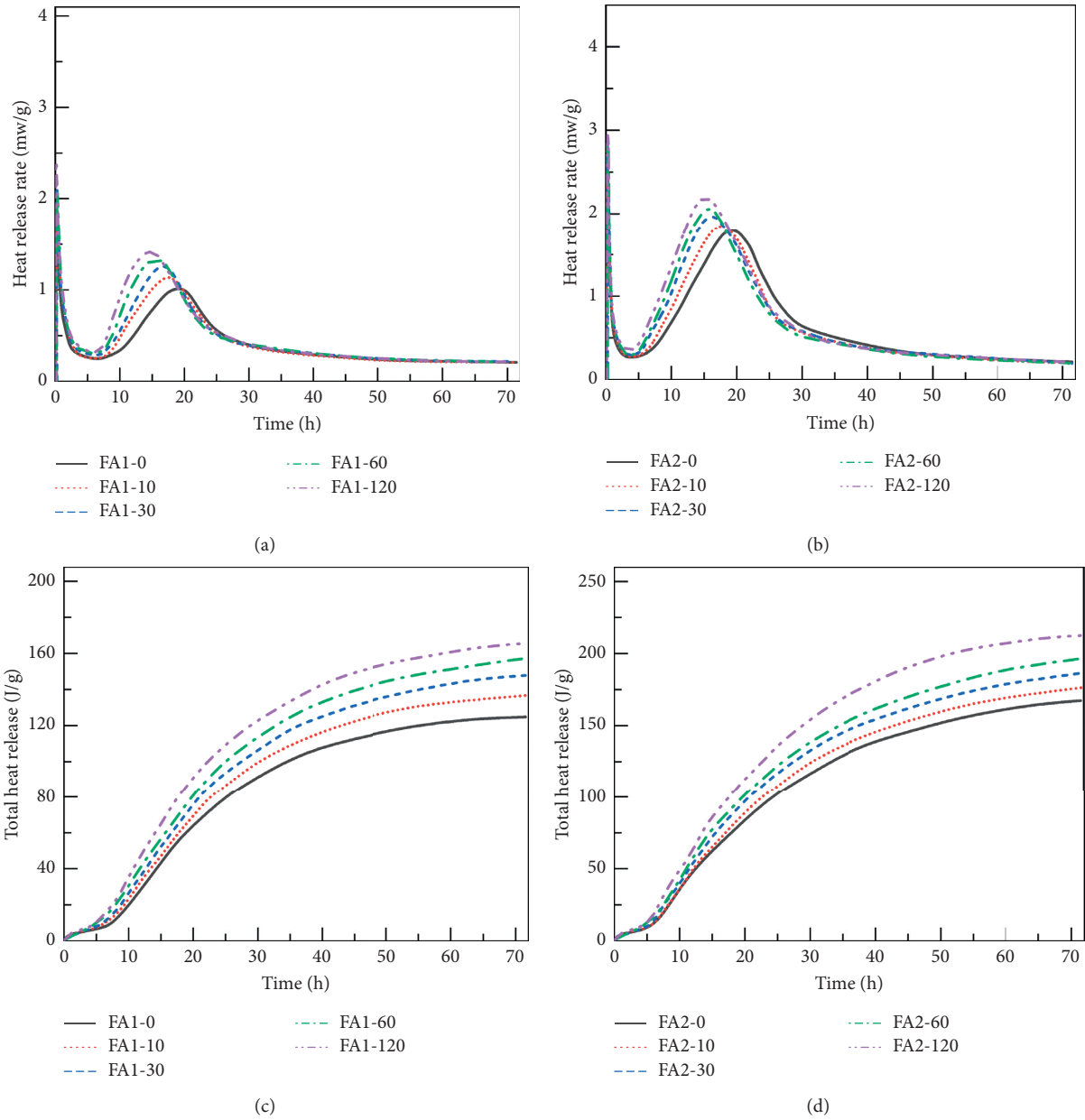
Figure 9: Calorimetry test results: (a, b) heat flow rate and (c, d) cumulative heat release.

Table 4: Kinetic data for the all the composites.

Samples	R_{max} (mW/g)	t_1 (hours)	t_2 (hours)	Cumulative heat release (J/g)
FA1-0	1.01	8.22	19.29	124.54
FA1-10	1.12	7.68	17.93	136.54
FA1-30	1.26	7.32	16.84	146.96
FA1-60	1.33	7.04	15.76	157.38
FA1-120	1.41	6.86	14.58	165.50
FA2-0	1.81	5.68	19.47	167.08
FA2-10	1.86	4.78	17.92	176.42
FA2-30	1.97	4.42	16.30	186.57
FA2-60	2.06	4.15	15.84	196.73
FA2-120	2.19	3.78	15.04	212.55

R_{max} is the maximum heat release rate, t_1 is the ending time of the induction period, and t_2 is the time reaching the main hydration peak.

(a)

(b)
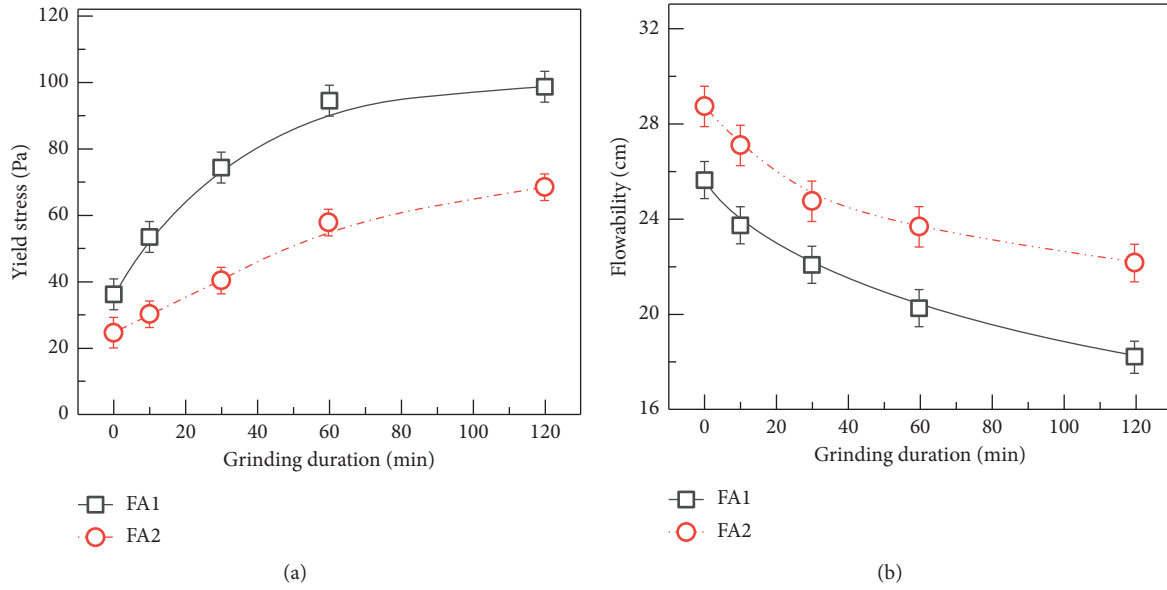
FIGURE 10: Rheological properties of the fresh slurry: (a) yield stress and (b) flowability.

(a)

(b)
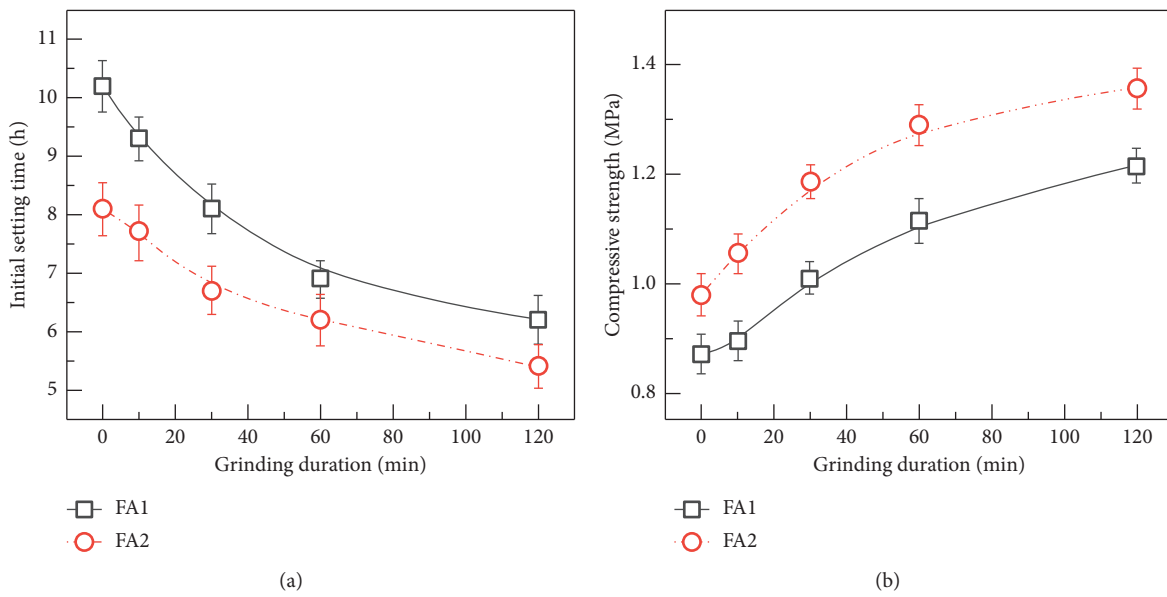
FIGURE 11: Initial setting time (a) and 28 d compressive strength (b).
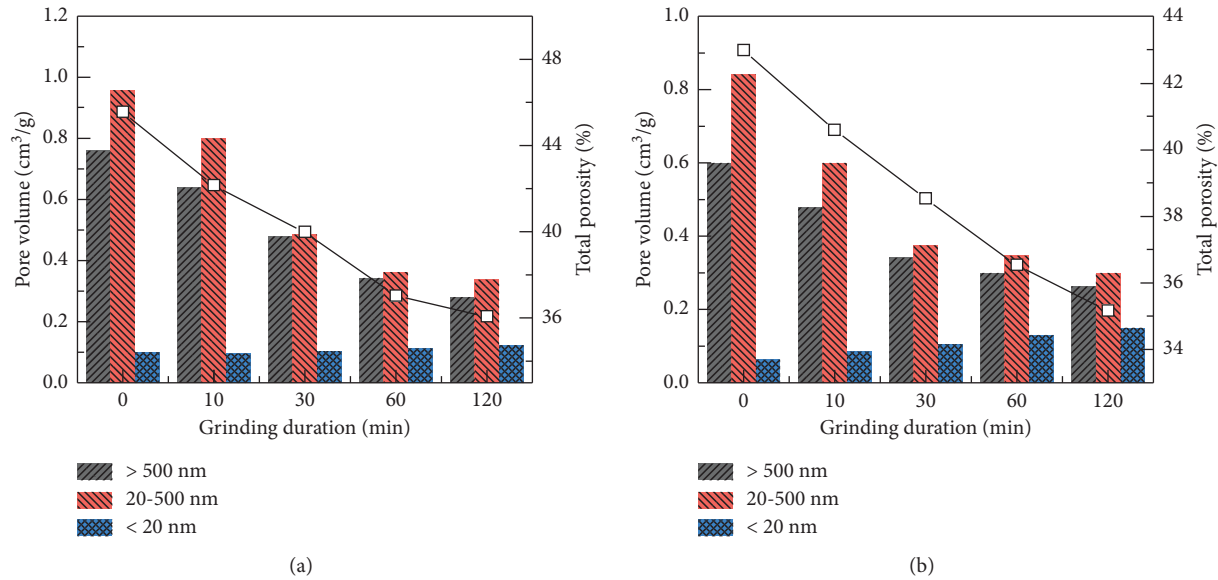
Figure 12: Pore structure of the samples after curing for 28 d: (a) FA1 and (b) FA2.

4. Conclusion

The low reactivity of FA limited its wide utilization in preparation of binder for cemented paste backfill (CPB). In the present work, FA was mechanically activated via wet-grinding with the aim of increasing its pozzolanic reactivity. The effect of wet-grinding was also investigated by dissolution and pozzolanic test. After that, the properties of CPB samples prepared using wet-ground FA was investigated. The results can lead to the following conclusions.

(1) Wet-grinding could decrease the particle size of FA to a more uniform distribution, with the increase in the specific surface area. This was accompanied by the content of crystalline phases in FA.

(2) The pozzolanic reactivity of wet-ground FA was increased according to the dissolution and pozzolanic tests. Wet-grinding promoted the dissolution of FA under alkaline conditions; at the same time, more hydration gels were formed during the pozzolanic test.

(3) Mechanical activation of FA increased the yield stress of the CPB slurry and then decreased the followability. The microstructure of FA showed a great impact on the rheological properties of CPB slurry.

(4) Mechanical activation of FA promoted the fast setting of the CPB samples. The reduction of the initial setting time was approximately 39.2% and 33.3% when the FA was ground for 120 h.

(5) Compressive strength of CPB samples after curing for 28 days increased by around 62.5% and 38.8% when adding the mechanically ground FA1 and FA2 for 120 min.

Data Availability

The data used to support the findings of this study are available from the corresponding author upon request.

Conflicts of Interest

The authors declare that they have no conflicts of interest.

Acknowledgments

References

[1] J. Shi, W. Huang, H. Han, and C. Xu, "Pollution control of wastewater from the coal chemical industry in China: environmental management policy and technical standards," *Renewable and Sustainable Energy Reviews*, vol. 143, Article ID 110883, 2021.

[2] L. Xue, W. Zhang, Z. Zheng et al., "Measurement and influential factors of the efficiency of coal resources of China's provinces: based on Bootstrap-DEA and Tobit," *Energy*, vol. 221, Article ID 119763, 2021.

[3] C. Fan, S. Guo, and H. Jin, "Numerical study on coal gasification in supercritical water fluidized bed and exploration of complete gasification under mild temperature conditions," *Chemical Engineering Science*, vol. 206, pp. 134–145, 2019.

[4] A. Bagheri, A. Nazari, J. G. Sanjayan, P. Rajeev, and W. Duan, "Fly ash-based boroaluminosilicate geopolymers: experimental and molecular simulations," *Ceramics International*, vol. 43, no. 5, pp. 4119–4126, 2017.

[5] C. Bobirică, J.-H. Shim, and J.-Y. Park, "Leaching behavior of fly ash-waste glass and fly ash-slag-waste glass-based geopolymers," *Ceramics International*, vol. 44, pp. 5886–5893, 2018.

[6] P. Duan, C. Yan, W. Zhou, and D. Ren, "Development of fly ash and iron ore tailing based porous geopolymer for removal of Cu(II) from wastewater," *Ceramics International*, vol. 42, no. 12, pp. 13507–13518, 2016.

[7] A. F. Abdalqader, F. Jin, and A. Al-Tabbaa, "Development of greener alkali-activated cement: utilisation of sodium carbonate for activating slag and fly ash mixtures," *Journal of Cleaner Production*, vol. 113, pp. 66–75, 2016.

[8] J. Cheung, A. Jeknavorian, L. Roberts, and D. Silva, "Impact of admixtures on the hydration kinetics of Portland cement," *Cement and Concrete Research*, vol. 41, no. 12, pp. 1289–1309, 2011.

[9] B. Guo, S. Nakama, Q. Tian, N. D. Pahlevi, Z. Hu, and K. Sasaki, "Suppression processes of anionic pollutants released from fly ash by various Ca additives," *Journal of Hazardous Materials*, vol. 371, pp. 474–483, 2019.

[10] Q. Tian, B. Guo, S. Nakama, L. Zhang, Z. Hu, and K. Sasaki, "Reduction of undesirable element leaching from fly ash by adding hydroxylated calcined dolomite," *Waste Management*, vol. 86, pp. 23–35, 2019.

[11] S. K. Pandey and T. Bhattacharya, "Mobility, ecological risk and change in surface morphology during sequential chemical extraction of heavy metals in fly ash: a case study," *Environmental Technology & Innovation*, vol. 13, pp. 373–382, 2019.

[12] D. P. Bentz, "Activation energies of high-volume fly ash ternary blends: hydration and setting," *Cement and Concrete Composites*, vol. 53, pp. 214–223, 2014.

[13] O. A. Abdulkareem, A. M. Mustafa Al Bakri, H. Kamarudin, I. Khairul Nizar, and A. E. A. Saif, "Effects of elevated temperatures on the thermal behavior and mechanical performance of fly ash geopolymer paste, mortar and lightweight concrete," *Construction and Building Materials*, vol. 50, pp. 377–387, 2014.

[14] T. Phoo-ngernkham, C. Phiangphimai, D. Intarabut et al., "Low cost and sustainable repair material made from alkali-activated high-calcium fly ash with calcium carbide residue," *Construction and Building Materials*, vol. 247, Article ID 118543, 2020.

[15] D. Adak, M. Sarkar, and S. Mandal, "Structural performance of nano-silica modified fly-ash based geopolymer concrete," *Construction and Building Materials*, vol. 135, pp. 430–439, 2017.

[16] Y. Li, X. Liu, Z. Li, Y. Ren, Y. Wang, and W. Zhang, "Preparation, characterization and application of red mud, fly ash and desulfurized gypsum based eco-friendly road base materials," *Journal of Cleaner Production*, vol. 284, Article ID 124777, 2021.

[17] I. Phummiphan, S. Horpibulsuk, T. Phoo-ngernkham, A. Arulrajah, and S.-L. Shen, "Marginal lateritic soil stabilized with calcium carbide residue and fly ash geopolymers as a sustainable pavement base material," *Journal of Materials in Civil Engineering*, vol. 29, Article ID 4016195, 2017.

[18] I. Cavusoglu, E. Yilmaz, and A. O. Yilmaz, "Sodium silicate effect on setting properties, strength behavior and microstructure of cemented coal fly ash backfill," *Powder Technology*, vol. 384, pp. 17–28, 2021.

[19] Y.-g. Chen, L.-l. Guan, S.-y. Zhu, and W.-j. Chen, "Foamed concrete containing fly ash: properties and application to backfilling," *Construction and Building Materials*, vol. 273, Article ID 121685, 2021.

[20] M. Mahedi, B. Cetin, and A. Y. Dayioglu, "Effect of cement incorporation on the leaching characteristics of elements from fly ash and slag treated soils," *Journal of Environmental Management*, vol. 253, Article ID 109720, 2020.

[21] P. Pongsopha, P. Sukontasukkul, T. Phoo-ngernkham, T. Imjai, P. Jamsawang, and P. Chindaprasirt, "Use of burnt clay aggregate as phase change material carrier to improve thermal properties of concrete panel," *Case Studies in Construction Materials*, vol. 11, Article ID e00242, 2019.

[22] M. I. M. Alzeer and K. J. D. MacKenzie, "Synthesis and catalytic properties of new sustainable aluminosilicate heterogeneous catalysts derived from fly ash," *ACS Sustainable Chemistry & Engineering*, vol. 6, no. 4, pp. 5273–5282, 2018.

[23] H. Rui, L. Zhang, L. Li, and L. zhu, "Solvent extraction of lithium from hydrochloric acid leaching solution of high-alumina coal fly ash," *Chemical Physics Letters*, vol. 771, Article ID 138510, 2021.

[24] S. Donatello, A. Palomo, and A. Fernández-Jiménez, "Durability of very high volume fly ash cement pastes and mortars in aggressive solutions," *Cement and Concrete Composites*, vol. 38, pp. 12–20, 2013.

[25] F. Moghaddam, V. Sirivivatnanon, and K. Vessalas, "The effect of fly ash fineness on heat of hydration, microstructure, flow and compressive strength of blended cement pastes," *Case Studies in Construction Materials*, vol. 10, Article ID e00218, 2019.

[26] A. K. H. Kwan and J. J. Chen, "Adding fly ash microsphere to improve packing density, flowability and strength of cement paste," *Powder Technology*, vol. 234, pp. 19–25, 2013.

[27] Q. Zeng, K. Li, T. Fen-chong, and P. Dangla, "Determination of cement hydration and pozzolanic reaction extents for fly-ash cement pastes," *Construction and Building Materials*, vol. 27, no. 1, pp. 560–569, 2012.

[28] Y. Zhao, Q. Jingping, M. A. Zhengyu, G. Zhenbang, and L. Hui, "Effect of superfine blast furnace slags on the binary cement containing high-volume fly ash," *Powder Technology*, vol. 375, pp. 539–548, 2020.

[29] J. Yang, Y. Su, X. He et al., "Pore structure evaluation of cementing composites blended with coal by-products: calcined coal gangue and coal fly ash," *Fuel Processing Technology*, vol. 181, pp. 75–90, 2018.

[30] K. Yildirim and M. Sümer, "Effects of sodium chloride and magnesium sulfate concentration on the durability of cement mortar with and without fly ash," *Composites Part B: Engineering*, vol. 52, pp. 56–61, 2013.

[31] R. Kumar, S. Kumar, and S. P. Mehrotra, "Towards sustainable solutions for fly ash through mechanical activation," *Resources, Conservation and Recycling*, vol. 52, no. 2, pp. 157–179, 2007.

[32] C. Qi and A. Fourie, "Cemented paste backfill for mineral tailings management: review and future perspectives," *Minerals Engineering*, vol. 144, Article ID 106025, 2019.

[33] H. Jiang, Z. Qi, E. Yilmaz, J. Han, J. Qiu, and C. Dong, "Effectiveness of alkali-activated slag as alternative binder on workability and early age compressive strength of cemented paste backfills," *Construction and Building Materials*, vol. 218, pp. 689–700, 2019.

[34] V. D. Cao, S. Pilehvar, C. Salas-Bringas et al., "Influence of microcapsule size and shell polarity on the time-dependent viscosity of geopolymer paste," *Industrial & Engineering Chemistry Research*, vol. 57, no. 29, pp. 9457–9464, 2018.

[35] J. Qiu, Y. Zhao, J. Xing, and X. Sun, "Fly ash/blast furnace slag-based geopolymer as a potential binder for mine backfilling: effect of binder type and activator concentration," *Advances in Materials Science and Engineering*, vol. 2019, Article ID 2028109, 12 pages, 2019.

[36] W. Liu, Z. Guo, C. Wang, and S. Niu, "Physico-mechanical and microstructure properties of cemented coal Gangue-Fly ash backfill: effects of curing temperature," *Construction and Building Materials*, vol. 299, Article ID 124011, 2021.

[37] I. Cavusoglu, E. Yilmaz, and A. O. Yilmaz, "Additivity effect on properties of cemented coal fly ash backfill containing water-reducing admixtures," *Construction and Building Materials*, vol. 267, Article ID 121021, 2021.

[38] Y. Zhao, J. Qiu, Z. Ma, and X. Sun, "Eco-friendly treatment of coal gangue for its utilization as supplementary cementitious materials," *Journal of Cleaner Production*, vol. 285, Article ID 124834, 2021.

[39] Y. Cheng, F. Huang, W. Li, R. Liu, G. Li, and J. Wei, "Test research on the effects of mechanochemically activated iron tailings on the compressive strength of concrete," *Construction and Building Materials*, vol. 118, pp. 164–170, 2016.

[40] P. L. Guzzo, F. B. Marinho de Barros, B. R. Soares, and J. B. Santos, "Evaluation of particle size reduction and agglomeration in dry grinding of natural quartz in a planetary ball mill," *Powder Technology*, vol. 368, pp. 149–159, 2020.

[41] S. Kucharczyk, M. Sitarz, M. Zajac, and J. Deja, "The effect of CaO/SiO 2 molar ratio of CaO-Al 2 O 3 -SiO 2 glasses on their structure and reactivity in alkali activated system," *Spectrochimica Acta Part A: Molecular and Biomolecular Spectroscopy*, vol. 194, pp. 163–171, 2018.

[42] S. Kucharczyk, M. Zajac, C. Stabler et al., "Structure and reactivity of synthetic CaO-Al$_2$O$_3$-SiO$_2$ glasses," *Cement and Concrete Research*, vol. 120, pp. 77–91, 2019.

[43] ASTM C191-13, *Standard Test Methods for Time of Setting of Hydraulic Cement by Vicat Needle*, ASTM Committee C01, West Conshohocken, PA, USA, 2013.

[44] Z. Giergiczny, "Fly ash and slag," *Cement and Concrete Research*, vol. 124, Article ID 105826, 2019.

[45] A. A. Siyal, M. R. Shamsuddin, N. E. Rabat, M. Zulfiqar, Z. Man, and A. Low, "Fly ash based geopolymer for the adsorption of anionic surfactant from aqueous solution," *Journal of Cleaner Production*, vol. 229, pp. 232–243, 2019.

[46] J. Yang, J. Huang, Y. Su et al., "Eco-friendly treatment of low-calcium coal fly ash for high pozzolanic reactivity: a step towards waste utilization in sustainable building material," *Journal of Cleaner Production*, vol. 238, Article ID 117962, 2019.

[47] H. Niu, P. Kinnunen, H. Sreenivasan, E. Adesanya, and M. Illikainen, "Structural collapse in phlogopite mica-rich mine tailings induced by mechanochemical treatment and implications to alkali activation potential," *Minerals Engineering*, vol. 151, Article ID 106331, 2020.

[48] N. Garg and J. Skibsted, "Dissolution kinetics of calcined kaolinite and montmorillonite in alkaline conditions: evidence for reactive Al(V) sites," *Journal of the American Ceramic Society*, vol. 102, no. 12, pp. 7720–7734, 2019.

[49] C. Kuenzel and N. Ranjbar, "Dissolution mechanism of fly ash to quantify the reactive aluminosilicates in geopolymerisation," *Resources, Conservation and Recycling*, vol. 150, Article ID 104421, 2019.

[50] M. Liu, H. Tan, and X. He, "Effects of nano-SiO2 on early strength and microstructure of steam-cured high volume fly ash cement system," *Construction and Building Materials*, vol. 194, pp. 350–359, 2019.

[51] H. C. Pedrosa, O. M. Reales, V. D. Reis, M. d. D. Paiva, and E. M. R. Fairbairn, "Hydration of Portland cement accelerated by C-S-H seeds at different temperatures," *Cement and Concrete Research*, vol. 129, Article ID 105978, 2020.

[52] G. Land and D. Stephan, "The effect of synthesis conditions on the efficiency of C-S-H seeds to accelerate cement hydration," *Cement and Concrete Composites*, vol. 87, pp. 73–78, 2018.

[53] F. Zou, C. Hu, F. Wang, Y. Ruan, and S. Hu, "Enhancement of early-age strength of the high content fly ash blended cement paste by sodium sulfate and C-S-H seeds towards a greener binder," *Journal of Cleaner Production*, vol. 244, Article ID 118566, 2020.

[54] S. Fan, B. Cao, N. Deng, Y. Hu, and M. Li, "Effects of ferrihydrite nanoparticle incorporation in cementitious materials on radioactive waste immobilization," *Journal of Hazardous Materials*, vol. 379, Article ID 120570, 2019.

[55] D. Siang Ng, S. C. Paul, V. Anggraini et al., "Influence of SiO2, TiO2 and Fe2O3 nanoparticles on the properties of fly ash blended cement mortars," *Construction and Building Materials*, vol. 258, Article ID 119627, 2020.

[56] S. Zhang, L. Yang, F. Ren, J. Qiu, and H. Ding, "Rheological and mechanical properties of cemented foam backfill: effect of mineral admixture type and dosage," *Cement and Concrete Composites*, vol. 112, Article ID 103689, 2020.

[57] J. Haiqiang, M. Fall, and L. Cui, "Yield stress of cemented paste backfill in sub-zero environments: experimental results," *Minerals Engineering*, vol. 92, pp. 141–150, 2016.

[58] Z. Li, T.-a. Ohkubo, and Y. Tanigawa, "Theoretical analysis of time-dependence and thixotropy of fluidity for high fluidity concrete," *Journal of Materials in Civil Engineering*, vol. 16, no. 3, pp. 247–256, 2004.

[59] X. Chen, X. Shi, J. Zhou, X. Du, Q. Chen, and X. Qiu, "Effect of overflow tailings properties on cemented paste backfill," *Journal of Environmental Management*, vol. 235, pp. 133–144, 2019.

[60] C. Qi, A. Fourie, Q. Chen, and Q. Zhang, "A strength prediction model using artificial intelligence for recycling waste tailings as cemented paste backfill," *Journal of Cleaner Production*, vol. 183, pp. 566–578, 2018.

[61] M. Fall, D. Adrien, J. C. Célestin, M. Pokharel, and M. Touré, "Saturated hydraulic conductivity of cemented paste backfill," *Minerals Engineering*, vol. 22, no. 15, pp. 1307–1317, 2009.

[62] S. Zhang, F. Ren, Z. Guo, J. Qiu, and H. Ding, "Strength and deformation behavior of cemented foam backfill in sub-zero environment," *Journal of Materials Research and Technology*, vol. 9, no. 4, pp. 9219–9231, 2020.

[63] B. Lothenbach, K. Scrivener, and R. D. Hooton, "Supplementary cementitious materials," *Cement and Concrete Research*, vol. 41, no. 12, pp. 1244–1256, 2011.

[64] S. Zhang, F. Ren, Y. Zhao, J. Qiu, and Z. Guo, "The effect of stone waste on the properties of cemented paste backfill using alkali-activated slag as binder," *Construction and Building Materials*, vol. 283, Article ID 122686, 2021.

[65] W. Xu, Y. Zhang, and B. Liu, "Influence of silica fume and low curing temperature on mechanical property of cemented paste backfill," *Construction and Building Materials*, vol. 254, Article ID 119305, 2020.

[66] W. Xu, Y. Zhang, X. Zuo, and M. Hong, "Time-dependent rheological and mechanical properties of silica fume modified cemented tailings backfill in low temperature environment," *Cement and Concrete Composites*, vol. 114, Article ID 103804, 2020.

[67] W. Xu, W. Chen, M. Tian, and L. Guo, "Effect of temperature on time-dependent rheological and compressive strength of fresh cemented paste backfill containing flocculants," *Construction and Building Materials*, vol. 267, Article ID 121038, 2021.

Research Article

The Influence of the Instantaneous Collapse of Tailings Pond on Downstream Facilities

Sha Wang [1,2] **Guodong Mei** [1,2] **Xuyang Xie** [1,2] **and Lijie Guo** [1,2]

[1]*BGRIMM Technology Group, No. 22, Beixing Road, Daxing District, Beijing 102628, Beijing, China*
[2]*National Centre for International Research on Green Metal Mining, No. 22, Beixing Road, Daxing District, Beijing 102628, Beijing, China*

Correspondence should be addressed to Guodong Mei; meiguodong@bgrimm.com and Lijie Guo; guolijie@bgrimm.com

To evaluate the evolutionary processes guiding the formation of the tailings-water mixtures produced by the instantaneous collapse of tailings ponds and the influence of these on downstream facilities, a 2D simulation model with reasonable boundary and working conditions derived from actual engineering practice was built in this study, and the relationship between dam-break elevation and impact on downstream facilities was also analyzed to determine the relevant mechanism of influence. Computational results indicated that lowering the dam-break elevation caused the maximum velocity and flooding depth, along with the flooded area at monitoring points, to gradually increase. The occurrence times of maximum velocity and flooding depth were also gradually moved forward as the breaking elevation was reduced; this effect is directly related to the increase in the total potential energy at the lower break elevations. Further simulations of sand-prevent dams with different heights located downstream from a tailings pond were carried out to identify methods for mitigating the impact of dam failure. The results revealed that increasing the height of the sand-prevent dam reduced the production of tailings mixtures. Based on the results, the construction of a sand-prevent dam with a crest elevation equal to that of the starter dam was recommended.

1. Introduction

Tailings ponds are specialized structures for the deposition of tailings produced by mining extraction [1]. For historical and policy purposes, tailings ponds in China can be characterized as being numerous but with small capacities and have often been constructed with little attention to design, with dam structures that do not meet stability requirements. The water levels in the reservoirs of upstream tailings ponds are prone to change when there is heavy rain or impervious structural failure [2–4]. Because of the complex physical and mechanical properties of tailings and their high levels of physical discreteness, the risk of dam break is extremely high when catastrophic floods [5] or earthquakes occur. Dam breaks in tailings ponds can result in sudden and significant damage [6], especially when there are facilities or densely populated villages downstream, and can cause serious consequences—such as casualties, property loss, and environmental pollution—that are difficult to remedy.

As the causes of tailings pond failure are numerous and complex, researchers have had to systematically investigate and analyze them. For example, Mei and Wang [7] conducted the statistical analysis and countermeasure research on the causes of tailings dam failure accidents in China. Berghe et al. [8] systematically analyzed the risks of tailings dam breakage; based on a Chinese case study, Wei et al. [9] proposed specific requirements for the design, construction, and management of tailings ponds. Dobry and Alvarez [10] analyzed post-earthquake dam-break accidents and found that failure typically occurred during or immediately after the earthquake and was induced by slope slide and flow. Robinson and Toland [11] discussed case histories covering a wide variety of embankment and foundation conditions and noted that seepage problems associated with foundation conditions have a pronounced impact on the overall ability of facilities to retain their tailings perimeters. Shakesby et al. [12, 13] studied the failure and subsequent development of

gold mine tailings dam flow slides based on a combination of multiple factors, including poor basal drainage, too-steep perimeter walls, wall saturation, and the effects on tailings saturation of the accumulation of basal sediments through the continued spitting of slurry during periods of heavy rainfall. Priulli et al. [14] presented a refined computing model for simulating rapid-flow movement across a 3D terrain. Rico et al. [15] carried out a detailed search and reevaluation of known historical cases of tailings dam failure in Europe and found that failure was most often related to unusual rainfall and that more than 90% of incidents occurred inactive mines, with only 10% occurring in abandoned ponds. Their results indicated an urgent need for EU regulations covering the technical standards of tailings disposal. Fourie et al. [16] assessed the 1994 Merriespruit, Virginia gold tailings dam failure, which resulted in 17 deaths, and found that it was produced by a large volume of metastable tailings and the overtopping and erosion of the impoundment wall, which combined to produce static liquefaction of the tailings and a consequent flow failure. Zhang et al. [17, 18] carried out an experimental model study on dam breakage and the tailings pond evolution law and proposed a model test method for predicting and preventing the dam-break process. Li [19] analyzed the influence of rainfall factors and safety warning technology on tailings dam breakage and, based on physical and numerical simulation of a dam example, determined the evolution rule and water flow characteristics for instantaneous and progressive tailings dam break. Mei [20] researched the mechanism of and online early-warning methods for tailing dam failure, and Xu [21] studied the dynamic process and post-failure effect of the overtopping failure of a tailings dam.

To evaluate the risk level of tailing dam failure accurately, Wang et al. [22] established a matter-element extension evaluation model. Considering that the stability of a tailings dam is affected by many random and fuzzy factors that are difficult to quantitatively estimate, Li et al. [23] conducted fuzzy theory-based research on tailings dam failure risk evaluation models and proposed a fuzzy theoretical model for the risk assessment of tailings ponds. Similarly, Liang et al. [24] proposed a dam-break risk assessment model based on variable weight synthesis and analytic hierarchy processes. Chen et al. [25] proposed a dam-break risk classification model based on interpretive structural modeling and factor frequency methods. Xiong [26] established the application of downstream dam-break risk fields to tailings ponds based on the use of geographic information systems and risk control theory. Zhang [27] also developed a risk assessment model and control strategy for tailings dam failure. Model testing and numerical modeling are both important tools for evaluating the serious consequences of tailings pond dam failure, and researchers including Li et al. [28], Li et al. [29], Wei et al. [30], Li [31], Liu [32], Lu [33], and Qin [34], have simulated tailings pond dam breaks under different working conditions. Nevertheless, there remains a lack of research on the impact of dam breakage on downstream areas.

If a dam is broken for any reason, its accumulated tailings can escape and flow downstream along the existing terrain. In this study, the evolution law of the spreading range, flow rate,

and submergence depth of the mixture of tailings and water under different dam-break elevations was determined using a 2D numerical simulation model of dam failure based on the Mike 21 hydrodynamics software package. A practical terrain- and dam data-based model of a tailings dam was established and, using a set of reasonable river bed resistance coefficients, an evaluation of the effects of tailings pond release on downstream facilities was carried out.

2. Governing Equations of the Dam-Break Simulation

The sand flow caused by tailings discharge after dam collapse is inherently a landslide or debris flow in nature and can be assumed to be a special form of movement between "fluid" and "granular body." This flow can be described by the dynamic equation and continuity equation similar to the fluid flow.

Therefore, this study is based on the following assumptions. The tailings sand is an isotropic continuum; the flow of the tailings sand conforms to the Bingham flow mode; the relationship between shear stress and shear strain is linear but does not pass through the origin; at a certain yield stress, the collapse of the tailings dam occurs under the condition that the dam is piled high. Thus, the water storage in the tailings dam corresponding to the overtopping water level of the tailings dam is the largest.

Based on a solution of the 2D incompressible average Navier–Stokes equation established using the Boussinesq and two-dimensional incompressible assumptions, the sand and water escape from the breakdown of a tailings pond can be approximately described by the following 2D average depth equations [35]:

Continuity equation:

$$\frac{\partial h}{\partial t} + \frac{\partial h\overline{u}}{\partial x} + \frac{\partial h\overline{v}}{\partial y} = hS. \tag{1}$$

Momentum equations:

$$\frac{\partial h\overline{u}}{\partial t} + \frac{\partial h\,\overline{u}^2}{\partial x} + \frac{\partial h\overline{v}\overline{u}}{\partial y} = f\overline{v}h - gh\frac{\partial \eta}{\partial x} - \frac{h}{\rho_0}\frac{\partial p_a}{\partial x} - \frac{gh^2}{2\rho_0}\frac{\partial \rho}{\partial x}$$

$$+ \frac{\tau_{sx}}{\rho_0} - \frac{\tau_{bx}}{\rho_0} - \frac{1}{\rho_0}\left(\frac{\partial s_{xx}}{\partial x} + \frac{\partial s_{xy}}{\partial y}\right)$$

$$+ \frac{\partial}{\partial x}\left(hT_{xx}\right) + \frac{\partial}{\partial y}\left(hT_{yy}\right) + hu_s S,$$

$$\frac{\partial h\overline{v}}{\partial t} + \frac{\partial h\overline{vu}}{\partial x} + \frac{\partial h\,\overline{v}^2}{\partial y} = -f\overline{u}h - gh\frac{\partial \eta}{\partial x} - \frac{h}{\rho_0}\frac{\partial p_a}{\partial y} - \frac{gh^2}{2\rho_0}\frac{\partial \rho}{\partial y}$$

$$+ \frac{\tau_{sy}}{\rho_0} - \frac{\tau_{by}}{\rho_0} - \frac{1}{\rho_0}\left(\frac{\partial s_{yx}}{\partial x} + \frac{\partial s_{yy}}{\partial y}\right)$$

$$+ \frac{\partial}{\partial x}\left(hT_{xy}\right) + \frac{\partial}{\partial y}\left(hT_{yy}\right) + hv_s S,$$

$$\tag{2}$$

where t is time, x and y are Cartesian spatial coordinates, η is the height of the water, d is still water depth, $h = \eta + d$ is the total water depth, $f = 2\Omega \sin \phi$ is the Coriolis parameter (where Ω is the angular velocity of rotation, ϕ is the latitude), g is the acceleration of gravity, ρ is the density of water, s_{xx}, s_{xy}, s_{yx}, and s_{yy} are the respective components of radiation, ρ_0 is the reference density of water, S is the flow size of the point source, and $\overline{u}$ and $\overline{v}$ are the velocity components in the x- and y-directions, respectively, which are determined to the average velocity by water depth as follows:

$$
\begin{aligned}
h\overline{u} &= \int_{-d}^{\eta} u \, \mathrm{d}z, \\
h\overline{v} &= \int_{-d}^{\eta} v \, \mathrm{d}z.
\end{aligned}
\tag{3}
$$

The lateral stress component comprehensively considers the influence of viscous and turbulent friction, differential advection, etc., whereas the vortex viscosity formula is estimated based on the average velocity gradient:

$$
\begin{aligned}
T_{xx} &= 2A\frac{\partial \overline{u}}{\partial x}, \\
T_{xy} &= A\left(\frac{\partial \overline{u}}{\partial y} + \frac{\partial v}{\partial x}\right), \\
T_{yy} &= 2A\frac{\partial \overline{v}}{\partial y}.
\end{aligned}
\tag{4}
$$

3. Dam-Break Simulation

3.1. Basic Information on the Tailings Pond Model. The starter dam modeled for this study was a clay core dam with bottom and crest elevations of 1,156.0 and 1,180.0 m, respectively, and an external slope ratio of 1 : 2.0. The final accumulation elevation of the dam crest was 1,195.0 m and the external slope ratio of the accumulation dam was 1 : 3.0. The tailings pond was a fourth-class pond with a total capacity of approximately 629,000 m^3. Several facilities such as villages and high-speed railway lines were located approximately 510 m downstream of the tailings pond to the southeast (see Figure 1 for details). The main cross section of the tailings pond is shown in Figure 2.

A flow chart of the tailings pond dam-breaking simulation is shown in Figure 3. The scope of calculation was determined based on the collection of a sufficient amount of survey, topography, and other basic data. The reliability, consistency, and representativeness of the data were then evaluated. The numerical scheme used to model the dam-break simulation was determined based on an analysis of reasons for dam break and outburst shape, duration, and elevation. Using the resulting calculation scheme, the terrain was digitized, the grid was divided to meet the requirements of computational accuracy, and reasonable calculation time series and boundary conditions were set. Finally, the resulting flow rate, inundation range, and depth of discharge were analyzed to obtain the effects of dam break on the downstream facilities.

3.2. Grid Division, Boundary Conditions, and Location of the Monitoring Points. A finite volume method based on the mesh center was used to spatially discretize the governing equations. The horizontal plane was covered in an unstructured mesh comprising a mixed grid of triangles and quadrilaterals to provide an optimal fitting to the complex geometric topography through an arrangement of small and large elements in key and non-key areas, respectively, while smoothing the boundary. The grid subdivision of the dam-break simulation, which is shown in Figure 4, adopted a grid size of 50 m and divided the study area into 59,061 elements. As all of the boundaries were closed, there was a zero flow velocity in the vertical direction.

To analyze the flow velocity and deposition of discharged material at the inclined shaft and drain opening during the discharge process, monitoring points were set at these locations to observe the changes in discharged material over time. The locations of the monitoring points are shown in Figure 5.

The break patterns of the tailings dam can be generally divided into total and local failure in terms of scale and instantaneous and gradual dam failure in terms of time. As the impact force of the flow causing the dam break is strong, the entire process from the beginning of the break to the formation of a stable rupture section is very short; therefore, the dam break can be treated as instantaneous and total collapse for safety reasons.

The amount of tailings and water discharged is directly related to the amount of water stored in the tailings pond. In this study, the storage capacity characteristic, corresponding to the accumulation elevation of +1195 m of the tailings dam, was set as the initial condition of the simulation, whose water storage amount was the largest. Thus, the debris flow formed by the dam break was also the largest. The crossing line between the tailings pond and mountain was defined as a dike, whose crest elevation was the current elevation. The tailings dam was simulated by the axis of the highest accumulation dam and defined as a dike with a constant elevation of the crest, whose elevation adopted the dam-break elevation. The sand-prevent dam used in this study was also defined as a dike, whose crest elevation was also set as a constant value. The other boundary conditions adopted current topographic data. A total of 60 time steps was set in this simulation, and each of the time step was 30 s.

3.3. Bed Resistance Parameter. A variation of Manning's coefficient was used as a shear force function to simulate the bed resistance parameter in modeling the different flow characteristics of tailings slurry and water. The relationship between the shear force and Manning's coefficient is shown in Figure 6.

In Figure 6, τ_c is the critical shear force as the tailings begin to flow, τ_{cu} is the critical shear force of the tailing slurry as it transitions from a yield pseudoplastic body to a Bingham plastic body, and M_l is the minimum Manning coefficient, which represents the bottom friction as the slurry begins to flow; here, $M = 1/n$, where n is the roughness coefficient. There are several facilities in the downstream
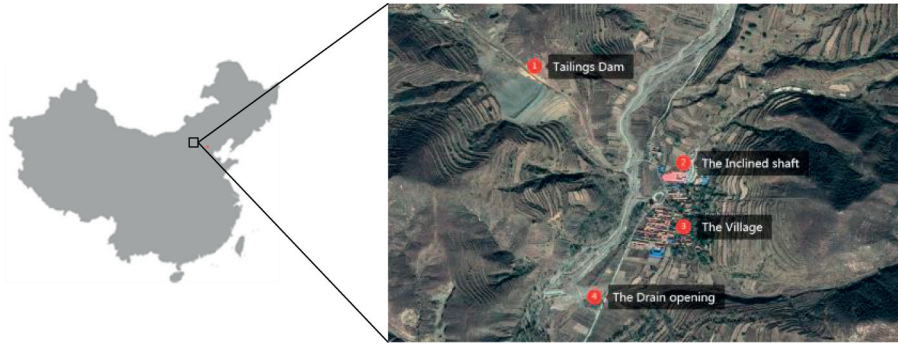
FIGURE 1: Locations of the tailings pond and nearby facilities.
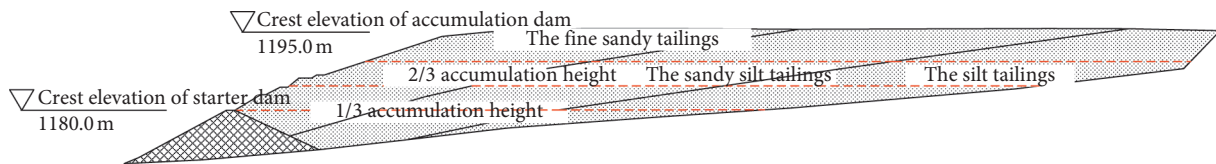
FIGURE 2: Cross section of tailings pond.

riverbed and the mountains on both sides are steep, with a few trees on the riverbed. The roughness values in Table 1 were used to select a minimum Manning coefficient of 3.2. A maximum Manning coefficient, which represents the bottom friction as the slurry transitions from a pseudoplastic body to a Bingham plastic body, of $M_u = 32$, was selected.

To assess the impact of dam breakage elevation on the downstream facilities, three different breaking elevations were modeled—two-thirds of the accumulation dam height, one-third of the accumulation dam height, and the elevation of the dam crest of the starter dam—and the resulting discharge evolution processes and distributions of tailings deposition were compared and analyzed.

3.4. Analysis of Tailings Evolution Results

3.4.1. Break Occurring Immediately above the Two-Thirds of Accumulation Dam Height Mark. Because an instantaneous dam break occurs quickly and the maximum flow appears in the initial stage of the break, the scope of spread within 30 min of breaking was analyzed. The corresponding elevation at two-thirds of the dam height was +1,190 m. The evolution of the tailings-and-water mixture flow following an instantaneous tailings pond collapse above this altitude is shown in Figure 7. In this case, the flow spreads downstream along the valley under the action of accumulated potential energy. 8.5 minutes after the dam break, the mixture of tailings and water reaches the inclined shaft opening and continues to spread downstream; 9.5 min after the dam break, tailings, and water flood the drain opening; 30 min after the break, the reservoir has ceased discharging. Although the quantity of mixed tailings and water at the inclined shaft is small, it is large at the drain opening; this effect is directly related to the respective elevations and topographic conditions of the two locations.

3.4.2. Instantaneous Breakage of the Dam at One-Third of Dam Height. The evolution process of tailings and water flow following a break at one-third of the dam height (elevation +1,185.0 m) is shown in Figure 8. The working conditions are similar to those occurring following the break at +1,190.0 m: 4.5 min after the dam break, the mixture of tailings and water reaches the inclined shaft; 6.5 min after the break, it reaches the drain opening; 30 min after the break, the discharge stops, and a large number of tailings and water have accumulated at the drain opening. The quantity of mixture accumulating at the inclined shaft, however, is less than that under the two-thirds case and does not affect its primary functionality.

3.4.3. Instantaneous Breakage at Starter Dam Crest Height. Finally, the breakage of the dam at the elevation of the crest of the starter dam was modeled. The evolution process of tailings-and-water flow is shown in Figure 9. Four minutes after the dam breaks, the mixture reaches the inclined shaft; 5.5 min later, the mixture reaches the drain opening.

3.5. Analysis of Flooding Depth and Flow Velocity. Under a basic assumption of our dam-break simulation, the total amount of discharge will be equivalent to the reservoir capacity above the elevation of the break. The changes in flooding depth and flow velocity, respectively, overtime at the monitoring points in front of the inclined shaft and drain opening downstream of the tailings pond are shown in Figures 10 and 11.

It is seen that the flooding depths at both monitoring points first increase to maximum values and then decrease gradually over time. As the dam-break elevation is reduced, the maximum flooding depth increases, and the maximum value is reached within a shorter time. This is directly related to the water-capacity curve of the tailings pond (i.e., the

```
┌─────────────────────────┐        ┌──────────────────────────┐
│ Geological              │        │ Determine the numerical  │
│ prospecting data        │        │ calculation range        │
│                         │        └──────────────────────────┘
│ Designing data          │                    │
│                         │                    ▼
│ Evaluation data         │───────▶┌──────────────────────────┐
│                         │        │ Collection and organization
│ Operation data          │        │ of basic data            │
│                         │        └──────────────────────────┘
│ Topographic and         │
│ geomorphic data         │
└─────────────────────────┘
```

┌──────────────────────────┐   ┌──────────────┐
│ Reliability   │
│ Consistency   │
│ Representativeness   │
└──────────────────────────┘

Compilation and evaluation of basic data

┌──────────────────────────┐
│ Analysis of dam-break causes │
│ The dam-break forms   │
│ Duration of dam break   │
│ Dam-break position   │
└──────────────────────────┘

Setting calculation scheme

┌──────────────────────────┐
│ Terrain digitization   │
│ Mesh generation   │
│ Design time series   │
│ Setting boundary conditions │
└──────────────────────────┘

Modeling and calculation

Results extraction and analysis

┌──────────────────────────┐
│ The dam-break flow   │
│ Flooded area of tailings   │
│ Results analysis   │
└──────────────────────────┘

FIGURE 3: Flow chart of numerical simulation of tailings pond dam break.

shape of the valley in which the pond is located). Reducing the dam-break position increases the total potential energy of the discharged material, and therefore the total energy of the discharged material, enhancing both the velocity and volume of flow. The maximum flooding depth at the drain opening exceeds that at the inclined shaft because the inclined shaft is located at a higher elevation than the drain opening.

The flow velocity curves in front of the inclined shaft and drain opening follow similar laws in terms of the forms of their respective flooding depth curves: as the elevation of dam break decreases, the maximum velocity gradually increases, and the time at which the maximum occurs gradually advances. After reaching its maximum, the velocity decreases gradually over time and finally settles into its initial state. In the second halves of the velocity curves, corresponding to the drain opening, the fluctuation in velocity decreases owing to the proximity of the closed boundary downstream of the drain opening. When the discharge reaches this boundary, it flows back under the
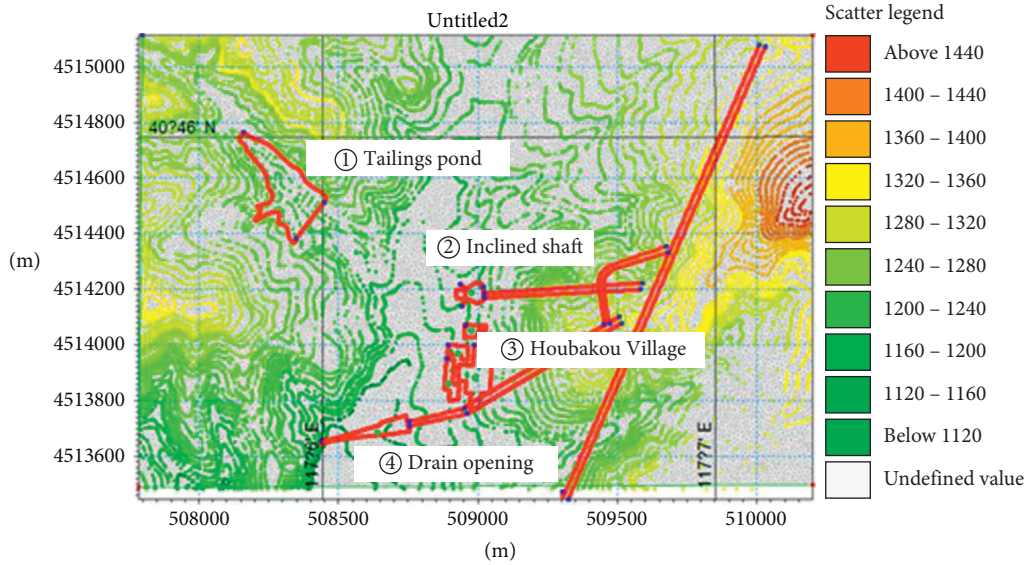
FIGURE 4: Element division of dam-break simulation.
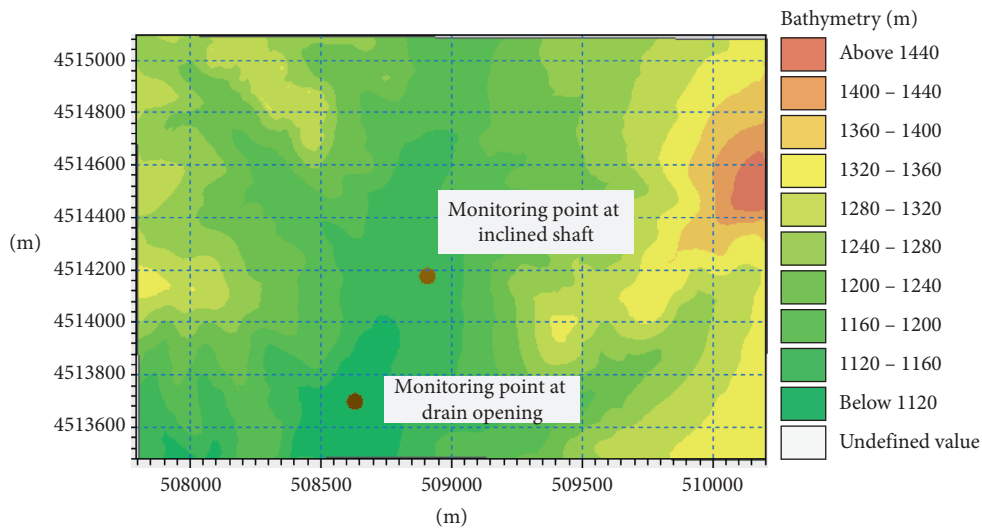
FIGURE 5: Locations of monitoring points.
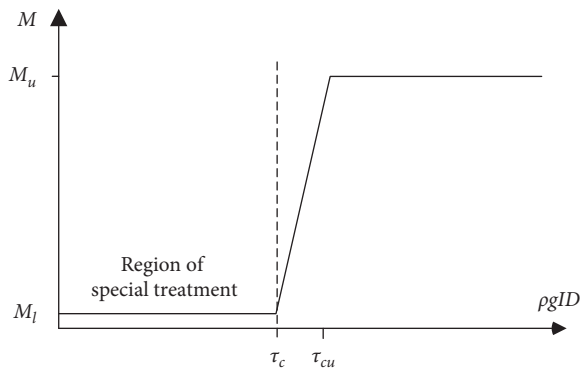
FIGURE 6: Relationship between shear force and Manning's coefficient.

action of boundary resistance, resulting in a decrease in the fluctuation of the velocity curve.

4. Influence of Sand-Prevent Dam on the Amount of Discharge

The tailings pond modeled in this study was an overhead reservoir with villages and high-speed railway facilities present within 1 km downstream. According to the analysis results described in Section 3, the dam-break tailings-and-water mixture would flood this infrastructure. To reduce the impact of discharge on the villages and high-speed railway facilities, we examined the effects of placing a sand-prevent dam, built using the same material used to construct the starter dam, 150.0 m downstream of the axis of the starter dam.

TABLE 1: Roughness coefficient n of the natural river bed [36].

Pattern of riverbed	Minimum value	Normal value	Maximum value
Flooded path with many weeds and deep pools or trees and undergrowth that severely retard water	0.075	0.100	0.150
No plants on the riverbed, the mountains on both side are steep, and trees and shrubs on the river banks are flooded at high water levels	0.030	0.040	0.050

(a)

(b)

(c)

(d)

(e)

(f)
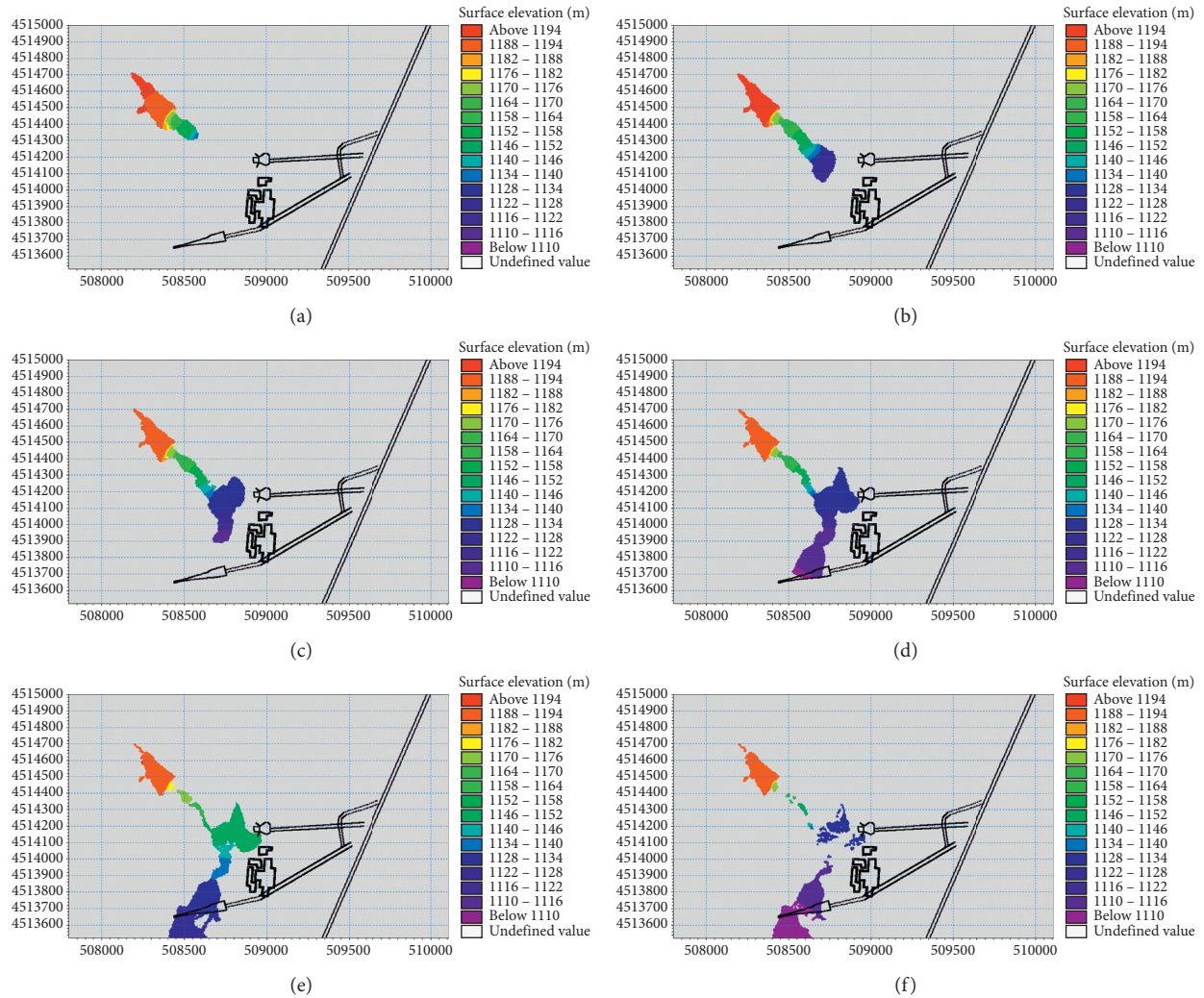
FIGURE 7: The evolution process of tailings and water flow following dam break at two-thirds of the accumulation dam height. (a) First minute; (b) third minute; (c) fifth minute; (d) tenth minute; (e) twentieth minute; (f) thirtieth minute.

(a)

(b)

FIGURE 8: Continued.

(c)

(d)

(e)

(f)
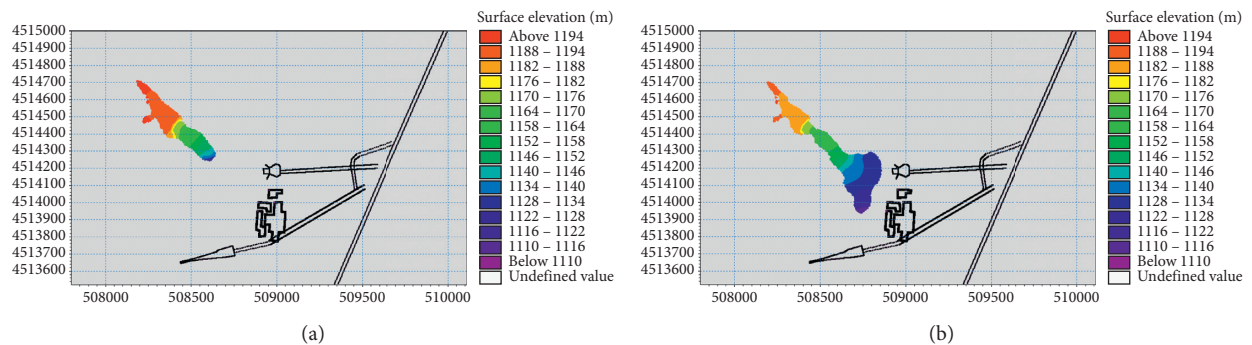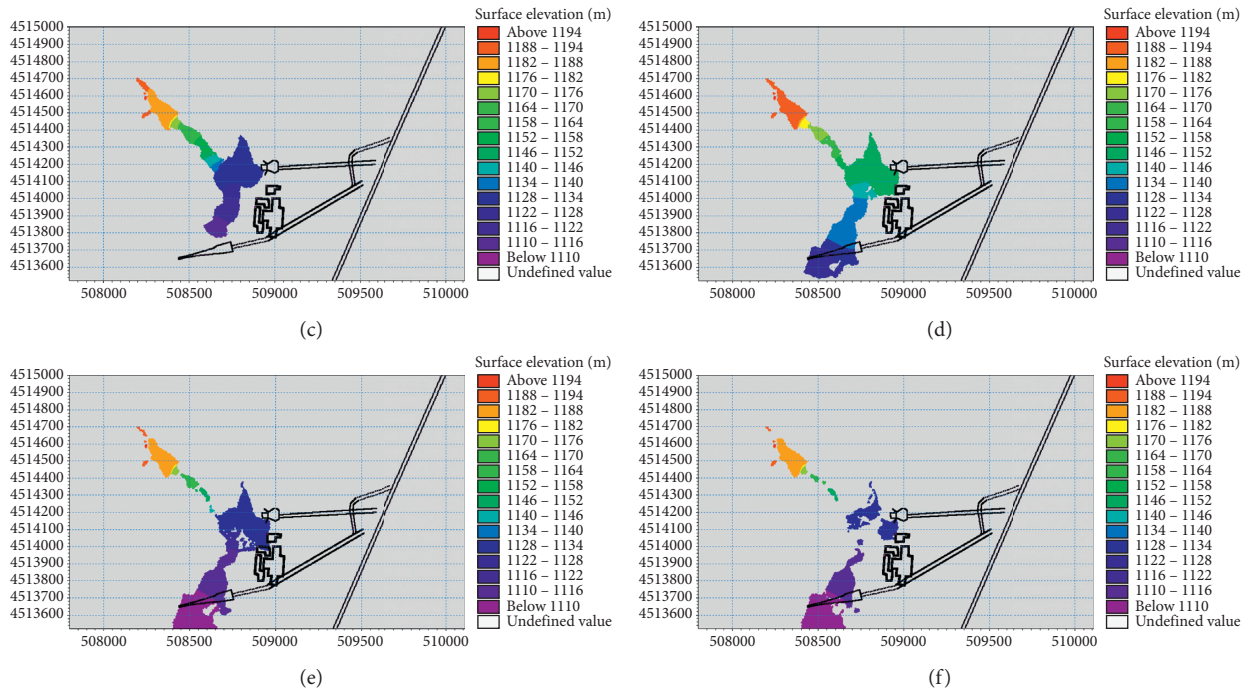
Figure 8: The evolution process of tailings-and-water flow following dam break at one-third of the accumulation dam height. (a) First minute; (b) third minute; (c) fifth minute; (d) tenth minute; (e) twentieth minute; (f) thirtieth minute. The tailings pond collapsed at the elevation of the starter dam crest instantly.

(a)

(b)

(c)

(d)

Figure 9: Continued.

(e)

(f)
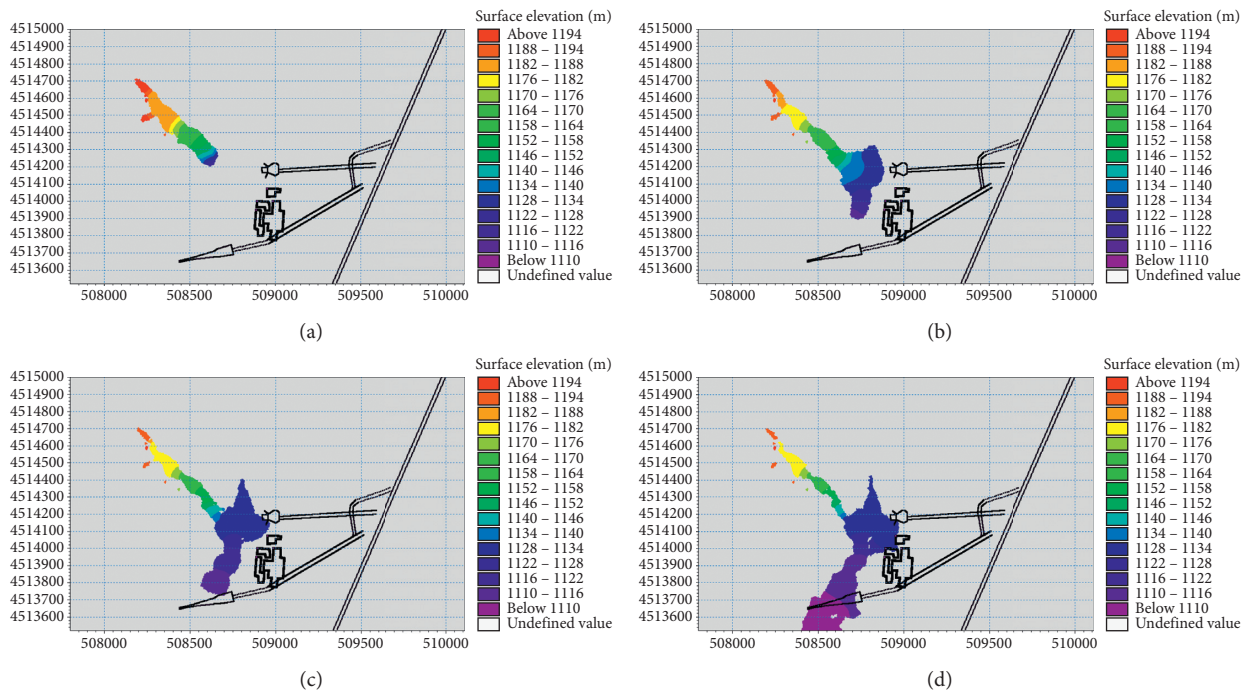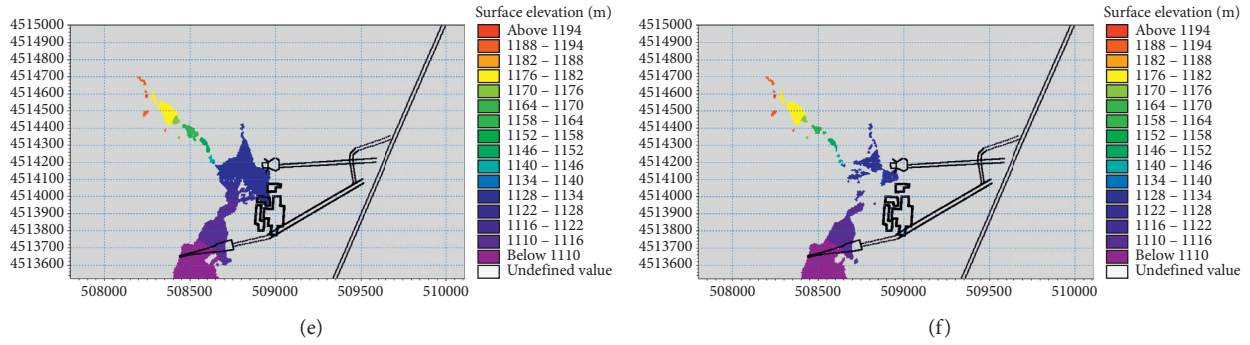
FIGURE 9: The evolution process of tailings-and-water flow following dam break at the crest of the starter dam. (a) First minute; (b) third minute; (c) fifth minute; (d) tenth minute; (e) twentieth minute; (f) thirtieth minute.

(a)

(b)
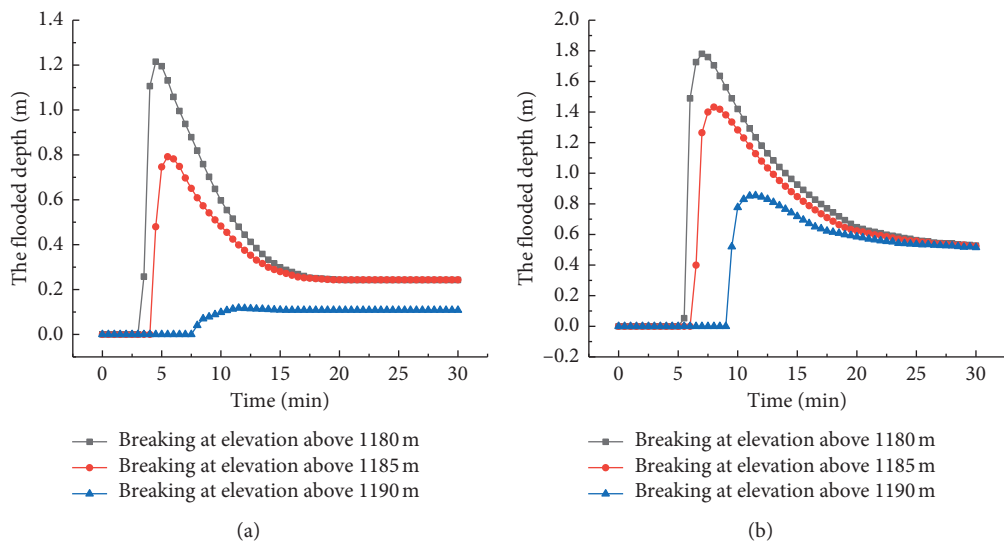
FIGURE 10: Time variation in flooding depth. (a) In front of the inclined shaft and (b) in front of the drain opening.

(a)

(b)
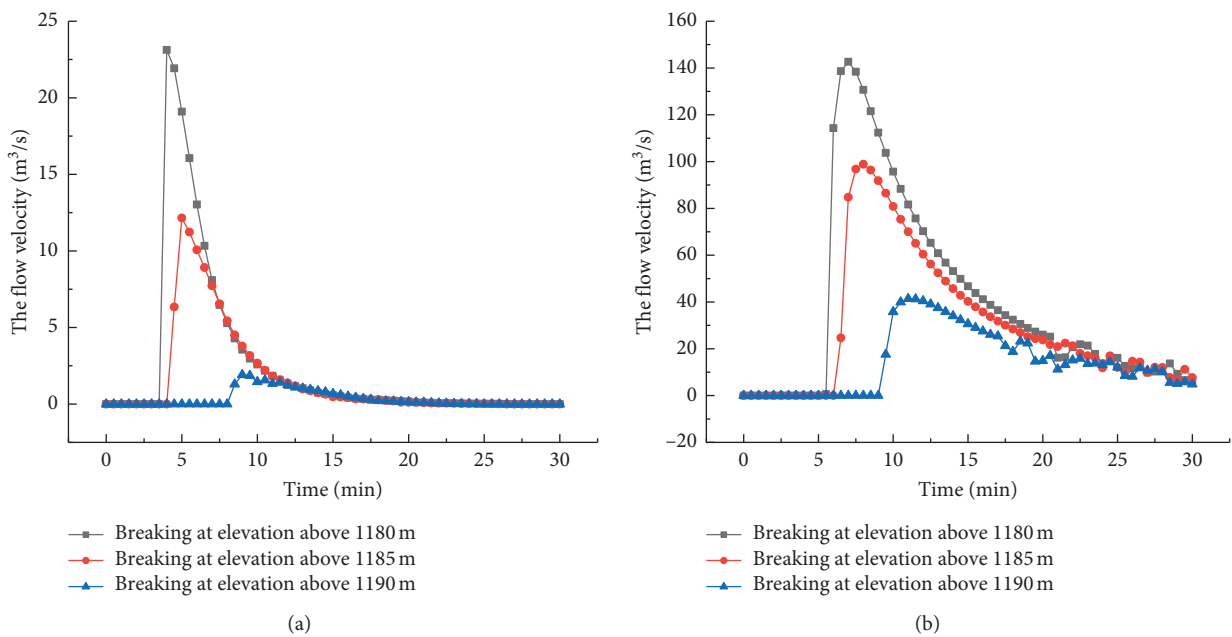
FIGURE 11: Time variation in velocity. (a) In front of the inclined shaft and (b) in front of the drain opening.

Three different sand-prevent dam schemes, with crest elevations of 1,180.0, 1,170.0, and 1,160.0 m respectively, were modeled. According to the analysis results presented in Section 3, the impact on downstream facilities would be most severe following a tailings dam break at the elevation of the starter dam crest. Therefore, for each sand-prevent model, we analyzed the evolution rules of discharge flow and submergence depth following a tailings dam break at an elevation of 1,180.0 m.

4.1. Analysis of Flooding Depth and Flow Velocity.
The discharge flow in front of the inclined shaft is shown in Figure 12. It is seen from the figure that the discharge flow evolution law is essentially the same at all three sand-prevent dam crest elevations; in each case, there is a steep increase from the initial flow value of zero and a gradual decrease following the peak of the curve. As the height of the sand-prevent dam increases, the curve decreases more sharply following the peak. At a sand-prevent dam crest elevation of 1,180.0 m, the discharge flow velocity at the inclined shaft is only 8.0% of that occurring without a sand-prevent dam.

The flooding depths in front of the inclined shaft under the respective sand-prevent dam models are shown in Figure 13. It is seen that the submergence depth evolution rules under the different sand-prevent dam schemes are also essentially the same; following a steep increase from an initial depth of zero, the depth peaks and then gradually decreases. For the sand-prevent dam with a height of 1,180.0 m, the maximum submergence depth in front of the inclined shaft is 0.13 mm, which is only 1.0% of the depth occurring without a sand-prevent dam; this indicates that the sand-prevent dam can intercept most of the discharge under this working condition.

The flow velocities at the drain opening under the respective sand-prevent dam models are shown in Figure 14. It is seen that the evolution rules are essentially the same, with each showing a steep increase from an initial velocity of zero and a gradual decrease in fluctuation after the peak. Increasing the height of the sand-prevent dam causes the curve to decrease more sharply after the peak. At a sand-prevent dam crest elevation of 1,180.0 m, the flow velocity at the drain opening is only 22.1% of that obtained without a sand-prevent dam.

The flooding depths at the drain opening under the respective sand-prevention models are shown in Figure 15, from which it is evident that the flooding depths at the drain opening follow essentially the same evolution law; in each case, there is a steep increase from an initial depth of zero and then a gradual decrease after the peak. At a sand-prevent dam crest elevation of 1,180.0 m, the maximum flooding depth at the drainage outlet is only 38.9% of that obtained without a sand-prevent dam, indicating that the sand-prevent dam can intercept most of the discharged tailings and water under this working condition.

4.2. Analysis of Discharge Velocity and Flooding Depth under Different Sand-Prevent Dam Schemes.
The maximum flooding depths at the inclined shaft and drain opening under each sand-prevention scheme are shown in Figure 16. As the height of the sand-prevent dam increases, the flooding depths at both positions gradually increase, indicating that the flooding depth near the downstream facilities will be directly related to the height of the sand-prevent dam. Increasing the height of the sand-prevent dam reduces the flooding depth, and, therefore the impact of a tailings dam break on the downstream area.

The maximum values of discharge velocity at the inclined shaft and drain opening under each sand-prevent dam scheme are shown in Figure 17. As the height of the sand-prevent dam increases, the discharge velocities at both locations gradually increase, indicating that the discharge velocities at the facilities downstream will be directly related to the height of the sand-prevent dam. Increasing the dam height will reduce the discharge flow velocity, thereby reducing the impact of a tailings pond dam break on the downstream facilities.

4.3. Discussion.
According to the existing Chinese national codes or regulations for design or safety of tailings pond, there is no suggestion regarding the construction of sand-prevent dams to reduce the impact of dam-break accidents. Only tailings collection dams are recommended in center-line tailings ponds, which are typically constructed in the downstream direction of the tailings dam and used to block tailings entrained by rainwater erosion.

In China, a tailings dam with inhabited areas or facilities downstream within 1 km is defined as a high-risk tailings dam, referred to as the "on-head" tailings dam; therefore, 1 km is a controlling distance. The spread range of dam-break debris flow is closely related to the characteristics of the discharged materials, and the influence range is more than 1 km under extreme conditions. For example, on November 5, 2015, the Fundao tailings pond in Samarco Iron Mine in Brazil collapsed owing to a small earthquake, which triggered the liquefaction of the super-high dam that was already close to saturation. At least 19 people were killed, with an estimated 32 million m^3 of tailings being discharged and flooding 158 houses in the village of Bento Rodrigues, 5 km downstream of the pond. On January 25, 2019, Brazil's Feijiao tailings dam collapsed, releasing up to 9.8 million m^3 of tailings, resulting in 270 deaths, with the main victims being residents of the Vila Ferteco community, 1 km away from the dam. The cases above show that, if no blocking measures are taken, dam collapse can have a significant impact on downstream areas, where residents or facilities exist. Moreover, from a safety perspective, distances beyond 1 km along the flow path should be studied further.

The theoretical research above shows that a sand-prevent dam located downstream of the tailings dam is an effective measure to reduce the consequences of dam collapse for residents or facilities that are downstream of the tailings pond. Therefore, from a safety perspective, a sand-prevent dam is suggested to be constructed to further ensure safety.

(a)

(b)

(c)

(d)
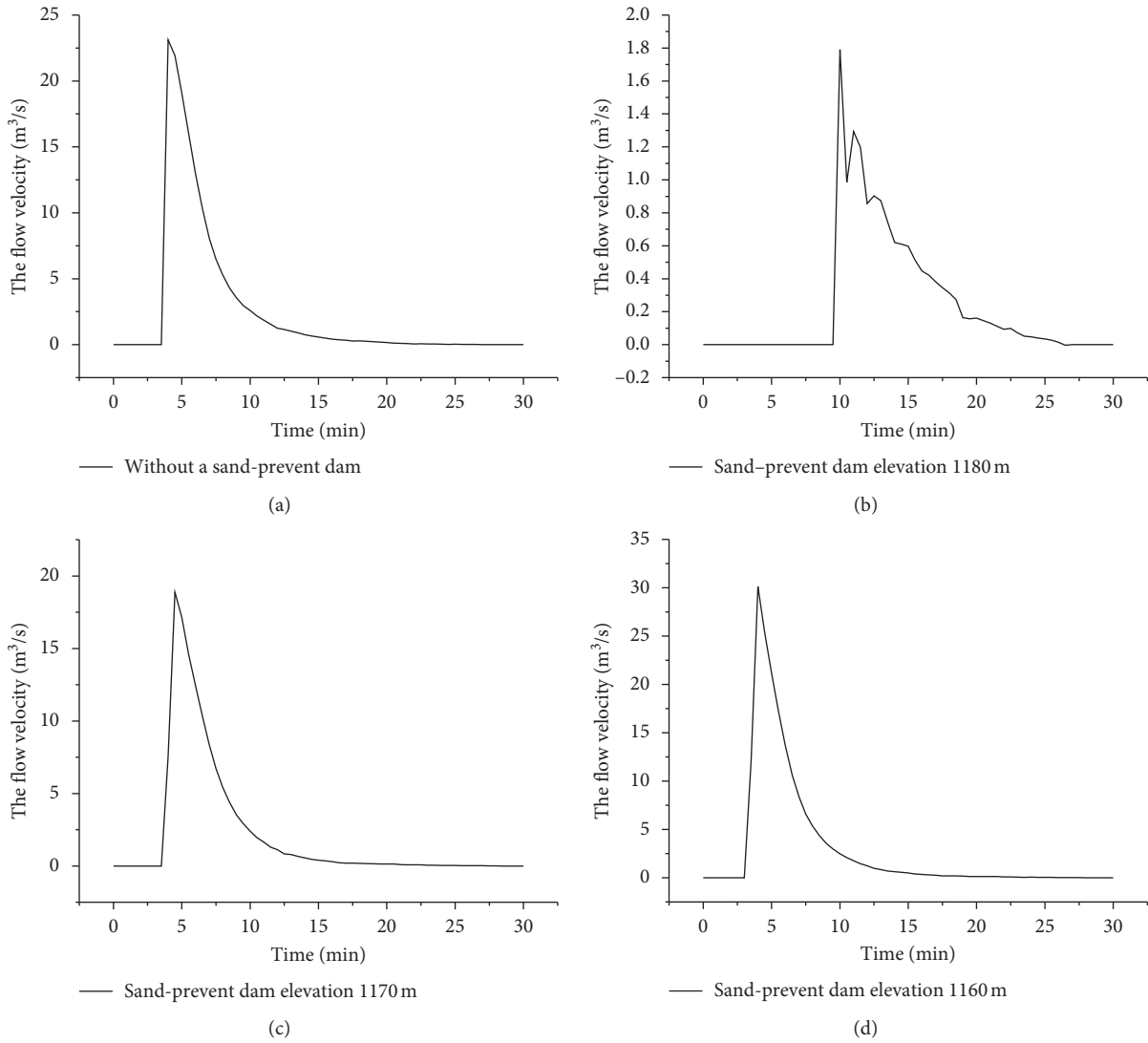
Figure 12: Evolution curves of discharge flow in front of the inclined shaft at different sand-prevent dam heights.

(a)

(b)

Figure 13: Continued.

(c) Sand-prevent dam elevation 1170 m

(d) Sand-prevent dam elevation 1160 m
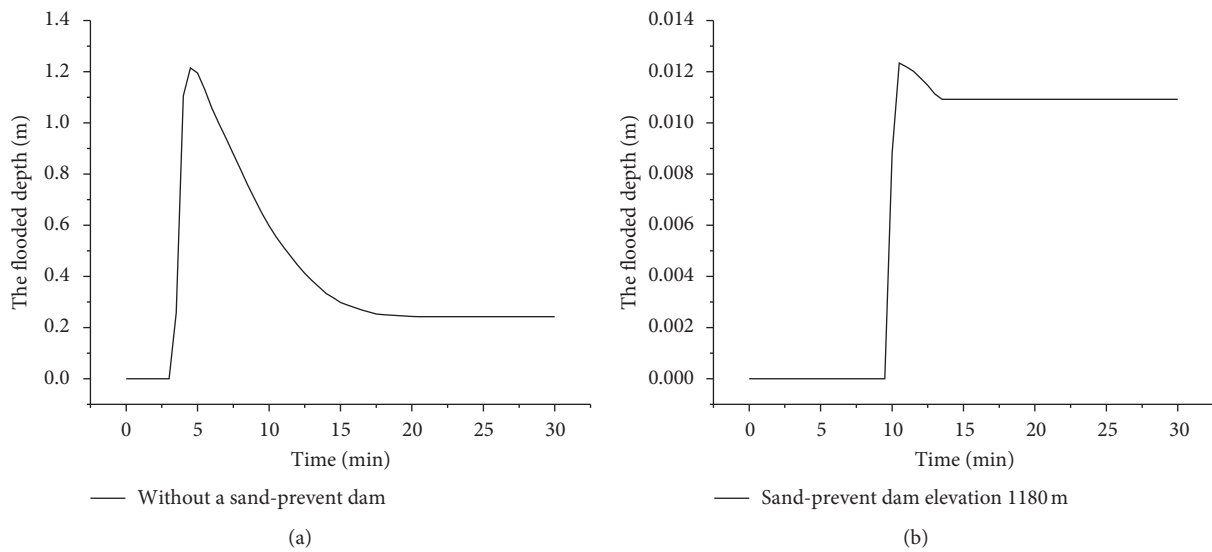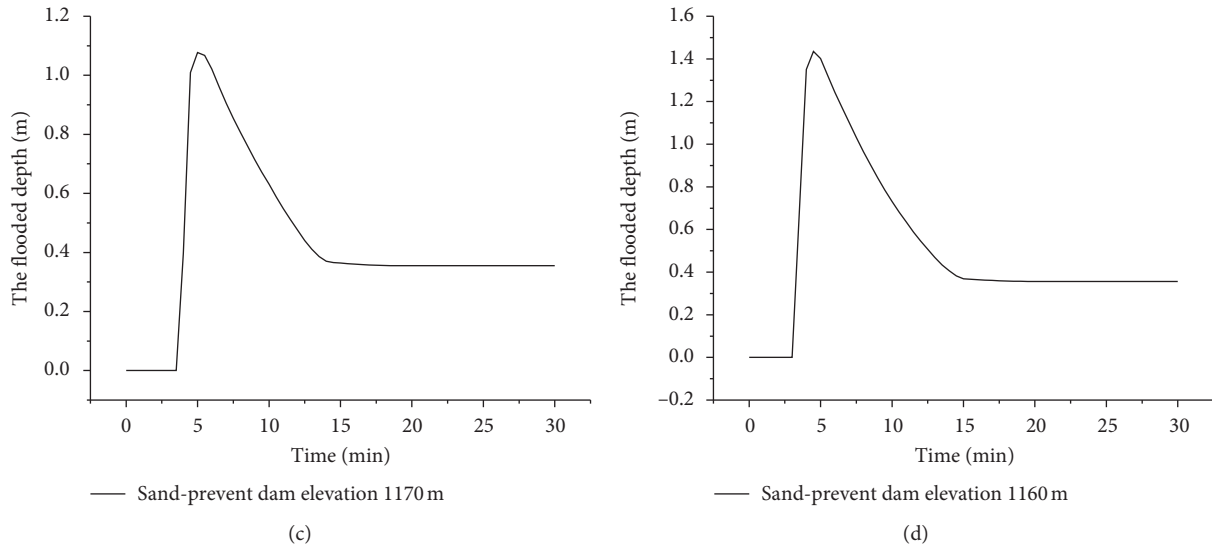
FIGURE 13: Evolution curves of flooding depth in front of the inclined shaft at different sand-prevent dam heights.

(a) Without a sand-prevent dam

(b) Sand-prevent dam elevation 1180 m

(c) Sand-prevent dam elevation 1170 m

(d) Sand-prevent dam elevation 1160 m
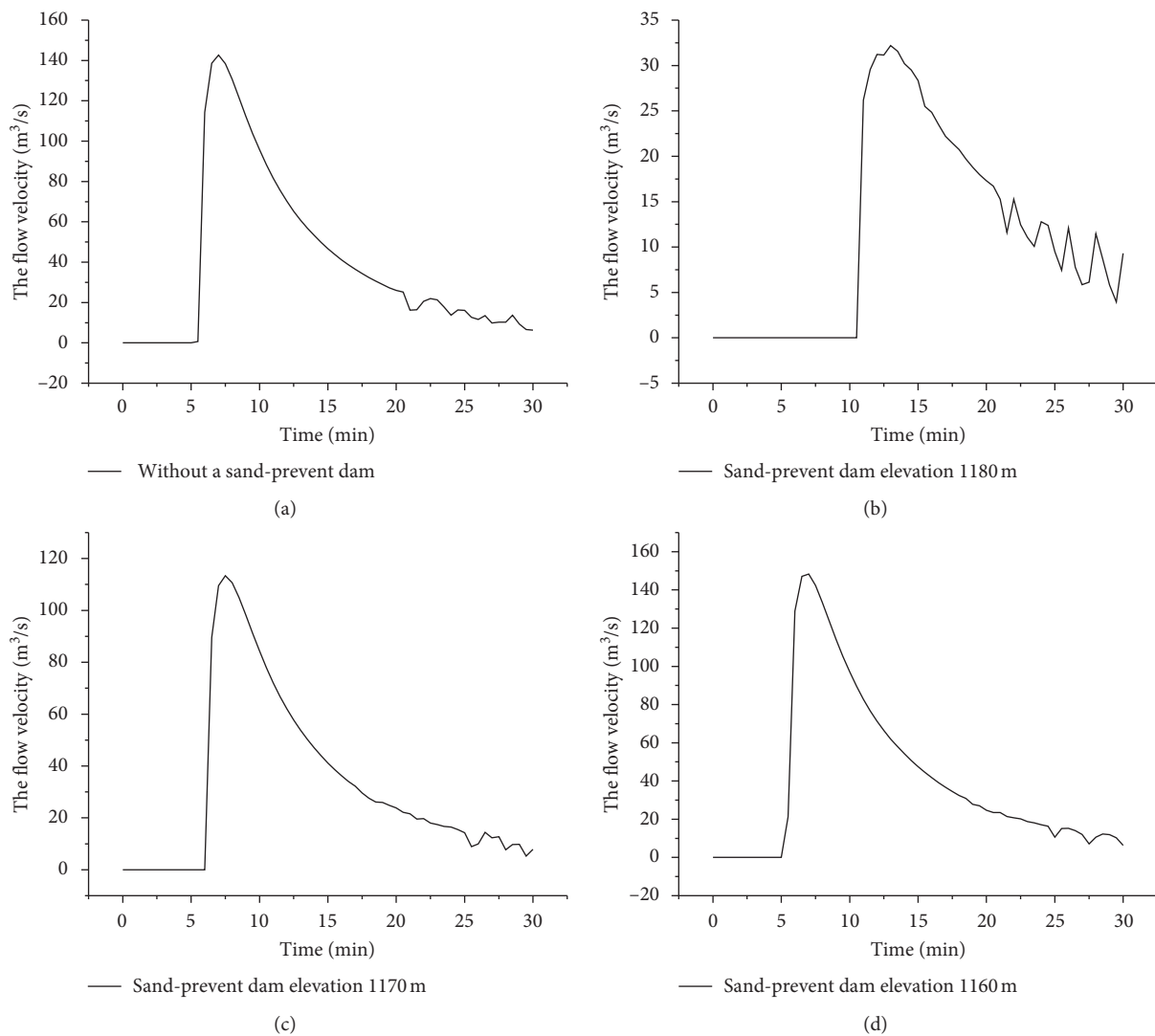
FIGURE 14: Evolution curves of discharge flow in front of drainage outlet at different sand-prevent dam heights.
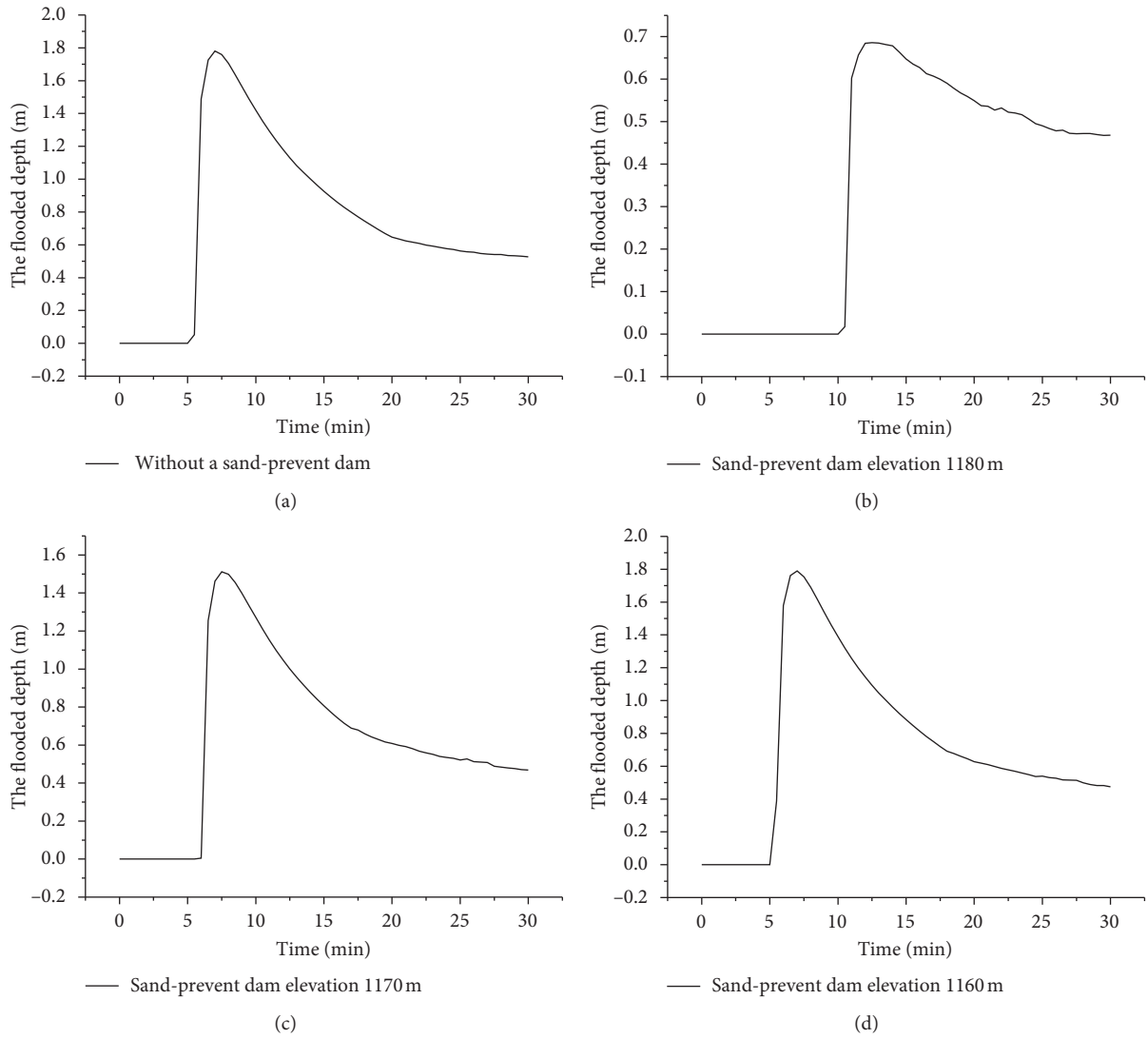
FIGURE 15: Evolution curves of flooding depth in front of drainage outlet at different sand-prevent dam heights.
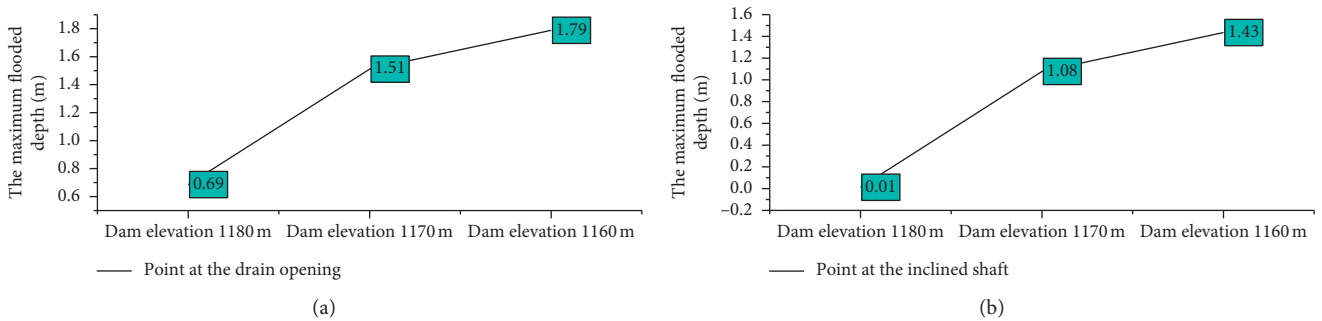
FIGURE 16: Maximum flooding depths in front of the inclined shaft and discharge outlet at different sand-prevent dam heights.
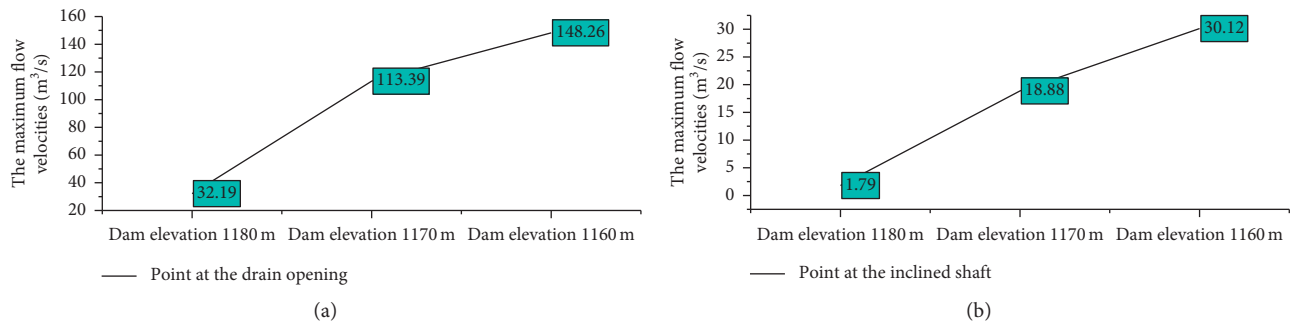
FIGURE 17: Maximum flow velocities in front of the inclined shaft and discharge outlet at different sand-prevent dam heights.

5. Conclusions

In this study, technical data obtained from an actual tailings dam project were used to quantitatively model the flooded area and flooding depth following dam breakage using numerical simulation. The impact of tailings pond dam failure on downstream facilities was analyzed, producing the following conclusions:

(1) Five minutes after dam breakage, the tailings-water mixture flow will have flooded the downstream high-speed railway facilities and drain opening, of which the scope of influence is longer than 1 km. This will seriously influence the normal operation of the railway and damage downstream villages and facilities, and a portion of the discharge will pile up in the natural riverbed with detrimental ecological impact.

(2) Numerical analysis of the dam-break process revealed that the evolution curves of flow velocity and flooding depth follow similar laws, with both increasing sharply, reaching a maximum value, and finally decreasing at a gradually slowing rate.

(3) The evolution curves of flow rate and submerged depth at typical positions in front of the inclined shaft and drain opening indicate that reducing the dam-breaking position causes the maximum velocities and submerged depths at these positions to increase gradually. Both effects are related to the fact that the discharge capacity of the reservoir increases as the breakage height of the dam decreases. Furthermore, the times of occurrence of maximum velocity and submerged depth will gradually advance as the dam-break elevation decreases because reducing the height of breakage increases the total potential energy accumulated at the dam-break position.

(4) Numerical modeling of the effects of placing sand-prevent projects with different heights revealed that increasing the height of the sand-prevent dam reduced the flooding depth and flow velocity of the discharge. For a sand-prevent dam with a crest height equal to that of the starter dam, the sub-merged depth and flow velocity of the tailings-and-water mixture in front of the inclined shaft will be only 1.0 and 8.0%, respectively, of the depth and

velocity achieved without a sand-prevent dam. Constructing a sand-prevent dam of this height will reduce the flooding and flow velocity in front of the drainage outlet to only 38.9 and 22.1% of the respective values without a sand-prevent dam. These results indicate that a sand-prevent dam with a crest elevation similar to that of the starter dam should be set up downstream of the overhead tailings pond to enhance the safety of nearby facilities and significantly reduce the impact of dam failure.

Data Availability

The data used to support the findings of this study are available from the corresponding author upon request.

Conflicts of Interest

The authors declare no conflicts of interest regarding the publication of this paper.

Acknowledgments

References

[1] Z. Lyu, J. Chai, Z. Xu, Y. Qin, and J. Cao, "A comprehensive review on reasons for tailings dam failures based on case history," *Advances in Civil Engineering*, vol. 2019, Article ID 4159306, 18 pages, 2019.

[2] J. C. Koppe, "Lessons learned from the two major tailings dam accidents in Brazil," *Mine Water and the Environment*, vol. 40, no. 1, pp. 166–173, 2021.

[3] J. R. Owen, D. Kemp, É. Lèbre, K. Svobodova, and G. Pérez Murillo, "Catastrophic tailings dam failures and disaster risk disclosure," *International Journal of Disaster Risk Reduction*, vol. 42, Article ID 101361, 2020.

[4] Icold, *Incident Case Records Tailings Dams Risk of Dangerous Occurrences*, United Nations Publications, Herndon, VA, USA, 2001.

[5] M. Rico, G. Benito, and A. Díez-Herrero, "Floods from tailings dam failures," *Journal of Hazardous Materials*, vol. 154, no. 1-3, pp. 79–87, 2008.

[6] P. Concha Larrauri and U. Lall, "Tailings dams failures: updated statistical model for discharge volume and runout," *Environments*, vol. 5, no. 2, p. 28, 2018.

[7] G. D. Mei and Y. H. Wang, "Statistics analysis and countermeasure study on tailings pond accidents in China," *Journal of Safety Science and Technology*, vol. 6, no. 3, pp. 211–213, 2010.

[8] J. F. V. Berghe, J. C. Ballard, M. Pirson, and U. Reh, "Risks of tailings dams failure," in *Proceedings of the 3rd International Symposium on Geotechnical Risk and Safety (ISGSR)*, Munich, Germany, June 2011.

[9] Z. Wei, G. Yin, J. G. Wang, L. Wan, and G. Li, "Design, construction and management of tailings storage facilities for surface disposal in China: case studies of failures," *Waste Management & Research: The Journal for a Sustainable Circular Economy*, vol. 31, no. 1, pp. 106–112, 2013.

[10] R. Dobry and L. Alvarez, "Seismic failures of Chilean tailings dams," *Journal of the Soil Mechanics and Foundations Division*, vol. 93, no. 6, pp. 237–260, 1967.

[11] K. E. Robinson and G. C. Toland, "Case histories of different seepage problems for mine tailings dams," *Mine Drainage*, vol. 39, pp. 781–800, 1979.

[12] R. A. Shakesby and J. R. Whitlow, "Failure of a mine waste dump in Zimbabwe: causes and consequences," *Environmental Geology and Water Sciences*, vol. 18, no. 2, pp. 143–153, 1991.

[13] S. G. Vick, "Failure of the Omai tailings dam: closure," *Geotechnical News*, vol. 15, pp. 49–55, 1997.

[14] M. Pirulli, M. Barbero, M. Marchelli et al., "The failure of the stava valley tailings dams (Northern Italy): numerical analysis of the flow dynamics and rheological properties," *Geoenvironmental Disasters*, vol. 4, no. 1, pp. 1–15, 2017.

[15] M. Rico, G. Benito, A. R. Salgueiro, A. Díez-Herrero, and H. G. Pereira, "Reported tailings dam failures," *Journal of Hazardous Materials*, vol. 152, no. 2, pp. 846–852, 2008.

[16] A. B. Fourie, G. E. Blight, and G. Papageorgiou, "Static liquefaction as a possible explanation for the merriespruit tailings dam failure," *Canadian Geotechnical Journal*, vol. 38, no. 4, pp. 707–719, 2001.

[17] L. T. Zhang, "Summary on the dam-break of tailings pond," *Journal of Hydraulic Engineering*, vol. 44, no. 5, pp. 594–600, 2013.

[18] L. T. Zhang, Q. L. Qi, Q. Li, and S. Zhang, "Experimental model study on the dam break and evolution law of tailings pond," *Journal of Hydraulic Engineering*, vol. 44, no. 5, pp. 594–600, 2013.

[19] H. G. Li, *Study on the Influence of Rainfall Factors on Tailings Dam Break and its Safety Warning Technology*, Degree of Doctor, University of Science and Technology Beijing, Beijing, China, 2017.

[20] G. D. Mei, *Research on Mechanism and Online Early-Warning Method for Tailings Dam Failure*, Degree of Doctor, University of Science and Technology Beijing, Beijing, China, 2015.

[21] Z. F. Xu, *Study on Dynamic Process of Overtop Dam Failure of Tailings Dam and its Influence after Failure*, Degree of Master, Kunming University of Science and Techonlogy, Kunming, China, 2019.

[22] J. M. Wang, M. T. Jia, J. Wang et al., "Risk evaluation of dam-break in tailings reservoir based on matter-element extension model," *Journal of Safety Science and Technology*, vol. 10, no. 4, pp. 96–102, 2014.

[23] Q. M. Li, X. Chen, Y. H. Wang et al., "Research on the evaluation model of dam failing risk of tailings reservoir based on fuzzy theory," *Journal of Safety Science and Technology*, vol. 4, no. 6, pp. 57–61, 2008.

[24] L. Liang, Q. Liu, and M. Li, "Dam-break risk assessment model of tailings reservoir based on variable weight synthesis and analytic hierarchy process," *Journal of Northeastern University*, vol. 12, no. 38, pp. 1790–1794, 2017.

[25] H. Chen, Y. Y. Chen, Q. H. Wang, L. Binyu, L. Ran, and W. Xianhua, "Tailings pond dam break risk classification study based on both ISM and factor frequency method," *China Safety Science Journal*, vol. 12, no. 28, pp. 150–156, 2018.

[26] L. Xiong, *The Establishment of the Downstream Risk Field of Tailings Dam Break based on GIS and Risk Control*, Degree of Master, Southwest University of Science and Technology, Mianyang, China, 2017.

[27] Y. Y. Zhang, *Research on Risk Assessment Model and Control Strategy for Tailings Dam Failure*, Degree of Doctor, Capital University of Economics and Business, Beijing, China, 2016.

[28] H. K. Li, X. Liang, H. H. Liu et al., "Three-dimensional numerical simulation of tailings dam failure based on Flow-3D," *Journal of Nanchang University*, vol. 41, no. 2, pp. 120–126, 2019.

[29] J. Y. Li, G. J. Wang, and B. Cui, "Simulation study on tailings dam failure under different topography and roughness," *Chinese Tungsten Industry*, vol. 3, pp. 1–6, 2019.

[30] W. L. Wei, Y. M. Shen, and G. C. Sun, "Numerical Simulation of 2D dam-break flood wave," *Journal of Hydraulic Engineering*, vol. 9, pp. 45–49, 2003.

[31] S. N. Li, *Study on Model and Numerical Simulation of Tailings Dam Break*, Degree of Master, Central South University, Changsha, China, 2010.

[32] C. Liu, *Numerical Simulation of Reservoir Dam Breaking Flood Based on Mike*, Degree of Master, Northwest A&F University, Xianyang, China, 2019.

[33] S. S. Lu, *Tailings Dam Flood Overtopping Model Test and Numerical Simulation*, Degree of Master, Nanchang Institute of Technology, Nanchang, China, 2019.

[34] Z. Qin, *Study on Guided Wave Charateristics in Dam Break Process of Tailings Reservoir*, Degree of Master, Jiangxi University of Science and Technology, Nanchang, China, 2019.

[35] G. S. Du, *Engineering Fluid Mechanics*, China Electric Power Press, Beijing, China, 2nd edition, 2014.

[36] C. G. Wu, *Hydraulics*, Higher Education Press, Beijing, China, 3rd edition, 1982.

Research Article

Behaviors and Overlying Strata Failure Law for Underground Filling of a Gently Inclined Medium-Thick Phosphate Deposit

Xiaoshuang Li,[1,2,3,4] Jiabo Geng,[1] Qihang Li [1] ,[1] Weijun Tian,[5] and Tao Zhou[1]

[1]*School of Resources and Environmental Engineering, Jiangxi University of Science and Technology, Ganzhou, Jiangxi 341000, China*
[2]*School of Civil Engineering, Shaoxing University, Shaoxing, Zhejiang 312000, China*
[3]*College of Civil Engineering, Qilu Institute of Technology, Jinan, Shandong 250200, China*
[4]*Sinosteel Maanshan General Institute of Mining Research Co. Ltd., Maanshan, Anhui 243000, China*
[5]*State Key Laboratory of Coal Mine Disaster Dynamics and Control, Chongqing University, Chongqing 400030, China*

Correspondence should be addressed to Qihang Li; 6720190072@mail.jxust.edu.cn

In this study, the No. 6 pit in the eastern mining area of the Jinning phosphate mine in China was taken as the research background. In order to reduce the cost of filling, an improved pillarless sublevel caving method is proposed. This method greatly improves the ore recovery rate by adding a recovery route. In addition, the combination of similar material simulation experiments and numerical simulations (discrete element and universal distinct element code) revealed the deformation and failure laws of the surrounding roof rock and the characteristics of the surface subsidence. The results indicate the following. (1) The similar simulation experimental results indicate that the deformation of the overlying rock layer originated from the direct roof of the goaf and gradually developed into the deep part of the rock layer. An irregular stepped caving zone formed in the goaf. The maximum surface subsidence was located above the phosphorus orebody, and it gradually decreased toward both sides. As the stope approached propulsion, the location of the maximum subsidence gradually moved toward the propulsion direction. (2) The numerical results revealed that the displacement of the overlying strata was nonlinear, and it decreased with increasing roof height. A support pressure concentration area was formed within a certain range of the stope roof. The numerical simulation results are basically consistent with the similar simulation experimental results.

1. Introduction

Among the major phosphate rock-producing countries, China has abundant phosphate rock resources but insufficient production and still needs to import some phosphate rocks. The main reason for this is that construction and production are restricted by the inclined mining method and gently inclined medium-thick ore bodies [1–4]. At present, most mines mainly adopt the shallow hole room-pillar method of underground mining, followed by the pillarless sublevel caving method and the bottom ore structure. However, practice has demonstrated that the room-pillar method of underground mining of medium-thick ore bodies causes a series of problems in rock drilling, ore

transportation, and roof management [5–8]. Currently, many valuable studies have been conducted on phosphate filling. Ding et al. analyzed the mechanism of surface subsidence and ground fissures caused by block caving and underground filling based on the law of displacement evolution, and the surface showed obvious segmentation characteristics [9]. Du et al. revealed the basic laws of roof caving and surface subsidence in the process of mining metals via pillarless sublevel caving [10]. Rui proposed that the pillarless sublevel caving method requires the formation of a cover layer with a certain thickness to achieve roof pressure management [11]. Ren proposed that it is more economical to adopt pillarless sublevel caving in open pit-to-underground mining [12].

The abovementioned methods cannot effectively verify the experimental results or systematically explain the failure evolution of the stope. With the proficient application of numerical simulation technology to phosphate filling, Xia used FLAC3D (Fast Lagrangian Analysis of Continua 3D) to simulate the specific characteristics of the ore body's structure in the main ore layer and revealed the evolutionary law of ground failure [13]. Wang et al. studied the distribution rate of the abutment pressure based on FLAC3D numerical simulations and proposed that retaining the coal safety pillar used to protect the inclination angle can increase the coal utilization rate [14]. Li et al. used the pillarless sublevel caving method to analyze the movement of pillars and pointed out the importance of optimizing the ore-drawing step based on the PFC3D (Particle Flow Code 3D) particle flow results [15].

In general, these methods have not been used to systematically study the destruction and evolution laws of inclined and gently inclined medium-thick ore bodies. In addition, they cannot take into account the economic benefits and result in the waste of recycled ore. Therefore, based on the geological conditions and mining technology of the No. 6 pit in the eastern mining area of the Jinning phosphate mine, we propose an improved pillarless sublevel caving method. This method reduces the ridge loss and improves the mining recovery rate. Based on similar physical model experiments and universal distinct element code (UDEC) numerical simulations, the evolution of the displacement and the failure of the overlying strata were obtained.

2. Similar Physical Model Experiments

2.1. Engineering Background. The No.6 pit in the eastern mining area of the Jinning Phosphate Mine is located in the hinterland of the Yunnan Plateau, China. It belongs to the Jinsha River system and is adjacent to the Nanpan River watershed in the south. This mine trends in the north-south direction, with a maximum elevation of 2483.5 m. The area has a subtropical monsoon climate, and the maximum annual rainfall is 1172.1 mm. The rainy season is mainly concentrated from May to October, accounting for 80% of the annual precipitation. There are no surface water bodies in the mining area except for small scattered reservoirs that intercept the streams in the foothills. The mining area is close to the middle section of the western wing of the Wangjiawan syncline, which is a monoclinic structure that strikes nearly north-south and dips eastward. The stratigraphic occurrence in the region strikes 335–355° to the north of Wangjiawan with an inclination angle of 40–50° and strikes 350-10° to the south of Wangjiawan with an inclination angle of 20–30°. The structure in the monoclinic area is relatively simple, and the secondary folds are not fully developed (Figure 1).

2.2. Similarity Criterion and Parameters. The transfer of phosphate ore from open pit-to-underground mining is a complex engineering system involving many factors [16]. In the similar simulation tests, we mainly considered the

following parameters: the thickness of the phosphate rock layer M, the thickness of each rock layer H, the compressive strength σ_c, the tensile strength σ_t, the bulk density γ, the elastic modulus E, the time t, and Poisson's ratio μ. The equation is

$$F\left(H, M, \sigma_c, \sigma_t, \gamma, E, \mu, t\right) = 0. \tag{1}$$

The following five similar criteria can be obtained by applying the dimensional analysis method:

$$\begin{cases} \pi_1 = \dfrac{\sqrt{H}}{t}, \\[2mm] \pi_2 = \dfrac{E}{\sigma_c}, \\[2mm] \pi_3 = \dfrac{\sigma_c}{\sigma_t}, \\[2mm] \pi_4 = \dfrac{\gamma H}{\sigma_c}, \\[2mm] \pi_5 = \dfrac{M}{H}. \end{cases} \tag{2}$$

Therefore, in order to make the model similar to the prototype, it needs to satisfy the following equations:

$$\begin{aligned} \frac{E_m}{E_p} &= \frac{\sigma_{tm}}{\sigma_{tp}}, \\[2mm] \frac{\sigma_{cm}}{\sigma_{cp}} &= \frac{\sigma_{tm}}{\sigma_{tp}}, \\[2mm] \frac{\sigma_{cm}}{\sigma_{cp}} &= \frac{\gamma_m \cdot H_m}{\gamma_p \cdot H_p}, \\[2mm] \frac{H_m}{H_p} &= \frac{M_m}{M_p}, \\[2mm] \frac{t_m}{t_p} &= \sqrt{\frac{H_m}{H_p}}. \end{aligned} \tag{3}$$

Based on the laboratory conditions, we conducted experiments on a rigid $3.0\,\mathrm{m} \times 0.30\,\mathrm{m} \times 2.0\,\mathrm{m}$ (length × width × height) model frame. The model design parameters are presented in Table 1.

2.3. Similar Material. In the experiment, we used fine river sands as the aggregates, calcium carbonate and gypsum as the cementing materials, and sodium tetraborate (boric acid) as the retarder [17–21]. The larger structural surfaces (faults) in the actual site were individually simulated by adding various additives (rosin, wood powder). The layer simulation method is to screen a mica powder and grease medium as the interlayer spacers on the layer's surface. The detailed proportioning steps are as follows:
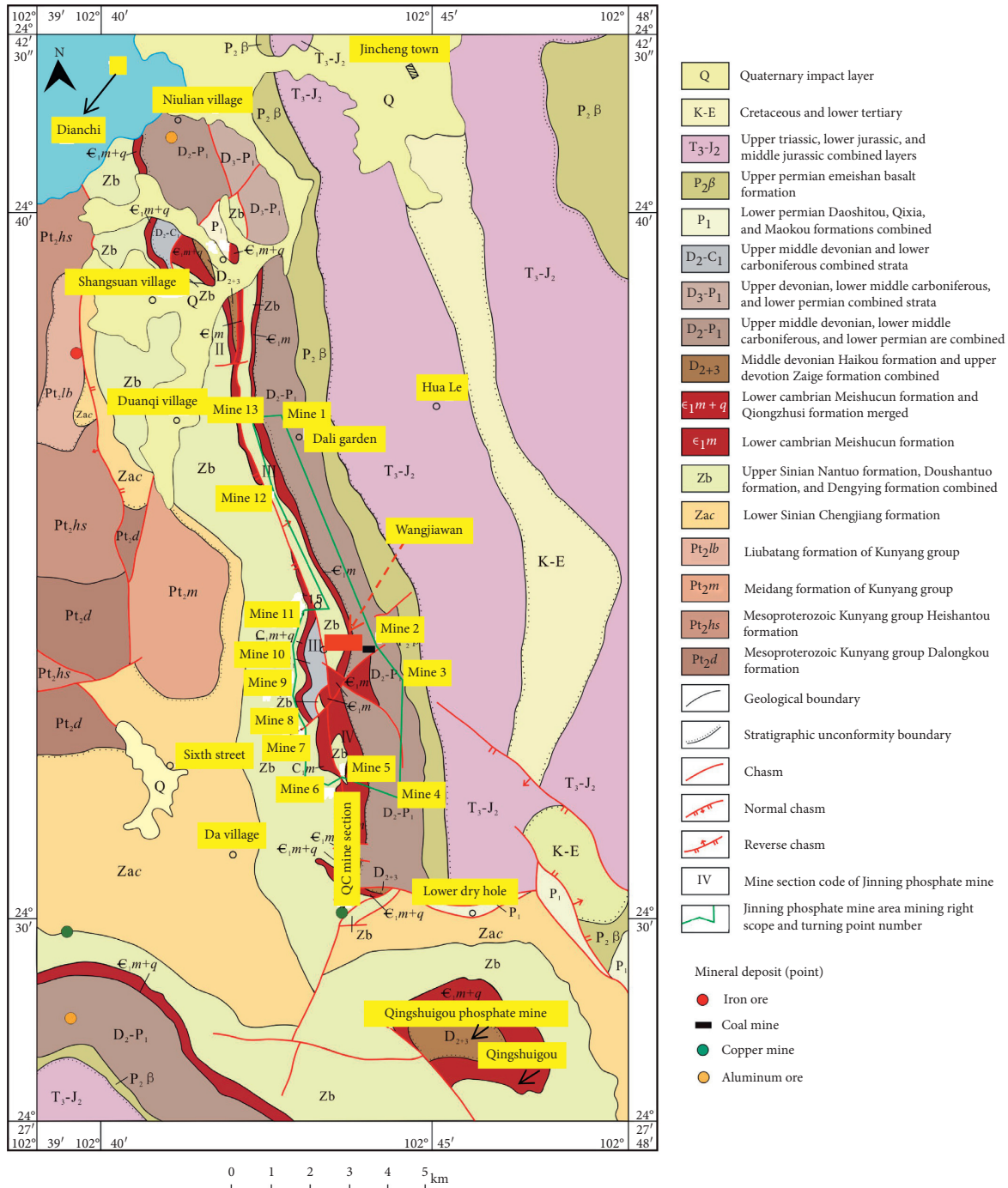
FIGURE 1: Regional geologic map of the Jinning phosphate mine.

(1) Brush the test mold with engine oil

(2) Weigh the sand, gypsum, and calcium carbonate in a certain proportion, mix, and stir evenly

(3) Add a certain amount of water containing borax, stir, and pour into the mold

(4) After drying for about four days, place the finished test piece (10 cm × 5 cm × 5 cm standard cylindrical test piece) on the servo pressure testing machine to measure its uniaxial compressive strength (Figure 2)

In order to reduce the error generated in the material proportioning process, we took the average value of the compressive strength of the three test pieces as the compressive strength of the material ratio number [22, 23]. The proportioning of the model similar material of the No. 6 pit in the eastern mining area is shown in Table 2.

2.4. Physical Model Making Process. First, we applied engine oil to the surface of the template. Then, we weighed the required sand, calcium carbonate, and gypsum and poured

TABLE 1: The parameter table of the model design.

Parameters	Numerical values
Model size ratio	1/240
Model length (mm)	3000
Model height (mm)	1040
Model width (mm)	300
Time similarity coefficient	1/16
Bulk weight similarity coefficient	0.81
Intensity similarity coefficient	1/296
External force similarity coefficient	5.86×10^{-8}
Modulus of elasticity	1/296
Poisson's ratio	1

them into the mixer to mix. We added a certain amount of retarder (borax) and water to the mixed material and mixed it evenly. The prepared material was poured into the model frame and was smoothed and compacted with a spatula. The template was placed on its side, and the material was poured. This process was repeated several times until the designed height of the physical model was reached. After drying for one week, we removed the template on both sides, continued to dry the sample for two weeks, and finally carried out the mining and observation experiments. During the production process, we used mica powder to separate the layers from each other. The actual physical model is shown in Figure 3.

3. Method

3.1. Improved Pillarless Sublevel Caving Method.
The pillarless sublevel caving method is mainly suitable for steeply inclined ore bodies with a medium or greater thickness, as well as inclined and gently inclined extremely thick ore bodies [24–27]. For moderately thick and gently inclined phosphate ore, this method will result in the loss of a large amount of ore. Therefore, we propose an improved pillarless sublevel caving method. This method is a new mining scheme in which a recycling route is added at the bottom, which greatly reduces the cost of filling (Figure 4(a)). Our method utilizes the space provided by the first segmented approach to induce natural falling of the surrounding roof rock. By digging the surrounding rock of the footwall to form a recycling route, the ore remaining in the stope can be fully recovered. In order to recover the ridge residue and the bottom wall residue, it is necessary to set up a recovery route in the surrounding rock under the residue. The essence of setting up the recovery route is to use the flow characteristics of the bulk to increase the recovery rate (Figure 4(b)). The flow of the bulk only occurs in a certain range above the discharge outlet. The calculation formula for this range is

$$R = 2.5\sqrt{0.5\beta Z^{\alpha}}. \tag{4}$$

In equation (4), R is the radius of the bulk flow range; Z is the height coordinate value; and α is the bulk flow parameter.

3.2. Simulation of Underground Mining and Displacement Monitoring.
An improved pillarless sublevel caving method was used to simulate the mining process in underground

mines. As shown in Figure 4(c), the distance between the adjacent mining approach and the recovery route is 11 m (4.6 cm). Every time an approach is advanced, the surface and the ground are measured and recorded after an hour-long interval. In the initial stage of mining, we only dug out part of the ore body. After the surrounding rock collapses, the surrounding rock without restriction on both sides will be scattered to the outside of the model. At this time, manual backfilling is required to form an overburden.

4. Results

4.1. Collapse Process and Theoretical Analysis of the Overlying Strata.
The collapse of the overlying strata is firstly the breaking of roof strata, then the instability of broken rock blocks, and finally directly to the surface cracking and collapse. The process is mainly divided into the following stages.

(1) Stable stage (the first to the second route): after the ore body of the two routes is mined out, the surrounding rock is stable and there is no falling phenomenon.

(2) Falling stage (the third to the fourth route): in this stage, the overlying roof gradually bends and deforms to falling. After the mining of the fourth approach, cracks appear in the overlying strata. About 2 hours later, the gravelly quartz sandstone in the roof partially collapses (Figure 5(a)).

(3) Caving stage (the fifth to the sixth route): with the development of mining, the width of the caving arch gradually increases, the slag falls from the vault, and the cracks continue to develop. At the end of the sixth recovery route, the gravelly quartz sandstone collapses as a whole, and the vault of the roof fall arch shows the phenomenon of bed separation, and more new cracks are produced (Figure 5(b)).

(4) Surface cracking and collapse stage: with the progress of mining, the layer separation phenomenon of falling arch roof intensifies. When the eighth mining approach is completed, the crack development speed is accelerated, tension joints appear on both sides of the model (Figure 6), and the crack length gradually extends downward. Finally, the surrounding rock between the two tension joints falls as a whole, resulting in surface cracking and settlement. In the subsequent excavation process, the crack length further increases, a new tension crack appears outside the initial crack, and the surface subsidence value gradually increases. However, due to the existence of the lower ridge ore body, the surface subsidence is slow and has obvious process. When the ridge is excavated through the mining recovery route, the overburden layer falls with the mining, or even the ore falls ahead of the mining, the overlying surrounding rock collapses faster, the scope expands, and the surface subsides further.

(a)   (b)

FIGURE 2: (a) Servo experimental equipment. (b) Typical uniaxial compression failure mode of rock samples.

TABLE 2: The proportioning table of the model similar material of the No.6 east mining area.

Lithology	Actual thickness (m)	Actual strength (MPa)	Simulated thickness (m)	Simulated strength (kPa)	Similar material ratio (sand : calcium carbonate : gypsum)
Quaternary cover layer	17.47	20.26	7.28	68.56	6 : 7 : 3
Gravel dolomite	59.00	95.86	24.58	323.52	3.5 : 5 : 6
Layered cryptocrystalline dolomite	17.00	88.32	7.08	298.85	3.8 : 5 : 5
Medium to coarse crystalline dolomite	45.00	80.00	18.75	270.69	4 : 2 : 8
Layered argillaceous dolomite	9.00	63.62	3.75	215.27	4 : 5 : 5
Pebbly quartz sandstone	17.80	88.32	7.42	298.85	3.8 : 5 : 5
Industrial phosphate rock	13.31	137.12	5.54	463.98	3 : 2 : 8
Low-grade phosphorus rock formation	21.94	118.00	9.14	399.28	3.2 : 3 : 7
Medium-thick layered dolomite	16.00	101.88	6.67	344.73	3.5 : 3 : 7
Medium-thick primary dolomite	33.50	98.50	13.96	333.29	3.5 : 3.5 : 6.5

4.2. Analysis of the Similar Physical Simulation Experiment Results. In the early stage of mining, the overlying rock underwent a small amount of movement (Figure 7(a)). After advancing to the sixth-level mining approach, along with the development of separations and fissures, the quartz sandstone above began to fall off (Figure 7(b)). When the tenth-level mining approach was excavated, the caving zone of the roof slab expended, and eventually, the old roof ruptured and the ground subsided (Figure 7(c)). During the entire collapse process, the overlying rock strata were first destroyed in the surrounding rock of the goaf and then developed to the deep part of the rock formation, forming an irregular stepped caving zone above the goaf (Figure 7(d)). In addition, the fissures in the overlying strata continued to develop, and there was obvious layering in the collapse area (Figure 6).

4.3. Overlying Strata and Ground Movement Law. According to the rock displacement monitoring results (Figures 8(a)–8(d)), the subsidence of the overlying rock strata changed dynamically with the advancement of the working face. The subsidence range gradually expanded

along the direction of the working face. With the advancement of the mining approach, the lower separation fissures of the overlying strata gradually closed. As the working face advanced, the separation fissures also extended forward and upward. In the case of sufficient mining, after the overlying rock above the ridge sank to the position of the ridge, the sinking speed became very slow or stopped. Therefore, the curve of the lower layer of the surrounding roof rock is wavy, and the closer it is to the roof of the orebody, the greater the difference between the peaks and valleys of the curve (Figure 8(a)). The surface subsidence curve is shown in Figure 8(d). The maximum surface subsidence occurred directly above the phosphorus ore body, and the maximum subsidence displacement gradually moved in the direction of the advancement.

4.4. Stress Variation Law of the Surrounding Rock in the Stope. As shown in Figures 9(a)–9(c), with the advancement of the mining approach, the stress in the overlying strata constantly changed. The stress concentration area affected the rock for about 50 m in front of the working face, and the peak stress appeared 20 m in front of the working face. In the process of
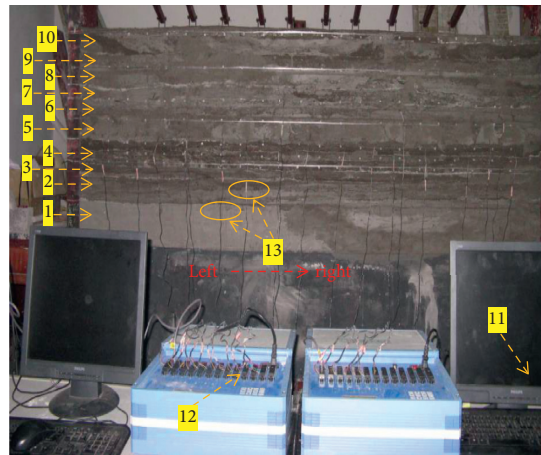
(1) Medium-thick primary dolomite
(2) Medium-thick layered dolomite
(3) Low-grade phosphorous rock formation
(4) Industrial phosphate rock
(5) Pebbly quartz sandstone
(6) Layered argillaceous dolomite
(7) Medium to coarse crystalline dolomite
(8) Layered cryptocrystalline dolomite
(9) Gravel dolomite
(10) Quaternary cover layer
(11) Data acquisition device
(12) Sensor equipment
(13) No. 1–19 displacement sensors position
     (from left to right)

FIGURE 3: The actual physical model.
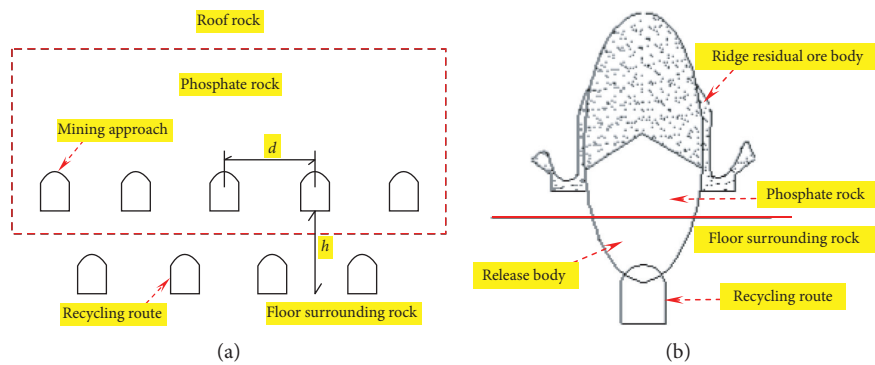
(a)

(b)
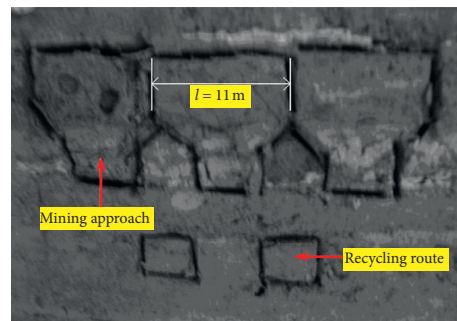
(c)

FIGURE 4: (a) Schematic diagram of the stope structure, (b) schematic diagram of the recovery route, and (c) excavation model diagram.

(a)

(b)
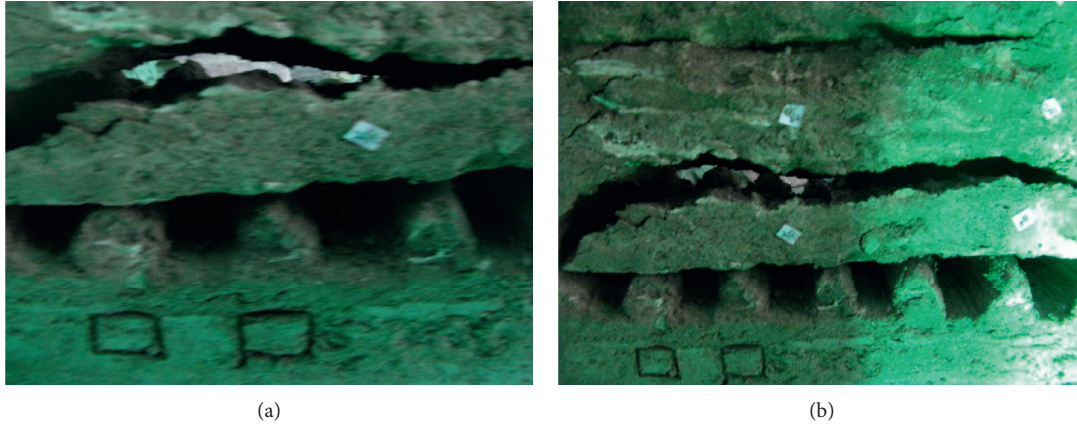
Figure 5: (a) The roof falling stage; (b) the block caving stage.

excavating and recycling roadways, the stress in the overlying strata of the stope also constantly changed and was more complex (Figures 9(d)–9(f)).

5. Discussion

5.1. Size and Boundary Conditions of the Numerical Simulation Model. In the field of mining engineering, UDEC numerical simulation technology has been applied to the static and dynamic analyses of deep underground mining caverns [28–30]. This technology can accurately analyze the fractures and slip induced by the destruction of the surrounding rock of the cavern. Based on the geological conditions and mechanical parameters of the No. 6 pit in the eastern mining area of the Jinning phosphate mine in the Yunnan phosphate group, the thickness of the phosphate rock in the discrete element model was set to 13.31 m. The X direction is the strike direction, and the part of the advancing length of the working face is 720 m. The Y direction has an average burial depth of 250 m. This model simulates a total of 10 layers, and the thickness of each layer is simulated according to the actual thickness (both the X and Y directions consider the 100-meter boundary influential area). Since the mine is an open pit mine (nearly shallowly buried phosphate layer), the strata cannot be omitted in this simulation. The model is 720 m × 250 m (length × height) (Figure 10).

The boundary conditions of the calculation model are as follows:

(1) Horizontal boundaries are constraints imposed on the left and right boundaries of the calculation model (the horizontal displacement of the boundary is zero)

(2) The bottom boundary of the calculation model is fixed (both the horizontal and vertical displacements of the bottom boundary are zero)

(3) The top of the calculation model is the free boundary

5.2. Material Constitutive Model and Failure Criterion. In our study, the ideal elastoplastic constitutive model was adopted for the rock mass, and the basic criterion of the rock material failure obeyed the Mohr-Coulomb relationship [31, 32]. Therefore, the linear failure surface formula corresponding to shear failure is

$$f_s = \sigma_1 - \sigma_3 N_\varphi + 2c\sqrt{N_\varphi}. \tag{5}$$

In equation (5), $N_\varphi = (1 + \sin\varphi)(1 - \sin\varphi)$; σ_1 is the maximum principal stress; σ_3 is the minimum principal stress; φ is the angle of internal friction; and c is the cohesion.

If $f_s < 0$, shear yielding occurs. When the normal stress becomes tensile stress, the Mohr-Coulomb criterion loses its practical significance. For simplicity, however, the yield surface extends to the area where σ_3 is equal to its tensile strength and the tensile strength σ^t. The minimum principal stress cannot exceed the tensile strength:

$$f_t = \sigma_3 - \sigma^t. \tag{6}$$

If $f_s \geq 0$, tension yielding occurs. The value that the tensile strength cannot exceed corresponds to the upper limit of the Mohr–Coulomb relationship. The maximum value is determined using the following formula:

$$\sigma^t_{max} = \frac{c}{\tan\varphi}. \tag{7}$$

We determined the physical and mechanical parameters of each layer in the model based on the test results. The physical and mechanical parameters of each layer are presented in Table 3.

5.3. Failure Process of Overlying Strata. In the mining process, in order to reflect the evolution of the movement and deformation of the rock layer, step-by-step excavation was adopted [33–38]. We advanced the work surface by a certain distance to perform an operation. When the second-level mining approach was advanced, the overlying strata remained basically unchanged (Figure 11(a)). When the sixth-level mining approach was continued, the gravelly quartz sandstone began to fail under the load of the overlying strata and its own weight (Figure 11(b)). As the advancement continued, the vertical deformation of the

(a)

(b)

(c)
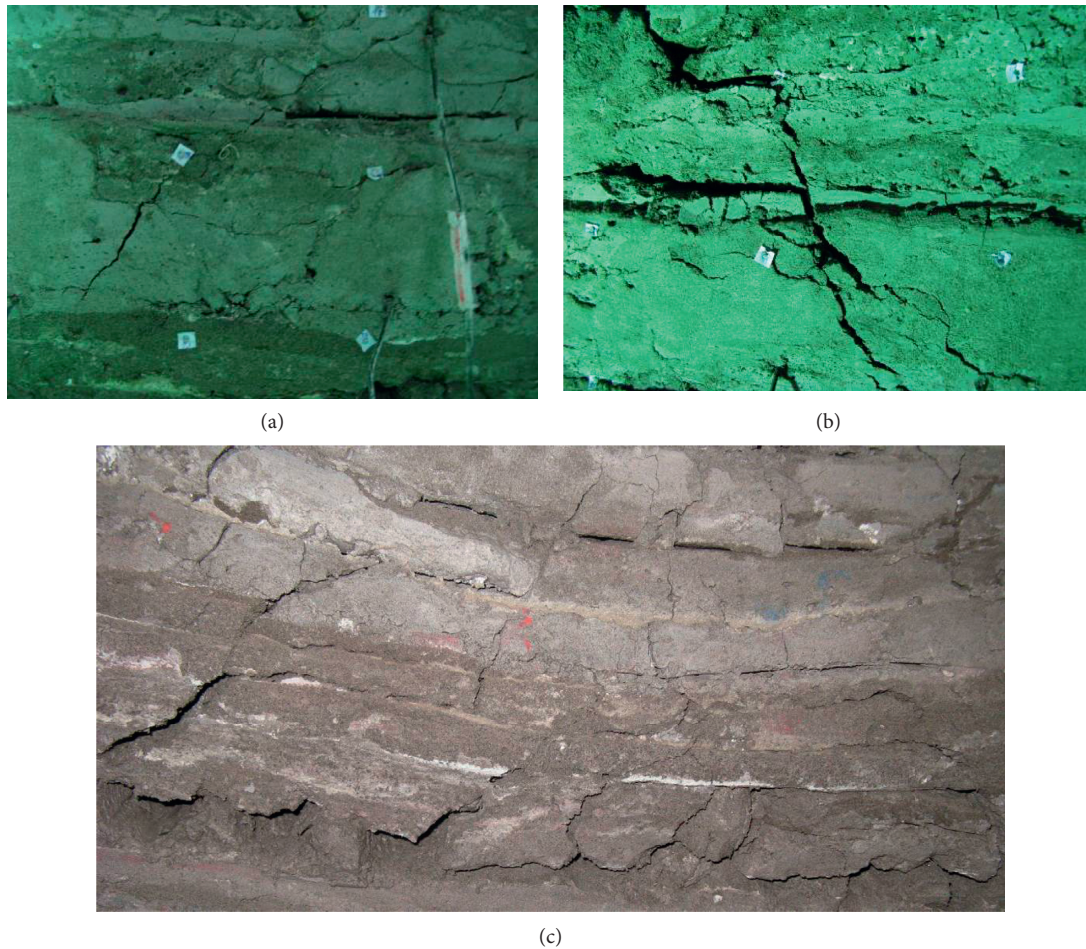
FIGURE 6: The phenomenon during the experiment. (a) Fissures that develop from the left upwards as the mining approach advances. (b) Fissures that develop form the right upwards as the mining approach advances. (c) Obvious stratification phenomenon during the collapse.

rock formation increased, causing tensile failure and breakage of the rock formation (Figure 11(c)). When the seventeenth-level mining approach was advanced, the broken rock block fell into the goaf, forming a trapezoidal collapse zone (Figure 11(d)). In the process of advancing the first-tenth recovery route, the deformation continued to increase and the old top dolomite cracked (Figures 12(a)–12(c)). When the sixteenth-level recovery route ended, the surface began to collapse, and the roof of the overlying rock was the most severely damaged [39, 40].

5.4. Displacement of the Overlying Strata. As shown in Figure 13, in the early stage of mining, the upper rock layer was less affected by the mining, and the vertical displacement was small. As the working face advanced, the area of the overlying rock strata affected by the mining continued to increase, and the subsidence value gradually increased. After the overlying rock above the ridge sank to the position of the ridge, the sinking speed became very slow or stopped, so the curve of the lower layer of the roof surrounding rock is wavy. The shorter the distance between the overlying strata and the

roof of the orebody, the greater the difference between the peaks and troughs of the curve. The closer it is to the phosphate rock layer, the wider the impact range and the greater the sinking value.

5.5. Variation Law of the Abutment Pressure of the Overlying Strata in the Stope. According to the results of the excavation using the simulated mining approach (Figures 14(a)–14(d)), the supporting pressure gradually stabilized as the working face advanced, and the peak value appeared at 20 m. The area affected by the mining in front of the working face was divided into three parts: (1) the areas severely affected by the mining (within 20 m); (2) the areas affected by the mining (within 60 m); and (3) the areas unaffected by the mining (beyond 60 m). The simulation results of the excavation of the recovery route show that the stress in front of the working face increased, and it constantly changed and became more complicated with the advancement of the recovery route (Figures 14(e)–14(h)).

The numerical simulation results are basically the same as the similar simulation experimental results. This is mainly

(a)

(b)

(c)

(d)
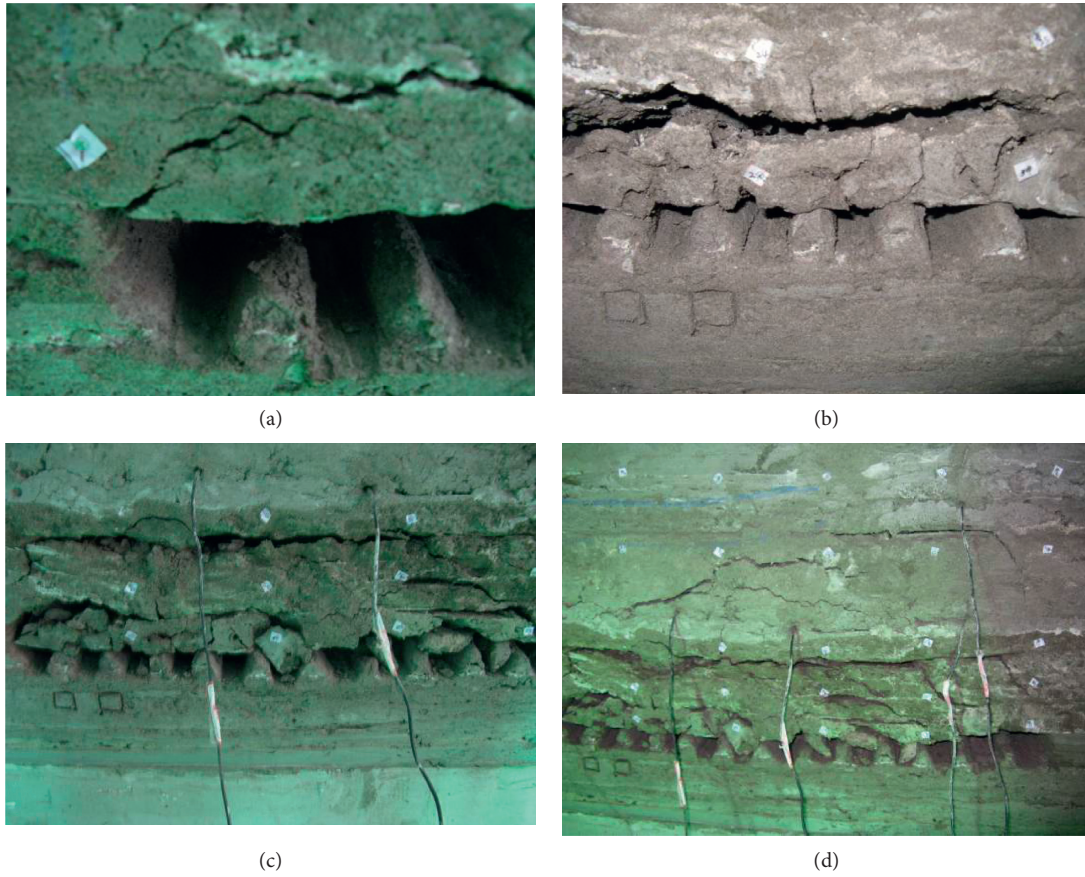
Figure 7: (a) Fissures appeared in the rock strata of the third-level mining approach. (b) Promotion of the sixth-level mining approach directly above the avalanche. (c) Promotion of the collapse of the top slab of the tenth-level mining approach. (d) The roof collapses after the mining is completed.

(a)

(b)

Figure 8: Continued.

(c)
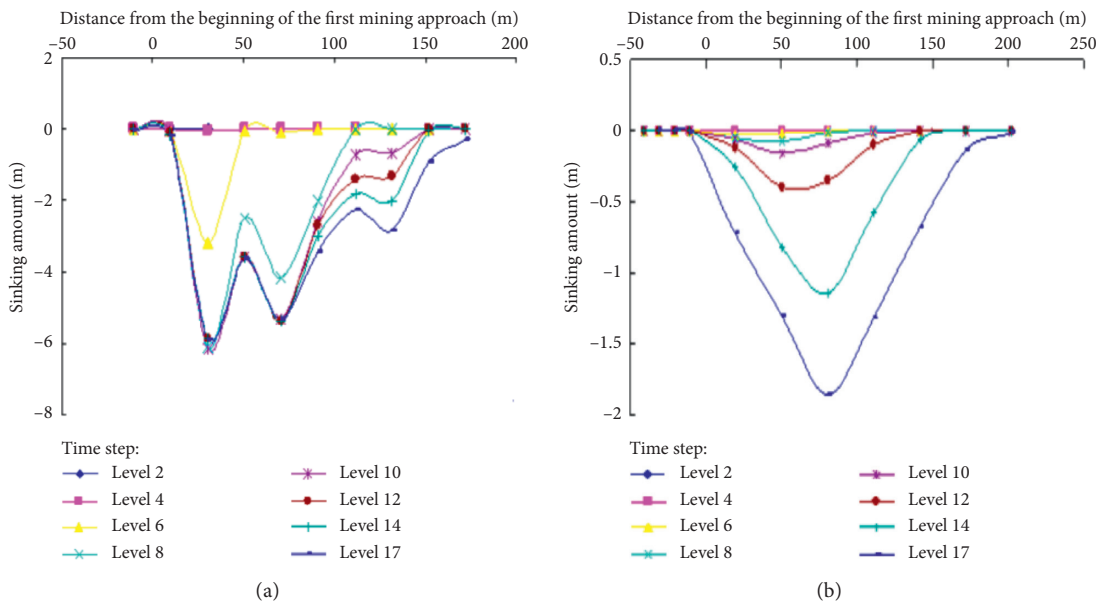
(d)
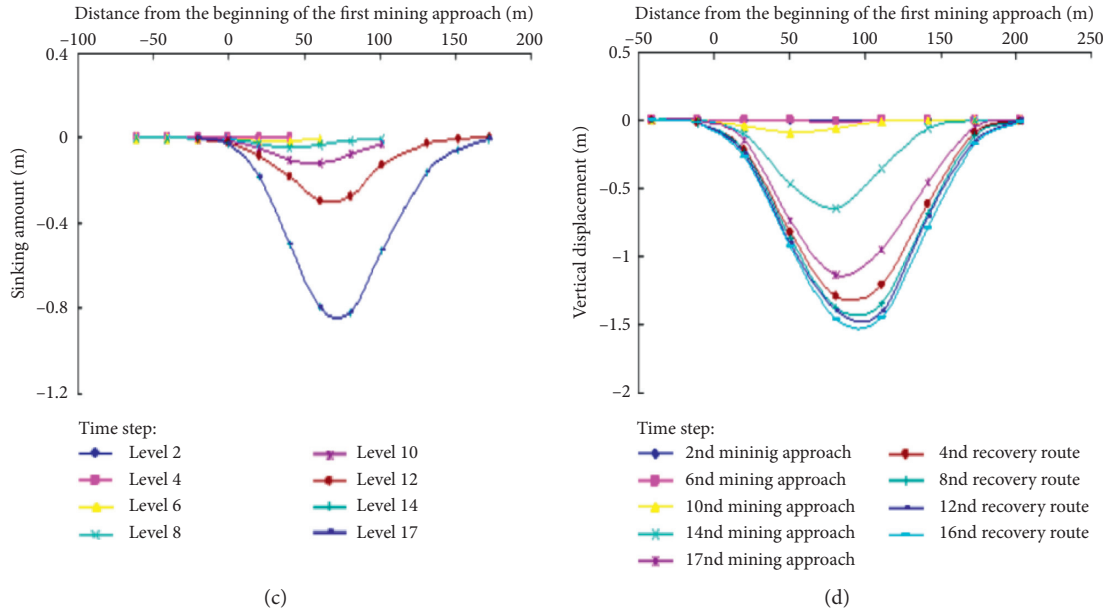
Figure 8: (a) The subsidence change curve of the rock formation (the second-level measuring points); (b) the subsidence change curve of the rock formation (the fourth-level measuring points); (c) the subsidence change curve of the rock formation (the seventh-level measuring points); and (d) the change curve of the surface subsidence and displacement (advancement via different approaches).

(a)

(b)

(c)

(d)

Figure 9: Continued.

(e)

(f)
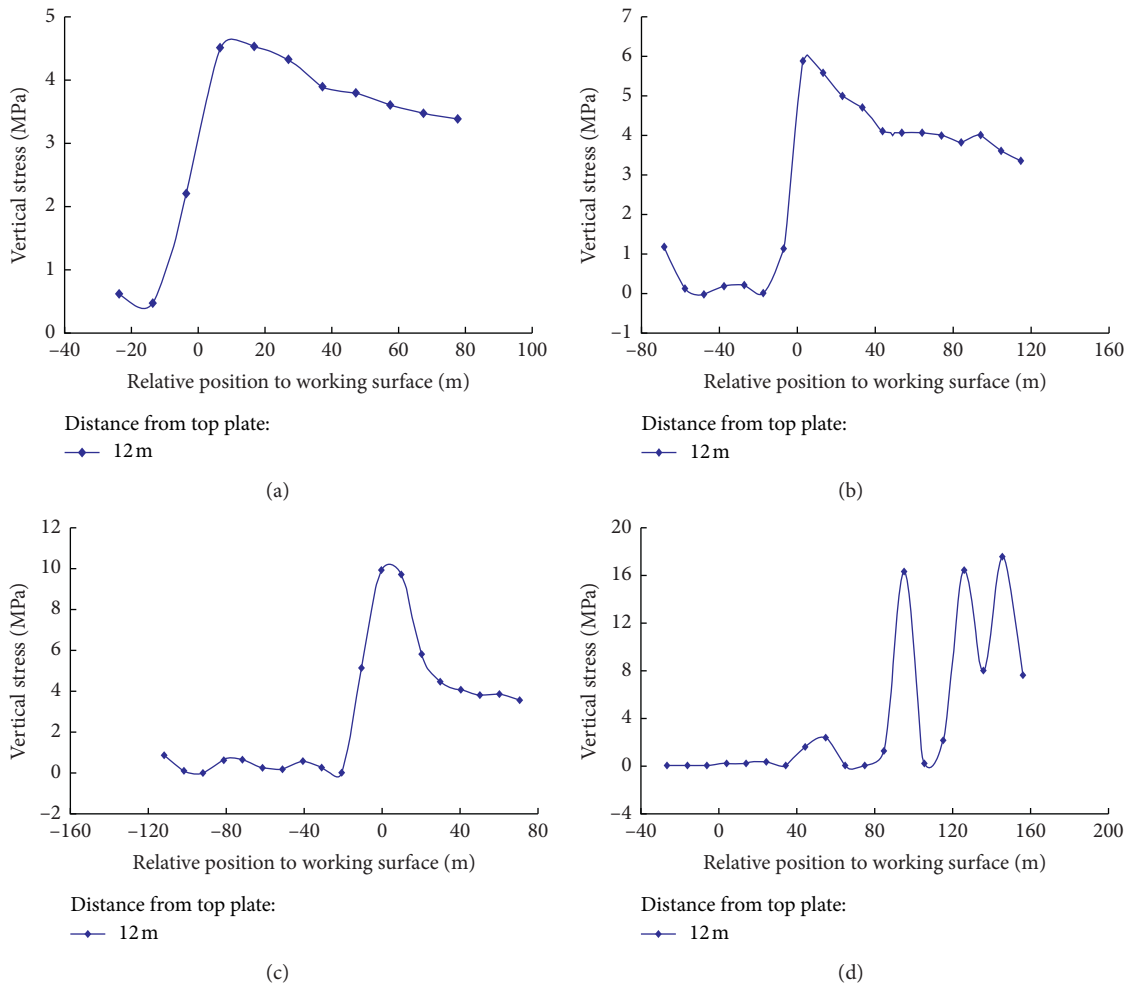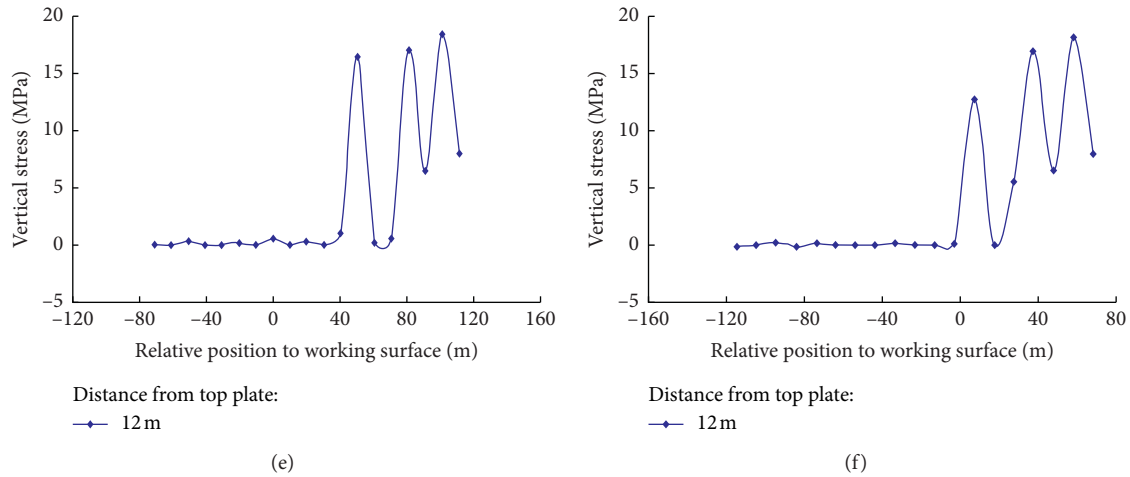
FIGURE 9: (a) The stress distribution diagram of the fourth-level mining approach; (b) the stress distribution diagram of the eighth-level mining approach; (c) the stress distribution diagram of the twelfth-level mining approach; (d) the stress distribution diagram of the fourth-level recovery route; (e) the stress distribution diagram of the eighth-level recovery route; and (f) the stress distribution diagram of the twelfth-level recovery route.

TABLE 3: The physical and mechanical properties of the rock.

Geotechnical type	Uniaxial compressive strength (MPa)	Uniaxial tensile strength (MPa)	Cohesion (MPa)	Internal friction angle (°)	Poisson's ratio	Density (kg/m^3)
Topsoil	*13.32	*0.13	*0.95	*40.00	*0.11	1800
Layered cryptocrystalline dolomite	18.17	1.04	*5.00	*42.50	*0.38	2580
Medium to coarse crystalline dolomite	28.20	2.26	*7.24	*44.20	*0.30	2610
Layered argillaceous dolomite	28.02	3.13	*5.76	*44.20	*0.25	2580
Pebbly quartz sandstone	52.99	2.20	*3.10	*43.68	*0.27	2620
Industrial phosphate rock	82.27	6.67	10.78	*43.40	*0.20	2660
Low-grade phosphate rock	70.80	4.38	*9.44	*43.60	*0.20	2566
Off-white medium-layered dolomite	50.50	3.07	*9.06	*60.00	*0.33	2500
Primary medium-thick layered dolomite	59.10	3.29	*9.07	*41.26	*0.23	2624

*Engineering analog data.
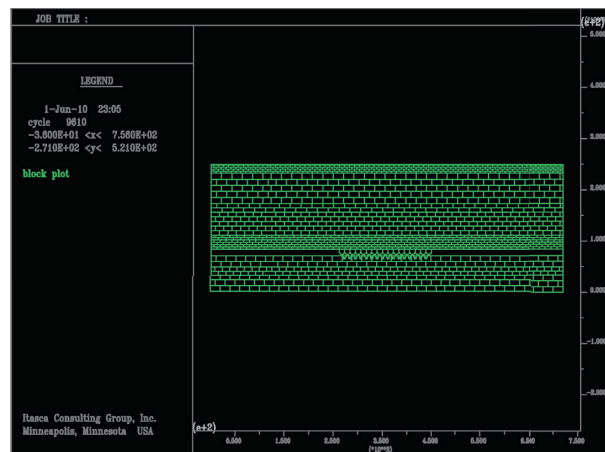
FIGURE 10: The numerical simulation model.

manifested as (1) the deformation and failure of the overlying rock strata started directly from the roof of the goaf. Then, they gradually developed toward the deep rock formation and collapsed. With the continuous advancement of the mining approach and the recovery route, an irregular trapezoidal collapse zone finally formed in the roof above the
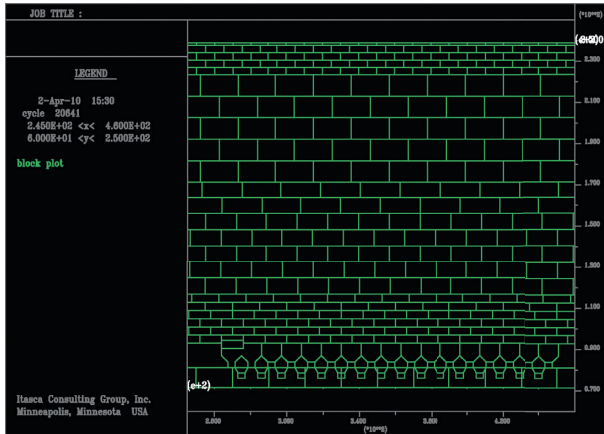
(a)
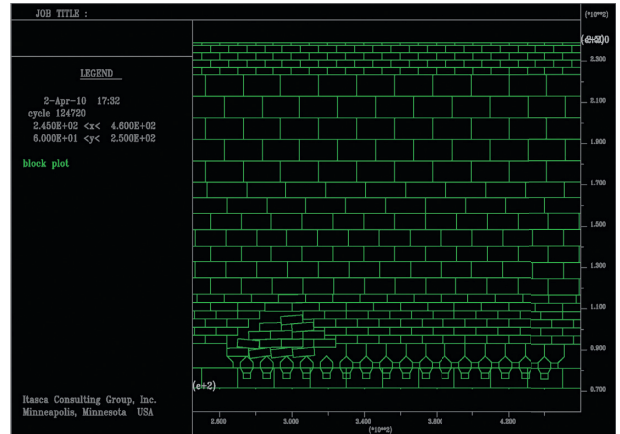
(b)
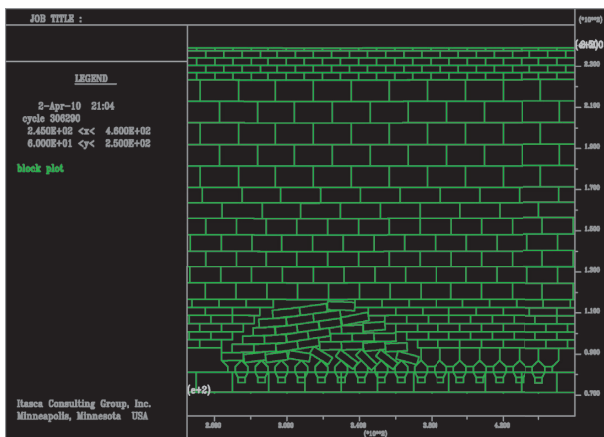
(c)
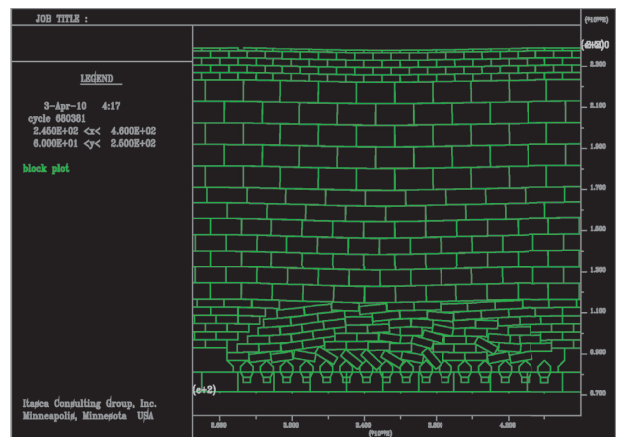
(d)

FIGURE 11: Roof failure process: (a) promotion of the second-level mining approach; (b) promotion of the sixth-level mining approach; (c) promotion of the tenth-level mining approach; and (d) promotion of the seventeenth-level mining approach.
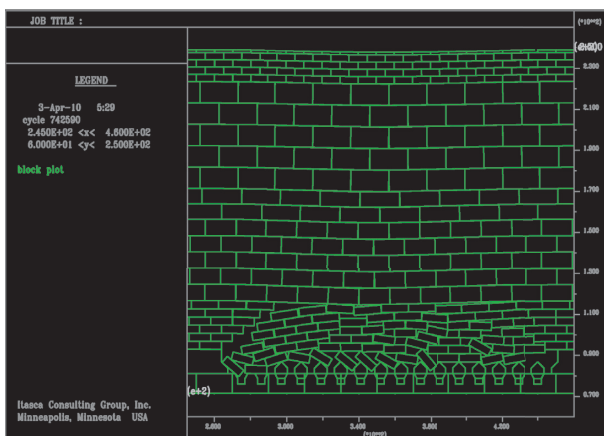
(a)
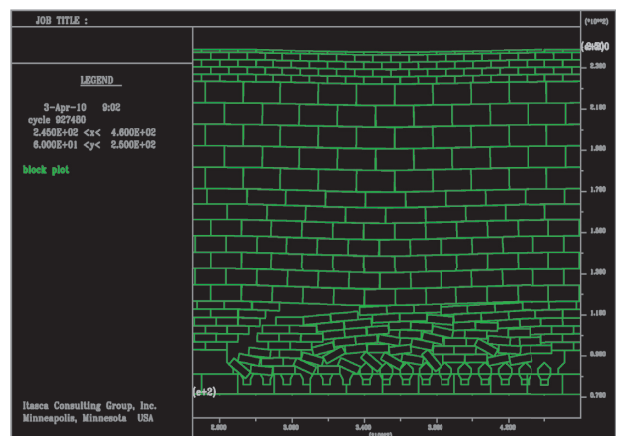
(b)

FIGURE 12: Continued.

(c)

(d)
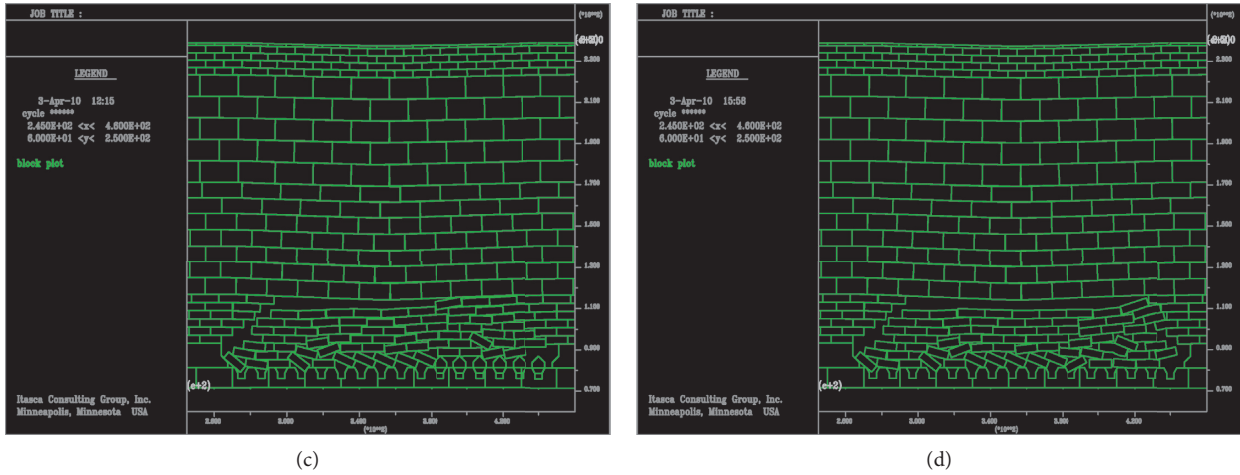
FIGURE 12: Roof failure process: (a) promotion of the second-level recycling route; (b) promotion of the sixth-level recycling route; (c) promotion of the tenth-level recycling route; and (d) promotion of the sixteenth-level recycling route.

(a)

(b)

FIGURE 13: Continued.

(c)

FIGURE 13: (a) Subsidence change curve of the rock formation (the second layer measuring points); (b) subsidence change curve of the rock formation (the fourth layer measuring points); and (c) subsidence change curve of the rock formation (the seventh layer measuring points).

(a)

(b)
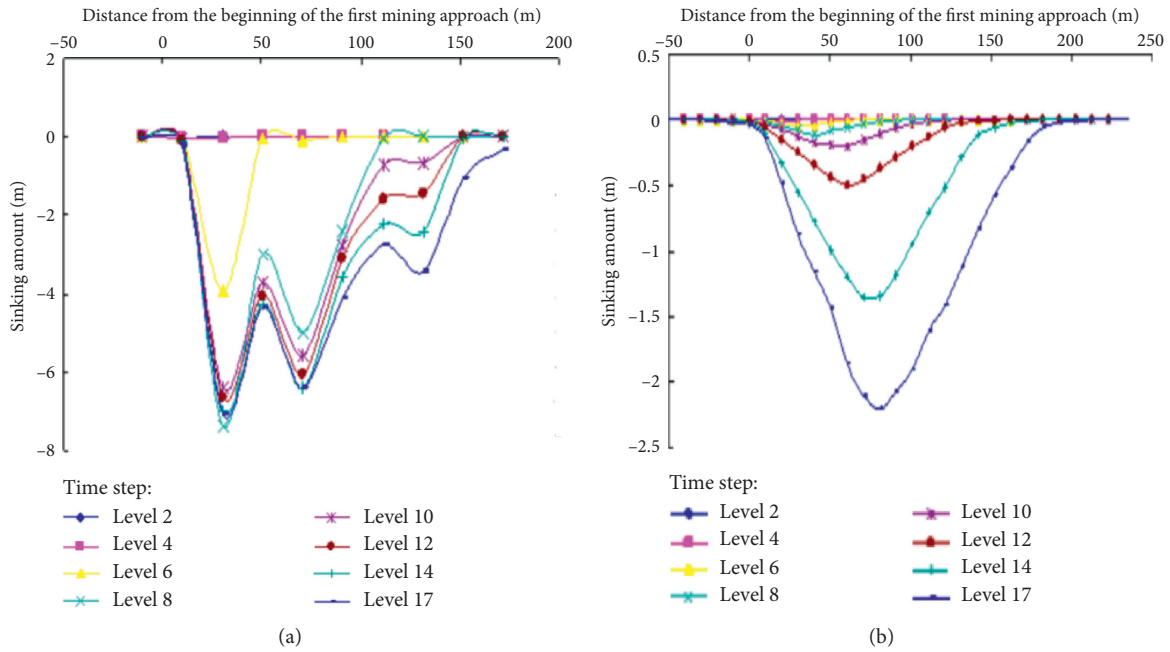
FIGURE 14: Continued.
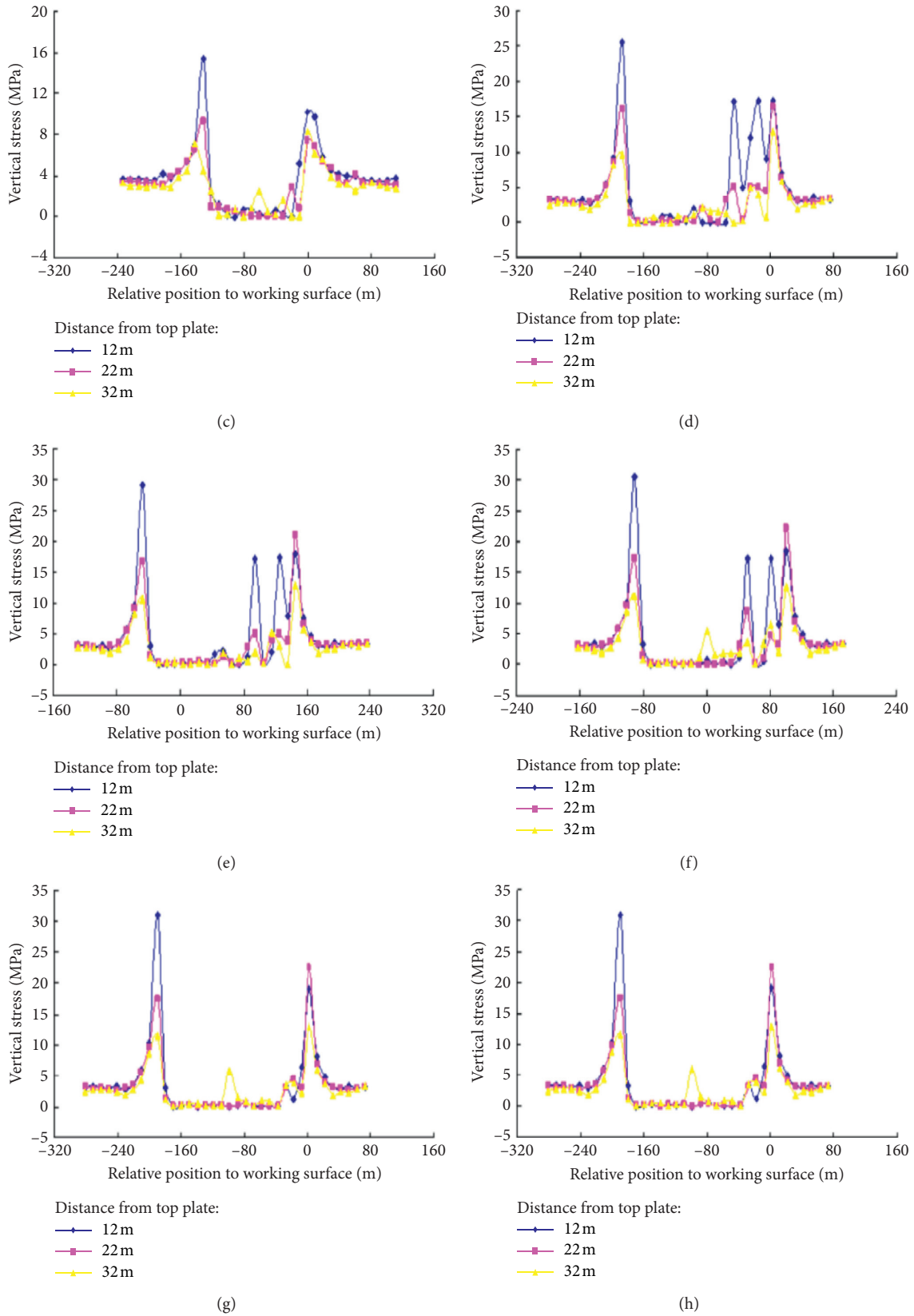
Figure 14: (a) Stress distribution diagram of the fourth-level mining approach; (b) stress distribution diagram of the eighth-level mining approach, (c) stress distribution diagram of the twelfth-level mining approach; (d) stress distribution diagram of the seventeenth-level mining approach; (e) stress distribution diagram of the fourth-level recovery route; (f) stress distribution diagram of the eighth-level recovery route; (g) stress distribution diagram of the twelfth-level recovery route; and (h) stress distribution diagram of the sixteenth-level recovery route.

goaf. (2) The displacement of the overlying strata decreased as the height of the roof increased. (3) The stress in the overlying strata of the stope constantly changed. As the working face advanced, the overburden stress near the working face increased.

6. Conclusions

In this study the deformation and failure laws of the surrounding roof rock and the characteristics of the surface subsidence were systematically investigated. The following conclusions were drawn:

(1) Based on the existing underground mining method and the actual situation of the Jinning Phosphate Mine, an improved pillarless sublevel caving method is proposed. It greatly improves the ore recovery rate and reduces the cost of filling.

(2) The similar simulation experimental results show that the deformation and failure of the overburden strata start directly from the roof of the goaf and then gradually develop into the deep part of the overburden strata, forming an irregular trapezoidal collapse zone above the goaf. The maximum surface subsidence is located directly above the goaf, and the position of the maximum subsidence gradually moves in the forward direction of the stope.

(3) The numerical simulation results show that the movement of the overlying strata is nonlinear. The subsidence displacement of the overlying strata decreases with increasing stope roof height. A support pressure concentration area forms within a certain range of the stope roof. The numerical simulation results are basically the same as the similar simulation experimental results.

Data Availability

The data used to support the findings of this study are included within the article.

Conflicts of Interest

The authors declare that there are no conflicts of interest regarding the publication of this paper.

Authors' Contributions

Conceptualization and software were done by Xiaoshuang Li; method and formal analysis were done by Qihang Li; original draft was prepared by Weijun Tian; and review and editing were done by Jiabo Geng and Tao Zhou.

Acknowledgments

References

[1] Q. F. Ge, X. S. Sun, W. G. Zhu, and Q. G. Chen, "Research of mining method for difficult-to-mine ore bodies in deep mine," *Advanced Materials Research*, vol. 962-965, pp. 1041–1046, 2014.

[2] R. N. Scoon and A. A. Mitchell, "A multi-stage orthomagmatic and partial melting hypothesis for the driekop platiniferous dunite pipe, eastern limb of the bushveld complex, south Africa," *South African Journal of Geology*, vol. 112, no. 2, pp. 163–186, 2009.

[3] A. Belkabir, H. L Gibson, E. Marcoux, D. Lentz, and S. Rziki, ""Geology and wall rock alteration at the Hercynian Draa Sfar Zn-Pb-Cu massive sulphide deposit," *Morocco*," *Ore Geology Reviews*, vol. 33, no. 3-4, pp. 280–306, 2008.

[4] A. H Abbas, "Environmental impacts of the gyp-sum mining operation at Maqna area, Tabuk, Saudi Arabia," *Environmental Geology*, vol. 41, no. 1-2, pp. 209–218, 2001.

[5] I. N Economopoulos and A. G. Vgenopoulos, "An approach concerning bauxites, bauxitization processes and mining in Greece," *Oryktos Ploutos*, vol. 109, pp. 21–34, 1998.

[6] W. Zhu, L. Chen, Z. Zhou, B. Shen, and Y. Xu, "Failure propagation of pillars and roof in a room and pillar mine induced by longwall mining in the lower seam," *Rock Mechanics and Rock Engineering*, vol. 52, no. 4, pp. 1193–1209, 2019.

[7] K. Skrzypkowski, W. Korzeniowski, K. Zagórski, and A. Zagórska, "Adjustment of the yielding system of mechanical rock bolts for room and pillar mining method in stratified rock mass," *Energies*, vol. 13, no. 8, p. 2082, 2020.

[8] M. A. A. Marzouk, D. Li, G. F. Ren, and C. R. Zhang, "Estimating deterioration rate of some carbonate rocks used as building materials under repeated frost damage process, China," *Advances in Materials Science and Engineering*, vol. 13, pp. 1–13, 2020.

[9] K. Ding, F. S. Ma, H. J. Zhao, J. Guo, J. J. Zhu, and M. H. Tian, "Monitoring and mechanism of ground movement and fissures formed by block caving and sublevel filling in the jingerquan nickel mine, China," *International Journal of Simulation. Systems, Science and Technology*, vol. 17, no. 22, 2016.

[10] C. F Du, J. H. Du, L. W. Guo, and G. Y. Tang, "Mechanism of capping rock collapse by no-pillar sublevel caving," *Journal of University of Science and Technology Beijing*, vol. 31, no. 6, pp. 667–673, 2009.

[11] Z. Y. Rui, "Technical economy and environmental protection of converting open-pit mining to underground mining," *World Mining Equipment*, vol. 6, pp. 13–19, 1999.

[12] S. C. Ren, "Determination of mining methods in the transition period of baiyin super large copper mine from open-pit to underground," *Non-ferrous Mines*, vol. 6, pp. 1–7, 1995.

[13] Z. Xia, Z. Tan, and Y. Miao, "Damage evolution mechanism of extraction structure during mining gently dipped orebody by block caving method," *Geotechnical & Geological Engineering*, vol. 38, no. 4, pp. 3891–3902, 2020.

[14] X.-q. Wang, X.-r. Meng, Z.-n. Gao, and Z.-h. Liu, "Optimal location of terminal line in sublevel caving face with suspendshift support in thinner thick-seam," *Journal of Coal Science and Engineering*, vol. 14, no. 4, pp. 600–603, 2008.

[15] B. Li, M. G. Xu, H. B. Cao, and Y. Li, "J. MA. "Numerical simulation to optimize the drawing pace of sublevel caving without sill pillar"," *Mining Research And Development*, vol. 2, pp. 5–7, 2012.

[16] Y. Y. Ruan, D. S. He, and R. Chi, "Review on beneficiation techniques and reagents used for phosphate ores," *Minerals*, vol. 9, no. 4, p. 253, 2019.

[17] G. Carbajal-Franco, E. Rendón-Lara, I. M. Abundez-Barrera, and A. Vásquez-Aguilar, "The mining of materials with similar electronic properties from the Crystallographic Open Database (COD)," *Materials Research Express*, vol. 7, no. 3, Article ID 035903, 2020.

[18] W.-b. Sun, F. Zhou, J.-l. Shao, H.-q. Du, and Y.-c. Xue, "Development status and prospects of mine physical similar material simulation experiments," *Geotechnical & Geological Engineering*, vol. 37, no. 4, pp. 3025–3036, 2019.

[19] S. Chen, H. Wang, J. Zhang, H. Xing, and H. Wang, "Experimental study on low-strength similar-material proportioning and properties for coal mining," *Advances in Materials Science and Engineering*, vol. 2015, Article ID 696501, 6 pages, 2015.

[20] K. Ciarkowska, L. Gargiulo, and G. Mele, "Natural restoration of soils on mine heaps with similar technogenic parent material: a case study of long-term soil evolution in Silesian-Krakow Upland Poland," *Geoderma*, vol. 261, pp. 141–150, 2016.

[21] Y. L. Jiang, D. F. Zhang, K. Wang, and X. Q. Zhang, "Mining-induced damage characteristics of floors during fully mechanized caving mining: a case study," *Advances in Materials Science and Engineering*, vol. 2018, Article ID 1513451, 11 pages, 2018.

[22] X. S. Li, Y. M. Wang, and K. Zhao, "Study on the law of ground pressure obliquity effect with gently inclined thin to medium thickness phosphate body from open-pit to underground," *Solid State Technology*, vol. 63, no. 4, pp. 6773–6781, 2020.

[23] X. S. Li, Y. M. Wang, and K. Zhao, "Research on deformation and failure character of underground surrounding rock and overlying strata transition from open-pit to underground mining," *Solid State Technology*, vol. 63, no. 4, pp. 6732–6757, 2020.

[24] W.-X. Li, C.-Y. Gao, X. Yin, J.-F. Li, D. L. Qi, and J.-C. Ren, "A visco-elastic theoretical model for analysis of dynamic ground subsidence due to deep underground mining," *Applied Mathematical Modelling*, vol. 39, no. 18, pp. 5495–5506, 2015.

[25] Y. Lin, "Research on computer stochastic simulation of large spacing pillar-less mining ore drawing," *Journal of Physics: Conference Series*, vol. 1649, Article ID 012023, 2020.

[26] C. B. Zhou, N. Jiang, and G. Luo, "Study on blasting vibration cumulative damage effect of medium-length hole mining," *Disaster Advances*, vol. 5, no. 4, pp. 468–473, 2012.

[27] W. X. Li, Q. L. Meng, L. Wen, X. M. Liu, and L. Liu, "Analysis of horizontal stress field and far field movements due to deep mining," *Chinese Journal of Rock Mechanics and Engineering*, vol. 29, no. 1, pp. 2630–2636, 2010.

[28] Y. L. Fang, "UDEC numerical simulation research of mining overlying strata movement regulation," *Applied Mechanics and Materials*, vol. 448-453, pp. 3884–3887, 2013.

[29] K. Moses and Y. Y. Xia, "UDEC-based stability analysis of jointed bedding slope and slope parameter optimization suggestions: a case study," *SN Applied Sciences*, vol. 2, no. 12, p. 1943, 2020.

[30] S. T Gu, Z. M Xiao, B. Y. Jiang, R. F. Huang, and P. Shan, "Research of rock burst risk induced by mining and field case in anticlinal control area," *Advances in Civil Engineering*, vol. 2018, Article ID 2632549, 10 pages, 2018.

[31] H. Jiang, "Simple three-dimensional Mohr-Coulomb criteria for intact rocks," *International Journal of Rock Mechanics and Mining Sciences*, vol. 105, pp. 145–159, 2018.

[32] T. Yu, "Statistical damage constitutive model of quasi-brittle materials," *Journal of Aerospace Engineering*, vol. 22, no. 1, pp. 95–100, 2009.

[33] P. Moczko, D. Pietrusiak, and J. Wieckowski, "Investigation of the failure of the bucket wheel excavator bridge conveyor," *Engineering Failure Analysis*, vol. 106, Article ID 104180, 2019.

[34] M. A. Sonnov, A. E. Rumyantsev, A. V. Trofimov, and V. B. Vilchinsky, "Numerical modeling of stress-and-strain behaviour of deposit deformed by mining operations using step-by-step calculation function in the CAE fidesys software system," *Mining Industry Journal/Gornaia Promyshlennost*, vol. 2020, no. 2, pp. 110–114, 2020.

[35] G. Liu, X.-T. Feng, Q. Jiang, Z. Yao, and S. Li, "In situ observation of spalling process of intact rock mass at large cavern excavation," *Engineering Geology*, vol. 226, pp. 52–69, 2017.

[36] S.-R. Wang and J.-L. Feng, "3D deformation effect and optimal excavated design of surface mine," *Journal of Coal Science and Engineering*, vol. 15, no. 4, pp. 361–366, 2009.

[37] X. S. Li, Y. M. Wang, K. Zhao, and S. Yang, "Research progress on the Key problems in transition from open-pit to underground mining for metal mines," *Metal Mine*, vol. 2019, no. 12, pp. 12–20, 2019.

[38] X. S. Li, K. Peng, J. Peng, and D. Hou, "Effect of thermal damage on mechanical behavior of a fine-grained sandstone," *Arabian Journal of Geosciences*, vol. 14, p. 1212, 2021.

[39] X. S. Li, Z. F. Liu, and S. Yang, "Similar physical modeling of roof stress and subsidence in room and pillar mining of a gently inclined medium-thick phosphate rock," *Advances in Civil Engineering*, vol. 2021, Article ID 6686981, 17 pages, 2021.

[40] X. S. Li, S. Yang, Y. Wang, W. Nie, and Z. Liu, "Macro-micro response characteristics of surrounding rock and overlying strata towards the transition from open-pit to underground mining," *Geofluids*, vol. 2021, Article ID 5582218, 18 pages, 2021.

Research Article

Development of Resonant Density Meter and Its Application in Tailings Backfilling

Xiaozhou Cheng [1,2]

[1]*China University of Mining and Technology (Xuzhou), No. 1 Jinshan East Road, Quanshan District, Xuzhou City, Jiangsu 221008, China*
[2]*Sinosteel Maanshan General Institute of Mining Research Co., Ltd.,, No. 666, Xitang Road, Economic Development Zone, Ma'anshan City, Anhui 243000, China*

Correspondence should be addressed to Xiaozhou Cheng; cxz3005@163.com

To solve the problems of low measurement accuracy, poor safety, and stability of the traditional pipeline liquid density meter, a MIMR-XZ6 pipeline liquid density meter was designed based on the vibration mathematical model of fluid flowing through the pipeline. The pipeline liquid densitometer mainly consisted of a vibration tube for the liquid passing by, a distributed inductance encircled around the inner wall of the vibration tube, a resistor, and a capacitor, respectively, connected to both ends of the inductance, and the inductor, resistor, and capacitor formed the RLC series resonant circuit; an excitation signal source which could generate an alternating current (AC) voltage signal in different frequencies was applied to both ends of the RLC series resonant circuit, and the AC voltage signal was connected to the series branch formed by the inductance and the capacitor to capture the electrical signals. In view of the practical application of this liquid pipe densitometer in tailings backfilling, the installation method of the liquid pipe densitometer is flexible, and the slurry flows in a fluent and stable manner, meeting the measuring requirement of the resonant concentration analyzer. The MIMR-XZ6 pipeline liquid densitometer was used for online detection of ore pulp density, and the precision of this densitometer met the needs of industrial applications.

1. Introduction

The medium measured by the concentration density was made up of a mixture of mineral slurry and water. The flow rate of ore pulp should not stay too slow in the whole mineral processing to avoid precipitation. Therefore, the concentration of ore pulp was an important operational parameter of mineral processing. In the process of pipeline transportation and beneficiation, an overlow concentration of ore pulp would lead to lower production efficiency, but an overhigh concentration would bring production accidents such as pipe plugging. How to measure the concentration accurately for guiding the production was important.

The online measurement instrument for slurry concentration was mainly γ-ray densitometer at present. But the γ-ray had radiation hazards. The differential-pressure densitometer could be measured with good precision for static liquid, but the pressure change caused by the flow of the medium would interfere with the correlation between the pressure difference and the density of the medium and cause a decrease in the measurement accuracy. The ultrasonic densitometer was very sensitive to bubbles, vibration, and flow in the medium, and the drift of the measurement reference was serious. It needed constant calibration during the working process and is hard to measure stably and reliably for a long time. Therefore, it was particularly important to find a safe and accurate online densitometer for pipeline liquid. This research of pipeline liquid densitometer was proposed in the context.

Greenwood and Bamberger [1] have studied computer-controlled sensors that measure the density of liquids or slurries in real time and deployed them at a base in the United States to monitor the characteristics of the slurries during the transfer of radioactive waste. Sickels [2] proposed

a device and method for determining the density and other characteristics of corrosive liquids (such as drilling mud). Using the relationship between the vibration frequency of the tuning fork and the density of the liquid between the walls of the fork, Tang et al. [3] proposed a tuning fork liquid density meter. Li and Cui [4] designed a new type of low-power and high-precision ultrasonic liquid medium density meter using the measurement principle of ultrasonic time difference method and the high-speed time-to-digital conversion chip TDC-GP2. Li et al. [5] prioritized pure water as the working medium when conducting static pressure tests on the online vibrating tube densitometer to obtain correction coefficients to ensure measurement accuracy.

The pipe would vibrate at different frequencies when the different density fluid flowed through. Hence, to measure the frequency of vibration of pipes, the density of fluid would be detected, and the MIMR-XZ6 pipeline liquid densitometer was developed in this theory. This novel pipeline liquid has an allowable range of true error and provides a good technical guarantee for the efficient and safe production of tailings backfilling operations.

2. The Mathematical Model of the Pipeline Liquid Density Meter

The mathematical model of vibration when the fluid flows through the pipeline is shown in equation (1). The measuring tube of the pipeline liquid density meter is shown in Figure 1. The waveforms of three different vibration modes on the tube length along the vertical and horizontal directions are shown in Figure 2 [6–8].

$$E \times I \frac{\partial^4 y(x,t)}{\partial x^4} + (\rho_w S_i + \rho_t S_t) \times \frac{\partial^2 y(x,t)}{\partial t^2} = 0. \quad (1)$$

In equation (1), E is the elastic modulus of the measuring tube; I is the second moment of the measuring tube to the central axis; S_i and S_t were, respectively, the cross-sectional areas of the tube occupied by the liquid in the tube through which the fluid flows and the cross-sectional area of the measuring tube; ρ_w and ρ_t were, respectively, the density of the liquid to be measured in the tube and the density of the measuring tube. Vibrating tubes were made of high-elastic alloy 42CrMo chrome-molybdenum alloy steel with a low hysteresis effect in the actual manufacturing process.

Solving equation (1) under a given boundary gave the vibration frequency of the horizontal measuring tube as follows [6–8]:

$$f = \frac{\lambda^2 \sqrt{E \times I / (\rho_w S_i + \rho_t S_t)}}{2\pi L^2}, \quad (2)$$

where λ is the constant associated with the boundary conditions and the vibration mode of the measuring tube and L is the length in the axial direction of the measuring tube.

The solution of density would be solved as follows [6–8]:

$$\rho_w = \frac{\lambda^4 E \times I / 4\pi L^4 f^2 - \rho_t S_t}{S_i}. \quad (3)$$

3. The Realization of Online Measurement Principle of the Pipeline Liquid Density Meter

The liquid density meter was mainly composed of a cavity vibration sensor, and its working principle is as shown in Figure 3. When the liquid flowed through the vibrating tube, the cavity vibrating sensor surrounded the vibrating tube through which the fluid flowed, and the inner and outer walls of the vibrating tube body were surrounded by an inductive coil, respectively, connected to the two lead ends of the inductive coil. Inductor, resistor, and capacitor formed an RLC series resonant circuit; the excitation signal source generated an AC voltage signal of different frequencies. The AC voltage is applied to both ends of the RLC series resonant circuit as an excitation signal. The AC voltage was connected to the series branch formed by the inductor coil and the capacitor, to capture the electrical signal at both ends of the series branch. When different fluids flowed through the vibrating tube, vibrations of different frequencies occurred. Resonance will appear when the frequency of the signal generated by the excitation signal source coincides with the frequency of the vibrating tube. The mixer outputted different harmonics between the resonant frequency and the signal frequency of the external excitation signal source. The density of the fluid was obtained by converting the frequency difference signal into an electrical signal through a detector, a filter, and an identifier. According to the above principle, we developed the pipe liquid density meter MIMR-XZ6 which is shown in Figure 4. The relationship between the frequency of vibration and the density of the liquid measured by the experiment is shown in Table 1.

It can be seen from Table 1 that the density of liquid measured by the developed liquid density meter had a smaller error than the true value, which was a reason for the range of error.

4. The Application of the Pipeline Liquid Density Meter in Tailings Backfilling

4.1. The Performance Analysis of Graded Tailings Backfilling Slurry. Cement-grade tailings backfilling slurry was the material that was mixed artificially by solid-liquid two-phase concrete. Its strength was affected by the sedimentation properties of the slurry previous solidification. The settling velocity and direction of filling material solid particles with different particle sizes were disordered in the mixing region. The mutual interference between the particles reduced the sedimentation speed of the particles, which resulted in the stickiness between the materials of the concrete mixture in the slurry. The force of gathering was not enough to resist the sinking of the coarse aggregate. The concrete mixture components were separated from each other, resulting in uneven internal composition and structure. The more the water was, the more the particle size distribution was unreasonable. The serious separation phenomenon in the slurry resulted in a negative impact on the strength of the filling [9–12].
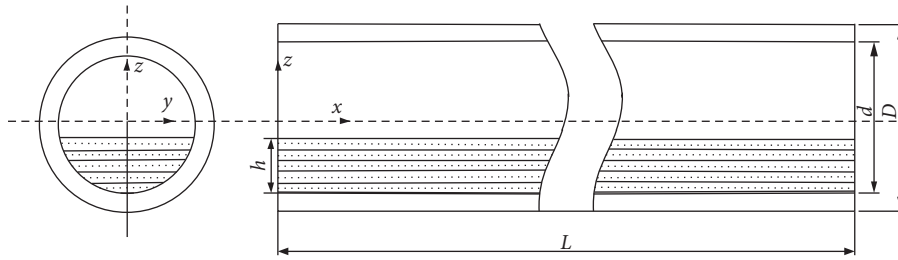
FIGURE 1: Schematic diagram of a measuring tube flowing through a liquid.
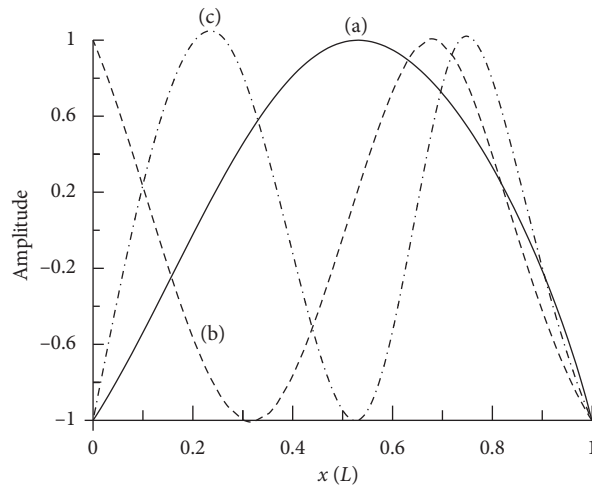
FIGURE 2: Waveforms of three different modes of vibration along with the vertical and horizontal directions over the length of the tube.
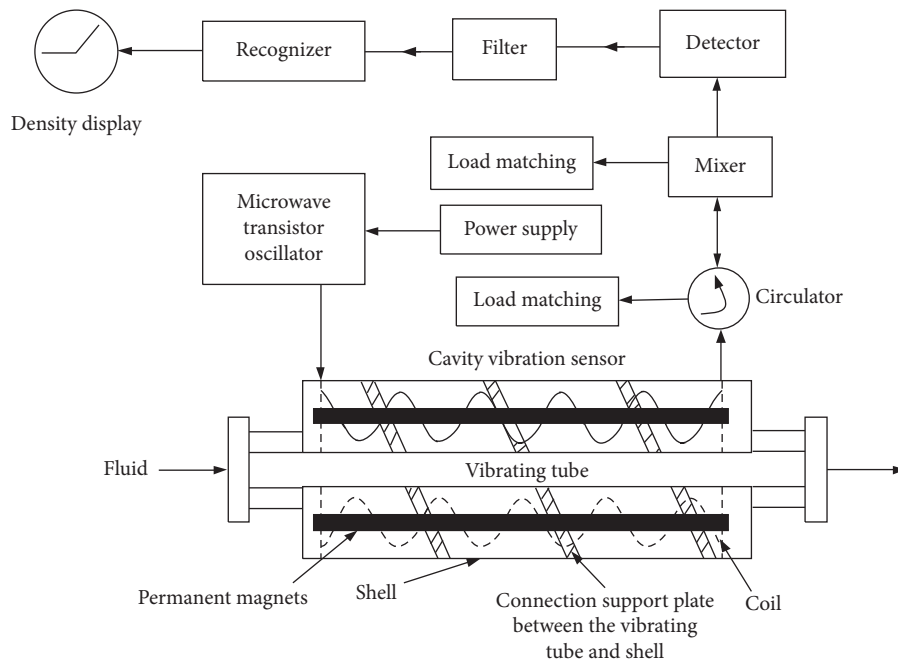
FIGURE 3: Liquid density meter online measurement principle realization diagram.

The sedimentation experiment was carried out on the filling slurry with different concentration ratios. The variation of the sedimentation performance of the slurry with the concentration Of the mixture was analyzed. The slurry was poured into the container and the mixture was stirred quickly. Then let it settle naturally during the experiment. The solid particles in the slurry sank gradually under the action of gravity. The upper clear water precipitated gradually.
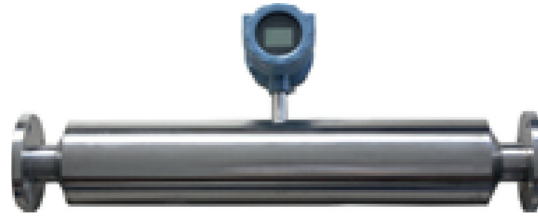
Figure 4: The real developed liquid density meter online measurement.

Table 1: The relationship between the frequency of vibration and the density of the liquid.

No.	Frequency of vibration (Hz)	The temperature of the liquid (°C)	Density (kg/m)		Error
			True value	Measurement	
1	744.15	22.8	998	998	0.00
2	683.45	21.5	1887	1886	−0.001
3	754.78	24.6	998	998	0.00
4	748.67	23.5	998	997	−0.001
5	739..80	22.4	998	998	0.00
6	733.72	21.4	998	998	0.00
7	836.65	22.3	1.00	1.00	0.00

The sedimentation performance of the slurry was directly reflected by observing the change of the height of the clear water layer. The sedimentation experiment resulted in various types of lime sand slurry with the concentration of 58%, 65%, and 72% and the test values of the settlement experiment are shown in Table 2. It can be seen from Table 2 that the sedimentation performance of the graded tailings had a great influence on the physical properties of the pack. The slurry was usually saturated at the initial stage after the agitation. The capillary pressure in the slurry and the solid particles are naturally compacted by the weight of the solid particles, resulting in a decrease in the volume of the slurry and dehydration.

The specific gravity, bulk density, grain size composition, and porosity of cement-grade tailings backfilling slurry influenced sedimentation directly. Its physical and chemical properties were different, resulting in its different performance. The bulk density and porosity of the slurry were larger. The larger the bulk density and porosity of the slurry, the fluffier the structure, the larger the compression coefficient, and the smaller the strength. The liquid phase water was discharged with time after filling in the goaf. The solid phase filling material particles shrink gradually under their gravity. Porosity decreased correspondingly and the bulk density of the slurry increased gradually. The structure tended to be dense and the strength was further improved [13–16].

Figure 5 shows the effect of the ratio of different coarse and fine sands and the concentration of the slurry on the strength of the filled test block when the ratio of lime to sand was 1 : 7. It could be seen from Figure 5 the ratio of the thickness of the coarse sand and the concentration of the slurry to the strength of the packed block. It did not exhibit regular changes. When the ratio of coarse to fine sand was 1 : 3.5 and the slurry concentration was 64.93%, the packing block had a good strength of 3.47 MPa.

4.2. Density Meter Installation. The resonant density meter adopts a pipeline design and flange connection, and it is easy to install. In this application, the density meter was installed at the bottom of the tailings sand tank. The density meter was used as a part of the tailings conveying pipeline. The density of the tailings can be measured when the tailings flow through the density meter. The installation position is shown in Figure 6.

4.3. The Application of the Pipeline Liquid Density Meter in Tailings Backfilling Process. The 10% overflow from the top of the cyclone and 25% overflow from high sulfur tailings, wastewater, and slurry mixed with the fine sand pool entered the thickener together. The fine mortar from the bottom of the thickener was driven into the fine sand pool by a ceramic plunger pump. The fine mortar coming out from the bottom of the fine sand pool was driven into the sand pool by the ceramic plunger pump after passing through the intermediate buffer pool. The slurry prepared according to a certain ratio of coarse sand coming out from the bottom of the fine sand pool through the intermediate buffer pool then entered the double screw mixer. The liquid pipe density meter monitored the slurry concentration. The cement was designed according to the optimal proportion of the sand-sand ratio. After being fed by the double-tube screw feeder, it was metered by a spiral electronic scale and sent to a high-speed activated double-helical mixer for uniform mixing. It was a highly efficient activated slurry for filling the mining bed. The system process of the specific tailings backfilling is shown in Figure 6.

The parameters of the system process in the tailings backfilling process were controlled by a computer. The control interface screenshot is shown in Figure 7. The ratio of coarse and fine sand of slurry during tailings backfilling operation, the concentration of the slurry, the

TABLE 2: The test values of the settlement experiment.

The ratio of ash and sand	The initial concentration (%)	The slurry weight after sedimentation (kg/m^3)	The concentration of slurry after sedimentation (%)	The volume ratio of settling water to slurry (%)	The volume ratio of settled water to total water (%)
	58	2.1	77.0	30.0	38.0
Cement free	65	2.1	78.0	18.0	28.0
	72	2.1	78.6	7.0	13.6
	58	2.1	77.0	29.0	37.3
1 : 4	65	2.1	78.0	18.0	28.0
	72	2.1	78.0	6.5	12.0
	58	2.1	76.7	27.0	35.0
1 : 6	65	2.1	77.0	15.0	23.9
	72	2.1	78.0	5.7	10.8
	58	2.1	76.0	25.0	33.8
1 : 8	65	2.1	77.0	15.0	23.8
	72	2.1	77.7	4.6	8.9
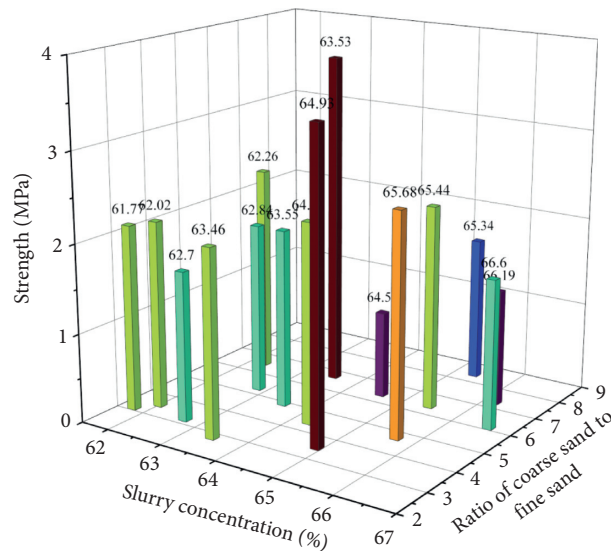
FIGURE 5: The effect of different ratios of coarse and fine sand and the concentration of slurry on the strength of the filled test block when the ratio of lime to sand is 1 : 7. *Notes.* The test block has a volume of 353.39 cm^3 and a cross-sectional area of 49.98 cm^2.

level of the sand pool, the hydration flow rate and the cement dosage every day, and the total amount of sand were learned through the online control system. One of the important control parameters was the concentration of the slurry which was measured by the liquid pipe density meter. The concentration of the slurry is shown in Figure 8.

It was seen from Figure 8, during the operation, the slurry concentration changed substantially with time at a concentration of 1650 kg/m^3. During the operation, if the concentration changed, the operator adjusted other process parameters opportunely. If we want to control the proportion of coarse sand, choose the appropriate ratio of sand and cement to meet the filing requirements of the mining method. Finally, a suitable concentration of filler slurry was selected to ensure that the tailings mixture material improved the structural strength of the deposit filling area while maintaining fluidity [17–20].
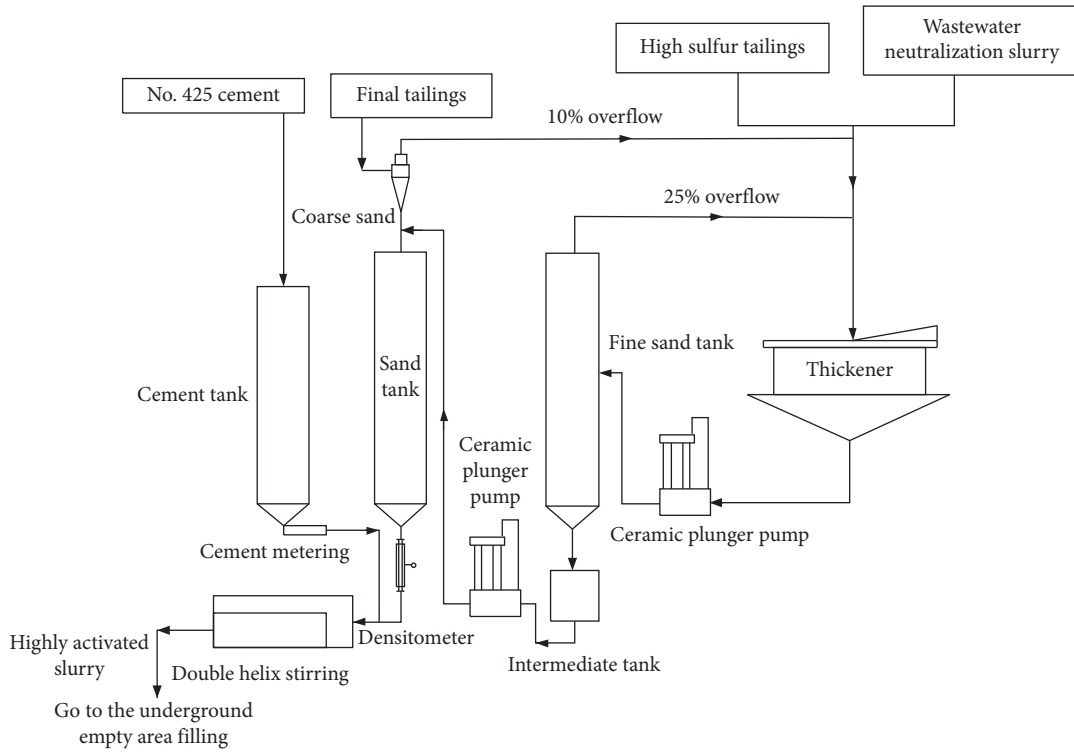
FIGURE 6: Tailings backfilling system process.
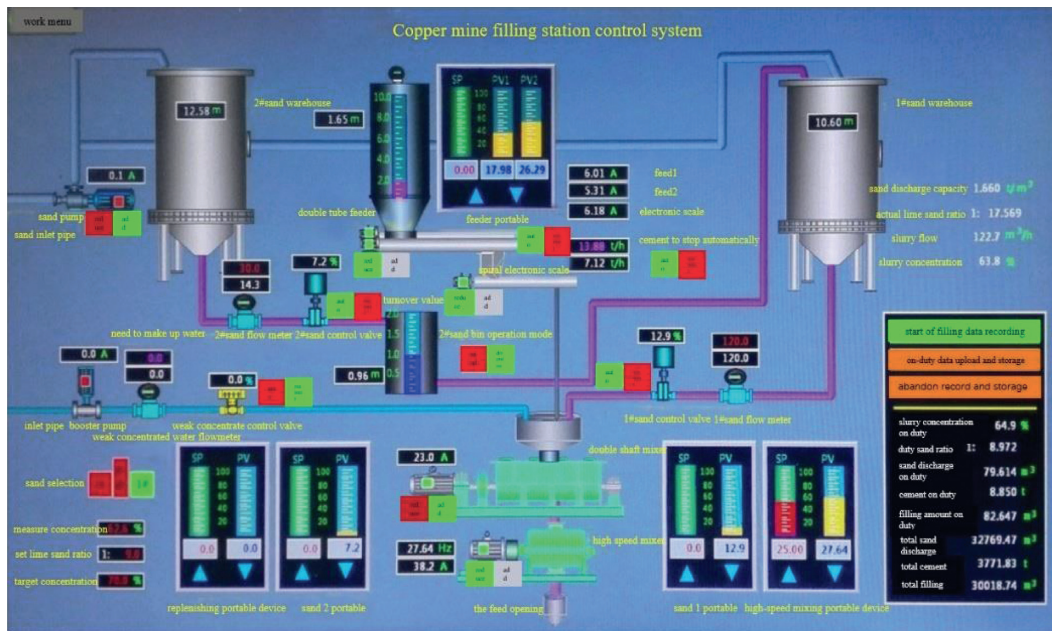
FIGURE 7: Screenshot of system process parameters for tailings backfilling.
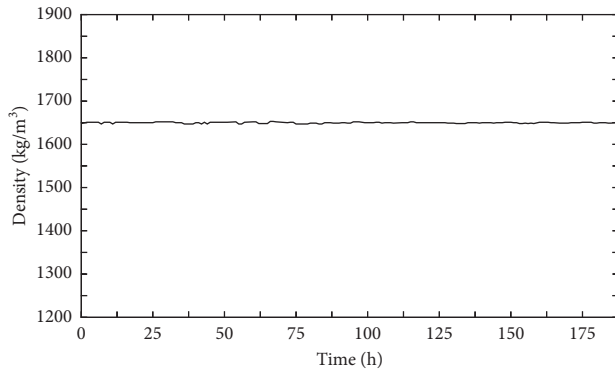
Figure 8: Relationship between slurry concentrations monitored over time during operation.

5. Conclusions

Starting from the mathematical model of the liquid pipeline density meter, this paper introduces its detection principle and its realization method. From the actual application information of the developed liquid pipeline density meter in tailings backfilling, the installation method of the liquid pipeline density meter is flexible and the slurry flows in a fluent and stable manner, meeting the measurement requirements of the resonant concentration analyzer.

The results from the on-site sampling and according showed that the deviation of the liquid pipeline densitometer measurement is about 1%, the deviation of the concentration measurement is about 3%, and the deviation value was stable and stayed in the range of allowable error in the whole process. The recorded data of ore pulp concentration and variation tendency had a certain relationship with the actual conditions in the production process, which provided specific technical support for the efficient and safe production of tailings backfilling operations.

Data Availability

Experimental data come from on-site sampling.

Conflicts of Interest

The author declares that there are have no conflicts of interest.

References

[1] M. S. Greenwood and J. A. Bamberger, "Ultrasonic sensor to measure the density of a liquid or slurry during pipeline transport," *Ultrasonics*, vol. 40, no. 1–8, pp. 413–417, 2002.

[2] R. E. Sickels, "Measuring the properties of a corrosive liquid," *Journal of Politics & Government Week*, vol. 7, no. 4, pp. 3085–3091, 2015.

[3] T. Tang, H. Yu, Q. Chen et al., "Design of tuning fork liquid density meter," *Journal of Yangtze University Natural Science Edition: Science and Engineering*, vol. 13, no. 22, pp. 14–18, 2016.

[4] K. Li and Y. Cui, "New ultrasonic liquid density meter based on time difference method and TDC–GP2," *Instrument Technique and Sensor*, vol. 431, no. 12, pp. 123–126, 2018.

[5] Z. Li, C. Han, and Z. Wang, "Analysis of static pressure correction test of online vibration tube liquid densitometer," *Oil-Gasfield Surface Engineering*, vol. 39, no. 6, pp. 29–32, 2020.

[6] I. Mnassri and A. E. Baroudi, "Vibrational frequency analysis of finite elastic tube filled with compressible viscous fluid," *Acta Mechanica Solida Sinica*, vol. 30, no. 4, pp. 435–444, 2017.

[7] J. A. S. Hidalgo, A. L. Gama, and R. M. Moreira, "Natural vibration frequencies of horizontal tubes partially filled with liquid," *Journal of Sound and Vibration*, vol. 408, pp. 31–42, 2017.

[8] A. El Baroudi, F. Razafimahery, and L. Rakotomanana, "Fluid-structure interaction within three-dimensional models of an idealized arterial wall," *International Journal of Engineering Science*, vol. 84, pp. 113–126, 2014.

[9] X. Peng and X. Yang, "Phenomenon and mechanism of settlement process of tailings backfill slurry," *China Mining Magazine*, vol. 26, no. 4, pp. 126–130, 2017.

[10] X. Chen, X. Yang, L. Guo et al., "Experimental study on the determination of cement content in cemented tailings backfill," *Nonferrous Metals Engineering*, vol. 8, no. 6, pp. 73–78, 2018.

[11] S. Zhu, Y. Hou, L. Chen et al., "Settlement performance and influencing factors of total tailings," *Chinese Journal of Underground Space and Engineering*, vol. 13, no. 4, pp. 931–937, 2017.

[12] S. Wang, S. Su, and F.-l. Wang, "Analysis of strength regularity of high concentration tailings cemented backfill," *Bulletin of the Chinese Ceramic Society*, vol. 38, no. 3, pp. 847–852, 2019.

[13] H. Hou, C. Li, S. Wang et al., "Settling velocity variation of mud layer and particle settling characteristics in thickening of tailings," *Journal of Central South University*, vol. 50, no. 6, pp. 1428–1436, 2019.

[14] R. Zhou, "Application of graded tailings cement filling in Wushan copper mine," *Nonferrous Metals*, vol. 62, no. 3, pp. 1-2, 2010.

[15] J. Gao, "Application of large-scale downward cementation filling mining method in Jinchuan nickel mine," *Mining Engineering*, vol. 59, pp. 136–139, 2005.

[16] Y. Teng, J. Ma, and J. Chen, "Study and application of tailings cementing backfilling technique in Xulou iron mine," *Modern Mining*, vol. 33, no. 2, pp. 65–68, 2017.

[17] P. M. Dighe, "Design simulation studies of pipe mounted boron concentration meter," *Annals of Nuclear Energy*, vol. 134, pp. 414–423, 2019.

[18] P. Wei and J. Wang, "Design of ultrasonic pulp concentration meter based on STM32," *Industrial Control Computer*, vol. 30, pp. 133-134, 2017.

[19] D. Gao, "Development of an intelligent non-contact ultrasonic densitometer," *Instrumentaion*, vol. 23, pp. 1–4, 2016.

[20] H. Zhao, J. Zhao, and C. Zhou, "Design of an weighting method concentration meter," *China Mining Magazine*, vol. 25, pp. 473–475, 2016.

Research Article

Effect of Tailings Fine Content on the Properties of Cemented Paste Backfill from the Perspective Packing Density

Haijun Wang,[1,2] Xiaogang Sun [ID],[2] Jianwen Wang,[1] Yun Duan,[1] Changsuo Zhang,[1] Jingping Qiu,[2] and Zhenbang Guo [ID][2]

[1]*BGRIMM Technology Group, Beijing 100160, China*
[2]*School of Resource and Civil Engineering, Northeastern University, Shenyang 110819, China*

Correspondence should be addressed to Xiaogang Sun; sunxiaogang@mail.neu.edu.cn

In order to quantitatively study the influence of tailings fine content on the properties of cemented paste backfill (CPB) and further understand the mechanism of tailings fine content acting, the concept of packing density was introduced in this study. The packing density of each tailings sample was measured by the wet packing method after the samples with various fine contents were prepared. Moreover, CPBs with different tailings fine contents were tested by the mini slump test, rheological test, uniaxial compressive strength (UCS) test, and mercury intrusion porosimetry test. The results demonstrated that the flow spread and UCS both increase first and then decrease with the increase of tailings fine content, while the yield stress shows an opposite trend. The fine content of tailings affects the flowability of fresh CPB mainly through the packing density. When the fine content is high, the influence of the specific surface area of tailings cannot be ignored. The packing density is an important factor affecting the strength of CPB, and there is an obvious linear relationship between the packing density and UCS. The pore structure of CPB samples with different tailing fine contents is significantly different, and the macroscopic packing density changes the strength of CPB by affecting the microscopic pores.

1. Introduction

Mining activities will inevitably have adverse effects on the environment, such as the generation of solid wastes (tailings and coal gangue) and geological disasters such as surface collapse and dam failure of tailings ponds [1–5]. Cemented paste backfill (CPB) technology has become one of the most effective methods to solve these problems in underground mining [6–9]. Its advantages include effective utilization of tailings waste, thus reducing the tailings disposal on the surface, alleviating the surface subsidence during underground mining, and reducing ore loss and dilution [10–12]. CPB is generally composed of tailings, cementitious materials, and mixing water [13–15]. The cementitious material is generally ordinary Portland cement (OPC), which aims to make CPB gain strength to support the surface after a certain curing age [16–19]. Since the backfill cost mainly comes from cementitious materials, it has become a trend to mix OPC

with solid wastes such as blast furnace slag and fly ash [20–27]. The solid content of CPB slurry is generally 70–85%, so as to achieve the desired consistency and make the slurry transported to the stope smoothly [28–30].

It is worth noting that tailings are the main components of the CPB, accounting for more than 66% of the mass [31]. This means that the properties of tailings cannot be ignored for CPB. Xiapeng et al. [32] studied the effect of initial sulphate content on the rheological properties of CPB. They found that with the increase of initial sulphate concentration, the yield stress decreases continuously, but the apparent viscosity shows an opposite trend. Li and Fall [33] explored the effect of the sulphate effect on the early strength of CPB. They reported that sulphate is not conducive to the increase of CPB strength in the early age. Fall et al. [2] concluded that the increase of tailings density will lead to the increase of cementitious material consumption, so it is beneficial to the increase of CPB strength. Qi et al. [34]

predicted the uniaxial compressive strength (UCS) of CPB by using the coupling model of boosted regression trees (BRT) and particle swarm optimization (PSO) and carried out sensitivity analysis on the influencing factors of the UCS. They believed that the influence of chemical composition of tailings cannot be ignored.

In addition to sulphate content and density, tailings particle size is also an important factor affecting CPB properties. Ke et al. [35] studied the effect of tailings fineness on the development of pore structure of CPB. The results show that the critical pore diameter and large pores decreased with the increase of tailings fineness. Deng et al. [36] observed that the CPB samples with finer particle sizes display a higher yield stress compared to the samples with coarser tailings particle sizes. On the basis of laboratory experiments and numerical simulation, Yang et al. believes that the cemented superfine unclassified tailings backfill prepared by reasonable mix proportion can achieve the function of subsidence control [10]. Cheng et al. studied [37] the effect of tailing particle gradation on the yield stress of fresh CPB. They concluded that particle gradation changed yield stress by affecting skeleton structure and pore structure. To sum up, tailings gradation has a significant impact on the performance of fresh or hardened CPB, and these studies have made significant contributions to understanding of the influence of tailings characteristics on CPB properties. However, on the other hand, there are few reports on the quantitative research on the influence of tailings grading, and the mechanism of tailings grading on flowability and UCS of CPB is also few. This is undoubtedly an obstacle to understanding the properties of CPB. Although Qiu et al. introduced the index of water film thickness (WFT) to quantify the influence of tailings fineness, the tailings sample does not contain coarse tailings [38]. Furthermore, rheological properties were not involved in the study of Qiu et al. [37, 39]. Therefore, it is necessary to further explore the influence of tailings particle size on CPB properties.

Based on the above discussion, the concept of packing density of tailing particles was introduced to quantify the influence of tailing particle size. After preparing tailings samples with different fine contents (<20 m), a series of related experiments were carried out, such as the mini slump test, rheological test, UCS test, mercury intrusion porosimetry (MIP) test, and so on. Moreover, because tailings particles are generally fine, the dry packing method often has great limitations in measuring tailings packing density, so the wet packing method was adopted to measure packing density. The purpose of this study is to further understand the influence of tailings fine content on CPB properties and to provide theoretical basis for the design of mine backfill mix.

2. Experimental

2.1. Materials.
In order to obtain tailings samples with different fine contents, the tailings from an iron mine in Liaoning Province, China, were adopted as the original material. The XQM-2 planetary ball mill was used for grinding at different times, and five tailings samples with different fine contents were obtained, which were 22.08%, 31.51%, 42.20%, 51.63, and 62.94%, respectively. The particle size distribution of tailings samples with various fine contents is shown in Figure 1. The main chemical components of tailings include SiO_2, Fe_2O_3, and Al_2O_3, and their mass percentages are 65.3%, 15.52%, and 2.89% respectively. The commercial OPC (namely, PO42.5R) generally used in mines in China was adopted, the specific surface area is 5808 cm^2/g, and the specific gravity is 3.3. The main physical and chemical properties of tailings and cement are given in Table 1. Furthermore, tap water was used as mixing water to obtain a fresh CPB slurry of desired consistency [26]. Detailed information on tap water can be found in [38].

2.2. Experimental Program.
The main purpose of this study is to study the influence of the fine content of tailings on the properties of fresh or hardened CPB, so other factors remain unchanged. The binder dosage and solid content are fixed at 8% and 72%, respectively, which are calculated from the following equations (equations (1) and (2)). In addition, the specific test scheme is given in Table 2.

$$BD_{w\%} = 100 * \frac{M_{binder}}{M_{tailings}}, \tag{1}$$

$$SC_{w\%} = 100 * \frac{M_{tailings} + M_{binder}}{M_{tailings} + M_{binder} + M_{water}}, \tag{2}$$

where $BD_{w\%}$ is the binder dosage, $SC_{w\%}$ is the solid content, and M_{binder}, $M_{tailings}$, and M_{water} represent the mass of dry binder, dry tailings, and water in the CPB, respectively.

2.3. Testing Procedures.
In this study, the wet packing method was used to measure the packing density of tailings. Detailed experimental procedures are given in [40]. The research results of Qiu et al. [38, 39, 41] showed the rationality of using the wet packing method to measure the density of tailings. The tailings and OPC were weighed according to a preset proportion, poured into a stirring container, and then mixed at a low speed for 1 minute to make the dry materials evenly mixed.

Once the dry materials were mixed evenly, different amounts of water (shown as various water-solid ratios in the abscissa of Figure 2) were added to the solid particle system. After fully stirring evenly, fresh slurry was poured into a cylindrical container with a diameter and height of 10 cm to measure the packing density. When the water content is low, the concentration of the mixed system increases with the increase of water content due to the effect of liquid bridge [42, 43]. When the water content exceeds a certain threshold, the concentration of the system decreases continuously if the water content continues to increase. Therefore, there is a threshold water content, at which time the system concentration reaches the maximum, and the maximum solid concentration can be regarded as the particle packing density. The concentration of the system can be obtained according to the following formulas:
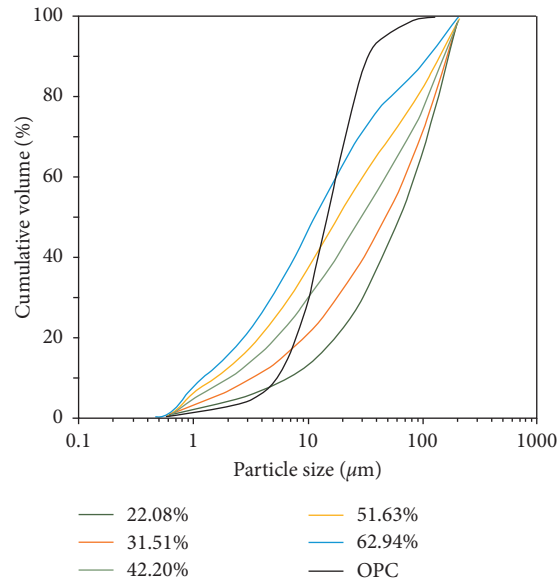
FIGURE 1: Particle size distribution of tailings and OPC.

TABLE 1: Main chemical and physical properties of OPC and tailings.

Physical properties	OPC	Tailings	Chemical composition (%)	OPC	Tailings
Specific gravity	3.3	3.02	SiO_2	21.43	65.3
<20 μm (%)	66.3	22.08	CaO	62.34	3.01
		31.51			
		42.20			
		51.63			
		62.94			
D_{10} (μm)	5.23	6.79	Fe_2O_3	5.06	15.52
		3.35			
		2.08			
		1.75			
		1.24			
D_{30} (μm)	10.18	30.13	Al_2O_3	4.25	2.89
		18.35			
		10.28			
		6.95			
		4.89			
D_{60} (μm)	17.8	86.23	MgO	2.61	0.58
		70.59			
		45.54			
		30.35			
		17.57			
Coefficient of uniformity	3.36	12.69	Na_2O	0.41	2.88
		21.05			
		23.33			
		17.39			
		14.18			
Coefficient of curvature	1.1	1.55	K_2O	0.73	8.76
		1.42			
		1.05			
		0.91			
		1.10			
—	—	—	SO_3	1.48	0.32

Coefficient of uniformity = D_{60}/D_{10}; coefficient of curvature = $(D_{30})^2/(D_{10} \times D_{60})$.

TABLE 2: Experimental program.

Binder dosage (%)	Solid content (%)	Fine content (%)
8	72	22.9
		28.2
		37.3
		46.9
		59.8

$$u = \frac{V - V_s}{V_s}, \qquad (3)$$

$$\varnothing = \frac{V_s}{V},$$

where V and V_s represent the volume of the cylindrical container and the volume of the solid particles in slurry, respectively. $\varnothing$ is the solid concentration of the system with various water contents. u is the voids ratio. It is worth noting that the voids ratio and solid concentration satisfy the following relationship:

$$\varnothing = \frac{1}{1 + u}. \qquad (4)$$

Due to the fine tailing particles, the mini slump cone was used to measure the flow spread of fresh CPB slurry and characterize the flowability of slurry. The top diameter of the mini slump cone is 5 cm, the bottom diameter is 10 cm, and the height is 15 cm. Detailed information on mini slump and mini slump test procedures can be found in [39].

The rheological properties of fresh CPB were tested by the Brookfield RSR-SST rheometer. A four-bladed vane with a diameter of 20 mm and a height of 40 mm was selected in this study [44]. Once the CPB mixture was ready, it is quickly poured into the sample cup of the rheometer. To ensure that all fresh CPB samples are at a reproducible reference state, preshear progress is performed before each rheological test [45]. During the preshear, a shear rate of $100\,s^{-1}$ is selected for a duration of 1 min. Subsequently, the shear rate decreases from $100\,s^{-1}$ to $0.003\,s^{-1}$ within 1 minute (Figure 3), and the data recorded during this stage were used to fit the rheological model [46]. Based on the experimental results, the correlation coefficients R^2 obtained by fitting the Bingham model (equation (5)) are all over 0.98, so it is reasonable to select this model to obtain the rheological parameters of CPB.

$$\tau = \tau_0 + \eta \cdot \gamma, \qquad (5)$$

where τ represents the shear stress (Pa); τ_0 and η represent the yield stress (Pa) and plastic viscosity (Pa·s), respectively; γ is the shear rate (s^{-1}).

The Humboldt HM-5030 with loading capacity of 50 kN was used to determine the UCS of the CPB. The loading method adopted the displacement loading, and the specific loading rate was 1 mm/min [24]. After the UCS test, a small piece was selected to soak in isopropanol for 24 hours to stop hydration, then vacuum dry to constant weight, and perform the MIP test. A mercury porosimeter of AutoPore IV 9510 was used for pore measurement in this study. This
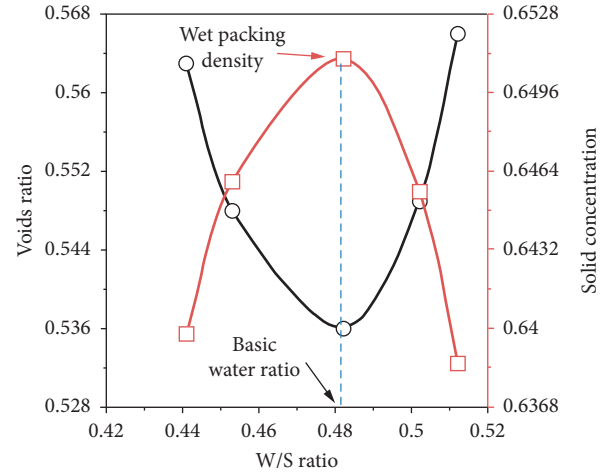
FIGURE 2: Wet packing test results for tailings.
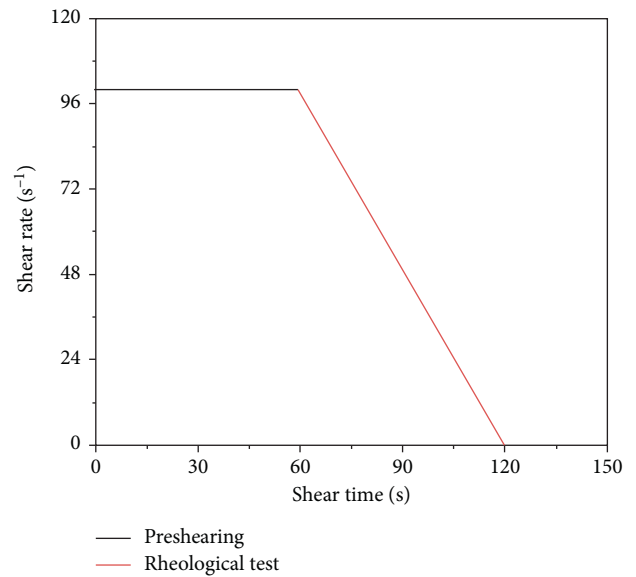
FIGURE 3: Applied rheological protocol.

instrument can achieve a maximum pressure of 414 MPa, and the measurable pore diameter range is $0.003–1000\,\mu$m.

It is worth noting that for the accuracy and reproducibility of the experimental results, each proportion of the sample is tested three times.

3. Results and Discussion

3.1. Effect of Tailings Fine Content on Packing Density.
Figure 2 shows the effect of water-solid (W/S) ratio on voids ratio and solid concentration (only sample with fine content of 42.20% is listed here, and other results are similar). It can be clearly seen from the figure that when the W/S ratio is less than the basic water ratio (also known as the optimal water-solid ratio, and the corresponding solid concentration is the wet packing density), the solid concentration increases with the increase of the W/S ratio. This is because the amount of water mixed at this time is not enough to fill all the voids

among the particles, and the formation of liquid bridges will reduce the particle spacing [40]. When the W/S ratio is greater than the basic water ratio, the suspension is formed and the tailings particles can be considered to be in a completely dispersed state [47]. Therefore, as the W/S ratio increases, the solid concentration gradually decreases. However, it should be noted that the basic water ratio is not necessarily equal to the minimum voids ratio. This is because when the minimum voids ratio occurs, there may be air trapped in the voids, resulting in a nonzero air proportion, as evidenced by the experimental results in the figure. Kwan et al. [47] also observed similar results when studying the wet packing density of concrete aggregates. Therefore, the basic water ratio should not be misunderstood as the minimum water ratio required to fill the voids among solid particles.

The variation of the packing density of the tailings particle system with different tailings fine contents under the wet and dry packing methods is shown in Figure 4. The packing density obtained by the dry packing method is in the range of 0.578–0.633, while that obtained by the wet packing method is in 0.585–0.651. Comparing the experimental results of the packing density under dry and wet conditions, it can be found that regardless of the fine content, the results obtained by the wet packing method are significantly greater than that obtained by the dry packing method, which indicates that the effect of water has a significant effect on the packing density of the tailings. This is because the tailing particles are fine, and the strong interparticle interaction forces (electrostatic force and van der Waals force) lead to the tailing particles attracting each other to form aggregates, thus resulting in loose packing [48]. In the dry packing test, this strong interaction cannot be eliminated, but the effect can be weakened to some extent by the action of water, so that the aggregates are dispersed and the particles are packed tightly [47]. This is the main reason why the dry packing method generally underestimates the packing density of fine particle systems. However, it is noteworthy that in the coarse particle system, because the interparticle forces are relatively small, the dry packing method can also achieve accurate results.

On the other hand, we can notice that with the increase of tailings fine content, the packing density increases sharply at first and then decreases slowly. According to the particle packing theory [39], when the fine content is less than 42.20%, the tailings are relatively coarse at this time. As the content of fine particles increases, the fine particles continue to fill the voids among the coarse particles, resulting in a significant increase in the overall packing density. This effect is called the filling effect of fine particles [39]. The increase of particle size distribution width may also be an important reason [49]. When the fine content is greater than 42.20%, the voids among the coarse particles have been basically filled at this time. If the fine content of the tailings is further increased, the fine tailings will pull apart the coarse tailings, which is the so-called "wedge effect" [50]. Moreover, coarse particles act as a wall, and fine particles adhere to the wall surface, which further increases the voids volume, the so-called "wall effect" [51]. To sum up, when the tailing fine content ranges from 22.08% to 62.94%, there exists an
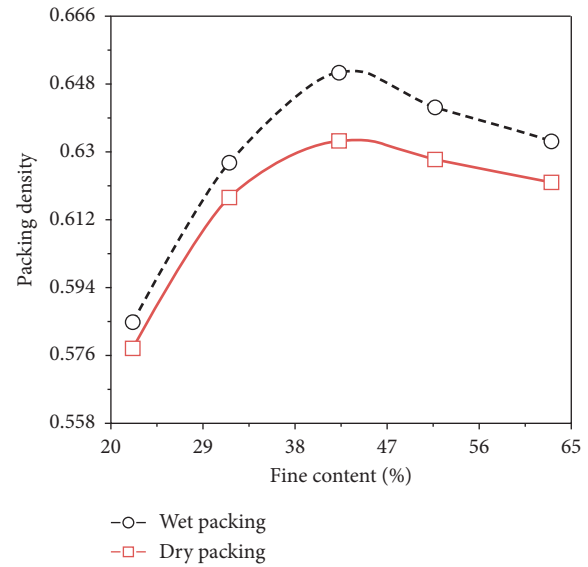
FIGURE 4: Results of the packing density measured by different methods.

optimal tailing fine content (42.20% in this study), which makes the packing density of the tailing particle system maximum.

3.2. Effect of Tailings Fine Content on Flow Spread.

Figure 5 shows the variation of the flow spread of fresh CPB slurry under different tailings fine contents (solid content is fixed at 72%). It is obvious from the figure that the flowability of CPB with various tailings fine contents is significantly different. When the fine content increases from 22.08% to 42.2%, the flow spread increases. However, when the fine content changes from 42.2% to 62.94%, the flow spread of fresh CPB slurry decreases significantly. The variation trend of flow spread with tailings fine content is similar to that of packing density with tailings fine content, which indicates that packing density affects the flowability of CPB slurry to a certain extent.

It is worth noting that when the coordinate system is established based on packing density and flow spread, the data points are very discrete and no obvious functional relationship appears (Figure 6). This shows that it is not comprehensive to study the flowability of CPB slurry only considering the factor of packing density. In other words, there are other important factors that affect the flowability of CPB. Qiu et al. [39] concluded that the specific surface area of tailings is also an important factor affecting the flow properties of fresh CPB slurry. When the fine content of tailings is between 22.08% and 42.2%, the influence of packing density on the flowability of CPB slurry is dominant. When the solid content is constant, the larger the packing density means that there is more water left after filling the particle voids, thus the greater the thickness of the water film formed on the particle surface and the smaller the friction resistance, thus improving the flow performance [52]. However, when the tailings fine content is between 42.2% and 62.94%, the influence of specific surface area of tailings
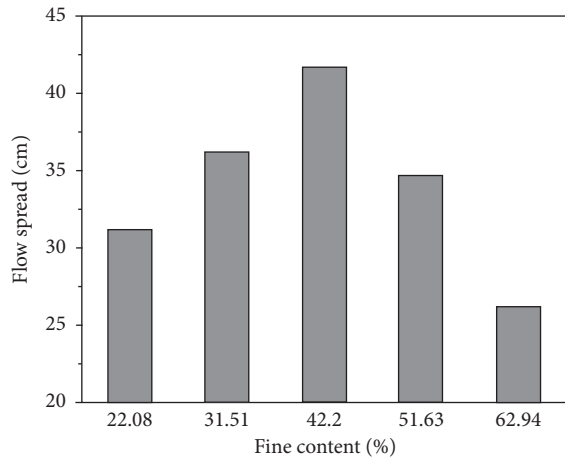
Figure 5: Flow spread variation with fine contents.

Figure 6: Relationship between packing density and flow spread.

Figure 7: Yield stress variation with fine contents.

cannot be ignored. On the one hand, the packing density is reduced, which means that there is less water available to form the water film. On the other hand, the specific surface area of tailings also increases sharply. Therefore, under the coupling action of packing density and specific surface area, the flowability of CPB decreases significantly in this range [39]. To sum up, it can be inferred that when solid content remains constant, if the packing density and specific surface area of tailings are coupled into a new index, the index will have a good function relationship with the flow spread of fresh CPB slurry. Of course, water content is also an important factor affecting slurry flow performance and generally not fixed. In this case, a comprehensive index including water content, particle packing density, and specific surface area must be the key to predict the flowability of CPB. The results of Guo et al. [41] and Kwan and Li [53] also prove this view.

3.3. Effect of Tailings Fine Content on Yield Stress. The yield stress of the fresh CPB slurry varies with the fine content of tailings as shown in Figure 7. Obviously, with the increase of tailings fine content, the yield stress decreases first and then increases. The reason for this phenomenon may be that the fine content of tailings changes the packing density of particles, thus affecting the free water content which contributes to flow [36]. The specific mechanism for the effect of packing density on yield stress is similar to that described in Section 3.2. It is worth noting that the packing density essentially reflects the result of particle physical packing, so the effect of hydration of cementitious materials cannot be taken into account. Although some studies have shown that the hydration of the binder has a significant effect on the rheological properties of CPB slurry [54, 55]. However, both the mini slump test and the rheological test were carried out quickly after the mixing was completed. In other words, these experiments were all completed within the induction period of hydration of the binder [56]. Therefore, it is reasonable to ignore the effect of hydration of the binder in this study.

In addition, a function fitting was carried out to explore the relationship between flow spread and yield stress
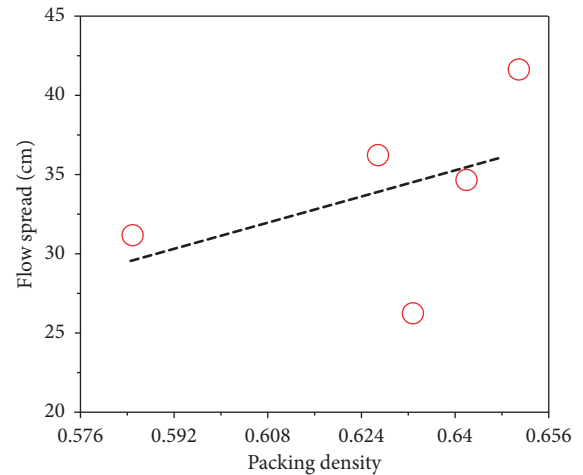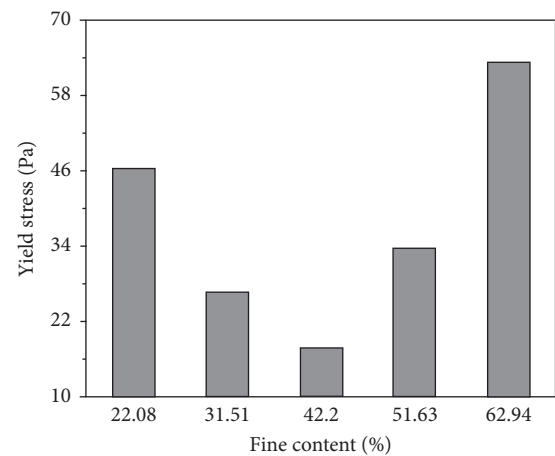
(Figure 8). The results show that there is an exponential relationship between flow spread and yield stress, and the correlation coefficient reaches 0.989. Therefore, the exponential model can be used as an empirical formula to estimate the yield stress by using the mini slump test, which has a certain significance for the engineering site. Liu et al. also reached a similar conclusion [56]. However, after comparing with the model in this study, it can be found that the coefficients in the two models are greatly different. This indicates that the composition of CPB has a great influence on the coefficient of the model, so the model with stronger applicability needs to be further studied.

3.4. Effect of Tailings Fine Content on UCS. The variation of UCS of CPB with tailings fine content after 28 days curing is shown in Figure 9 (solid content is 72%). With the increase of tailings fine content, the UCS of CPB first increases to the maximum value of 1.65 MPa and then decreases slowly. For example, when the tailings fine content increases from 22.08% to 42.2%, the strength of CPB increases by 30%. However, when the tailings fine content increases from
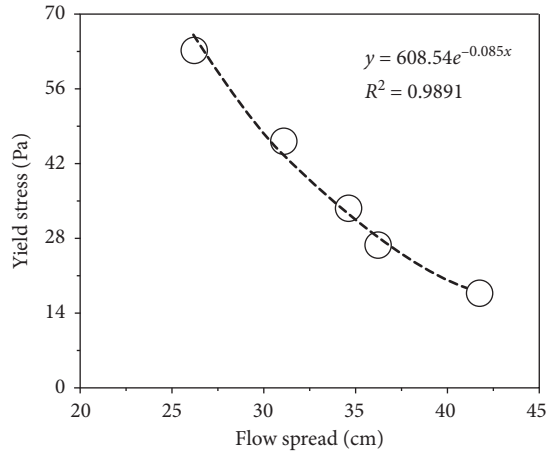
FIGURE 8: Correlation between flow spread and yield stress for fresh CPB.

FIGURE 9: UCS variation with fine contents.

42.2% to 62.94%, the corresponding strength decreases by 9.1%. The variation trend of strength is consistent with that of packing density. This indicates that the packing density is an important factor affecting the strength of CPB. A fitting analysis was conducted to further analyze the relationship between strength and packing density, and the results are shown in Figure 10. As can be seen from the figure, there is a good linear relationship between strength and packing density, and the correlation coefficient reaches 0.97. This means that the packing density of tailings can be used to predict the strength of CPB. The mechanism by which packing density affects CPB strength is further analyzed in the following section.

Wu et al. introduced Talbot gradation theory to study the influence of grain size distribution of waste rock on the cemented waste rock backfill (CWRB), and the results showed that when the gradation Talbot index was between 0.4 and 0.6, CWRB showed the best UCS and UPV performance [57]. Sevim and Demir used Dinger–Funk particle size distribution modulus (q) to explore the influence of fly ash particle size distribution on the compressive and flexural strength of fly ash-blended cement mortars, and the results revealed that when q is 0.4, mortars yield the best mechanical properties [58]. Therefore, it is necessary to explore the quantitative relationship between tailing particle size distribution and UCS for the purpose to further understand the mechanism of tailing particle size distribution affecting CPB properties. Here, the gradation Talbot index (t, obtained according to equation (6)) is used to correlate the UCS of the CPB, and the result is shown in Figure 11. The larger the t value is, the coarser the tailing particles are. Therefore, with the increase of tailings fine content, t value must decrease. It can be seen from Figure 11 that the UCS of CPB presents a good quadratic polynomial relationship with t value (the correlation coefficient reaches 0.929). When t is 0.38, the strength value of CPB is the maximum. In other words, when t is 0.41, the packing density of the particle system at this time is the largest, which is proved by the experimental results of tailings fine content and packing density in Section 3.1.
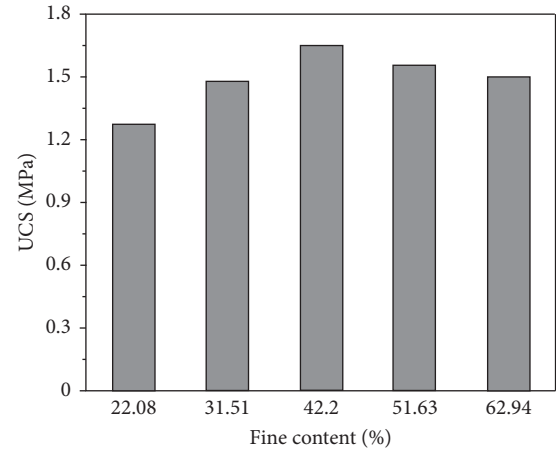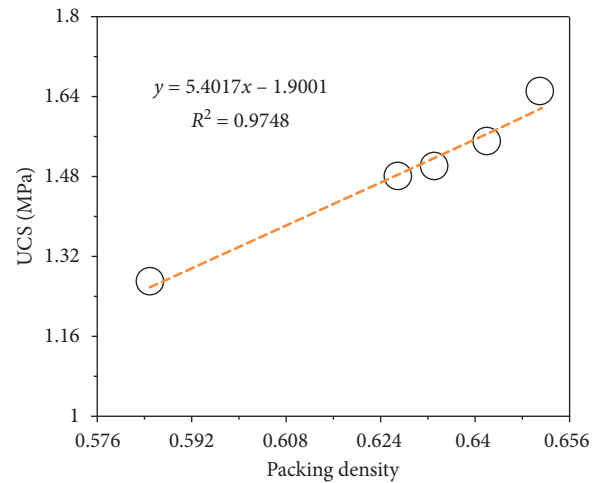
FIGURE 10: Relationship between packing density and UCS.

Furthermore, these results are consistent with the conclusions of Wu et al. [31, 59] and Zhang et al. [60].

$$P_i = 100 * \left(\frac{D_i}{D_{\max}} \right)^t, \tag{6}$$

where D_i is the particle size of tailings (μm); $D_{\max}$ is the maximum tailings particle size (μm); P_i represents the tailing volume percentage with particle size smaller than that occupied by D_i (%); P_i represents the volume percentage of tailings with particle size less than D_i (%).

3.5. Effect of Tailings Fine Content on Pore Structure. It is well known that the strength of CPB is essentially determined by its internal microstructure [61]. Figure 12 shows the pore size distribution of CPB with different tailings fine contents (curing time is 28 days). It can be clearly seen from the figure that when the tailings fine content is 42.2%, its pore distribution curve is at the far left, which indicates that this CPB sample has a finer pore structure. The samples with tailings fineness content of 62.94% and 22.08% have obviously poor
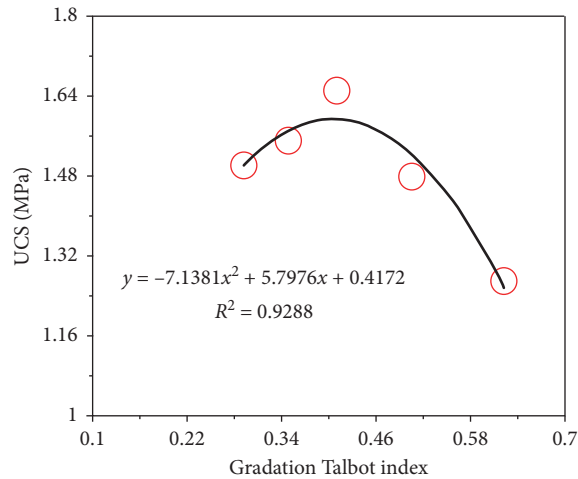
FIGURE 11: Relationship between gradation Talbot index and UCS.
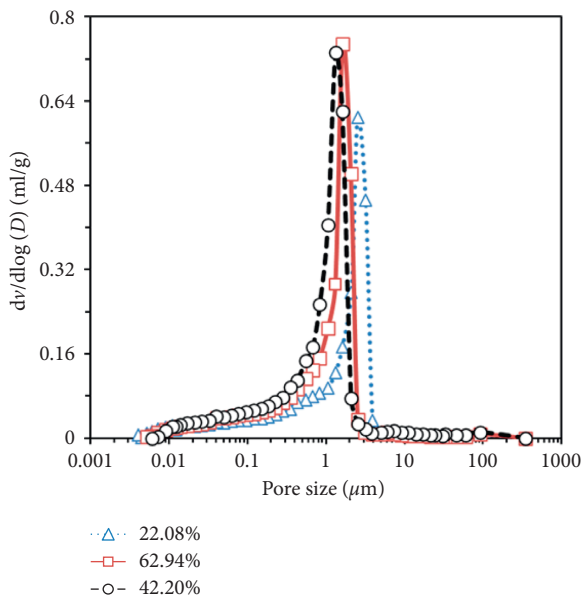
FIGURE 12: MIP test results under different fine contents.

pore structure, but the pore structure of the former is better than that of the latter. This is consistent with the results of packing density, indicating that the macroscopic packing density affects the strength of CPB by affecting the microscopic pores.

4. Conclusions

Based on the experimental results and discussion in this study, the following conclusions can be drawn:

(1) The packing density of tailings obtained by the dry packing method is less than that obtained by the wet packing method. With the increase of tailing fine content, the packing density increases first and then decreases.

(2) With the increase of tailings fine content, the flow spread of fresh CPB increases first and then decreases

significantly, while the yield stress shows an opposite trend. There is an exponential relationship between flow spread and yield stress of fresh CPB. The tailings fine content mainly affects the flowability and rheological properties of the CPB slurry through the packing density, but when the fine content is high, the influence of specific surface area of tailings cannot be ignored.

(3) With the increase of tailings fine content, the UCS of CPB increases first and then decreases slightly. The packing density is an important factor affecting the strength of CPB, and there is an obvious linear relationship between the packing density and the UCS of CPB. When the gradation Talbot index is 0.41, the strength of the CPB reaches the maximum.

(4) The pore structure of CPB samples with different tailings fine content is obviously different. The macroscopic packing density changes the strength of CPB by affecting the microscopic pores.

It is worth noting that the hydration of the binder was not considered in this study, so the coupling effect of hydration of binders and packing density on CPB performances will be the focus of our future work.

Data Availability

The [DATA TYPE] data used to support the findings of this study are included within the article.

Conflicts of Interest

The authors declare that they have no conflicts of interest.

Acknowledgments

References

[1] M. Fall, T. Belem, S. Samb, and M. Benzaazoua, "Experimental characterization of the stress-strain behaviour of cemented paste backfill in compression," *Journal of Materials Science*, vol. 42, no. 11, pp. 3914–3922, 2007.

[2] M. Fall, M. Benzaazoua, and S. Ouellet, "Experimental characterization of the influence of tailings fineness and density on the quality of cemented paste backfill," *Minerals Engineering*, vol. 18, no. 1, pp. 41–44, 2005.

[3] L. Yang, W. Xu, E. Yilmaz, Q. Wang, and J. Qiu, "A combined experimental and numerical study on the triaxial and dynamic compression behavior of cemented tailings backfill," *Engineering Structures*.vol. 219, Article ID 110957, 2020.

[4] J. Wang, J. Fan, and P. Qin, "Pullution of aromatic compounds and elements of a coal gangue dump from Fengfeng

Coal Mine 5, China," *World Journal of Engineering*, vol. 8, no. 1, pp. 15–22, 2011.

[5] Q. Hu, B. Lei, K. Ma, and T. Wang, "Analysis of surface mining subsidence laws under thick alluvial Quandian Mine," *World Journal of Engineering*, vol. 11, no. 3, pp. 247–256, 2014.

[6] C. Qi and A. Fourie, "Cemented paste backfill for mineral tailings management: review and future perspectives," *Minerals Engineering*, vol. 144, Article ID 106025, 2019.

[7] G. Wang, L. Yang, and Y. S. Zhang, "Modularized design of coal-mine paste filling station based on fuzzy theory," *World Journal of Engineering*, vol. 15, no. 6, pp. 743–750, 2018.

[8] Q. Chen, S. Sun, Y. Liu, C. Qi, H. Zhou, and Q. Zhang, "Experimental and numerical study on immobilization and leaching characteristics of fluoride from phosphogypsum based cemented paste backfill," *International Journal of Minerals, Metallurgy and Materials*, 2021.

[9] D. Wang, Q. Zhang, Q. Chen, C. Qi, Y. Feng, and C. Xiao, "Temperature variation characteristics in flocculation settlement of tailings and its mechanism," *International Journal of Minerals, Metallurgy and Materials*.vol. 27, no. 11, pp. 1438–1448, 2020.

[10] L. Yang, J. Qiu, H. Jiang, S. Hu, H. Li, and S. Li, "Use of cemented super-fine unclassified tailings backfill for control of subsidence," *Minerals*, vol. 7, no. 11, p. 216, 2017.

[11] J. Qiu, L. Yang, X. Sun, J. Xing, and S. Li, "Strength characteristics and failure mechanism of cemented super-fine unclassified tailings backfill," *Minerals*, vol. 7, no. 4, p. 58, 2017.

[12] A. Ghirian and M. Fall, "Coupled behavior of cemented paste backfill at early ages," *Geotechnical and Geological Engineering*, vol. 33, no. 5, pp. 1141–1166, 2015.

[13] G. Wang, Y. S. Zhang, L. Yang, and S. Zhang, "Paste-filling weighing control system optimization based on neural network," *World Journal of Engineering*, vol. 14, no. 2, pp. 155–158, 2017.

[14] M. Fall, D. Adrien, J. C. Célestin, M. Pokharel, and M. Touré, "Saturated hydraulic conductivity of cemented paste backfill," *Minerals Engineering*, vol. 22, no. 15, pp. 1307–1317, 2009.

[15] E. Yilmaz, M. Benzaazoua, T. Belem, and B. Bussière, "Effect of curing under pressure on compressive strength development of cemented paste backfill," *Minerals Engineering*, vol. 22, no. 9-10, pp. 772–785, 2009.

[16] J. Haiqiang, M. Fall, and L. Cui, "Yield stress of cemented paste backfill in sub-zero environments: experimental results," *Minerals Engineering*, vol. 92, pp. 141–150, 2016.

[17] J. Qiu, Z. Guo, L. Li, S. Zhang, Y. Zhao, and Z. Ma, "A hybrid artificial intelligence model for predicting the strength of foam-cemented paste backfill," *IEEE Access*, vol. 8, pp. 84569–84583, 2020.

[18] A. Wu, Y. Wang, H. Wang, S. Yin, and X. Miao, "Coupled effects of cement type and water quality on the properties of cemented paste backfill," *International Journal of Mineral Processing*, vol. 143, pp. 65–71, 2015.

[19] S. Ridha, A. I. Abd Hamid, and C. K. A. H. C. Ku, "Influence of different brine water salinity on mechanical properties of fly ash-based geopolymer cement," *International Journal of Structural Integrity*, vol. 9, no. 12, 2018.

[20] H. Jiang, M. Fall, E. Yilmaz, Y. Li, and L. Yang, "Effect of mineral admixtures on flow properties of fresh cemented paste backfill: assessment of time dependency and thixotropy," *Powder Technology*, vol. 372, pp. 258–266, 2020.

[21] K. Salhi and B. Mezghiche, "Effects of slag of blast furnace and sand of dune on durability of mortar and concrete," *World Journal of Engineering*, vol. 8, no. 1, pp. 23–28, 2011.

[22] M. Ozkaymak, S. Selimli, D. Kaya, and U. Uzun, "Searching the fertility potential of iron and steel industry blast furnace slag," *World Journal of Engineering*, vol. 13, no. 6, pp. 482–486, 2016.

[23] S. Raj, A. K. Rai, and V. G. Havanagi, "Suitability of stabilized copper slag and fly ash mix for road construction," *World Journal of Engineering*, vol. 15, no. 3, pp. 336–344, 2018.

[24] H. Jiang, Z. Qi, E. Yilmaz, J. Han, J. Qiu, and C. Dong, "Effectiveness of alkali-activated slag as alternative binder on workability and early age compressive strength of cemented paste backfills," *Construction and Building Materials*, vol. 218, pp. 689–700, 2019.

[25] F. Cihangir, B. Ercikdi, A. Kesimal, A. Turan, and H. Deveci, "Utilisation of alkali-activated blast furnace slag in paste backfill of high-sulphide mill tailings: effect of binder type and dosage," *Minerals Engineering*, vol. 30, pp. 33–43, 2012.

[26] S. Bechar and D. Zerrouki, "Effect of natural pozzolan on the fresh and hardened cement slurry properties for cementing oil well," *World Journal of Engineering*, vol. 15, no. 4, pp. 513–519, 2018.

[27] L. Zeghichi and Z. Benghazi, "Physical effects of natural pozzolana on alkali-activated slag cement," *World Journal of Engineering*, vol. 8, no. 2, pp. 141–146, 2011.

[28] S. Zhang, F. Ren, Z. Guo, J. Qiu, and H. Ding, "Strength and deformation behavior of cemented foam backfill in sub-zero environment," *Journal of Materials Research and Technology*, vol. 9, no. 4, pp. 9219–9231, 2020.

[29] D. Wu, M. Fall, and S. J. Cai, "Coupling temperature, cement hydration and rheological behaviour of fresh cemented paste backfill," *Minerals Engineering*, vol. 42, pp. 76–87, 2013.

[30] B. Ercikdi, F. Cihangir, A. Kesimal, H. Deveci, and İ. Alp, "Utilization of water-reducing admixtures in cemented paste backfill of sulphide-rich mill tailings," *Journal of Hazardous Materials*, vol. 179, no. 1–3, pp. 940–946, 2010.

[31] J. Wu, M. Feng, X. Ni, X. Mao, Z. Chen, and G. Han, "Aggregate gradation effects on dilatancy behavior and acoustic characteristic of cemented rockfill," *Ultrasonics*, vol. 92, pp. 79–92, 2019.

[32] P. Xiapeng, M. Fall, and S. Haruna, "Sulphate induced changes of rheological properties of cemented paste backfill," *Minerals Engineering*, vol. 141, Article ID 105849, 2019.

[33] W. Li and M. Fall, "Sulphate effect on the early age strength and self-desiccation of cemented paste backfill," *Construction and Building Materials*, vol. 106, pp. 296–304, 2016.

[34] C. Qi, A. Fourie, Q. Chen, and Q. Zhang, "A strength prediction model using artificial intelligence for recycling waste tailings as cemented paste backfill," *Journal of Cleaner Production*, vol. 183, pp. 566–578, 2018.

[35] X. Ke, X. Zhou, X. Wang, T. Wang, H. Hou, and M. Zhou, "Effect of tailings fineness on the pore structure development of cemented paste backfill," *Construction and Building Materials*, vol. 126, pp. 345–350, 2016.

[36] X. J. Deng, B. Klein, D. J. Hallbom, B. de Wit, and J. X. Zhang, "Influence of particle size on the basic and time-dependent rheological behaviors of cemented paste backfill," *Journal of Materials Engineering and Performance*, vol. 27, no. 7, pp. 3478–3487, 2018.

[37] H.-y. Cheng, S.-c. Wu, X.-q. Zhang, and A.-x. Wu, "Effect of particle gradation characteristics on yield stress of cemented paste backfill," *International Journal of Minerals, Metallurgy and Materials*, vol. 27, no. 1, pp. 10–17, 2020.

[38] J. Qiu, Z. Guo, L. Yang, H. Jiang, and Y. Zhao, "Effect of tailings fineness on flow, strength, ultrasonic and microstructure characteristics of cemented paste backfill,"

Construction and Building Materials, vol. 263, Article ID 120645, 2020.

[39] J. Qiu, Z. Guo, L. Yang, H. Jiang, and Y. Zhao, "Effects of packing density and water film thickness on the fluidity behaviour of cemented paste backfill," *Powder Technology*, vol. 359, pp. 27–35, 2020.

[40] H. H. C. Wong and A. K. H. Kwan, "Packing density of cementitious materials: Part 1-measurement using a wet packing method," *Materials and Structures*, vol. 41, no. 4, pp. 689–701, 2008.

[41] Z. Guo, J. Qiu, H. Jiang, J. Xing, X. Sun, and Z. Ma, "Flowability of ultrafine-tailings cemented paste backfill incorporating superplasticizer: insight from water film thickness theory," *Powder Technology*, vol. 381, pp. 509–517, 2021.

[42] M. Zhao, X. Zhang, and Y. Zhang, "Effect of free water on the flowability of cement paste with chemical or mineral admixtures," *Construction and Building Materials*, vol. 111, pp. 571–579, 2016.

[43] B. A. Kounakoff, L. Hanzic, and J. C. M. Ho, "Limestone and silica fume to improve concurrent flowability-segregation limits of concrete," *Magazine of Concrete Research*, vol. 69, no. 23, pp. 1189–1202, 2017.

[44] Z. Zhang, Y. Li, L. Ren, Z. Guo, H. Jiang, and N. Liu, "Evaluation of rheological parameters of slag-based paste backfill with superplasticizer," *Advances in Materials Science and Engineering*, vol. 2021, Article ID 6673033, 11 pages, 2021.

[45] S. Ma, Y. Qian, and S. Kawashima, "Experimental and modeling study on the non-linear structural build-up of fresh cement pastes incorporating viscosity modifying admixtures," *Cement and Concrete Research*, vol. 108, pp. 1–9, 2018.

[46] K. P. Singh, A. Kumar, and D. R. Kaushal, "Pressure drop calculation for fly ash slurry using rheological model," *World Journal of Engineering*, vol. 16, no. 6, pp. 751–767, 2019.

[47] A. K. H. Kwan, L. G. Li, and W. W. S. Fung, "Wet packing of blended fine and coarse aggregate," *Materials and Structures*, vol. 45, no. 6, pp. 817–828, 2012.

[48] A. K. H. Kwan and H. H. C. Wong, "Packing density of cementitious materials: Part 2-packing and flow of OPC + PFA + CSF," *Materials and Structures*, vol. 41, no. 4, pp. 773–784, 2008.

[49] H. Ye, X. Gao, R. Wang, and H. Wang, "Relationship among particle characteristic, water film thickness and flowability of fresh paste containing different mineral admixtures," *Construction and Building Materials*, vol. 153, pp. 193–201, 2017.

[50] A. K. H. Kwan, K. W. Chan, and V. Wong, "A 3-parameter particle packing model incorporating the wedging effect," *Powder Technology*, vol. 237, pp. 172–179, 2013.

[51] A. K. H. Kwan and W. W. S. Fung, "Packing density measurement and modelling of fine aggregate and mortar," *Cement and Concrete Composites*, vol. 31, no. 6, pp. 349–357, 2009.

[52] W. Xu, M. Tian, and Q. Li, "Time-dependent rheological properties and mechanical performance of fresh cemented tailings backfill containing flocculants," *Minerals Engineering*, vol. 145, Article ID 106064, 2020.

[53] A. K. H. Kwan and L. G. Li, "Combined effects of water film, paste film and mortar film thicknesses on fresh properties of concrete," *Construction and Building Materials*, vol. 50, pp. 598–608, 2014.

[54] S. Haruna and M. Fall, "Time- and temperature-dependent rheological properties of cemented paste backfill that contains superplasticizer," *Powder Technology*, vol. 360, pp. 731–740, 2020.

[55] W. Xu, W. Chen, M. Tian, and L. Guo, "Effect of temperature on time-dependent rheological and compressive strength of fresh cemented paste backfill containing flocculants," *Construction and Building Materials*, vol. 267, Article ID 121038, 2021.

[56] H. Liu, X Sun, H Du et al., "Effects and threshold of water film thickness on multi-mineral cement paste," *Cement and Concrete Composites*.vol. 112, Article ID 103677, 2020.

[57] J. Wu, H. Jing, Q. Yin, B. Meng, and G. Han, "Strength and ultrasonic properties of cemented waste rock backfill considering confining pressure, dosage and particle size effects," *Construction and Building Materials*.vol. 242, Article ID 118132, 2020.

[58] Ö. Sevim and İ. Demir, "Optimization of fly ash particle size distribution for cementitious systems with high compactness," *Construction and Building Materials*, vol. 195, pp. 104–114, 2019.

[59] J. Wu, M. Feng, J. Xu, P. Qiu, Y. Wang, and G. Han, "Particle size distribution of cemented rockfill effects on strata stability in filling mining," *Minerals*, vol. 8, no. 9, p. 407, 2018.

[60] T. Zhang, Q. Yu, J. Wei, and P. Zhang, "A new gap-graded particle size distribution and resulting consequences on properties of blended cement," *Cement and Concrete Composites*, vol. 33, no. 5, pp. 543–550, 2011.

[61] E. Yilmaz, T. Belem, B. Bussière, and M. Benzaazoua, "Relationships between microstructural properties and compressive strength of consolidated and unconsolidated cemented paste backfills," *Cement and Concrete Composites*, vol. 33, no. 6, pp. 702–715, 2011.

Review Article

Advances in Understanding the Alkali-Activated Metallurgical Slag

Kuisheng Liu [ID],[1] **Zengqi Zhang** [ID],[2] **and Jianwei Sun** [ID][3]

[1]*Beijing Urban Construction Group Co., Ltd, Beijing 100088, China*
[2]*School of Metallurgical and Ecological Engineering, University of Science and Technology Beijing, Beijing 100083, China*
[3]*Department of Civil Engineering, Tsinghua University, Beijing 100084, China*

Correspondence should be addressed to Zengqi Zhang; zzq4816@163.com

Received 14 April 2021; Accepted 8 May 2021; Published 25 May 2021

Academic Editor: Tingting Zhang

This paper summarized and reviewed the mechanism and macro-performance of alkali-activated metallurgical slag, including steel slag, copper slag, ferronickel slag, and lead-zinc slag. Better activated method and alkali-activator are still needed to be developed to improve the performance of the metallurgical slag with low reactivity. Besides, the chemical components' variation of these metallurgical slags from different regions will lead to unpredictable performance, which needs further study.

1. Introduction

It is widely accepted that alkali-activated material (AAM) is a potential alternative for ordinary Portland cement (OPC) [1]. These materials are commonly generated by alumino-silicate precursor, which can be obtained from solid industrial waste, such as granulated blast furnace slag (GBFS), fly ash, mineral processing tailings [2], catalyst residues, waste glass, waste ceramic, coal bottom ash [3], rice husk ash [4], palm oil fuel ash, etc. [5]. In 2016, approximately 1.45 Gt CO_2, which is about 8% of CO_2 total emissions from human activities, was released from the cement industry [6]. About 50%–60% CO_2 emission of cement industry comes from the calcination of limestone. Therefore, the replacement of OPC by AAM is recognized as one potential way to reduce carbon emission [7]. Life-cycle analysis (LCA) of alkali-activated materials has been thoroughly discussed by Habert. According to the statistics of different studies, LCA of AAM reduces approximately 40%–80% CO_2 emissions compared to an OPC baseline [1]. Need to add that the baselines of OPC are specified inconsistently among various reports because the mix design, local conditions (such as transport distances and cost of electricity generation) as well as industry and environmental policy significantly affect the baseline [1].

Compared to OPC, AAM could have superior properties through reasonable design. Better acids and sulfate resistance [8], higher strength [9], and higher temperature resistance [10] were reported in AAM. These advantages of AAM are mainly achieved by the presence of aluminosilicate gel such as hydrated calcium aluminosilicate gel (C-A-S-H) and hydrated sodium aluminosilicate gel (N-A-S-H). These two kinds of aluminosilicate gel are different from the main product, namely, C-S-H in cement. A highly crosslinked silicon structure of Q3 and Q4 with less bound water was found in aluminosilicate gel due to the substitution of aluminum for silicon [11], which contributed to the better properties of AAM. Furthermore, AAM shows a better performance in alkali-aggregated reactions (AAR) compared to OPC [12].

According to the different precursors activated, AAM is commonly divided into two different binder systems [5]. The primary type of alkali-activated binder is high-calcium alkali-activated binder mainly derived from alkali-activated blast furnace slag (AAS) [13]. The secondary-type binder system is the so-called "geopolymer" mainly derived from alkali-activated fly ash (AAF). The former system is dominated by C-A-S-H products with a tobermorite-like structure (mainly Q2 with smaller parts of Q1 and Q3) [14]. The main product in geoploymer is N-A-S-H with a zeolitic-like

structure (mainly Q4 with few Q3) [12]. Blast furnace slag is more reactive than fly ash, as a higher pH and temperature is needed to activate the fly ash [5]. This means AAS has a wider range of activators compared to AAF, such as sodium carbonate and sodium sulfate. Besides the different gels in these two systems, a wide range of secondary phases such as hydrotalcite and AFm-like crystal were observed in AAS [15].

Recently, various metallurgical slags are generated in the production of metal processing, such as steel slag, copper slag, ferronickel slag, and lead-zinc slag. Steel slag is a solid waste generated during the conversion of iron into steel, which is about 15% of the crude steel output [16, 17]. Copper slag is an industrial by-product produced by the copper-making process, whose yield is 2–3 times that of copper output [18, 19]. Ferronickel slag as an industrial waste comes from the process of nickel-iron alloy production [20, 21]. Approximately 12–14 tons of ferronickel slag per ton of nickel is produced [22, 23]. The main solid waste generated during lead and zinc production is lead-zinc slag. According to statistics, the extraction cost per 100 tons of lead and zinc is 71 tons of lead slag and 96 tons of zinc slag [24, 25]. It is estimated that the annual production of steel slag, copper slag, ferronickel slag, and lead-zinc slag each year worldwide is 200 million tons, 70 million tons, 150 million tons, and 25 million tons, respectively [17, 23]. Although the yield of these slags is high, the utilization rate is low. For example, until now, the steelmaking industry produced nearly 1.2 billion tons of steel slag in China, and only less than 30% slag is recycled and applied in some low value-added fields [26, 27]. Most of metallurgical slags are stockpiled in an open field. Dealing with a large amount of industrial waste is a severe challenge to global environmental governance. The best way to solve this problem is to transform metallurgical slags into new materials with high added value, which will also bring huge economic benefits to the society.

Most metallurgical slags are used as potential alternative materials in civil engineering. They are usually used as aggregates or fillers in place of other conventional sand and stone materials due to their low activity [28, 29]. Powdered slag has higher market value as compared to granulous slags for construction. A possible application for those solid wastes is to produce alkali-activated materials because they are high-quality aluminosilicate resources. With the further implementation of the concept of sustainable development, the research on cement with less clinker and no clinker has been paid more attention. Alkali-activated material as a kind of inorganic polymer material has great potential and is expected to be an alternative to cement and concrete. Meanwhile, in recent decades, with the development of mine cemented backfill technology in underground mine backfill, more and more mines use cementitious materials and alternative binders to replace conventional hydraulic back-filling at home and abroad [30]. Compared to building materials, the quantity of mine backfill material is large and the strength requirement is easily met. When alkali-activated materials are used to replace other conventional materials for mine backfill, it helps to effectively deal with the solid wastes, substantially preserve natural resources and energy,

and create the conditions for reducing potentially harmful waste disposal costs. Hence, it indicates that alkali-activated material is suitable for mine backfill.

Within this context, the purpose of this paper is to review steel slag, copper slag, ferronickel slag, and lead-zinc slag as a precursor in alkali-activated material. The challenges and opportunities of using slags in alkali-activated material are also discussed.

2. Alkali-Activated Steel Slag Material

2.1. Physical Properties and Chemical Composition. The type of modern steel determines the elimination of different impurities in the steelmaking process. In terms of carbon steel, it can be produced in a ladle furnace (LF), an electric arc furnace, and a basic oxygen furnace (BOF) in different countries [30–32]. Thus, depending on the type of furnace, steel slag can be broadly classified into three categories, i.e., BOF steel slag, EAF steel slag, and LF steel slag [33]. As for steel slag in alkali-activated material, it usually refers to BOF steel slag, which is also called converter steel slag [34]. Today, in China and the United States, BOF steel slag makes up approximately 70% and 40% of steelmaking, respectively [35, 36]. BOF steel slag is rock-like and dark. The density is 3–3.6 kg/m^3, which is higher than the natural aggregate [37]. The water absorption rate of steel slag is 0.4%–3.5% [38, 39]. BOF steel slag is very hard and not easy to be ground due to its high Fe content, so BOF steel slag and its products have good abrasion resistance [37, 38].

Different chemical compositions are heavily affected by steel slag type. BOF slag has more FeO than EAF steel slag and less SiO$_2$ than LF steel slag [35, 37]. The main chemical compositions of BOF steel slag are presented in Figure 1. In general, BOF steel slag primarily consists of 35%–50% CaO, 15%–35% Fe$_2$O$_3$, 10%–20% SiO$_2$, 2%–10% MgO, 0%–5% MnO, 1%–7% Al$_2$O$_3$, 1%–3% P$_2$O$_5$, and 0%–2% TiO$_2$. It is worth noting that there is a great difference in Fe$_2$O$_3$ content. High Fe$_2$O$_3$ content in steel slag plays an important role in grinding and application quality of steel slag. However, with the improvement of magnetic separation technology of BOF slag, the Fe$_2$O$_3$ content in BOF slag has been effectively reduced [26, 37]. The chemical composition analysis on newly produced slag has showed that the total amount of Fe$_2$O$_3$ is less than 20%.

Steelmaking slag is usually air-cooled to ambient conditions, and so BOF steel slag is highly crystallized [38, 39]. Those oxides in BOF steel slag form different mineralogical compositions. Essential mineral phases in BOF steel slag are tricalcium silicate (C$_3$S), dicalcium silicate (C$_2$S), CaO-FeO-MnO-MgO solid solution (RO phase), dicalcium ferrite (C$_2$F), tetracalcium aluminoferrite (C$_4$AF), merwinite (Ca$_3$MgSi$_2$O$_8$), lime (free CaO), and periclase (free MgO) [16, 26, 37, 40]. The Fe mainly exists in forms such as RO phase, C$_4$AF, and C$_2$F, and these phases have no sufficient reactivity. During cooling, C$_2$S undergoes polymorphic transformations, where β-C$_2$S transforms γ-C$_2$S at approximately 500°C, resulting in volumetric expansion of 12% [37–39]. A small amount of C$_3$S and β-C$_2$S with dense structure and large crystal size have low reactivity, while
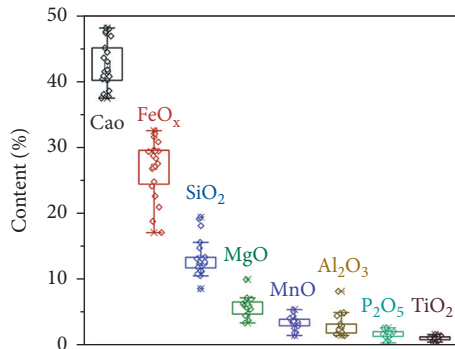
FIGURE 1: The chemical composition of BOF steel slag.

γ-C_2S is considered to have a negligible cementitious capability [41]. Therefore, BOF steel slag powder can result in poor hardening reaction after prolonged curing at room temperatures but show better cementitious properties under the action of chemical activator. The content of free CaO increases with the alkalinity of steel slag. And, even the content in BOF steel slag is up to 10%, which has a negative impact on the stability of steel slag products. Although the contents of free CaO and MgO in BOF steel slag have become very low with the improvement of heat and vapour process, the stability of steel slag should be considered when it is used as aggregate [37, 42, 43].

2.2. Reaction Mechanism of Alkali-Activated Steel Slag.
Compared to amorphous GBFS, fly ash, and metakaolin, the biggest challenge of steel slag as a precursor is its high crystallization. Therefore, it should have different inorganic polymerization mechanisms between alkali-activated steel slag materials and alkali-activated amorphous slag materials. Although few in number, some publications regarding the exploration of the reaction mechanism of steel slag in the production of alkali-activated materials do exist in literature.

The hydration sensitivity and even mechanical behavior of the material to activation depends on several factors, such as the phase compositions and fineness of the precursor, the curing conditions and alkaline conditions containing initial alkalinity, and the type and concentration of activator used [37]. Wang et al. [44] changed the pH value of NaOH solution in NaOH-activated steel slag and studied effects on kinds and morphologies of hydration products. They found that although increasing the initial alkalinity could promote the early hydration of active components like C_2S, C_3S, and $C_{12}A_7$, it had little effect on their late-age hydration degree [44]. As for inert components like Fe phases, the hydration degree of steel slag was still very low even under strong alkaline conditions [44]. They also found that changing the alkaline conditions did not change the type of hydration products [44].

The alkaline activator has a very important function. According to research findings, compared to sodium sulfate, sodium hydroxide, and sodium carbonate as activators, liquid sodium silicate (water glass) could activate steel slag more efficiently and is an appropriate activator for alkali-

activated steel slag materials [34, 37, 45, 46]. Sun et al. [47] had investigated the hydration properties and microstructure characteristics of alkali-activated steel slag binder[47]. According to their findings, both hydration processes and products between water glass-activated steel slag and Portland cement were similar: (i) five hydration stages including the rapid exothermic stage, the dormant stage, the acceleration stage, the deceleration stage, and the steady stage and (ii) C-(A)-S-H gel and crystalline $Ca(OH)_2$ as the main hydration products [47]. The increasing of the moduli of water glass solution from 0.5 to 2.0 lead tothe finerpore structure and higher mechanical strength [48]. Meanwhile, additional silicate had a retarding effect on the development of hydration process and the formation of hydration products [48]. However, increasing modulus had a negligible impact on the type of products of alkali-activated steel slag [48]. In addition, they also conducted detailed comparisons between the alkali-activated steel slag binder and Portland cement with the same water/binder ratio of 0.45 due to similar reaction conditions [47]. They found that alkali-activated steel slag has a faster reaction, fewer hydration products, poorer crystallization of $Ca(OH)_2$, a lower Ca/Si ratio, and a similar Al/Si ratio of gels than Portland cement [47]. Meanwhile, in terms of microstructure, alkali-activated steel slag hardened paste had more pores and looser microstructure causing long-term adverse impact on strength development [47].

Liu et al. [49] investigated the early age evolution including microstructure and reaction degree of alkali-activated steel slag from multiple perspectives under high curing temperature. They used ground steel slag with a specific surface area of $440\,m^2/kg$, SiO_2/Na_2O molar ratio equal to 2.42 in the activator, and curing temperature of $60°C$ [49]. The most important conclusion is that they demonstrated the type of gel product [49]. According to their findings, the nano-C-S-H and nano-C-A-S-H gel first condensed due to the dissolution Si and Al phases, and then the formation of C-A-S-H gel was continuously conducted at longer curing time because Si-O-Si bond translated into Si-O-Al [49]. Kang et al. [50] synthesized a novel CeO_2-loaded porous NaOH-activated steel slag-silica fume catalyst for photocatalytic water-splitting of hydrogen production, and they found that three-dimensional polymeric structure C-S-H gel ($Ca_{1.5}SiO_{3.5}\cdot xH_2O$) was the main phase in the alkali-activated steel-slag-based material.

2.3. Properties of Alkali-Activated Steel Slag.
The potential utilization of alkali-activated steel slag as an alternative binder has been drawing much attention recently. However, unfortunately, its strength is very low even under strong alkaline conditions. The reason is that less active components limit the amount of hydration products from steel slag, although the activation effect of alkaline condition on hydration of steel slag is obvious. Wang et al. [44] and Sun et al. [47] found that the strength of alkali-activated steel slag is far from the strength of cement. The compressive strength of alkali-activated steel slag is only 30%–40% of that of cement slurry [47]. But, adding 20% GBFS can increase the 28-day

compressive strength by 40% [51]. So steel slag as a solo precursor is not an ideal material for the production of alkali-activated materials. In most studies on alkali-activated steel slag materials, better cementitious property is achieved by blending with other materials like GBFS, fly ash, and metakaolin.

When blended with blast furnace slag, alkali-activated GBFS-steel slag material shows significant cementitious properties in the presence of alkaline activator. You et al. [52] systematically studied the effect of steel slag on properties of alkali-activated GBFS material at room temperature. The Na_2O content was 4% by total weight of precursors and the modulus of water glass was 1.5 in all the alkali-activated mortars [52]. The content of steel slag was 50% by mass in the precursor [52]. Hydration process, strength, autogenous and drying shrinkages, pore structure, water absorption, and chloride ion penetration resistance of mortars were investigated [52]. They found that adding steel slag could decrease the hydration heat but prolong the setting time and improve workability [52]. Furthermore, incorporating steel slag could increase water absorption, reduce autogenous and drying shrinkage, and chloride ion penetration resistance [52]. The reason was that the replacement of steel slag could significantly increase the total porosity of the matrix due to its lower activity and the consequent less products [52]. You et al. [53] also investigated corrosion behavior of low-carbon steel reinforcement in alkali-activated GBFS and alkali-activated GBFS-steel slag under simulated marine environment. They found that the corrosion products were hematite and goethite [53]. The addition of steel slag had a beneficial influence on corrosion resistance due to improved interface transition zone between reinforcements and mortars [53].

Several studies have been undertaken to understand the investigation effects of steel slag on hydration properties of alkali-activated fly ash materials. Song et al. [54] used steel slag with various replacement levels (0, 10%, 20%, 30%, 40% and 50% by mass) to replace fly ash for alkali-activated binary composite material. They evaluated the influence of steel slag on setting times, flowability, viscosity, strength, absorptivity, and microstructural properties at standard curing conditions [54]. Adding steel slag obviously increased the setting times and flowability but decreased the viscosity [54]. The optimum content of steel slag was found to be 20% due to the negligible 28-day compressive strength loss and best flexural strength, elasticity modulus, and absorptivity [54]. The reason for the development of the strength was the formation and coexistence of C-S-H gel and C-A-S-H gel exhibiting better bonding [54]. Guo and Yang [55] synthesized engineered cementitious composite by using fly ash-steel slag activated by water glass with the modulus of 1.5 and polyvinyl alcohol fibers. They also thought C-S-H gel and N-A-S-H gel as self-healing products had a positive effect on self-healing property [55]. However, Niklioć et al. [56] had different conclusions about the type of reaction product and the development of compressive strength due to high curing temperature of 65°C at the early age. They thought that the main products were N-(C)-A-S-H gel along with N-A-S-H gel [56]. They found that steel slag up to 30% in the range of 0%–40% positively affects the strength

evolution [56]. The 28-day compressive strength of alkali-activated fly ash mortar containing 30% steel slag exceed 35 MPa, and the study by Guo X had come to the same conclusions [56–58]. Niklioć et al. [56]also evaluated the thermal resistance of alkali-activated fly ash-steel slag materials. They found that steel slag had a negative effect on the thermal resistance,i.e.,the mechanical and dimensional stability was above 600°C [56].

Bai et al. [59] and Furlani et al. [60] investigated the content and fineness of steel slag as a precursor on the properties of alkali-activated metakaolin material. In the study by Bai et al. [59], they set two curing conditions (exposed curing at room temperature, sealed curing, and moist curing) and four substitution rates (0, 10%, 20%, and 40%). Mechanical properties, acid and alkali erosion endurance, and microstructure were investigated [59]. They found that adding 10% steel slag could ensure the optimum properties and moist curing was the best curing method [59]. The highest compressive strength and bending strength could reach 70 MPa and 8 MPa, respectively [59]. Moreover, microstructure was enhanced due to beneficial physical and chemical reactions between the active components of steel slag and metakaolin [59]. According to the research of Furlani et al. [60], two steel slag maximum particle sizes ($250 \mu m$ and $125 \mu m$) were used to replace metakaolin (0%, 20%, 40%, 60%, 80%, and 100% by mass). They found that finer steel slag could play a better role, and 40% steel slag was the best dosage [60]. They thought that the increase of compressive strength was attributed to the formation of stronger mechanical bonds replacing part of the original N-A-S-H gel [60].

Besides the binary systems above, steel slag is commonly mixedwith slag to form ternary and other composite systems. It is also expected to be an effective way to use steel slag. In alkali-activated fly ash-GBFS-steel slag ternary system by Song et al. [61], water glass with a modulus of 1.6 was used as activator, and composite additive of GBFS-steel slag varied from 10% to 50%. The optimum content of GBFS-steel slag was found to be 40% [61]. The setting time, initial flow, and early and later compressive strength of paste increased due to the presence of steel slag [61]. In addition, the brittleness decreased by adding steel slag [61]. More gel products formed by hydration of GBFS-steel slag refined the pore structure, which was the main reason for the improvement of strength [61]. In alkali-activated ultrafine palm oil fuel ash-steel slag composite system, Yusuf at al. [62] evaluated the contributions of steel slag on compressive strength and shrinkage of pastes and mortars. The dosage of steel slag varied from 0% to 80% for pastes and 0% to 60% for mortars [62]. They found that steel slags reduced shrinkage by refining pores, eliminating microcracks, and increasing the density and strength of microstructure [62].

3. Alkali-Activated Copper Slag

3.1. Properties of Copper Slag. Copper slag (CS) is a by-product generated from the refining of copper. About 2.2 tons of copper slag will be produced for each ton of copper

produced [63], and about 40 million tons of CS are produced annually in the world [64]. Depending on different cooling processes, CS can be divided into two different groups, namely, granulated water-cooled slag and air-cooled slag [64]. Granulated CS (GCS) contains an amorphous phase, which mainly consists of iron oxides, silicon dioxide, and calcium oxide [65]. Air-cooled slag with a slower cooling process mainly contains crystalline phases, which consist of similar chemical components [66]. Figure 2 shows the typical XRD patterns of GCS and air-cooled CS. Table 1 shows the chemical composition and mineral composition of copper slag cooled with different processes in other studies. Mineral composition of granulated water-cooled CS and air-cooled CS usually contains same mineral components, namely, magnetite (Fe_3O_4) and fayalite (Fe_2SiO_4) [67]. Figure 3 shows the statistical chemical content of copper slag from other studies.

The common utilization options of copper are recovering of the metal and producing value-added products, such as abrasive and cutting tools, tiles, glass, road-base construction, pavement, as well as cement and concrete [74]. Due to the amorphous nature of Granulated CS, the hydration properties of GCS are more active compared to air-cooled CS [73], which means granulated CS is more suitable for supplementary cementitious materials, while air-cooled CS is more suitable to be used as aggregate in concrete [75, 76].

Using granulated CS as supplementary cementitious material involves an optimal dosage of 5%–15% [77]; a higher dosage of GCS decreases the strength of the cementitious material [78]. Thus, this utilization method is not enough for utilizing GCS. Alkali-activated CS has been investigated by some researchers. CS can be used as a filling material activated by sodium hydroxide [70]. About 20–30 MPa compressive strength of the binder of alkali-activated CS was achieved [79–81], which shows that alkali-activated granulated CS is a potential environment-friendly material for replacing cement.

3.2. Mechanism of Alkali-Activated Copper Slag.
The mechanism of alkali-activated granulated copper slag is different when different activators are used [82]. Compressive strength result shows that the activation effect of sodium silica (SS) is better than sodium hydroxide (SH) [82], as the binder compressive strength of sodium silica is 5–6 times higher than that of sodium hydroxide.

The mineralogical characterization of alkali-activated CS with XRD shows that different products were formed when different activators were used. In SS-activated GCS, a weak peak, which represents the poor crystallinity of C-S-H, was formed. In SH-activated GCS, a sharp peak occurs at the similar position of weak peak in SS, which represents the plombierite (tobermorite 14 Å) [82].

The reaction products in the pastes of CS activated with SS are mostly amorphous C–S–H gels with higher degrees of polymerization, which bond the matrix together with fewer pores. However, the products formed in the pastes of CS activated with SH contain some highly crystalline

plombierite, and the matrix is loose and porous [82]. Besides, quantitative XRD shows that the original crystal in GCS, especially the fayatite and monticellite, are reduced in SS-activated GCS. This can be interpreted as the original crystal in GCS dissolved and participated in the formation of product [82]. The reaction degree of alkali-activated CS of different activators is consistent with the compressive strength and XRD result. CS reaction degree of SH and SS are 37.8% and 47.8%, respectively.

The different mechanisms of SH and SS were determined by pH and $[SiO_4]^{4-}$ concentrations. CS surface will dissolve with the attack of OH^-, Ca^{2+} and $[SiO_4]^4$ were dissolved into the solution to form the product. Compared to SH, although the pH of SS is lower, more $[SiO_4]^{4-}$, which dissolved slower than Ca^{2+}, is provided in SS. This can be explained that although the initial reaction rate of SS is slower than SH, the total heat release of SS is higher than SH [73]. The precipitation of the product might also be hindered when OH^- is excessive [82].

3.3. Performance of Alkali-Activated Copper Slag.
Alkali-activated GCS has the potential to be used as a construction material. The compressive strength of GCS varies when different activators are used. SS is more effective than SH, and a higher modulus of SS increases the compressive strength of alkali-activated CS mortar [75]. Twenty-eight-day compressive strength of alkali-activated CS can reach 20 MPa, and the strength can still develop before 90 days [73].

SH is not a suitable activator for GCS, and 28-day compressive strength of SH-activated GCS is lower than 5 MPa [73, 82]. The strength development of later stage (90 days) is not developed [73]. This might due to the products of SH-activated CS containing highly crystalline plombierite, which is small in specific surface area and thus loosens the matrix [82].

Shrinkage of alkali-activated CS was also investigated [81]; drying shrinkage of alkali-activated CS is higher than Portland cement due to refined pore structures of alkali-activated CS. Increasing of both alkali content and modulus will increase the shrinkage of alkali-activated CS. The porosity result shows that the increasing of alkali dosage refines the pore structure [81]. Similar with Portland cement, shrinkage was smaller after 14 days. Therefore, it is suggested that a lower alkali content and modulus is more effective for controlling the shrinkage of alkali-activated CS.

4. Alkali-Activated Ferronickel Slag

4.1. Raw Material Properties of Ferronickel Slag.
Ferronickel slag is an industrial waste obtained from ferronickel alloy production. The ferronickel industry uses two main smelting technologies: the electric furnace method and the blast furnace method. The electric furnace method is currently the main method of ferronickel alloy production, while the blast furnace method is only used in parts of eastern China. According to the differences of raw material and manufacturing technology, ferronickel slag can be

(a)   (b)
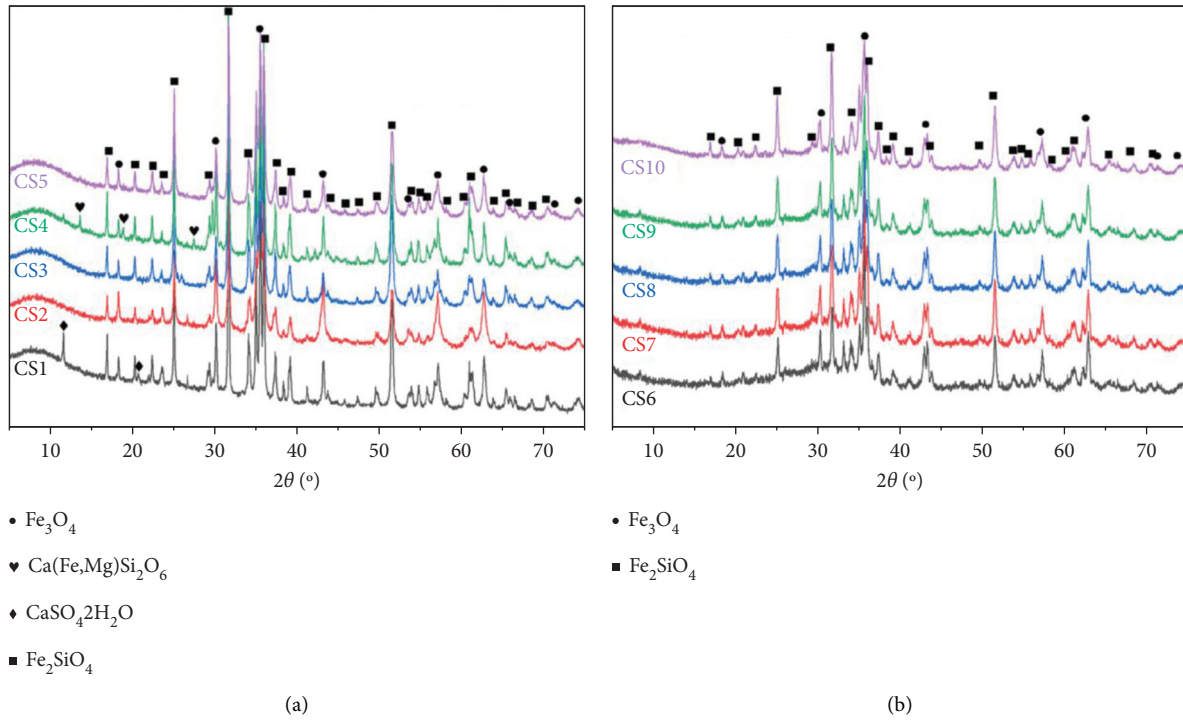
FIGURE 2: XRD patterns of the copper slag samples. (a) Air-cooled samples. (b) Water-cooled samples [67].

TABLE 1: Chemical composition of copper slag (M = magnetite, F = fayalite, H = hematite, D: diopside, C: clinoferrosilite).

Material	Fe_2O_3	SiO_2	CaO	Al_2O_3	MgO	Cooling process	Mineral composition	Ref.
1	59.78	25.18	3.75	3.51	0.69	Air-cooled	M, F, D	[67]
2	59.94	21.68	1.76	2.83	1.13	Air-cooled	F, H	[68]
3	44.21	35.29	1.82	2.7	1.14	Water-cooled	M, F	[67]
4	47.01	33.4	4.0	3.5	1.39	Water-cooled	F, H	[69]
5	30.48	39.14	13.41	7.76	2.09	—	M, F, C, D	[66]
6	53.11	28.70	3.87	5.8	1.56	—	F	[70]
7	65.27	27	2	3	0.29	—	—	[71]
8	57.8	30.53	1.6	2.8	1.49	—	—	[72]
9	49.6	34.17	4.29	4.67	0.71	Air-cooled	M, F	[73]
10	44.05	34.74	2.66	10.52	1.03	Water-cooled	M, F	[73]
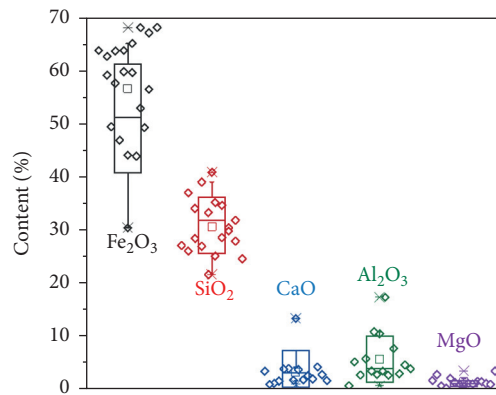
FIGURE 3: Statistical chart of content of copper slag.

categorized as electric furnace ferronickel slag (EFFS) and blast furnace ferronickel slag (BFFS) with different chemical and mineralogical compositions. In addition, the cooling method of the molten slag has an important influence on its composition. The chemical compositions of ferronickel slag obtained from different sources are presented in Table 2. In general, BFFS are composed of SiO_2, Al_2O_3, and CaO, as BFFS has a large amount of amorphous phase [83, 84]. EFFS is mainly composed of SiO_2, MgO, and Fe_2O_3, and its mineral composition is mainly composed of crystalline phases, such as enstatite, forsterite, and dropsied. EFFS can be divided into air-cooled slag and water-cooled slag depending on different cooling methods. Generally, EFFS generated from laterite ore contains a high FeO/Fe_2O_3 and low MgO, whereas that from garnierite ore contains low Fe_2O_3 and high MgO [85–89]. The chemical composition of air-cooled EFFS differs only relatively little from that of water-cooled EFFS. However, the glassy phase content of water-cooled EFFS is higher than that of air-cooled EFFS. It can be seen that the nature of ferronickel slag depends on its source and treatment process.

4.2. Reaction Mechanism of Alkali-Activated Ferronickel Slag. The reaction process of alkali-activated ferronickel slag is similar to that of alkali-activated slag/fly ash. The reaction of alkali-activated BFFS can be simplified as in Figure 4. After the addition of the activator solution, the structure of the BFFS is first attacked by the alkaline solution; then, BFFS is subsequently depolymerized to low polymer or silicate and aluminate tetrahedral units. Finally, the depolymerized substances polymerize to form the crystalline product strätlingite and amorphous product C-A-S-H, which is responsible for the high strength of alkali-activated BFFS [83]. BFFS tends to form strätlingite rather than hydrotalcite, mainly because of the high aluminum content of BFFS and the small amount of magnesium dissolved, which is mainly present in the form of spinel and forsterite with a stable structure, and hardly reacts in alkaline solutions. The Ca/Si and Al/Si ratios of C-A-S-H are 0.64 and 0.57–1.44, respectively. The difference in composition between EFFS and BFFS results in the generation of different hydration products. Hydroxysodalite was found in the reaction products of alkali-activated low-calcium and low-magnesium EFFS with kaolinite that exhibited higher strength [89]. Maragkos et al. [88] found that increasing the OH^- concentration could enhance the dissolution of silicon and aluminum in EFFS. And high SiO_2/Na_2O ratio can promote the condensation reaction. The presence of alkali metal cations plays a catalytic role and has an important influence on gel hardening and crystallization. Compared to NaOH, KOH provides more inorganic polymer precursors, as the larger K^+ size contributes to the formation of larger silicate oligomers, to which $Al(OH)_4^-$ tends to bind; thus, better solidification and higher compressive strength are obtained [95]. The main product of alkali-activated high-Mg EFFS/fly ash is N-A-M-S-H, where the magnesium dissolved in EFFS participates in the reaction and is incorporated into the N-A-S-H molecular structure [99, 100]. There are three typical phases identified in water-quenched high Mg EFFS, namely, FNS I, II, and III phases, which are Mg-Si phase, Si-Ca-Al phase, and Gr-Fe phase, respectively [94]. The FNS I phase (Mg-Si phase) is more prone to dissolve and preferentially participate in the reaction process than the other two phases. The dissolved Mg from FNS is mainly involved in the formation of hydrotalcite and N-M-S-H gels. The heavy metals in ferronickel slag mainly include Mn, Cr, and Ni. Wang et al. [83] reported that the alkali-activated matrix has a good stabilization effect on heavy metals, which greatly reduces the risk of heavy metals leaching. Cao et al. [94] found that Cr exists in EFFS in the form of Gr-Fe phase, which remains stable under the activation of alkali. Cr could not be detected during the leaching process. According to Komnitsas et al. [101], alkali-activated EFFS encapsulated the heavy metals such as Pb, Cr, and Ni. Therefore, heavy metals could not leach out from the concrete and maintained the structural integrity. In summary, alkali-activated ferronickel slag is an environmentally friendly material, and there is no problem of heavy metal leaching.

4.3. Properties of Alkali-Activated Ferronickel Slag. Wang et al. [83] found that alkali-activated BFFS showed comparable compressive strength and lower 7-day autogenous shrinkage to the alkali-activated slag. And BFFS activated by Ms = 0.5 waterglass obtained the highest compressive strength (70 MPa) at 90 days. Xu et al. [92] investigated the type and content of solid activators on the compressive strength of alkali-activated BFFS. The results showed that alkali-activated BFFS with Na_2SiO_3/Na_2CO_3 activators have a denser microstructure, lower porosity, and smaller pore size than alkali-activated BFFS with Na_2SiO_3 or NaOH activators. The compressive strength of the $Na_2SiO_3/$ Na_2CO_3 sample can reach 96 MPa when the Na_2O content is 0.107 mol. It had been shown that low-calcium EFFS can also be used to prepare alkali-activated materials with superior properties. According to Maragkos et al. [88], the properties of alkali-activated EFFS depends on the solid to liquid ratio (S/L). The optimum quantities of S/L and NaOH concentrations were 5.6 g/mL and 7 M, respectively. Under optimum conditions, the alkali-activated EFFS exhibited a very high compressive strength of 118 MPa and a very low water absorption of about 0.8%. Komnitsas et al. [89] investigated the performance of sodium-silicate-activated EFFS/kaolin-based materials. They found that only aging period had a very significant effect on the final compressive strength while heating time and the temperature had a negligible effect on strength development. The alkali-activated samples showed excellent resistance to freeze-thaw cycles. However, the strength declined in acidic environment due to the formation of halite, magnesium calcite, calcite, aragonite, and akermanite on the surface of the immersed samples. Sakkas et al. [87] evaluated the effect of fire exposure on the alkali-activated EFFS materials. The results showed that these samples had a low thermal conductivity and high fire resistance like commercial fire-resisting materials. It is even possible to prepare alkali-activated ferronickel slag concrete, which belongs to the category of ultrahigh performance concrete, with a

TABLE 2: Chemical composition of ferronickel slag.

Material	SiO$_2$	Al$_2$O$_3$	FeO	Fe$_2$O$_3$	MgO	CaO	MnO	Gr$_2$O$_3$	NiO	Types of ores source	Ref.
BFFS	29.95	26.31		1.55	8.93	25.19	2.25	2.3	0.01	China	[83]
BFFS	33.15	21.94		2.15	12.54	22.5	3.36	2.08	0.02	China	[84]
BFFS	37.2	21.37		1.72	10.53	24.82				China	[90]
BFFS	36.7	18.11		1.83	11.63	28.77				China	[91]
BFFS	22.26	18.97		2.87	7.81	33.9	2.87			China	[92]
EFFS-W	46.1	4.46		12.25	27.12	6.75	0.79	1.5	0.19	China	[84]
EFFS-W	50.48	3.08		10.37	32.61	1.01	0.62	1.37	0.06	China	[84]
EFFS-W	44.9	4.94		14.36	23.29	8.24	0.98	2.47	0.13	China	[84]
EFFS-W	47.61	6.56		13.24	15.94	11.49		0.7		China	[93]
EFFS-W	45.23	5.91		9.74	24.17	8.93		1.14	0.29	China	[94]
EFFS-W	53.1	2.4		11.3	32.3	0.23				Soci´et´e Le Nickel (SLN), New Caledonia	[23]
EFFS-W	41.14	13.79	34.74		3.59	0.71		5.41	0.14	Laterites LARCO, Greece	[87]
EFFS-W	40.29	10.11	37.69		5.43	3.65		2.58	0.09	Laterites LARCO, Greece	[88]
EFFS-W	32.74	8.32	38.8	0.76	2.76	3.73		3.07	0.1	Laterites LARCO, Greece	[89]
EFFS-W	32.74	8.32		43.83	2.76	3.73		3.07		Laterites LARCO, Greece	[95]
EFFS-W	51.93	2.92		12.98	30.87	0.5				Garnierite ore, New Caledonia	[85]
EFFS-W	52.52	2.33		10.8	33.16	0.27				Garnierite ore, New Caledonia	[96]
EFFS-W	53.29	2.67		11.9	31.6	0.42		1.08	0.1	Garnierite ore, New Caledonia	[86]
EFFS-W	52.27	6.19		4.2	26.93	8.77			0.04	China	[96]
EFFS-W	58.1	2.29		11.1	26.5	0.29				SNNC, South Korea	[97]
EFFS-A	62.8	1.95		7.13	24.7	2.07				SNNC, South Korea	[97]
EFFS-A	51.23	3.66		8.06	31.91	1.52				China	[98]

EFFS-A: air-cooled EFFS slag; EFFS-W: water-cooled EFFS slag.
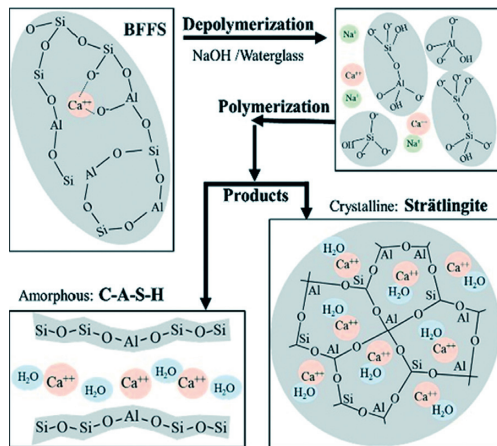
FIGURE 4: Reaction mechanism of alkali-activated blast furnace ferronickel slag [83].

strength of up to 120 MPa. Komnitsas et al. [101] reported that NO_3^- or SO_4^{2-} ions reduced the strength of alkali-activated EFFS due to the fact that they consumed most of the available moles of alkali activators, hindering the polymerization reaction and therefore producing a limited number of gels.

According to the literature, it was found that an EFFS with a high MgO content is not very well utilized due to the low reactivity and high magnesium oxide content, which may lead to bulk stability problems [8]. Cao et al. [102] used EFFS with high MgO content as a partial replacement for blast furnace slag to prepare alkali-activated cements (AACs). The results showed that the incorporation of less than 40% FNS has no significant effect on the setting time; however, the incorporation of 60% FNS will not only

prolong the setting time but also reduce the compressive strength. For Na_2SiO_3-activated AACs, increasing EFFS content in the mixture will lead to the increase of autogenous shrinkage, drying shrinkage, and total porosity. For NaOH-activated AACs, the autogenous shrinkage and drying shrinkage are decreased with the addition of EFFS, while the total porosity is increased. Kuri et al. [103] reported that EFFS replacing part of the fly ash reduced workability and shortened setting time but increased compressive strength, with 75% EFFS being the optimum content. They found that Mg was involved in the formation of N-M-A-S-H and therefore did not cause bulk stability problems, whereas Komnitsas et al. [89, 95] argued that magnesium acted as chemically inert in alkali-activated EFFS materials. It also depends on the source of the FNS. It is closely related to the source of ferronickel slag. Yang et al. [100] further suggested that EFFS can improve the thermal stability of alkali-activated materials by replacing some of the fly ash, and can effectively reduce the shrinkage of alkali-activated materials below 600°C.

5. Alkali-Activated Lead-Zinc Slag

5.1. Characterization of Lead-Zinc Slag. Lead-zinc slag is a by-product of the lead and zinc production industry, generated from the ores during smelting [104, 105]. It is reported that the production of 1t of lead and zinc discharges 7,100 kg and 9,600 kg slag [24], respectively. These lead-zinc slags are generally landfilled, not only occupying large areas of arable land but also polluting the environment due to the leaching of heavy metals and the radiation of nuclides.

The chemical composition of lead-zinc slag changes depending on the ores, the fluxes, the smelting process, and

TABLE 3: Chemical compositions of lead-zinc slag.

Composition	SiO$_2$	FeO$_x$	CaO	Al$_2$O$_3$	ZnO	Cr$_2$O$_3$	PbO	MgO	SO$_3$	MnO	Ref.
1	31.34	32.26	18.34	4.26	8.20	—	2.69	1.72	1.19	—	[104]
2	18.89	39.15	13.92	8.52	13.95	0.19	1.37	2.05	3.77	1.12	[105]
3	30.67	29.73	12.48	7.27	6.39	—	—	3.27	3.06	2.97	[24]
4	34.92	24.98	20.50	5.07	3.63	—	1.12	2.36	1.11	—	[106]
5	24.33	33.70	22.10	2.46	11.11	—	3.63	2.71	0.39	—	[107]
6	43.09	14.99	23.05	6.22	4.01	—	—	1.58	—	—	[108]
7	14.68	41.96	4.50	4.7	2.82	—	10.34	1.43	6.51	—	[109]
8	35.50	46.37	11.53	3.85	6.02	—	4.03	4.65	0.24	—	[109]
9	21.39	28.10	23.11	3.56	9.47	—	4.06	5.44	0.37	—	[110, 111]
10	24.88	31.38	22.14	2.46	10.77	—	3.74	2.71	—	—	[112]
11	21.56	31.57	3.05	1.73	6.18	—	12.28	0.15	8.01	—	[113]
12	18.08	34.28	17.91	8.17	9.21	—	1.22	1.93	1.41	1.33	[114]
13	18.30	26.10	15.60	5.5	14.00	—	3.60	—	—	—	[115]
14	11.30	52.90	3.30	5.5	9.80	—	1.40	—	—	—	[115]
15	32.50	16.25	27.50	9.25	5.00	1.30	—	2.13	—	—	[116]
16	27.1	35.30	17.95	7.65	1.30	—	0.03	4.70	—	—	[117]
17	21.90	33.70	18.10	10.4	6.92	—	0.69	—	1.58	—	[118]
18	23.00	33.40	20.00	1.89	11.20	—	3.50	—	0.7	—	[118]
19	27.50	33.80	19.40	7.4	—	—	—	2.10	—	—	[119]
20	21.40	28.10	23.10	3.6	—	—	—	5.44	—	—	[119]
21	25.70	33.95	18.90	5.41	5.01	—	2.47	1.41	—	0.656	[120]
22	29.79	54.19	3.87	0.01	5.82	0.03	0.11	2.91	0.02	3.22	[121]
23	29.66	55.57	2.77	0.02	4.34	0.01	—	2.28	0.02	4.42	[121]
24	30.03	51.13	8.08	0.74	6.28	0.01	0.11	0.85	—	2.13	[121]
25	32.89	27.67	27.48	0.49	2.32	—	0.02	5.33	0.11	3.61	[121]
26	31.15	41.23	15.38	0.26	1.98	—	0.06	3.68	0.07	5.91	[121]
27	30.52	47.52	14.49	0.06	3.80	—	0.18	1.68	8.00	1.48	[121]
28	41.87	26.14	21.71	6.12	2.71	—	—	0.65	—	0.92	[121]
29	39.87	22.67	21.49	10.19	2.82	—	—	0.19	—	0.62	[121]
30	40.07	18.91	22.62	11.2	1.23	—	—	2.41	—	1.40	[121]
31	43.30	23.50	20.59	4.73	3.12	0.43	—	1.50	—	1.80	[121]
32	43.34	20.68	22.29	8.06	1.65	0.23	—	2.06	—	1.39	[121]
33	30.76	30.09	11.80	7.28	—	—	—	3.32	2.41	—	[122]
34	17.01	34.33	13.14	6.84	12.20	0.13	0.82	0.85	2.5	1.12	[123]

the impurities in the coke and the iron. The chemical compositions of lead-zinc slag from different research papers [24, 104–123] are summarized in Table 3. It could be found in Table 3 that the major composition of lead-zinc slag is FeO$_x$, SiO$_2$, CaO, Al$_2$O$_3$, and ZnO. As shown in Figure 5, the major constituents of the lead-zinc slag, in decreasing order of wt%, were the following: FeO$_x$ (34%, ranging from 27% to 37%), SiO$_2$ (28%, ranging from 21% to 33%), CaO (17%, ranging from 14% to 23%), ZnO (8%, ranging from 3% to 10%), and Al$_2$O$_3$ (5%, ranging from 2% to 8%). Figure 5 also shows that the contents of the major compositions of lead-zinc slag are significantly different from various areas and the smelting factory. Some heavy and toxic elements, such as Pb, Zn, Cd, Cr, Mn, Cu, etc., could be found in lead-zinc slag, which limits its utilization due to the large leaching risk. The density of lead-zinc slag ranges from 3.6 g/cm^3 to 3.9 g/cm^3 [105, 118, 124], which is larger than that of traditional aluminosilicate waste due to high iron oxide content.

The phase composition of lead-zinc slag greatly changes depending on the ores, the fluxes, the smelting process, and the cooling method. The lead-zinc slag was reported to be mostly composed of an iron-silica-lime glass matrix and the content of the glass phase in lead-zinc slag is generally larger
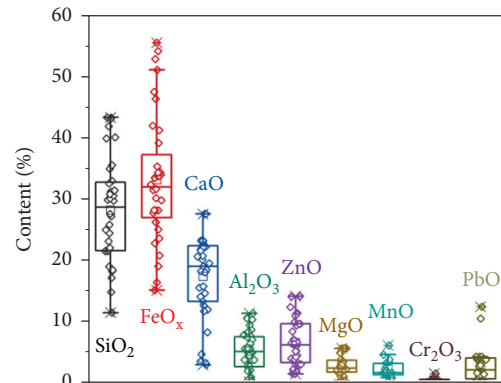
FIGURE 5: Major compositions of lead-zinc slag (data from Table 1).

than 80% [24, 115, 117]. The kinds of the crystal phases in lead-zinc slag are also dependent on the ores and fluxes. Figure 6 provides an example of the XRD pattern of lead-zinc slag, which proves that most components are amorphous. As shown in Figure 6, the crystal phases in lead-zinc slag are ZnS, FeS, FeO, Fe$_3$O$_4$, and Pb metal, which is consistent with the results reported by Weeks [105]. Xia et al.
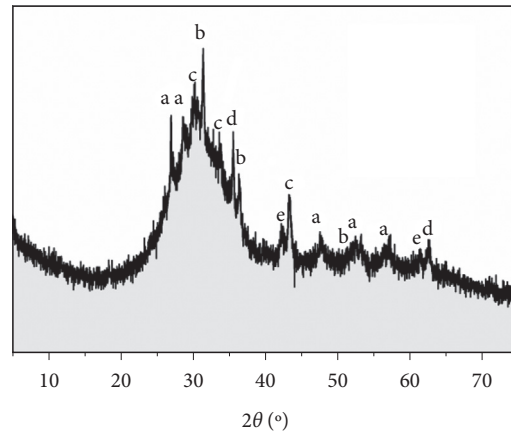
a: ZnS
b: Pb
c: FeS
d: Fe$_3$O$_4$
e: FeO

Figure 6: XRD pattern of lead-zinc slag.
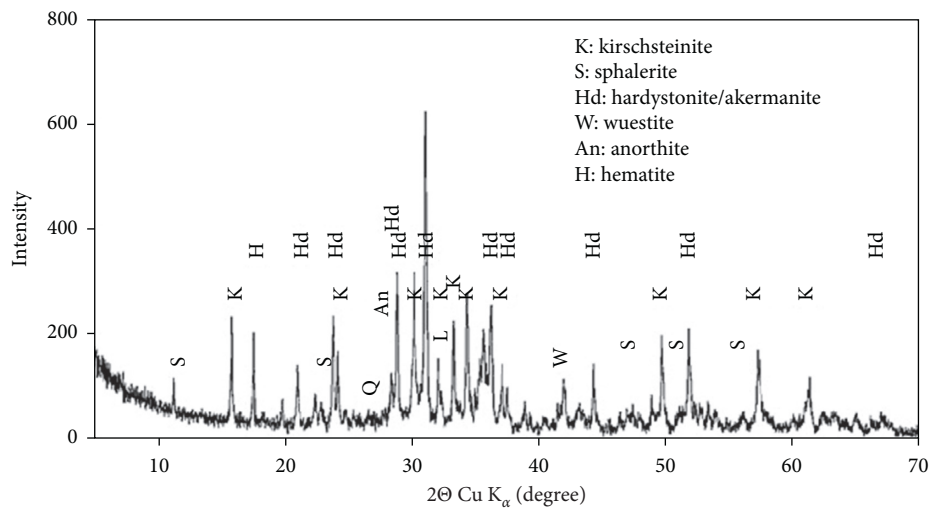
(a)
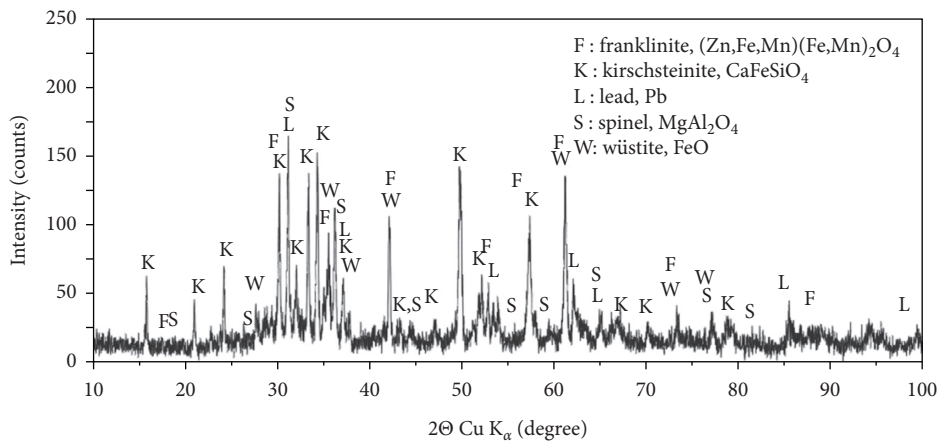
(b)

Figure 7: XRD of lead-zinc slag with high percentage of crystal phases. (a) Lead-zinc slag from Belgium [120]. (b) Lead-zinc slag from Brazil [110].
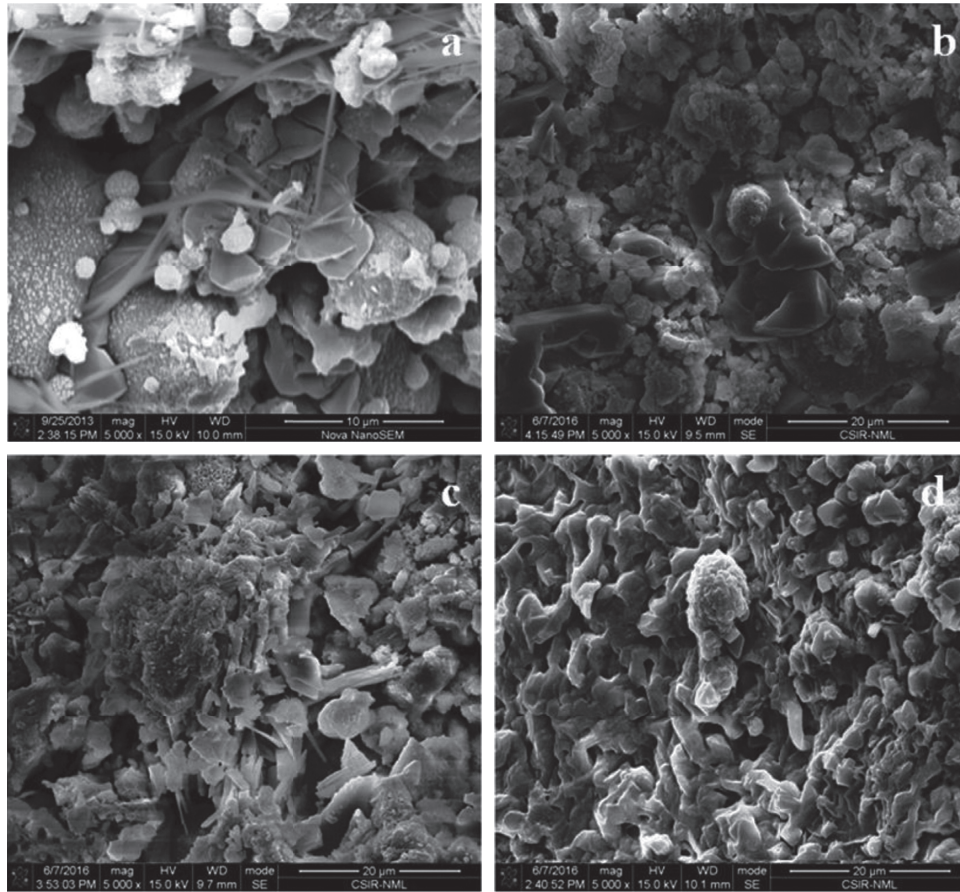
FIGURE 8: Morphology of fly ash-zinc composite geopolymer. (a) 100% fly ash. (b) 60% fly ash and 40% zinc slag. (c) 20% fly ash and 80% zinc slag. (d) 100% zinc slag. Data from [117].

[122] reported that the small amount of crystal phases is ringwoodite and Fe metal. Spinel [24, 104, 107, 110, 112, 125, 126], calcium iron silicate [117], magnesioferrite [117], fayalite [125], Olivine [104, 110], kirschsteinite [125], hedenbergite [104, 125], willemite [110, 112], melilite [1, 8, 10, 22], and franklinite [126] were also found in lead-zinc slag from various areas. Due to the difference in smelting processes, two kinds of lead-zinc slag were reported to be composed mainly of crystal phases and their XRD patterns are provided in Figure 7.

5.2. Reaction Mechanism of the Alkali-Activated Lead-Zinc Slag. Similar to the blast furnace slag [127], fly ash [128], and rice husk ash [129], most of the lead-zinc slag is composed by amorphous aluminosilicate phases. So the reaction process of alkali-activated lead-zinc slag is similar to the traditional alkali-activated materials: dissolution and dispersion of raw materials, rearrangement and exchange of dissolved species, gelation and solidification, and continuous gel evolution toward crystallization [130, 131].

The leaching risk of the heavy metals in lead-zinc slag is the key factor that limits its application as construction materials. Alkali-activated material is an effective system for the solidification of heavy metals. But, high Si content and low Al content in lead-zinc slag make it difficult to form a

rigid Al-Si network structure [117]. The lack of AlO_4- unit tend to decrease the capacity of alkali-activated materials for element immobilization since the heavy metals mainly bonded with alumina tetrahedron [132]. So, some studies were conducted by mixing the lead-zinc slag with fly ash and alkalis to form a geopolymer [113, 117, 119]. The morphology of the fly ash-zinc slag composite geopolymer was reported by Nath [117]. It was found that the reaction products were refined with the increasing of the zinc slag content (see Figure 8). Zhang [24] has also studied the self-cementation of lead-zinc slag through alkali-activated materials and found that the solidification efficiency was larger than 90% for most of the heavy metals. The physical encapsulation was found to be the main mechanism of the solidification of the heavy metals in alkali-activated materials.

5.3. Properties of the Alkali-Activated Lead-Zinc Slag Material. The performance of the alkali-activated materials containing lead-zinc slag is also dependent on the properties of the raw materials. Xia et al. [122] found that the compressive strength of hardened alkali-activated materials decreases with the increasing of the lead-zinc slag content. It means that lead-zinc slag has a negative effect on the performance of the alkali-activated materials. It was supposed that the

high iron content in lead-zinc slag tend to be oxidized and the oxidation might increase the porosity and volume of solidified body, which ultimately resulted in decrease of compressive strength. But, Nath [117] found that the relatively high CaO content in lead-zinc slag results in the formation of Ca-rich dense gel and the development of compact microstructure. The 28-day compressive strength of alkali-activated zinc slag even reached 71 MPa. And the highest compressive strength even reaches 96 MPa. It means that the dispersion of the chemical composition of raw materials significantly affects the mechanical performance of the alkali-activated lead-zinc slag.

6. Conclusion and Outlook

The main mineral phases in steel slag are tricalcium silicate, dicalcium silicate, RO phase, tetracalcium aluminoferrite, etc. The phase composition of steel slag is similar to that of cement and thus steel slag has the potential cementitious property. But, the low activity of steel slag is the biggest obstacle and challenge to the proper utilization of alkali-activated steel slag materials. Moreover, there is great uncertainty about the hydration mechanism of the steel slag as a solo precursor.

Copper slag is mainly composed of crystal phases, i.e., magnetite (Fe_3O_4) and fayalite (Fe_2SiO_4). The utilization of copper slag as an alkali-activated material depends on the cooling process of the copper slag. Granulated water-cooled copper slag with a relatively higher amorphous phase is more suitable for alkali activation. In terms of activator, sodium hydroxide is less effective than water glass due to the formation of the high crystalized product. Although many studies have evaluated the mechanical properties of alkali-activated copper slag, heavy metal leaching assessment should be considered in the future study as copper usually contains heavy metals.

BFFS has good reactivity due to the large amount of amorphous phase; therefore, alkali-activated BFFS has superior mechanical properties. The reaction products are strätlingite and C-A-S-H. The reactivity of EFFS is closely related to its source and treatment process. EFFS generated from laterite ore contains a low MgO, whereas that from garnierite ore contains a high MgO. The amorphous phase content of EFFS with low Mg content is high, while the amorphous phase content of EFFS with high Mg content is low, and there are a large number of Mg-containing crystals for the main mineral phases in EFFS, namely, forsterite (Mg_2SiO_4), enstatite ($MgSiO_3$, and clinoenstatite ($MgSiO_3$). Good properties can be obtained in fly ash-based alkali-activated materials by incorporating EFFS, and the generation of the amorphous phase N-M-A-S-H leads to a denser microstructure. There is no negative impact on the environment due to the utilization of ferronickel slag in the alkali-activated materials.

The chemical composition of lead-zinc slag significantly changes depending on the ores, the fluxes, the smelting process, and the impurities in the coke and the iron. Thus, the phase composition and the reaction activity of lead-zinc slag and the mechanical performance of alkali-activated lead-zinc slag reported in different papers are quite inconsistent. Generally, the lead-zinc slag is composed of iron-silica-lime amorphous phases. In order to improve the mechanical property and the solidification efficiency for heavy metals, lead-zinc slag is usually mixed with fly ash or granulated blast furnace slag to form a geopolymer.

There are few studies to fully understand the properties of alkali-activated metallurgical slag composite system, and in-depth research on durability is still a new topic. Better activated methods and alkali-activators are still needed to improve the performance of the metallurgical slag with low reactivity. It is expected that the acid-activated method may be an alternative method due to the high contents of iron, calcium, and magnesium in metallurgical slag. The chemical composition of the metallurgical slag is closely dependent on the ores, the fluxes, and the smelting process. Thus, the relationship between the chemical composition and the reactivity of metallurgical slags needs to be constructed. If these problems are solved, they will bring great environmental benefits to slag yards and enormous economic benefits to steel industries.

Data Availability

Previously reported data were used to support this study. These prior studies are cited at relevant places within the text as references.

Conflicts of Interest

The authors declare that they have no conflicts of interest.

Acknowledgments

References

[1] J. L. Provis, "Alkali-activated materials," *Cement and Concrete Research*, vol. 114, pp. 40–48, 2018.

[2] J. Ye, W. Zhang, and D. Shi, "Performance evolutions of tailing-slag-based geopolymer under severe conditions," *Journal of Sustainable Cement-Based Materials*, vol. 4, no. 2, pp. 101–115, 2015.

[3] R. Siddique, "Design and development of self-compacting concrete made with coal bottom ash," *Journal of Sustainable Cement-Based Materials*, vol. 4, no. 3-4, pp. 225–237, 2015.

[4] S. K. Das, J. Mishra, S. M. Mustakim, A. Adesina, C. R. Kaze, and D. Das, "Sustainable utilization of ultrafine rice husk ash in alkali activated concrete: characterization and performance evaluation," *Journal of Sustainable Cement-Based Materials*, pp. 1–19, 2021.

[5] J. L. Provis, "Geopolymers and other alkali activated materials: why, how, and what?," *Materials and Structures*, vol. 47, no. 1-2, pp. 11–25, 2014.

[6] R. M. Andrew, "Global Co_2 emissions from Cement Production (1928–2017)," *Earth System Science Data*, vol. 10, pp. 2213–2239, 2018.

[7] E. Gartner and H. Hirao, "A review of alternative approaches to the reduction of CO_2 emissions associated with the

manufacture of the binder phase in concrete," *Cement and Concrete Research*, vol. 78, pp. 126–142, 2015.

[8] T. A. Aiken, W. Sha, J. Kwasny, and M. N. Soutsos, "Resistance of geopolymer and Portland cement based systems to silage effluent attack," *Cement and Concrete Research*, vol. 92, pp. 56–65, 2017.

[9] M. Albitar, M. S. Mohamed Ali, P. Visintin, and M. Drechsler, "Durability evaluation of geopolymer and conventional concretes," *Construction and Building Materials*, vol. 136, pp. 374–385, 2017.

[10] A. M. M. A. Bakri, H. Kamarudin, M. Binhussain, I. K. Nizar, A. R. Rafiza, and Y. Zarina, "Comparison of geopolymer fly ash and ordinary portland cement to the strength of concrete," *Advanced Science Letters*, vol. 19, no. 12, pp. 3592–3595, 2013.

[11] P. K. Sarker and S. McBeath, "Fire endurance of steel reinforced fly ash geopolymer concrete elements," *Construction and Building Materials*, vol. 90, pp. 91–98, 2015.

[12] P. Duxson, J. L. Provis, G. C. Lukey, F. Separovic, and J. S. J. Van Deventer, "29Si NMR study of structural ordering in aluminosilicate geopolymer gels," *Langmuir*, vol. 21, no. 7, pp. 3028–3036, 2005.

[13] N. R. Rakhimova and R. Z. Rakhimov, "A review on alkali-activated slag cements incorporated with supplementary materials," *Journal of Sustainable Cement-Based Materials*, vol. 3, no. 1, pp. 61–74, 2014.

[14] I. G. Richardson, A. R. Brough, G. W. Groves, and C. M. Dobson, "The characterization of hardened alkali-activated blast-furnace slag pastes and the nature of the calcium silicate hydrate (C-S-H) phase," *Cement and Concrete Research*, vol. 24, no. 5, pp. 813–829, 1994.

[15] M. Ben Haha, G. Le Saout, F. Winnefeld, and B. Lothenbach, "Influence of activator type on hydration kinetics, hydrate assemblage and microstructural development of alkali activated blast-furnace slags," *Cement and Concrete Research*, vol. 41, no. 3, pp. 301–310, 2011.

[16] İ. Yüksel, "A review of steel slag usage in construction industry for sustainable development," *Environment, Development and Sustainability*, vol. 19, no. 2, pp. 369–384, 2017.

[17] S. Zhuang and Q. Wang, "Inhibition mechanisms of steel slag on the early-age hydration of cement," *Cement and Concrete Research*, vol. 140, Article ID 106283, 2021.

[18] J. Łabaj, L. Blacha, M. Jodkowski, A. Smalcerz, M. Fröhlichová, and R. Findorak, "The use of waste, fine-grained carbonaceous material in the process of copper slag reduction," *Journal of Cleaner Production*, vol. 288, 2021.

[19] Z. Zulhan and N. Agustina, "A novel utilization of ferro-nickel slag as a source of magnesium metal and ferroalloy production," *Journal of Cleaner Production*, vol. 292, Article ID 125307, 2021.

[20] J. Sun, Z. Wang, and Z. Chen, "Hydration mechanism of composite binders containing blast furnace ferronickel slag at different curing temperatures," *Journal of Thermal Analysis and Calorimetry*, vol. 131, no. 3, pp. 2291–2301, 2018.

[21] J. Sun, J. Feng, and Z. Chen, "Effect of ferronickel slag as fine aggregate on properties of concrete," *Construction and Building Materials*, vol. 206, pp. 201–209, 2019.

[22] A. K. Saha, M. N. N. Khan, and P. K. Sarker, "Value added utilization of by-product electric furnace ferronickel slag as construction materials: a review," *Resources, Conservation and Recycling*, vol. 134, pp. 10–24, 2018.

[23] Q. D. Nguyen, A. Castel, T. Kim, and M. S. H. Khan, "Performance of fly ash concrete with ferronickel slag fine aggregate against alkali-silica reaction and chloride diffusion," *Cement and Concrete Research*, vol. 139, Article ID 106265, 2021.

[24] P. Zhang, F. Muhammad, L. Yu et al., "Self-cementation solidification of heavy metals in lead-zinc smelting slag through alkali-activated materials," *Construction and Building Materials*, vol. 249, Article ID 118756, 2020.

[25] M. Alwaeli, "Investigation of gamma radiation shielding and compressive strength properties of concrete containing scale and granulated lead-zinc slag wastes," *Journal of Cleaner Production*, vol. 166, pp. 157–162, 2017.

[26] Y. Jiang, T.-C. Ling, C. Shi, and S.-Y. Pan, "Characteristics of steel slags and their use in cement and concrete-A review," *Resources, Conservation and Recycling*, vol. 136, pp. 187–197, 2018.

[27] X. Wang, X. Li, X. Yan, C. Tu, and Z. Yu, "Environmental risks for application of iron and steel slags in soils in China: a review," *Pedosphere*, vol. 31, no. 1, pp. 28–42, 2021.

[28] S. N. Chinnu, S. N. Minnu, A. Bahurudeen, and R. Senthilkumar, "Recycling of industrial and agricultural wastes as alternative coarse aggregates: a step towards cleaner production of concrete," *Construction and Building Materials*, vol. 287, Article ID 123056, 2021.

[29] Q. Dong, G. Wang, X. Chen, J. Tan, and X. Gu, "Recycling of steel slag aggregate in portland cement concrete: an overview," *Journal of Cleaner Production*, vol. 282, Article ID 124447, 2021.

[30] D. Q. Deng, L. Liu, Z. L. Yao, K. I.-I. L. Song, and D. Z. Lao, "A practice of ultra-fine tailings disposal as filling material in a gold mine," *Journal of Environmental Management*, vol. 196, pp. 100–109, 2017.

[31] B. Li, Y. Wang, L. Yang, and Y. Zhang, "Sulfate resistance and hydration products of steam cured steel slag blended cement mortar under dry-wet cycle," *Journal of Sustainable Cement-Based Materials*, vol. 8, no. 6, pp. 353–366, 2019.

[32] C. A. C. Balaguera and M. A. G. Botero, "Multiphase phosphate cements from steel slags," *Journal of Sustainable Cement-Based Materials*, pp. 1–20, 2020.

[33] M. Salman, Ö. Cizer, Y. Pontikes et al., "Cementitious binders from activated stainless steel refining slag and the effect of alkali solutions," *Journal of Hazardous Materials*, vol. 286, pp. 211–219, 2015.

[34] C. Shi and S. Hu, "Cementitious properties of ladle slag fines under autoclave curing conditions," *Cement and Concrete Research*, vol. 33, no. 11, pp. 1851–1856, 2003.

[35] C. Thomas, J. Rosales, J. A. Polanco, and F. Agrela, *Steel Slags*, pp. 169–190, Elsevier Ltd, Amsterdam, Netherlands, 2019.

[36] M. Češnovar, K. Traven, B. Horvat, and V. Ducman, "The potential of ladle slag and electric arc furnace slag use in Synthesizing alkali activated materials; the influence of curing on mechanical properties," *Materials (Basel)*, vol. 12, 2019.

[37] V. A. Nunes and P. H. R. Borges, "Recent advances in the reuse of steel slags and future perspectives as binder and aggregate for alkali-activated materials," *Construction and Building Materials*, vol. 281, Article ID 122605, 2021.

[38] A. M. Kaja, K. Schollbach, S. Melzer, S. R. van der Laan, H. J. H. Brouwers, and Q. Yu, "Hydration of potassium citrate-activated BOF slag," *Cement and Concrete Research*, vol. 140, Article ID 106291, 2021.

[39] T. He, Z. Li, S. Zhao, Z. Zhao, and X. Zhao, "Effect of reductive component-conditioning materials on the composition, structure, and properties of reconstructed BOF slag," *Construction and Building Materials*, vol. 255, Article ID 119269, 2020.

[40] G. C. Wang, "Slag use as an aggregate in concrete and cement-based materials," in *The Utilization of Slag in Civil Infrastructure Construction*, pp. 239–274, Elsevier Ltd, Amsterdam, Netherlands, 2016.

[41] J. Feng and J. Sun, "A comparison of the 10-year properties of converter steel slag activated by high temperature and an alkaline activator," *Construction and Building Materials*, vol. 234, Article ID 116948, 2020.

[42] P. S. Humbert and J. Castro-Gomes, "CO_2 activated steel slag-based materials: a review," *Journal of Cleaner Production*, vol. 208, pp. 448–457, 2019.

[43] Q. Wang, D. Wang, and S. Zhuang, "The soundness of steel slag with different free CaO and MgO contents," *Construction and Building Materials*, vol. 151, pp. 138–146, 2017.

[44] Q. Wang, J. Yang, and P. Yan, "Influence of initial alkalinity on the hydration of steel slag," *Science China Technological Sciences*, vol. 55, no. 12, pp. 3378–3387, 2012.

[45] C. Shi, "Characteristics and cementitious properties of ladle slag fines from steel production," *Cement and Concrete Research*, vol. 32, no. 3, pp. 459–462, 2002.

[46] W. Ni, E. Wang, J. Li, and H. Sun, "Cementing properties of steel slag activated by sodium silicates and sodium hydroxide," *Journal of University of Science and Technology Beijing Mineral Metallurgy Material*, vol. 12, pp. 464–468, 2005.

[47] J. Sun, Z. Zhang, S. Zhuang, and W. He, "Hydration properties and microstructure characteristics of alkali-activated steel slag," *Construction and Building Materials*, vol. 241, Article ID 118141, 2020.

[48] J. Sun and Z. Chen, "Effect of silicate modulus of water glass on the hydration of alkali-activated converter steel slag," *Journal of Thermal Analysis and Calorimetry*, vol. 138, no. 1, pp. 47–56, 2019.

[49] Z. Liu, D.-W. Zhang, L. LI, J.-X. Wang, N.-N. Shao, and D.-M. Wang, "Microstructure and phase evolution of alkali-activated steel slag during early age," *Construction and Building Materials*, vol. 204, pp. 158–165, 2019.

[50] L. Kang, Y. J. Zhang, L. Zhang, and K. Zhang, "Preparation, characterization and photocatalytic activity of novel CeO2 loaded porous alkali-activated steel slag-based binding material," *International Journal of Hydrogen Energy*, vol. 42, no. 27, pp. 17341–17349, 2017.

[51] Y. Zhou, J. Sun, and Y. Liao, "Influence of ground granulated blast furnace slag on the early hydration and microstructure of alkali-activated converter steel slag binder," in *Journal of Thermal Analysis and Calorimetry*Springer, Berlin, Germany, 2020.

[52] N. You, B. Li, R. Cao, J. Shi, C. Chen, and Y. Zhang, "The influence of steel slag and ferronickel slag on the properties of alkali-activated slag mortar," *Construction and Building Materials*, vol. 227, Article ID 116614, 2019.

[53] N. You, J. Shi, and Y. Zhang, "Corrosion behaviour of low-carbon steel reinforcement in alkali-activated slag-steel slag and Portland cement-based mortars under simulated marine environment," *Corrosion Science*, vol. 175, Article ID 108874, 2020.

[54] W. Song, Z. Zhu, Y. Peng et al., "Effect of steel slag on fresh, hardened and microstructural properties of high-calcium fly ash based geopolymers at standard curing condition," *Construction and Building Materials*, vol. 229, Article ID 116933, 2019.

[55] X. Guo and J. Yang, "Intrinsic properties and micro-crack characteristics of ultra-high toughness fly ash/steel slag based geopolymer," *Construction and Building Materials*, vol. 230, Article ID 116965, 2020.

[56] I. Niklioć, S. Marković, I. Janković-Častvan et al., "Modification of mechanical and thermal properties of fly ash-based geopolymer by the incorporation of steel slag," *Materials Letters*, vol. 176, pp. 301–305, 2016.

[57] X. Guo and G. Xiong, "Resistance of fiber-reinforced fly ash-steel slag based geopolymer mortar to sulfate attack and drying-wetting cycles," *Construction and Building Materials*, vol. 269, Article ID 121326, 2021.

[58] X. Guo and X. Pan, "Mechanical properties and mechanisms of fiber reinforced fly ash-steel slag based geopolymer mortar," *Construction and Building Materials*, vol. 179, pp. 633–641, 2018.

[59] T. Bai, Z.-G. Song, Y.-G. Wu, X.-D. Hu, and H. Bai, "Influence of steel slag on the mechanical properties and curing time of metakaolin geopolymer," *Ceramics International*, vol. 44, no. 13, pp. 15706–15713, 2018.

[60] E. Furlani, S. Maschio, M. Magnan et al., "Synthesis and characterization of geopolymers containing blends of unprocessed steel slag and metakaolin: the role of slag particle size," *Ceramics International*, vol. 44, no. 5, pp. 5226–5232, 2018.

[61] W. Song, Z. Zhu, S. Pu et al., "Efficient use of steel slag in alkali-activated fly ash-steel slag-ground granulated blast furnace slag ternary blends," *Construction and Building Materials*, vol. 259, Article ID 119814, 2020.

[62] M. O. Yusuf, M. A. Megat Johari, Z. A. Ahmad, and M. Maslehuddin, "Shrinkage and strength of alkaline activated ground steel slag/ultrafine palm oil fuel ash pastes and mortars," *Materials & Design*, vol. 63, pp. 710–718, 2014.

[63] B. Gorai and R. K. Jana, "Characteristics and utilisation of copper slag-a review," *Resources, Conservation and Recycling*, vol. 39, no. 4, pp. 299–313, 2003.

[64] R. K. Dhir, J. de Brito, R. Mangabhai, and C. Q. Lye, *Sustainable Construction Materials: Copper Slag*, Woodhead Publishing, Cambridge, UK, 2017.

[65] İ. Alp, H. Deveci, and H. Süngün, "Utilization of flotation wastes of copper slag as raw material in cement production," *Journal of Hazardous Materials*, vol. 159, no. 2-3, pp. 390–395, 2008.

[66] A. Nazer, J. Payá, M. V. Borrachero, and J. Monzó, "Use of ancient copper slags in Portland cement and alkali activated cement matrices," *Journal of Environmental Management*, vol. 167, pp. 115–123, 2016.

[67] D. Wang, Q. Wang, and Z. Huang, "Reuse of copper slag as a supplementary cementitious material: reactivity and safety," *Resources, Conservation and Recycling*, vol. 162, Article ID 105037, 2020.

[68] B. Traynor, C. Mulcahy, H. Uvegi, T. Aytas, N. Chanut, and E. A. Olivetti, "Dissolution of olivines from steel and copper slags in basic solution," *Cement and Concrete Research*, vol. 133, Article ID 106065, 2020.

[69] Y. Feng, Q. Yang, Q. Chen et al., "Characterization and evaluation of the pozzolanic activity of granulated copper slag modified with CaO," *Journal of Cleaner Production*, vol. 232, pp. 1112–1120, 2019.

[70] W. Lan, A. Wu, and P. Yu, "Development of a new controlled low strength filling material from the activation of copper slag: influencing factors and mechanism analysis," *Journal of Cleaner Production*, vol. 246, Article ID 119060, 2020.

[71] P. R. Prem, M. Verma, and P. S. Ambily, "Sustainable cleaner production of concrete with high volume copper slag," *Journal of Cleaner Production*, vol. 193, pp. 43–58, 2018.

[72] R. Sharma and R. A. Khan, "Influence of copper slag and metakaolin on the durability of self compacting concrete," *Journal of Cleaner Production*, vol. 171, pp. 1171–1186, 2018.

[73] J. Liu and R. Guo, "Hydration properties of alkali-activated quick cooled copper slag and slow cooled copper slag," *Journal of Thermal Analysis and Calorimetry*, vol. 139, no. 6, pp. 3383–3394, 2020.

[74] C. Shi, C. Meyer, and A. Behnood, "Utilization of copper slag in cement and concrete," *Resources, Conservation and Recycling*, vol. 52, no. 10, pp. 1115–1120, 2008.

[75] W. Wu, W. Zhang, and G. Ma, "Mechanical properties of copper slag reinforced concrete under dynamic compression," *Construction and Building Materials*, vol. 24, no. 6, pp. 910–917, 2010.

[76] B. M. Mithun and M. C. Narasimhan, "Performance of alkali activated slag concrete mixes incorporating copper slag as fine aggregate," *Journal of Cleaner Production*, vol. 112, pp. 837–844, 2016.

[77] W. A. Moura, J. P. Gonçalves, and M. B. L. Lima, "Copper slag waste as a supplementary cementing material to concrete," *Journal of Materials Science*, vol. 42, no. 7, pp. 2226–2230, 2007.

[78] K. S. Al-Jabri, R. A. Taha, A. Al-Hashmi, and A. S. Al-Harthy, "Effect of copper slag and cement by-pass dust addition on mechanical properties of concrete," *Construction and Building Materials*, vol. 20, no. 5, pp. 322–331, 2006.

[79] J. Singh and S. Singh, "Development of alkali-activated cementitious material using copper slag," *Construction and Building Materials*, vol. 211, pp. 73–79, 2019.

[80] J. Singh and S. P. Singh, "Synthesis of alkali-activated binder at ambient temperature using copper slag as precursor," *Materials Letters*, vol. 262, Article ID 127169, 2020.

[81] J. Singh and S. P. Singh, "Evaluating the alkali-silica reaction in alkali-activated copper slag mortars," *Construction and Building Materials*, vol. 253, Article ID 119189, 2020.

[82] Z. Yan, Z. Sun, J. Yang, H. Yang, Y. Ji, and K. Hu, "Mechanical performance and reaction mechanism of copper slag activated with sodium silicate or sodium hydroxide," *Construction and Building Materials*, vol. 266, Article ID 120900, 2021.

[83] D. Wang, Q. Wang, S. Zhuang, and J. Yang, "Evaluation of alkali-activated blast furnace ferronickel slag as a cementitious material: reaction mechanism, engineering properties and leaching behaviors," *Construction and Building Materials*, vol. 188, pp. 860–873, 2018.

[84] Y. Huang, Q. Wang, and M. Shi, "Characteristics and reactivity of ferronickel slag powder," *Construction and Building Materials*, vol. 156, pp. 773–789, 2017.

[85] M. Nuruzzaman, J. O. Camargo Casimiro, and P. K. Sarker, "Fresh and hardened properties of high strength self-compacting concrete using by-product ferronickel slag fine aggregate," *Journal of Building Engineering*, vol. 32, Article ID 101686, 2020.

[86] A. K. Saha and P. K. Sarker, "Sustainable use of ferronickel slag fine aggregate and fly ash in structural concrete: mechanical properties and leaching study," *Journal of Cleaner Production*, vol. 162, pp. 438–448, 2017.

[87] K. Sakkas, P. Nomikos, A. Sofianos, and D. Panias, "Utilisation of FeNi-Slag for the production of inorganic polymeric materials for construction or for passive fire protection," *Waste and Biomass Valorization*, vol. 5, no. 3, pp. 403–410, 2014.

[88] I. Maragkos, I. P. Giannopoulou, and D. Panias, "Synthesis of ferronickel slag-based geopolymers," *Minerals Engineering*, vol. 22, no. 2, pp. 196–203, 2009.

[89] K. Komnitsas, D. Zaharaki, and V. Perdikatsis, "Geopolymerisation of low calcium ferronickel slags," *Journal of Materials Science*, vol. 42, no. 9, pp. 3073–3082, 2007.

[90] A. Qi, X. Liu, Z. Wang, and Z. Chen, "Mechanical properties of the concrete containing ferronickel slag and blast furnace slag powder," *Construction and Building Materials*, vol. 231, Article ID 117120, 2020.

[91] Q. Liu, S. Chen, W. Lin, A. Qi, and Z. Chen, "Experimental behaviors of prefabricated members made of ferronickel slag concrete," *Construction and Building Materials*, vol. 261, Article ID 120519, 2020.

[92] L. Xu, X. Wang, C. Guan, W. Wu, and L. Zhang, "The effect of activators on the mechanical properties and microstructure of alkali-activated nickel slag," *Advances in Civil Engineering*, vol. 2020, Article ID 1764108, 17 pages, 2020.

[93] B. Li, B. Huo, R. Cao, S. Wang, and Y. Zhang, "Sulfate resistance of steam cured ferronickel slag blended cement mortar," *Cement and Concrete Composites*, vol. 96, pp. 204–211, 2019.

[94] R. Cao, Z. Jia, Z. Zhang, Y. Zhang, and N. Banthia, "Leaching kinetics and reactivity evaluation of ferronickel slag in alkaline conditions," *Cement and Concrete Research*, vol. 137, Article ID 106202, 2020.

[95] K. Komnitsas, D. Zaharaki, and V. Perdikatsis, "Effect of synthesis parameters on the compressive strength of low-calcium ferronickel slag inorganic polymers," *Journal of Hazardous Materials*, vol. 161, no. 2-3, pp. 760–768, 2009.

[96] T. Yang, X. Yao, and Z. Zhang, "Geopolymer prepared with high-magnesium nickel slag: characterization of properties and microstructure," *Construction and Building Materials*, vol. 59, pp. 188–194, 2014.

[97] Y. C. Choi and S. Choi, "Alkali-silica reactivity of cementitious materials using ferro-nickel slag fine aggregates produced in different cooling conditions," *Construction and Building Materials*, vol. 99, pp. 279–287, 2015.

[98] M. Zhai, H. Zhu, G. Liang et al., "Enhancing the recyclability of air-cooled high-magnesium ferronickel slag in cement-based materials: a study of assessing soundness through modifying method," *Construction and Building Materials*, vol. 261, Article ID 120523, 2020.

[99] J. C. Kuri, M. N. N. Khan, and P. K. Sarker, "Workability, strength and microstructural properties of ground ferronickel slag blended fly ash geopolymer mortar," *Journal of Sustainable Cement-Based Materials*, pp. 1–18, 2020.

[100] T. Yang, Q. Wu, H. Zhu, and Z. Zhang, "Geopolymer with improved thermal stability by incorporating high-magnesium nickel slag," *Construction and Building Materials*, vol. 155, pp. 475–484, 2017.

[101] K. Komnitsas, D. Zaharaki, and G. Bartzas, "Effect of sulphate and nitrate anions on heavy metal immobilisation in ferronickel slag geopolymers," *Applied Clay Science*, vol. 73, pp. 103–109, 2013.

[102] R. Cao, B. Li, N. You, Y. Zhang, and Z. Zhang, "Properties of alkali-activated ground granulated blast furnace slag blended with ferronickel slag," *Construction and Building Materials*, vol. 192, pp. 123–132, 2018.

[103] J. C. Kuri, M. N. N. Khan, and P. K. Sarker, "Fresh and hardened properties of geopolymer binder using ground high magnesium ferronickel slag with fly ash," *Construction and Building Materials*, vol. 272, Article ID 121877, 2021.

[104] V. Ettler and Z. Johan, "12years of leaching of contaminants from Pb smelter slags: geochemical/mineralogical controls and slag recycling potential," *Applied Geochemistry*, vol. 40, pp. 97–103, 2014.

[105] C. Weeks, R. J. Hand, and J. H. Sharp, "Retardation of cement hydration caused by heavy metals present in ISF slag used as aggregate," *Cement and Concrete Composites*, vol. 30, no. 10, pp. 970–978, 2008.

[106] V. Ettler, M. Komárková, J. Jehlička et al., "Leaching of lead metallurgical slag in citric solutions-implications for disposal and weathering in soil environments," *Chemosphere*, vol. 57, no. 7, pp. 567–577, 2004.

[107] N. Seignez, A. Gauthier, D. Bulteel et al., "Effect of Pb-rich and Fe-rich entities during alteration of a partially vitrified metallurgical waste," *Journal of Hazardous Materials*, vol. 149, no. 2, pp. 418–431, 2007.

[108] N. Seignez, A. Gauthier, D. Bulteel, D. Damidot, and J.-L. Potdevin, "Leaching of lead metallurgical slags and pollutant mobility far from equilibrium conditions," *Applied Geochemistry*, vol. 23, no. 12, pp. 3699–3711, 2008.

[109] V. Ettler, Z. Johan, B. Křibek, O. Šebek, and M. Mihaljevič, "Mineralogy and environmental stability of slags from the Tsumeb smelter, Namibia," *Applied Geochemistry*, vol. 24, no. 1, pp. 1–15, 2009.

[110] L. R. P. De Andrade Lima and L. A. Bernardez, "Characterization of the lead smelter slag in santo amaro, bahia, Brazil," *Journal of Hazardous Materials*, vol. 189, no. 3, pp. 692–699, 2011.

[111] L. R. P. de Andrade Lima and L. A. Bernardez, "Evaluation of the chemical stability of a landfilled primary lead smelting slag," *Environmental Earth Sciences*, vol. 68, no. 4, pp. 1033–1040, 2013.

[112] N.-H. Yin, Y. Sivry, F. Guyot, P. N. L. Lens, and E. D. van Hullebusch, "Evaluation on chemical stability of lead blast furnace (LBF) and imperial smelting furnace (ISF) slags," *Journal of Environmental Management*, vol. 180, pp. 310–323, 2016.

[113] S. Onisei, Y. Pontikes, T. Van Gerven et al., "Synthesis of inorganic polymers using fly ash and primary lead slag," *Journal of Hazardous Materials*, vol. 205-206, pp. 101–110, 2012.

[114] T. C. Alex, A. M. Kalinkin, S. K. Nath et al., "Utilization of zinc slag through geopolymerization: influence of milling atmosphere," *International Journal of Mineral Processing*, vol. 123, pp. 102–107, 2013.

[115] C. Atzeni, L. Massidda, and U. Sanna, "Use of granulated slag from lead and zinc processing in concrete technology," *Cement and Concrete Research*, vol. 26, no. 9, pp. 1381–1388, 1996.

[116] S. H. G. Mosavinezhad and S. E. Nabavi, "Effect of 30% ground granulated blast furnace, lead and zinc slags as sand replacements on the strength of concrete," *KSCE Journal of Civil Engineering*, vol. 16, pp. 989–993, 2012.

[117] S. K. Nath, "Fly ash and zinc slag blended geopolymer: immobilization of hazardous materials and development of paving blocks," *Journal of Hazardous Materials*, vol. 387, Article ID 121673, 2020.

[118] R. Barna, P. Moszkowicz, and C. Gervais, "Leaching assessment of road materials containing primary lead and zinc slags," *Waste Management*, vol. 24, no. 9, pp. 945–955, 2004.

[119] M. Albitar, M. S. Mohamed Ali, P. Visintin, and M. Drechsler, "Effect of granulated lead smelter slag on strength of fly ash-based geopolymer concrete," *Construction and Building Materials*, vol. 83, pp. 128–135, 2015.

[120] N. Saikia, G. Cornelis, G. Mertens et al., "Assessment of Pb-slag, MSWI bottom ash and boiler and fly ash for using as a fine aggregate in cement mortar," *Journal of Hazardous Materials*, vol. 154, no. 1-3, pp. 766–777, 2008.

[121] J. Touray, "Primary phases and natural weathering of old lead–zinc," *The Canadian Mineralogist*, vol. 39, pp. 873–888, 2001.

[122] M. Xia, F. Muhammad, L. Zeng et al., "Solidification/stabilization of lead-zinc smelting slag in composite based geopolymer," *Journal of Cleaner Production*, vol. 209, pp. 1206–1215, 2019.

[123] B. Tripathi and S. Chaudhary, "Performance based evaluation of ISF slag as a substitute of natural sand in concrete," *Journal of Cleaner Production*, vol. 112, pp. 672–683, 2016.

[124] M. Alwaeli, "Application of granulated lead-zinc slag in concrete as an opportunity to save natural resources," *Radiation Physics and Chemistry*, vol. 83, pp. 54–60, 2013.

[125] V. Ettler, O. Legendre, F. Bodenan, and J.-C. Touray, "Primary phases and natural weathering OF old lead zinc pyrometallurgical slag from pribram, Czech Republic," *The Canadian Mineralogist*, vol. 39, no. 3, pp. 873–888, 2001.

[126] N. Seignez, D. Bulteel, D. Damidot, A. Gauthier, and J. L. Potdevin, "Weathering of metallurgical slag heaps: multi-experimental approach of the chemical behaviours of lead and zinc," *Waste Management and the Environment III*, vol. 92, pp. 31–40, 2006.

[127] M. Palacios, Y. F. Houst, P. Bowen, and F. Puertas, "Adsorption of superplasticizer admixtures on alkali-activated slag pastes," *Cement and Concrete Research*, vol. 39, no. 8, pp. 670–677, 2009.

[128] G. Xu and X. Shi, "Characteristics and applications of fly ash as a sustainable construction material: a state-of-the-art review," *Resources, Conservation and Recycling*, vol. 136, pp. 95–109, 2018.

[129] P. Sturm, G. J. G. Gluth, H. J. H. Brouwers, and H.-C. Kühne, "Synthesizing one-part geopolymers from rice husk ash," *Construction and Building Materials*, vol. 124, pp. 961–966, 2016.

[130] M. C. G. Juenger, F. Winnefeld, J. L. Provis, and J. H. Ideker, "Advances in alternative cementitious binders," *Cement and Concrete Research*, vol. 41, no. 12, pp. 1232–1243, 2011.

[131] S. Zhao, F. Muhammad, L. Yu et al., "Solidification/stabilization of municipal solid waste incineration fly ash using uncalcined coal gangue-based alkali-activated cementitious materials," *Environmental Science and Pollution Research*, vol. 26, no. 25, pp. 25609–25620, 2019.

[132] C. Fernández-Pereira, Y. Luna-Galiano, M. Pérez-Clemente et al., "Immobilization of heavy metals (Cd, Ni or Pb) using aluminate geopolymers," *Materials Letters*, vol. 227, pp. 184–186, 2018.

Research Article

Study on the Relationship between Pore Structure and Uniaxial Compressive Strength of Cemented Paste Backfill by Using Air-Entraining Agent

Fengwen Zhao,[1] **Jianhua Hu** ⓘ,[1] **Dongjie Yang** ⓘ,[1] **Ye Kuang,**[1] **Hongxing Xiao,**[2] **Minghua Zheng,**[2] **and Xueliang Wang**[2]

[1]*School of Resources and Safety Engineering, Central South University, Changsha, Hunan 410081, China*
[2]*Hubei Sanning Mining Co., Ltd., Yichang, Hubei 443100, China*

Correspondence should be addressed to Dongjie Yang; yangdjxx@csu.edu.cn

To control pores in the backfill, the air-entraining agents (AEAs) are used as an admixture to realize the pore structure changes under artificial action and explore the effect of pore structure on strength. Two AEAs at different dosages were added to the backfill. The relationship was then analyzed between them from the macro- and mesoscopic aspects. The results indicate that AEA can regulate pore structure changes of AEACPB. With the increase in AEA content, the total pore volume of different pore sizes in AEACPB increases, in which the proportion of big and medium pore gradually increases while the proportion of small pore gradually decreases. The AEACPB's UCS is linearly negatively correlated with the porosity and pore percentage, which is the primary factor affecting the AEACPB of the pore structure. When the total pores' volume in the AEACPB is constant, the influence of different pore structures differs. A higher proportion of small pores leads to a linear increase in strength; a higher proportion of medium pores leads to a linear decrease in strength; and a higher proportion of big pores leads to an exponential decrease in strength. And the fractal dimension has a linear negative correlation with the UCS by fractal theory analysis.

1. Introduction

As an important indicator of mine filling, the backfill strength has multiple influencing factors. They can be divided into macro and micro aspects according to the perspective of analysis. In the macroscopic aspect, the composition of filling material had a significant effect on strength. The results report that macro factors such as cement–sand ratio, slurry concentration, solids content of tailings, and fine tailings have a significant impact on strength [1–3]. In the microscopic aspect, this study was performed on microscopic substance and reported that the sulfate, type, shape, and quantity of hydration products have an important influence on strength [4–7]. However, the pore structure is a major factor affecting the pore material's strength [8–10].

The strength is considerably influenced by pores, and the pore structure is changed to achieve the influence strength. It is very important that to achieve the change of pore structure through some methods and means for to study the effect of pore on strength. Dai et al. examined the relationships between pores structure and strength by changing the water–binder ratio of concrete and reported that as the water–binder ratio increased, the average pores size increased while the porosity decreased, and the strength first increased and then decreased, indicating that the pores structure was an important factor determining the concrete strength [11]. Huo et al. then analyzed the relationship between harmful pores having a size of $>0.2 \mu$m and concrete strength in different curing ages. They reported that, during the curing period of 7–28 days, pore structure and uniaxial compressive strength (UCS) considerably changed; moreover, the pore structure and strength change tended to stabilize during the curing period of 28–90 days. Thus, there is a certain relationship between pore structure characteristics and strength [12]. However, these methods will not

only cause pore structure changes but also affect other factors, and air-entraining agent (AEA) is a type of admixture that can introduce a large number of bubbles into the backfill to generate pores, thus changing the pore structure in the backfill. Note that it can change the pore structure in the backfill under the condition that the ratio of other materials remains unchanged so as to achieve an individual change of pores in the same age and achieve the purpose of artificially controlling the pore structure. Studies report that adding AEA to the pore material can effectively change the pore structure and improve the material's performance [13–15]. Furthermore, we performed quantitative description of pore structure to analyze the effect of pore on strength. Moreover, the analysis methods of pore structure primarily include mercury injection test, nuclear magnetic resonance (NMR), and scanning electron microscopy (SEM). Jiang et al. measured the porosity and pores size distribution of concrete by mercury injection [16]. Zou et al. observed the evolution law of the concrete mesopore structure in the curing process using SEM [17]. Hu et al. used SEM to observe and analyze the hydration products and pore structure characteristics in the backfill [18, 19]. And Liu et al. examined the distribution characteristics of various pore sizes using NMR spectroscopy [20]. All of the abovementioned techniques can be used to analyze pores' characteristics and achieve the acquisition of relevant characteristics of pore structure. And there are not many studies on quantitative analysis of backfill pores by using these techniques.

The amount of data and quantitative study of pore and strength are insufficient in this study. Tailings, tailings sludge, fly ash, and other raw materials were used to manufacture backfill samples, whereas AEAs (sodium abietate (SA) and triterpenoid saponins (SJ)) were used to regulate the backfill's pore structure. They were cured in a standard curing box (20°C and 99% humidity) for seven days and then tested by UCS, NMR, and SEM. By establishing the relationship model between the strength of the cemented paste backfill with an additional air-entraining agent (AEACPB) and the pores' structure, the quantitative relationship research between pore structure and the strength is then realized. Thus, the relationship between strength of backfill and pores is comprehensively analyzed.

2. Materials and Methods

2.1. Materials. Tailings, fly ash, and tailings sludge were obtained from the Sanning Mine, Hubei, China. They were analyzed using a sieving method, laser particle size analyzer (Mastersizer 2000), and X-ray diffraction (XRD). Their physical properties (Table 1) and particle size distribution (Figure 1 and 2) were as follows. AEAs were then provided by a supplier based in Shandong province, and the physical properties of the AEAs are shown in Table 2. In this study, Portland cement was sourced from Changsha Xinxing Cement Factory; its physical properties are shown in Table 3. Ordinary tap water of Changsha was used.

TABLE 1: Physical properties of the materials.

Class	Tailings	Tailing sludge	Fly ash
Apparent density (kg/m^3)	2626	2653	1990
Packing density (kg/m^3)	1464	923	650
Surface moisture content (%)	0.120	0.974	0.049
Hydroxyllapatite (%)	10.15	60.94	—
Quartz (%)	6.91	2.24	61.55
Hematite (%)	12.75	—	1.46
Albite (%)	—	8.38	15.99
Plagioclase (%)	—	11.42	—
Muscovite (%)	—	—	20.99
Illite (%)	—	9.76	—
Dolomite (%)	69.65	6.30	—

Incremental volume (%)

Particle size (mm)

- 0.075
- 0.15
- 0.3
- 0.6
- 1.18
- 2.36
- 4.75
- 9.5
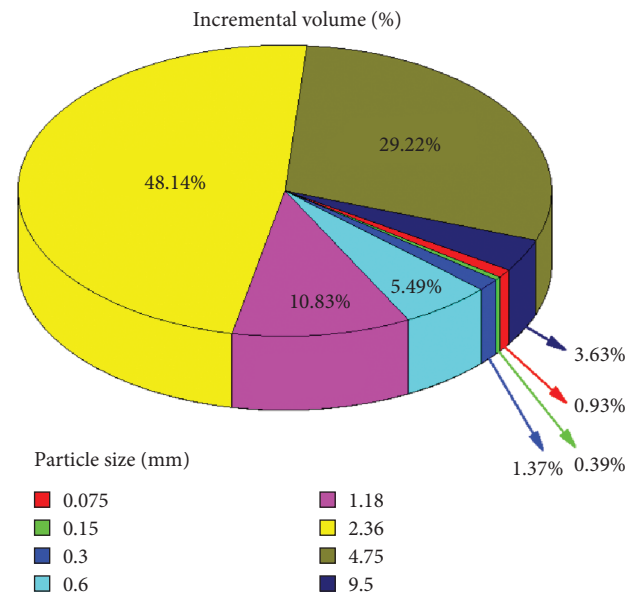
FIGURE 1: Particle size distribution of tailings.
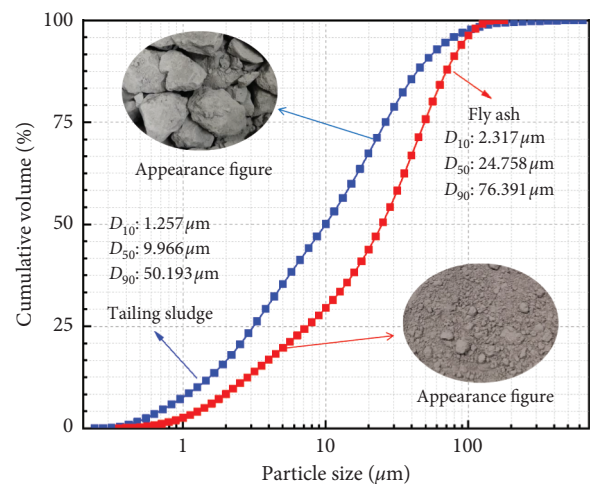
FIGURE 2: Particle size distribution of tailing sludge and fly ash.

2.2. Experimental

2.2.1. Experimental Scheme Design. Tailing and tailings sludge are regarded as aggregates. Cement and fly ash are

TABLE 2: The main characteristics of used AEA.

Main components	Appearance	pH
SA	White powder	10
SJ	Pale-yellow powder	6

TABLE 3: Physical parameters of the cement.

Chemical component	$3CaO·SiO_2$	$2CaO·SiO_2$	$3CaO·Al_2O_3$	$4CaO·Al_2O_3·Fe_2O_3$
Content	52.8	20.7	11.5	8.8
Physical properties	Apparent density (kg/m³)	Packing density (kg/m³)	—	—
Numerical value	3100	1300	—	—

regarded as cementing material. In this study, the dosages of AEAs (SA and SJ) include three types. In order to meet the requirement of the Tiaoshuihe Phosphate Mine, the ratio of cement to tailing is 1 : 10 and concentration is 80%. The specific ratios (Table 4) of this experiment are as follows.

The manufacturing of AEACPB specimen according to GB/T50081-2002 is as follows. First, every raw material is weighed as per the design requirement, and these materials are mixed evenly by blender. Then, the filling slurry is injected into cylindrical mold ($\varphi 50 \times 100$ mm). And the specimens are cured in a curing box (20°C and 99% humidity) for 7 days after demolding. Finally, the samples were tested with SEM, NMR, and UCS.

2.2.2. Experimental Test

(i) SEM analysis is undertaken using a Quanta-200. The test objects are fragments of 1 mm² picked from the center of damaged samples. Moreover, surface dusts are cleared and metal conductive films are applied before test.

(ii) NMR analysis is undertaken using a MesoMR23-060H. The test objects are complete samples cured for 7 days. First, they are pumped dry and then soaked, so as to ensure they are fully saturated. Finally, the samples are tested.

(iii) The UCS test is performed using a compressor no. 01000405, and its loading rate is 0.2 kN/s. The UCS value is then obtained through a force measurement system analysis. The reference standard for this experiment is ASTM D2166/D2166M-16.

The experiment process is shown in Figure 3.

3. Results

3.1. NMR Results

3.1.1. T_2 Spectrum Distribution. For the AEACPB sample treated with saturated water, NMR T_2 spectrum can reflect the pore size distribution feature of the pores in the AEACPB. Furthermore, there is a certain functional relationship between the pore size and T_2, which can be expressed as follows [21, 22]:

TABLE 4: Mixture proportions for the AEACPB.

Code	Tailings	Tailing sludge	Fly ash	Cement	Water	SA	SJ
		(kg/m³)				By wt% of the cement	
SA1	1500	400	200	150	562	0.2	—
SA2	1500	400	200	150	562	0.4	—
SA3	1500	400	200	150	562	0.6	—
SJ1	1500	400	200	150	562	—	0.2
SJ2	1500	400	200	150	562	—	0.4
SJ3	1500	400	200	150	562	—	0.6

Note. "wt%" represents solid mass percentage.

$$r \approx T_2 \rho_2 F_s, \quad (1)$$

where r is pore radius (μm); T_2 is transverse relaxation time (ms); ρ_2 is transverse surface relaxation strength (μm/ms); and F_s is pores' shape factor (for spherical pore, $F_s = 3$, and for tube bundle pore, $F_s = 2$).

Because pores' structure of AEACPB was similar to that of concrete, the parameter ρ_2 (12 nm/ms) could be got as per related study [23]. AEA could densify pore, so the pore could be regarded as spherical shape ($F_s = 3$). Therefore, the relationship between r and T_2 is as follows:

$$r \approx 36 \times 10^{-9} \times T_2. \quad (2)$$

Combining equation (2) and T_2 spectrum, the T_2 spectrum included pore size and T_2 value can be got (Figure 4). Figure 4 shows that the T_2 spectrum is primarily divided into three peaks from big to small; moreover, it can then be divided into small, medium, and big pores, of which the small pores are the main ones (the largest area). As the AEA content increases, the first peak in the T_2 spectrum gradually increases, which shows that the small pores gradually increase with the increase of AEA content. However, the second and third peaks did not change much, indicating that the AEA had little effect on the medium and big pores. In Figure 4, 20 nm is the boundary of the pore size whether it is harmful to the strength. As per relevant research, when the pore size is >20 nm, the pores are harmful to the strength; otherwise, they are not harmful [24]. Figure 4 shows that the small pores in the first peak of the T_2 spectrum are primarily pores of <20 nm, which have little
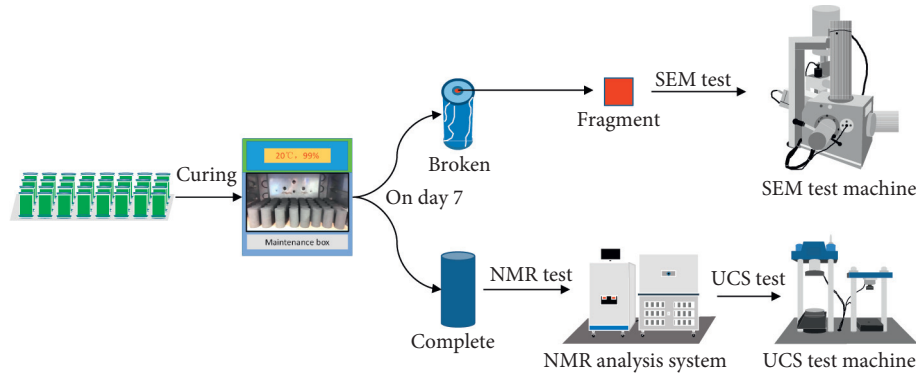
Figure 3: Experiment process with sample preparation, UCS tests, and SEM.

(a)

(b)
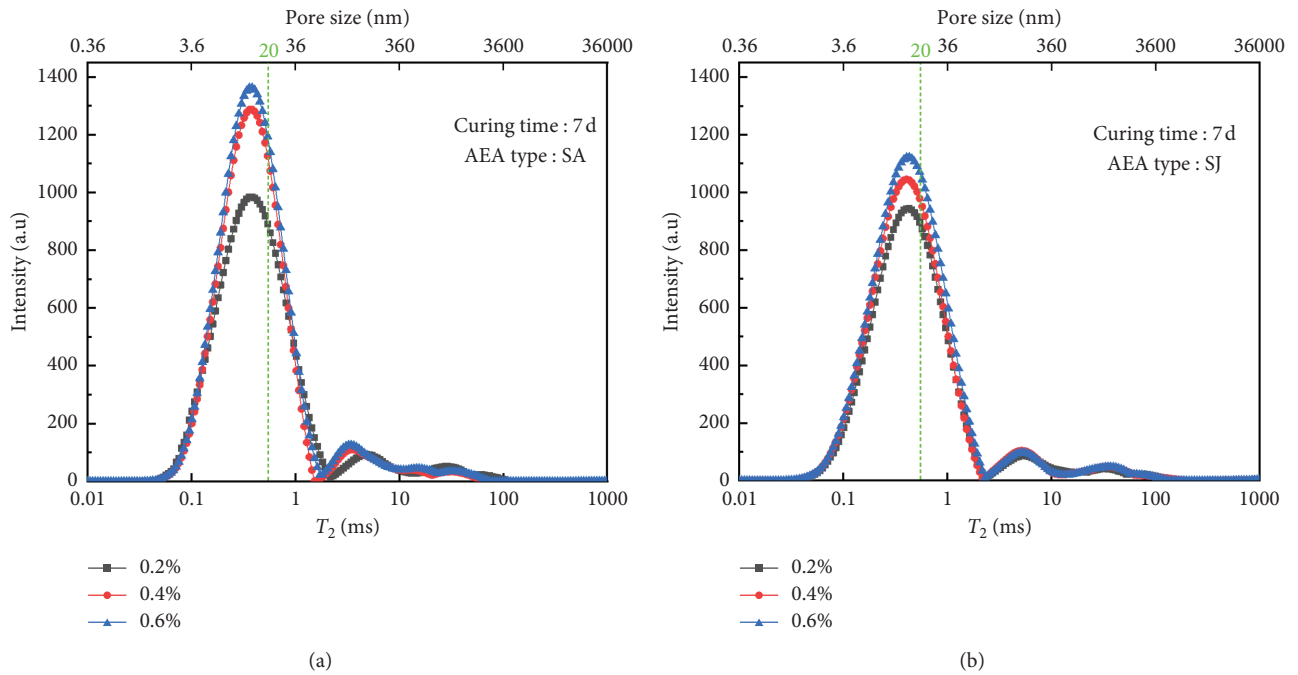
Figure 4: NMR T_2 spectral distribution of AEACPB samples incorporating different concentration of AEA.

impact on the strength deterioration. However, the second and third peaks are primarily medium and big pores of >20 nm, which have a harmful effect on strength.

3.1.2. T_2 Spectrum Peak Area. In the AEACPB sample, there is a certain correlation between the T_2 spectral area and the amount of fluid contained. The peak areas and their proportions reflect the number of pores and their proportions in the AEACPB sample. Table 5 shows the peak areas and their proportions in the AEACPB samples under different AEA contents. Table 5 shows that as the content of the AEA increases, both the area of each peak and the total area gradually increase, which indicates that the AEA addition introduces a large number of bubbles, which makes the pore volume increase. However, the proportion of the first peak area decreases, indicating that although a large number of bubbles can be introduced with increase in AEA content, the proportion of small bubbles decreases and the proportion of

big and medium bubbles gradually increases, which is harmful to AEACPB strength.

3.2. SEM Analysis. In addition to using NMR, SEM can be used to study the distribution feature of pores in the AEACPB sample. The SEM images can be used to observe the pore distribution feature of some areas in the AEACPB sample. The SEM image is then processed using binarization, and the distribution of black and white areas in the binarization image can reflect pore distribution. The binarization processing is that the solid part and pore part in SEM image can be transformed into black and white regions by using threshold grayscale segmentation. The processing principle is as follows [25, 26]:

$$f(i, j) = \begin{cases} 0, & f(i, j) < T, \\ 1, & f(i, j) \geq T, \end{cases} \tag{3}$$

where T is the threshold grayscale.

TABLE 5: T_2 spectral peak areas and their proportions of AEACPB samples doped with different AEA.

AEA type	Dosage (%)	Peak area and its proportion						
		The first	Proportion	The second	Proportion	The third	Proportion	Total area
SA	0.2	32467.06	0.9167	1825.85	0.0516	1124.81	0.0318	35417.72
	0.4	37077.48	0.9141	2113.89	0.0521	1368.23	0.0337	40559.60
	0.6	40486.61	0.9094	2511.36	0.0564	1524.25	0.0342	44522.23
SJ	0.2	29724.96	0.9274	1407.53	0.0439	918.32	0.0287	32050.81
	0.4	32293.20	0.9162	1803.33	0.0512	1150.57	0.0326	35247.10
	0.6	36562.98	0.9126	2141.14	0.0534	1361.33	0.0340	40065.45

According to equation (3), the SEM binarization image is composed by setting pixel point to 0 where the gray level is lower than T, i.e., the black point (solid part) and setting pixel point to 1 where the gray level is higher than or equal to T, i.e., the white point (pore part). The porosity that is measured is from the macro aspect using NMR, but SEM can be used to obtain the pore percentage from the micro aspect. The black and white areas in the binarization image are composed of a number of pixel points. The white areas in the binarization image are added, and the pore percentage of the sample can then be obtained by calculating the area percentage of the white area in the area of the entire picture. Figure 5 shows the SEM image and its binarization image of AEACPB samples. Figure 5 shows that the pores are primarily divided into three forms, namely, small, medium, and big pores. Among them, there are primarily small pores, and the proportion of big and medium pores is not much, which is consistent with the results obtained in Section 3.2.

3.3. Porosity and Pore Percentage. Porosity and pore percentage are two methods for calculating the total pore volume percentage of AEACPB. The porosity is directly obtained by NMR, but the pore percentage is obtained by obtaining the SEM binarization image. Figure 6 shows the changes of porosity and pore percentage with AEA content. Figure 6 shows that as the content of the AEA increases, both the porosity and the pore percentage increase; however, the pore percentage is lesser than the porosity. The total volume of the AEACPB sample remains unchanged; therefore, the amount of pores increased. This indicates that AEA can effectively increase amount of pore in AEACPB because AEA can introduce a large number of bubbles during the stirring process of filling slurry, and these bubbles will then form pores after the AEACPB is hardened. With additional AEA content, more bubbles will be introduced, resulting in an increase in the amount of the pore with an increase in AEA content. However, the main composition of SA-type and SJ-type AEA is different, and the bubbles produced by the two kinds of AEA are different. SA-type AEA will produce a large number of bubbles, while SJ-type AEA will produce a small number of bubbles, which leads to the difference of the backfill pore formed in the latter, and the porosity of the backfill with SA-type AEA is higher.

3.4. Strength Characteristics. Strength is an important feature of the AEACPB, and its size is of great significance.

The strength change curve of the AEACPB was observed with the different contents of the two external AEAs on seven days (Figure 7). Figure 7 shows that as the content of the AEA increases, the strength gradually decreases, which indicates that AEA addition has a certain effect on the AEACPB strength. This is because the AEA can introduce a large number of bubbles in the AEACPB, resulting in a large number of pores in the AEACPB. Moreover, the different content of AEA can create pores with different pore sizes in the AEACPB, and pores with different pore sizes have different effects on the AEACPB strength. When the content of the AEA increases, pores with larger pore size will be generated in the AEACPB, which leads to a decrease in the AEACPB strength. It is shown in Section 3.3 that porosity increases with the increase of AEA content. The increase of porosity leads to the decrease of strength, and the porosity of the backfill with SA is greater than that of the backfill with SJ, so the strength of the backfill with SA is relatively low.

4. Discussion and Analysis

4.1. Relationship between Strength and Porosity and Pore Percentage. In the AEACPB sample, porosity embodies the total pore feature; moreover, it has an inevitable connection with strength. Certain studies have reported that there is a certain functional relationship between porosity and strength [19, 27]. Now, two techniques are used to obtain the relationships between strength and porosity and pore percentage (Figure 8). Figure 8 shows that the relationship between porosity and strength is better ($R^2 = 0.92$); however, that between pore percentage and strength is worse ($R^2 = 0.68$). The relationships between them are as follows:

$$y = -0.4x_1 + 3.62,$$
$$y = -0.31x_2 + 2.84, \tag{4}$$

where y is strength (MPa); x_1 is porosity (%); and x_2 is pore percentage (%).

Figure 8 shows that no matter the porosity or the pore percentage, their increase will lead to a decrease in strength because total pore volume increases because of the increase in AEA content. Furthermore, the proportion of big and medium pores in the total pores increases, resulting in a decrease in the compactness of the AEACPB; therefore, the strength is reduced.
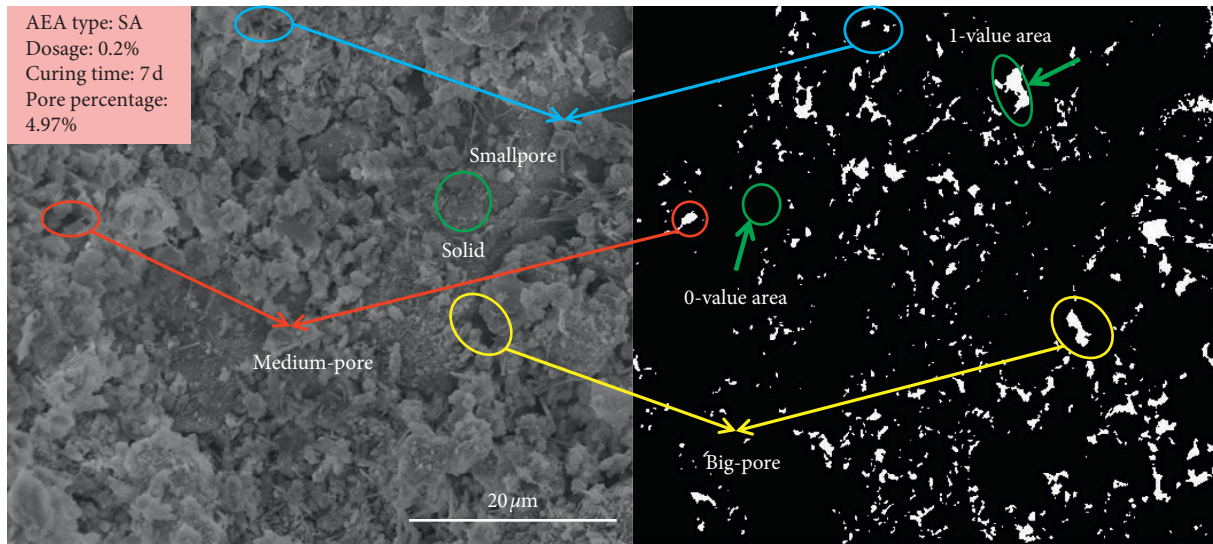
FIGURE 5: SEM and its binarization image of AEACPB.
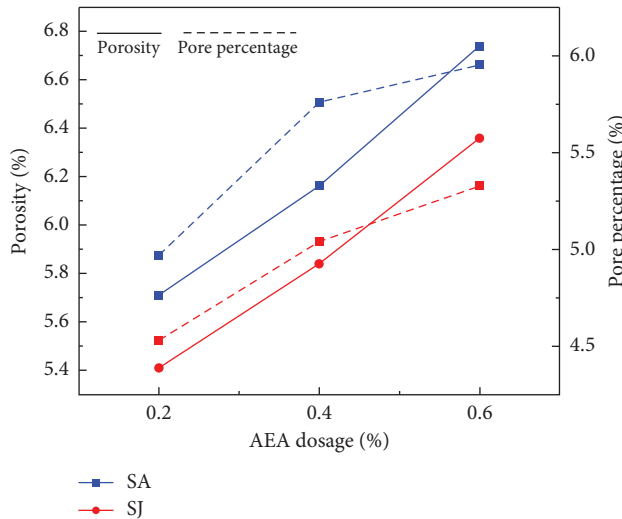
FIGURE 6: Changes of porosity and pore percentage with AEA content.

Curing time: 7 d

FIGURE 7: Variation characteristics of AEACPB strength with AEA content.

$$y = -5.23 \times 10^{-20} e^{12.76x_3} + 1.38, \tag{7}$$

where y is strength (MPa) and x is T_2SPAP (%). Among them, x_1 is first peak, x_2 is second peak, and x_3 is third peak.

The above formulas show that the strength is linearly proportional related to the area percentage of the first peaks, linearly inversely related to the area percentage of the second peaks, and exponentially related to the area percentage of the third peaks. This demonstrates that when the total pores' volume of the AEACPB sample remains unchanged, the proportion of small pores is larger, and the strength increases linearly. However, when the proportion of medium pores is larger, the strength linearly decreases. Moreover, when the proportion of big pores increases, the strength

4.2. Relationship between Strength and T_2SPAP. Studies report that when the pore size is >20 nm, it is a harmful pore [22]. Note that there are three peaks on the T_2 spectrum, whereas the pore size is >20 nm. Here, we examined the effect of different pore size on strength. Figure 9 shows the relationships between the three T_2 spectrum peaks area percentage (T_2SPAP) and the strength, respectively, where (a), (b), and (c) show the relationships between the first, second, and third peaks area percentage and the strength, respectively. Moreover, Figure 9 shows that there is a certain functional relationship between them, and the relationship is very good ($R^2 > 0.9$). Furthermore, the relationships between them are as follows:

$$y = 0.63x_1 - 56.38, \tag{5}$$

$$y = -0.39x_2 + 3.13, \tag{6}$$

FIGURE 8: Relationship between strength and porosity and pore percentage.

FIGURE 9: Relationship between strength and T_2SPAP. (a) First peak; (b) second peak; and (c) third peak.

appears to exponentially decrease. This indicates that small pores have certain benefits on strength; however, medium pores have certain damage to strength and big pores have the greatest damage to strength. Therefore, the proportion of medium and big pores in the AEACPB should be minimized. Li et al. reported that more harmful pores having sizes of >0.2 μm have the greatest impact on strength reduction [27]. By comparing the slopes of equations (5) and (6), small pores have a greater and beneficial effect on strength. Figure 9(c) shows that when the proportion of big pores reaches a certain amount, they have the greatest and harmful impact on strength; otherwise, the impact on strength is reduced. In these three types of pores, the amount of small pores should increase as much as possible, followed by the amount of medium pores. Furthermore, the amount of big pores should be avoided to exceed that fixed value as much as possible. If backfill needs the addition of AEA, note that a small amount of AEAs should be added, so that it is beneficial to the strength because it can effectively increase the proportion of small pores.

4.3. The Relationship between Fractal Dimension and UCS.

As an important parameter of fractal geometry, fractal dimension can quantitatively describe the complexity of geometry. The combination of fractal theory and NMR can be used to study the pore characteristics in the AEACPB, so as to explain the change of strength from the complexity of pores. There is a certain functional relationship between the fractal dimension D and T_2, and the relationship is as follows [15, 19]:

$$l_g(S_v) = (3 - D)l_g(T_2) + (D - 3)l_g(T_{2\max}), \qquad (8)$$

where S_v is the percentage between pore cumulative volume with pore size less than r and total pore volume and $T_{2\max}$ is the T_2 value corresponding to the maximum pore size.

TABLE 6: Fractal dimension of various pores.

Groups	Small pore			Medium pore			Big pore		
	k	D_s	R^2	k	D_m	R^2	k	D_b	R^2
SA1	2.599	0.401	0.88	0.034	2.966	0.98	0.018	2.982	0.97
SA2	2.039	0.961	0.82	0.031	2.969	0.99	0.011	2.989	0.99
SA3	1.707	1.293	0.81	0.03	2.97	0.97	0.012	2.988	0.99
SJ1	2.584	0.416	0.88	0.032	2.968	0.98	0.016	2.984	0.98
SJ2	2.227	0.773	0.87	0.037	2.963	0.98	0.017	2.983	0.98
SJ3	1.621	1.379	0.86	0.031	2.969	0.97	0.015	2.985	0.98
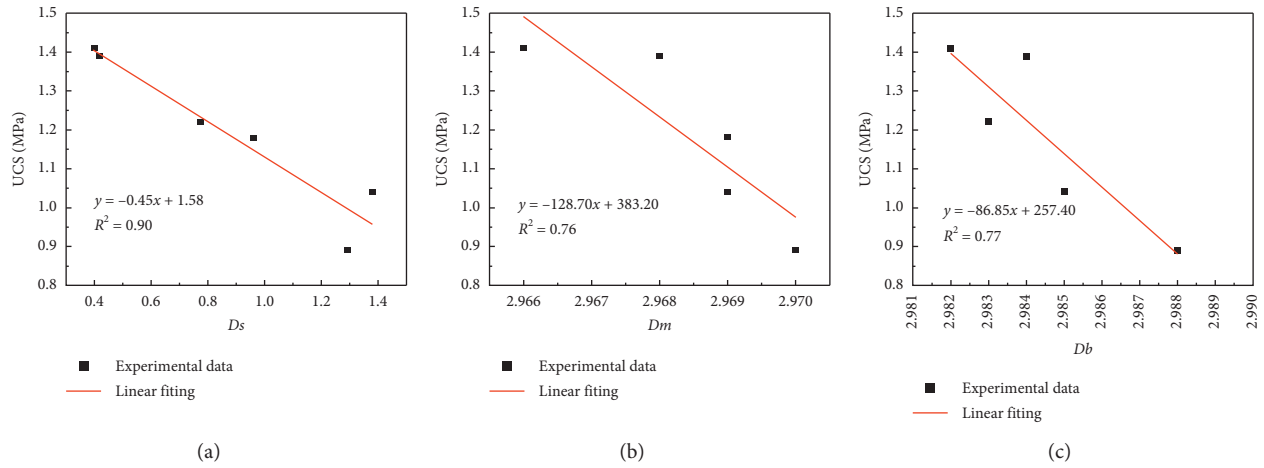
FIGURE 10: The relationship between UCS and the fractal dimension of various pores.

It can be found from equation (8) that the relationship between $\lg(S_v)$ and $\lg(T_2)$ is linear, and the sum of the slope k and D is 3. The results shown in Table 6 can be obtained through the calculation of formula (8). By fitting the relationship between the fractal dimension and strength of various types of pores, we can get the result as shown in Figure 10. Among them, Ds, Dm, and Db represent the fractal dimensions of small, medium, and big pores, respectively. It can be seen from Table 6 that R^2 of the small pores is all above 0.8, indicating that the fractal property of the small pores is good. The fractal dimensions of big and medium pores are all 0.97 and above, indicating that the fractal properties of big and medium pores are very good. It can be seen from Figure 10 that R^2 of the relationship between the fractal dimension of small pores and strength is 0.9, while that of medium pores and big pores is 0.76 and 0.77, respectively, which indicates that the relationship between fractal dimension of small pores and strength is strong, while that of medium pores and big pores is weak. The functional relationship between them is as follows:

$$\begin{aligned} y &= -0.45x_1 + 1.58, \\ y &= -128.70x_2 + 383.20, \\ y &= -86.85x_3 + 257.40, \end{aligned} \tag{9}$$

where y represents UCS (MPa), and x represents the fractal dimension. Among them, x_1 is Ds, x_2 is Dm, and x_3 is Db.

It can be seen from Figure 10 that the strength decreases with the increase of fractal dimension. This is similar to the result obtained by Ding Ziwei and others in the study of the relationship between the pore fractal dimension and strength of sandstone, and Xie Chao and others also obtained similar results in the study of concrete [28, 29]. There are two reasons for this phenomenon, because the larger the fractal dimension, the more complex the pores. Firstly, the larger the fractal dimension is, the more pores with larger pore size will be, and the compactness of AEACPB will be decreased, which will cause great damage to the strength and reduce the strength. Studies have shown that the pore size becomes larger as the fractal dimension increases [28]. Second, the larger the fractal dimension, the more types of pore shapes. Irregular pores have a certain influence on the strength, and a large number of irregular pores reduce the strength.

5. Conclusion

The pore structure of the backfill has significant effect on strength. Note that AEA is added to regulate the pore structure of the backfill. Moreover, UCS, NMR, and SEM were used for the tests, and the relationships between pores' structure and backfill strength were quantitatively studied.

(1) For NMR analysis of AEACPB, there are three primary peaks in the T_2 spectrum, which can be divided into big, medium, and small pores as per the size of the pore structure. The pore size is primarily small pores (the largest area). As the content of the

AEA increases, both the area of each peak and the total area are gradually increasing; however, the proportion of the first peak area is decreasing.

(2) The strength of the AEACPB is linearly negative correlation with porosity and pore percentage. Because the porosity and pore percentage increase, the strength of the AEACPB decreases.

(3) Pore structures of different scales have different action mechanisms on AEACPB strength. When the total pores in the AEACPB are constant, the higher the proportion of small pore, the strength linearly increases; the higher the proportion of medium pore, the strength linearly decreases; and the higher the proportion of big pore, the strength decreases exponentially. To improve the AEACPB strength, the external AEA should be adjusted as much as possible to effectively increase the amount of small pores, followed by the amount of medium pores, and avoid the amount of big pores.

(4) Through the analysis of fractal theory, all types of pores are fractal, and the fractal dimension has a linear negative correlation with the UCS.

Data Availability

The data used to support the findings of this study are available from the corresponding author upon request.

Conflicts of Interest

The authors declare that they have no conflicts of interest regarding the publication of this paper.

Acknowledgments

References

[1] T.-Y. Qi, G.-R. Feng, Y.-R. Li, Y. Guo, J. Guo, and Y. Zhang, "Effects of fine gangue on strength, resistivity, and microscopic properties of cemented coal gangue backfill for coal mining," *Shock and Vibration*, vol. 2015, Article ID 752678, 11 pages, 2015.

[2] W. Xu, P. Cao, and M. Tian, "Strength development and microstructure evolution of cemented tailings backfill containing different binder types and contents," *Miner*, vol. 8, no. 4, pp. 1–15, 2018.

[3] Q. Zhang, Z. Wang, S. Rong et al., "Early strength characteristics and microcosmic influence mechanism analysis of cemented filling body of full tailings in deep mine," *Nonferrous Metals Engineering*, vol. 9, no. 6, pp. 97–104, 2019.

[4] W. Li and M. Fall, "Sulphate effect on the early age strength and self-desiccation of cemented paste backfill," *Construction and Building Materials*, vol. 106, pp. 296–304, 2016.

[5] H. Rong, M. Zhou, and H. Hou, "Pore structure evolution and its effect on strength development of sulfate-containing cemented paste backfill," *Miner*, vol. 7, no. 1, pp. 1–9, 2017.

[6] W. Xu, W. Pang, and M. Ding, "Experiment on evolution of microstructures and long-term strength model of cemented backfill mass," *Journal of Central South University*, vol. 46, no. 6, pp. 2333–2341, 2015.

[7] X. Li, B. Wand, J. You et al., "Study on mechanical properties and microstructure of the cemented tailings backfill," *China Mining Magazinne*, vol. 25, no. 6, pp. 169–172, 2016.

[8] W. Zhang, B. Li, H. Wang et al., "Analysis of pore structures and their relations with strength of hardened cement paste," *Journal of Wuhan University of Technology-Materials Science and Engineering*, vol. 20, no. 1, pp. 114–125, 2005.

[9] H. Zhao, Q. Xiao, D. Huang, and S. Zhang, "Influence of pore structure on compressive strength of cement mortar," *The Scientific World Journal*, vol. 2014, Article ID 247058, 12 pages, 2014.

[10] S. Jin, J. Zhang, and S. Han, "Fractal analysis of relation between strength and pore structure of hardened mortar," *Construction and Building Materials*, vol. 135, pp. 1–7, 2017.

[11] Y. Dai, P. Gao, H. Lin et al., "Effect of pore structure on the compressive strength of foamed concrete," *New Building Materials*, vol. 3, pp. 130–133, 2018.

[12] J. Huo, X. Cao, and X. Wang, "Influence of natural pumice concrete pore structure on its compressive strength," *Journal of the Chinese Ceramic Society*, vol. 39, no. 3, pp. 734–739, 2020.

[13] Y. Chang, "Study on the effect of different air entraining agents on the performance of concrete," *Contemporary Chemical Industry*, vol. 47, no. 10, pp. 2114–2117, 2018.

[14] J. H. Hu, Y. Kuang, T. Zhou, and F. Zhao, "Influence of air entraining agent on strength and microstructure properties of cemented paste backfill," *IEEE Access*, vol. 7, pp. 140899–140907, 2019.

[15] J. Hu, F. Zhao, Y. Kuang, D. Yang, M. Zheng, and L. Zhao, "Microscopic characteristics of the action of an air entraining agent on cemented paste backfill pores," *Alexandria Engineering Journal*, vol. 59, no. 3, pp. 1583–1593, 2020.

[16] L. Jiang and Y. Guan, "Pore structure and its effect on strength of high-volume fly ash paste," *Cement and Concrete Research*, vol. 29, no. 4, pp. 631–633, 1999.

[17] C. Zou, G. Long, Y. Xie et al., "Evolution of multi-scale pore structure of concrete during steam-curing process," *Microporous Mesoporous Mater*, vol. 288, pp. 1–11, 2019.

[18] J. Hu, Q. Ren, Q. Jiang, R. Gao, L. Zhang, and Z. Luo, "Strength characteristics and the reaction mechanism of stone powder cement tailings backfill," *Advances in Materials Science and Engineering*, vol. 2018, Article ID 8651239, 14 pages, 2018.

[19] J.-H. Hu, Q.-F. Ren, D.-J. Yang et al., "Cross-scale characteristics of backfill material using NMR and Fractal Theory," *Transactions of Nonferrous Metals Society of China*, vol. 30, no. 5, pp. 1347–1363, 2020.

[20] L. Liu, Z. Fang, C. Qi, B. Zhang, L. Guo, and K.-I. Song, "Experimental investigation on the relationship between pore characteristics and unconfined compressive strength of cemented paste backfill," *Construction and Building Materials*, vol. 179, pp. 254–264, 2018.

[21] J. Hu, F. Zhao, Q. Ren et al., "Microscopic characterization and strength characteristics of cemented backfill under

different humidity curing conditions," *Royal Society Open Science*, vol. 6, pp. 1–14, 2019.

[22] Z. Jiang, H. Deng, T. Liu, G. Tian, and L. Tang, "Study on microstructural evolution of marble under cyclic dynamic impact based on NMR," *IEEE Access*, IEEE Access, vol. 7, pp. 138043–138055, 2019.

[23] J. Li, H. Liu, K. Ai et al., "An NMR-based experimental study on the pore structure of the hydration process of mine filling slurry," *Advances in Civil Engineering*, vol. 2018, Article ID 4720356, 12 pages, 2018.

[24] Z. Wu and H. Lian, *High-Performance Concrete*, China Railway Press, Beijing, China, 1999.

[25] J. Hu, Q. Ren, X. Ding et al., "Trans-scale relationship analysis between the pore structure and macro parameters of backfill and slurry," *Royal Society Open Science*, vol. 6, no. 6, pp. 1–16, 2019.

[26] J. Hu, Q. Jiang, Q. Ren et al., "Cross scale correlation characteristics of pore structure and meso parameters of filling body," *Transactions of Nonferrous Met. Metals Society of China*, vol. 28, no. 10, pp. 2154–2163, 2018.

[27] W. Li, Z. Wang, L. Guo et al., "Correlation between early strength and pore structure of cemented tailing backfill sample," *China Mining Magazinne*, vol. 27, no. 10, pp. 143–147, 2018.

[28] C. Xie, Q. Wang, S. Li et al., "Relations of pore fractral dimension to pore structure and compressive strength of concrete under different water to binder ratio and curing condition," *Journal of the Chinese Ceramic Society*, vol. 34, no. 12, pp. 3695–3702, 2015.

[29] Z. Ding, X. Li, Q. Tang et al., "Study on correlation between fractal characteristics of pore distribution and strength of sandstone particles," *Chinese Journal of Rock Mechanics and Engineering*, vol. 39, pp. 1–10, 2020.

Research Article

New Definition of Ultrafine Particles in Mine Paste and Its Relationship with Rheological Properties

Jincheng Xie, Dengpan Qiao ⓘ, Runsheng Han, Tao Deng, and Jun Wang

Kunming University of Science and Technology, Kunming 650000, Yunnan, China

Correspondence should be addressed to Dengpan Qiao; 20030033@kust.edu.cn

Mine backfill paste is generally composed of tailings and coarse aggregates. In engineering practice, the definitions in fill material classification are vague. In this paper, the size range of ultrafine particles is defined by the Stokes sedimentation test and hydraulic coarseness method. The size range of ultrafine particles is affected not only by the geometric size of the particles but also by the physical characteristics of the particles themselves. This definition has more comprehensive considerations and stricter physical and mathematical significance than the traditional definition of ultrafine particles based only on size. There is a strong correlation between ultrafine particles in fill materials and the rheological properties of the mine backfill paste. In this study, through experiments and correlation analysis, it was found that the content of ultrafine particles is positively correlated with the plastic viscosity of the mine backfill paste, and its growth range is exponential. The coarse aggregate content is positively correlated with the yield stress of the mine backfill paste. A regression analysis model was established for the rheological properties of mine backfill paste. The model has few factors and high correlation, so it can simply and efficiently predict the rheological properties of mine backfill paste and guide engineering practice.

1. Introduction

Mine backfill paste is often made by mixing coarse aggregate, tailings, cement, and water. Many studies on the rheological properties of mine backfill paste mention that ultrafine particles have a significant influence on the rheological properties of the paste. However, there is no unified scientific and objective basis for the definition of ultrafine particles. In the study of sediment, particles with a particle size less than 0.01 mm are called fine particles, which is more accurate in academic research [1]. There is no strict definition of fine-grained tailings in the mining industry. Yin et al. [2] thought that the average particle size is less than 0.03 mm, and tailings with a particle size less than 0.019 mm and content greater than 10% are called fine-grained tailings. Researchers studying mine backfill paste think that the paste can only be formed if the content of under-20 μm particles is not less than 15%. Many studies [3, 4] show that under-

20 μm particle content has a significant impact on paste fluidity, and the paste has better fluidity when under-20 μm content is 15–20%. Wang et al. [5] studied the influence of different particle size ranges on the slurry bleeding rate by uniform design. The test results showed that tailing particles with a particle size of 20–37 μm had the greatest influence on the slurry bleeding rate. Wu et al. [6] said that the average particle size of ultrafine tailings is less than 30 μm, with the content of particles below 19 μm more than 50%, the content of particles above 37 μm less than 30%, and the content of particles above 74 μm less than 10%. Kang et al. [7] used the L-tube model to measure and calculate the flow parameters of the filling slurry in the Duda lead-zinc mine. The results showed that, within a certain range, increasing the under-20 μm fine particles is beneficial to improve the fluidity of the slurry. Xu et al. [8] tested the rheological properties of gangue filling slurry with different gradation aggregates, and the results showed that particles from 0 to 30 μm had the

greatest influence on the rheological properties of the slurry. In a study of the particle flocculation mechanism, Mehta [9] said that the boundary between sticky and nonsticky particles should be $20\,\mu$m. Viscous particles significantly influence the formation of the slurry flocculation structure.

In conclusion, many studies in the literature have pointed out that the content of ultrafine particles has an important influence on the rheological properties of paste. A size of $20\,\mu$m is often used as the dividing line for the ultrafine particle size range, with particles smaller than $20\,\mu$m used as ultrafine particles. However, the reason why $20\,\mu$m is used as the dividing line has not been clearly pointed out in the literature, and there is no clear theoretical derivation, only empirical limits were obtained through many experiments. There are significant differences in apparent density, particle size distribution, and shape sizes of different mine filling materials. If only the particle size is used for demarcation, it seems that the classification criteria are too singular, unscientific, and objective. In engineering practice, due to the improvement of mineral processing technology, most mine tailings have reached the category of "mud" in soil mechanics. It is urgent to make a scientific and systematic definition of the size of ultrafine particles and clarify their physical conditions to study the influence of ultrafine particles on the rheological properties of paste more scientifically and systematically.

2. Definition of Ultrafine Particles

The research object of this paper is ultrafine particles, and the main research aspect is the rheological properties of mine backfill paste, so the hydrodynamic performance of particles in water should be studied. Cement is usually used as the cementing material in the mine backfill paste, and cement in powder form undergoes a hydration reaction in water to form cement floc, which is a network or chain polymer with irregular shape, but it is still the finest particle in the mine backfill paste, that is, the slowest settling particle in the filling material. The authors think that the settling velocity of ultrafine particles in water should be similar to or the same as that of cement floc; that is, the maximum hydraulic roughness of cement floc should be regarded as the demarcation standard for ultrafine particles.

In the definition of ultrafine particles, it is necessary to measure the hydraulic coarseness of cement flocs, which is measured by the sedimentation balance method in this paper. The basic principle of the settling balance method is to calculate the particle size distribution of particles by measuring the mass of the particles settled in the liquid medium at different times [10, 11]. Its main feature is that the particles are not affected by ultrasound, stirring, and other factors in the measurement process, and the method does not destroy the structure of the particles or break up flocs. It is based on the Stokes principle: the correlation between settling velocity and particle size is as follows:

$$v_x = \frac{g\left(\rho_s - \rho_w\right)X^2}{18\eta}, \tag{1}$$

where v_x is the settling velocity, ρ_s and ρ_w are the densities of powder and water, respectively, X is the diameter of the spherical particles, and η is the viscosity of the liquid medium (usually water or another pure viscous fluid). From this formula, it can be seen that the settling velocity is proportional to the diameter of the particles. The larger the diameter, the faster the settling velocity, and the smaller the diameter, the slower the settling velocity. The expression of particle diameter can be obtained from the following:

$$X = \sqrt{\frac{18\eta v_x}{g\left(\rho_s - \rho_w\right)}}, \tag{2}$$

where X represents the Stokes diameter, and its physical meaning is the diameter of a sphere with the same settling velocity as particles of this size. Therefore, the diameter obtained by the Stokes sedimentation method is also called the effective diameter.

A schematic diagram of the settlement balance method is shown in Figure 1.

After time t_i, the effective mass m_i of particles settling on the tray is

$$m_i = M\int_{X_i}^{X_{\max}} f_{(X)}d_X + \int_{X_{\min}}^{X_i} \frac{vt_i}{H}f_{(X)}d_X, \tag{3}$$

where M is the total theoretical mass on the settling balance, H is the settling height, that is, the distance from the settling balance to the liquid level, and $f_{(X)}$ is the particle size distribution frequency function. X_i is the critical Stokes particle size corresponding to t_i time; that is, after t_i time, only the particles with particle size greater than or equal to X_i finish settling, and the rest remain in the liquid phase. According to formula (2), the calculation formula is as follows:

$$X = \sqrt{\frac{18\eta H/t_i}{g\left(\rho_s - \rho_w\right)}}. \tag{4}$$

Therefore, the particle size distribution can be calculated by measuring the $m_i - t_i$ curve, combined with formulas (3) and (4).

However, if the above method is to be extended to the measurement of floc gradation, appropriate changes must be made because the cement powder will undergo a hydration reaction in water, which will cause the density of the floc to change. Second, floc particles are nonstrict spheres, and the concept of an equivalent sphere should be used to replace floc particles equivalently.

First, the Stokes principle is used to analyze the force of the floc, as shown in Figure 2. Flocculant moves at a uniform speed because of its balanced force in water, which is affected by three forces: gravity, buoyancy, and viscous resistance.

Therefore, through the analysis,

$$G = F_V + F_b. \tag{5}$$

At the same time, according to the concept of equivalent spheres and the Stokes viscous resistance formula,
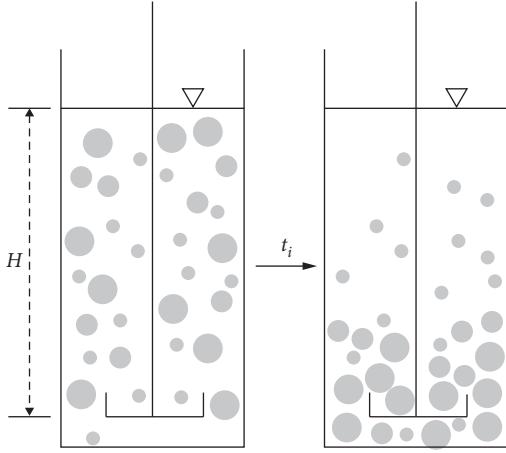
FIGURE 1: Schematic diagram of the settlement balance method.
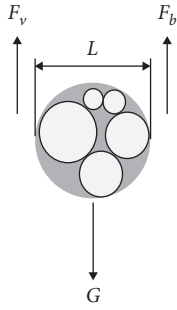
FIGURE 2: Force analysis of flocculation microbeads.

$$G = \frac{4}{3} \pi \rho_S g a^3 + \rho_w v_{\text{viod}} g,$$

$$F_b = \frac{4}{3} \pi \rho_w g a^3 + \rho_w v_{\text{viod}} g,$$

$$F_V = 3 \pi \eta L v_L,$$

$$L = (\beta + 1)^{1/3} * 2a.$$

$$(6)$$

Based on the above four formulas, the settling velocity of flocs can be obtained:

$$v_L = \frac{2g(\rho_s - \rho_w)a^2}{9\eta(\beta + 1)^{1/3}}. \tag{7}$$

It can be seen from the above formula that the sedimentation rate of floc is similar to Stokes sedimentation, which depends on the particle size of the floc equivalent sphere. The larger the particle size, the faster the sedimentation rate, and the smaller the particle size, the slower the sedimentation rate. However, it is noted that there is still a basic water demand rate β in the above formula, which should be considered in the experimental analysis. According to formula (7), the $m_i - t_i$ curve can be measured by the sedimentation balance method, and the particle size distribution of flocs can be calculated.

The equivalent particle size formula of the floc is

$$a_i = \sqrt{\frac{(\beta + 1)^{1/3} \times 18\eta H/t_i}{g(\rho_s - \rho_w)}}. \tag{8}$$

The equivalent particle size distribution function of the floc can be obtained according to the above formula and the measured $m_i - t_i$ curve.

2.1. Measurement Test of Cement Floc Gradation. Equations (7) and (8) can effectively measure the equivalent ball gradation of floc. The test device used in the test is shown in Figure 3. Its main components are the precision balance, boom, settling tray, and beaker. The suspender is connected to the weight of the balance to transfer the mass of the settling pan to the balance. The mass reduced by the weight of the balance is the mass of floc settlement increased in the settling pan. The mass-time curve of the balance can be recorded in real time to measure the floc gradation.

The specific steps of the test are as follows: (1) remove 20 g of slurry from the slurry test and put it into a settling beaker and inject a certain amount of water into the beaker for dilution so that the volume of water in the beaker reaches a fixed value, the purpose of which is to ensure that the settling height is consistent every time. (2) Stir the liquid in the beaker to make the flocs disperse evenly. (3) Place the settling tray at the bottom of the beaker. (4) With the boom connected to the balance, start the measurement program to record the curve of the balance quality as it changes with time. The test device is shown in Figure 3.

2.2. Experimental Results and Analysis of Floc Gradation. The floc gradation was measured using the test scheme. The sedimentation rate and time curve is shown in Figure 4 using a water-cement ratio of 1 : 1 as an example. The cumulative floc sedimentation rate first increased rapidly with time and then slowed. This occurs because large particles have a very fast sedimentation rate, and the cumulative sedimentation rate reached approximately 40% in only one second, with the diameter of the floc settled at this time larger than 100 μm. Next, the sedimentation rate of the floc began to decrease gradually, which was due to the diameter of the floc beginning to decrease, and the sedimentation rate reached 70% within approximately 50 s, when the diameter of the floc in the water was less than 5 μm. Then, the sedimentation rate decreased further until 200 s, when the sedimentation rate reached more than 90%, and there was almost no floc in the water.

The floc gradation curve was obtained by calculation, and the particle size distribution curves with different water-cement ratios (1 : 1, 1.6 : 1, and 2 : 1) are shown in Figure 5.

As shown in Figure 5, the floc particle size is mainly distributed between 10 and 100 μm, and the particle size of 1 to 10 μm accounts for a small part; the floc particle size increased from the minimum to about 80 μm, and its particle size frequency began to decrease, then the floc particle content gradually decreased, and finally the floc particle size reached less than 200 μm.
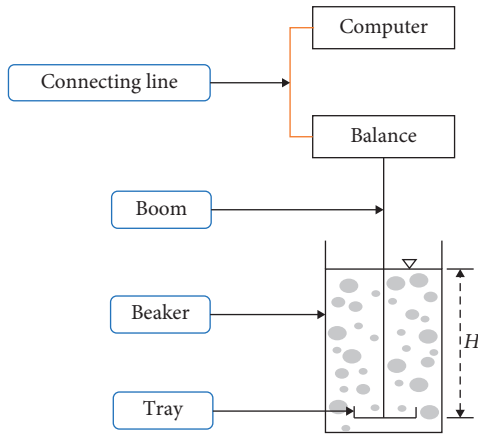
FIGURE 3: Settlement balance test.
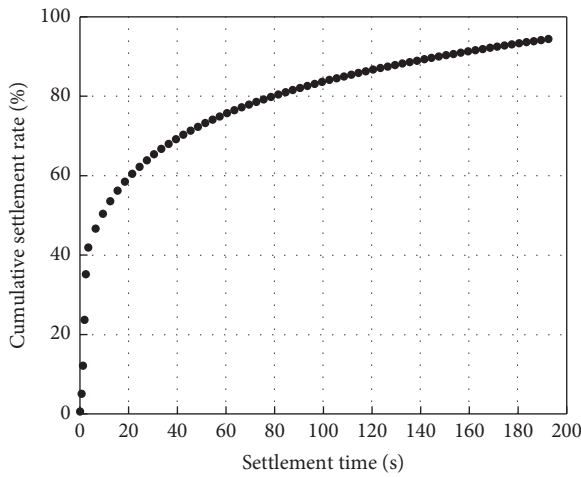
FIGURE 4: Sedimentation curve of flocculated microbeads.
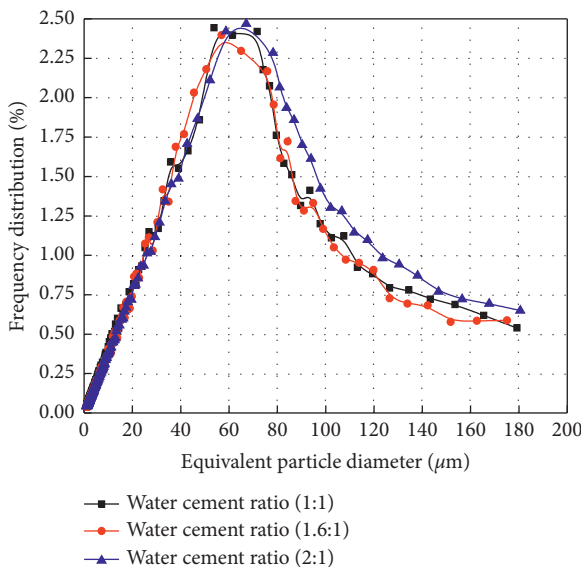
FIGURE 5: Gradation curve of flocculated microbeads.

Importantly, for mine backfill paste, the mass ratio of cement to water is generally above 1 : 1, which means that the volume of water is more than three times that of the cement powder, and the content of water in the mortar is far greater than that of cement. Under this condition, the distribution trend and content of the floc gradation are almost unchanged under three different water-cement ratios. It is noted that with the increase of the water-cement ratio, the curve shifts, but the amplitude is very small. Overall, the three sets of curves are almost at the same level, so it seems that they are within the mortar ratio range of paste. In essence, this is because the cement content in the mortar is small, and many gaps remain between floc particles after the cement hydration reaction is completed. However, due to the relatively large water content in mortar, the change in water quantity has little influence on the particle size of the floc equivalent sphere.

The results of the floc gradation test show that the particle size of floc is mainly distributed between 10 and 100 μm, and the particle size of 1 to 10 μm accounts for a small part; when the floc size reaches about 80 μm, its frequency begins to decrease, then gradually decreases, and finally the floc size reaches less than 200 μm. More than 99% of flocs have a Stokes particle size within 200 μm, so the boundary Stokes particle size of the flocs is 200 μm. Then, taking the Stokes particle size of 200 μm as the boundary condition, the ultrafine tailings particles should have a matching settling velocity (the liquid medium is water or pure viscous fluid), and on this basis, their mechanical effects in the movement process are the same.

Assuming that the settling velocity of cement floc with the largest Stokes equivalent particle size is v_x, the settling velocity of tailings in water should satisfy the following formula:

$$v_x \geq \frac{g\left(\rho_p - \rho_w\right)X^2}{18\eta}. \tag{9}$$

From this, the following formula is derived:

$$X \leq \sqrt{\frac{18\eta v_x}{g\left(\rho_p - \rho_w\right)}}, \tag{10}$$

where η is the viscosity of water, ρ_p is the apparent density of the tailings, and ρ_W is the apparent density of water. Substitute the settlement velocity formula of cement floc to obtain

$$X \leq \sqrt{\frac{8 \times 10^{-6}\left(\rho_s - \rho_w\right)}{(\beta + 1)^{1/3}\left(\rho_p - \rho_w\right)}}. \tag{11}$$

As shown in formula (11), the particle size range of ultrafine tailings is related to the density of water tailings, flocs, and the basic water demand rate of flocs. Compared with the definition of ultrafine tailings by most scholars, the particle size of ultrafine tailings is no longer a fixed particle size range but rather changes with the apparent density of the tailings.

The old and new definitions of ultrafine particles of waste rock and wind sand in Jinchuan are compared in Table 1. Under the old definition, the content of ultrafine waste rock and wind sand particles is 2%, so the two kinds of filling materials cannot be distinguished from the content of ultrafine particles. Thus, the numerical relationship between ultrafine particle content and rheological properties cannot be determined from the relationship. The new definition of ultrafine particles effectively avoids this problem. In the new definition, the content of ultrafine particles in waste rock and river sand is different, and there is a significant gap to conform to the facts. This proves that the new definition of ultrafine particles has wider applicability.

3. Rheological Test of Mine Backfill Paste

This paper mainly studies the relationship between ultrafine particles and the rheological properties of mine backfill paste. After ultrafine particles were defined, the rheological properties of the mine backfill paste with different filler ratios were evaluated by rheological testing.

The RheoCAD500 concrete rheometer produced in France was used in the test, as shown in Figure 6. The rheometer has two modes: manual control and program control. In manual mode, the torque or speed can be adjusted as required. The program control mode can be used with either a fast scheme or an expert scheme, which can be selected for torque or speed, respectively. The fast scheme is used to identify the maximum torque of the paste. The logarithmic curve of the shear rate and shear stress is first decreased and then increased, with the number and duration of each step programmed. The advantage of this program is that it does not need to know the sample well and will automatically identify the rotation speed corresponding to the required maximum torque. The expert scheme is flexible and can be set according to needs for the loading step time, but it does not provide the corresponding maximum speed under a given torque.

The double helix (1#) rotor was selected for the test. The internal program of the computer was set to increase the rotor speed from 0 rpm to 250 rpm and then decrease it from 250 to 0 rpm. There were 100 speed points in total. Each speed point lasted for 5 s, with the data at each 1 s interval averaged.

Expert mode was used in the study to detect the process of the paste changing from a solid state to a fluid state. The loading and thixotropic control of the RheoCAD500 rheometer is shown in Figure 7.

To ensure the rotor was covered with paste, the volume of paste added was from 30 mm to the top of the rotor and 30 mm from the bottom of the rotor. Temperature has a significant influence on rheological characteristics. To eliminate this influence, the test temperature was controlled at 20°C. The rheological test scheme of the mine backfill paste is shown in Table 2, where the mine backfill paste used in the test met the limit concentration condition of the paste, and the paste was homogeneous and had no segregation.

3.1. Basic Physical Parameters of Filling Materials. In this study, the crushed waste rock aggregate and desert sand of the Jinchuan Company were selected as filling aggregate for research. The basic physical parameters of waste rock and wind sand are shown in Table 3.

According to the safety technical standards for cemented filling, the maximum particle size of cemented filling aggregate should not exceed 1/5 of the conveying pipe diameter. Most conveying pipes in the Jinchuan Mine stope are steel pipes or plastic pipes with an inner diameter of 150 mm, so the maximum particle size of waste rock should not exceed 20 mm. Broken waste rock aggregate with a maximum particle size of 12 mm was used in this project. The gradation or particle size distribution of crushed stone aggregate is an important property of aggregate that determines the packing density of the aggregate, amount of filling cement, and pipe transportation performance.

It can be seen from Table 4 that the maximum size of the waste stone was 12 mm. Approximately, 50% of the waste stone was above 4.75 mm, and approximately, 70% was above 2.36 mm. The coarse particle content was too high and the fine material content was too low for the coarse particles to be suspended.

Desert sand is a natural aggregate collected naturally. For example, in desert areas, it is an ideal filling material with spherical particles and 90% quartz sand. See Tables 5 and 6 for the physical parameters of desert sand. The chemical composition of sand is shown in Table 5.

It can be seen from the above that desert sand is mainly SiO_2, and the content of SiO_2 is higher than that of the other four materials in the table, which are inert materials.

It can be seen from Table 6 that desert sand is less than 1.18 mm, with a particle size distribution characterized as "fewer coarse particles, more middle particles, and fewer fine particles." Approximately, 50% of the desert sand had a grain size below 0.3 mm, and more than 99% had a grain size below 0.6 mm. The content of the fine portion is too high, but the content of the coarse material is too small.

According to the definition of ultrafine particles, the particle size and content of ultrafine particles of waste rock and wind sand are calculated, and the results are shown in Table 7.

As shown in Table 7, the ultrafine particle content of desert sand is 31% and that of waste rock is 9%.

4. Influence of Aggregate Gradation on Rheological Parameters

The rheological properties and the Herschel–Bulkley (H-B) model of the waste rock-desert sand paste with different concentrations, cement contents, and proportions were obtained by rheological tests. The rheological parameters were mainly affected by paste properties such as concentration and cement content. Most studies have shown that the proportion of thick and thin parts of filling aggregate also significantly affects the rheological parameters of mine backfill paste.

TABLE 1: Comparison of new and old definitions of ultrafine particles.

Type	Ultrafine particle content (old definition) (%)	Ultrafine particle content (new definition) (%)
Waste rock (Jinchuan)	2	9
River sand (Jinchuan)	2	14.9

FIGURE 6: RheoCAD500 rheometer.
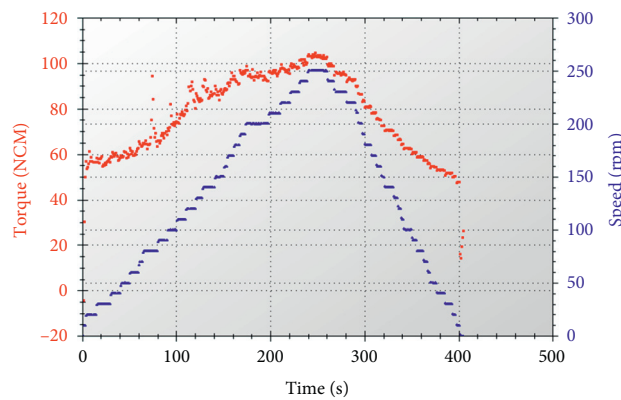
FIGURE 7: Loading and thixotropic control of the RheoCAD500 rheometer.

TABLE 2: Rheological test of paste filling material.

Type of aggregate	Aggregate gradation	Mass concentration (%)	Amount of cement added (kg/m^3)	Rheological parameters
Waste rock-desert sand	5 : 5 6 : 4 7 : 3	78, 79, 80, 81, 82, 83, 84	240, 260, 280, 310	

4.1. Effect of Ultrafine Particles on Plastic Viscosity of Paste.

Most studies show that the proportion of ultrafine content in mine backfill paste has a significant influence on the fluidity of the mine backfill paste. The ultrafine tailing content (excluding cement flocs) in the mine backfill paste and the plastic viscosity of mine backfill paste are plotted as follows:

As shown in Figure 8, the influence of the ultrafine aggregate content on the plastic viscosity of the mine backfill

TABLE 3: Physical parameters of filling aggregate.

Type of aggregate	Density (t/m³)	Loose bulk density (t/m³)	Moisture content (%)	Porosity (%)	Compactness of stacking (%)
Waste rock	2.625	1.623	1.255	40.4	59.6
Desert sand	2.570	1.519	0.219	40.9	59.1

TABLE 4: Gradation of waste rock.

Particle size (mm)	$(d_{imax} + d_{imin})/2$ (mm)	Frequency degree distribution (%)	Negative accumulation distribution (%)	Fuller distribution (%)	Frequency difference
9.5–12	10.75	10.62	100	100.00	−12.32
4.75 – <9.5	7.125	37.97	89.38	77.06	15.34
2.36 – <4.75	3.555	20.67	51.41	54.43	4.65
1.18 – <2.36	1.77	7.17	30.74	38.41	−4.00
0.6 – <1.18	0.89	7.57	23.57	27.23	−0.30
0.3 – <0.6	0.45	5.03	16	19.36	−0.64
0.15 – <0.3	0.225	2.43	10.97	13.69	−1.58
0.075 – <0.15	0.1125	2.97	8.54	9.68	−1.12
<0.075	0.0375	5.57	5.57	5.59	−0.02

TABLE 5: Chemical composition of desert sand.

Component	SiO_2	MgO	Fe_2O_3	SO3	Al_2O_3	CaO	Cr_2O_3	Na_2O	K_2O	TiO_2	Others
Desert sand	91.90	1.10	2.43	—	2.13	2.44	—	—	—	—	—

TABLE 6: Gradation of desert sand.

Particle size (mm)	$(d_{imax} + d_{imin})/2$ (mm)	Frequency degree distribution (%)	Negative accumulation distribution (%)	Fuller distribution (%)	Frequency difference
0.6–1.18	0.89	0.83	100	100.00	−37.42
0.3–<0.6	0.45	48.87	99.17	61.75	30.78
0.15–<0.3	0.225	21.17	50.30	43.67	8.38
0.075–<0.15	0.1125	21.13	29.13	30.88	8.08
<0.075	0.0375	8.00	8.00	17.83	−9.83

TABLE 7: Range and content of ultrafine particles of fill aggregate.

Type of aggregate	Apparent density (kg/m³)	Size range of ultrafine particles (<μm)	Content of ultrafine particles (%)
Desert sand	2570	120	31
Waste rock	2625	118	9

paste is the same at different graduations. With an increase in ultrafine aggregate content, the plastic viscosity of the mine backfill paste increases, and given the same gradation, the increasing trend of different cement contents is approximately the same, which shows that the ultrafine particle content is undoubtedly the main factor affecting the plastic viscosity of the mine backfill paste.

It is noted that the absolute plastic viscosity is different with different cement contents, and it is obvious from the figure that the plastic viscosity of the mine backfill paste increases with an increase in cement content (given the same ultrafine particle content), which means that the cement content is also a factor affecting the plastic viscosity of the mine backfill paste. Therefore, a comparison chart of the

relationship between the ultrafine particle content (including cement, floc, and ultrafine tailings) and plastic viscosity of different grades is analyzed.

As shown in Figure 9, the ultrafine particle content is positively correlated with plastic viscosity, and the plastic viscosity increases with an increase in ultrafine particle content. At the same mass concentration, the ultrafine particle content determines the plastic viscosity. Given the same ultrafine particle content, the higher the mass concentration of the mine backfill paste, the higher the plastic viscosity. Different grades will also cause a change in plastic viscosity. The higher the waste rock content of the mine backfill paste, the lower the plastic viscosity at the same concentration. The higher the waste rock content, the fewer
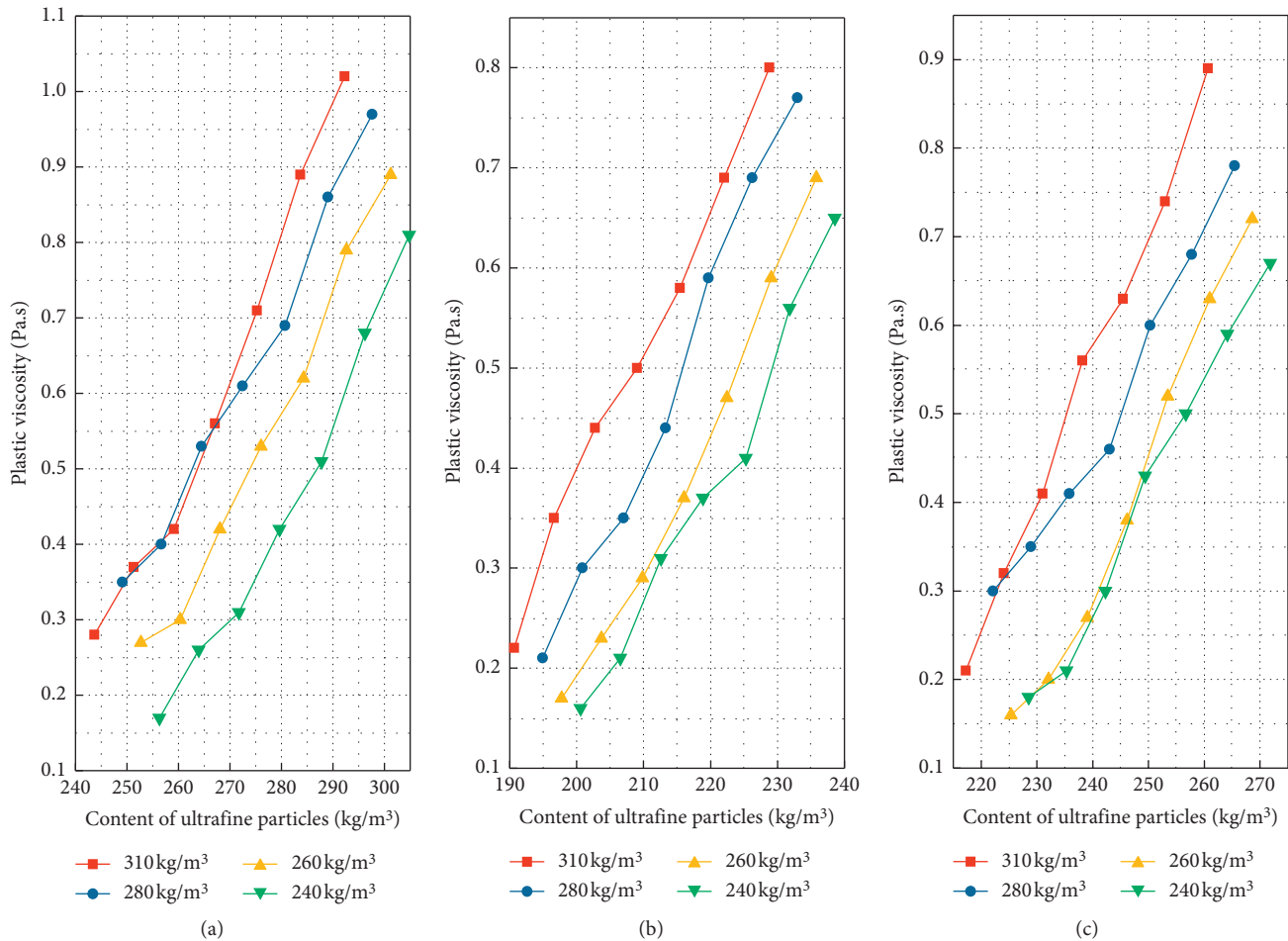
FIGURE 8: Relationship between the ultrafine tailing content and plastic viscosity under different gradations. (a) Waste rock : desert sand = 5 : 5. (b) Waste rock : desert sand = 6 : 4. (c) Waste rock : desert sand = 7 : 3.

the ultrafine particles in the mine backfill paste, leading to a decrease in plastic viscosity.

Thus, it is not scientifically appropriate to use only the content of ultrafine particles as a factor to measure the change in plastic viscosity of the mine backfill paste. In the mine backfill paste, the most important condition for paste formation is the addition of water, which fills the pores between particles. Excess water maintains the movement transmission between particles. The addition of water causes paste flow and paste formation. Thus, the relationship between ultrafine particle content and water determines the plastic viscosity of the mine backfill paste. Therefore, the ratio of the mass of the ultrafine particles to the mass of the water is taken as a dependent variable, and the relationship between it and the plastic viscosity of the paste is examined by graphing it.

As shown in Figure 10, the ratio of the mass of the ultrafine particles to the mass of the water under different gradations is taken as the plastic viscosity of the paste as the dependent variable. The plastic viscosity of the paste increases exponentially with an increase in the ratio. Regression analysis of the data shows that the data conform to an exponential equation. Regression results show that the R^2 of the fitted

curve is 94.13%, and the correlation between factors is very high. The analysis of variance (Table 8) shows that the F value of the regression curve is 4313, and the regression result of the equation is highly significant. Therefore, the ratio of ultrafine particles to water can be used as the standard to calculate and measure the plastic viscosity of mine backfill paste, which makes it more convenient to calculate and regress the plastic viscosity of the mine backfill paste.

4.2. Effect of Coarse Aggregate Content on Yield Stress of Paste. The rheological model of mine backfill paste meets the H-B model. It contains two important parameters: plastic viscosity and yield stress. Most studies show that the plastic viscosity of the paste is highly influenced by the fine particle content in the paste, while the yield stress is mostly influenced by the coarse aggregate in the paste.

To analyze the influence of the coarse aggregate in the paste on the plastic viscosity of the paste, the experimental data were plotted, taking the ratio of the coarse aggregate (aggregate larger than ultrafine particle size) to the water mass at the same gradation, different cement content, and different concentrations as independent variables and the
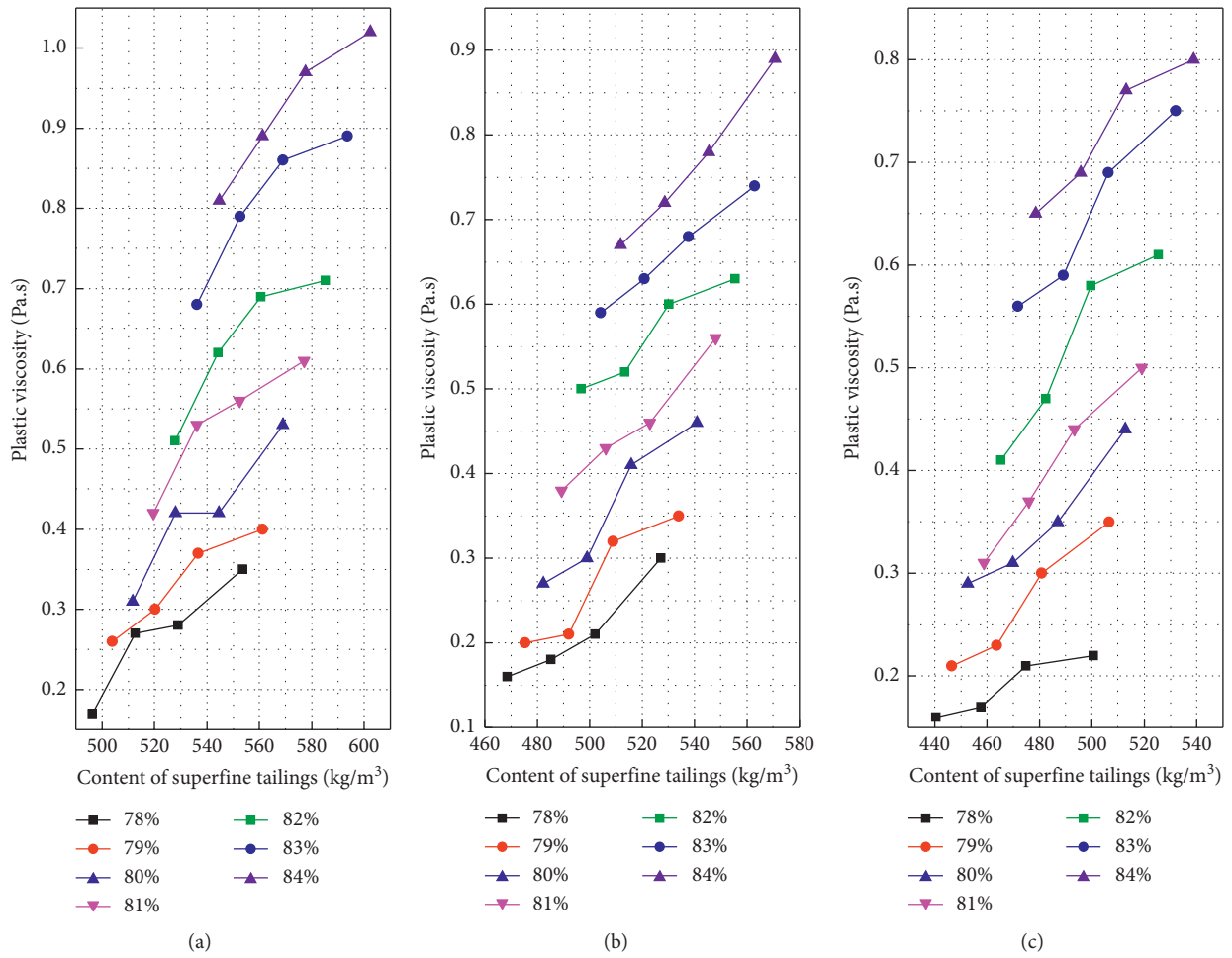
FIGURE 9: Relationship between ultrafine particle content and plastic viscosity at different gradations. (a) Waste rock : desert sand = 5 : 5. (b) Waste rock : desert sand = 6 : 4. (c) Waste rock : desert sand = 7 : 3.

Model	Allometric1
Equation	$y = a*x^\wedge b$
Plot	Plastic viscosity
a	0.17657
b	3.18822
Reduced Chi-Sqr	0.00364
R-square(COD)	0.92314
Adj. R-square	0.9222

● Plastic viscosity
— Fitting curve
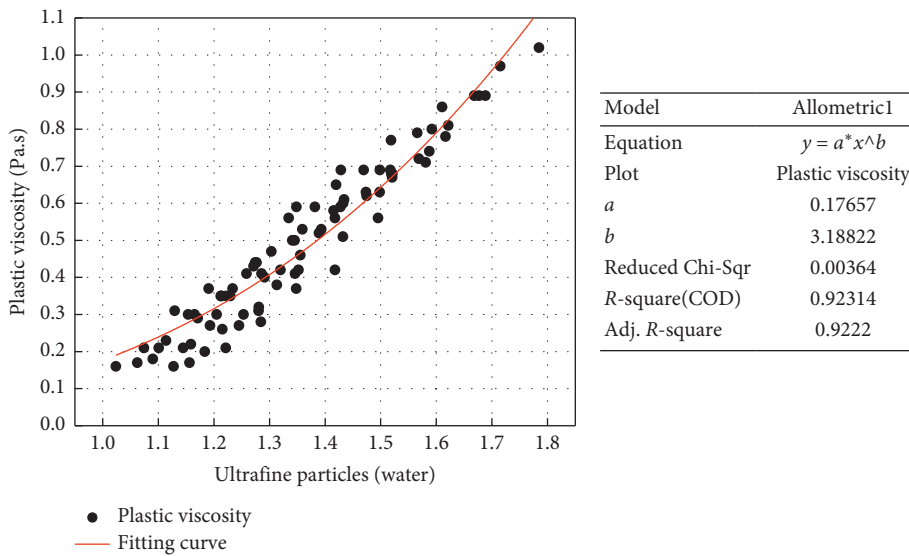
FIGURE 10: Relationship between the ratio of the mass of the ultrafine particles to the mass of the water and the plastic viscosity.

TABLE 8: ANOVA.

	DF	Sum of squares	Mean square	F value	Prob > F
Regression	2	23.64582	11.82291	4313.05949	0
Residual	82	0.22478	0.00274		
Uncorrected total	84	23.8706			
Corrected total	83	3.87821			

Model	Allometric1
Equation	$y = a*x^b$
Plot	Yield stress
a	5.25754
b	1.70581
Reduced Chi-S	5.35289
R-square(COD)	0.86792
Adj. R-square	0.86284

(a)

Model	Allometric1
Equation	$y = a*x^b$
Plot	Yield stress
a	4.63751
b	1.70862
Reduced Chi-S	4.43518
R-square(COD)	0.874
Adj. R-square	0.86915

(b)

Model	Allometric1
Equation	$y = a*x^b$
Plot	Yield stress
a	4.71376
b	1.31523
Reduced Chi-Sqr	1.40867
R-square(COD)	0.88439
Adj. R-square	0.87995

(c)
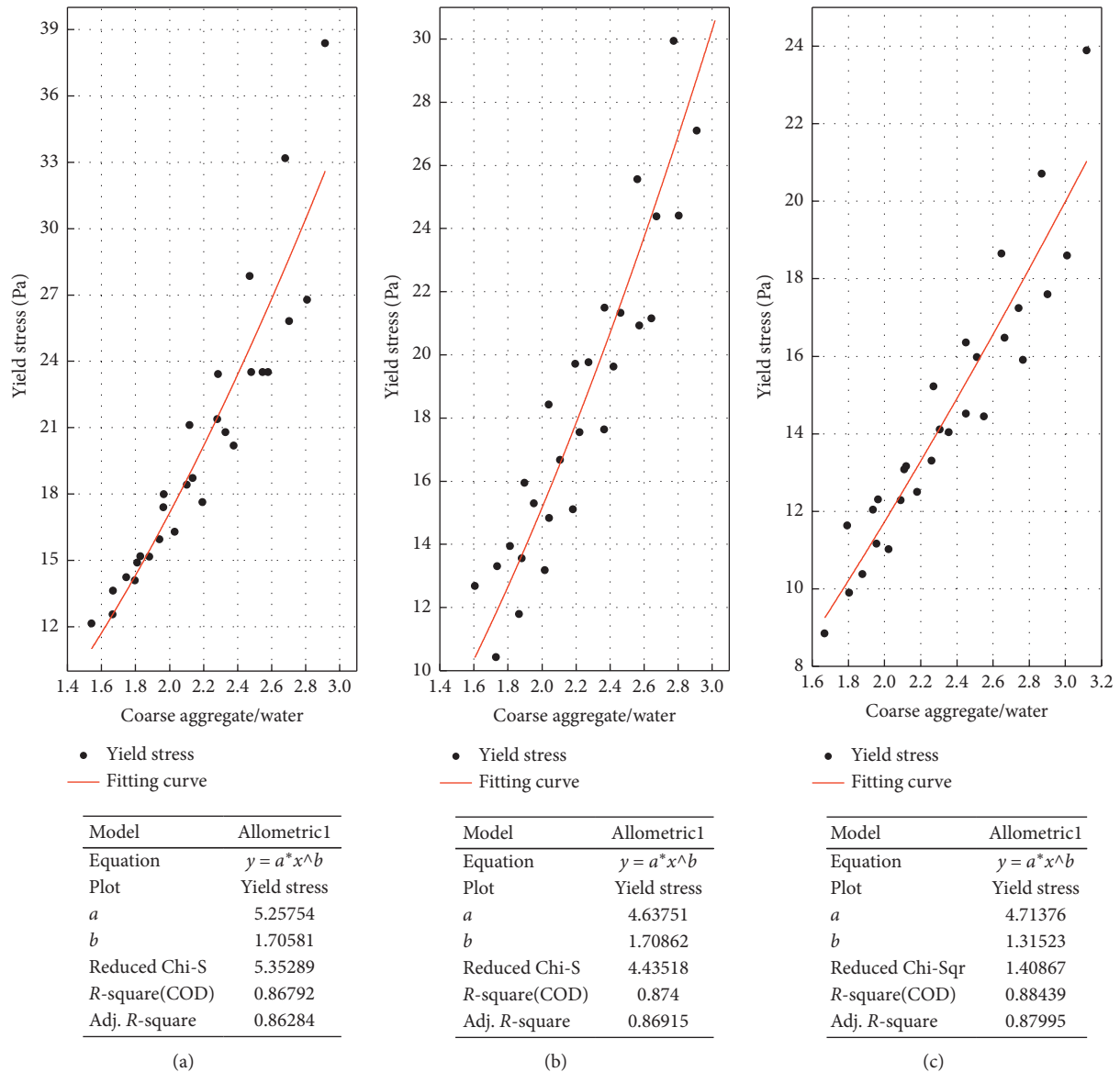
FIGURE 11: Relationship between the ratio of the mass of the coarse aggregate to the mass of the water and yield stress. (a) Waste rock : desert sand = 5 : 5. (b) Waste rock : desert sand = 6 : 4. (c) Waste rock : desert sand = 7 : 3.

yield stress of the mine backfill paste as the dependent variable.

As shown in Figure 11, the coarse aggregate content (aggregates larger than ultrafine particle size) in the waste rock-desert sand paste has a significant influence on the yield stress of the mine backfill paste. As shown in the figure, a change in coarse aggregate content causes a change in yield stress in the paste, and the ratio of coarse aggregate to water is positively correlated with yield stress; that is, an increase in coarse aggregate content leads to an increase in the yield stress of the paste. An increase in coarse aggregate content undoubtedly reduces the porosity of the paste and increases the possibility of friction between aggregates in the paste, which leads to an increase in the yield stress of the paste. The

above relations exist and are obvious in waste rock-desert sand paste with different gradations.

The yield stress of the paste increases exponentially with an increase in the ratio of aggregate to mass in the paste. The regression equation of a $5:5$ waste rock-desert sand ratio is $y = 5.26 \times^{1.71}$, $R^2 = 0.86$, the regression equation of a $6:4$ waste rock-desert sand ratio is $y = 4.64 \times^{1.71}$, $R^2 = 0.87$, and the regression equation of a $7:3$ waste rock-desert sand ratio is $y = 4.71 \times^{1.41}$, $R^2 = 0.88$. It can be seen from the above regression equations that the mass ratio of coarse aggregate to water can clearly characterize the yield stress of mine backfill paste with different proportions.

5. Conclusion

Mine backfill paste generally consists of tailings, coarse aggregate, cement, and water. In engineering practice, the definition of filling material classification is very vague. In this study, the size range of ultrafine particles was defined by the Stokes sedimentation test and hydraulic coarseness method. The relationship between ultrafine particles and the rheological properties of the paste was analyzed, and the following conclusions were obtained:

(1) The size range of ultrafine particles depends on the maximum hydraulic coarseness of the cement flocculation structure and the physical properties of the particles themselves. Within the range of the water-cement ratio of mine backfill paste, the maximum hydraulic coarseness of the cement flocculation structure changes slightly, and the Stokes particle size of the floc is less than $200\,\mu$m. The range of ultrafine particles of fine aggregates, such as tailings, can be determined on this basis, which comprehensively considers the physical characteristics and size of particles and has relatively strict physical and mathematical definitions.

(2) There is a strong correlation between the ultrafine particle content in the mine backfill paste and the rheological properties of the mine backfill paste. The higher the ultrafine particle content, the greater the plastic viscosity of the mine backfill paste, with an exponentially increasing growth rate. The higher the coarse aggregate content, the greater the yield stress of the mine backfill paste. This conclusion is consistent with most studies in the literature. The mass ratio of ultrafine particle content to water content in paste reflects the amount of ultrafine particle content. The model of the rheological properties of waste rock-desert sand series paste is established by regression analysis. The model is simple, with few factors and high correlation. It can accurately predict the rheological properties of the mine backfill paste, which can be beneficial in guiding engineering practice.

Data Availability

All the data used to support this study are included within the article.

Conflicts of Interest

The authors declare that they have no conflicts of interest.

References

[1] Z. Zhu, T. Yang, M. Zhao et al., "Preliminary study on critical criteria of floc development and floc network development in cohesive fine sediment," *Sediment Research*, no. 1, pp. 20–25, 2009.

[2] G. Yin, X. Jing, W. Zuo'an et al., "Model test and field measurement of seepage characteristics of coarse and fine tailings dams," *Chinese Journal of Rock Mechanics and Engineering*, vol. 29, no. s2, pp. 3710–3718, 2010.

[3] M. Fall, J. Célestin, and H. F. Sen, "Potential use of densified polymer-pastefill mixture as waste containment barrier materials," *Waste Management*, vol. 30, no. 12, pp. 2570–2578, 2010.

[4] O. H. Wallevik and J. E. Wallevik, "Rheology as a tool in concrete science: the use of rheographs and workability boxes," *Cement and Concrete Research*, vol. 41, no. 12, pp. 1279–1288, 2011.

[5] H. Wang, A. Li, A. Wu et al., "New definition of paste based on full tailings gradation," *Journal of Central South University (Natural Science Edition)*, no. 2, pp. 557–562, 2014.

[6] A. Wu, S. Yang, H. Wang et al., "Present situation and trend of ultra-fine paste disposal technology," *Mining Technology*, vol. 11, no. 3, pp. 4–8, 2011.

[7] R. Kang, P. Liang, and Z. Yao, "Study on fluidity of coarse aggregate filling slurry in Duda lead-zinc mine," *Mining Research and Development*, no. 3, pp. 14–18, 2017.

[8] W. Xu, B. Yang, S. Yang et al., "Experimental study on the correlation between rheological properties and particle size distribution of gangue filling slurry," *Journal of Central South University (Natural Science Edition)*, vol. 47, no. 4, pp. 1282–1289, 2016.

[9] A. J. Mehta, "Problems in linking the threshold condition for the transport of cohesionless and cohesive sediment grain," *Journal of Coastal Research*, vol. 10, no. 1, pp. 170–177, 1994.

[10] H. Oshida, H. Masuda, K. Fukui et al., "Particle size measurement with an improved sedimentation balance method and microscopic method together with computer simulation of necessary sample size," *Advanced Powder Technology*, vol. 12, no. 1, pp. 79–94, 2001.

[11] K. Fukui, H. Yoshida, and T. Higashiguchi, "Effects of initial slurry concentration distribution on the particle size distribution measured with a sedimentation balance method," *Advanced Powder Technology*, vol. 15, no. 2, pp. 181–200, 2004.

Research Article

Damage Strengthening Constitutive Model of Cemented Paste Backfill

Kangli Cheng [ID],[1] **Bingbing Tu** [ID],[2] **Lang Liu** [ID],[1,3] **Bo Zhang** [ID],[1] and **Huafu Qiu** [ID][1]

[1]*Energy School, Xi'an University of Science and Technology, Xi'an 710054, China*
[2]*College of Science, Xi'an University of Science and Technology, Xi'an 710054, China*
[3]*Key Laboratory of Western Mines and Hazards Prevention, Ministry of Education of China, Xi'an 710054, China*

Correspondence should be addressed to Kangli Cheng; xustckl@163.com, Bingbing Tu; tubingbing9@xust.edu.cn, Lang Liu; liulang@xust.edu.cn, and Bo Zhang; bozhang@xust.edu.cn

In order to consider the influence of mesoscopic characteristics of materials on the constitutive model of cemented paste backfill (CPB), the uniaxial compression variables and the damage constitutive model, considering the influence of porosity and pore size of filling materials, were derived based on the strain equivalence principle and Weibull probability distribution function. The nuclear magnetic resonance (NMR) tests and unconfined compression strength (UCS) tests were carried out on 8 groups of CPB specimens with different slurry concentrations and cement-tailings ratios. Then, the expression of damage strengthening coefficient is determined, and the stress-strain curves measured by the theoretical model were compared with the experimental ones. The results show that the uniaxial compression constitutive model proposed is in good agreement with UCS test results and can effectively describe the damage evolution law and the development process of stress-strain curve of CPB under uniaxial compression. The 28-day compressive strength of CPB can reach 8 MPa, the residual strength is about 1~2 MPa, the elastic modulus is about 200~2000 MPa, and the porosity is about 3~5%. The CPB with slurry concentration of 74% and 76% and cement-tailings ratio of 1 : 4 and 1 : 6 is more reasonable, and the relevant mechanical parameters are more stable.

1. Introduction

In recent years, the global industrialization process is accelerating, the demand for mineral resources is increasing, the mining rate is increasing, and the tailings accumulation is increasing [1]. The storage of tailings wastes not only wastes land resources but also causes increasingly serious environmental problems (water pollution, air pollution, surface collapse, vegetation destruction, etc.) [2, 3]. Backfill mining technique is widely used in underground mine engineering because of its advantages of saving tailings waste storage place, reducing environmental pollution, effectively controlling ground pressure in goaf, ensuring safe operation, and so on [4–6]. Cemented paste backfill (CPB) is a kind of multiphase material formed by mixing a certain proportion of tailings and water with cement as the main cementation material and through mixing, vibrating, curing, and other

processes. It has the advantages of no pollution, low energy consumption, and good roof connection performance when used in underground mine filling [7, 8]. Whether the strength of CPB meets the requirements is an important basis for the effective implementation of backfill mining technology [9, 10].

At present, scholars have systematically studied the mechanical properties of CPB and achieved remarkable results. Hou et al. [11] studied the damage characteristics and energy dissipation analysis of CPB with different curing ages under uniaxial compression. Zhao et al. [12] explored the destruction process and mechanical properties of CPB with different slurry concentrations through uniaxial compression acoustic emission test. Yi et al. [13] discussed the damage and destruction evolution process of CPB with different waste rock contents through uniaxial compression real-time CT scanning mechanical test. In order to obtain the

constitutive model of filling material, Liu et al. [14] and Zhao et al. [15] established the damage constitutive model of CPB by introducing the effective damage rate parameter on the basis of Weibull distribution law. Wang et al. [16] set up the damage evolution and constitutive model of CPB by using the damage mechanics theory and considering the delamination effect and studied the mechanical properties of different layered CPB. Cui and Fall [17] built an elastic-plastic evolution model to research the important role of hydration of gelling agent on the mechanical behavior and property evolution of CPB. Wang et al. [18] established the paste damage constitutive model at different initial temperatures and proposed the paste temperature-time coupling damage constitutive model through parameter regression of the constitutive model. Cui and Fall [19] set up a thermo-hydro-mechanical chemical coupling model for CPB and studied the mechanical characteristics under multiphysical environment. Liu et al. [20] built the constitutive equation based on damage mechanics through the mechanical test of CPB with different cement-tailings ratios and discussed the reasonable matching between CPB and rock.

Wittmann et al. [21] believed that due to the differences in representational scales and research methods, according to the internal structure characteristics of the cemented tailings backfill, the mechanical properties of the backfill can be generally described in three different scales (macroscale, mesoscale, and microscale). In macroscale, the cemented tailings backfill is a single homogeneous body formed by mixing cement, tailings, and water cementing. Studies at this scale cannot reveal the relationship between the internal structure, composition, and mechanical properties of the backfill [22]. In mesoscale, the cemented tailings backfill can be regarded as a multiphase composite material composed of tailings, gel matrix, and initial defects (pores and cavities). Existing researches on the constitutive model of CPB mostly consider the influence of external factors such as material composition and ratio, external environment, and loading mode. In other words, the mechanical properties of backfill were studied from the macroscopic scale, while the influence of microscopic properties such as pore defects in the material on the mechanical effects of backfill was ignored. During the process of hydration and hardening, the intercalated pores of hydrated calcium silicate (C-S-H) gel, capillary pores formed by evaporation and loss of water not involved in hydration reaction, and bubble pores formed by residual air during slurry mixing formed in CPB [23, 24]. This makes the CTB have the properties of porous material, the pore distribution is complex, and the pore size spans the microcosmic and microscale. The formation, destruction, and expansion of initial pores will have a significant impact on the strength, stiffness, damage failure, and other basic mechanical parameters [25–28].

Considering the influence of mesoscopic pore characteristics of CPB, a damage constitutive model based on damage strengthening coefficient is derived. Then, the effectiveness of the model is verified by combining nuclear magnetic resonance (NMR) test and unconfined compression strength (UCS) test, and the damage evolution law of CPB under uniaxial compression is analyzed, which

provides a basis for understanding the basic mechanical properties of CPB.

2. Damage Strengthening Coefficient

Porosity and pore size are important parameters affecting the mechanical properties of CPB [29–31]. In this paper, the porosity and pore size of the CPB specimen are taken as the initial defect measurement index of the material, and the damage strengthening coefficient of the CPB is defined as

$$\alpha = f(P, d), \tag{1}$$

where α is the damage strengthening coefficient; P is the porosity; and d is the pore size.

Referring to the functional relationship between pore size and strength of concrete material [31], the relationship between damage strengthening coefficient of CPB and porosity and pore size is defined as

$$\alpha = Gd^H (1 + P)^k + c, \tag{2}$$

where G, H, and c are the test parameter, which are related to the slurry concentration, cement-tailings ratio, tailings type, cement type, etc.

3. Damage Constitutive Model

3.1. Model Establishment. According to the principle of strain equivalence proposed by Professor Lemaitre [32], a famous French scholar, any stress-strain constitutive relation of damaged materials under uniaxial loading can be derived from the constitutive equation of nondestructive materials, as long as the nominal stress in the constitutive relation of nondestructive materials is replaced by the effective stress after damage. Assuming that the effective bearing area of the CPB specimen is A in the nondestructive state and A_1 after loading damage, the nominal stress of the section under loading is as follows:

$$\sigma = \frac{F}{A}. \tag{3}$$

The effective stress σ^* on the effective section is

$$\sigma^* = \frac{F}{A_1}. \tag{4}$$

The damage variable D is defined as

$$D = \frac{A - A_1}{A}. \tag{5}$$

In combination with equations (3)–(5), it is obtained that

$$\sigma^* = \frac{\sigma}{(1 - D)}. \tag{6}$$

Then,

$$\sigma = (1 - D)\sigma^*. \tag{7}$$

From $\sigma^* = E\varepsilon$, the damage constitutive equation of CPB can be obtained as follows:

$$\sigma = E(1-D)\varepsilon, \tag{8}$$

where E is the elastic modulus of CPB.

Previous studies [14, 15] have shown that the mechanical properties of mesoscopic heterogeneity of quasibrittle materials obey a certain statistical law. According to the shape characteristics of stress-strain curve of CPB, the nominal damage variable D_0 is selected to obey the two-parameter Weibull distribution equation:

$$D_0 = 1 - \exp\left[-\left(\frac{\varepsilon}{a}\right)\right]^m, \tag{9}$$

where ε is the strain; m and a are the coefficient related to the physical and mechanical properties of CPB, and it is not negative.

At the initial stage of compression, the pores in the CPB are compacted. The existence of pore structure weakens the material properties of CPB and accelerates the damage rate. In this paper, the influence of pore structure on the damage degree of CPB specimen is characterized by the damage strengthening coefficient as shown in equation (2), and the damage variable D is defined as

$$D = \alpha D_0. \tag{10}$$

By introducing equation (9) into equation (11), we obtain

$$D = \alpha\left(1 - \exp\left[-\left(\frac{\varepsilon}{a}\right)\right]^m\right). \tag{11}$$

By introducing equation (11) into equation (8), it is obtained that

$$\sigma = E\varepsilon\left\{1 - \alpha\left(1 - \exp\left[-\left(\frac{\varepsilon}{a}\right)^m\right]\right)\right\} \tag{12}$$

The results are as follows:

$$\sigma = (1-\alpha)E\varepsilon + \alpha E\varepsilon\,\exp\left[-\left(\frac{\varepsilon}{a}\right)^m\right]. \tag{13}$$

Under the action of stress, the CPB specimens are gradually damaged, and the internal structure is destroyed. When the strain exceeds a certain limit and the external stress is at a low stress level again, the internal structural damage tends to be stable, but the specimen still has a certain residual strength. Based on this, the damage threshold γ is introduced. When the strain is γ, the damage variable in the CPB reaches the maximum damage D_γ, and the corresponding stress is residual strength. Then, the two-stage damage variable and damage constitutive equation are defined:

$$D = \begin{cases} \alpha\left(1 - \exp\left[-\left(\frac{\varepsilon}{a}\right)\right]^m\right), & (\varepsilon < \gamma) \\ \\ D_\gamma, & (\varepsilon \geq \gamma) \end{cases}, \tag{14}$$

$$\sigma = \begin{cases} (1-\alpha)E\varepsilon + \alpha E\varepsilon\,\exp\left[-\left(\frac{\varepsilon}{a}\right)^m\right], & (\varepsilon < \gamma) \\ \\ \sigma_\gamma, & (\varepsilon \geq \gamma) \end{cases}.$$

3.2. Model Establishment.

According to the damage constitutive equation of CPB, the stress-strain curve of the whole process is obtained as shown in Figure 1. It can be seen from Figure 1 that the constitutive curve satisfies the following four boundary conditions:

(1) $\varepsilon = 0$, $\sigma = 0$; (2) $\varepsilon = 0$, $d\sigma/d\varepsilon = E$; (3) $\sigma = \sigma_{pk}$, $\varepsilon = \varepsilon_{pk}$; (4) $\sigma = \sigma_{pk}$, $d\sigma/d\varepsilon = 0$, where σ_{pk}, ε_{pk}, and E are the peak stress, peak load strain, and elastic modulus.

According to (1), (2), (3), and (4) of the stress-strain curve, the sum of two undetermined parameters in equation (14) can be determined. Among them, conditions (1) and (2) are naturally satisfied.

By introducing condition ③ into equation (13), it is obtained that

$$\sigma_{pk} = (1-\alpha)E\varepsilon_{pk} + \alpha E\varepsilon_{pk}\exp\left[-\left(\frac{\varepsilon_{pk}}{a}\right)^m\right]. \tag{15}$$

Then,

$$\frac{\sigma_{pk}}{E\varepsilon_{pk}} = (1-\alpha) + \alpha\,\exp\left[-\left(\frac{\varepsilon_{pk}}{a}\right)^m\right]. \tag{16}$$

The derivation of (13) is obtained:

$$\frac{d\sigma}{d\varepsilon} = (1-\alpha)E + \alpha E\,\exp\left[-\left(\frac{\varepsilon}{a}\right)^m\right]\left[1 - m\left(\frac{\varepsilon}{a}\right)^m\right]. \tag{17}$$

By substituting condition (4) into equation (17), it is obtained that

$$\frac{d\sigma_{pk}}{d\varepsilon_{pk}} = (1-\alpha)E + \alpha E\,\exp\left[-\left(\frac{\varepsilon_{pk}}{a}\right)^m\right]\left[1 - m\left(\frac{\varepsilon_{pk}}{a}\right)^m\right]. \tag{18}$$

Because of the elastic modulus $E \neq 0$, then,

$$(1-\alpha) + \alpha\,\exp\left[-\left(\frac{\varepsilon_{pk}}{a}\right)^m\right]\left[1 - m\left(\frac{\varepsilon_{pk}}{a}\right)^m\right] = 0. \tag{19}$$

The result is obtained from simultaneous solution equations (16) and (17):

$$\left(\frac{\varepsilon_{pk}}{a}\right)^m = \frac{\left(\sigma_{pk}/E\varepsilon_{pk}\right)}{m\left[\left(\sigma_{pk}/E\varepsilon_{pk}\right) - (1-\alpha)\right]}. \tag{20}$$

Make the equation $t = (\sigma_{pk}/E\varepsilon_{pk}) - (1-a)$ true; we can get that

$$m = \frac{-\sigma_{pk}}{E t\varepsilon_{pk}(\ln t - \ln \alpha)},$$

$$a = \varepsilon_{pk}^{((m+1)/m)}\left[\frac{mtE}{\sigma_{pk}}\right]^m. \tag{21}$$

4. Laboratory Test

4.1. Material Characteristics.

CPB is mainly composed of cementitious agent, aggregate, and water. The test water is ordinary urban tap-water. The test cement is PO425 [33, 34] ordinary Portland cement produced by Jidong Heidelberg (Jingyang) Cement Co., Ltd. The test aggregate is tailings
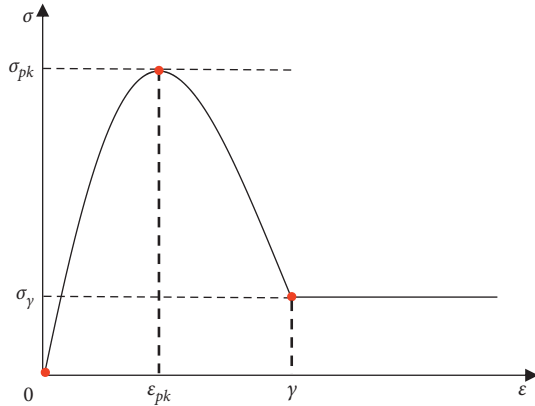
FIGURE 1: Stress-strain curves.

from a copper mine. The density of cement clinker is 2.87 g/cm^3, grain size d_{50} is $11\,\mu$m, the initial setting time is 162 min, the final setting time is 203 min, and the 28-day compressive strength is 41.5 MPa. The main chemical composition of cement is CaO (accounting for 64.1%), SiO$_2$ (accounting for 19.2%), Al$_2$O$_3$ (accounting for 4.50%), Fe$_2$O$_3$ (accounting for 3.33%), MgO (accounting for 1.82%), and S (accounting for 1.06%).

Figure 2(a) shows the particle size distribution of tailings measured by laser particle size distribution analyzer. The figure shows that $d_{10} = 8.54\,\mu$m, $d_{20} = 66.9\,\mu$m, $d_{50} = 129\,\mu$m, $d_{60} = 163\,\mu$m, the nonuniformity coefficient $C_u = 19.08$, and the curvature coefficient $C_c = 3.22$. The grading curve of tailings is smooth and continuous, the slope is gentle, the grading is good, the compactness is easy to obtain, the compressibility is low, the strength is high, and the engineering property is excellent. Figure 2(b) shows the chemical composition of tailings measured by X-ray fluorescence spectrometer (XRF). Among them, CaO content is less than 10%, which is low calcium tailings.

4.2. Specimen Making.
According to GB/T 50266-2013 "standard for test methods of engineering rock mass" [35], eight groups of cylinder specimens with cement-tailings ratios of 1 : 4, 1 : 6, 1 : 8, and 1 : 10, slurry concentration of 70%, 72%, 74%, 76%, and 78%, and curing age of 28 days under standard environment were made. The number of specimens in each group is 4, including 3 UCS tests and 1 NMR test. The slurry composition of CPB is shown in Table 1, and the specific test idea and process are shown in Figure 3.

4.3. Analysis on the Influence of Slurry Concentration and Cement-Tailings ratio

4.3.1. Analysis of NMR Test Results.
Figure 4 shows the influence of slurry concentration and cement-tailings ratio on porosity and pore size of CPB. It can be seen from Figure 4(a) that with the increase of the slurry concentration, the porosity of the CPB gradually decreases. When the slurry concentration increases from 72% to 74%, the

porosity obviously decreases with a larger gradient, while with the continuous increase of the slurry concentration, the porosity remains about 3%. It can be seen from Figure 4(b) that with the decrease of the cement-tailings ratio, the porosity of the CPB gradually increases. When the cement-tailings ratio decreases from 1 : 8 to 1 : 10, the porosity increases obviously with a larger gradient, while when the cement-tailings ratio increases from 1 : 8 to 1 : 4, the porosity remains about 3%.

It can be seen from Figures 4(a) and 4(b) that the proportion of large pore (>50 nm) gradually increases and that of small pore (<50 nm) gradually decreases with the increase of slurry concentration or cement-tailings ratio of CPB. The porosity of CPB body is about 3~5%. From the point of view of microscopic characteristics, the slurry concentration with 74% and 76% and cement-tailings ratio with 1 : 4 and 1 : 6 are reasonable.

4.3.2. Analysis of USC Test Results.
Figure 5 shows the influence of slurry concentration and cement-tailings ratio of CPB on elastic modulus, peak strength, and residual strength. It can be seen from Figure 5 that the elastic modulus, peak strength, and residual strength of the CPB increase with the increase of the slurry concentration or the cement-tailings ratio. The 28-day compressive strength can reach 8 MPa, residual strength can reach 1~2 MPa, and elastic modulus is approximately 200~2000 MPa, respectively. When the slurry concentration is 74% and 76%, the mechanical properties are similar.

5. Model Validation and Analysis

5.1. Theoretical Model Validation.
The basic mechanical parameters such as elastic modulus, peak stress, and peak load strain can be obtained from the UCS test of CPB. Combined with the model parameter equation (equations (14), (20), and (21)), the damage strengthening coefficient a and damage threshold γ of 8 groups of CPB specimens under different slurry concentrations and cement-tailings ratios can be fitted, and the corresponding Weibull statistical distribution parameters m and a can be calculated, as shown in Table 2. The elastic modulus of CPB is calculated by E_{50} method [18, 36]. E_{50} refers to 50% of the maximum stress of concrete materials in the whole process from loading to destruction divided by its corresponding strain value. The residual strength is taken as the maximum curvature point in the descending section of the stress-strain curve and the average stress after the point. The damage threshold is the strain value at the same stress value as the residual strength in the theoretical curve.

In order to validate the correctness of the damage constitutive model of CPB based on the damage strengthening coefficient established in this paper, the constitutive model calculated by the theoretical model is compared with the UCS test results, and the evolution of damage variables in the whole stress-strain process is analyzed, as shown in Figure 6.

(a)

(b)
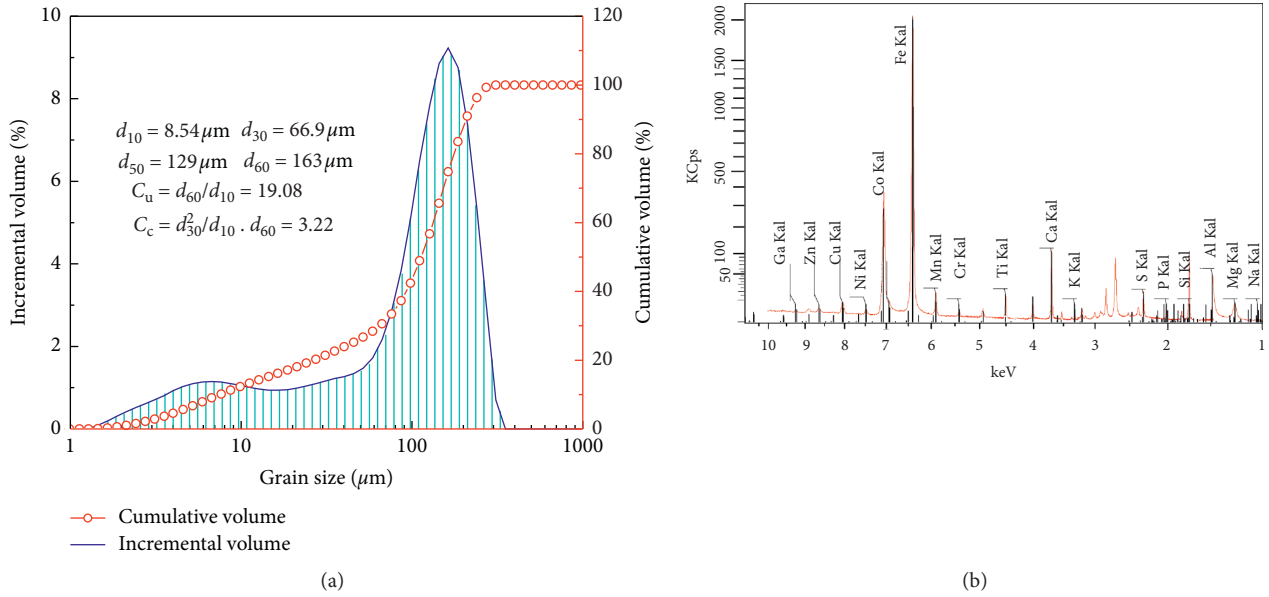
FIGURE 2: Material characteristics of tailings. (a) Particle size distribution of tailings; (b) X-ray fluorescence pattern of tailings.

TABLE 1: Composition of filling slurry.

Number	Cement-tailings ratio	Slurry concentration (%)	Tailings (kg)	Cement (kg)	Water (kg)
1	1 : 4	70	1.08	0.27	0.58
2	1 : 4	72	1.11	0.28	0.54
3	1 : 4	74	1.14	0.28	0.50
4	1 : 4	76	1.17	0.29	0.46
5	1 : 4	78	1.20	0.30	0.42
6	1 : 6	76	1.25	0.21	0.46
7	1 : 8	76	1.30	0.16	0.46
8	1 : 10	76	1.33	0.13	0.46
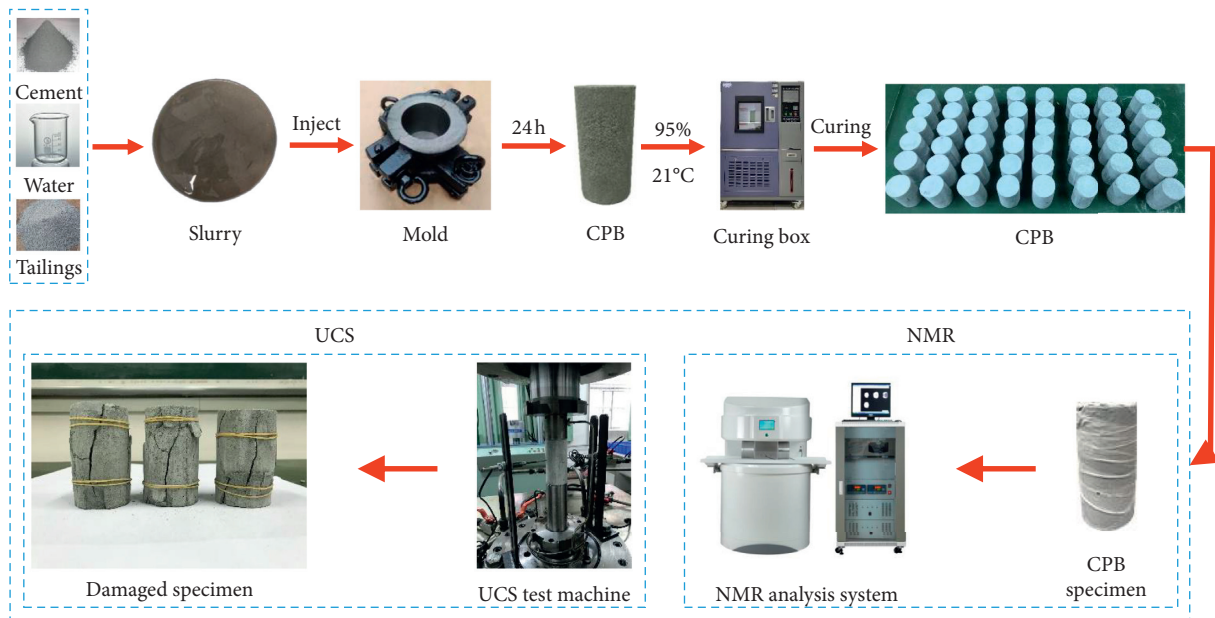
FIGURE 3: Experimental flow picture.

(a)

(b)
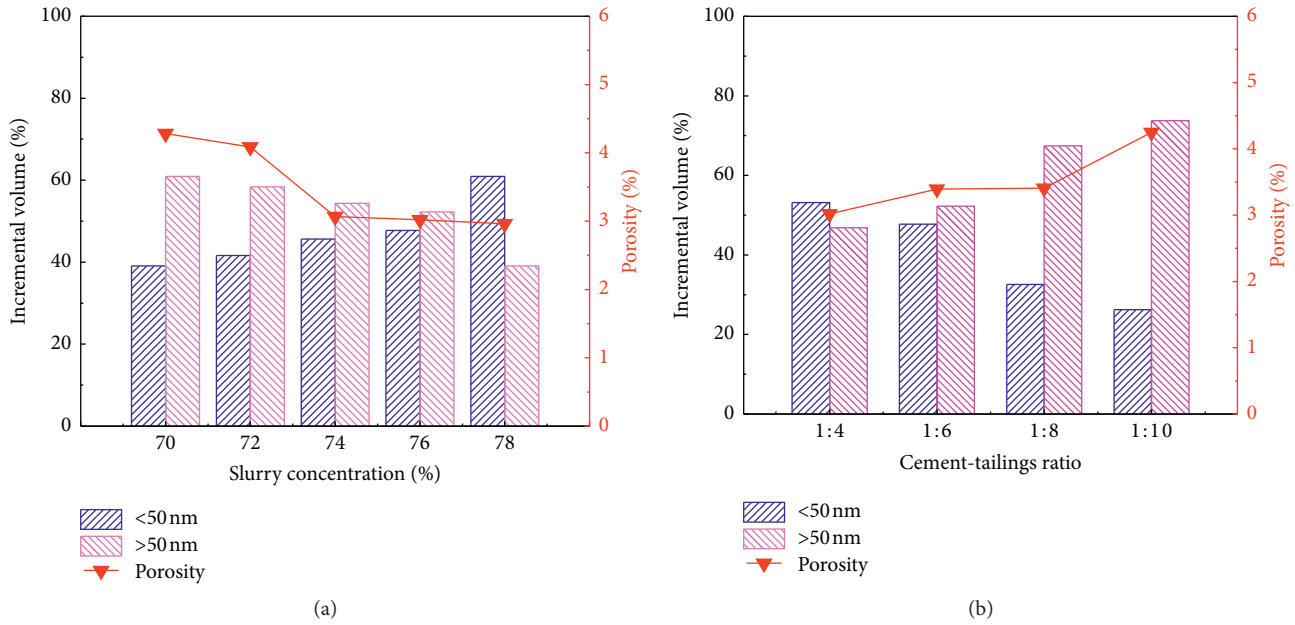
FIGURE 4: Porosity and pore size distribution of CPB. (a) Slurry concentration effect; (b) cement-tailings ratio effect.

(a)

(b)
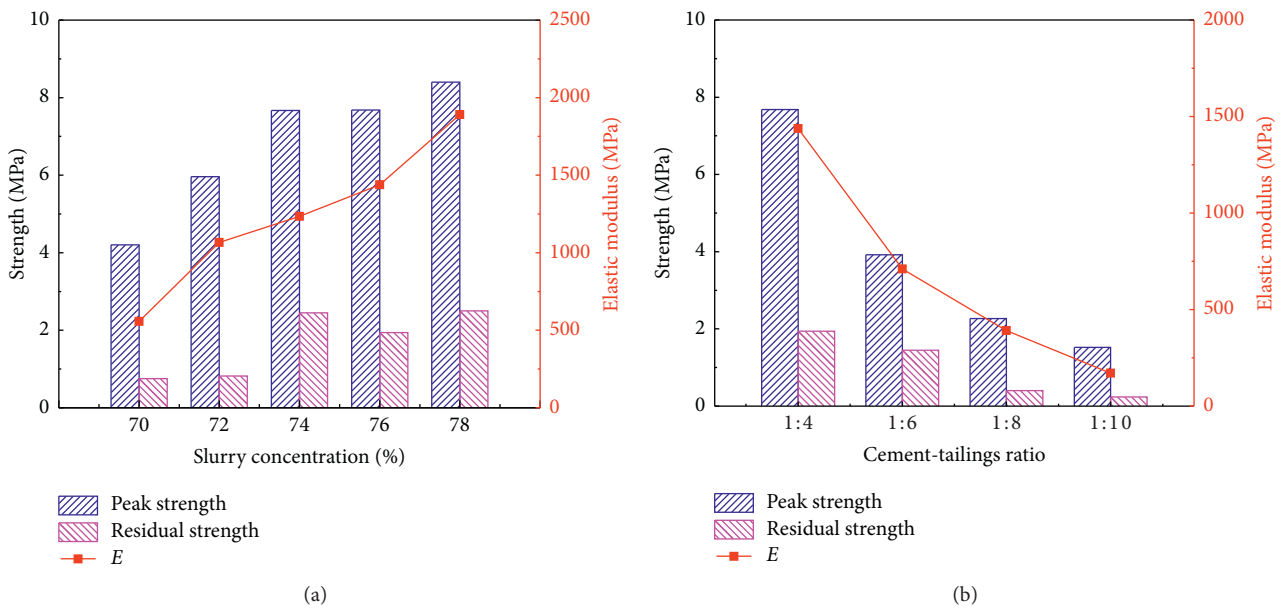
FIGURE 5: Basic mechanical parameters of CPB. (a) Slurry concentration effect; (b) cement-tailings ratio effect.

It can be seen from Figure 6 that the theoretical curve obtained from the damage constitutive calculation based on the damage strengthening coefficient proposed in this paper is in good agreement with the UCS test curve, which can effectively reflect the basic mechanical characteristics of the CPB under uniaxial compression. It can be seen from the distribution of damage variables in Figure 6 that the damage development trend of CPB with different cement-tailings ratios is similar, and they all approximate to the growth trend of the shape of the word "factory." With the increase of

axial strain, the damage variable increases gradually. When the axial strain reaches the peak load strain, the damage increases exponentially. When the axial strain reaches the damage threshold, the damage variable tends to 90%. When the damage variable is about 0.25, the stress reaches the peak. The ratio of peak load strain to damage variable corresponding to damage threshold is about 0.25 under different cement-tailings ratios. The results show that when the damage variable reaches 1/4 of the threshold damage variable, the stress-strain curve shows a downward trend, the

TABLE 2: Parameters of damage constitutive model.

Number	Elastic modulus (MPa)	Peak stress (MPa)	Peak load strain (%)	Residual strength (MPa)	α	m	a (%)	γ (%)
1	557.83	4.20	0.97	0.75	1.20	3.83	1.47	1.61
2	1066.64	5.96	0.73	0.82	1.16	3.70	1.09	1.25
3	1234.73	7.67	0.71	2.45	1.12	7.78	0.93	0.96
4	1437.79	7.68	0.69	1.94	1.06	3.75	1.01	1.18
5	1890.97	8.40	0.56	2.50	1.02	4.23	0.79	0.92
6	710.14	3.92	0.71	1.51	1.18	4.59	1.04	1.06
7	391.09	2.27	0.80	0.40	1.22	2.95	1.28	1.43
8	170.31	1.52	0.85	0.22	1.24	3.17	1.48	1.65

(a)

(b)

(c)

(d)
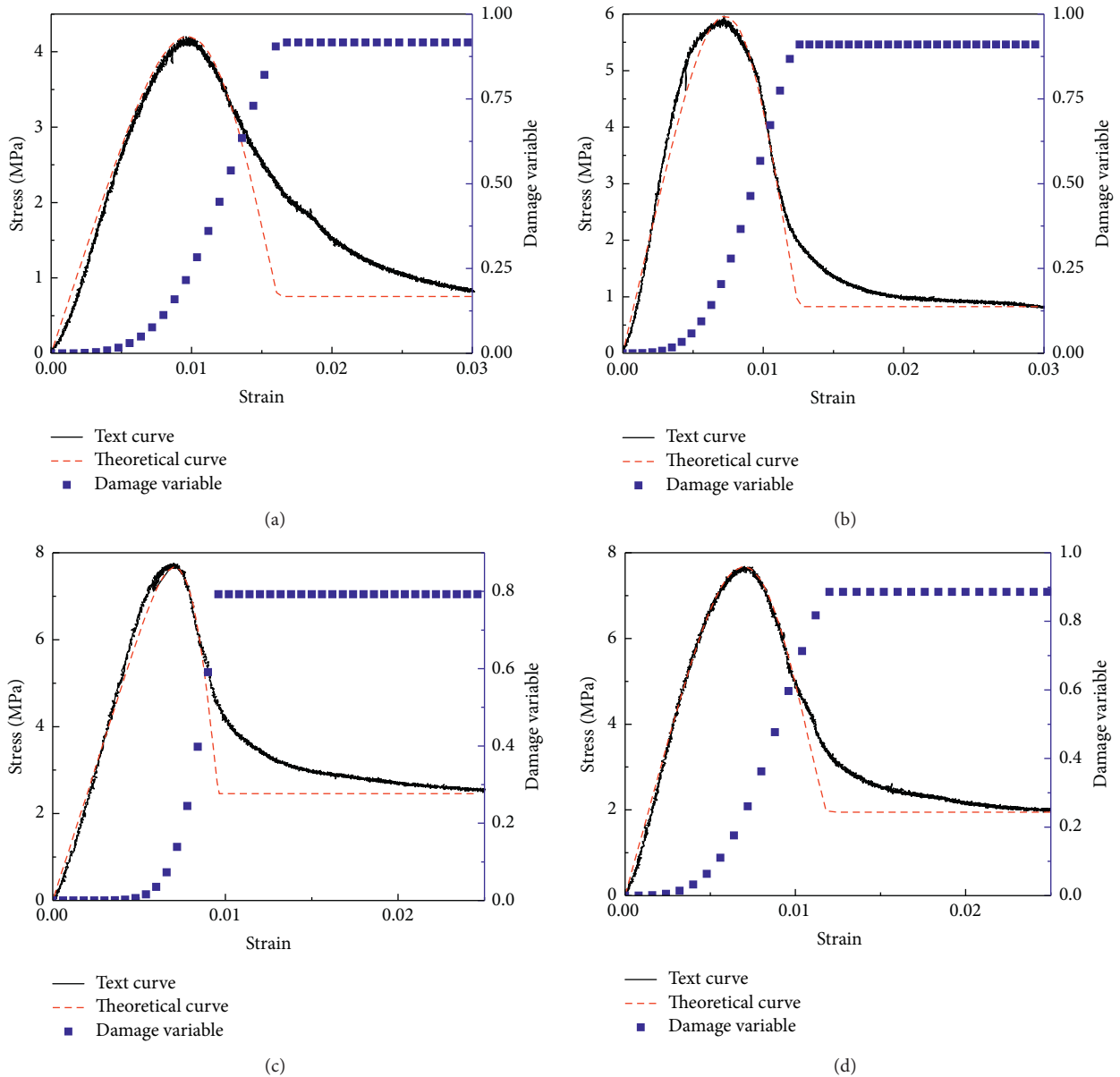
FIGURE 6: Continued.

(e)

(f)

(g)

(h)
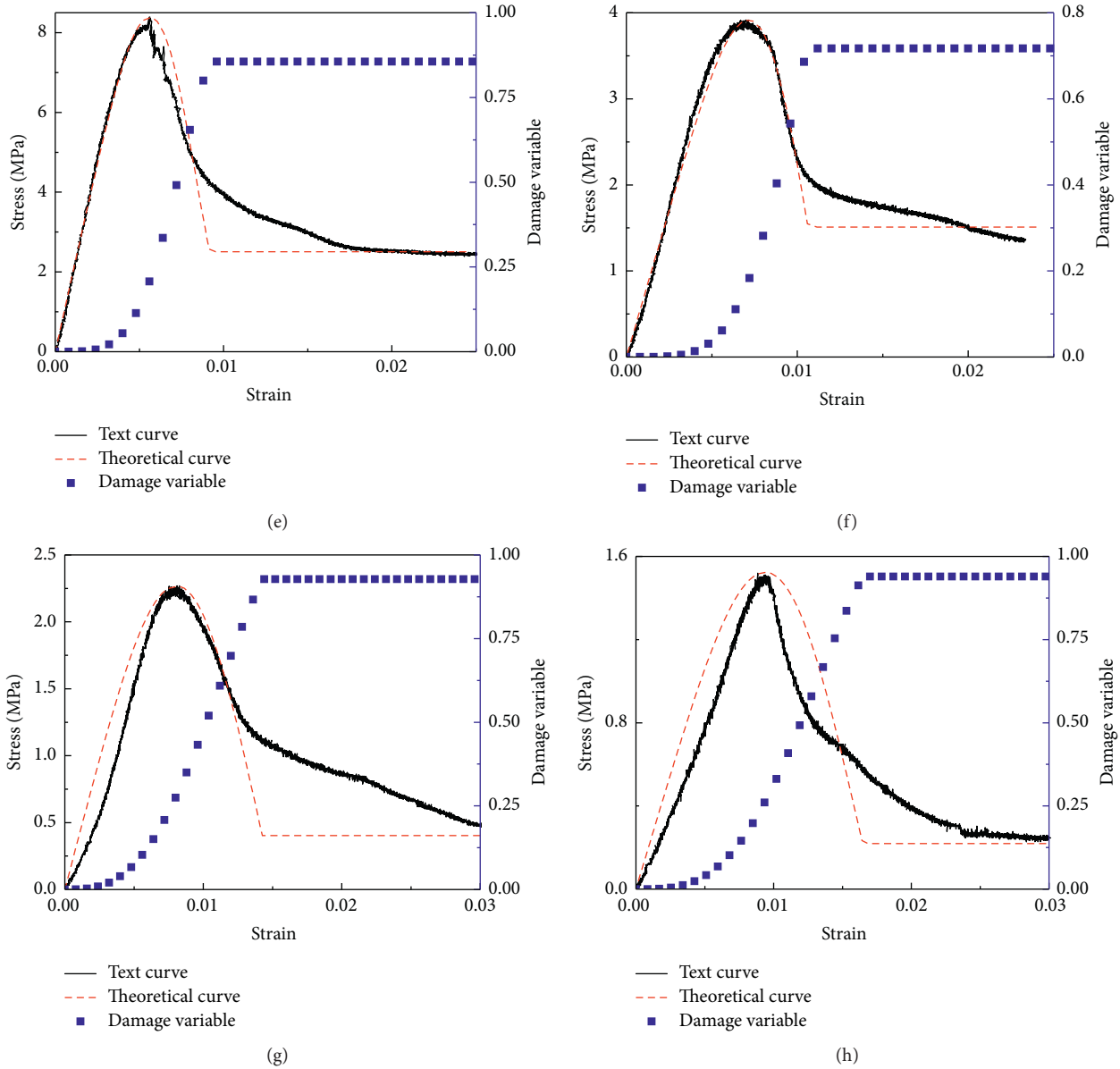
Figure 6: Damage variable and comparison of damage constitutive models. (a) Cement-tailings ratio is 1 : 4 and slurry concentration is 70%; (b) cement-tailings ratio is 1 : 4 and slurry concentration is 72%; (c) cement-tailings ratio is 1 : 4 and slurry concentration is 74%; (d) cement-tailings ratio is 1 : 4 and slurry concentration is 76%; (e) cement-tailings ratio is 1 : 4 and slurry concentration is 78%; (f) cement-tailings ratio is 1 : 6 and slurry concentration is 76%; (g) cement-tailings ratio is 1 : 8 and slurry concentration is 76%; (h) cement-tailings ratio is 1 : 10 and slurry concentration is 78%.

damage growth rate is accelerated, and the CPB is easy to be destroyed.

5.2. Analysis of Damage Strengthening Coefficient.
According to the analysis of the NMR test results, the main pore type of CPB is capillary pore, and the pore size range is $2.5 \sim 10^4$ nm. When analyzing the influence of pore size on material strength, the pore size should be classified and the influence coefficient should be calculated in different pore size areas. In this paper, the pore size is taken as the average value, and then the expression of damage strengthening coefficient and

the relevant parameters in equation (2) are taken with reference to [31], and then equation (2) is expressed as

$$\alpha = 1.365 d^{0.156.} (1 + P)^k + c. \tag{22}$$

MATLAB is used to fit equation (22) with two parameters, and the fitting equation of damage strengthening coefficient is obtained in equation (23); the results are shown in Figure 7.

$$\alpha = 1.365 d^{0.156.} (1 + P)^{0.1558} - 0.7583. \tag{23}$$
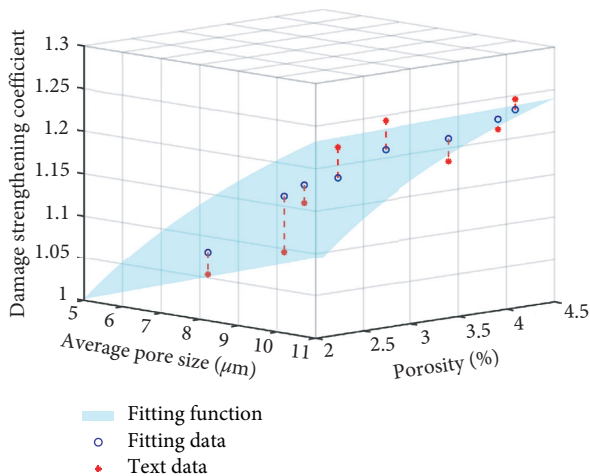
FIGURE 7: Fitting effect drawing of damage strengthening factor.

6. Conclusion

In this paper, a damage constitutive model based on the damage strengthening coefficient is proposed, considering the influence of microcosmic pore characteristics of CPB. The validity of the theoretical model is verified by UCS test and NMR test. The exponential expression of damage strengthening coefficient is given, which can effectively describe the stress-strain relationship and damage evolution process of CPB under uniaxial compression. The main conclusions are as follows:

(1) Under uniaxial compression, when the damage variable is about 0.25, the stress reaches the peak value. The ratio of peak load strain to damage variable corresponding to damage threshold is about 0.25.

(2) The 28-day compressive strength of CPB can reach 8 MPa, the residual strength is about 1~2 MPa, the elastic modulus is about 200~2000 MPa, the porosity is about 3~5%, the damage strengthening coefficient is about 1~1.2, and the damage threshold is about 1~1.5%.

(3) From the perspective of microscopic characteristics, the CPB with slurry concentration of 74% and 76% and cement-tailings ratio of 1 : 4 and 1 : 6 is more reasonable, and the relevant mechanical parameters are more stable.

Data Availability

Data are available from the corresponding author upon request.

Conflicts of Interest

Liu Lang, Cheng Kangli, Tu Bingbing, Zhang Bo, and Qiu Huafu declare that they have no conflicts of interest.

Acknowledgments

References

[1] L. Dong, X. Tong, X. Li, J. Zhou, S. Wang, and B. Liu, "Some developments and new insights of environmental problems and deep mining strategy for cleaner production in mines," *Journal of Cleaner Production*, vol. 210, no. 2, pp. 1562–1578, 2019.

[2] L. Dong, W. Shu, X. Li, and J. Zhang, "Quantitative evaluation and case studies of cleaner mining with multiple indexes considering uncertainty factors for phosphorus mines," *Journal of Cleaner Production*, vol. 183, no. 5, pp. 319–334, 2018.

[3] K. Zhao, S. T. Zhu, K. P. Zhou et al., "Research on mechanical properties and damage law of tantalum-niobium ore cemented tailings backfill," *Journal of Mining & Safety Engineering*, vol. 3, pp. 413–419, 2019.

[4] G. Huang, S. J. Cai, Y. D. Zhang, and D. Wu, "Experimental and modeling study on the strength of tailings backfill in underground mine," *Applied Mechanics & Materials*, vol. 522-524, pp. 1390–1393, 2014.

[5] Z. H. Wu, H. G. Ji, H. Q. Jiang, Z.-J. Qi, and Y. P. Kou, "Study of mechanical properties of frozen saline cemented tailings backfill," *Rock and Soil Mechanics*, vol. 41, no. 6, pp. 1874–1880, 2020.

[6] X. Zhang, M. Zhao, L. Liu et al., "Numerical simulation on heat storage performance of backfill body based on tube-in-tube heat exchanger," *Construction and Building Materials*, vol. 265, no. 9, p. 120340, 2020.

[7] R. L. Hu, Z. Q. Yue, L. C. Wang, and S. J. Wang, "Review on current status and challenging issues of land subsidence in China," *Engineering Geology*, vol. 76, no. 1-2, pp. 65–77, 2004.

[8] R. Rankine, M. Pacheco, and N. Sivakugan, "Underground mining with backfills," *Soils and Rocks*, vol. 30, no. 2, pp. 93–101, 2007.

[9] B. Ercikdi, A. Kesimal, F. Cihangir, H. Deveci, and İ. Alp, "Cemented paste backfill of sulphide-rich tailings: Importance of binder type and dosage," *Cement and Concrete Composites*, vol. 31, no. 4, pp. 268–274, 2009.

[10] M. Fall, M. Benzaazoua, and E. G. Saa, "Mix proportioning of underground cemented tailings backfill," *Tunnelling and Underground Space Technology*, vol. 23, no. 1, pp. 80–90, 2008.

[11] Y. Q. Hou, S. H. Yin, Y. Cao et al., "Analysis of damage characteristics and energy dissipation of cemented tailings backfill with different curing ages under uniaxial compression," *Journal of Central South University (Science and Technology)*, vol. 7, pp. 1955–1965, 2020.

[12] K. Zhao, W. J. Xie, P. Zeng et al., "Experimental study on damage characteristics of cemented tailings backfill failure process with different concentration," *Journal of Applied Acoustics*, vol. 7, pp. 543–549, 2020.

[13] X. F. Yi, C. K. Liu, and Y. Wang, "Experimental study on the meso-mechanical properties of cemented waste rock-tailings backfill (CWRB) using in-situ X-ray CT scanning," *Rock and Soil Mechanics*, vol. 10, pp. 1–8, 2020.

[14] Z. X. Liu, Q. L. Liu, and W. G. Dang, "On softening-hardening intrinsically constitutive model for damage of tailings-cemented filling body," *Journal of Shandong University of Science and Technology (Natural Science)*, vol. 2, pp. 36–41, 2012.

[15] S. G. Zhao, D. L. Su, W. R. Wu et al., "Study on damage model of backfill based," *China Mining Magazine*, vol. 2, pp. 106–111, 2017.

[16] J. Wang, W. D. Song, Y. Y. Tan et al., "Damage constitutive model and strength criterion of horizontal stratified cemented backfill," *Rock and Soil Mechanics*, vol. 5, pp. 1731–1739, 2019.

[17] L. Cui and M. Fall, "An evolutive elasto-plastic model for cemented paste backfill," *Computers and Geotechnics*, vol. 71, pp. 19–29, 2016.

[18] Y. Wang, A. X. Wu, H. J. Wang et al., "Damage constitutive model of cemented tailing paste under initial temperature effect," *Chinese Journal of Engineering*, vol. 39, no. 1, pp. 31–38, 2017.

[19] L. Cui and M. Fall, "A coupled thermo-hydro-mechanical-chemical model for underground cemented tailings backfill," *Tunnelling and Underground Space Technology*, vol. 50, pp. 396–414, 2015.

[20] Z. X. Liu, X. B. Li, T. G. Dai et al., "On damage model of cemented tailings backfill and its match with rock mass," *Rock and Soil Mechanics*, vol. 9, pp. 1442–1446, 2006.

[21] F. H. Wittmann, P. E. Roelfstra, and H. Sadouki, "Simulation and analysis of composite structures," *Materials Science and Engineering*, vol. 68, no. 2, pp. 239–248, 1985.

[22] X. L. Du and L. Jin, "Applications of meso-scale analysis methods on the studyof the physical/mechanical properties of concrete," *Shuili Xuebao*, vol. 3, pp. 355–371, 2016.

[23] B. Pichler, S. Scheiner, and C. Hellmich, "From micron-sized needle-shaped hydrates to meter-sized shotcrete tunnel shells: micromechanical upscaling of stiffness and strength of hydrating shotcrete," *Acta Geotechnica*, vol. 3, no. 4, pp. 273–294, 2008.

[24] B. Pichler, C. Hellmich, and J. Eberhardsteiner, "Spherical and acicular representation of hydrates in a micromechanical model for cement paste: prediction of early-age elasticity and strength," *Acta Mechanica*, vol. 203, no. 3-4, pp. 137–162, 2009.

[25] X. L. Du and L. Jin, "Research on effective mechanical proerties of concrete composite material with pores," *Engineering Mechanics*, vol. 6, pp. 70–77, 2012.

[26] W. B. Xu, W. D. Pang, and M. L. Ding, "Experiment on evolution of microstructures and long-term strength model of cemented backfill mass," *Journal of Central South University (Science and Technology)*, vol. 46, no. 6, pp. 2333–2341, 2015.

[27] D. S. Shi and A. Wang, "Effect of slag fine aggregate concrete pore structure on compressive strength," *Concrete*, vol. 3, pp. 80–83, 2016.

[28] C. Lian, Y. Zhuge, and S. Beecham, "The relationship between porosity and strength for porous concrete," *Construction and Building Materials*, vol. 25, no. 11, pp. 4294–4298, 2011.

[29] Erniati, M. W. Tjaronge, Zulharnah, and U. R. Irfan, "Porosity, pore size and compressive strength of self compacting concrete using sea water," *Procedia Engineering*, vol. 125, pp. 832–837, 2015.

[30] S. Jin, J. Zhang, and S. Han, "Fractal analysis of relation between strength and pore structure of hardened mortar," *Construction and Building Materials*, vol. 135, pp. 1–7, 2017.

[31] D. Li, Z. Li, C. Lv, G. Zhang, and Y. Yin, "A predictive model of the effective tensile and compressive strengths of concrete considering porosity and pore size," *Construction and Building Materials*, vol. 170, pp. 520–526, 2018.

[32] J. Lemaitre, "How to use damage mechanics," *Nuclear Engineering and Design*, vol. 80, no. 2, pp. 233–245, 1984.

[33] L. Liu, J. Xin, C. Huan, C. Qi, W. Zhou, and K.-I. Song, "Pore and strength characteristics of cemented paste backfill using sulphide tailings: effect of sulphur content," *Construction and Building Materials*, vol. 237, pp. 117452–117512, 2020.

[34] L. Liu, J. Xin, C. C. Qi, H. Jia, and K.-I. Song, "Experimental investigation of mechanical, hydration, microstructure and electrical properties of cemented paste backfill," *Construction and Building Materials*, vol. 263, pp. 1–12, 2020.

[35] MOHURD, *GB/T. 50266-2013, Standard for test methods of engineering rock mass*, MOHURD, vol. 1, p. 28, China, 2013.

[36] Y. Wang, *Initial Temperature-Dependence of Multi-Field Property Correlation and Mechanics Behaviors for Cemented Paste Backfill*, University of Science and Technology Beijing, Beijing, China, 2017.

Research Article

Evaluation of Backfill Operation Models Using SBSC and IFAHP Approach

Yan Li (ID)

School of Business, Xi'an University of Finance and Economics, Xi'an 710100, China

Correspondence should be addressed to Yan Li; liyan@xaufe.edu.cn

As the mine backfill is recognized as one promising technique for the sustainable development, it is crucial to explore the backfill operation mechanism for the mining industry. At present, the self-management and outsourcing model are generally selected to apply in backfill operation and management worldwide. The advantages are insufficient from the strategic and sustainable perspective. Therefore, the study proposes joint venture alliance and concerns the superiority on mine backfill management. In order to evaluate the models, this study puts forward the integrated method which involves combination of SBSC and IFAHP. A strategic and hierarchical framework of SBSC on the basis of sustainability is formulated, which includes 6 perspectives and 16 secondary indexes. Simultaneously, the IFAHP approach is used for determination of the weights of indexes and calculation of the final score, which enables to assess mine backfill operation activity more objectively. The results show that the self-management model provides little advantages whereas the outsourcing model is the better operation mechanism. By contrast, joint venture alliance is rated as the optimal backfill operation model of the mining industry. The research findings of this study would help the mining industry to evaluate objectively and make an appropriate decision on the backfill operation model in the mining industry.

1. Introduction

Mine backfill has been widely used worldwide. The building process of the backfill station was associated with several steps including feasibility analysis, design, procurement, construction, installation, and debugging; the backfill operating process did not begin until the employees finished training of professional skills (as shown in Figure 1). For the management of the backfill station, some countries such as Chile and South America adopted the traditional self-management model. Therefore, the mining industries need to spend several years and much energy on the preparation activity before conducting the operational process of the backfill station.

Some countries proposed the outsourcing model, which has been practiced in business management in various fields ranging from IT/IS to logistics [1]. Some mining industries have outsourced noncore business activity to the private partner or service provider, even recently the scope of outsourcing expanded to certain core business [2]. There are

instances like South Africa and Canada where the backfill project was outsourced to service providers with expertise. The reasons for outsourcing are acquisition of specialized competencies, good flexibility in adapting to the environment and geology, and reduction of cost mainly including fixed assets [3]. Moreover, outsourcing is conducive to strategic enhancement of industry core competencies [4]. However, there were reports from Indian coal mining industries which showed unsatisfactory conclusions with respect to outsourcing by empirical evidence [5, 6]. In addition, there may be other deficiencies including increase in extra cost and disclosure of confidential information [7]. Moreover, the top risk of outsourcing is that the quality of the product or service is not fully controlled [3].

At present, the mining industries dominantly adopt self-management or outsourcing as the backfill operation model worldwide. In China, the mining industries generally select the self-management model. However, joint venture alliance was still under-appreciated in terms of backfill operation mechanism and was rarely used. Joint venture alliance
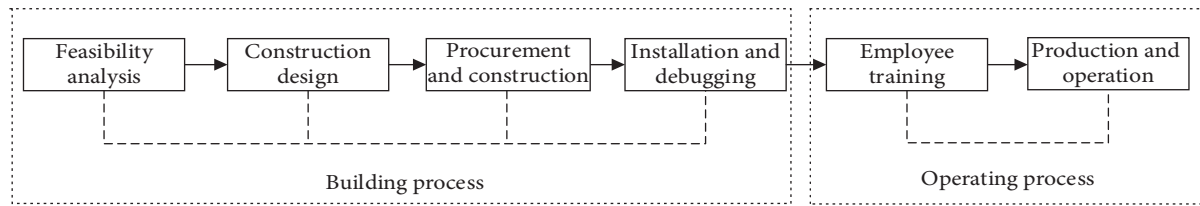
FIGURE 1: Building and operating process of mine backfill.

provided access to special technology and skill from alliance partners [8]. Generally, the industries need to select the alliance partner with complementary resource such as market, expertise, and capital investment [9]. Furthermore, joint venture alliance highlighted long-term reciprocal commitment and mutual trust so that competitive advantage of alliance was reinforced. Nevertheless, joint venture alliance was yet unsatisfactory, and there may exist some risks including selection of alliance partner, poor flexibility, and constraint of the government policy [10, 11].

The inefficient management model is unfavorable for the development of mine backfill; therefore, it is crucial to make decision on selecting the appropriate backfill operation model. Multicriteria decision-making (MCDM) technology contributes to assess and determine the best alternative in the case of conflicting criteria and objectives. There have been some studies on exploring decision-making by MCDM including Analytic Hierarchy Process (AHP) [12], Analytical Network Process (ANP) [13], PROMETHEE [14], Decision-Making Trial and Evaluation Laboratory (DEMATEL) [15], Technique for Order Preference by Similarity to Ideal Solution (TOPSIS) [16], Data Envelopment Analysis (DEA) [17], Vlse Kriterijumska Optimizacija Kompromisno Resenje (VIKOR) [18], linear programming, and hybrid approach such as fuzzy AHP [19]. MCDM techniques are classified as individual and hybrid methods, of which AHP, RPOME-THEE, ELECTRE, TOPSIS, ANP, and VIKOR are considered as the most frequent applications in energy decision [20]. Fuzzy MCDM has been widely used since fuzzy sets are conducive to tackling uncertainties and vagueness, from which intuitionistic fuzzy decision-making was developed. Xue (2021) applied the intuitionistic fuzzy set to explore the database retrieval and decision-making based on the uncertain database [21]. Garg (2020) developed the fuzzy set and addressed the complex interval-valued q-rung orthopair fuzzy set (IVq-ROFS) to deal with uncertain information in the decision-making process [22]. Puri (2017) concerned a new set of weights methodology for multicomponent data envelopment analysis (MC-DEA) with uncertain data to measure interval efficiencies, which has been applied to banks in India [23]. Moreover, researchers tend to utilize integrated MCDM involving two or more methods to find optimal results. Sustainable balanced scorecard (SBSC) is a tool to build the concept framework on the basis of sustainability for more efficient operation of the organization [24]. There was no literature that integrate SBSC with intuitionistic fuzzy AHP (IFAHP) for performance evaluation. In order to select the optimal model among self-management, outsourcing, and proposed joint venture alliance, the study attempts to establish the conceptual framework for evaluation of backfill operation. Moreover, the study tries to adopt the hybrid MCDM methods combing SBSC with IFAHP to make the optimal and appropriate decision for mine backfill industries.

2. Review of Literature

2.1. SBSC. SBSC was developed on the basis of BSC, which was proposed by Professor Kaplan and Norton for the first time [25]. BSC broke through traditional evaluation criteria viewing only financial indexes as a measure of organizational performance and took the nonfinancial issue into account; therefore, a balanced and strategic framework with the financial factor and nonfinancial factor was formulated, which covered four perspectives including financial, customers, internal operations, learning, and growth.

However, the BSC method focused only on the internal management of organization, but ignored the surroundings in which the organization was admitted to keep sustainable development. Figge (2002) expressed the process of social and environmental impact on business activities and incorporated social and environmental issues into the strategic framework of SBSC; correspondingly, nonmarket became the fifth perspective [26]. Sidiropoulos (2004) supported sustainable indexes into operational performance [27]. Möller and Schaltegger (2005) embedded eco-efficiency indexes into sustainable performance measure [28]. Hubbard (2009) proposed that the organization should be responsible for stakeholders and modified the SBSC framework structure lying in stakeholders' perspective [29]. Tsalis (2013) addressed the SBSC approach that contributed to enhance social responsibility awareness of the industry [30]. As a result, both the eco-efficiency element and sustainability element were integrated into the hierarchical evaluation system of SBSC in which economic, environmental, and social factors were combined. Simultaneously, the environmental and social perspective help stimulate growth of the value added [31, 32].

2.2. IFAHP. IFAHP is a comprehensive evaluation method formulated by combining intuitionistic fuzzy sets and AHP. The AHP method was employed to quantify experience and subjective judgment of experts, which was proposed by Saaty [33]. Although a noticeable advantage of AHP was that the method enables to transform qualitative analysis into the quantitative issue, and expert judgment with ambiguity has not been considered. Therefore, the degree of membership

derived from fuzzy mathematics was introduced to the AHP approach. However, this method cannot provide a quantitative description of hesitation and abstention, and the subjectivity of the evaluation remains strong. The intuitionistic fuzzy set was further integrated to AHP, in which the hesitancy degree enables to show the hesitation situation in the evaluation process. IFAHP was developed by Xu and Liao, which covers the degree of membership, the degree of nonmembership, and hesitancy degree [34]. With respect to IFAHP, there are several extremely significant advantages. Since the hesitancy degree may explain the hesitation of experts, the IFAHP approach can effectively solve the subjectivity of expert decision-making in the evaluation process. Moreover, the weights of indexes are obtained by experts scoring, while its consistency test fails, the correction is fulfilled by adjusting the iterative parameters, so there is no need to gather experts for scoring again [35]. However, IFAHP also has certain deficiency including dramatic increase in computational complexity due to the addition of the degree of nonmembership.

2.3. Proposed Backfill Operation Models

2.3.1. Self-Management Model. As shown in Figure 2, the first model is the self-management model [4]. For the self-management model, the mine owner is committed to setting up a department of mine backfill, by which the activities of mine backfill are operated. Therefore, all of businesses involving mine backfill are controlled by the mine owner. The model requires that the mine owner enables to possess the backfill technology and expertise and provides enough financial support. The benefits and risks arising from backfill activities are held by the mine owner.

2.3.2. Outsourcing Model. As shown in Figure 2, the second model is the outsourcing model [4]. For the outsourcing model, the mine owner takes effort to select appropriate vendors or service providers as the operator employed for backfill operation service and management. Backfill vendors and backfill service providers are expected to provide physical resources, expertise, and sophisticated technology which are applied for mine backfill. According to classification of outsourcing engagement, there are four scopes of task outsourced including out-tasking, comanaged services, managed services, and full outsourcing [36]. However, there are certain possibilities that some risk might emerge such as cost escalation and inadequate performance of vendors [37].

2.3.3. Joint Venture Alliance. As shown in Figure 2, the third model is joint venture alliance [4]. For joint venture alliance, the mine owner is admitted to build an organizational alliance with the backfill vendor on the basis of institutional trust. The critical factors for the backfill vendor selected as the alliance partner are specialist knowledge, expertise, and professional equipment possessed by the vendor. All of the operational activities of backfill are controlled by joint venture alliance. Compared with the transaction relation, joint venture alliance is beneficial to reduce costs and time [38]. The mine owner and alliance partner share the rewards and risks according to the proportion of equity investment [39].

3. Methodology

It is crucial for the mining industry to select an appropriate backfill operation model. The flow chart of performance evaluation of the mine backfill operation model is shown in Figure 3. In the first step, the experts group is formed, in which the experts specialized in expertise and management knowledge of mine backfill are invited to participate in assessment of backfill operation models. In the second step, six perspectives of SBSC and performance indexes in terms of mine backfill are identified. In the third step, each expert in the group measures the importance degree of indexes and constructs the complementary matrix of IFPR. In addition, each expert is required to provide the evaluation matrix of three backfill operation models. In the fourth step, the intuitionistic fuzzy consistency judgment matrix is calculated, and the consistency test of the matrix is conducted by which the validity of the calculation result is determined. While the consistency test may fail, the parameter could be used to adjust until the consistency test is passed instead of scoring by experts again. In the fifth step, the weights of indexes and total weights are calculated. Subsequently, weighted results for each model are conducted, and final scores are obtained. Finally, the mine backfill operation models are summarized.

3.1. Identify SBSC Perspectives and Performance Indexes The SBSC method takes account of the sustainability issue. Some scholars insert sustainable indexes into the conceptual framework of BSC, while others incorporate eco-efficiency indexes into the BSC [40]. However, with green mining emphasized by more countries worldwide, this study prefers to address the environmental perspective and social perspective to the proposed SBSC evaluation framework. Therefore, there are six perspectives constructed for the performance measurement framework of the mine backfill including financial, stakeholders, internal process, learning and growth, and environmental and social perspective. As shown in Table 1, the performance indexes within the financial perspective are total capital input, operational cost optimization, and profit variance [24, 41, 42], whereas the stakeholders' perspective comprises indexes such as mine owner satisfaction, backfill vendor satisfaction, and regulatory satisfaction [11, 43, 44]. The internal process perspective involves mining-separation-backfill balance, flexibility, communication and collaboration efficiency [3, 45, 46]; whereas the learning and growth perspective comprises of training and development, technological innovation capability, and knowledge sharing [46–48]. The environmental perspective includes reduction of environmental impact and tailings utilization [45, 49]; the social perspective consists of employee accident and health of

(a)   (b)   (c)
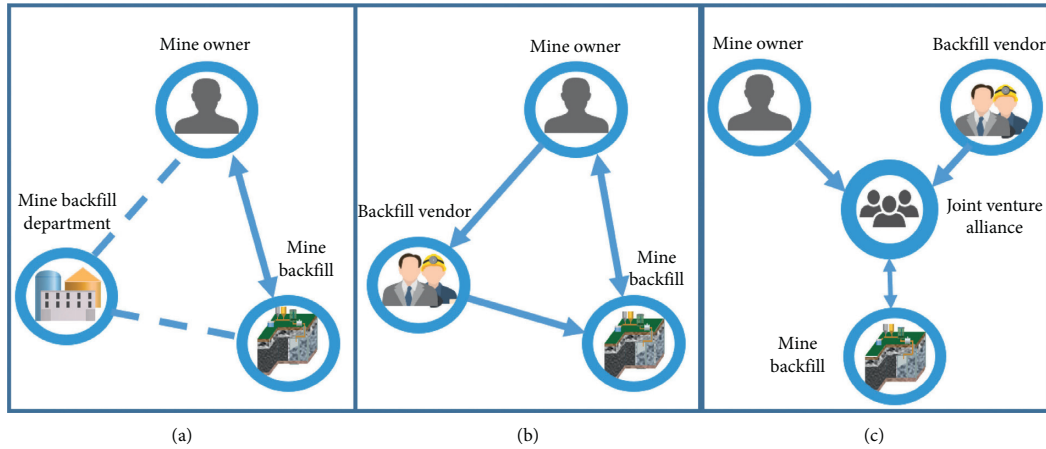
FIGURE 2: Schematic diagram of the proposed backfill operation models.
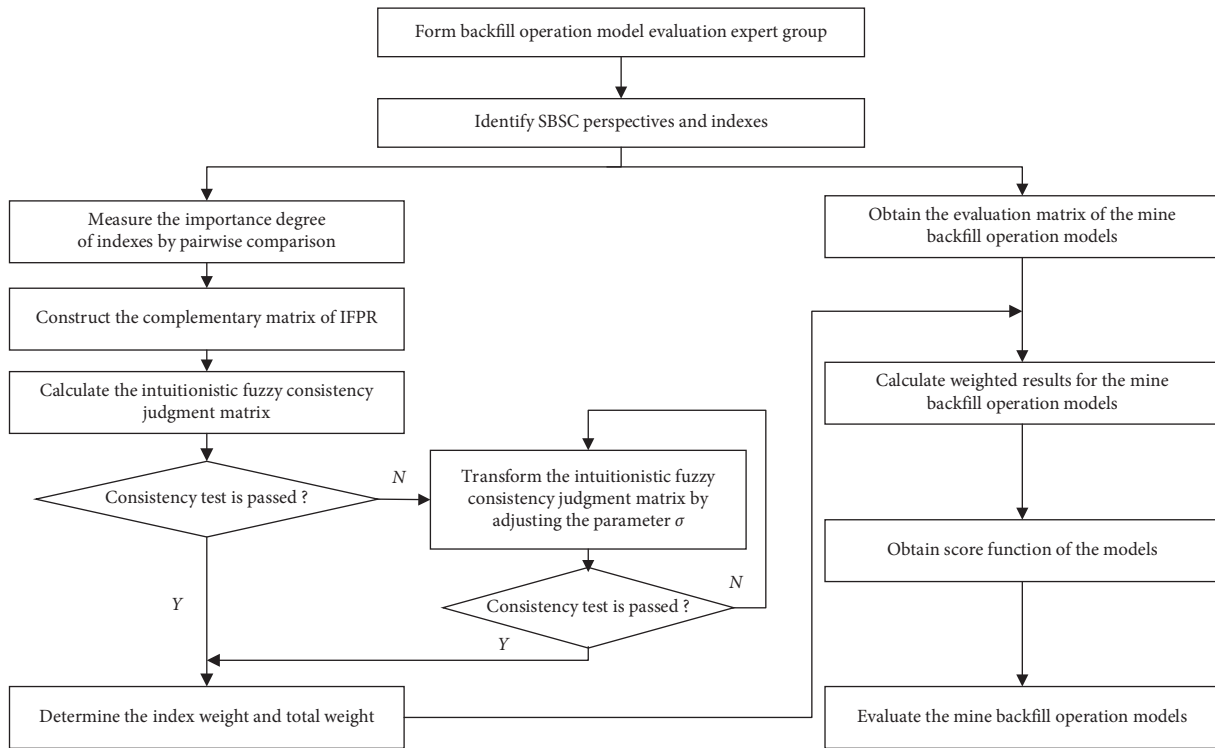
FIGURE 3: Flow chart of evaluation of mine backfill operation models.

residents [49, 50]. The definitions and descriptions of the indexes are shown in Table 1.

3.2. Steps of IFAHP

3.2.1. Construction of the Complementary Matrix of IFPR Let a set of alternatives $C = \{c_1, c_2, \ldots, c_n\}$. The experts give the preference degree by comparing c_i with c_j, $i, j = 1, 2, \ldots, n$. Generally, the experts need to provide the preference degree including the membership degree and nonmembership degree. However, it is very possible that

experts feel hesitant to quickly give the degree of membership. Therefore, compared with the fuzzy preference relation, the intuitionistic fuzzy preference relation (IFPR) proposes the issue of the hesitation degree. IFPR on the set C is represented by a complementary matrix $A = (r_{ij})_{n \times n}$, where $r_{ij} = (\mu_{ij}, \nu_{ij})$, and μ_{ij} is called the membership degree [35], and it indicates the degree to which c_i is more important than c_j, and ν_{ij} is denoted as the nonmembership degree [35], and it represents the degree to which c_j is more important than c_i. Both μ_{ij} and ν_{ij} are satisfied with the conditions including $\mu_{ij} \in [0, 1]$, $\nu_{ij} \in [0, 1]$, $0 \leq \mu_{ij} + \nu_{ij} \leq 1$, and $\mu_{ij} = \nu_{ji}$. The hesitation degree or degree of uncertainty

TABLE 1: Description of evaluation indexes.

Evaluation indexes	Description	References
Financial perspective (B1)		
Total capital input (C1)	Investment related to mine backfill including equipment, technology, professional technicians, and managers	Agrawal et al. [41]
Operational cost optimization (C2)	Optimization of expense items associated with operational activities	Lee et al. [42]
Profit variance (C3)	Comparison of actual profit and planned profit	Epstein et al. [24]
Stakeholders' perspective (B2)		
Mine owner satisfaction (C4)	Satisfaction degree of mine owner with financial and backfill operational management	Lin et al. [43]
Backfill vendor satisfaction (C5)	Satisfaction degree of backfill vendor with financial and empowerment	Moon et al. [11]
Regulatory satisfaction (C6)	Compliance with standards and rules from regulatory bodies	Modak et al. [44]
Internal process perspective (B3)		
Mining-separation-backfill balance (C7)	Mining, separation, and backfill process remain closed-loop connection	Qi et al. [45]
Flexibility (C8)	Ability to adapt to environmental and market changes	Baatartogtokh et al. [3]
Communication and collaboration efficiency (C9)	Effectiveness of communication and collaboration among stakeholders	Tsai et al. [46]
Learning and growth perspective (B4)		
Training and development (C10)	Improvement of employee's capacity by training of expertise and skill	Modak et al. [44]
Technological innovation capability (C11)	Motivation and capacity to continuously improve technology	Khaleie et al. [48]
Knowledge sharing (C12)	Sharing knowledge and information associated with backfill activities among stakeholders	Tsai et al. [46]
Environmental perspective (B5)		
Tailings utilization (C13)	Minimization of risk of environmental pollution through implementing backfill technology	Liu et al. [49]
Reduction of environmental impact (C14)	Percentage of tailings backfilled to underground voids	Qi et al. [45]
Social perspective (B6)		
Employee accident (C15)	Occupational accident rate of employee	Zhao et al. [50]
Health of residents (C16)	Impact on community residents' health condition	Liu et al. [51]

π_{ij} is calculated through $\pi_{ij} = 1 - \mu_{ij} - \nu_{ij}$. In order to quantify the degree of preference by pairwise comparison, the related evaluation scale is proposed by Atanassov [52], as shown in Table 2.

3.2.2. Consistency Test. The process of consistency test shows the improvement of IFAHP compared to the traditional AHP method, which reflects validity of the conclusion. Based on the complementary matrix of IFPR $A = (r_{ij})_{n \times n}$, the matrix $\overline{A} = (\overline{r}_{ij})_{n \times n}$ is obtained by the way of calculation, which is denoted as the intuitionistic fuzzy consistency judgment matrix.

When $j > i+1$, then $\overline{r}_{ij} = (\overline{\mu}_{ij}, \overline{\nu}_{ij})$ [53],

$$\overline{\mu}_{ij} = \sqrt[j-i-1]{\frac{\prod_{t=i+1}^{j-1} \mu_{it}\mu_{tj}}{\sqrt[j-i-1]{\prod_{t=i+1}^{j-1} \mu_{it}\mu_{tj}} + \sqrt[j-i-1]{\prod_{t=i+1}^{j-1} (1-\mu_{it})(1-\mu_{tj})}}}, \quad j > i+1, \tag{1}$$

$$\overline{\nu}_{ij} = \sqrt[j-i-1]{\frac{\prod_{t=i+1}^{j-1} \nu_{it}\nu_{tj}}{\sqrt[j-i-1]{\prod_{t=i+1}^{j-1} \nu_{it}\nu_{tj}} + \sqrt[j-i-1]{\prod_{t=i+1}^{j-1} (1-\nu_{it})(1-\nu_{tj})}}}, \quad j > i+1. \tag{2}$$

When $j = i+1$, then $\overline{r}_{ij} = (\mu_{ij}, \nu_{ij})$;
When $j < i$, then $\overline{r}_{ij} = (\overline{\nu}_{ji}, \overline{\mu}_{ji})$.

The values of μ_{ij}, $\overline{\mu}_{ij}$, ν_{ij}, and $\overline{\nu}_{ij}$ are subsequently brought into the following formula for the consistency test [53]:

TABLE 2: IFAHP pairwise comparison scale and meaning.

Meaning	Scale
Compared with two factors, i is extremely better than j	(0.90,0.10,0.00)
Compared with two factors, i is strongly better than j	(0.80,0.15,0.05)
Compared with two factors, i is obviously better than j	(0.70,0.20,0.10)
Compared with two factors, i is slightly better than j	(0.60,0.25,0.15)
Compared with two factors, i is equivalent to $j(i \neq j)$	(0.50,0.30,0.20)
Compared with two factors, j is slightly better than i	(0.40,0.45,0.15)
Compared with two factors, j is obviously better than i	(0.30,0.60,0.10)
Compared with two factors, j is strongly better than i	(0.20,0.75,0.05)
Compared with two factors, j is extremely better than i	(0.10,0.90,0.00)

$$d(\overline{A}, A) = \frac{1}{2(n-1)(n-2)} \sum_{i=1}^{n} \sum_{j=1}^{n}$$
$$\cdot \left(\left|\overline{\mu}_{ij} - \mu_{ij}\right| + \left|\overline{\nu}_{ij} - \nu_{ij}\right| + \left|\overline{\pi}_{ij} - \pi_{ij}\right| \right). \tag{3}$$

If $d(\overline{A}, A) < 0.1$, it means $\overline{A}$ passed the consistency test.

If $d(\overline{A}, A) \geq 0.1$, it means $\overline{A}$ does not pass the consistency test. However, it is not indispensable that the experts provide the preference degree once again. The parameter σ is set and used for iteration, where $\sigma \in [0, 1]$. The parameter σ is changed in steps of -0.01 from 1 through the iteration process; correspondingly, the intuitionistic fuzzy consistency judgment matrix is adjusted:

$$\tilde{\mu}_{ij} = \frac{\left(\mu_{ij}\right)^{1-\sigma} \left(\overline{\mu}_{ij}\right)^{\sigma}}{\left(\mu_{ij}\right)^{1-\sigma} \left(\overline{\mu}_{ij}\right)^{\sigma} + \left(1 - \mu_{ij}\right)^{1-\sigma} \left(1 - \overline{\mu}_{ij}\right)^{\sigma}}, \quad i, j \in [1, n] \tag{4}$$

$$\tilde{\nu}_{ij} = \frac{\left(\nu_{ij}\right)^{1-\sigma} \left(\overline{\nu}_{ij}\right)^{\sigma}}{\left(\nu_{ij}\right)^{1-\sigma} \left(\overline{\nu}_{ij}\right)^{\sigma} + \left(1 - \nu_{ij}\right)^{1-\sigma} \left(1 - \overline{\nu}_{ij}\right)^{\sigma}}, \quad i, j \in [1, n]. \tag{5}$$

According to abovementioned two formulas, the values of $\tilde{u}_{ij}$ and $\tilde{v}_{ij}$ are calculated, and the adjusted intuitionistic fuzzy consistency judgment matrix $\tilde{A} = (\tilde{r_{ij}})_{n \times n}$ is obtained, where $\tilde{r}_{ij} = (\tilde{u_{ij}}, \tilde{v_{ij}})$. While $\tilde{A}$ and A are brought to the following formula and the consistency test still fails, the adjusting process by the parameter is repeatedly conducted until the consistency test is passed:

$$d(\overline{A}, A) = \frac{1}{2(n-1)(n-2)} \sum_{i=1}^{n} \sum_{j=1}^{n} \left(\left|\tilde{\mu}_{ij} - \mu_{ij}\right| + \left|\overline{\nu}_{ij} - \nu_{ij}\right| + \left|\overline{\pi}_{ij} - \pi_{ij}\right| \right). \tag{6}$$

3.2.3. Determination of Weights. The relative weight of each index is calculated by the following formula on the basis of the intuitionistic fuzzy consistency judgment matrix [53]:

$$\omega_{i=} \left[\frac{\sum_{j=1}^{n} \overline{\mu}_{ij}}{\sum_{i=1}^{n} \sum_{j=1}^{n} \left(1 - \overline{\nu}_{ij}\right)}, 1 - \frac{\sum_{j=1}^{n} \left(1 - \overline{\nu}_{ij}\right)}{\sum_{i=1}^{n} \sum_{j=1}^{n} \overline{\mu}_{ij}} \right]. \tag{7}$$

The weight of each secondary index and the corresponding first-level index is aggregated and weighted in accordance with the algorithm of the intuitionistic fuzzy value, and the total weight is obtained. The following are related formulas [35]:

$$\omega_1 \otimes \omega_2 = \left(\mu_{\omega 1} \mu_{\omega 2}, \nu_{\omega 1} + \nu_{\omega 2} - \nu_{\omega 1} \nu_{\omega 2}\right), \tag{8}$$

$$\omega_1 \otimes \omega_2 = \left(\mu_{\omega 1} + \mu_{\omega 2} - \mu_{\omega 1} \mu_{\omega 2}, \nu_{\omega 1} \nu_{\omega 2}\right), \tag{9}$$

$$\omega(C_i) = \omega_{B_k} \otimes \omega_{c_i}, k, i \in [1, n]. \tag{10}$$

3.2.4. Calculation of Final Evaluation. The score function and ranking function are calculated through the following formulas based on the intuitionistic fuzzy value [53]. Generally, the higher the score function value, the better the evaluation of this backfill operation model. The higher the ranking function value, the lower the evaluation of this backfill operation model:

$$H(\omega) = \frac{1 - \nu_{ij}}{2 - \mu_{ij} - \nu_{ij}}, \tag{11}$$

$$\rho(\omega) = 0.5 \left(1 + \pi_{\omega}\right) \left(1 - \mu_{\omega}\right). \tag{12}$$

4. Results and Discussion

4.1. Results

4.1.1. Establishing the Complementary Matrix of IFPR There are ten experts in the panel with rich technology knowledge and management experience in the field of mine backfill in China. The experts are invited to provide their preference degree including IFPR of first-level indexes and IFPR of secondary indexes. Moreover, the membership degree and nonmembership degree given by ten experts

need to be arithmetically averaged. So the complementary matrices of IFPR are determined:

$$A = \begin{bmatrix} (0.5, 0.5) & (0.570, 0.265) & (0.430, 0.405) & (0.510, 0.305) & (0.590, 0.255) & (0.640, 0.230) \\ (0.265, 0.570) & (0.5, 0.5) & (0.380, 0.480) & (0.450, 0.385) & (0.520, 0.290) & (0.560, 0.270) \\ (0.405, 0.430) & (0.480, 0.380) & (0.5, 0.5) & (0.550, 0.275) & (0.640, 0.230) & (0.670, 0.215) \\ (0.305, 0.510) & (0.385, 0.450) & (0.275, 0.550) & (0.5, 0.5) & (0.580, 0.260) & (0.610, 0.245) \\ (0.255, 0.590) & (0.290, 0.520) & (0.230, 0.640) & (0.260, 0.580) & (0.5, 0.5) & (0.530, 0.285) \\ (0.230, 0.640) & (0.270, 0.560) & (0.215, 0.670) & (0.245, 0.610) & (0.285, 0.530) & (0.5, 0.5) \end{bmatrix},$$

$$A_1 = \begin{bmatrix} (0.5, 0.5) & (0.550, 0.275) & (0.560, 0.270) \\ (0.275, 0.550) & (0.5, 0.5) & (0.510, 0.305) \\ (0.270, 0.560) & (0.305, 0.510) & (0.5, 0.5) \end{bmatrix},$$

$$A_2 = \begin{bmatrix} (0.5, 0.5) & (0.540, 0.280) & (0.560, 0.270) \\ (0.280, 0.540) & (0.5, 0.5) & (0.500, 0.330) \\ (0.270, 0.560) & (0.330, 0.500) & (0.5, 0.5) \end{bmatrix},$$

$$A_3 = \begin{bmatrix} (0.5, 0.5) & (0.530, 0.285) & (0.520, 0.290) \\ (0.285, 0.530) & (0.5, 0.5) & (0.500, 0.310) \\ (0.290, 0.520) & (0.310, 0.500) & (0.5, 0.5) \end{bmatrix}, \qquad (13)$$

$$A_4 = \begin{bmatrix} (0.5, 0.5) & (0.485, 0.335) & (0.500, 0.320) \\ (0.305, 0.510) & (0.5, 0.5) & (0.530, 0.285) \\ (0.295, 0.530) & (0.285, 0.530) & (0.5, 0.5) \end{bmatrix},$$

$$A_5 = \begin{bmatrix} (0.5, 0.5) & (0.560, 0.270) \\ (0.270, 0.560) & (0.5, 0.5) \end{bmatrix},$$

$$A_6 = \begin{bmatrix} (0.5, 0.5) & (0.590, 0.255) \\ (0.255, 0.590) & (0.5, 0.5) \end{bmatrix}.$$

4.1.2. Consistency Test. The intuitionistic fuzzy consistency judgment matrix on first-level indexes $\overline{A}$ can be calculated by using equations (1) and (2):

$$\overline{A} = \begin{bmatrix} (0.5, 0.5) & (0.5700, 0.2650) & (0.4483, 0.2497) & (0.5000, 0.1945) & (0.5840, 0.1427) & (0.6178, 0.1291) \\ (0.2650, 0.5700) & (0.5, 0.5) & (0.3800, 0.4800) & (0.4283, 0.2593) & (0.5260, 0.1976) & (0.5552, 0.1687) \\ (0.2497, 0.4483) & (0.4800, 0.3800) & (0.5, 0.5) & (0.5500, 0.2750) & (0.6280, 0.1176) & (0.6619, 0.1080) \\ (0.1945, 0.5000) & (0.2593, 0.4283) & (0.2750, 0.5500) & (0.5, 0.5) & (0.5800, 0.2600) & (0.6090, 0.1228) \\ (0.1427, 0.5840) & (0.1976, 0.5260) & (0.1176, 0.6280) & (0.2600, 0.5800) & (0.5, 0.5) & (0.5300, 0.2850) \\ (0.1291, 0.6178) & (0.1687, 0.5552) & (0.1080, 0.6619) & (0.1228, 0.6090) & (0.2850, 0.5300) & (0.5, 0.5) \end{bmatrix}. \qquad (14)$$

Putting A and $\overline{A}$ into equation (3), we get $d(\overline{A}, A) = 0.0625 < 0.1$, and it means $\overline{A}$ passes the consistency test. Similarly, the intuitionistic fuzzy consistency judgment matrix on secondary indexes $\overline{A}_1$, $\overline{A}_2$, $\overline{A}_3$, $\overline{A}_4$, $\overline{A}_5$, and $\overline{A}_6$ are brought to equations (1) and (2) for the consistency test. It is found that $d(\overline{A}_1, A_1) = 0.0637 < 0.1$, $d(\overline{A}_2, A_2) = 0.0646 < 0.1$, $d(\overline{A}_3, A_3) = 0.0741 < 0.1$, $d(\overline{A}_4, A_4) = 0.0839 < 0.1$, $d(\overline{A}_5, A_5) = 0 < 0.1$, and $d(\overline{A}_6, A_6) = 0 < 0.1$, which demonstrate that the seven intuitionistic fuzzy consistency judgment matrices pass the consistency test at one time.

4.1.3. Determining Weight. According to equation (7), the weights of six first-level indexes are obtained:

$$\omega_{B1} = (0.1590, 0.8234),$$
$$\omega_{B2} = (0.1590, 0.8234),$$
$$\omega_{B3} = (0.1593, 0.8237),$$
$$\omega_{B4} = (0.1303, 0.7859),$$
$$\omega_{B5} = (0.1013, 0.7482),$$
$$\omega_{B6} = (0.0856, 0.7277).$$

$$(15)$$

Similarly, the same method is used to bring the intuitionistic preference relation matrix of secondary indexes into equation (7). Then, the weight of each secondary index and its corresponding first-level index is aggregated by using equation (10); hence, the total weight integrated first-level index with the secondary index is obtained and shown in Table 3:

$$\omega(C_j) = \omega_{B1} \otimes \omega_{C1} = (0.1590, 0.8234) \otimes (0.3201, 0.6499)$$
$$= (0.0509, 0.9382).$$

$$(16)$$

4.1.4. Evaluation of the Models. Ten experts are asked to rate the abovementioned backfill operation models on the IFAHP pairwise comparison scale. The arithmetic average of ten evaluation scores is taken as the expert evaluation result, by which the intuitionistic fuzzy evaluation matrix is constructed, as shown in Table 4. The evaluation results of the backfill operational models including $M1$, $M2$, and $M3$ are calculated through using the algorithm for the intuitionistic fuzzy value including equations (8) and (9). The score function is calculated by applying equation (11). The ranking function is calculated by applying equation (12).

$M1 = \oplus_{i=1}^{16} \quad M_{1j} \otimes \omega(C_j) = (0.41, 0.48) \otimes \quad (0.0509, 0.9382) \oplus (0.56, 0.33) \otimes (0.0405, 0.9237) \oplus (0.57, 0.35) \otimes (0.0340, 0.9144) \oplus (0.72, 0.21) \otimes (0.0418, 0.9251) \oplus (0.57, 0.29) (0.0335, 0.9080) \oplus (0.67, 0.25) \otimes (0.0288, 0.8984) \oplus (0.66, 0.26) \otimes (0.0487, 0.9350) \oplus (0.57, 0.32) \otimes (0.0404, 0.9232) \oplus (0.59, 0.32) \otimes (0.0346, 0.9149) \oplus (0.32, 0.60) \otimes (0.0388, 0.9191) \oplus (0.35, 0.57) \otimes (0.0349, 0.9111) \oplus (0.39, 0.53) \otimes (0.0282, 0.8975) \oplus (0.51, 0.39) \otimes (0.0495, 0.8707) \oplus (0.62, 0.31) \otimes (0.0359, 0.8308) \oplus (0.64, 0.29) \otimes (0.0433, 0.8657) \oplus (0.61, 0.31) \otimes (0.0300, 0.8163) = (0.2882, 0.3409)$

$M2 = \oplus_{i=1}^{16} (M_{2j} \otimes \omega(C_j)) = (0.3370, 0.2859)$

$M3 = \oplus_{i=1}^{16} (M_{3j} \omega(C_j)) = (0.3394, 0.2814)$

$H(1) = 0.4808$, $H(2) = 0.5186$, and $H(3) = 0.5210$

$\rho(1) = 0.4879$, $\rho(2) = 0.4565$, and $\rho(3) = 0.4555$

4.2. Discussion. This study focuses on how to make decision on the optimal backfill operation model in the mining industries and proposes joint venture alliance. The score

TABLE 3: Weight of each index and total weight.

First-level index	Secondary index	Total weight
B1 (0.1590,0.8234)	C1 (0.3201, 0.6499)	(0.0509, 0.9382)
	C2 (0.2555, 0.5680)	(0.0405, 0.9237)
	C3 (0.2137, 0.5151)	(0.0340, 0.9144)
B2 (0.1313,0.7872)	C4 (0.3187, 0.6482)	(0.0418, 0.9251)
	C5 (0.2550, 0.5678)	(0.0335, 0.9080)
	C6 (0.2191, 0.5226)	(0.0288, 0.8984)
B3 (0.1593,0.8237)	C7 (0.3060, 0.6315)	(0.0487, 0.9350)
	C8 (0.2537, 0.5642)	(0.0404, 0.9232)
	C9 (0.2172, 0.5172)	(0.0346, 0.9149)
B4 (0.1303,0.7859)	C10 (0.2976, 0.6222)	(0.0388, 0.9191)
	C11 (0.2675, 0.5848)	(0.0349, 0.9111)
	C12 (0.2164, 0.5212)	(0.0282, 0.8975)
B5 (0.1013,0.7482)	C13 (0.4885, 0.4863)	(0.0495, 0.8707)
	C14 (0.3548, 0.3279)	(0.0359, 0.8308)
B6 (0.0856,0.7277)	C15 (0.5058, 0.5068)	(0.0433, 0.8657)
	C16 (0.3503, 0.3252)	(0.0300, 0.8163)

TABLE 4: Intuitionistic fuzzy evaluation matrix of the models.

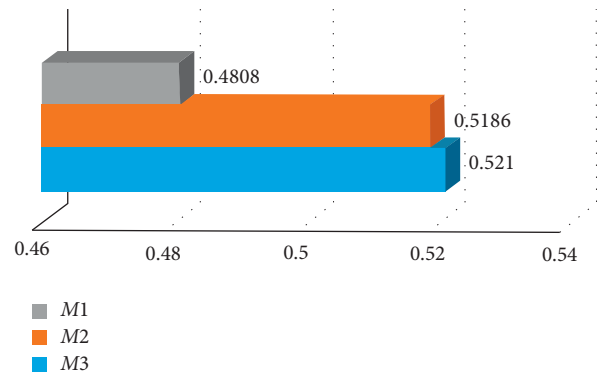| M_{1j}	M_{2j}	M_{3j}
(0.41, 0.48)	(0.62, 0.28)	(0.74, 0.20)
(0.56, 0.33)	(0.65, 0.25)	(0.71, 0.21)
(0.57, 0.35)	(0.69, 0.22)	(0.73, 0.21)
(0.72, 0.21)	(0.66, 0.23)	(0.74, 0.20)
(0.57, 0.29)	(0.69, 0.21)	(0.74, 0.18)
(0.67, 0.25)	(0.73, 0.19)	(0.71, 0.20)
(0.66, 0.26)	(0.69, 0.23)	(0.62, 0.28)
(0.57, 0.32)	(0.74, 0.19)	(0.61, 0.26)
(0.59, 0.32)	(0.69, 0.22)	(0.64, 0.25)
(0.32, 0.60)	(0.62, 0.29)	(0.58, 0.32)
(0.35, 0.57)	(0.44, 0.50)	(0.53, 0.39)
(0.39, 0.53)	(0.56, 0.36)	(0.58, 0.33)
(0.51, 0.39)	(0.69, 0.23)	(0.65, 0.27)
(0.62, 0.31)	(0.70, 0.22)	(0.66, 0.23)
(0.64, 0.29)	(0.71, 0.22)	(0.71, 0.22)
(0.61, 0.31)	(0.66, 0.27)	(0.69, 0.22)

FIGURE 4: Comparison chart of the score function of the models.

functions of the models are clearly shown in Figure 4. As seen from the graph, the highest rating is joint venture alliance, with a score function of 0.5210, which is viewed as

TABLE 5: Score function of the secondary index on the three backfill operation models.

Secondary index	Total weight	M_{1j}	M_{2j}	M_{3j}
Total capital input (C1)	(0.0509, 0.9382)	0.4685	0.6545	0.6822
Operational cost optimization (C2)	(0.0405, 0.9237)	0.6036	0.6818	0.7547
Profit variance (C3)	(0.0340, 0.9144)	0.6019	0.7156	0.7312
Mine owner satisfaction (C4)	(0.0418, 0.9251)	0.7383	0.6937	0.7453
Backfill vendor satisfaction (C5)	(0.0335, 0.9080)	0.6228	0.7182	0.7547
Regulatory satisfaction (C6)	(0.0288, 0.8984)	0.6944	0.7500	0.7593
Mining-separation-backfill balance (C7)	(0.0487, 0.9350)	0.6852	0.7130	0.7340
Flexibility (C8)	(0.0404, 0.9232)	0.6126	0.7570	0.6546
Communication and collaboration efficiency (C9)	(0.0346, 0.9149)	0.6239	0.7156	0.6549
Training and development (C10)	(0.0388, 0.9191)	0.3704	0.6514	0.6757
Technological innovation capability (C11)	(0.0349, 0.9111)	0.3981	0.4717	0.6182
Knowledge sharing (C12)	(0.0282, 0.8975)	0.4352	0.5926	0.5648
Tailings utilization (C13)	(0.0495, 0.8707)	0.5545	0.7130	0.6147
Reduction of environmental impact (C14)	(0.0359, 0.8308)	0.6449	0.7222	0.6759
Employee accident (C15)	(0.0433, 0.8657)	0.6636	0.7290	0.6937
Health of residents (C16)	(0.0300, 0.8163)	0.6389	0.6822	0.7290
Final score		0.4808	0.5186	0.5210

the optimal strategic operation mechanism for mine backfill in the study. The next to be followed closely is the outsourcing model, which has a score function of 0.5186. However, compared with other models, the self-management model receives a lower score function of 0.4808, and this implies that the outsourcing model is suboptimal decision-making whereas the self-management model has fewer advantages.

The intuitive fuzzy evaluation matrix is transformed into the score function by using equation (11), as seen in Table 5. There are 16 secondary indexes constructed under 6 perspectives, among which the financial perspective covers 3 criteria including total capital input, operational cost optimization, and profit variance, and the top importance of these indexes for evaluating the backfill operation business is given to joint venture alliance with scores of 0.6822, 0.7547, and 0.7312. This indicates that joint venture alliance has the advantages in reducing investment cost, optimizing cost structure, and profitability, which is followed by the outsourcing model. For the stakeholders' perspective, there are three secondary indexes under the first-level index, which are mine owner satisfaction, backfill vendor satisfaction, and regulatory satisfaction. Similarly, in the models, joint venture alliance receives the highest importance of 0.7453, 0.7547, and 0.7593. This manifests mine owners and ventures as well as regulators who have high satisfaction with joint venture alliance. The internal process perspective covers three secondary indexes, in which the highest score of mining-separation-backfill balance is given to the joint venture alliance whereas the outsourcing model receives the top importance of flexibility, communication and collaboration efficiency. It shows the superiority of the outsourcing model over other models in adaptability and communication capability. The fourth perspective, learning and growth, includes three secondary indexes, and joint venture alliance is rated as the top importance with regard to training and development and technological innovation capability whereas the outsourcing model is considered the highest importance with respect to knowledge sharing. It

demonstrates that joint venture alliance has a greater impact on employee learning and technical improvement of the mining industry. For the environmental perspective, the outsourcing model receives the top score about tailings utilization and reduction of environmental impact, which implies that the model helps promote environmental protection. For the social perspective, joint venture alliance is rated as the top importance in regard to employee accident and health of residents, which shows that this model plays the significant role in fulfilling corporate social responsibility. In summary, joint venture alliance has greater advantages than the self-management and outsourcing model.

5. Conclusion

It is indispensable for the mining industry to find an appropriate backfill operational mechanism which will facilitate the development of the mine backfill business; therefore, this study proposes joint venture alliance; on this basis, the model is compared with the self-management and outsourcing model by the way of the integrated methods. In order to assess three operation models, the study puts forward the hierarchical framework and evaluation system of mine backfill business evaluation, and the IFAHP method is used to estimate the optimal model. It is found to draw the following conclusions through adopting the proposed approach.

(1) This study establishes a strategic and hierarchical framework for evaluating the backfill operation model in the mining industry, which fully takes into account sustainability and includes 6 perspectives and 16 secondary indexes. In addition to financial, stakeholders, internal process, and learning and growth perspectives, environmental and social perspectives are integrated into the framework.

(2) Considering the hesitant degree existing under the fuzzy environment and the fuzzy mathematical thought, this study proposes the IFAHP approach,

which is applied to determine the relative weight of each index and total weight and calculate the final score. Due to superiority of the IFAHP approach, this method enables to reveal objectivity in the process of model evaluation. Therefore, the integrated method is addressed through applying SBSC along with the IFAHP approach, which better shows the combination of several factors concerned including strategy, sustainability, hierarchy, and objectivity.

(3) There are self-management and outsourcing generally used as backfill operation models worldwide, whose advantages are insufficient from the strategic and sustainability perspective. The novelty of this study lies in proposing joint venture alliance and exploring its superiority in the mine backfill management. Through comparison and evaluation of the models including joint venture alliance, self-management, and outsourcing, the results show that joint venture alliance receives the top score, next is followed by the outsourcing model, and the last one is the self-management model. Thus, joint venture alliance is considered as the optimal operation mechanism of the mine backfill, followed by the outsourcing model, and the self-management model has few advantages compared with the other models.

Data Availability

All data are valid and included within this paper.

Conflicts of Interest

The authors declare that they have no conflicts of interest.

Acknowledgments

References

[1] A. Gunasekaran, Z. Irani, K.-L. Choy, L. Filippi, and T. Papadopoulos, "Performance measures and metrics in outsourcing decisions: a review for research and applications," *International Journal of Production Economics*, vol. 161, pp. 153–166, 2015.

[2] ICC, *Coal Mining Is Private Participation the Answer?*, Indian Chamber of Commerce, Kolkata, India, 2013.

[3] B. Baatartogtokh, W. S. Dunbar, and D. Van Zyl, "The state of outsourcing in the Canadian mining industry," *Resources Policy*, vol. 59, pp. 184–191, 2018.

[4] R. Sivakumar, D. Kannan, and P. Murugesan, "Green vendor evaluation and selection using AHP and Taguchi loss functions in production outsourcing in mining industry," *Resources Policy*, vol. 46, pp. 64–75, 2015.

[5] NCL, "Northern coalfields limited," Annual Report 2014-15, NCL, Madhya Pradesh, India, 2015.

[6] SECL, "Himalaya granites limited," 29th Annual Report 2014-15, South Eastern Coalfields Limited, Chattisgarh, India, 2015.

[7] F. Nan, Y. Chen, H. Feng, D. Li, and M. Li, "To outsource or not: the impact of information leakage risk on information security strategy," *Information &Management*, vol. 57, Article ID 103215, 2020.

[8] T. K. Das and B.-S. Teng, "Instabilities of strategic alliances: an internal tensions perspective," *Organization Science*, vol. 11, no. 1, pp. 77–101, 2000.

[9] J. Y. Murray and M. Kotabe, "Performance implications of strategic fit between alliance attributes and alliance forms," *Journal of Business Research*, vol. 58, no. 11, pp. 1525–1533, 2005.

[10] V. Durmaz and L. Zheng, "The effect of joint ventures on airline competition: the case of American airlines, British airways and iberia joint business," *Procedia-Social and Behavioral Sciences*, vol. 210, pp. 430–439, 2015.

[11] Y. Moon, T. Yao, and B. Jiang, "Outsourcing versus joint venture from vendor's perspective," *International Journal of Production Economics*, vol. 129, no. 1, pp. 23–31, 2011.

[12] O. Demirtas, "Evaluating the core capabilities for strategic outsourcing decisions at aviation maintenance industry," *Procedia - Social and Behavioral Sciences*, vol. 99, pp. 1134–1143, 2013.

[13] Y. Tjader, J. H. May, J. Shang, L. G. Vargas, and N. Gao, "Firm-level outsourcing decision making: a balanced scorecard-based analytic network process model," *International Journal of Production Economics*, vol. 147, pp. 614–623, 2014.

[14] A. Makan and F. Ahmed, "Sustainability assessment of large-scale composting technologies using Promethee method," *Journal of Cleaner Production*, vol. 261, Article ID 121244, 2020.

[15] H.-Y. Wu, "Constructing a strategy map for banking institutions with key performance indicators of the balanced scorecard," *Evaluation and Program Planning*, vol. 35, no. 3, pp. 303–320, 2012.

[16] G. Ozkaya and C. Erdin, "Evaluation of smart and sustainable cities through a hybrid MCDM approach based on ANP and TOPSIS technique," *Heliyon*, vol. 6, Article ID e05052, 2020.

[17] R. Davoudabadi, S. M. Mousavi, and V. Mohagheghi, "A new decision model based on DEA and simulation to evaluate renewable energy projects under interval-valued intuitionistic fuzzy uncertainty," *Renewable Energy*, vol. 164, pp. 1588–1601, 2020.

[18] C. Tian, J.-J. Peng, S. Zhang, J.-Q. Wang, and M. Goh, "A sustainability evaluation framework for WET-PPP projects based on a picture fuzzy similarity-based VIKOR method," *Journal of Cleaner Production*, vol. 289, Article ID 125130, 2020.

[19] M. Tavana, M. Zareinejad, D. Di Caprio, and M. A. Kaviani, "An integrated intuitionistic fuzzy AHP and SWOT method for outsourcing reverse logistics," *Applied Soft Computing*, vol. 40, pp. 544–557, 2016.

[20] M. Çolak and İ. Kaya, "Prioritization of renewable energy alternatives by using an integrated fuzzy MCDM model: a real case application for Turkey," *Renewable and Sustainable Energy Reviews*, vol. 80, pp. 840–853, 2017.

[21] Y. Xue, Y. Deng, and H. Garg, "Uncertain database retrieval with measure - based belief function attribute values under intuitionistic fuzzy set," *Information Sciences*, vol. 546, pp. 436–447, 2021.

[22] H. Garg, Z. Ali, and T. Mahmood, "Algorithms for complex interval-valued q-rung orthopair fuzzy sets in decision making based on aggregation operators,AHP,andTOPSIS," *Expert Systems*, vol. 38, no. 1, 2021.

[23] J. Puri, S. P. Yadav, and H. Garg, "A new multi-component DEA approach using common set of weights methodology and imprecise data: an application to public sector banks in India with undesirable and shared resources," *Annals of Operations Research*, vol. 259, no. 1-2, pp. 351–388, 2017.

[24] M. J. Epstein and P. S. Wisner, "Using a balanced scorecard to implement sustainability," *Environmental Quality Management*, vol. 11, no. 2, pp. 1–10, 2001.

[25] R. S. Kaplan and D. P. Norton, "The balanced scorecard: measures that drive performance," *Harvard Business Review*, vol. 70, pp. 71–99, 1992.

[26] F. Frank, T. Hahn, and S. Schaltegger, "The sustainability balanced scorecard-linking sustainability management to business strategy," *Business Strategy and the Environment*, vol. 11, pp. 269–284, 2002.

[27] M. Sidiropoulos, Y. Mouzakitis, E. Adamides, and S. Goutsos, "Applying sustainable indicators to corporate strategy: the eco-balanced scorecard," *Environmental Research, Engineering Management*, vol. 1, pp. 28–33, 2004.

[28] A. Möller and S. Schaltegger, "The sustainability balanced scorecard as a framework for eco-efficiency analysis," *Journal of Industrial Ecology*, vol. 9, no. 4, pp. 73–83, 2005.

[29] H. Graham, "Measuring organizational performance: beyond the triple bottom line," *Business Strategy and the Environment*, vol. 18, pp. 177–191, 2009.

[30] T. A. Tsalis, I. E. Nikolaou, E. Grigoroudis, and K. P. Tsagarakis, "A framework development to evaluate the needs of SMEs in order to adopt a sustainability-balanced scorecard," *Journal of Integrative Environmental Sciences*, vol. 10, pp. 3-4, 2013.

[31] I. Dias-Sardinha, L. Reijnders, and P. Antunes, "From environmental performance evaluation to eco-efficiency and sustainability balanced scorecards," *Environmental Quality Management*, vol. 12, no. 2, pp. 51–64, 2002.

[32] M. Radu, "Empirical study on the indicators of sustainable performance-the sustainability balanced scorecard, effect of strategic organizational change," *Amfiteatru Economic*, vol. 32, pp. 451–469, 2012.

[33] T. L. Saaty, *The Analytic Hierarchy Process*, McGraw-Hill, New York, NY, USA, 1980.

[34] H. Liao, Z. Xu, and X.-J. Zeng, "Distance and similarity measures for hesitant fuzzy linguistic term sets and their application in multi-criteria decision making," *Information Sciences*, vol. 271, pp. 125–142, 2014.

[35] H. Liao and Z. Xu, "Consistency of the fused intuitionistic fuzzy preference relation in group intuitionistic fuzzy analytic hierarchy process," *Applied Soft Computing*, vol. 35, pp. 812–826, 2015.

[36] R. Nada, "A multidimensional framework for understanding outsourcing arrangement," *Journal of Supply Chain Management*, vol. 43, pp. 3–15, 2007.

[37] C. Samantra, S. Datta, and S. S. Mahapatra, "Risk assessment in IT outsourcing using fuzzy decision-making approach: an Indian perspective," *Expert Systems with Applications*, vol. 41, no. 8, pp. 4010–4022, 2014.

[38] D. N. Burton, D. W. Dobler, and S. L. Starling, *World Class Supply Management-The Key to Supply Chain Management*, McGraw-Hill, New York, NY, USA, 7th edition, 2003.

[39] L. Cacciolatti, A. Rosli, J. L. Ruiz-Alba, J. Chang, and J. Chang, "Strategic alliances and firm performance in startups with a social mission," *Journal of Business Research*, vol. 106, pp. 106–117, 2020.

[40] M.-T. Lu, C.-C. Hsu, J. J. H. Liou, H.-W. Lo, and H.-W. Lo, "A hybrid MCDM and sustainability-balanced scorecard model to establish sustainable performance evaluation for international airports," *Journal of Air Transport Management*, vol. 71, pp. 9–19, 2018.

[41] S. Agrawal, R. K. Singh, and Q. Murtaza, "Outsourcing decisions in reverse logistics: sustainable balanced scorecard and graph theoretic approach," *Resources, Conservation and Recycling*, vol. 108, pp. 41–53, 2016.

[42] A. H. I. Lee, H.-Y. Kang, C.-F. Hsu, and H.-C. Hung, "A green supplier selection model for high-tech industry," *Expert Systems with Applications*, vol. 36, no. 4, pp. 7917–7927, 2009.

[43] X. Lin and C. L. Wang, "Enforcement and performance: the role of ownership, legalism and trust in international joint ventures," *Journal of World Business*, vol. 43, no. 3, pp. 340–351, 2008.

[44] M. Modak, K. Pathak, and K. K. Ghosh, "Performance evaluation of outsourcing decision using a BSC and Fuzzy AHP approach: a case of the Indian coal mining organization," *Resources Policy*, vol. 52, pp. 181–191, 2017.

[45] C. Qi and A. Fourie, "Cemented paste backfill for mineral tailings management: review and future perspectives," *Minerals Engineering*, vol. 144, Article ID 106025, 2019.

[46] F. M. Tsai, M.-L. Tseng, M. Lim, and K.-J. Wu, "Assessing a hierarchical sustainable solid waste management structure with qualitative information: policy and regulations drive social impacts and stakeholder participation," *Resources, Conservation and Recycling*, vol. 168, Article ID 119740, 2021.

[47] M. Modak, K. K. Ghosh, and K. Pathak, "A BSC-ANP approach to organizational outsourcing decision support-A case study," *Journal of Business Research*, vol. 103, pp. 432–447, 2019.

[48] S. Khaleie, M. Fasanghari, and E. Tavassoli, "Supplier selection using a novel intuitionist fuzzy clustering approach," *Applied Soft Computing*, vol. 12, no. 6, pp. 1741–1754, 2012.

[49] L. Liu, P. Yang, C. Qi, B. Zhang, L. Guo, and K.-I. Song, "An experimental study on the early-age hydration kinetics of cemented paste backfill," *Construction and Building Materials*, vol. 212, pp. 283–294, 2019.

[50] H. Zhao and N. Li, "Evaluating the performance of thermal power enterprises using sustainability balanced scorecard, fuzzy Delphic and hybrid multi-criteria decision making approaches for sustainability," *Journal of Cleaner Production*, vol. 108, pp. 569–582, 2015.

[51] L. Liu, Z. Fang, C. Qi, B. Zhang, L. Guo, and K.-I. Song, "Experimental investigation on the relationship between pore characteristics and unconfined compressive strength of cemented paste backfill," *Construction and Building Materials*, vol. 179, pp. 254–264, 2018.

[52] K. T. Atanassov, "More on intuitionistic fuzzy sets," *Fuzzy Sets and Systems*, vol. 33, no. 1, pp. 37–45, 1989.

[53] Z. Xu, "Intuitionistic preference relations and their application in group decision making," *Information Sciences*, vol. 177, no. 11, pp. 2363–2379, 2007.

Research Article

Durability Analysis of Sludge Solidified with Soda Residue Subjected to Dry-Wet and Freeze-Thaw Cycles

Jun He [iD]**, Lei Zhang, and Chi Zhang**

School of Civil Engineering, Architecture and Environment, Hubei University of Technology, Wuhan 430068, China

Correspondence should be addressed to Jun He; hjunas@163.com

Soda residue (SR), ground-granulated blast-furnace slag (GGBS), and quicklime (QL) were employed for solidifying sewage sludge, which is a technique for sustainable development by transforming industrial solid waste and sludge into engineering fill material such as backfill material in mine or abandoned caverns. The durability of solidified sludge against dry-wet and freeze-thaw cycles was investigated by unconfined compressive strength (UCS), X-ray diffraction, scanning electron microscopy, and nuclear magnetic resonance tests. The results demonstrated that the SR-GGBS-QL solidified sludge had good dry-wet and freeze-thaw durability. In general, UCS increased at first, but then it decreased to some degree with the increase in dry-wet and freeze-thaw cycles. The cycle number for peak UCS depended on the durability test types and SR content. The UCS values after seven dry-wet cycles or ten freeze-thaw cycles were higher than the initial values before cycles. The main products detected in SR-GGBS-QL solidified sludge were ettringite, hydroaluminite, and calcium silicate hydrate (C-S-H). In addition, some pollutants such as copper, arsenic, and chromium were stabilized. The weakening effect on the microstructure of the solidified sludge occurred after dry-wet or freeze-thaw cycles. However, the hydration reaction continued with the increase of dry-wet and freeze-thaw cycles, leading to an increase in the amount of hydration products (especially C-S-H) and compact microstructure. These contributed to high UCS values and good dry-wet and freeze-thaw durability. The strength and failure strain of solidified sludge still met the requirement of filling materials after dry-wet or freeze-thaw cycles.

1. Introduction

As a byproduct of municipal wastewater treatment, sewage sludge has been dramatically produced every year in the world and needs to be treated urgently. Owing to its high moisture content, high content of organic and harmful substances, and poor mechanical performance, sewage sludge was usually solidified or stabilized by curing agent and skeleton materials. Various binders, such as cement, lime, silica fume, phosphogypsum, and some inorganic cementitious materials, have been usually used as curing agents to solidify sludge [1–7]. And skeleton materials used in sludge included bentonite, soil, slag, municipal solid waste, and incineration bottom ash and fly ash [6–13]. More and more solid wastes were investigated on the potential to be used as curing agent or skeleton materials.

Soda residue (SR) is a main waste generated in soda industry, and soda residue pollution has become an important factor that destroys the environment and restricts the development of the salt chemical industry. SR has been used as soil amendment, filling materials in salt caverns, sea reclamation, and filling embankment [14, 15]. Owing to its components (such as $CaCO_3$, $CaSO_4$, and $CaCl_2$) and granulometric composition (mainly of silt), SR has the potential to be used as a curing agent and skeleton material. For example, SR has been used as one of the main raw materials to prepare a new nonclinker to solidify soil [16]. SR can provide active components to strengthen the skeleton effect when used as a modification agent in muddy soil [17]. When SR is used as solidifier of soft soil, the sulfate and chloride in SR help to form hydration products, such as ettringite and calcium chloroaluminate hydrates, which can improve the strength of the soil [18]. All these studies deepened the understanding of the properties of SR and extended the potential of its applications in solidifying sludge as both curing agent and skeleton material.

Solidified sludge can be used as the stable and safe filler which meets the engineering requirements and environmental requirements [19]. For example, Lin et al. [9] found that calcium bentonite was a favorable additive to improve the effectiveness of cement to solidify sewage sludge due to its good mechanical properties and advantage to immobilize of pollutants such as alkalinity, organics, copper, and zinc. They concluded that the unconfined compressive strength (UCS) of the treated sludge after 7 days and 28 days could meet the requirement of landfilling and construction material, respectively. Dohnalkova et al. [20] used cement and fly ash to solidify the neutralisation sludge and found that the solidified sludge could be used as a filler material for recultivation and installation of technological units in landfills and a buffer layer or underlayer in the construction of roads or subfloors. One of the possible engineering applications is using solidified sludge as backfill material in mine or abandoned caverns, which can solve the problem of waste disposal and the potential geologic disasters associated with sludge disposal. For example, the shortage of backfill materials is one of the factors that restrict the development of backing mining technology in China; then municipal construction wastes, mine tailings, and some chemical solid wastes including sludge were proposed to be used as filling materials in backfill mining [21]. Therefore, the solidified sludge can be considered as a filling material when there is a large amount of available sludge near the mining area or abandoned caverns. Particularly, adoption of solid waste around the mining area or abandoned caverns as sludge solidifier is a promising approach to restore a safe and green environment.

Dry-wet and freeze-thaw cycles might have effects on the engineering properties of solidified sludge and the stability and safety of sludge pile or backfill. From the previous researches about the durability of solidified sludge (see Table 1), it can be observed that the changes of strength with the dry-wet and freeze-thaw cycles are different due to the difference in sludge type, solidified agent, durability type, and testing conditions. The dry-wet cycle testing conditions, such as drying temperature and time and wetting mode and time, have significant effects on the strength. Under the effect of dry-wet cycles with different testing conditions, the solidified sludge may present monotonous increase [8, 23], increase first and then decrease [12, 22], or monotonous decrease [10, 13, 23]. The freeze-thaw cycle testing conditions, such as the freezing temperature, the thawing temperature, and the durations, have varying effects on the strength. Some solidified sludge showed a decrease in strength after freeze-thaw cycles [10, 12, 25], while some presented an increase first and then decrease [22, 24]. Nowadays, little relevant literature is available on the curing and skeleton effects of SR when it is used as a modification agent in sludge and subjected to dry-wet and freeze-thaw cycles.

The aim of this study was to investigate the effects of dry-wet and freeze-thaw cycles on the strength properties of solidified sludge. The sewage sludge was solidified with SR, ground-granulated blast-furnace slag (GGBS), and quicklime (QL). Sludge samples solidified with 3 different SR contents were cured for 28 days and subjected to different numbers of dry-wet cycle or freeze-thaw cycle. The strength and microstructural and mineralogical characteristics were investigated by unconfined compressive strength tests, X-ray diffraction (XRD), nuclear magnetic resonance (NMR), and scanning electronic microscopy (SEM) technologies. The results from this study are helpful in understanding the durability of SR-GGBS-QL solidified sludge when used as a filling material.

2. Materials and Methods

2.1. Materials. The tested sewage sludge was taken from Wuhan Donghu Domestic Sewage Treatment Plant, and its properties are shown in Table 2. The sewage sludge has high contents of water and organic matter and high values of the liquid limit, plastic limit, and plasticity index. The curing agents used are composed of SR, GGBS, and QL. The physical properties and chemical compositions of the GGBS and SR can be found in He et al.'s study [18]. Xue and Chen [11] found that the particles in the size range of 0.075 to 0.85 mm were conducive to skeleton formation in sludge. About 75% of the SR particles have a size between 0.075 and 0.85 mm [18], ensuring that SR has a positive effect on the formation of skeleton in sewage sludge. QL can quickly reduce the moisture content of the sludge and activate GGBS [11, 26]. The CaO content in the QL used was more than 98%.

2.2. Testing Scheme and Procedure

2.2.1. Testing Scheme. The testing scheme is shown in Table 3. The content is defined as the mass ratio of solidifier to wet sludge. According to the research of He et al. [18], Xue and Chen [11], and the results of preliminary experiments, the GGBS and QL contents were determined and fixed. In order to make the full use of SR, the SR content was the highest compared to those of other additives, and different contents were tested. The 30%, 40%, and 50% SR contents are denoted by S3, S4, and S5, respectively, in the text.

2.2.2. Sample Preparation. The SR and GGBS were dried in an oven at 60°C and 105°C, respectively, for 24 h. Then, the SR and GGBS were ground and passed through a 1 mm sieve. The solidifiers and the sewage sludge were mixed and stirred thoroughly and then sealed and maturated at 30°C for 3 days. Considering the exothermic effect of QL and the need to maintain the consistency of the test conditions, 30°C was selected for the maturation of all the samples. After 3 days of maturation, the moisture content of the mixture dropped to a low value (the moisture contents of samples S3, S4, and S5 were 85.8%, 82.1%, and 68.2%, respectively). It was conducive to sample preparation and subsequent tests. Before sample preparation, a layer of petroleum jelly was evenly spread on the inner wall of the mold (diameter 3.91 cm and height 8 cm), and then the mixture was put into the mold in 3 layers. Each layer was vibrated and compacted by a compactor to eliminate the air in the sample until the height did not change. When the air bubbles were eliminated, the

TABLE 1: Previous literatures on durability of solidified sludge.

Reference	Solidified agents	Soil type	Durability type	Cured days and one cycle condition	Results of strength
Hu [12]	Inorganic cementitious materials (20%)	Sewage sludge	Freeze-thaw	28 days, −20°C (24 h) + 20°C (24 h)	Decrease from 100 kPa (before cycle) to 50 kPa (6th) then keep constant
			Dry-wet	—	Increase from 200 kPa (before cycle) to 400 kPa (1st) and decrease to 300 kPa (7th) then destroyed
Hu [12]	Inorganic cementitious materials (20%) + waste incineration bottom ash	Sewage sludge	Dry-wet	—	Increase from 250 kPa (before cycle) to 600 kPa (1st) and decrease to 400 kPa (4th) and then destroyed
Li [10]	Conditioned with fly ash + lime + ferric chloride and then dewatered	Sewage sludge	Freeze-thaw	28 days, −20°C (5 h) + 10~20°C (3 h)	Decrease slightly and strength loss ratio is about 15% (12th)
			Dry-wet	28 days, 60°C (24 h) + immerse at 20°C (24 h)	Decrease slightly and strength loss ratio is about 10% (12th)
Li [8]	Bentonite (10~20%) + cement (20~60%)	Sewage sludge	Dry-wet	28 days, 60°C (24 h) + immerse at 20°C (24 h)	Increase after 12 cycles, the higher the cement content, the more the difference
Yang et al. [13]	Soil + quicklime (20%) + curing agent (10%)	Sewage sludge	Dry-wet	28 days, 35°C (12 h) + adsorb water through porous stone + 20°C (24 h)	Decrease rapidly (≤5 cycles) and then tend to be stable
Wang et al. [22]	MgO (7%) + fly ash (3%)	Dredge sludge	Freeze-thaw	28 days, −20°C (24 h) + 20°C (24 h)	Increase from 900 kPa (before cycle) to 1910 kPa (16th) and then decrease to 1400 kPa (20th)
			Dry-wet	28 days, 40°C (24 h) + immerse at room temperature (24 h)	Increase from 900 kPa (before cycle) to 2320 kPa (8th) and then decrease to 1700 kPa (20th)
Liu et al. [23]	Cement (100, 150, and 200 kg/m³)	Dredge sludge	Dry-wet	28 days, 60°C (8 h) + vacuum saturation at 20°C (16 h)	Decrease after cycle for 100 kg/m³ and increase for 150 and 200 kg/m³
Wang et al. [24]	Cement (5, 10, and 15%)	Lead-polluted soil	Freeze-thaw	28 days, −15°C (3 h) + 20 ± 1°C (3 h)	Increase when the cycles increase from 1 to 3 and then decrease
Hou et al. [25]	Sodium silicate (3%)	Loess	Freeze-thaw	7 days, −15°C (12 h) + 15°C (12 h)	Decrease from 3935 kPa (before cycle) to 577 kPa (20th)

TABLE 2: Basic characteristics of the sludge.

Parameters	Value				
Moisture (%)	566				
pH	6.45				
Organic matter content (%)	35				
Specific surface area (m²/kg)	203.0				
Atterberg limits	Liquid limit (%)		Plastic limit (%)		Plasticity index
	380.31		62.92		317.39
Main chemical compositions (%)	SiO_2	P_2O_5	Al_2O_3	Fe_2O_3	CaO
	45.1	16.4	12.9	6.7	5.6
Heavy metals (mg/kg dry sludge)	Cu	Zn	Pb	Cd	Cr	Ni
	0.326	22.190	3.778	0.160	0.974	0.566

vibration or compaction would not affect the density of the mixture sample under high water content [26]. Then, the sample was demolded and cured in a curing box with a temperature of 20 ± 1°C and a humidity of >90% for 28 days.

2.2.3. Dry-Wet Cycles and Freeze-Thaw Cycles. Since there is no standard method for dry-wet cycle test at present, the dry-wet cycle was referred to the test method proposed by the Japanese Highway Association and Kamei et al. [27, 28].

TABLE 3: Summary of testing scheme.

Testing program		SR content (%)	GGBS content (%)	QL content (%)	Curing time (days)	Number of cycles
Dry-wet cycles	UCS	30, 40, 50	20	12	28	0, 1, 2, 3, 4, 5, 6, 7
	XRD	50				0, 1, 6, 7
	SEM	50				0, 3, 6
	NMR	50				0, 3, 6
Freeze-thaw cycles	UCS	30, 40, 50	20	12	28	0, 1, 3, 6, 10
	XRD	50				0, 1, 10
	SEM	50				0, 1, 6
	NMR	50				0, 1, 10

Before the dry-wet cycle, the mass and volume of the samples after being cured for 28 days were measured. The sample was dried at $20 \pm 1°C$ for 24 h and then put into a beaker. Water was added to the beaker until the sample was submerged. The sample was immersed in water for another 24 h. This process was one dry-wet cycle. The strength tends to be stable after 7 cycles [23], so the number of dry-wet cycle was selected as 0~7. In order to prevent moisture from evaporating during the freeze-thaw cycles, the sample was wrapped with plastic wrap and put in the freezer. The freeze-thaw cycles were carried out with reference to the test method proposed by the American Society for Testing and Materials [29], Wang et al. [24], and Hou et al. [25]. The process of each freeze-thaw cycle was designed as follows: $-15°C$ for 24 h and $20°C$ for another 24 h. 1, 3, 6, and 10 freeze-thaw cycles were implemented on the samples. Then, the mass, UCS, and moisture content of the samples were measured after the dry-wet or freeze-thaw cycles.

2.2.4. Testing Methods. The UCS test was conducted based on the Standard for Geotechnical Testing Method (GB/T 50123-2019) [30]. The vertical load was applied at a constant displacement rate of 1.18 mm/min until the specimen failed. In order to achieve reliable results, two replicate specimens were prepared for each test, and the average value and margin of error of the results were reported. The specimens after UCS tests were used for XRD and SEM analyses. In XRD analysis (Bruker AXS, Madison, WI, USA), the specimen was firstly dried at $50°C$ and milled into fine particles and then scanned with a rate of $2°/min$ from $10°$ to $75°$. The specimen was cut into blocks of about 1 cm³ and dried at $50°C$. A block after drying was taken for SEM analysis (SU8010, Hitachi Ltd., Tokyo, Japan). Although drying at $50°C$ might lead to shrinkage and change the microstructure to some degree, the mineral compositions can be revealed in SEM images. Another batch of specimens with SR content of 50% (see Table 3) was prepared and subjected to dry-wet or freeze-thaw cycles. Then, a cylinder specimen was sampled using a small syringe and put into the NMR analysis (MicroM12-025VR, Suzhou Niumag Analytical Instrument Corporation, Suzhou, China). The T_2 distribution of the inversion curve generated by NMR analysis can be used to estimate the pore size distribution. The soil pores are assumed as ideal spheres; then, the diameter of the pore is proportional to T_2 [31].

3. Results and Discussion

3.1. Dry-Wet Cycles

3.1.1. Unconfined Compressive Strength. The stress-strain curves and UCS of solidified sludge subjected to dry-wet cycles are shown in Figure 1. The values of failure strain for all samples were in the range of 1% and 2%, with the brittle failure characteristics. In general, sample S5 had higher UCS compared with samples S4 and S3, and the difference between S4 and S3 was negligible. This indicated that sufficient amount of SR was needed to play the curing and skeleton roles in solidified sludge. The slight decrease in UCS after the 1st drying-wetting cycle could be observed for all samples. The UCS increased until the 5th or 6th cycle and then decreased slightly. After seven dry-wet cycles, the UCS for samples S5, S4, and S3 were 557.30, 320.77, and 346.16 kPa, respectively, which were 1.36, 1.16, and 1.45 times of those before dry-wet cycle.

Zhang et al. [32] proposed that the requirements of filling engineering were the UCS higher than 200 kPa and the failure strain less than 2.8% after being cured for 28 days. The minimum common standard for compressive strength in the Czech Republic is 400 kPa for the additive granulate for embankments and backfills for other constructions [20]. The minimum UCS required in the USA is 350 kPa after 28 days of curing for waste deposited on the landfill as a structural or substrate material [33]. Generally, all the samples after dry-wet cycles had the UCS greater than 200 kPa and failure strain less than 2.8% [31], which meet the requirements of filling engineering. The limit UCS of 400 kPa [20] can be met for sample S5 even after seven dry-wet cycles and the UCS for samples S4 and S3 close to 350 kPa [33].

3.1.2. Mass Loss Rate. Variations in the mass loss rate of solidified sludge with dry-wet cycles are shown in Figure 2. The mass loss rate (Δ_m) is defined as

$$\Delta_m = \frac{m_0 - m_n}{m_0} \times 100\%, \quad (1)$$

where m_0 and m_n are the mass of the sample before dry-wet cycle and after the nth cycle, respectively. It can be seen that Δ_m of solidified sludge increases firstly and then becomes stable after three dry-wet cycles. The Δ_m for sample S4 was lower than that of samples S5 and S3. More hydration products and higher filling and cementing effects might contribute to the lower Δ_m for sample S4 than sample S3. The

(a)

(b)

(c)

(d)
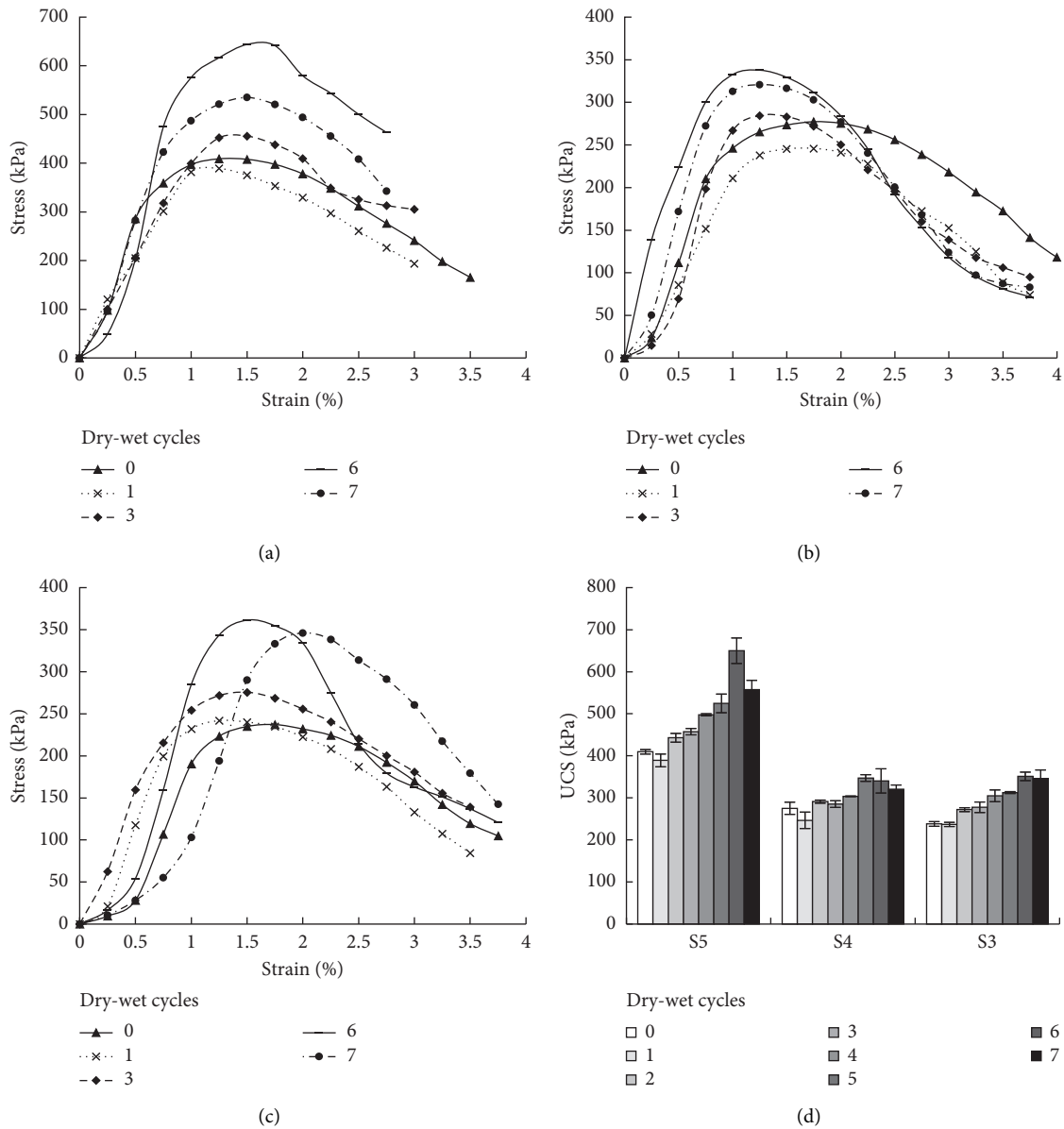
FIGURE 1: The stress-strain curves for samples (a) S5; (b) S4; (c) S3; and (d) UCS under dry-wet cycles.

dissolution of some substances in sample S5 such as ardealite (as will be shown in Figure 3(b)) might contribute to the greater than sample S4. All the values of Δ_m were less than 4%, similar to the results reported by Li [10].

3.1.3. Moisture Content.
Variations in moisture content of the solidified sludge with dry-wet cycles are shown in Figure 4. The initial moisture content of the samples before dry-wet cycle decreased with the increase in SR content. The sample before the cycle was unsaturated, so the initial moisture content was lower than that after the 1st dry-wet cycle. The increase in moisture content and sharp increase in Δ_m for the 1st dry-wet cycle might partly contribute to the slight decrease in UCS (Figure 1(d)). Generally, the moisture content decreased as the dry-wet cycles increased from one to seven.

3.2. Freeze-Thaw Cycles

3.2.1. Unconfined Compressive Strength.
The stress-strain and UCS of solidified sludge subjected to freeze-thaw cycles are shown in Figure 5. Similar to those subjected to dry-wet cycles, the stress-strain curves show obvious brittle failure characteristics, with failure strains between 1.3% and 2%. The UCS values of sample S5 after freeze-thaw cycles were higher than samples S4 and S3. When the sample subjected to one freeze-thaw cycle, the UCS increased significantly. The UCS for samples S5 and S4 decreased for the further cycles, while the UCS for sample S3 decreased after the 6th cycle. After ten freeze-thaw cycles, the UCS for samples S5, S4, and S3 were 454.26, 345.52, and 365.80 kPa, respectively, which were 1.11, 1.25, and 1.54 times of those before cycles. Similar to the results of dry-wet cycles, the UCS of sample S5 exceeded the limit of 400 kPa [20], and the UCS
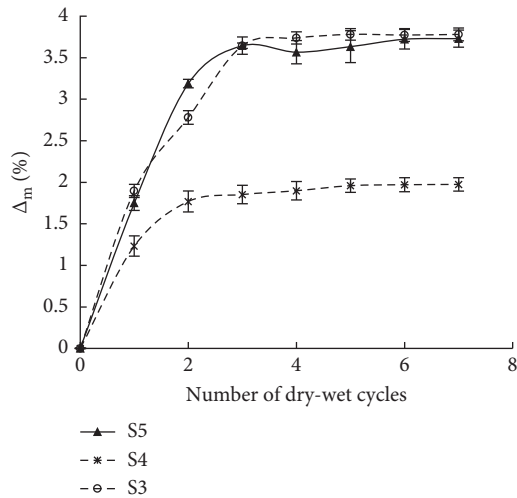
FIGURE 2: Variations in mass loss rate with dry-wet cycles.

of samples S4 and S3 was greater than or close to 350 kPa [33]. The UCS and failure strain of all the samples after ten freeze-thaw cycles met the requirements of filling engineering [32].

3.2.2. Moisture Content. Variations of moisture content of the solidified sludge with freeze-thaw cycles are shown in Figure 6. The lower moisture content was observed on the samples after one freeze-thaw cycle. Different from the samples subjected to dry-wet cycles, the samples in freeze-thaw cycles were sealed, and no water exchange with the environment occurs. The drop of moisture content for the 1st freeze-thaw cycle might be attributed to the variations of composition under the effect of temperature change, such as more assumption of portlandite and formation of calcium silicate hydrate (as will be shown in Figures 3(c) and 7(g) and 7(h)). After 10 freeze-thaw cycles, the moisture content of samples S3, S4, and S5 was 79.12%, 70.43%, and 67.24%, respectively. The moisture content reduction is 2.64%, 4.88%, and 1.01% compared with the samples before freeze-thaw cycles.

3.3. Microstructural Characteristics. The XRD patterns and SEM images for the solidified sludge are shown in Figures 3 and 7. The results from Figure 3(a) demonstrated that the amount of portlandite ($Ca(OH)_2$) decreased with the increase in SR content. Portlandite originated mainly from QL, and the QL content was same for samples S5, S4, and S3. Therefore, the low content of portlandite in sample S5 indicated that more QL had participated in hydration reactions. The ettringite ($Ca_5Al_2(SO_4)_3(OH)_{12} \cdot 26H_2O$) and bentorite ($Ca_6Cr_2(SO_4)_3(OH)_{12} \cdot 26H_2O$) formed in all samples, which were of lower content for sample S3. Ettringite formed from sulfate in SR and portlandite, which were needle-like and could be observed clearly in Figures 7(a) and 7(b). The formation of ettringite can transform free water into bound water, connect the particles, and fill the pores. These effects helped to improve the

short-term and long-term strength of solidified sludge [28]. Bentorite is a Cr^{3+} analogue of ettringite, indicating that the interaction between solidifier and pollutions in the sludge occurred. Portlandite reacted with chloride in SR to form hydrocalumite ($Ca_2Al(OH)_6Cl \cdot 2H_2O$) which was a layered bimetallic hydroxide and could adsorb heavy metals in the sludge [34]. In addition, geminate ($Cu^{2+}2As^{2+}5O_7 \cdot 3H_2O$) or stichtite ($Mg_6Cr_2CO_3(OH)_{16} \cdot 4H_2O$) could be detected at 2θ of 11.1°, indicating that some pollutants, such as copper, arsenic, and chromium in the sludge, might have been stabilized. Calcium silicate hydrate (C-S-H) was also detected in all samples, although some peaks might be overlapped by other phases [10]. Some C-S-H could also be observed in Figure 7(b). Ardealite ($Ca(SO_4)$ $(PO_3(OH)) \cdot 4H_2O$) can be detected in samples S5 and S4, which easily formed in sulfate environment when SR content was high [35].

Figures 3(b) and 7(c)~7(f) show the XRD patterns and SEM images of sample S5 subjected to different number of dry-wet cycles. With the increase in dry-wet cycles, the content of portlandite decreased, while the ettringite peaks showed an increase trend. This indicated that the hydration reaction continued with the increase in dry-wet cycles. The ardealite peak disappeared after the 1st dry-wet cycle. Ardealite is a monoclinic crystal system, and the sulfate in ardealite can be replaced [35]. Besides needle-like ettringite, more C-S-H gels could be observed in samples after dry-wet cycles (Figures 7(c) and 7(d)). After six dry-wet cycles, some C-S-H gels on the surfaces of portlandite crystal and more compact microstructure could be observed, which contributed to the higher UCS than that before dry-wet cycle.

Figures 3(c) and 7(g)~7(j) show the XRD patterns and SEM images of sample S5 subjected to different freeze-thaw cycles. As shown in Figure 3(c), the XRD pattern for sample after the 1st freeze-thaw cycle was different from that before cycle. Ardealite after the 1st freeze-thaw cycle was weaker, similar to that after dry-wet cycles. Halite (NaCl) could not be observed before freeze-thaw cycle, while the peaks of halite were strongly highlighted after freeze-thaw cycles. Meanwhile, the peaks of hydrocalumite were much lower, indicating that the chloride in hydrocalumite transformed into halite. The transformation might provide phases such as calcium and aluminum to form other hydration products. The peaks of ettringite, bentorite, and portlandite were also lower after the 1st freeze-thaw cycle. Large-dimension ettringite occurred in the sample after the 1st freeze-thaw cycle (Figure 7(h)) might have an adverse effect on the microstructure due to the uneven expansion. However, the higher peaks of C-S-H in Figure 3(c) and more C-S-H gels in Figure 7(h) contributed to the increase in UCS after the 1st freeze-thaw cycle. Compared with the 1st freeze-thaw cycle, halite peaks decreased slightly while portlandite and hydrocalumite peaks increased for the sample after ten freeze-thaw cycles. Many C-S-H gels and compact microstructure was observed in samples after 10 freeze-thaw cycles (Figures 7(i) and 7(j)).

In addition, geminite and stichtite peaks still existed after dry-wet or freeze-thaw cycles, indicating that the pollutants were still stabilized in the solidified sludge. SR, GGBS, and

(a)

(b)

(c)
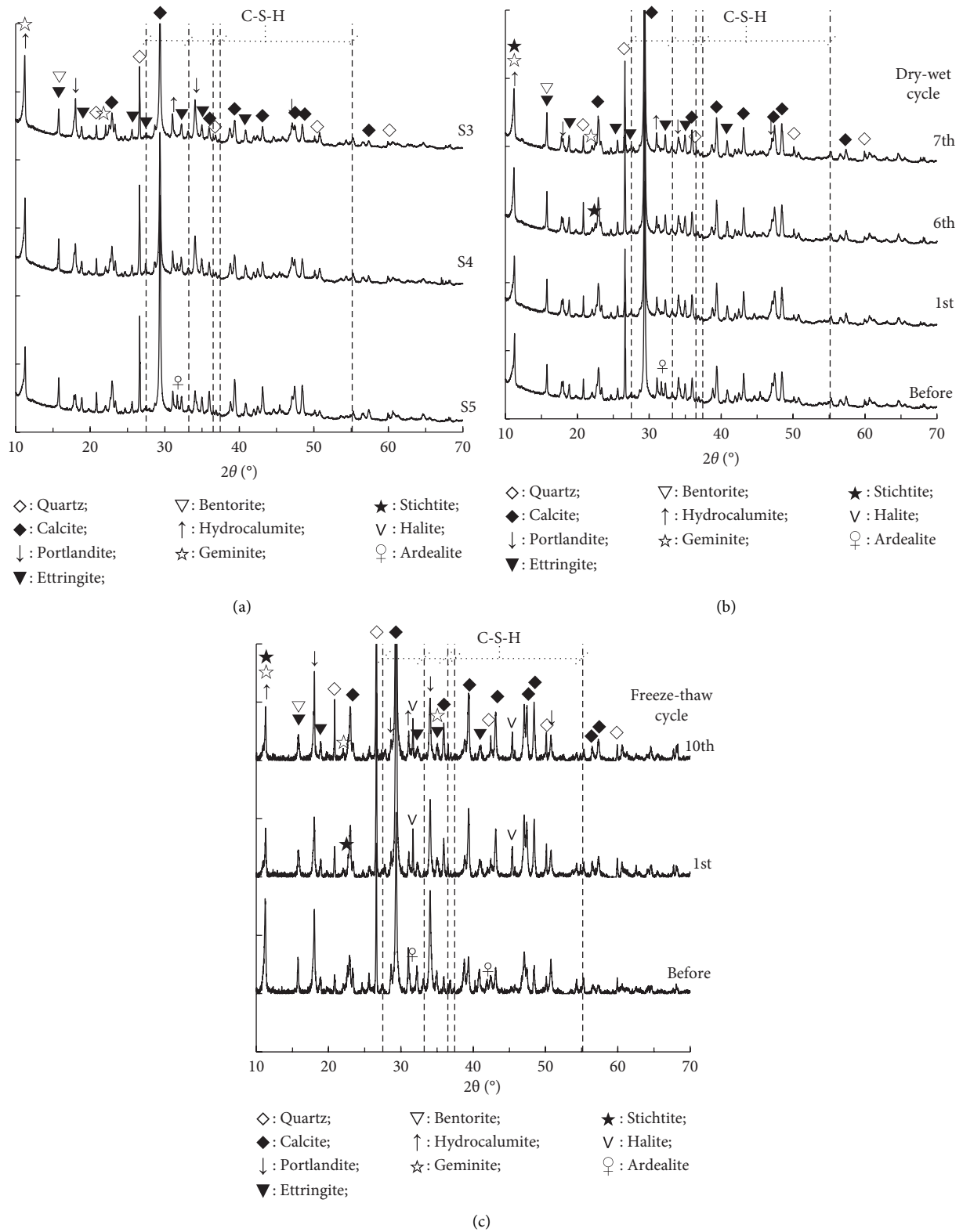
Figure 3: XRD diagram for (a) samples S5, S4, and S3 before cycle; and sample S5 under the effects of (b) dry-wet cycles and (c) freeze-thaw cycles.
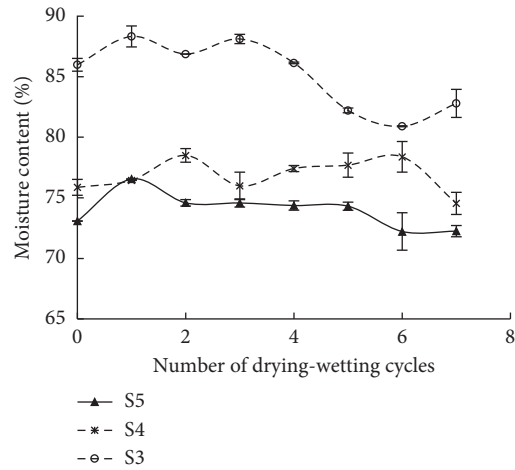
FIGURE 4: Variations in moisture content with dry-wet cycles.
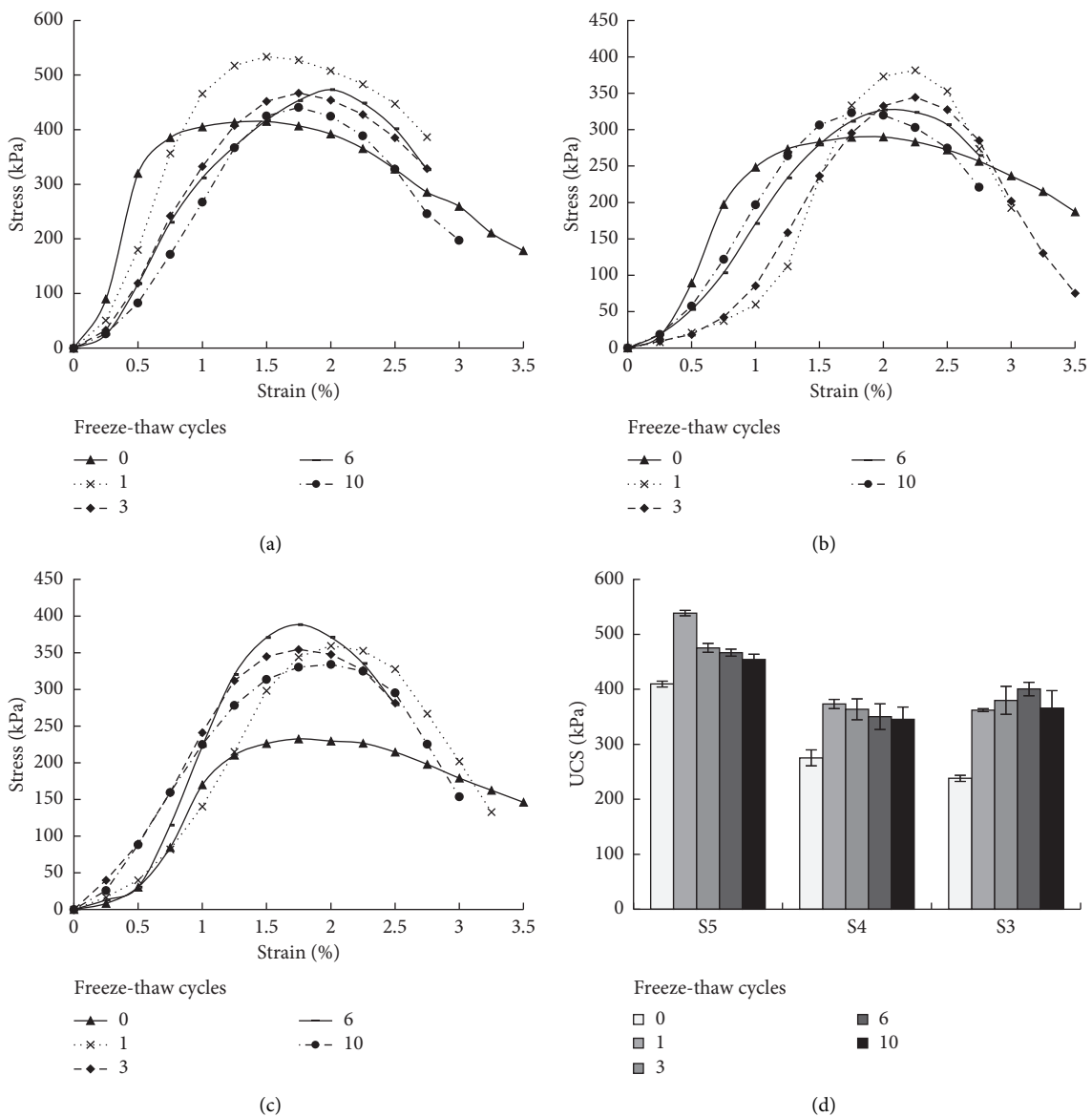

FIGURE 5: The stress-stain curves for samples (a) S5; (b) S4; (c) S3; and (d) UCS under freeze-thaw cycles.
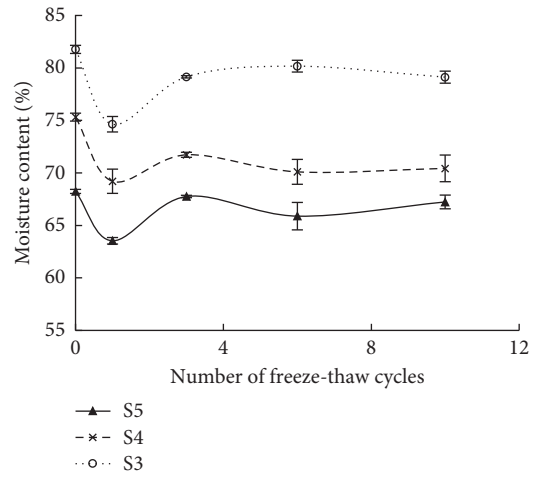
Figure 6: Variations in moisture content with freeze-thaw cycles.

(a)

(b)

(c)

(d)

(e)

(f)

Figure 7: Continued.

(g)

(h)

(i)

(j)
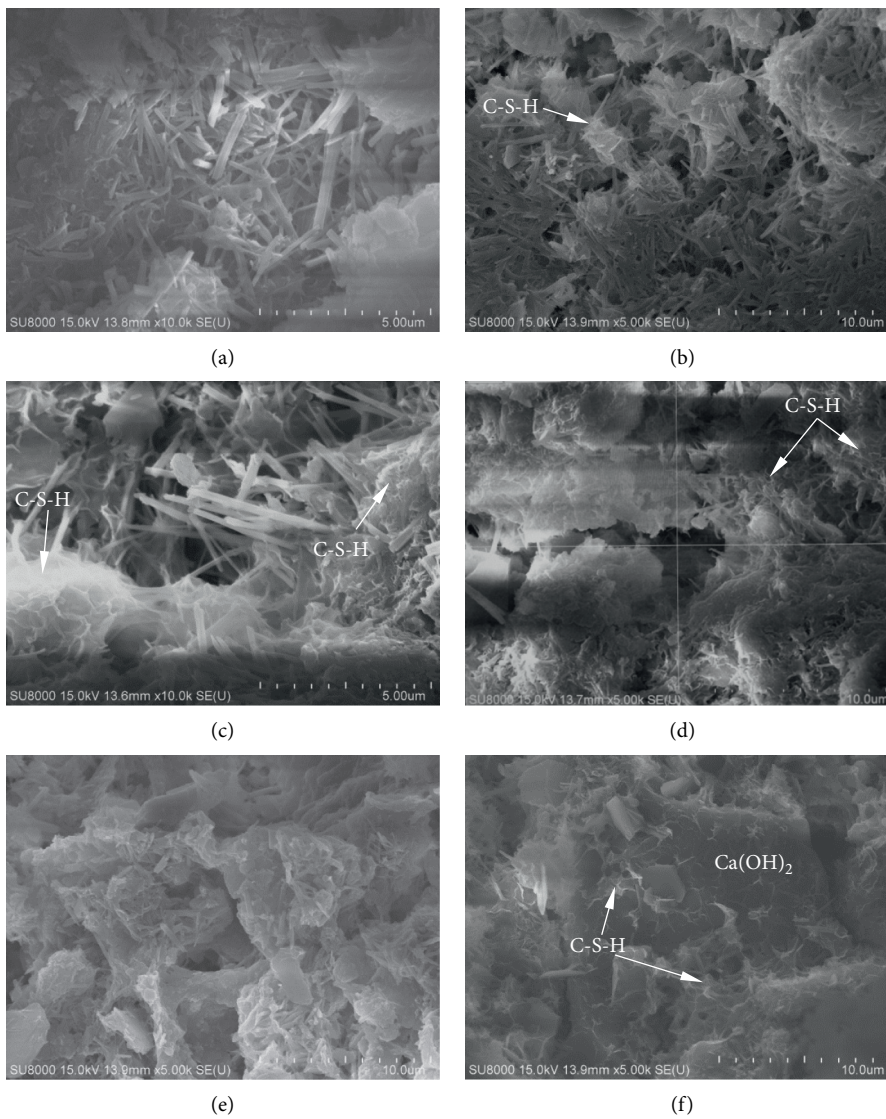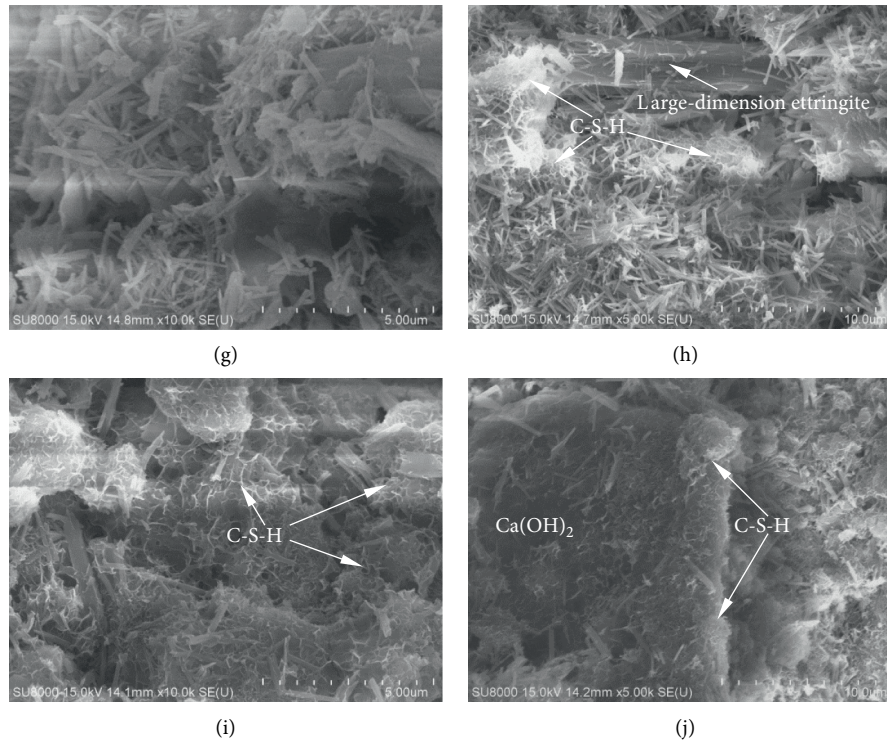
FIGURE 7: SEM images for sample S5 ((a), (b)) before cycle; ((c), (d)) after 3 dry-wet cycles; ((e), (f)) after 6 dry-wet cycles; ((g), (h)) after 1 freeze-thaw cycle; and ((i), (j)) after 6 freeze-thaw cycles.

Drying-wetting cycles

▲ 0
⊖ 3
✕ 6

(a)

Freeze-thaw cycles

▲ 0
⊖ 1
✕ 10

(b)
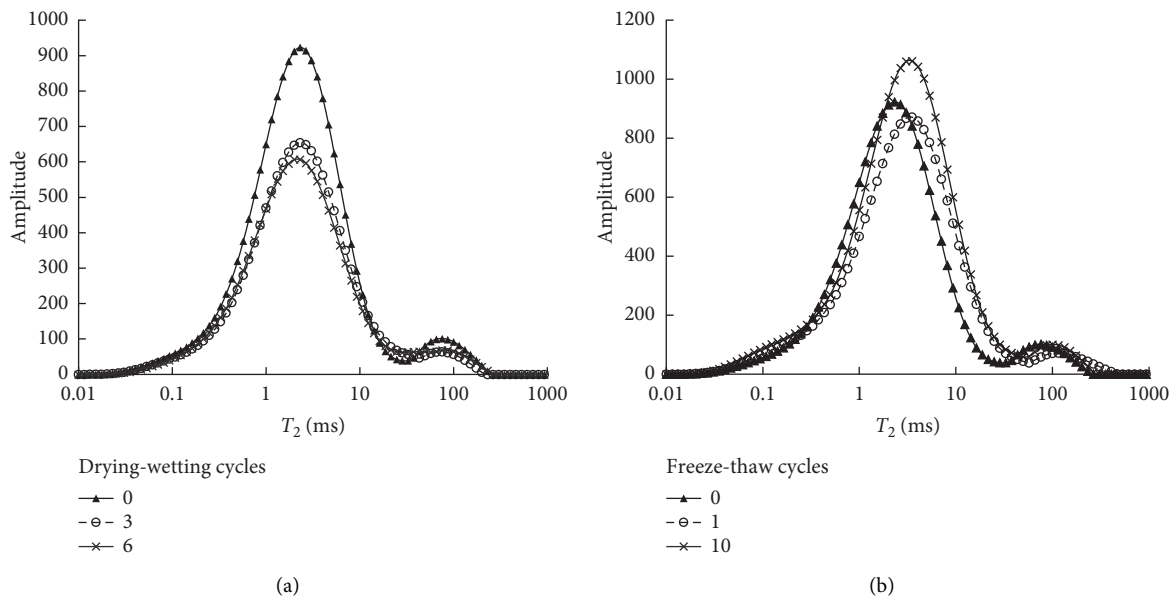
FIGURE 8: Effect of (a) dry-wet cycle and (b) freeze-thaw cycle on the T2 distribution curves of solidified sludge.

QL as solidifiers of sludge showed a good performance on stabilizing pollutants under dry-wet or freeze-thaw cycle environment.

The T_2 distributions from NMR analysis for the solidified sludge subjected to dry-wet and freeze-thaw cycles are shown in Figure 8. The T_2 distribution showed a bimodal distribution. With the increase in dry-wet cycles, the values of T_2 at the peak amplitude did not vary, but the peak values of amplitude decreased, indicating the decrease in pore volume. This improved the UCS and dry-wet durability of the sample. Different from the distribution after dry-wet cycles, the T_2 distribution after the 1st freeze-thaw cycle

moved right. The increase in the value of T_2 at the peak amplitude indicated that the pore size increased after the 1st freeze-thaw cycle. This might be attributed to the frost swell and the formation of large-dimension ettringite as shown in Figure 7(h). However, the decrease in the amplitude of the T_2 peaks helped to increase the UCS, along with the increase in the amount of C-S-H gels (Figure 7(h)). When the freeze-thaw cycles increased to ten, the peak amplitude increased, indicating the destructive effect on microstructure from the repeated freeze-thaw and a decrease in UCS.

Although the sludge, solidifier, and testing method used in this study were different from the references, the results of SR-GGBS-QL solidified sludge under dry-wet and freeze-thaw cycles were similar to those reported by Li et al. [8], Hu [12], Wang et al. [22], and Liu et al. [23]. Dehydrated shrinkage and water absorption swelling in dry-wet cycles, or frost swelling and thaw softening in freeze-thaw cycles, might weaken the microstructure [8]. If the adverse effects were less than the cementation effect from hydration reaction (especially the formation of C-S-H), the solidified sludge showed good durability. The factors such as phosphorus originated from sludge, chlorine and sulfur originated from SR [18], activation of GGBS by QL [26], and skeleton effect of SR particles [12] all played important roles in SR-GGBS-QL solidified sludge against dry-wet and freeze-thaw cycles. It should be noted that the dry-wet cycles and freeze-thaw cycles are no more than 10 in this study. The effect of further cycles should be investigated, which will be addressed in the future studies. The results in this study demonstrated that the SR-GGBS-QL solidified sludge had a good mechanical performance when used as a fill material under dry-wet and freeze-thaw environment.

4. Conclusions

A series of strength and microstructure tests were carried out on the SR-GGBS-QL solidified sludge subjected to dry-wet or freeze-thaw cycles. The main conclusions are as follows:

(1) The stress versus strain of the solidified sludge cured for 28 days showed a brittle failure characteristic, with the failure strain less than 2%, regardless of the SR content, dry-wet cycle, or freeze-thaw cycle.

(2) With the increase in dry-wet cycles, the UCS of the solidified sludge increased first and then decreased after the 5th or 6th cycle, except for a slight decrease after the 1st cycle. The sharp increase in mass lost rate and the increase in moist content contributed to the UCS decrease for the 1st cycle. The frequent fluctuations in moist content during the dry-wet cycles might do harm to the microstructure of the solidified sludge. However, the hydration reaction continued, especially more ettringite and C-S-H formed during the dry-wet cycles, which contributed to a lower pore volume, compact microstructure, and a higher UCS than those before the cycles.

(3) After the 1st freeze-thaw cycle, the UCS of the solidified sludge increased markedly owing to the transformation of hydrocalumite and the formation of more C-S-H. With the further increase in freeze-thaw cycles, the UCS of the solidified sludge decreased, whereas the values after ten cycles were higher than those before the cycles. The frost swell and large-dimension ettringite formation led to enlargement of the pores, but C-S-H gels and compact microstructure after ten freeze-thaw cycles helped to maintain a high UCS.

(4) Under the effects of dry-wet cycles and freeze-thaw cycles, the UCS values of the solidified sludge were greater than 400 kPa (for sample S5) or close to 350 kPa (for samples S4 and S3), which met the strength requirement of filling materials. Moreover, pollutants, such as copper, arsenic, and chromium, were stabilized in the solidified sludge. Therefore, it is believed that SR-GGBS-QL solidified sludge has good dry-wet and freeze-thaw durability.

Data Availability

The data used to support the findings of this study are available from the corresponding author upon request.

Conflicts of Interest

The authors declare that they have no conflicts of interest regarding the publication of this paper.

Acknowledgments

References

[1] L. Lang, N. Liu, and B. Chen, "Investigation on the strength, durability and swelling of cement- solidified dredged sludge admixed fly ash and nano-SiO$_2$," *European Journal of Environmental and Civil Engineering*, pp. 1–21, 2020.

[2] R. Ke, H. X. Wang, Y. Z. Tan, and L. H. Wang, "Solidification of high organic matter content sludge by cement, lime and metakaolin," *Periodica Polytechnica Civil Engineering*, vol. 63, no. 1, pp. 53–62, 2019.

[3] Y. J. Chen, X. X. He, S. H. Zhang, X. Tan, and Y. Wan, "Strength and microstructure properties of solidified sewage sludge with two types of cement-based binders," *Scientific Reports*, vol. 10, no. 1, 2020.

[4] D. X. Wang, S. J. Di, X. Y. Gao, R. H. Wang, and Z. G. Chen, "Strength properties and associated mechanisms of magnesium oxychloride cement-solidified urban river sludge," *Construction and Building Materials*, vol. 250, Article ID 118933, 2020.

[5] W. Xiao, X. Yao, F. Y. Zhang, and A. Perrot, "Recycling of oily sludge as a roadbed material utilizing phosphogypsum-based cementitious materials," *Advances in Civil Engineering*, vol. 2019, Article ID 6280715, , 2019.

[6] F. Y. Liu, C. G. Zhu, K. J. Yang, J. F. Ni, J. Hai, and S. H. Gao, "Effects of fly ash and slag content on the solidification of

river-dredged sludge," *Marine Georesources and Geo-technology*, vol. 39, no. 1, 2019.

[7] P. Chen, B. Feng, Y. J. Lin, and C. Lin, "Solidification and stabilization of sewage sludge and MSWI bottom ash for beneficial use as construction materials," *Journal of Materials in Civil Engineering*, vol. 31, no. 1, 2019.

[8] L. Li, W. Zhu, C. Lin, and T. Ohki, "Study of wet and dry properties of solidified sludge," *Rock and Soil Mechanics*, vol. 30, no. 10, pp. 3001–3004, 2009.

[9] C. Lin, W. Zhu, and J. Han, "Strength and leachability of solidified sewage sludge with different additives," *Journal of Materials in Civil Engineering*, vol. 25, no. 11, pp. 1594–1601, 2013.

[10] Y. L. Li, *Study on landfill and durability of sewage sludge solidified with skeleton builders*, PhD Dissertation, Huazhong University of Science and Technology, Wuhan, China, 2013.

[11] Q. Xue and Y. J. Chen, "Experimental study on municipal sludge dewatering capacity by using quicklime and slag," *Desalination and Water Treatment*, vol. 54, no. 6, pp. 1499–1506, 2015.

[12] X. T. Hu, *Experimental study on physical and mechanical characteristics of solidified municipal sludge under complicated environment*, PhD Dissertation, Liaoning Technical University, Fuxin, China, 2016.

[13] A. W. Yang, S. K. Yang, G. F. Xu, and W. Zhang, "Study of the long-term deformation characteristics of municipal sludge solidified soil under the coupling action of dry-wet cycles and initial static deviatoric stress," *Advances in Civil Engineering*, vol. 2020, Article ID 8824414, , 2020.

[14] S. Yan, J. Hou, and R. Liu, "Research on geotechnical properties and environmental effect of mixture of soda waste and fly ash," *Rock and Soil Mechanics*, vol. 27, pp. 2305–2308, 2006.

[15] J. Yang, Z. Liu, C. Yang, H. Li, Q. Lu, and X. Shi, "Mechanical and microstructural properties of alkali wastes as filling materials for abandoned salt caverns," *Waste and Biomass Valorization*, vol. 12, no. 3, pp. 1581–1590, 2021.

[16] J. Y. Sun and X. Gu, "Engineering properties of the new non-clinker incorporating soda residue solidified soil," *Journal of Building Materials*, vol. 17, no. 6, pp. 1031–1035, 2014.

[17] Z. X. Yang and J. G. Xie, "A new embankment filling technic applied on muddy soil by using alkali slug and waste cement concrete as modification," *Highway Engineering*, vol. 35, no. 1, pp. 72–75, 2010.

[18] J. He, X. K. Shi, Z. X. Li, L. Zhang, X. Y. Feng, and L. R. Zhou, "Strength properties of dredged soil at high water content treated with soda residue, carbide slag, and ground granulated blast furnace slag," *Construction and Building Materials*, vol. 242, pp. 118–126, 2020.

[19] G. Zhen, X. Lu, X. Cheng, H. Chen, X. Yan, and Y. Zhao, "Hydration process of the aluminate 12CaO·7Al2O3-assisted Portland cement-based solidification/stabilization of sewage sludge," *Construction and Building Materials*, vol. 30, pp. 675–681, 2012.

[20] B. Dohnálková, R. Drochytka, and J. Hodul, "New possibilities of neutralisation sludge solidification technology," *Journal of Cleaner Production*, vol. 204, pp. 1097–1107, 2018.

[21] J. G. Liu, X. W. Li, and T. He, "Application status and prospect of backfill mining in Chinese coal mines," *Journal of China Coal Society*, vol. 45, no. 1, pp. 141–150, 2020.

[22] D. Wang, J. Xiao, F. He, and Y. Zhou, "Durability evolution and associated micro-mechanisms of carbonated reactive MgO-fly ash solidified sludge from East Lake, China," *Construction and Building Materials*, vol. 208, pp. 1–12, 2019.

[23] W. H. Liu, J. W. Shu, X. L. Sun, Y. Hua, and F. F. Li, "Shear strength variations of solidified sludge during drying-wetting cycles," *Journal of Civil and Environmental Engineering*, vol. 41, no. 4, pp. 10–18, 2019.

[24] Q. Wang, Y. T. Yin, J. Y. Cui, and R. Tang, "Research of the strength model of cement solidified lead-contaminated soil under freezing and thawing cycles," *Journal of Glaciology and Geocryology*, vol. 39, no. 3, pp. 623–628, 2017.

[25] X. Hou, W. Ma, G. Y. Li, Z. W. Zhou, and Y. T. Huang, "Effects of freezing-thawing cycles on mechanical properties of loess solidified by sodium silicate," *Journal of Glaciology and Geocryology*, vol. 40, no. 1, pp. 86–93, 2018.

[26] Y. Yi, L. Gu, S. Liu, and A. J. Puppala, "Carbide slag-activated ground granulated blastfurnace slag for soft clay stabilization," *Canadian Geotechnical Journal*, vol. 52, no. 5, pp. 656–663, 2015.

[27] The Professional Standards Compilation Group of Japan, *Method of Wetting and Drying Test for Water Absorption of Rocks, Method for Soil Testing*, Japan Highway Society Handbook, Japan, 2001.

[28] T. Kamei, A. Ahmed, and T. Shibi, "The use of recycled bassanite and coal ash to enhance the strength of very soft clay in dry and wet environmental conditions," *Construction and Building Materials*, vol. 38, no. 1, pp. 224–235, 2013.

[29] The Professional Standards Compilation Group of American, *Standard Test Methods for Freezing and Thawing Compacted Soil-Cement Mixtures*, American Society for Testing and Materials, West Conshohocken, PA, USA, 2003.

[30] The Professional Standards Compilation Group of People's Republic of China, *Standard for Geotechnical Testing Method*, China Planning Press, Beijing, China, 2019.

[31] J. Xu, Y. Li, C. Ren, and W. Lan, "Damage of saline intact loess after dry-wet and its interpretation based on SEM and NMR," *Soils and Foundations*, vol. 60, no. 4, pp. 911–928, 2020.

[32] C. L. Zhang, W. Zhu, L. Li, G. J. Fang, and T. Ohki, "Field test of dike construction with solidified lake dredged material," *China Harbour Engineeing*, vol. 147, no. 1, pp. 27–29, 2007.

[33] US Environmental Protection Agency, *Stabilisation/Solidification of CERCLA and RCRA Wastes, Physical Tests, Chemical Testing Procedures, Technology Screening, and Field Activities*, U.S. Environmental Protection Agency, Cincinnati, OH, USA, EPA/625/6-89/022, 1989.

[34] M. Chrysochoou and D. Dermatas, "Evaluation of ettringite and hydrocalumite formation for heavy metal immobilization: literature review and experimental study," *Journal of Hazardous Materials*, vol. 136, no. 1, pp. 20–33, 2006.

[35] M. Secco, G. I. Lampronti, M.-C. Schlegel, L. Maritan, and F. Zorzi, "Degradation processes of reinforced concretes by combined sulfate-phosphate attack," *Cement and Concrete Research*, vol. 68, pp. 49–63, 2015.

Research Article

ECT Image Recognition of Pipe Plugging Flow Patterns Based on Broad Learning System in Mining Filling

Xuebin Qin [ID],[1] **ChenChen Ji,**[1] **Yutong Shen** [ID],[1] **Pai Wang** [ID],[1] **Mingqiao Li** [ID],[1] **and Junle Zhang** [ID][2]

[1]*College of Electrical and Control Engineering, Xi'an University of Science and Technology, 58 Yanta Road, Xi'an 710054, China*
[2]*Shaanxi Institute of Metrology Science, Dongyi Road, Yanta District, Xi'an 710065, China*

Correspondence should be addressed to Xuebin Qin; qinxb@xust.edu.cn

The process of mining filling, when the slurry is transported to the goaf by the filling pipeline, is very important to find the location and size of the caking in the filling pipeline in time for the safe and stable operation of the mine filling pipeline. It is an important research work to detect different flow patterns after two-dimensional section reconstruction in closed filling pipeline based on ECT (electrical capacitance tomography) visualization method. Slurry flow in pipeline is regarded as a two-phase flow, and the multishape distribution was reconstructed into images by ECT and intelligently recognized by broad learning system (BLS) algorithm. BLS is a feedforward neural network with few optimization parameters and fast training speed. In this paper, three features of two-phase sample images, the number of regional blocks, the roundness of regional blocks, and barycenter of regional blocks, are combined with network structure of BLS to recognize different flow patterns. Through the simulation, the recognition accuracy of two-phase fillback image is more than 99%. This conclusion indicates the effectiveness of BLS to predict different two-phase flow patterns; it also provides a new solution for the pattern recognition of the flow pattern in the mining filling pipeline.

1. Introduction

In the filling pipeline from the surface to the goaf, due to the unstable slurry flow pattern, there is a large density difference between the upper and lower parts of the pipe. The transport velocity is too low to make the coarse slurry deposit at the bottom of the pipe, which can easily cause serious blockage in the junction section between the horizontal pipeline and the vertical (or inclined) pipeline [1, 2]. ECT visualization and BLS image recognition technology are helpful for rapid detection and slurry location in pipe blockage.

As slurry materials and proportions, strength and other factors lead to different flow conditions [3]; ECT visualization of pipeline cross section focuses on the permittivity of the medium in backfill pipeline. A possible option is to dynamically observe the internal conditions of the pipeline in the area where the blockage is most likely to occur a priori. ECT is a visualization technique for two-dimensional or three-dimensional image reconstruction of limited mediums

or mixtures in a closed container [4]. ECT technology has the advantages of high accuracy and low cost. Its hardware mainly includes capacitive sensor, acquisition circuit, and computer. The capacitive sensor may be composed of 8 or 12 or 16 electrodes, in which each electrode travels around the closed container at an equal distance and is attached to the outer wall of backfill pipeline. When the ECT system is working, a set of independent capacitance data is collected through different excitation orders of electrodes to the computer for image reconstruction. From this set of independent capacitance data, the permittivity distribution of the slurry flow is inverted by image reconstruction algorithm. ECT technology has great potential for applications such as multiphase flow detection [5], combustion imaging [6], and fluidized bed solid particle monitoring [7]. In this paper, ECT technology is used to detect the insulation of mining fillings.

The classic image reconstruction algorithms of ECT technology include linear back projection (LBP) [8], Landweber [9], and Tikhonov regularization [10]. These

algorithms have advantages and disadvantages. For example, using LBP algorithm has fast imaging speed but low accuracy, while the result of using the Landweber algorithm is that the image quality depends on parameters. Accuracy and efficiency have become the main obstacle for the field application of ECT technology, and it is also the main research direction of relevant scientific researchers. Wang Pai used least squares-support vector machines (LS-SVM) method to predict the capacitance error caused by the soft field, the fitness function of annealing particle swarm optimization (APSO) algorithm is constructed according to the capacitance error, and the image reconstruction with high precision is realized by searching for the best resolution [11]. Zhang proposed the ECT image reconstruction algorithm based on the compressed sensing theory and used the discrete Fourier transform basis to sparse the original image gray signal, and l_1 – norm regularization and primal-dual interior point method were used to reconstruct the image [12]. ECT is becoming more mature with the advent of many fast and accurate reconstruction algorithms.

ECT algorithms include forward and inverse problem solving. The forward problem refers to the establishment of mathematical model based on the distribution of permittivity in sensitive field and boundary conditions of sensitive field so as to obtain the mutual capacitance between electrode pairs. The inverse problem is to reconstruct the distribution of permittivity in sensitive field by the sensitivity of the field and the measured capacitance data and take the image as the final representation. However, the unprocessed reconstructed images cannot meet the requirements of the site. In order to achieve intelligent and integrated operation flow, ECT technology still needs various postprocessing, among which flow pattern recognition is the basic requirement. AbdeelJ Roman extracted the features of the space average permittivity and the position of the center of mass and combined them and used neural network to automatically identify the liquid-vapor two-phase flow patterns of refrigerant in horizontal tubes. The final experiment showed that the classification results of the nine flow patterns reached an average accuracy of 98.1% [13]. By using long short-term memory (LSTM) method, which can overcome the gradient disappearance or escalation, Rafael Johansen provided a successful application scenario for the flow pattern identification of annular, plug, slug, stratified, and wavy flow regimes [14]. Image reconstruction of two-phase flow and flow pattern identification as a link in the field assembly line, their training speed, and classification accuracy has important influence on the subsequent operation.

In this paper, the ECT system is used to reconstruct the two-dimensional cross-sectional image inside the mining filling pipeline, and the broad learning system (BLS) provides a new idea for the flow pattern recognition inside the filling pipeline [15].

BLS is a novel neural network framework, which has the advantages of fewer parameters to be optimized and shorter training time compared with deep structural neural network. The simple BLS network is suitable for processing small sample sets of low dimensions and establishing online

learning model efficiently. BLS network structure is flexible, and it can be used in combination with other networks. For example, the features extracted by convolutional neural network (CNN) are combined with the output of BLS feature layer to enhance the ability of network prediction or classification under the premise of optimal training time. In this paper, the idea of combining features is adopted to realize flow pattern identification.

This paper is organized as follows: in Section 2, the basic principles of BLS theory are introduced. In Section 3, three artificial feature extraction methods are described. In Section 4, artificial feature extraction method and BLS are combined to enhance the ability of model recognition. The reconstruction results are analyzed and evaluated through simulation in Section 5. Concluding remarks are presented in Section 6.

2. BLS Theory

The predecessor of BLS is random vector functional-link neural network [16] (RVFLNN), which essentially belongs to feedforward neural network (FNN). BLS network consists of mapping layer, enhancement layer, and output layer. A BLS network is shown in Figure 1. First, input data is mapped to "feature nodes" through sparse weight mapping, and these "feature nodes" form the mapping layer. Second, the output of the mapping layer serves as the input of the enhancement layer and is activated by the "enhancement node." Finally, the output of the mapping layer and the output of the enhancement layer are combined as the input vector of the output network, and the corresponding weight is calculated by the Moore–Penrose generalized inverse.

The main network relations of each layer are as follows:

$$\text{mapping layer}: Z = \phi(XW_e + \beta_e),$$
$$\text{enhancement layer}: H = \xi(ZW_h + \beta_h), \quad (1)$$
$$\text{output layer}: Y = [Z|H]W^m,$$

where X is the input data; Y is known label data; $\phi(\cdot)$ is the identity mapping function; $\xi(\cdot)$ is the $\tan sig$ activation function $(\tan sig(x) = (2/(1 + e^{-2x})) - 1)$; W_e, W_h, and W^m are weights of mapping layer, enhancement layer, and output layer, respectively; β_e and β_h are biases; Z and H are the outputs of the mapping layer and the enhancement layer, respectively.

Set the input data to $X_{m \times n}$ (m is the number of samples in the training set and n is the number of pixels). A column vector whose entries are all constants adds to the end of $X_{m \times n}$ and the new matrix is written as $X_{m \times (n+1)}$, so equation (1) can be abbreviated as

$$Z = \phi(XW_{ee}), \quad (2)$$

where W_{ee} is a randomly generated $(n + 1) \times N_1$ weight matrix (N_1 is the number of "feature nodes" in the mapping layer). It is a necessary processing to sparse W_{ee} to effectively reduce the linear correlation of new "feature nodes."

The output $Z_{m \times N_1}$ of the mapping layer is the input to the enhancement layer. Similarly, equation (1) can be abbreviated as
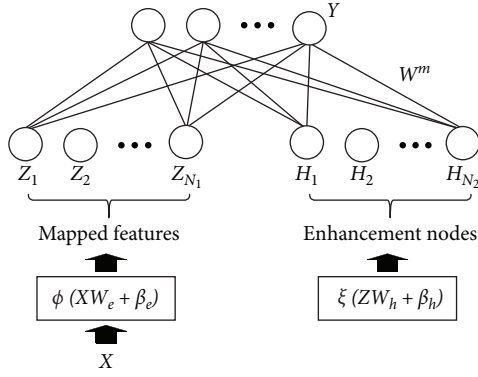
Figure 1: Network model of BLS.

$$H = \xi\left(ZW_{hh}\right), \tag{3}$$

where W_{hh} is the randomly generated weight matrix of $(N_1 + 1) \times N_2$ (N_2 is the number of "enhancement nodes" of the enhancement layer). The orthonormal basis of W_{hh} was used to improve the feature extraction ability of the enhancement layer. $[Z|H]_{m \times (N_1 + N_2)}$ is obtained by combining the output features of the mapping layer and the enhancement layer. $A (A = [Z|H]_{m \times (N_1 + N_2)})$ directly establishes the mapping equation (1) with label data Y. In order to solve the weight W^m of the output layer, the optimization of equation (1) is established as

$$\underset{W^m}{\arg\min}\ \left\|Y - AW^m\right\|_2^2 + \lambda\left\|W^m\right\|_2^2, \tag{4}$$

where λ is a parameter close to the l_2 − norm and regularization method is adopted to prevent model overfitting.

To solve for weight W^m is to solve for the Moore−Penrose generalized inverse.

$$W^m = \left(A^T A + \lambda I\right)^{-1} A^T Y. \tag{5}$$

The BLS network model is mainly composed of $W1$ of the mapping layer, $W2$ of the enhancement layer, and $W3$ of the output layer. Since there is no need for backpropagation during training, the training time is very short. In addition, BLS can provide incremental learning similar to migration learning when dealing with big data, including incremental enhancement node, incremental feature node, and incremental input data. Incremental learning avoids data retraining and greatly saves training time.

3. Feature Extraction

In this paper, the BLS network is used to identify the flow pattern inside the mining filling pipeline, and the characteristics of the filling body are added to the branches of the original BLS network to further improve the recognition accuracy. These are three different functions and their extraction methods.

3.1. Number of Regional Blocks.
Obtaining the number of area blocks is an important index to judge the pipeline

blockage. Based on OpenCV library, the binary image of two-phase flow is used to obtain the number of blocks in the pipeline.

3.2. Circularity of Regional Block.
Block shape complexity can be described by shape coefficient. For example, the circularity coefficient of stratified flow is small, while that of bubble flow is large.

$$ff = 4\pi \cdot \frac{S}{C^2}, \tag{6}$$

where S represents the area of the block and C represents the perimeter of the block.

3.3. Barycenter of Regional Block.
Barycenter reflects the location information of the region block. For example, pixels barycenter of stratified flow is near the bottom of the pipe, and pixels barycenter of circulation is generally near the center. Barycenter position of the block is calculated by means of moment based binary image of two-phase flow section [17].

$$M_{00} = \sum_I \sum_J v(i, j),$$

$$M_{10} = \sum_I \sum_J i \cdot v(i, j),$$

$$M_{01} = \sum_I \sum_J j \cdot v(i, j), \tag{7}$$

$$x_c = \frac{M_{10}}{M_{00}},$$

$$y_c = \frac{M_{01}}{M_{00}},$$

where M_{00} is the area of the white area of the image block. $v(i, j)$ represents the pixel value of the white region on the binary image, where (i, j) is the coordinate on the image; M_{10} and M_{01}, respectively, represent the accumulation of coordinate values in the x direction and y direction of the white area on the binary image. (x_c, y_c) are the barycentric coordinates.

4. Proposed Method

For the three features extracted from sample sets, the number of regional blocks, circularity, and the barycentric coordinates are represented by P_1, P_2, P_3, respectively. After combining them, $P = \begin{bmatrix} P_1 & P_2 & P_3 \end{bmatrix}$ is obtained, where P_1, P_2, P_3 is the matrix of $m \times 1$, $m \times q$, and $m \times 2q$, respectively, m is the number of sample sets, and the value of q is equal to the number of categories to be classified. The number of categories in this article is 6; then $q = 6$ is set.

If $P^{(i)} = \begin{bmatrix} P_1^{(i)} & P_2^{(i)} & P_3^{(i)} \end{bmatrix}$ calculated from the ith sample image, then the calculated value of the circular degree corresponding to the sample is placed in the front position of matrix $P_2^{(i)}$, and the remaining position is filled with 0; the

barycentric coordinate is placed in the front position of matrix $P_3^{(i)}$, and the remaining position is filled with 0.

As shown in Figure 2, the BLS mapping layer is augmented with "feature node," and the output of the mapping layer is combined with the feature matrix P to form a new matrix $[Z|P]$. After the normalization of P, the input of BLS's enhancement layer is also $[Z|P]$:

$$
\begin{aligned}
H^* &= \xi\left([Z|P]W_{hh}\right), \\
Y &= [Z|P|H^*]W^m = A^*W^m,
\end{aligned}
\tag{8}
$$

where H^* is the output of the enhancement layer; $A^* = [Z|P|H^*]$, representing the input to the output layer.

Additional features are added to the BLS architecture to ensure the accuracy of identification; and because the amount of data for additional features is small, it hardly affects the training speed.

5. Simulation and Experiment

5.1. The Data Set. The data set in this article simulates ECT to reconstruct a two-dimensional cross-sectional image of a mining filling pipeline, and the size of each sample image is 64×64 pixels. There are 6 types of flow patterns: single bubble, double bubbles, three bubbles, four bubbles, stratified, and annular flow. The data set includes training set, training set label, test set, and test set label. The training set has a total of 3000 images, including 500 images of different categories. The test set has a total of 500 images, with 100 images for each category. Part of the training set is shown in Figure 3.

After the pixels of the sample image are compressed to 32×32 pixels, and row by row into a 1 by 2 row vector 1×1024, the training set is a 3000×1024 matrix and the test set is a 500×1024 matrix.

The training set label and the test set label are matrices of 3000×6 and 500×6, respectively. The elements of the label matrix are 0 and 1. The row corresponds to different samples and the column corresponds to different categories.

5.2. Feature Representation. Based on the feature extraction method proposed in Section 4, three features are extracted from the reconstructed binary image by ECT. Figure 4 shows a sample of stratified flow. The image size is 64×64 pixels. The number of regional blocks is 1, the barycenter coordinate is (31,45), and the circularity is 0.5344. It can be seen from this sample that the barycenter of the stratified flow image is downward, and the circularity is small.

5.3. Simulation Result. In order to verify the influence of additional features on BLS network flow pattern identification, this paper discusses three groups of schemes, namely, BLS network to train data, the combination of BLS networks with individual features to train data, and the combination of BLS networks with three features to train data.

5.3.1. BLS Network Training Results. Adjust the number of feature nodes and enhancement nodes in BLS network, and

the training accuracy, test accuracy, and training time are shown in Table 1.

As shown in the first row of Table 1, the numbers of feature nodes and enhancement nodes were set as 200 and 2000, respectively, and the training accuracy was 99.57% after the training set data was input into the BLS network, and the training time was 0.5787 s; the test accuracy is 66.96% after the test set data was input into BLS network.

In Table 1, the number of feature nodes was set to 200. With the increase of the number of enhanced nodes, the test accuracy is improved by a small margin. The number of enhancement nodes was fixed at 10000. With the increase of the number of feature nodes, the accuracy of the test set decreases by a small margin. This indicates that the enhancement layer of BLS greatly influences the training results. Since the activation function of BLS enhancement layer is $\tan \text{sig}(\cdot)$, it has the ability to fit nonlinear functions, which is also the core function of BLS network.

The training accuracy of BLS network is close to 100%, but the test accuracy is low, which is a typical overfitting phenomenon. There are two possible reasons for the overfitting phenomenon in BLS network:

(1) The mapping layer is a direct linear transformation system, whose extracted features are not sufficiently expressive or have few extracted features

(2) There are too many parameters in the enhancement layer, which overfits the training set, resulting in poor performance of the model on the test set

5.3.2. Combination of Features. The main reasons for the poor classification results of two-phase flow by single BLS network are the limitations of network architecture and insufficient feature extraction ability. In this section, the additional extracted features, including P_1 (the number of regional blocks), P_2 (the circularity of the regional blocks), and P_3 (the barycenter coordinates of the regional blocks), are combined with the "feature nodes" of the BLS mapping layer, respectively. The classification results of the two-phase flow by this network are shown in Table 2.

As shown in the first row of Table 2, 200 feature nodes and 2000 enhancement nodes were set, respectively. When feature nodes of BLS and P_1 are combined, the accuracy rate of test set is 76.73% and the training time is 0.6187 s. When P_2 is combined with feature nodes, the accuracy of test set is 97.13% and the training time is 0.6754 s. When P_3 is combined with feature nodes, the accuracy of test set is 97.13% and the training time is 0.6754 s.

Combine the three additional features P_1, P_2, and P_3 into $P = \begin{bmatrix} P_1 & P_2 & P_3 \end{bmatrix}$; three additional features, P_1, P_2, and P_3, are combined into $P = \begin{bmatrix} P_1 & P_2 & P_3 \end{bmatrix}$, and P is combined with feature nodes of BLS mapping layer. The identification results of the two-phase flow data set are shown in Table 3.

As shown in the first row of Table 3, the numbers of feature nodes and enhancement nodes were set as 200 and 2000, respectively. The training accuracy was 99.68% and the training time was 0.6083 s after the training data was input
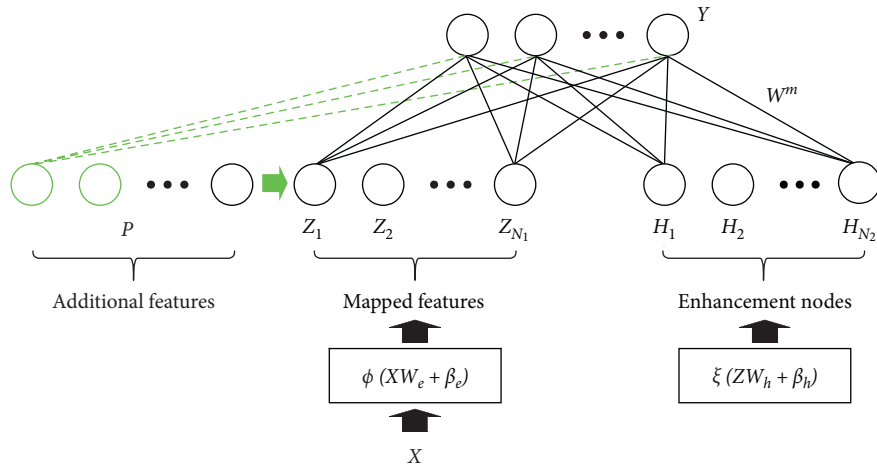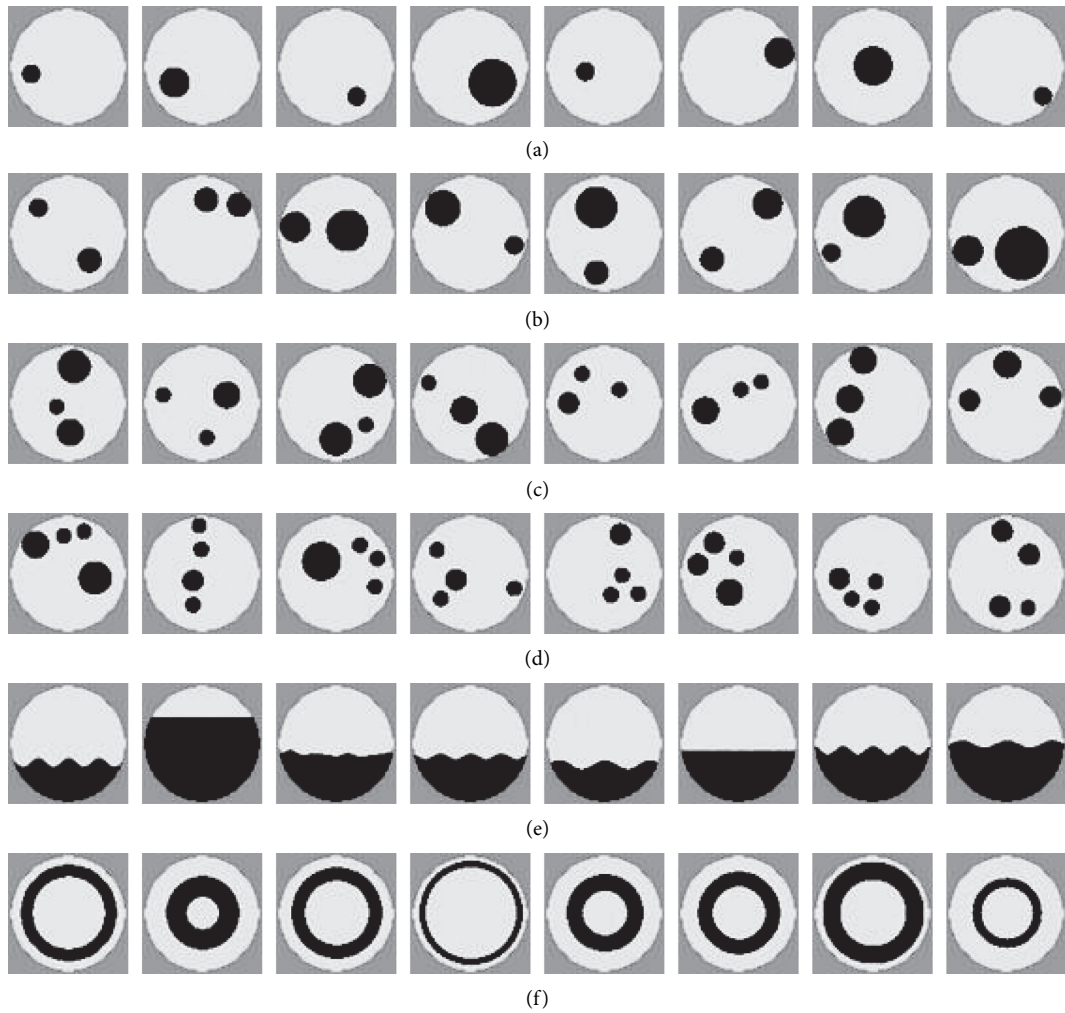
Figure 2: Network model of BLS.

(a)

(b)

(c)

(d)

(e)

(f)

Figure 3: Presentation of partial sample sets. (a) Single bubble. (b) Two bubbles. (c) Three bubbles. (d) Four bubbles. (e) Stratified. (f) Annular.

(a)   (b)
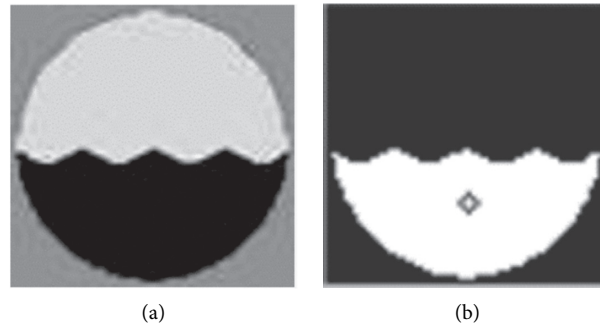
FIGURE 4: Feature extraction of ECT reconstructed images. (a) Reconstructed gray-scale image. (b) Reconstructed binary image.

TABLE 1: The result of BLS.

Feature nodes	Enhancement nodes	Training accuracy (%)	Testing accuracy (%)	Training time (s)
200	2000	99.57	66.96	0.5787
200	4000	99.84	68.92	1.3383
200	6000	99.87	69.98	2.1988
200	8000	99.76	69.80	4.3135
200	10000	99.91	70.34	6.6591
200	12000	99.66	68.56	9.3596
500	10000	99.53	70.34	7.0168
2000	10000	99.85	67.14	14.5632
4000	10000	99.72	68.21	45.6702

TABLE 2: The result of adding one feature to BLS.

Feature nodes	Enhancement nodes	Testing accuracy (%)			Training time (s)		
		P_1	P_2	P_3	P_1	P_2	P_3
200	2000	76.73	97.13	98.35	0.6187	0.6754	0.7246
200	4000	82.06	97.28	98.52	1.1592	1.2627	1.3174
200	6000	83.30	97.46	98.76	2.1641	2.3541	4.2512
200	8000	83.84	97.59	98.89	4.3135	4.2429	4.5854
200	10000	84.19	97.63	98.86	6.2257	6.2466	6.3350
200	12000	82.95	97.35	98.49	9.3698	9.3321	9.1278
500	10000	80.82	97.41	98.21	7.1576	7.2756	7.1853
2000	10000	75.66	97.25	98.43	14.2775	14.5853	14.4428
4000	10000	73.89	97.33	98.37	46.4412	47.1185	47.6614

TABLE 3: The result of adding three features to BLS.

Feature nodes	Enhancement nodes	Training accuracy (%)	Testing accuracy (%)	Training time (s)
200	2000	99.98	99.54	0.6083
200	4000	99.94	99.67	1.2704
200	6000	99.98	99.76	2.2515
200	8000	99.95	99.79	4.0251
200	10000	99.90	99.82	6.0906
200	12000	99.96	99.65	9.1225
500	10000	99.99	99.81	7.3056
2000	10000	99.92	99.85	14.0437
4000	10000	99.93	99.87	47.9779

into BLS network; the test accuracy is 66.54% when test data was input into BLS network.

The results of Table 2 show that P_1 improves BLS network to some extent, but the effect is not significant; P_2 and P_3 have significant improvement effect on BLS network and high accuracy of test set. The results of Table 3 show that the test accuracy is close to 100% when P_1, P_2, and P_3 jointly affect the BLS network. The training time of the BLS network

with the additional features is similar to that of the single BLS network, which hardly affected the training speed.

6. Summary and Prospect

In order to better analyze the distribution of blockage material in filling pipeline comprehensively, this paper proposes to adopt ECT method to observe the blockage area visually. According to the permittivity of the plugging material, six shapes of fluids (single-bubble, double-bubble, three-bubble, four-bubble, stratified, and annular flow) in the cross-sectional view are simulated. A fusion method of artificial features and BLS was proposed to recognize the flow pattern of blocked pipes in the gray image reconstructed by ECT. The training set and test set have 3000 and 500 sample images, respectively. In the simulation, the BLS network that can be quickly trained is used to identify the flow pattern of two-phase flow images. Due to the lack of feature extraction ability of BLS network, the simulation results show that the identification effect of test set is poor. In view of this situation, this paper used the method of non-neural network to extract three additional features, which are the number of regional blocks, the circularity of regional blocks, and the barycenter coordinates of regional blocks. Three different features are combined with feature nodes of BLS mapping layer to realize high accuracy test set recognition. In addition, the training time is almost unaffected because of the small amount of data of the additional features selected. Further work is to extract fewer and more prominent features from ECT reconstructed images, thereby improving the accuracy and speed of recognition.

Data Availability

The data used in this paper were randomly generated by programming and simulation software, including the training set and the test set (the reconstructed images of the ECT system were taken as samples).

Conflicts of Interest

The authors declare that they have no conflicts of interest.

Acknowledgments

References

[1] R. Gao, K. Zhou, Y. Zhou, and C. Yang, "Research on the fluid characteristics of cemented backfill pipeline transportation of mineral processing tailings," *Alexandria Engineering Journal*, vol. 59, no. 6, pp. 4409–4426, 2020.

[2] J. Zhang, W. Guo, and H. Li, "Effects of backfill soil on pipeline's mechanical response subjected to perilous rock impact," *Engineering Review*, vol. 40, no. 1, pp. 25–31, 2020.

[3] C. Qi, A. Fourie, Q. Chen, and Q. Zhang, "A strength prediction model using artificial intelligence for recycling waste tailings as cemented paste backfill," *Journal of Cleaner Production*, vol. 183, pp. 566–578, 2018.

[4] M. Meribout and I. M. Saied, "Real-time two-dimensional imaging of solid contaminants in gas pipelines using an electrical capacitance tomography system," *IEEE Transactions on Industrial Electronics*, vol. 64, no. 5, pp. 3989–3996, 2017.

[5] Y. Shi, M. Wang, and M. Shen, "Characterization of oil-water two-phase flow in a horizontal pipe with multi-electrode conductance sensor," *Journal of Petroleum Science and Engineering*, vol. 146, pp. 584–590, 2016.

[6] Y. Jia and Q. Chen, "Theoretical analysis of the dielectric characteristics of plasma flame and imaging plasma flame using Electrical Capacitance Tomography," in *Proceedings of the IEEE International Conference on Imaging Systems & Techniques*, Beijing, China, October 2013.

[7] X. Li, A. J. Jaworski, and X. Mao, "Bubble size and bubble rise velocity estimation by means of electrical capacitance tomography within gas-solids fluidized beds," *Measurement*, vol. 117, pp. 226–240, 2018.

[8] B. Matusiak, M. J. Da Silva, U. Hampel, and A. Romanowski, "Measurement of dynamic liquid distributions in a fixed bed using electrical capacitance tomography and capacitance wire-mesh sensor," *Industrial & Engineering Chemistry Research*, vol. 49, no. 5, pp. 2070–2077, 2010.

[9] H. Yan, Y. F. Wang, and Y. G. Zhou, "Three-dimensional electrical capacitance tomography reconstruction by the Landweber iterative algorithm with fuzzy thresholding," *IET Science Measurement & Technology*, vol. 8, no. 6, pp. 487–496, 2014.

[10] L. Wang, X. Liu, D. Chen, H. Yang, and C. Wang, "ECT image reconstruction algorithm based on multiscale dual-channel convolutional neural network," *Complexity*, vol. 2020, Article ID 4918058, 2020.

[11] Tsinghua University, *Sensor Research; Reports from Tsinghua University Provide New Insights into Sensor Research (A Deep Learning Compensated Back Projection for Image Reconstruction of Electrical Capacitance Tomography)*, Tsinghua University, Beijing, China, 2020.

[12] Z. Cao, L. Ji, and L. Xu, "Iterative reconstruction algorithm for electrical capacitance tomography based on Calderon's method," *IEEE Sensors Journal*, vol. 18, no. 20, pp. 8450–8462, 2018.

[13] A. J. Roman, P. J. Kreitzer, J. S. Ervin, M. S. Hanchak, and L. W. Byrd, "Flow pattern identification of horizontal two-phase refrigerant flow using neural networks," *International Communications in Heat and Mass Transfer*, vol. 71, pp. 254–264, 2016.

[14] R. Johansen, T. G. Ostby, A. Dupré, and S. Mylvaganam, "Long short-term memort neural networks for flow regime identification using ECT," in *Proceedings of the 9th World Congress on Industrial Process Tomography*, Bath, UK, September 2018.

[15] C. L. P. Chen and Z. Liu, "Broad learning system: an effective and efficient incremental learning system without the need for deep architecture," *IEEE Transactions on Neural Networks and Learning Systems*, vol. 29, no. 1, pp. 10–24, 2017.

[16] S. Feng and C. L. P. Chen, "Fuzzy Broad learning system: a novel neuro-fuzzy model for regression and classification," *IEEE Transactions on Cybernetics*, vol. 50, no. 2, pp. 414–424.

[17] T. Tibyani and S. I. Kamata, "Registering 3D objects triangular meshes using an interest point detection on barycentric coordinates," in *Proceedings of the 2012 International Conference on Informatics, Electronics & Vision (ICIEV)*, Dhaka, Bangladesh, May 2012.

Research Article

Investigation of Freeze-Thaw Resistance of Stabilized Saline Soil

Yongxiang Zhou [ID],[1,2,3] **Qingfeng Guan** [ID],[1,2,3] **and Peiyu Yan**[4]

[1]*Institute of Building Materials, China Academy of Building Research, Beijing 100013, China*
[2]*State Key Laboratory of Building Safety and Built Environment, Beijing 100013, China*
[3]*National Engineering Research Center of Building Technology, Beijing 100013, China*
[4]*Department of Civil Engineering, Tsinghua University, Beijing 100084, China*

Correspondence should be addressed to Yongxiang Zhou; zhouyxt@126.com

In this paper, three freezing-thawing tests are designed to study the freeze-thaw resistance of stabilized sulfate type saline soil. The results show that different destructive modes and erosion extents are caused by different freeze-thaw conditions. The destructive effect from salt tends to be limited if there is no external water intrusion. When sufficient water is provided, ice expansion, dissolution recrystallization of salts, and ettringite growth during the thawing phase may take place. Soil water potential is used for analysis and explanation of the driving force and water migration in the stabilized soil. Pressure potential caused by the air sealed in the stabilized soil specimen leads to early water concentration in the outer parts of the specimen, and the surface layer is first eroded under the freeze-thaw cycles. A high percentage of soil stabilizer can improve the freeze-thaw resistance of stabilized soil, but a sufficiently long curing period plays a more important role. This study provides useful insights for improving the freeze-thaw resistance of solidified saline soil in road engineering.

1. Introduction

There is a large amount of inland saline soil distributed widely in northwest China. Saline soil is a type of soil whose salt content exceeds a certain threshold, and some common classifications include chlorine saline soil, sulfate saline soil, and carbonate saline soil. Among these, sulfate saline soil occupies the largest area in northwest China and is most harmful for roadbed engineering [1]. It may be necessary to build roads in saline soil zones due to exploration and exploitation of mineral resources such as salt lakes. However, the content of soluble chloride and sulfate salt in saline soil is very high, and the mass percent of saline soil may exceed 30%, which can often cause road engineering hazards such as dissolution, salt expansion, frost damage, and frost heaving [2–4]. In a harsh saline soil environment, ordinary concrete will severely corrode, and its service life is only a few years. Such a harsh environment will pose a severe threat to the durability of ordinary concrete and severely limit the feasibility of using concrete for construction.

One of the most effective technical solutions is to use stabilized saline soil as a base or subbase of roads, sometimes even as a pavement for low-grade roads. Methods of soil stabilization can generally be divided into physical reinforcement (mechanical force stabilization and heat treatment stabilization) [5, 6], chemical stabilization (trinity mixture fill stabilization, modern curing agent stabilization, salt solution, and asphalt stabilization) [7–10], and biological stabilization (microbiologically induced calcite precipitation, MICP) [11–15]. The relevant properties of stabilized soil have undergone significant improvement, and application technologies of stabilized soil are becoming increasingly advanced [16, 17].

It should be noted that the environment in northwest China is harsh, with hot summers and dry and cold winters, especially in the northwest of Qinghai-Tibet plateau where the sunshine is strong, the annual average temperature is below 5.1°C, and the temperature difference between day and night is high with an extreme minimum temperature of −29°C to −34°C [18]. During the long winters, highway

engineering structures experience severe freeze-thaw cycles many times. Similar to expansive clay, saline soil has a high sodium sulfate content that may expand or shrink through crystallization or dissolution with moisture change. It also has the properties of relatively high solubility and corrosivity. In cold areas, road and railroad engineers need to consider problems such as roadbed swelling and frost boiling resulting from the presence of sulfate saline soil [19].

Many previous studies have investigated the damage mechanism of the freeze-thaw cycle in saline soil in cold areas. In a cold environment, the migration and accumulation of free water in saline soil are affected by the cooling rate and temperature gradient [20]. The freezing of water in saline soil is a dynamic process of hydrothermal and salt-mechanical interaction [21, 22]. It has been reported that the frost deformation of saline soil can be divided into three steps [23]. The first is a salt heaving period when the temperature is higher than the freezing point of water; sodium sulfate will form, and the amount of free water decreases as the temperature decreases. The second step is a salt heaving and frost heaving period when the temperature is between the freezing point and the salt swelling temperature. Hence, salt heave and frost heave occur at the same time, resulting in a rapid volume expansion. The last step is the frost heaving period when the temperature continues to decrease and is lower than the salt swelling temperature, and finally the frost heaving appears. To investigate the mechanism of the salt heaving effect on saline soil, previous studies [24, 25] have proposed a thermo-hydro-salt-mechanical coupled model considering a phase change and stated that the most important method for the protection of constructions in saline soil areas is to effectively prevent the migration, accumulation, and phase change of water and salt [26, 27].

Based on existing research [17, 28, 29] on saline soil such as salt crystallization, salt and water transfer, salt deformation and frost heave, and a water-heat-salt coupled model, many researchers [7, 16, 30, 31] have conducted investigations to improve the freezing resistance of saline soil. However, these have been for natural saline soil. The freezing resistance of stabilized saline soil, especially saline soil stabilized by cement-based materials, has not yet received sufficient attention, and the understanding of mechanisms such as freeze-thaw damage and improvement of freezing resistance deserves further attention. There is no special test or standard to evaluate the freezing resistance of stabilized saline soil, which is not conducive to promoting the use of saline soil stabilized by cement-based material in severe cold areas. Successfully stabilizing saline soil and improving its durability are of important significance for solving road traffic problems in the saline soil areas in northwest China.

Herein, we therefore study the freezing resistance of saline soil stabilized by cement-based materials. We focus on salt crystallization, salt and water transfer, and the migration driving force of stabilized saline soil under different methods of water supply in freezing and thawing conditions. We firstly design three types of water supply tests and transfer the cured samples of stabilized saline soil of different ages

into a freezer to undergo different freeze-thaw cycles. Then, we record the appearance and measure the unconfined compressive strength and cumulative mass loss of samples. Finally, we introduce a soil water potential model to explain the damage mechanism and failure mode of stabilized saline soil under different water supply methods.

2. Materials and Test Methods

2.1. Saline Soil.
A typical natural sulfate saline soil from Golmud, Qinghai Province, China, was used in this study. This soil is local salinized clay that contains about 4% soluble salts (mainly sodium sulfate) on a dry-weight basis. The physical properties and chemical analysis of the saline soil are detailed in Tables 1 and 2, respectively.

2.2. Soil Stabilizer.
The saline soil has an extremely high content of soluble salt, especially chlorine and sulfate. According to the principles of hydration hardening of cement-based materials and the chemical excitation principles of binder materials, we designed a wide variety of proportions of curing agents by referencing previous studies and then tested their effectiveness in stabilizing the saline soil in Qinghai Province. After several optimizations and trials, we found that mixing ordinary Portland cement, fly ash, and ground granulated blast furnace slag in a certain proportion can provide the best curing effect. The soil stabilizer used in this study therefore consists of 20% Portland cement, 20% fly ash, and 60% ground granulated blast furnace slag by weight. The chemical compositions of these cementitious materials are given in Table 3.

2.3. Test Methods

2.3.1. Preparing, Curing, and Unconfined Compressive Strength (UCS) Testing of Specimens.
The Sieved saline soil and the soil stabilizer were mechanically mixed. The mass of the soil stabilizer accounted for 10%, 15%, or 20% of the total weight of the dry sample, and then water was added. The mixing was continued until the fresh mixture became homogeneous. The water content was controlled to ensure that the sample reached the maximum dry density, that is, the optimum water content [32] The fresh mixture was then placed into a cylindrical mold with a 50 mm diameter and a 50 mm height and compacted to 100% of the maximum dry density. After being demolded, specimens were sealed in plastic bags and placed into a curing environment at a constant temperature of $20 \pm 2°C$ and 100% relative humidity (standard curing conditions). The designed curing ages were 7 and 28 days. The specimens were taken out from the curing room 1 day before the designed age and saturated in water for 24 hours before UCS testing [33]. The level of water was about 2 cm higher than the top of the specimens. In the UCS testing, a constant loading rate was controlled at about 1 mm/min.

2.3.2. Test Methods for Freeze-Thaw Cycles of Stabilized Saline Soil.
Since there is no standard method for evaluating the freeze-thaw resistance of stabilized soil in China at

TABLE 1: Physical properties of saline soil.

Plastic limit (%)	Liquid limit (%)	Plasticity index (%)	Optimum water content (%)	pH value of soil solution	Cl$^-$ concentration of soil solution (mg/L)[b]	SO$_4^{2-}$ concentration of soil solution (mg/L)[b]	Soluble salt content (%)
16.56	20.98	4.42	15.5	9.48	886.50	3326.20	4.0

[a]The solution was prepared at a mass rate of soil to deionized water ratio of 1 : 2.5. [b]The solution was prepared at a mass rate of soil to deionized water ratio of 1 : 10.

TABLE 2: Chemical composition of saline soil (% by weight).

Loss on ignition	SiO$_2$	Al$_2$O$_3$	CaO	Fe$_2$O$_3$	MgO	K$_2$O	Na$_2$O	SO$_3$	Cl$^-$	P$_2$O$_5$	Total
10.09	48.67	11.13	9.45	4.09	3.58	2.53	3.77	4.76	0.97	0.19	99.22

TABLE 3: Chemical analysis of Portland cement, slag, and fly ash (% by weight).

Materials	SiO$_2$	Al$_2$O$_3$	Fe$_2$O$_3$	CaO	MgO	Na$_2$O$_{eq}$	SO$_3$	Loss on ignition
Cement	22.80	4.55	2.82	65.34	2.74	0.55	2.92	3.90
Slag	34.63	13.92	0.29	38.28	10.52	—	0.25	0.25
Fly ash	57.60	21.90	7.70	3.87	1.68	0.41	4.05	0.43

present, and the testing methods of concrete are not suitable to adopt, this study modified and designed three test methods by referring to the ASTM D560-16 [34] freeze-thaw test method as follows.

Test I: Cyclic freeze-thaw test of all-round water supply to specimens without pressure. At the end of the curing period, the specimens, whose surfaces were wet, were placed into a moist room at a constant temperature of 20°C and relative humidity of 100%. After 24 hours, a water-saturated felt pad was placed between the specimens and the carriers, and the sample was placed in a freezing cabinet at a constant temperature of -25 ± 2°C for 12 hours. It was then moved to the moist room at a constant temperature of 20 ± 2°C and a RH >95% again to thaw for 11 hours. During the thawing period, all the side surfaces and upper top surface of the samples of saline soil were wetted by mist and then supplied with free water. In such a high relative humidity, we consider that the test samples were close to being soaked in water, so all the surfaces in contact with the mist had similar water supply conditions as the bottom surface of the specimen that was in contact with the felt pad. In every freezing and thawing step, it was necessary to keep the water-saturated felt pad in place, so sufficient potable water was available to permit the specimens to absorb water by capillary action.

To measure the mass loss of specimens after thawing, two firm strokes were given on all surfaces of each specimen with a wire scratch brush according to the method presented in ASTM D560-16. Before and after this step, the mass changes of specimens were recorded for calculating the percentage of cumulative mass loss (PCML). After brushing, the specimens were turned over endways before they were placed on the water-saturated pads.

The above procedures constitute one cycle (24 hours) of freezing and thawing. It should be noted that no extra pressure was applied in the process of supplying water to the specimens, which is different from the case when specimens are immersed into water where there is a pressure difference created by the water depth on the specimen surface.

Test II: Cyclic freeze-thaw test of unidirectional water supply to specimens without pressure. In this test, specimens from the curing storage were placed directly in sealed plastic bags, on the bottom of which one hole with a diameter of about 1 mm was created at the center of each specimen. In this test, a piece of water-saturated felt pad was always placed between the sealed bags holding the specimens and carriers, so that water could move to the bottom of each specimen through the holes.

The mass change of each specimen was measured every three cycles until thorough destruction took place. The water content of the specimens at a temperature of 105°C at the end of the curing period was recorded in order to obtain the critical value at the time when complete destruction occurred. If the mass increase is regarded as the increase of water content during freeze-thaw cycles, the critical water content can be calculated.

In Test II, the procedure continued as in Test I, but without giving two firm strokes on all areas of specimens and turning specimens over endways when they were placed on the water-saturated pad.

Test III: Cyclic freeze-thaw test without external water supply. In this test, specimens were placed in sealed plastic bags in order to separate them from moisture in the freezing and thawing steps. The remaining procedure continued in the same way as in Test II.

The water supply patterns in these three tests are sketched in Figure 1. In addition, other groups of specimens were cured under standard curing conditions with their strength determined simultaneously with the samples affected by the freeze-thaw cycles.

3. Results and Analysis

Experimental UCS data obtained from the three tests are given in Table 4.

3.1. Test I. Figure 2 shows the PCML of specimens in Test I. The changing patterns in UCS have a similar tendency to that in PCML. With increasing numbers of freezing-thawing
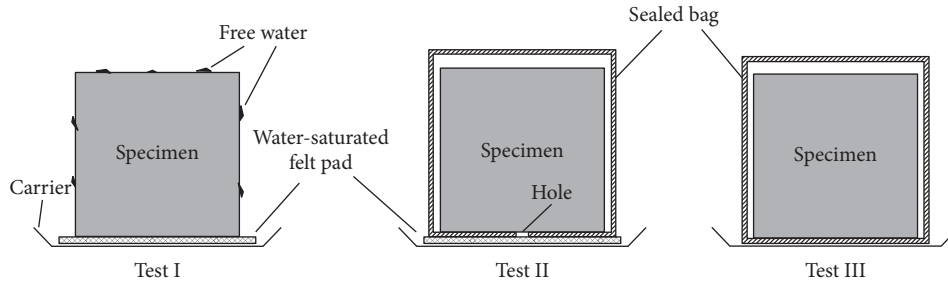
FIGURE 1: Sketch of the water supply conditions in the three tests.

TABLE 4: Changes in UCS of stabilized soil after freeze-thaw cycles in three tests.

Specimen group	Percent of stabilizer (%)	Age (days)	Initial strength[a] (MPa)	UCS after 12 cycles (MPa)				UCS after 24 cycles (MPa)				UCS after 60 cycles (MPa)			
				SS[b]	Test I	Test II	Test III	SS	Test I	Test II	Test III	SS	Test I	Test II	Test III
1	10		4.4	6.8	1.5	—[c]	4.4	9	—	—	2.1	9.5	—	—	1.2
2	15	7	5.4	8.3	2.6	3.9	5.9	9.9	—	—	3.6	11.2	—	—	2.9
3	20		7.1	9.8	3.9	4.9	6.9	11.1	—	—	5.4	13.5	—	—	5.0
4	10		7.1	9	3.6	5.1	7.1	9.5	2	2.6	5.6	9.8	—	1.0	4.0
5	15	28	10	9.9	5	5.8	10.0	11.7	2.8	6.2	7.3	12	—	5.1	7.4
6	20		10.7	11.4	5	6.3	10.3	13.1	4.8	6.9	8.9	14.4	3.5	6.5	7.6

[a]Initial strength means the value of the strength at the end of the curing period. [b]SS means the synchronous strength of the specimens cured under standard conditions. [c]— means the group of specimens were destroyed in or before this cycle.
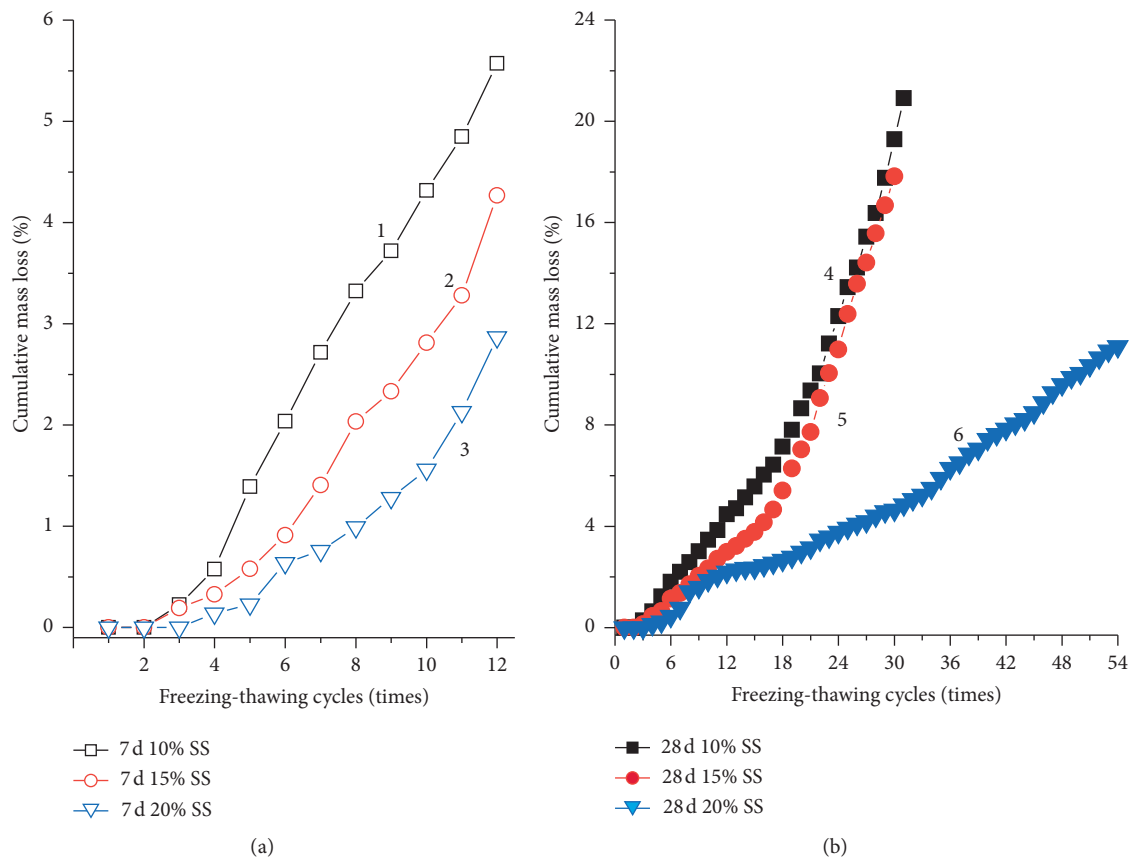

(a)

(b)

FIGURE 2: Cumulative mass loss of specimens with curing periods of 7 days (a) and 28 days (b) in Test I (SS means soil stabilizer).

cycles, the UCS decreases gradually until destruction occurs. The PCML of specimens with curing period of 7 days (specimen groups 1–3 in Table 4) begins to increase rapidly after five or six cycles. After eight or nine cycles, cracks appear one after another on these specimens. The failure patterns of these specimens are shown in Figure 3.

The UCS and PCML results reveal that the repeated freeze-thaw under the condition of all-round water supply to specimens has a strong destructive effect on the specimens with a short curing period. Furthermore, this destructive effect cannot be effectively reduced by increasing the content of the soil stabilizer. This is proved by the fact that the specimens stabilized by 20% stabilizer performed a little better than the ones with 10% stabilizer, yet they were destroyed completely after 12-18 cycles.

The PCML values of groups 4–6 with a curing period of 28 days were 5.5%, 3.8%, and 2.4%, respectively, at the end of the 15th cycle and increased slowly. After 15 cycles, the PCML of group 6 specimens maintained a slow increase. However, for groups 4 and 5, the PCML of specimens started to rise steeply. Erosion in these specimens took place from the surface towards the core with water incursion, but visible cracks were hardly seen before 24 cycles. The PCML of specimens stabilized by 20% soil stabilizer did not exceed 5%, even after 30 cycles, and the UCS remained more than 3 MPa after 60 cycles. Therefore, a sufficiently long curing period is important to improve the freeze-thaw resistance of stabilized saline soil.

3.2. Test II. In this test, water migrated from the water-saturated felt pad to the center bottom of a specimen through a hole in an otherwise sealed bag. Similar to Test I, it is obvious that the freeze-thaw resistance of the specimens cured for short period is not as good as that for specimens cured for a longer period.

However, for the specimens with a curing term of 7 days, the failure pattern in Test II is distinctly different from that in Test I. In Test II, there was no obvious change in the mass and volume of specimens before six cycles. After six cycles, specimens of group 1 (10% stabilizer) began to rapidly expand in the upper part until the whole specimen fell apart to powder. The typical failure pattern of group 1 after night cycles is shown in Figure 4(a). The specimens of group 2 (15% stabilizer) and group 3 (20% stabilizer) still had 3-4 MPa UCS after 12 cycles but began to increase rapidly in mass and in volume after 12 cycles. The typical failure pattern of group 3 after 24 cycles is shown in Figure 4(b).

Conversely, the severe erosion phenomena did not show up in the specimens cured for 28 days. These specimens had no evident change in mass or appearance, even after 60 cycles. In Test II, the erosion extent of the specimens cured for 7 days exceeded that in Test I, while it was the opposite case for the specimens cured for 28 days. This conclusion can be deduced from the changes in UCS (Table 4).

3.3. Test III. In this test, specimens were separated from external moisture by sealed bags. The UCS data in Table 4 show that this had the least destructive effect on the stabilized soil specimens compared to the other two tests. However, the decreasing UCS data indicate that the destruction may be due to the salt in the soil.

4. Discussion

4.1. Failure Pattern of Specimens. As a result of rich sodium sulfate, large amounts of ettringite may form during hydration of the stabilizer-soil mixture (Figure 5; the rod-shaped phases are ettringites). However, in Test III, in addition to the negative influence of low temperature on potential activity of the soil stabilizer, crystallization of sulfate in the stabilized soil affected by repeated freeze-thaw is also a main cause of the reduction in the mechanical properties of specimens.

Despite many studies on the crystallization of sodium sulfate over the last 150 years, the reason why it generates damage remains controversial. Sodium sulfate has two stable phases at room temperature, thenardite (an anhydride) and mirabilite (a decahydrate), as well as a metastable phase [35–37]. At low temperature, the solubility of sodium sulfate largely decreases so that the pore liquid in the stabilized soil reaches supersaturation, which is a necessary condition for the occurrence of crystallization pressure [38, 39]. With decreasing temperature, both thenardite and mirabilite precipitate from a saturated sodium sulfate solution. Thenardite is the most abundant phase when precipitation occurs at low relative humidity in a porous material [40, 41]. As the temperature decreases and the amount of free water reduces, the salt concentration in the solution increases while the water activity decreases. A lower water activity is beneficial to the formation of thenardite. In micropores, precipitation of anhydrous sodium sulfate is promoted due to water activity reduction. Furthermore, crystallization of thenardite can generate tensile hoop stresses of the order of 10–20 MPa, which is higher than that caused by mirabilite at the same supersaturation ratios [42–44].

Figure 6 shows the changes in pore characteristics of specimens affected by freeze-thaw cycles in Test III. Curve 3 indicates that salt crystallization may be one of the factors that causes a higher porosity of specimens cured for short periods. Curve 2 appears close to Curve 1. This reveals that salt crystallization has little effect on specimens with a longer curing term after 12 cycles.

In Test III, the specimens are in a dry condition, which means only air is present in the macropores and meso-pores, while any liquid tends to be in the micropores. Therefore, part of the sodium sulfate dissolves in the liquid in the micropores where the solution reaches a saturated state, and the rest of the sodium sulfate acts as part of the soil skeleton. The destructive effect is induced only from the sodium sulfate dissolved in the pore liquid, where crystallization of the sulfate and water can take place during the freeze-thaw cycles. The sulfate acting as the soil skeleton has little damage effect on the specimen given that there is no external moisture. In addition, the presence of a large volume of voids can relax the stress caused by crystallization of the salt and water. Arora et al. [45–47] pointed out that freeze-thaw cycles did not have any detrimental effect on cement-treated mixtures of
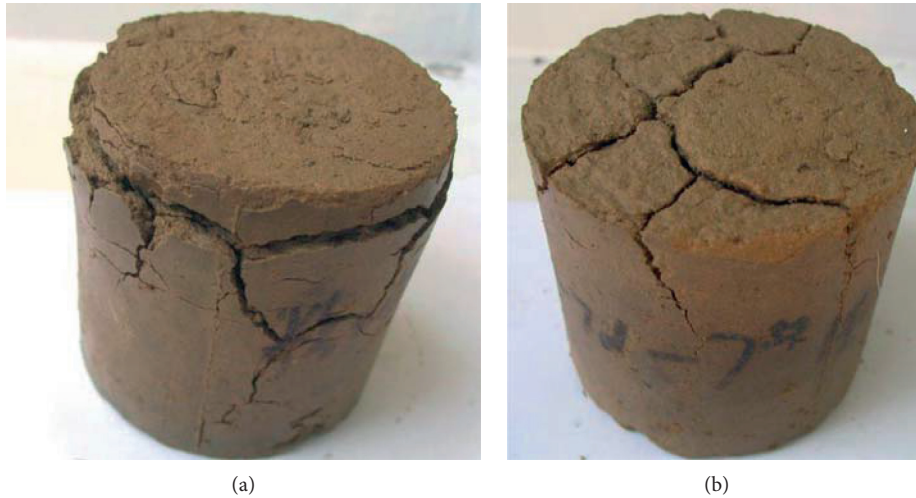
(a)

(b)

FIGURE 3: Appearance of representative specimens of group 2 (a) and group 3 (b) after nine cycles in Test I.
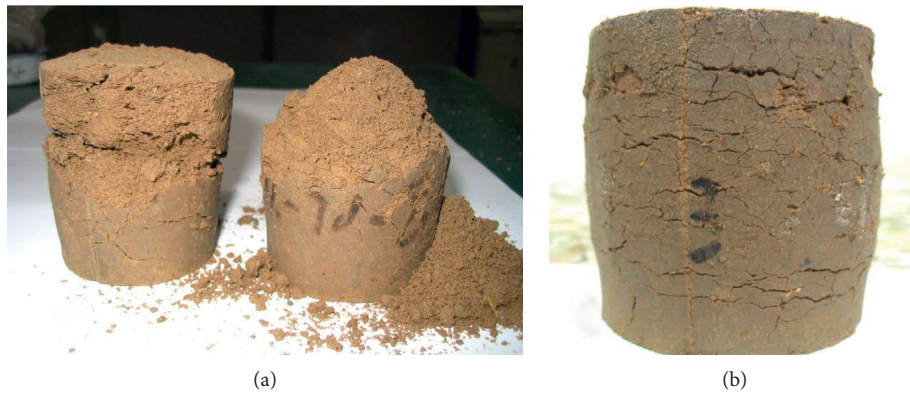

(a)

(b)

FIGURE 4: Appearance of representative samples of group 1 (a) after nine cycles and group 3 (b) after 24 cycles in Test II.
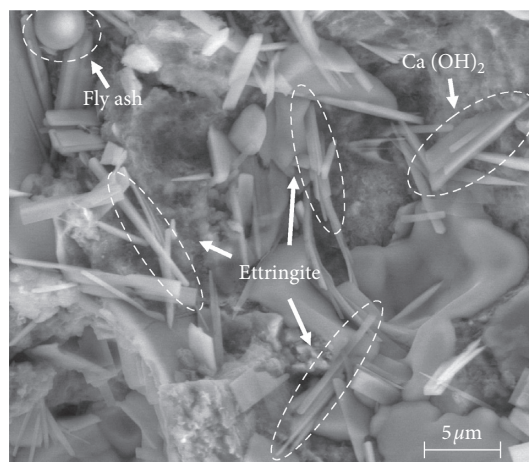
FIGURE 5: SEM image of saline soil stabilized by 15% stabilizer at an age of 7 days.

nonsaline sandy soil even though specimens were placed in a humidity chamber for thawing. Thus, the decrease in UCS shows the presence of the decay effect resulting from salt crystallization, but this effect is far slighter than those in Test I and Test II, where external water can invade specimens during the cyclic freeze-thaw process. Therefore, water content is a key factor in freeze-thaw damage of stabilized saline soil.

FIGURE 6: Pore size distribution of specimens stabilized by 10% stabilizer.

FIGURE 7: Percentage of mass increase of specimens in Test II (group 5 and 6 specimens were not destroyed completely after 60 cycles.).

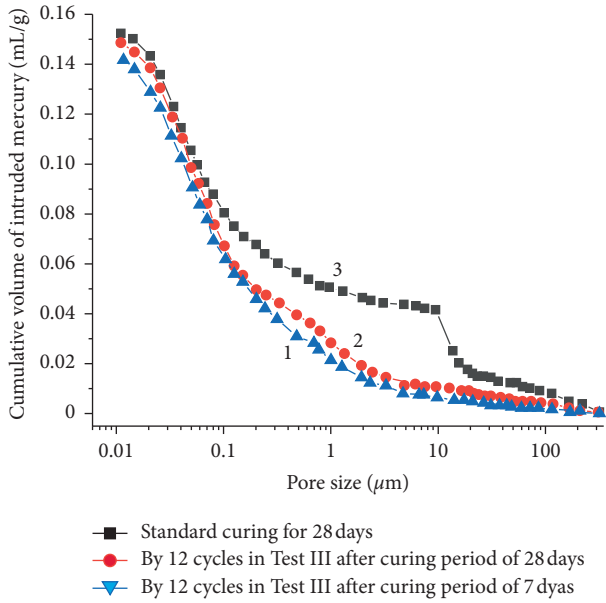In Test I and Test II, the freeze-thaw resistance of specimens cured for 28 days was much higher than that of specimens cured for 7 days. This is because the former specimens have a more compacted microstructure to prevent external water invasion. In addition, before repeated freezing and thawing, long-term curing is helpful for pozzolanic activity development of the soil stabilizer and for strength growth of specimens. Water intrusion damage is partly due to the expansion stress of ice. With increasing water content, more and more pores are filled with liquid, and thus the risk of frost damage grows. At the same time, more salt serving as part of the solid skeleton is dissolved into the pore liquid. This means that the salt solution in the specimen increases, and hence the zone influenced by the salt solution enlarges. When the temperature is lowered, crystallization of salts may cause serious damage to specimens. Moreover, the presence of moisture provides a necessary condition for growth of ettringite in the thawing steps. Expansion of ettringite can lead to serious damage in a hardened specimen.

When water content reaches a critical value, the specimen is rapidly destroyed in a freezing test. Figure 7 presents the percentage of mass increase of specimens in Test II. For the specimens cured for 7 days, when the percentage of mass increase reaches about 3.5%, corresponding with a water content of 18% (the water content of specimens is about 14.5% at the end of the curing period), complete destruction of the whole specimen occurs. For the specimens cured for 28 days, the critical value of percentage of mass increase is above 4.5%, corresponding with a water content of 20%. It should be noted that the time at which the water content of a specimen reaches a critical value is determined by its hydraulic conductivity. The longer the curing period, the lower the hydraulic conductivity that the specimen possesses.
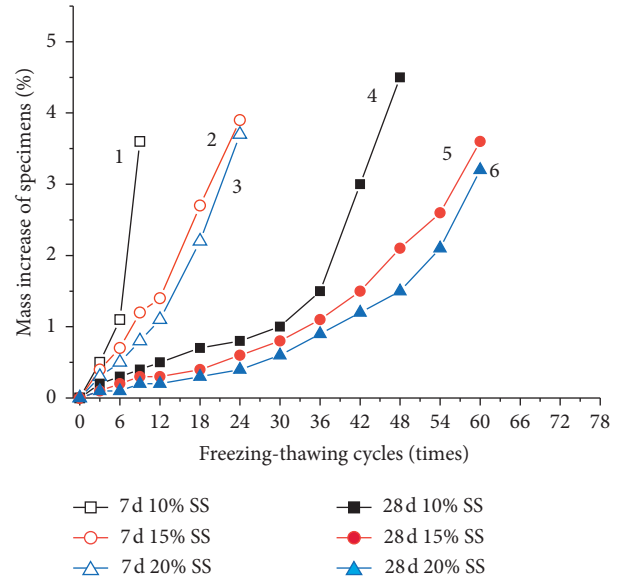
As noted above, the specimens with short-term curing have two obviously different failure patterns under the conditions of all-round (Test I) and unidirectional (Test II) water supply to specimens. In Test I, erosion of specimens begins from the surface layers and goes on towards the core with water invading, until the whole specimen is separated into several blocks by the expanding crystal phases of water and salt (Figure 3). In Test II, expansion first takes place in the upper part of a specimen, followed by crushing of the whole specimen (Figure 4). The cause of the two failure patterns is related to the migration of external water into specimens and internal moisture within specimens during the freeze-thaw cycles.

4.2. Driving Force of Water Migration. In agrology, soil water potential is defined to characterize the total potential energy of water in soil. It can be defined as the Gibbs free energy in thermodynamics [48, 49]:

$$dG = VdP - SdT + \sum_{1}^{n} \frac{\partial G}{\partial ci}dci + \frac{\partial G}{\partial \theta}\theta + dw_g, \quad (1)$$

where G is the Gibbs free energy, $V\,dP$ is the pressure potential caused by a change of pressure P, V is the volume, $-SdT$ is the temperature potential caused by a change of temperature T, and S is the entropy. The third term on the right-hand side of this equation is the solute potential caused by change in concentration c_i of the ith kind of solute, the fourth term is the matric potential caused by change of water content θ, and dw_g is gravity potential. Potential gradient is the driving force of water migration. Soil water migrates along the normal direction of the equipotential plane from high potential to low potential.

When focusing on the problem of water migration in solidified soil, the gravity potential and solute potential in the

soil water potential can be ignored [21, 50]. As the influence created by temperature change on other aspects such as surface tension of water, matric potential, and pressure potential largely exceeds the change of temperature potential [51], especially for small-scale specimens in which the temperature gradient is small, the term $-SdT$ can be ignored and other factors deserve more attention. Thus, (2) can be simplified as [52]

$$dG = VdP + \frac{\partial G}{\partial \theta} d\theta. \qquad (2)$$

Matric potential is generated by the holding effect of the soil matric on moisture, which is dominated by either the adsorption effect at low water content or capillary attraction at high water content. Therefore, it is a function with respect to water content, θ. As the matric potential is a negative value, the term for soil water suction is defined as its opposite number. Soil water suction, F_{su}, can be expressed as

$$F_{su} = -\frac{\partial G}{\partial \theta} d\theta = a \left(\frac{\theta}{\theta s} \right)^b, \qquad (3)$$

where θs is the saturation water content, and a and b are empirical constants. Equation (3) indicates that soil water suction has a decreasing power relation with water content before the saturated water content is reached. In [53], it was found experimentally that soil water potential in frozen soil increases at a power rate with decreasing temperature. According to (3), it can be explained by equivalently decreasing the water content when the liquid water in pores turns gradually into ice at low temperatures. Furthermore, soil water suction is also elevated due to increasing surface tension with decreasing temperature.

Before freezing, external water tends to be sucked into the specimen by a matric potential gradient between the surface and the core of the specimen when the specimen is in contact with water. When freezing, external water first ices. Due to the surface energy effect of soil particles on water and the salt dissolving in the water, the freezing point of water in the specimen decreases, so the external water source supply is shut off. Consequently, not much water enters the specimen during the freezing step. When thawing, the thawing front progresses from the outside towards the core of the specimen. The outer side of this thawing front maintains a relatively low water content and thereby a higher soil water suction compared with the inner side, where thawed liquid is sucked towards the outer side of the thawing front. Thus, water suction occurs with a progressing thawing front mainly during the thawing step.

4.3. Patterns of Water Migration.
The similarity between Tests I and II is the pressure-free water supply; i.e., no extra water pressure or air pressure is applied throughout the testing process. Besides, the difference between these two tests is that Test I adopts the all-round method of water supply to ensure there is sufficient free water on the surface of the specimens, whereas Test II supplies limited water in one direction from the bottom of samples, and the other surfaces of samples are always in a dry state.

In Test I, no extra pressure is exerted on specimens except for atmospheric pressure when water is supplied from all directions. Therefore, air in the pores of the core of the specimen is sealed by water on the surface and cannot escape. Figure 8(a) sketches external water migration in connected pores from the surface towards the core under the conditions of Test I. Before freezing, external water is sucked from the surface of the specimen through capillaries. By assuming that the solidified soil is an isotropic material, considering only the connected pores from the surface to the inside, and assuming cylindrical capillaries, a model of external water invading the specimen is as given in Figure 8(b), where water in the specimen is neglected due to the low water content, resulting in the macropores and mesopores being in an almost dry state.

If gravity action is not considered, soil water potential consists of matric potential and pressure potential. The intruding water compresses the air, so the inner pressure increases. When the pressure difference between the inner and outer parts equals the additional pressure created by the concave meniscus in the capillary, the external water stops intruding. The pressure difference can be expressed by the Young-Laplace equation:

$$\Delta P = P - P_0 = \gamma \left(\frac{1}{R_1} + \frac{1}{R_2} \right), \qquad (4)$$

where P is the inner air pressure, P_0 is the external atmospheric pressure, γ is the surface tension of water, and R_1 and R_2 are two radii of the meniscus curvature. The inner air pressure can be estimated by the ideal gas law equation:

$$PV = nRT, \qquad (5)$$

where n is the number of moles of air and R is the ideal gas constant. Before the beginning of the freezing step, the inner air may be regarded as being under isothermal compression. Therefore, the change of air volume can be obtained from

$$\Delta V = \frac{V_0 (P_0 - P)}{P} = -\frac{\Delta P V_0}{(P_0 + \Delta P)}, \qquad (6)$$

where V_0 is the original volume of the inner air, corresponding with pressure P_0. The absolute value of ΔV is the volume of intruded water, ΔV_w:

$$\Delta V_w = \frac{V_0}{(1 + P_0 / (\gamma (1/R_1 + 1/R_2)))}. \qquad (7)$$

When the temperature is lowered to T_2, which is above the freezing point of the external water, the inner air shrinks until the pressure difference can balance the additional pressure from the concave meniscus. The volume of intruded water can be calculated according to

$$\Delta V_w = V_0 \left(1 - \frac{P_0 T_2}{T_0 (P_0 + \gamma (1/R_1 + 1/R_2))} \right). \qquad (8)$$

Furthermore, γ increases with decreasing temperature, which promotes water intrusion. V_0 can be estimated according to
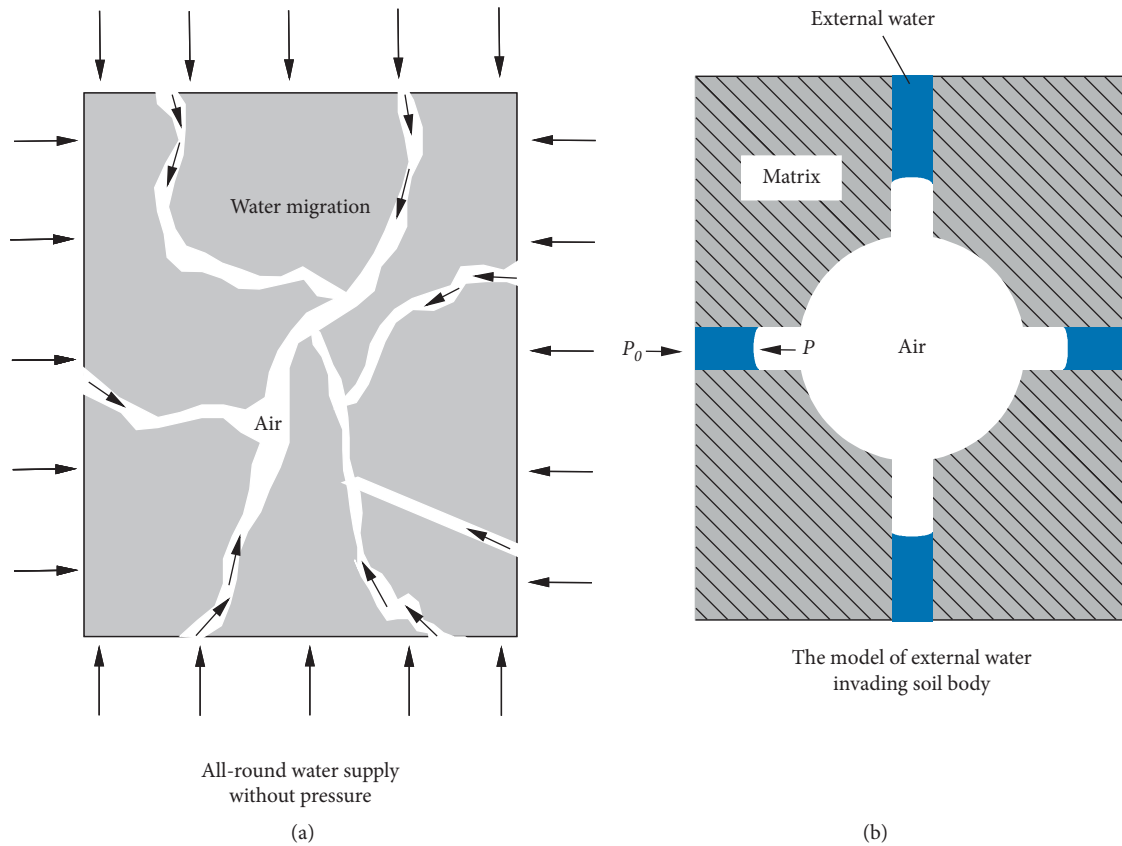
Figure 8: Sketch of water migration and the simplified model of Test I.

$$V_0 = V_{sp} - \frac{m_s}{\rho_s} - \frac{m_l}{\rho_l}, \tag{9}$$

where V_{sp} is the volume of the specimen, m_s and m_l are the dry mass and moist mass, respectively, of the specimen at the end of curing, and ρ_s and ρ_l are the density of soil particles and the density of water, respectively.

Once freezing occurs, external water cannot intrude any more, even though the inner air pressure continues to decrease and soil water suction increases. However, the negative/suction pressure generated is the driving force that sucks free water from the thawing front in the thawing step.

In Test I, due to the presence of this air pressure potential, external water is kept out of the specimen core and accumulates only in the outer part, where the microstructure of the specimen is firstly eroded. This is why erosion takes place from the surface towards the core in Test I. With a short curing period, the pozzolanic reactivity of the soil stabilizer cannot fully develop. Therefore, the specimen is not compact enough, and there are some big flaws in the microstructure, through which external water can intrude the core of the specimen. An uncompacted microstructure leads to high hydraulic conductivity. Accordingly, these specimens fail early. This is why the specimens cured for a short period are destroyed as in Figure 3.

Unlike Test I, no pressure potential appears under the experimental condition of unidirectional water supply to specimens because the pressure in pores connected with air always equals atmospheric pressure. Thus (2) can be further simplified to

$$dG = \frac{\partial G}{\partial \theta} d\theta + dw_g. \tag{10}$$

Equation (10) reveals that the water migration depends on the gradient of the matric potential and the gravity potential. In Test II, water migrates from the bottom of the specimen upwards. Figure 9 sketches the water migration and water content distribution in the specimen under this condition. Since water content in the top part is always lower than that in the bottom part before the whole specimen reaches saturation, the gradient of matric potential always drives water upwards.

Since external water is obtained only through the hole from the water-saturated felt pad, it is not sufficient, and the intruded water is fully dispersed in the specimen due to the action of soil water suction. Therefore, the water content even in the bottom part cannot reach the critical value at which the specimen is completely destroyed, and the bottom can keep sucking water from the environment.

Thus, each part of the specimen strives to acquire water to reach the balance of the soil water potential, leading to full dispersion of water in the whole specimen. Therefore, it is difficult to accumulate water in some parts, for example, the bottom. This is why the destructive phenomenon of specimens under this condition occurs later than that under the conditions of all-round water supply to specimens. Only when the

Figure 9: Sketch of water migration and water content distribution before saturation in Test II.

water content in the whole specimen synchronously reaches the critical value, will frost damage suddenly occur.

When water content in the matric is low, the holding effect on water mainly depends on adsorption. Therefore, the method of capillary rise is not suitable for estimation of intruded water. With increasing water content, more sodium sulfate dissolves into the pore liquid and then rises to the upper part, together with migrating moisture. Expansion and destruction of specimens occur firstly in the upper part, which proves that cumulative salt in the pore liquid is the most significant cause leading to specimen failure in Test II. After 12 cycles, the content of the dissoluble salt in the upper and lower halves of specimens belonging to group 2 was measured. The results revealed that the salt content in the lower half was only 81% of that in the upper half, which confirms that the salt moved from the lower part and accumulated in the upper part during the cyclic freeze-thaw processes. Moreover, the uneven distribution of salt may produce osmotic potential and then further affect the migration of water.

5. Conclusion

By designing three test methods for freeze-thaw cycles of stabilized saline soil, this study has investigated the freeze-thaw resistance of saline soil stabilized by cement-based material

under different types of water supply. It has also analyzed the failure modes of the specimens and the role of salt and water in the freezing and thawing process. The concept of soil water potential has been introduced, and the dynamic mechanism and migration of water and salt have been described through theoretical models. The effect of water content on the freeze-thaw resistance of stabilized saline soil has also been discussed. The main conclusions of this study are as follows.

In cyclic freeze-thaw tests, external water is one of the most important factors in the destruction of stabilized saline soil. Different failure patterns are caused by different water supply patterns in freeze-thaw tests. If no external water is supplied, specimens have no obvious appearance of erosion, even though the UCS gradually decreases with increasing number of freeze-thaw cycles.

Under the condition of all-round water supply to specimens, the pressure potential caused by the inner air leads to water accumulating first in the outer part of the specimen. For specimens with a long-term curing period, erosion from the surface towards the core is a distinct characteristic of the failure pattern.

Under the condition of unidirectional water supply to specimens, air pressure potential is eliminated and

matric potential drives moisture to migrate from the bottom upwards, finally dispersing all over the specimen. The sulfate in the lower part of the specimen is dissolved and then carried to the upper part. Gradual accumulation of salt causes the specimen to turn into powder when a certain water content is reached.

The water content is an important factor for appearance of macroscopical frost damage. In this study, the estimated critical value of water content was about 18%–20%.

The pozzolanic reactivity of soil stabilizer is reduced by low temperature. A high percentage of soil stabilizer can improve the freeze-thaw resistance of stabilized soil, but a sufficiently long curing period plays a more important role.

Abbreviations

a and b: Empirical constants
c_i: Concentration of the ith kind of solute
F_{su}: Soil water suction
G: Gibbs free energy, J
m_s and m_l: Specimen dry mass and moist mass at end of curing, kg
n: Number of moles of air
P: Air pressure, Pa
P_0: External atmospheric pressure, Pa
R: Ideal gas constant
R_1 and R_2: Radii of meniscus curvature, m
r: Pore radius, m
S: Entropy
T: Temperature, K
T_2: Final temperature, K
V: Air volume, m^3
V_{sp}: Volume of specimen, m^3
V_0: Original volume of inner air, m^3
w_g: Work done by gravity on water, J
α_{H2O}: Water activity
γ: Surface tension of water, mN/m
ΔV: Volume difference of air of intruded water, m^3
ΔV_w: Volume of intruded water, m^3
θ: Water content of soil body
θ_s: Saturation water content
ρ_s and ρ_l: Density of soil particles and density of water, kg/m^3.

Data Availability

All the data included in this study are available upon request by contacting the corresponding author.

Conflicts of Interest

The authors declare that there are no conflicts of interest regarding the publication of this paper.

References

[1] S. Zhang, J. Zhang, Y. Gui, W. Chen, and Z. Dai, "Deformation properties of coarse-grained sulfate saline soil under the freeze-thaw-precipitation cycle," *Cold Regions Science and Technology*, vol. 177, Article ID 103121, 2020.

[2] B. Yang, Z. Qin, Q. Zhou, H. Li, L. Li, and X. Yang, "Pavement damage behaviour of urban roads in seasonally frozen saline ground regions," *Cold Regions Science and Technology*, vol. 174, Article ID 103035, 2020.

[3] H. Li, Y. Lai, L. Wang et al., "Review of the state of the art: interactions between a buried pipeline and frozen soil," *Cold Regions Science and Technology*, vol. 157, pp. 171–186, 2019.

[4] H. Li, Y. Lai, and L. Li, "Impact of hydro-thermal behaviour around a buried pipeline in cold regions," *Cold Regions Science and Technology*, vol. 171, Article ID 102961, 2020.

[5] H. Zhang, X. Yuan, Y. Liu, J. Wu, X. Song, and F. He, "Experimental study on the pullout behavior of scrap tire strips and their application as soil reinforcement," *Construction and Building Materials*, vol. 254, Article ID 119288, 2020.

[6] S. M. Hejazi, M. Sheikhzadeh, S. M. Abtahi, and A. Zadhoush, "A simple review of soil reinforcement by using natural and synthetic fibers," *Construction and Building Materials*, vol. 30, pp. 100–116, 2012.

[7] S. Zhang, X. Yang, S. Xie, and P. Yin, "Experimental study on improving the engineering properties of coarse grain sulphate saline soils with inorganic materials," *Cold Regions Science and Technology*, vol. 170, Article ID 102909, 2020.

[8] Y. Liu, Q. Wang, S. Liu et al., "Experimental investigation of the geotechnical properties and microstructure of lime-stabilized saline soils under freeze-thaw cycling," *Cold Regions Science and Technology*, vol. 161, pp. 32–42, 2019.

[9] Q. Lv, L. Jiang, B. Ma, B. Zhao, and Z. Huo, "A study on the effect of the salt content on the solidification of sulfate saline soil solidified with an alkali-activated geopolymer," *Construction and Building Materials*, vol. 176, pp. 68–74, 2018.

[10] P. Sargent, *The Development of Alkali-Activated Mixtures for Soil Stabilisation*, Woodhead Publishing Limited, Sawston, UK, Cambridge, 2015.

[11] M. Naveed, J. Duan, S. Uddin, M. Suleman, Y. Hui, and H. Li, "Application of microbially induced calcium carbonate precipitation with urea hydrolysis to improve the mechanical properties of soil," *Ecological Engineering*, vol. 153, Article ID 105885, 2020.

[12] T. Zhang, Y.-L. Yang, and S.-Y. Liu, "Application of biomass by-product lignin stabilized soils as sustainable Geomaterials: a review," *Science of the Total Environment*, vol. 728, Article ID 138830, 2020.

[13] C. Zhang, D. Li, J. Jiang et al., "Evaluating the potential slope plants using new method for soil reinforcement program," *Catena*, vol. 180, pp. 346–354, 2019.

[14] F. Kalantary and M. Kahani, "Evaluation of the ability to control biological precipitation to improve sandy soils," *Procedia Earth and Planetary Science*, vol. 15, no. 21, pp. 278–284, 2015.

[15] L. A. van Paassen, C. M. Daza, M. Staal, D. Y. Sorokin, W. van der Zon, and M. C. M. Van Loosdrecht, "Potential soil reinforcement by biological denitrification," *Ecological Engineering*, vol. 36, no. 2, pp. 168–175, 2010.

[16] W. Zhang, J. Ma, and L. Tang, "Experimental study on shear strength characteristics of sulfate saline soil in Ningxia region under long-term freeze-thaw cycles," *Cold Regions Science and Technology*, vol. 160, pp. 48–57, 2019.

[17] C. C. Ikeagwuani and D. C. Nwonu, "Emerging trends in expansive soil stabilisation: a review," *Journal of Rock Mechanics and Geotechnical Engineering*, vol. 11, no. 2, pp. 423–440, 2019.

[18] F. Wang, X. Qin, and R. Sun, "The investigation of concrete durability under natural condition of Caerhan Salt Lake," *Bulletin of the Chinese Ceramic Society*, vol. 4, no. 21, pp. 16–22, 2002.

[19] A. Mardani-Aghabaglou, İ. Kalıpcılar, G. İnan Sezer, A. Sezer, and S. Altun, "Freeze-thaw resistance and chloride-ion penetration of cement-stabilized clay exposed to sulfate attack," *Applied Clay Science*, vol. 115, pp. 179–188, 2015.

[20] X. Long, G. Cen, L. Cai, and Y. Chen, "Model experiment of uneven frost heave of airport pavement structure on coarse-grained soils foundation," *Construction and Building Materials*, vol. 188, pp. 372–380, 2018.

[21] J. Zhang, Y. Lai, J. Li, and Y. Zhao, "Study on the influence of hydro-thermal-salt-mechanical interaction in saturated frozen sulfate saline soil based on crystallization kinetics," *International Journal of Heat and Mass Transfer*, vol. 146, Article ID 118868, 2020.

[22] X. Wan, Q. Hu, and M. Liao, "Salt crystallization in cold sulfate saline soil," *Cold Regions Science and Technology*, vol. 137, pp. 36–47, 2017.

[23] X. Zhao, A. Shen, Y. Guo, P. Li, and Z. Lv, "Pavement mechanic response of sulfate saline soil subgrade section based on fluid-structure interaction model," *International Journal of Pavement Research and Technology*, vol. 10, no. 6, pp. 497–506, 2017.

[24] D. Wu, Y. Lai, and M. Zhang, "Thermo-hydro-salt-mechanical coupled model for saturated porous media based on crystallization kinetics," *Cold Regions Science and Technology*, vol. 133, pp. 94–107, 2017.

[25] R. Bai, Y. Lai, M. Zhang, and J. Ren, "Study on the coupled heat-water-vapor-mechanics process of unsaturated soils," *Journal of Hydrology*, vol. 585, Article ID 124784, 2020.

[26] D. Wang, Q. Wang, and Z. Huang, "New insights into the early reaction of NaOH-activated slag in the presence of CaSO4," *Composites Part B: Engineering*, vol. 198, Article ID 108207, 2020.

[27] S. Zhuang and Q. Wang, "Inhibition mechanisms of steel slag on the early-age hydration of cement," *Cement and Concrete Research*, vol. 140, Article ID 106283, 2021.

[28] J. Liu, P. Yang, and Z. Yang, "Electrical properties of frozen saline clay and their relationship with unfrozen water content," *Cold Regions Science and Technology*, vol. 178, no. 159, Article ID 103127, 2020.

[29] Q. Wang, J. Qi, S. Wang, J. Xu, and Y. Yang, "Effect of freeze-thaw on freezing point of a saline loess," *Cold Regions Science and Technology*, vol. 170, Article ID 102922, 2020.

[30] J. Xu, Y. Li, W. Lan, and S. Wang, "Shear strength and damage mechanism of saline intact loess after freeze-thaw cycling," *Cold Regions Science and Technology*, vol. 164, Article ID 102779, 2019.

[31] R. Tang, G. Zhou, J. Wang, G. Zhao, Z. Lai, and F. Jiu, "A new method for estimating salt expansion in saturated saline soils

[32] during cooling based on electrical conductivity," *Cold Regions Science and Technology*, vol. 170, Article ID 102943, 2020.

[32] J. Ren, "The damage mechanism and failure prediction of concrete under wetting-drying cycles with sodium sulfate solution," *Construction and Building Materials*, vol. 264, Article ID 120525, 2020.

[33] RIOH, Test Methods of Materials Stabilized with Inorganic Binders for Highway Engineering (JTG E51–2009), 2009.

[34] ASTM International, Methods for Freezing and Thawing Compacted Soil-Cement Mixtures, 2016.

[35] J. Ren, Y. Lai, R. Bai, and Y. Qin, "The damage mechanism and failure prediction of concrete under wetting-drying cycles with sodium sulfate solution," *Construction and Building Materials*, vol. 264, Article ID 120525, 2021.

[36] Y. Wang, I.-M. Chou, M. Zheng, and X. Hou, "Acquisition and evaluation of thermodynamic data for mirabilite-thenardite equilibria at 0.1 MPa," *The Journal of Chemical Thermodynamics*, vol. 111, pp. 221–227, 2017.

[37] A. I. Vavouraki and P. G. Koutsoukos, "Kinetics of crystal growth of mirabilite in aqueous supersaturated solutions," *Journal of Crystal Growth*, vol. 338, no. 1, pp. 189–194, 2012.

[38] P. Vazquez, C. Thomachot-Schneider, K. Mouhoubi et al., "Sodium sulfate crystallisation monitoring using IR thermography," *Infrared Physics & Technology*, vol. 89, pp. 231–241, 2018.

[39] T. A. Saidov, L. Pel, and G. H. A. Van Der Heijden, "Crystallization of sodium sulfate in porous media by drying at a constant temperature," *International Journal of Heat and Mass Transfer*, vol. 83, pp. 621–628, 2015.

[40] P. A. J. Donkers, K. Linnow, L. Pel, M. Steiger, and O. C. G. Adan, "Na2SO4·10H2O dehydration in view of thermal storage," *Chemical Engineering Science*, vol. 134, pp. 360–366, 2015.

[41] C. Rodriguez-Navarro, E. Doehne, and E. Sebastian, "How does sodium sulfate crystallize? Implications for the decay and testing of building materials," *Cement and Concrete Research*, vol. 30, no. 10, pp. 1527–1534, 2000.

[42] R. J. Flatt, "Salt damage in porous materials: how high supersaturations are generated," *Journal of Crystal Growth*, vol. 242, no. 3-4, pp. 435–454, 2002.

[43] E. M. Winkler and P. C. Singer, "Crystallization pressure of salts in stone and concrete," *Geological Society of America Bulletin*, vol. 83, no. 11, pp. 3509–3514, 1972.

[44] G. W. Scherer, "Stress from crystallization of salt," *Cement and Concrete Research*, vol. 34, no. 9, pp. 1613–1624, 2004.

[45] S. Arora and A. H. Aydilek, "Class F fly-ash-amended soils as highway base materials," *Journal of Materials in Civil Engineering*, vol. 17, no. 6, pp. 640–649, 2005.

[46] M. H. Gorakhki and C. A. Bareither, "Unconfined compressive strength of synthetic and natural mine tailings amended with fly ash and cement," *Journal of Geotechnical and Geoenvironmental Engineering*, vol. 143, no. 7, 2017.

[47] I. Bozbey, M. K. Kelesoglu, B. Demir et al., "Effects of soil pulverization level on resilient modulus and freeze and thaw resistance of a lime stabilized clay," *Cold Regions Science and Technology*, vol. 151, pp. 323–334, 2018.

[48] J. W.. Gibbs, "A method of geometrical representation of the thermodynamic properties of substances by means of surfaces," *Transactions of Connecticut Academy of Arts and Sciences*, vol. 8, pp. 382–404, 1873.

[49] X. Zhao, Study on Water-Salt Transport and HTSPE Coupled Model of the Saline Soil in Western Jilin, 2018.

[50] Z. Li, Q. Xue, T. Katsumi, and T. Inui, "Electric-hydraulic-chemical coupled modeling of solute transport through

landfill clay liners," *Applied Clay Science*, vol. 101, pp. 541–552, 2014.

[51] Z. D. Lei, S. X. Yang, and S. C. Xie, Kinetic of Soil Wate, 1988.

[52] Y. D. Qin, Soil physics Encyclopedia of Earth Sciences Series, pp. 686–693, 2003.

[53] Y. Ji, G. Zhou, X. Zhao et al., "On the frost heaving-induced pressure response and its dropping power-law behaviors of freezing soils under various restraints," *Cold Regions Science and Technology*, vol. 142, pp. 25–33, 2017.

Research Article

Effect of Different Activators on Rheological and Strength Properties of Fly Ash-Based Filling Cementitious Materials

Liu Fangfang [ID], Feng Xiyang, and Chen Li

Yunnan Land and Resources Vocational College, Kunming 650000, China

Correspondence should be addressed to Liu Fangfang; liufangfag@yugoco.com

In this paper, lime, gypsum, NaOH, and Na_2SO_4 are mainly used to study the activation degree and activation mechanism of fly ash, and L9 (3^4) orthogonal table is used for the orthogonal test. The influence of different activators on the rheological and strength properties of slurry was analyzed. The microstructure and hydration products of fly ash cement cementitious body were studied by SEM and XRD. The results show that the bleeding rate of slurry containing activator fly ash system is between 2.24% and 3.37%, which is much higher than that of pure cement slurry (9.25%). Therefore, the addition of this system can improve the fluidity of slurry, and the optimal scheme is $a_3b_2c_2d_2$. The results show that the compressive strength of cement with activator fly ash system is much lower than that of pure cement, but the increase of strength is between 31% and 85%, which is much greater than that of pure cement (35%–46%). The optimal scheme is $A_2B_2C_3D_3$ or $A_3B_2C_3D_3$ at 3 days and $A_1B_3C_2D_3$ at 28 days. According to the scanning results of SEM and XRD, the addition of activator can significantly improve the hydration degree of fly ash and form a more complex network structure without obvious gap.
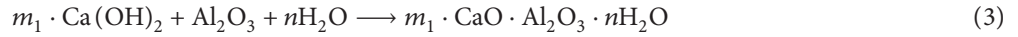
1. Introduction

tWith the development of mining technology, filling method is considered a future development direction for an increasing number of large, medium, and small mines, and the reduction of filling cost has always been the research emphasis of scholars all over the world [1, 2]. Fly ash mainly refers to fine particles generated from coal combustion, the particle size of which is 1–100 m and the main chemical compositions are SiO_2 and Al_2O_3 [3]. By the end of 2020, the annual production of fly ash in China has reached 580 million tons. If the fly ash is released into the air, it will seriously affect the air quality, but if it is stacked on the ground, it will not only pollute the local environment but also inevitably cause a waste of resources. Since fly ash is enriched with Si, Al, Ca, and other chemical substances [4], it can be used to substitute some types of cement in the fields of concrete [5, 6] or mine filling [7–9]. This is a generally accepted treatment method. However, as an inert material, fly ash can substitute cement as much as possible only when its internal potential activity is fully stimulated. For this purpose, it is affirmatively necessary to study the excitation principle and mode of fly ash.
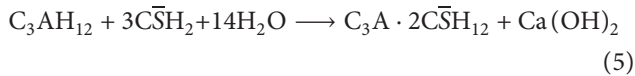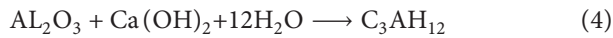
In the physical excitation mode, the particle size of fly ash is changed by mechanical milling technology, so its particle fineness is improved, and specific surface area is increased, which facilitates the dissolution of elements such as SiO_2 and Al_2O_3 and the penetration of Ca^{2+}, thereby improving the activity of fly ash [10, 11]. As for the chemical excitation mode, different fly ash excitants are added to stimulate the internal potential activity of fly ash [12]. Fu et al. [13] developed a compound additive and its ratio to effectively activate fly ash by using the methods of orthogonal design and uniform design and working out a computer program. Sun et al. [14] studied the mechanism and persistence of different chemical excitants stimulating the activity of fly ash by using XRD, SEM, EDS, and other devices and determined the optimal combination of excitants by single mixing and double mixing. Hoang et al. [15] investigated the compressive strength of fly ash cement gelatin at 5°C and 20°C by using three different additives, that is, sodium thiocyanate, diethanolamine, and glycerin. The results showed that cement hydration is promoted after these three additives are added, and the content of calcium carboaluminate in hydration products is increased, and the

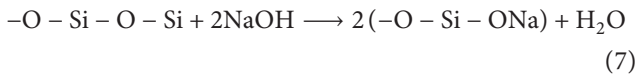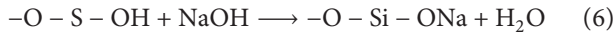compressive strength of gelatin is also improved to a certain extent.

Al$_2$O$_3$ and SiO$_2$ stored in fly ash bind with Ca^{2+} in slurry to form calcium silicate and calcium aluminate, so that the internal structure of gelatin becomes denser, and its long-term strength is improved [16]. The reaction mechanism is as follows.

CaO in cement reacts with water to generate Ca(OH)$_2$:

$$CaO + H_2O \longrightarrow Ca(OH)_2 \tag{1}$$

Al$_2$O$_3$ and SiO$_2$ in fly ash continue to react chemically with Ca(OH)$_2$ to generate CaO·SiO$_2$ and CaO·Al$_2$O$_3$:

$$m_1 \cdot Ca(OH)_2 + SiO_2 + nH_2O \longrightarrow m_1 \cdot CaO \cdot SiO_2 \cdot nH_2O \tag{2}$$

$$m_1 \cdot Ca(OH)_2 + Al_2O_3 + nH_2O \longrightarrow m_1 \cdot CaO \cdot Al_2O_3 \cdot nH_2O \tag{3}$$

However, Ca^{2+} in slurry is not enough for Al$_2$O$_3$ and SiO$_2$. Hence, excitant is added to the slurry to supplement Ca^{2+} needed by Al$_2$O$_3$ and SiO$_2$ and also to crack the internal structure of fly ash. Then, the excitant reacts chemically with Al$_2$O$_3$ dissolved from fly ash in the solution containing CaO to generate ettringite (Aft). The reaction mechanism is as follows:

$$AL_2O_3 + Ca(OH)_2 + 12H_2O \longrightarrow C_3AH_{12} \tag{4}$$

$$C_3AH_{12} + 3C\bar{S}H_2 + 14H_2O \longrightarrow C_3A \cdot 2C\bar{S}H_{12} + Ca(OH)_2 \tag{5}$$

Excitant is added to also increase the concentration of OH- in the slurry [17], so that the reaction speed between fly ash and Ca(OH)$_2$ is improved. In addition, it also has a certain promoting effect on the early strength of gelatin. The reaction mechanism is as follows:

$$-O-S-OH + NaOH \longrightarrow -O-Si-ONa + H_2O \tag{6}$$

$$-O-Si-O-Si + 2NaOH \longrightarrow 2(-O-Si-ONa) + H_2O \tag{7}$$

According to the above analysis, excitant can be added to densify the gelatin, generate more stable hydration products, and improve the compressive strength of gelatin.
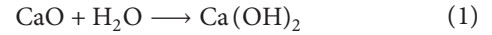
2. Composition of Test Materials

The test materials used include fly ash produced by China Huadian Group Kunming Power Plant; 32.5# Portland slag cement produced by Beikong Cement Plant; lime powder with calcium content ≥85% and fineness ≥180 meshes produced by Kunming Maoshan Qiangda Lime Building Materials Factory; and gypsum powder produced by Yunnan Hongshi Mining Co., Ltd., as well as NaoH, Na$_2$SO$_4$, and other chemical additives.

3. Characteristics of Fly Ash

The fly ash has a density of 1.8~2.3 g/cm^3, bulk density of 0.6~0.9 g/cm^3, measured bulk density of 0.79 g/cm^3, and compacted bulk density of 1.26 g/cm^3. Its chemical composition and technical indexes are shown in Tables 1 and 2, respectively.

4. Characteristics of Cement

The cement has a density of 3.01~3.15 g/cm^3, bulk density of 1.3~1.8 g/cm^3, measured bulk density of 1.35 g/cm^3, and compacted bulk density of 1.95 g/cm^3. Its chemical composition is shown in Table 3.

4.1. Test Program. In this paper, four different excitants are used to perform compound activation test on fly ash. Because the activation effect on fly ash varies among different excitants, the test program is designed by the orthogonal test in this paper. According to a great number of preliminary studies, the four excitants used in this test are determined: lime, gypsum, NaOH, and Na$_2$SO$_4$. L9(3^4) orthogonal table is used for orthogonal test. The specific test programs are shown in Tables 4 and 5, respectively.

According to the test method by Huang et al. [18], the evenly mixed slurry is poured into a standard triple test mold (7.07 cm ∗ 7.07 cm ∗ 7.07 cm) and then cured for 24 h and demoulded after tamping. The specimen is watered every 3 d and covered with water-retaining material, and cured for 3 d, 7 d, and 28 d at room temperature.

The evenly mixed slurry is poured into a measuring cylinder with a measuring range of 200 mL until reaching the 100 mL scale. The bleeding amount of the slurry is recorded at 2 h, and the bleeding rate is calculated according to formula (8) [19], where V is the total volume of slurry; ΔV is the secreted water.

The slurry prepared is poured into a slump barrel with both top and bottom openings. The slump barrel is placed vertically upward and then lifted at a constant speed. The maximum diffusion diameter of the slurry, that is, the fluidity of slurry, is measured by a straight rule.

4.2. Test Equipment. The microstructure of fly ash cement gelatin and the morphology of its hydration products are observed by Philips XL30 ESEM-TMP SEM (Figure 1(a)) and D/Max 2200 XRD (Figure 1(b)) provided by Research Center for Analysis and Measurement, Kunming University of Science and Technology.

TABLE 1: Chemical composition of fly ash.

Composition	Fe_2O_3	SiO_2	Al_2O_3	CaO	MgO	Na_2O	K_2O	SO_3	Loss on ignition
Content (%)	11.26	51.79	22.95	2.89	1.6	0.46	0.9	0.06	7.69

TABLE 2: Technical indexes of fly ash.

Item	Unit of measurement	Technical index	Test value
Fineness	%	≤8 (0.08 screen residue)	1.1
Loss on ignition	%	≤5.0	7.69
Water demand	%	≤95	90
Water content	%	≤1.0	0.03
SO3	%	≤3.0	0.06
Free CaO	%	≤4.0	Trace amount

TABLE 3: Chemical composition of P.S 32.5 cement.

Composition	SiO_2	Al_2O_3	Fe_2O_3	CaO	MgO	K_2O	SO_3	Total
Content (%)	19.97	6.34	3.74	65.74	1.11	1.1	0.12	98.12

TABLE 4: Orthogonal table design of compound activation test.

Level	A	B	C	D
	Lime dosage (%)	Gypsum dosage (%)	NaOH dosage (%)	Na_2SO_4 dosage (%)
1	8	4	1	2
2	12	5	2	3
3	16	6	3	4

TABLE 5: Orthogonal test scheme of compound activation.

Test no.	A	B	C	D
	Lime dosage (%)	Gypsum dosage (%)	NaOH dosage (%)	Na_2SO_4 dosage (%)
FH-1	8	4	1	2
FH-2	8	5	2	3
FH-3	8	6	3	4
FH-4	12	4	2	4
FH-5	12	5	3	2
FH-6	12	6	1	3
FH-7	16	4	3	3
FH-8	16	5	1	4
FH-9	16	6	2	2

Notes: the ratio of cement to fly ash is 1 : 1; the water-cement ratio is 0.5.

5. Analysis of Test Results

5.1. Fluidity Analysis of Slurry. According to Table 6, slurry containing the system of excitant and fly ash has a bleeding rate of 2.24%~3.73% and a fluidity of 110 mm~155 mm. The bleeding rate and fluidity of unmixed cement mortar are 9.25% and 150 mm, respectively. According to field filling experience, the slurry has a paste property if its bleeding rate is below 5% [20]. Therefore, it is believed that the system of excitant and fly ash can be added to improve the fluidity of slurry and ensure that no segregation or pipe blockage occurs during the slurry transportation. The primary cause is that although the lime used in the test is hydrated lime $(Ca(OH)_2)$, it still contains a small amount of quicklime (CaO). The digestion reaction between CaO and water continues to generate $Ca(OH)_2$, and $Ca(OH)_2$ particles are in the form of colloidal dispersion. The diameter of these particles is about 1 m, and their surface is covered by a thick water film. As indicated by a large number of particles and large total surface area, lime has a good water-retaining property, so that the slurry has a certain stability without excess water secretion. There is no big difference in fluidity between unmixed cement mortar and slurry containing the system of excitant and fly ash, so no detailed analysis is conducted, and only the bleeding rate of slurry is analyzed by multiple linear regression and variance analysis, as shown in the following formula:

$$y = 4.32 - 13.67x_1 - 2.5x_2 + 6.5x_3 + 9x_4, \qquad (8)$$

where y is the bleeding rate of slurry; x_1 is the lime dosage, %; x_2 is the gypsum dosage, %; x_3 is the NaoH dosage, %; x_4 is the Na_2SO_4 dosage.

The negative correlation coefficient R^2 of curve fitting is 0.848, indicating that the regression of this equation is significant and the curve fitting is highly accurate.

(a)

(b)

Figure 1: Morphology and phase test. (a) SEM. (b) XRD.

Table 6: Rheological properties of slurry.

Test No.	A Lime dosage (%)	B Gypsum dosage (%)	C NaOH dosage (%)	D Na$_2$SO$_4$ dosage (%)	Syneresis rate (%)	Fluidity (mm)
FH-1	1 (8)	1 (4)	1 (1)	1 (2)	3.47	131
FH-2	1	2 (5)	2 (2)	2 (3)	3.17	140
FH-3	1	3 (6)	3 (3)	3 (4)	3.73	155
FH-4	2 (12)	1	2	3	3.14	145
FH-5	2	2	3	1	3.02	138
FH-6	2	3	1	2	2.94	115
FH-7	3 (16)	1	3	2	2.45	136
FH-8	3	2	1	3	2.4	112
FH-9	3	3	2	1	2.24	110
KD-12	0	0	0	0	9.25	150

Notes: KD-12 is unmixed cement mortar; KD-11 is fly ash containing 50 additives, without excitant.

Variance analysis is carried out on the bleeding rate of slurry. According to Table 6, the influence of each factor on the bleeding rate of slurry from big to small is as follows: lime dosage > NaOH dosage > Na$_2$SO$_4$ dosage > gypsum dosage; the optimal scheme is A$_3$B$_2$C$_2$D$_2$, that is, 16% lime, 5% gypsum, 2% NaOH, and 3% Na$_2$SO$_4$ (due to limited space, variance analysis is not described).

5.2. Strength Analysis of Fly Ash Cement Gelatin. For some specimens that have reached the curing period, the compressive strength test is carried out by 200-C-1 compression-testing machine manufactured by Wuxi Building Materials Instrument Factory, and the test results are shown in Figure 2. Other specimens are divided by a cutting machine, and a small part in the middle is retained and placed in industrial alcohol to stop its hydration reaction. When necessary, the specimen is taken out and carbon sprayed on its surface, and then it can be scanned by SEM [21].

According to Figure 2, when the curing period is only 3 d, the addition of excitant can improve the compressive strength of fly ash cement gelatin, but its maximum strength value is far less than that of ordinary Portland cement. According to Figure 3, with the increase of curing period and when it reaches 7 d, the strength value of the gelatin containing the system of excitant and fly ash is 68%~85%, and that of the

gelatin without excitant is 46%~60%. When the curing period reaches 28 d, the strength value of the gelatin containing the system of excitant and fly ash is 37%~78%, and that of the gelatin without excitant is 35%~68%. Therefore, excitant can be added to increase the hydration speed of fly ash and enhance the compressive strength of fly ash cement gelatin. When the curing period reaches 90 d or 180 d, the compressive strength of gelatin containing the system of excitant and fly ash is greater than that of ordinary Portland cement.

Multivariate linear regression analysis and variance analysis are carried out on the compressive strength of gelatin containing the system of excitant and fly ash at 3 d, 7 d, and 28 d, as shown in formulas (9)–(11):

$$y = 0.45 + 0.02x_1 - 0.06x_2 + 0.28x_3 + 0.04x_4. \quad (9)$$

The F-value test method is adopted, and the critical value of F-test is $F_{0.95}$ (4.5) = 5.19 < F = 61.95. The regression equation is significant and the negative correlation coefficient $R_2 = 0.9644$, where y is the compressive strength of gelatin; x_1 is the lime dosage, %; x_2 is the gypsum dosage, %; x_3 is the NaOH dosage, %; x_4 is the Na$_2$SO$_4$ dosage.

$$y = 4.62 + 0.001x_1 - 0.41x_2 + 1.63x_3 - 0.23x_4. \quad (10)$$

The F-value test method is adopted, and the critical value of F-test is $F_{0.95}$ (4.5) = 5.19 < F = 71.12. The
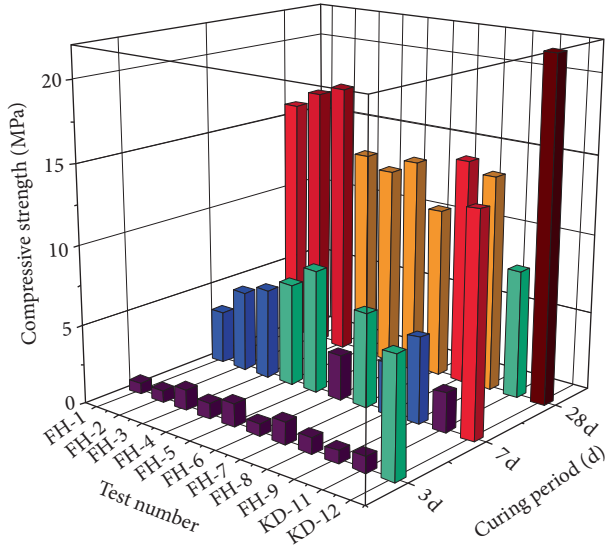
FIGURE 2: Variation of compressive strength of cementitious materials with different ratios.
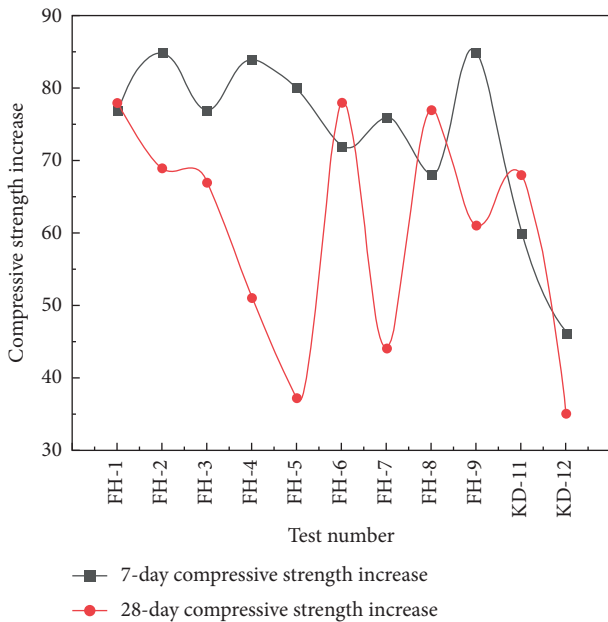

FIGURE 3: Increase of compressive strength with curing age.

regression equation is significant and the negative correlation coefficient $R_2 = 0.9689$, where y is the compressive strength of gelatin; x_1 is the lime dosage, %; x_2 is the gypsum dosage, %; x_3 is the NaoH dosage, %; x_4 is the Na$_2$SO$_4$ dosage.

$$y = 16.24 - 0.49x_1 + 0.72x_2 - 0.50x_3 + 0.46x_4. \quad (11)$$

The F-value test method is adopted, and the critical value of F-test is F0.95 $(4.5) = 5.19 < F = 302.44$. The regression equation is significant and the negative correlation coefficient $R_2 = 0.99259$, where y is the compressive strength of gelatin; x_1 is the lime dosage, %; x_2 is the gypsum dosage, %; x_3 is the NaoH dosage, %; x_4 is the Na$_2$SO$_4$ dosage.

Variance analysis is carried out on the compressive strength of gelatin containing the system of excitant and fly ash at 3 d, 7 d, and 28 d, and the analysis results are shown in Table 7. According to Table 7, the fluence of each factor on the early strength of gelatin from big to small is as follows: NaOH dosage > lime dosage > Na$_2$SO$_4$ dosage > gypsum dosage. The optimal scheme is A$_2$B$_2$C$_3$D$_3$ or A$_3$B$_2$C$_3$D$_3$ (the influence and optimal scheme for gelatin with a curing period of 7 d and 3 d are the same, so they are not listed). The influence on long-term strength from big to small is as follows: lime dosage > gypsum dosage > Na$_2$SO$_4$ dosage > NaOH dosage, and the optimal scheme is A$_1$B$_3$C$_2$D$_3$.

6. Analysis of Gelatin Morphology and Phase Test Results

6.1. SEM Analysis of Hydration Products. According to Figure 4(a), the solid particles in the slurry are uniformly dispersed in the fly ash cement gelatin without the addition of excitant upon the curing period of 3 d. There are few hydration products, and only a small amount of C-S-H flocs and tabular Ca(OH)$_2$ are produced, leading to loose gelatin structure and no stable structure. According to Figure 4(b), compared with gelatin at 3 d, the gelatin at 28 d has a large amount of acicular AFt, which extend and cross each other to form a denser network structure.
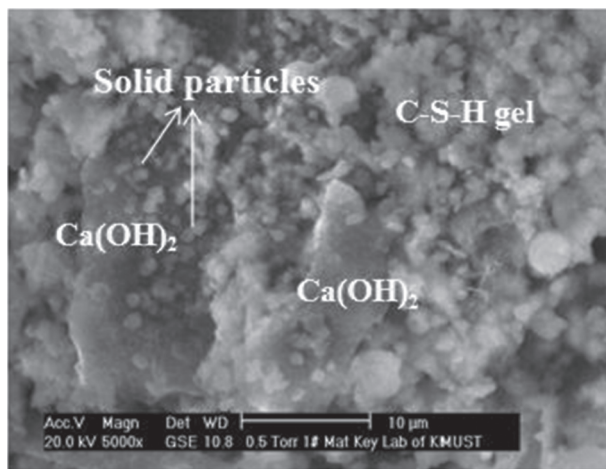
According to Figure 5(a), although the curing period of gelatin containing excitant is only 3 d, the solid particles have been wrapped by hydration products, and the particles are connected through AFt to form a dense network structure. Compared with Figure 4(a), the hydration of fly ash is obviously improved, the hydration products are increased, the network structure formed is more complex, and the gelatin is more dense. According to Figure 5(b) in which excitant is added, compared with Figure 4(b), the hydration of the gelatin is more significant, the internal structure is denser, and the hydration products are more complex, mainly including C–S–H gelatin, AFt, Ca(OH)$_2$, and CaCO$_3$. In addition, AFt becomes thicker and denser, so that all particles are tightly connected into one piece, and no obvious gap can be seen.

6.2. XRD Analysis of Hydration Products. As can be seen from Figure 6(a), the hydration reaction of the specimen after curing for 3 d generates substances such as Ca(OH)$_2$(C), AFt(E), and C-S-H gelatin. With the increase of hydration cycle, the diffraction peak of Ca(OH)$_2$ decreases obviously, which is mainly due to the chemical reaction between Ca(OH)$_2$ and quartz (Q) or mullite in fly ash, resulting in new hydration products. However, the diffraction peak of AFt basically has no change, which indicates that the reaction speed of fly ash is slow without excitant, resulting in a low growth in the strength of gelatin.
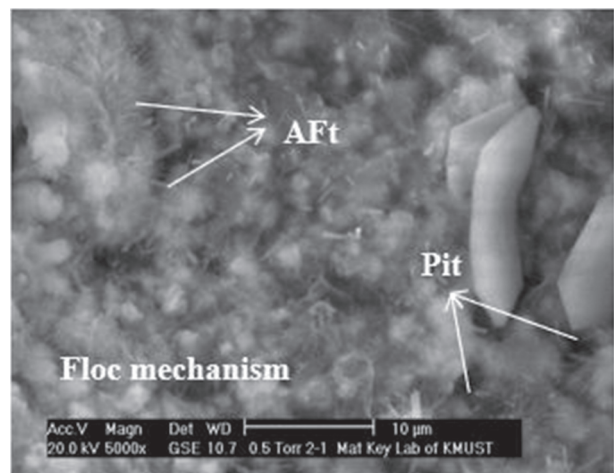
As can be seen from Figure 7(a), since the excitant contains Ca(OH)$_2$, the diffraction peak of Ca(OH)$_2$ in Figure 7(a) is higher than that of Ca(OH)$_2$ in Figure 6(a). Therefore, gelatin with t excitant has a greater early strength. The diffraction peak of Ca(OH)$_2$ in Figure 7(b) is obviously lower than that of Ca(OH)$_2$ in Figure 7(a), and the

TABLE 7: Analysis results of orthogonal test for compressive strength of slurry.

Test No.		A Lime dosage	B Gypsum dosage	C NaOH dosage	D Na$_2$SO$_4$ dosage	Compressive strength (MPa)		
						3 d	7 d	28 d
FH-1		1 (8)	1 (4)	1 (1)	1 (2)	0.73	3.43	15.87
FH-2		1	2 (5)	2 (2)	2 (3)	0.75	5.17	16.93
FH-3		1	3 (6)	3 (3)	3 (4)	1.32	5.77	17.53
FH-4		2 (12)	1	2	3	1	6.53	13.4
FH-5		2	2	3	1	1.51	7.87	12.67
FH-6		2	3	1	2	0.78	2.87	13.6
FH-7		3 (16)	1	3	2	1.43	6	10.8
FH-8		3	2	1	3	1.05	3.33	14.33
FH-9		3	3	2	1	0.81	5.4	13.67
	K$_1$	2.8	3.16	2.56	3.05			
	K$_2$	3.29	3.31	2.56	2.96			
	K$_3$	3.29	2.91	4.26	3.37			
Comprehensive strength at 3 d	K1 = K1/3	0.933	1.053	0.853	1.017		C > A > D > B	
	K2 = K2/3	1.097	1.103	0.853	0.987			
	K3 = K3/3	1.097	0.97	1.42	1.123			
	Range	0.164	0.133	0.567	0.136			
Optimal scheme		A$_2$ or A$_3$	B$_2$	C$_3$	D$_3$		A$_2$B$_2$C$_3$D$_3$ or A$_3$B$_2$C$_3$D$_3$	
	K$_1$	50.33	40.07	43.8	42.2		A > B > D > C	
	K$_2$	39.67	43.93	44	41.33			
	K$_3$	38.8	44.8	41	45.27			
Compressive strength at 28 d	K1 = K1/3	16.78	13.36	14.6	14.07			
	K2 = K2/3	13.22	14.64	14.67	13.78			
	K3 = K3/3	12.93	14.93	13.67	15.09			
	Range	3.84	1.58	1	1.31			
Optimal scheme		A$_1$	B$_3$	C$_2$	D$_3$		A$_1$B$_3$C$_2$D$_3$	

(a)

(b)

FIGURE 4: Microstructure of cementite after 3 days and 28 days when fly ash content is 50% without activator. (a) 3 d curing period; (b) 28 d curing period.
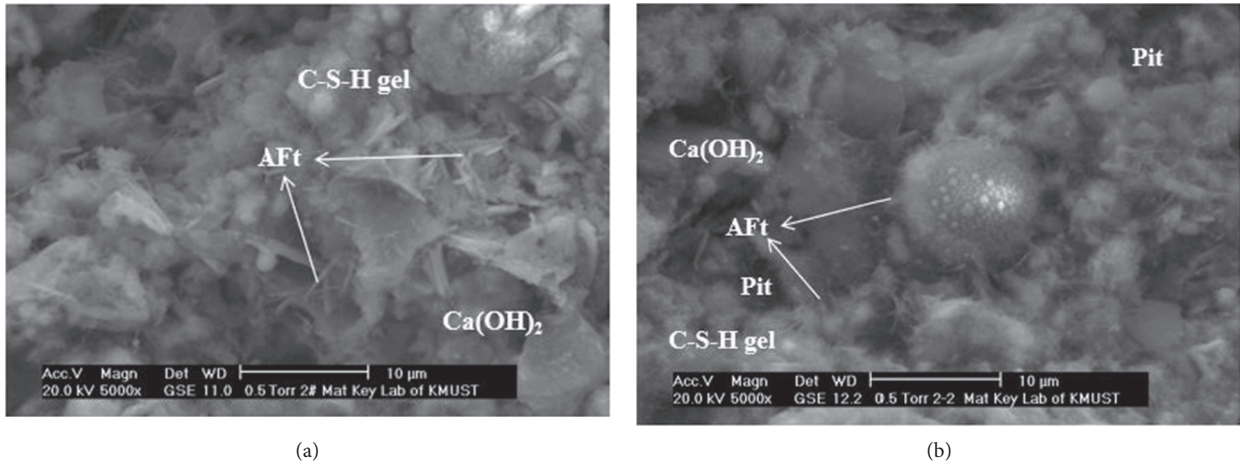
FIGURE 5: Microstructure of cementitious body after 3 days and 28 days with 50% fly ash and activator. (a) 3 d curing period; (b) 28 d curing period.
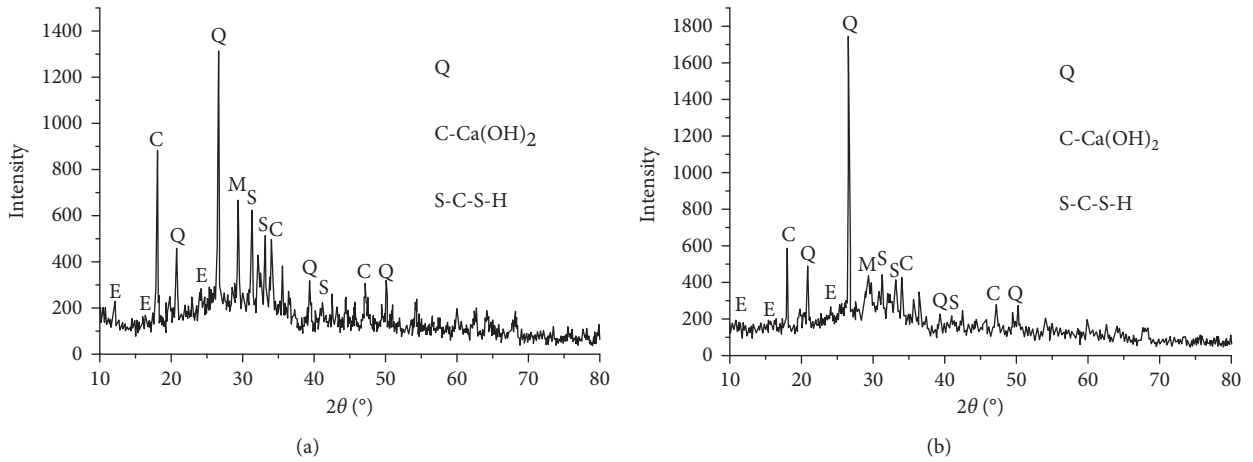

FIGURE 6: XRD patterns of hydration products at different ages with 50% fly ash without activator. (a) 3-day hydration; (b) 28-day hydration.
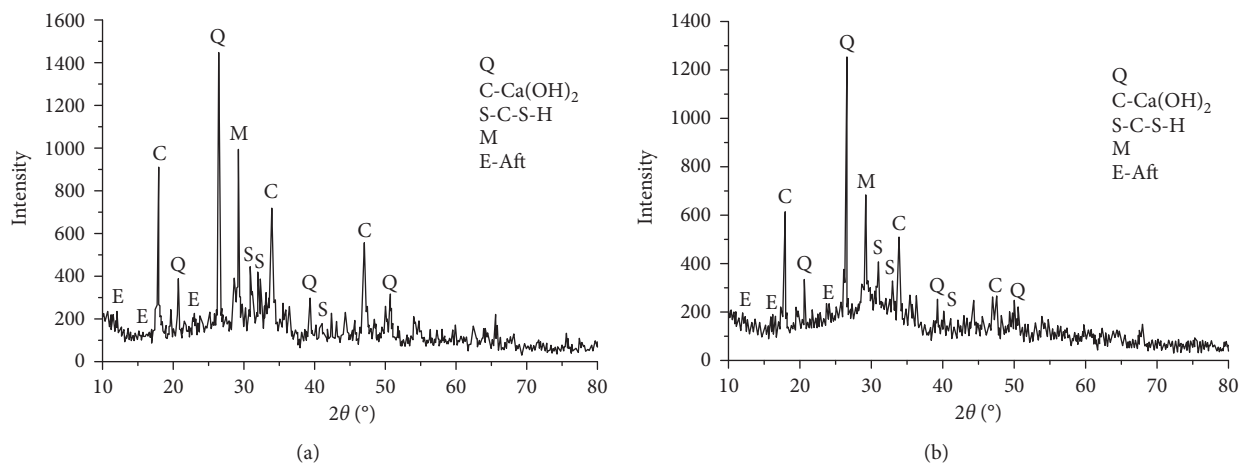

FIGURE 7: XRD patterns of hydration products with 50% fly ash and activator at different ages. (a) 3-day hydration; (b) 28-day hydration.

diffraction peaks of mullite, quartz, and other substances in Figure 7(b) are all decreased. This is mainly because as the excitant is added, the active SiO_2 released from quartz reacts with $Ca(OH)_2$ in the slurry to form complex hydration products and increase the compressive strength of gelatin. The diffraction peak of $Ca(OH)_2$ in Figure 7(b) is significantly lower than that of $Ca(OH)_2$ in Figure 7(a), and the diffraction peaks of mullite, Shi Ying, and other substances in Figure 7(b) have all decreased. This is mainly due to the pozzolanic reaction between the active SiO_2 released from and $Ca(OH)_2$ in the slurry due to the addition of activator, which forms more complex hydration products and increases the compressive strength of the gel.

7. Conclusions

(1) The bleeding rate of slurry containing the system of excitant and fly ash is 2.24%~3.73%, which is far less than that of unmixed cement mortar (9.25%). Its fluidity is 110 mm~155 mm, which is not much different from that of unmixed cement mortar (150 mm). The influence of four excitants on the bleeding rate of slurry from big to small is lime dosage > NaOH > Na_2SO_4 > gypsum dosage, and the optimal scheme is $A_3B_2C_2D_2$.

(2) The influence of each factor on the early strength of gelatin from big to small is NaOH dosage > lime dosage > Na_2SO_4 dosage > gypsum dosage, and the optimal scheme is $A_2B_2C_3D_3$ or $A_3B_2C_3D_3$. The influence on long-term strength from big to small is lime dosage > gypsum dosage > Na_2SO_4 dosage > NaOH dosage, and the optimal scheme is $A1B_3C_2D_3$. The amount of excitant can be determined according to the strength requirements of the filling body.

(3) From the microstructure of gelatin, it can be seen that the addition of excitant makes the hydration products of fly ash more complex, mainly including C-S-H gelatin, AFt, $Ca(OH)_2$, and $CaCO_3$. In addition, with the increase of curing period, AFt becomes denser and coarser, so that the particles are tightly connected into one piece without obvious gap, and the internal structure is denser. The results of XRD analysis show that excitant can be added to stimulate the activity of fly ash, generate more complex hydration products, and increase the compressive strength of fly ash cement gelatin.

(4) According to test results, it is considered that the addition of excitant fly ash system can improve the fluidity of slurry, increase the long-term strength of filling body, and reduce its early strength. The added amount of compound excitant can be appropriately adjusted according to the needs of the mines, thereby achieving the purpose of controlling the strength of filling body.

Data Availability

The data used to support the findings of this study are included within the article.

References

[1] D. Y. Gao, Z. Liu, and Z.L. Cheng, "2D Ni-Fe MOF nanosheets reinforced poly(vinyl alcohol) hydrogels with enhanced mechanical and tribological performance," *Colloids and Surfaces A: Physicochemical and Engineering Aspects*, vol. 610, pp. 1259–1264, 2021.

[2] J. Liu, Z. Zhou, A. Wu, and Y. M. Wang, "Preparation and hydration mechanism of low concentration bayer red mud filling materials," *Chinese Journal of Engineering*, vol. 42, no. 11, pp. 1457–1464, 2020.

[3] X. Guo, X. Guo, S. Xin, and Y. Liu, "Zeolite from coal fly ash by hydrothermal synthesis and characterization," *Bulletin of the Chinese Ceramic Society*, vol. 35, no. 2, pp. 525–528, 2016.

[4] S. Amulya, A. U. Ravi Shankar, and M. Praveen, "Stabilisation of lithomargic clay using alkali activated fly ash and ground granulated blast furnace slag," *International Journal of Pavement Engineering*, vol. 21, no. 9, pp. 1114–1121, 2020.

[5] S. Kumar, P. Murthi, A. Paul, G. Ravindran, and S. Kumar, "Impact resistance and strength development of fly ash based self-compacting concrete," *Silicon*, no. 19, pp. 1–12, 2020.

[6] V. Saraswathy, S. Muralidharan, K. Thangavel, and S. Srinivasan, "Influence of activated fly ash on corrosion-resistance and strength of concrete," *Cement and Concrete Composites*, vol. 25, no. 7, pp. 673–680, 2003.

[7] B. Wang, L. Zhang, J. Zhao et al., "Activation experiment study on high volume fly ash filling material," *Coal Engineering*, vol. 46, no. 10, pp. 192–195, 2016.

[8] D. Wu, B. Yang, and L. Yucheng, "Transportability and pressure drop of fresh cemented coal gangue-fly ash backfill(CGFB) slurry in pipe loop," *Powder Technology*, vol. 284, pp. 218–224, 2015.

[9] B. Yin, T. Kang, J. Kang et al., "The research of the hydration kinetics process and hydration mechanism of fly ash paste filling materials," *Chinese Journal of Rock Mechanics and Engineering*, vol. 37, no. 2, pp. 4384–4394, 2018.

[10] M. Mollamahmutoğlu and Y. Yilmaz, "Potential use of fly ash and bentonite mixture as liner or cover at waste disposal areas," *Environmental Earth Sciences*, vol. 40, no. 11-12, pp. 1316–1324, 2001.

[11] L. Zhongtao, M. A. Baoguo, Y. Jiujun et al., "Effects of fineness on activity character of fly ash," *Advanced Materials Research*, vol. 266, pp. 114–117, 2011.

[12] L. S. Zhang, G. H. Li, W. Huang, X. C. He, F. Jiang, and T. C. Liu, "The effect of slate powder on fly ash in suppressing alkali activity of slate aggregate," *Applied Mechanics and Materials*, vol. 357-360, pp. 1450–1454, 2013.

[13] D. Fu, *Study on Activation of Fly Ash and its Application in Grouting Engineering*, Central South University, Hunan, China, 2003.

[14] G. Sun, Q. Tang, L. Zhang, and C. Wang, "Early activation effect and mechanism of high-volume fly ash," *Journal of Harbin Engineering University*, vol. 40, no. 3, pp. 540–547, 2019.

[15] K. Hoang, H. Justnes, and M. Geiker, "Early age strength increase of fly ash blended cement by a ternary hardening accelerating admixture," *Cement and Concrete Research*, vol. 81, pp. 59–69, 2016.

[16] M. Zhang and J. Yang, "Study on the application of excitant in cement gelatin with high volume fly-ash," *Materials Reports*, vol. 21, no. 6, pp. 146–148, 2017.

[17] H. L. Wang and X. D. Zhang, "Study on the effect of fly ash mix amount in large volume pile cap concrete on heat of hydration," *Applied Mechanics and Materials*, vol. 744–746, pp. 832–836, 2015.

[18] S. Huang, J. Jiang, N. Yang et al., *Contemporary Concrete Technology*, Science and Technology Press, Xi'an, Shaanxi, China.

[19] H. Jiao, A. Wu, H. J. Wang, X.-H. Liu, S. K. Yang, and Y. T. Xiao, "Experiment study on the flocculation settlement characteristic of unclassified tailings," *Journal of University of Science and Technology Beijing*, vol. 32, no. 12, pp. 1437–1441, 2011.

[20] A. Wu and H. Wang, *Theory and Technology of Paste Filling in Metal Ore*, Science Press, Beijing, China, 2015.

[21] L. Dong, Q. Gao, S. Nan, and J. Du, "Performance and hydration mechanism of new super fine cemented whole-tailings backfilling materials," *Journal of Central South University (Science and Technology)*, vol. 44, no. 4, pp. 1571–1577, 2013.

Research Article

The Mechanism of Reinforced Backfill Body with Flexible Mesh

Xiaosheng Liu [ID],[1,2] **Weijun Wang,**[1] **Quan Liu,**[2] **and Chao Yuan**[1]

[1]*School of Resources, Environment and Safety Engineering, Hunan University of Science and Technology, Xiangtan 411201, China*
[2]*Changsha Institute of Mining Research Co., Ltd., Changsha 410012, China*

Correspondence should be addressed to Xiaosheng Liu; 13681996@qq.com

The backfill of metal mines is easily damaged by the disturbance due to their low strength. We proposed a method that uses flexible meshes as the backfill skeleton to enhance the strength of the backfill. The physical and mechanical properties of the flexible mesh-reinforced filling body are investigated by combining theoretical analysis and laboratory experiments. The strengthening effect is remarkable with the flexible meshes. With the friction-passive resistance between the high-strength reinforcement material and the filling body, the insufficient tensile strength of the filling body is compensated and the reinforcement is improved. The ultimate compressive strength is increased by 1.07 to 1.35 times, and the elastic modulus is increased by 1.08 to 4.42 times. We concluded that the essence of strengthening the flexible mesh-reinforced filling is to increase the cohesive force of the filling and increase the ability to resist external load damage.

1. Introduction

Mine backfill is the cementing of tailings, cement, and other aggregates into the excavation area. Backfilling is an indispensable part of mine operation to stabilize mine stress concentration and dispose of mine waste. Generally, there are three types of backfill, including the hydraulic fill (slurry and dense slurry fills), the paste fill (coarse tailings, medium tailings, and fine tailings), and the rock fill (cemented and noncemented) [1]. These three types are adapted to different mining scenarios. How to improve the strength of the filling body and whether it is meaningful to reinforce the filling body with filling body mesh are still unclear. This motivated our study on the mechanical characteristics of reinforced backfill body with flexible mesh.

Annor (2002) studied the characteristics and behavior of composite backfill material. Yin et al (2019) provided an innovative method for the placement of gangue backfilling material in steep underground coal mines [2]. They found when the strength of the backfill body does not meet the requirements, flexible materials or steel mesh will be added according to the site conditions.

Reinforced strengthening technology refers to the technology that mixes or implants reinforced materials with

relatively high-strength and elastic modulus into the reinforced body to improve the mechanical properties of the reinforced body, represented by the reinforced soil technology. After a long time of development of reinforced soil technology, the theory and application have achieved fruitful results. For example, Wang Zhijie [3], Zhou Bin et al. [4], and He Zhijun et al. [5] have proved that geogrid can significantly improve the maximum axial stress of reinforced soil through large-scale biaxial compression test; Shi Youzhi [6] concluded that the reinforced soil interface is a weak sliding surface through the pull-out test of different reinforced materials and considered that the interface antisliding stability should be calculated in the reinforced soil engineering design; and Lei Shengyou et al. [7] carried out damage soil. The results show that the strength of reinforced soil is the highest, that of plain soil is the second, and that of damaged soil is the least. In practical applications, the use of geogrids (Wang et al., 2019), geotextiles (Chang L., 2019), gravel (Liu W., 2019), and fibers (Hu Y., 2019) to reinforce roadbeds, dams, slopes, and retaining walls has become a common method and approach [8–11].

However, due to the late start of backfill reinforcement technology, there are relatively few studies and applications of reinforcement technology theory in the field of mine

filling. For example, Bernie (2017) studied engineering backfill fiber as an environmental solution to cost reduction [12]. Liu X. (2019) investigated the filling method of the suspended reinforced filling body [13]. Liu Q. (2019) studied the mechanical properties and reinforcement of the filling body with weak interlayer [14].

But the research on the reinforcement of filling bodies is mostly fiber reinforcement. Deng (2005) studied the mechanical properties, damage, and stability of the filling body in extralarge stope of Anqing copper mine [15]. Sun et al. (2018) performed an experimental study on the mechanical properties of polypropylene fiber high water materials [16]. Ma et al. (2016) and Li et al. (2016) carried out the macro- and microtests of fiber-reinforced paste filling materials [17, 18]. Yi et al. (2015) and Yi et al. (2018) studied the compressive behavior of fiber-reinforced cemented paste backfill [19, 20].

Although a relatively optimistic effect has been achieved in enhancing the strength of the filling body, fiber reinforcement increases the strength of the filling body while also reducing the fluidity of the filling slurry, which brings new challenges to the efficient activation preparation and long-distance transportation of filler slurry.

In view of the problems mentioned above, this paper proposes a new reinforcement technology that can solve the difficulties in preparing filler slurry and long-distance transportation caused by fiber reinforcement. It is a composite body with flexible mesh as the tensile and flexible framework of the backfill. The higher tensile performance of the three-dimensional flexible grid and the compressive performance of the filling body complement each other, which improves the overall strength and stability of the filling body. This paper uses a combination of theory and laboratory experiments to analyze the strength and degeneration characteristics of the flexible grid-reinforced filling body and study its strengthening mechanism.

2. Experiment

2.1. Materials and Equipment.
The reinforced material flexible grid is made of polyethylene. The specifications are as follows: the diameter of the rope is 1 mm, the tensile strength of the single rope is 15 kg, the mesh size is 20 mm × 20 mm, and the layer spacing is 20 mm.

The filler slurry aggregate adopts the whole tailings of a gold mine, the specific gravity is 2.71, the loose bulk density is 1.07 t/m^3, the average particle size is 63 μm, and the 200 mesh accounts for 70%. The tailings are medium and coarse tailings; the filling cementing material is Hunan Changsha Pingtang Cement Factory produces P·O42.5 ordinary Portland cement.

The test loading equipment uses a 60-ton YNS-Y600 electrohydraulic servo rigid control material testing machine to perform uniaxial compression tests on the specimens with a test accuracy of 0.001 kN. The equipment has multiple loading control methods of force, deformation, displacement, stress, and strain and can realize impact-free conversion among various methods during the test. The load sensor is used to directly measure the force, which can overcome the disadvantages of the influence of the piston friction of the hydraulic sensor, and the measurement is accurate. The maximum loading capacity is 600 KN. The displacement measurement error is less than 0.5%.

2.2. Test Program.
In order to reduce the influence of the size effect on the test results, a cube test block with a size of 100 mm × 100 mm × 100 mm was made. A total of 6 sets of tests were prepared, with 3 test blocks in each group, numbered S1 ∼ S3 (without flexible grid-reinforced) and J1 ∼ J3 (flexible grid-reinforced). The parameters are designed as shown in Table 1.

According to the test design, a total of 18 filling body test blocks are made, and the manufacturing process of reinforced filling body test block is shown in Figure 1. The molding and demoulding test block was moved to a constant temperature and humidity curing box with a temperature of (20 ± 2)°C and humidity of (95 ± 5)% and cured for 28 days, as shown in Figure 2.

The loading method of test is displacement loading, and the loading rate is controlled at 0.5 mm/min. The loading process of the specimen is shown in Figures 3 and 4.

3. Results

3.1. Mechanical Properties of the Filling Body.
The stress-strain curve of the filled test block is shown in Figure 4. The ultimate compressive strength and elastic modulus of the filling body after reinforcement have been improved to a certain extent, especially for the strength of the filling body in the postdestructive stage, as shown in Table 2.

The ultimate compressive strength and elastic modulus of the J1 group increased by 0.14 MPa and 0.027 GPa, respectively. The strengthening coefficients were 1.07 and 1.08, respectively. The ultimate compressive strength and elastic modulus of the J2 group increased by 0.098 MPa and 0.025 GPa, respectively. The strengthening coefficients were 1.20 and 1.41. The ultimate compressive strength and elastic modulus of the J3 group increased by 0.104 MPa and 0.032 GPa, respectively, and the strengthening coefficients were 1.36 and 1.81, respectively.

This improvement of elastic modulus is obvious when the lime–sand ratio is relatively small (i.e., when its own compressive strength is low), and when the lime–sand ratio is relatively large (the compressive strength is higher), the improvement is limited. Of course, the precision of the improvement may relate to the calculation method. But since we used the same method when calculating the two experiments (with and without mesh), the relative improvement is reliable.

3.2. Failure Mode.
The failure modes of the backfill samples before and after reinforcement are quite different. The failure mode of the backfill before reinforcement is affected by various factors and the mode is complex, mainly including large shear failure, tensile failure, tension-shear composite failure, and slip failure. The failure mode of the filling body

TABLE 1: Parameter design of reinforced backfill.

Number	Cement sand ratio	Concentration (%)	Number	Cement sand ratio	Concentration (%)
S1	1 : 4	66	J1	1 : 4	66
S2	1 : 10	66	J2	1 : 6	66
S3	1 : 15	66	J3	1 : 8	66

FIGURE 1: 3D flexible grid reinforcement of filling body.

FIGURE 2: Curing of constant temperature and humidity test block for filling body.

FIGURE 3: Loading process of backfill specimen.

after reinforcement is relatively simple and mainly dominated by small shear failure, as shown in Figure 5.

The flexible three-dimensional mesh layer is closely connected, and the force transmission characteristics are better. At the same time, the shear strength of the mesh ribs is higher than the shear failure strength of the filling body, and the shear stress cannot cut the flexible ribs to form a large shear surface. Under the action of the flexible three-dimensional grid, the internal stress distribution of the filling body changes, the stress concentration is reduced, and large-area shear failure is avoided, which indirectly improves the load-bearing strength of the filling body. Therefore, the flexible three-dimensional grid-reinforced filling body is subjected to axial compression, from local large-area failure to relatively uniform small shear failure, and the outline of the filling body remains relatively complete after the failure and the surrounding fragments caused by shear failure. The block size is relatively uniform, and there will be no peeling of large blocks.

3.3. Deformation Characteristics. The deformation characteristics of the reinforced backfill are generally similar to those of the plain backfill. The difference is only reflected in the postpeak failure stage. The reinforced backfill exhibits more obvious hardening in the postpeak failure stage. The deformation characteristics can be summarized into five stages: ① in the compaction stage, the filling body undergoes void compaction and structural surface closure; ②in the elastic deformation stage, the stress and strain at this stage are linearly related, and this stage is affected by the interlayer and changes; ③ in the plastic deformation stage, the filling body occurs in this stage plastic deformation and cracks begin to occur; ④ in the strain softening stage, the stress at this stage decreases with the increase of the strain of the filling body; and ⑤ in the strain hardening stage, the stress at this stage increases with the increase of the compression deformation of the filling body specimen, and there is a tendency of exceeding the ultimate failure strength.

4. Discussion

4.1. Mechanical Strengthening Mechanism. The strengthening mechanism of the flexible grid is the coupling effect between the grid and the filling. The tensile and non-compressive properties of the flexible grid make up for the low tensile strength of the reinforced body and improve the resistance of the filling to damage, as shown in Figure 6. The force of the longitudinal ribs and the interlayer connecting ribs of the reinforced filling body is transmitted to the adjacent longitudinal ribs and the vertical transverse ribs through the connecting nodes between the ribs.
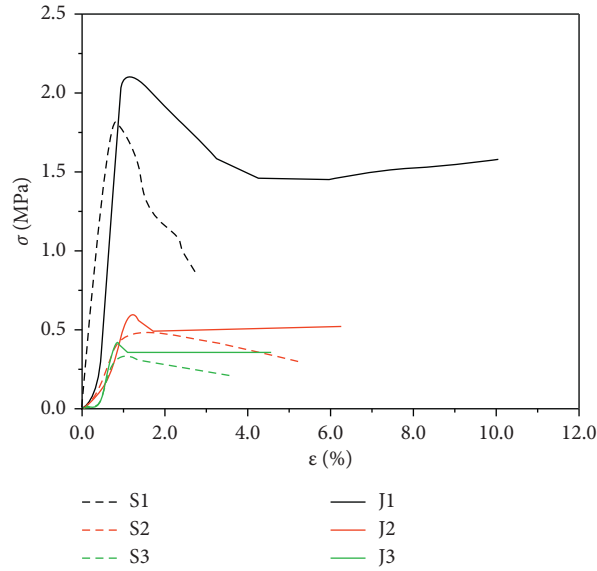
FIGURE 4: Stress-strain curve of backfill before and after reinforcement.

TABLE 2: Comparison of some mechanical parameters of backfill before and after reinforcement.

Ratio	Without flexible grid-reinforced		Flexible grid-reinforced	
	Ultimate strength (MPa)	Elastic modulus (GPa)	Ultimate strength (MPa)	Elastic modulus (GPa)
1 : 4	1.88	0.29	2.02	0.31
1 : 10	0.49	0.06	0.59	0.08
1 : 15	0.29	0.04	0.39	0.07

FIGURE 5: Comparison of filling failure modes before and after reinforcement.
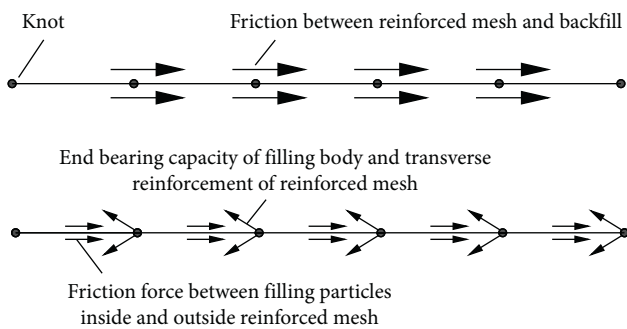
FIGURE 6: Coupling relationship between flexible grid and stiffener.

The ribs may be pulled out to cause displacement under tension. However, the ribs are squeezed under the action of the filling body's own weight and external load, and the friction and biting force between the filling body and the grid prevent the grid and the filling body from generating relative displacement. The force model of the flexible grid is shown in Figure 7.

According to the theoretical model of stiffened force, the force and deformation of the stiffened body lead to the force of each force element:

$$\Delta T = T_z - T_y, \tag{1}$$

where T_z and T_y are, respectively, the lateral deformation and tension transferred from the connection knots of the two ends of the force element to the brace.

Under the action of external load and dead weight, the total frictional resistance between the filling body of the force-bearing element and the tendons is

$$F = \pi \sigma_y dL \, \mu, \tag{2}$$

where L is the length of the force receiving unit, μ is the friction factor of the contact surface between the brace and the filling body, and d is the diameter of the rib.
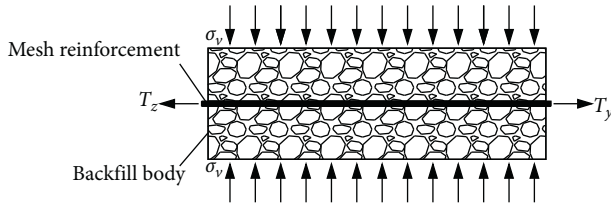
FIGURE 7: Stress model of flexible grid reinforcement.

FIGURE 8: Variation of lateral stress of filling body under the same normal stress.

FIGURE 9: Mechanical balance diagram of reinforced backfill.

According to the principle of mechanical balance, when F is less than ΔT, there will be a relative displacement between the rib and the filling body; when F is greater than ΔT, the relative balance between the rib and the filling body will not be displaced, and the force-bearing unit body remains stable. Therefore, the flexible grid-reinforced filling body should meet the following necessary conditions: ① the surface of the reinforced material is rough enough to generate greater antisliding friction between the reinforcement mesh and the filling body; ② the reinforced material has higher tensile strength and the elastic modulus constitute the conditions for the relative displacement trend; and ③ the filling body has sufficient density to produce sufficient interaction force with the reinforced material.

4.2. Mechanical Strength Characteristics of Reinforced Backfill. Reinforced backfill is a material composite with different material properties, and the elastic modulus of the reinforced material is much greater than that of the filling body. Therefore, the coupling effect of the reinforcement material and the filling body includes the shear resistance of the filling body, the synergistic effect of the friction resistance of the reinforcement, and the tensile strength of the reinforcement.

Under the Poisson effect, the lateral deformation of the reinforced backfill exerts a lateral pulling force on the reinforcement. At the same time, the lacing bars will exert a force in the opposite direction on the filling body to limit the lateral expansion and deformation of the filling body. The lateral restraint force reduces the lateral deformation pressure of the stiffened backfill. Under the same axial deformation, the minimum principal stress borne is smaller than that of the plain backfill, as shown in Figure 8. In Figure 8, (a) is the molar circle in the undamaged state of the plain backfill and (b) is the molar circle in the ultimate failure state of the plain backfill.

According to the Mohr–Coulomb theory, the relationship between σ_{1f} and σ_{3f} in the limit equilibrium state is

$$\sigma_{1f} = 2c \tan\left(\frac{\varphi}{2} + \frac{\pi}{4}\right) + \sigma_{3f}\tan^2\left(\frac{\varphi}{2} + \frac{\pi}{4}\right). \tag{3}$$

However, for reinforced fillings, under external load conditions, in addition to transverse and longitudinal stresses, the fillings are also subjected to the lateral force T of the reinforced material and the reaction force R of the fillings. The subisolator with broken body structure is subjected to force analysis, and the force is shown in Figure 9.

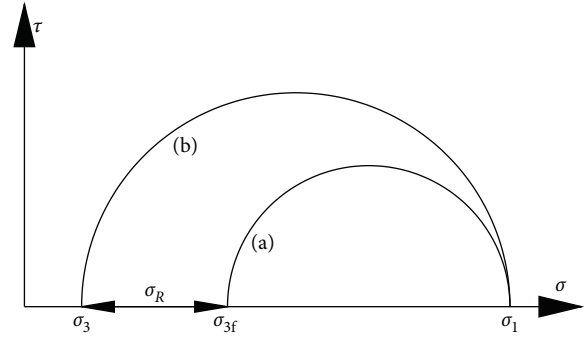The reinforcement of the backfill adopts a flexible mesh. The interaction effect of the horizontal, vertical, and interlayer connecting ribs of the flexible mesh is good. Reinforced backfill is only subjected to the limit state analysis of tensile strength. Assuming that the angle between the fracture surface of the reinforced filling body and the horizontal plane is α, according to the static balance principle, we can obtain
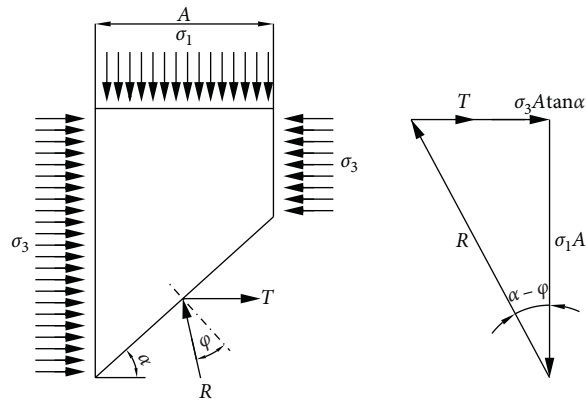
$$T + \sigma_3 A \tan a = R \sin(\alpha - \varphi), \tag{4}$$

where the tensile force of the brace can be calculated by

$$T = \frac{R_t \cdot A \cdot \tan\alpha}{\Delta L \cdot \Delta H}, \tag{5}$$

where ΔH is the vertical layer spacing of the three-dimensional flexible grid; ΔL is the horizontal layer spacing of the three-dimensional flexible grid; and R_t is the tensile strength of the flexible ribs.

In formula (4), the reaction force R of the backfill can be calculated by the following formula:

$$R = \frac{\sigma_1 \cdot A}{\cos(\alpha - \varphi)}. \tag{6}$$

Substituting formula (6) and formula (5) into formula (4), we obtain

$$\sigma_1 = \left(\sigma_3 + \frac{R_t}{\Delta L \cdot \Delta H}\right)\tan\alpha \times \cot(\alpha - \varphi). \tag{7}$$
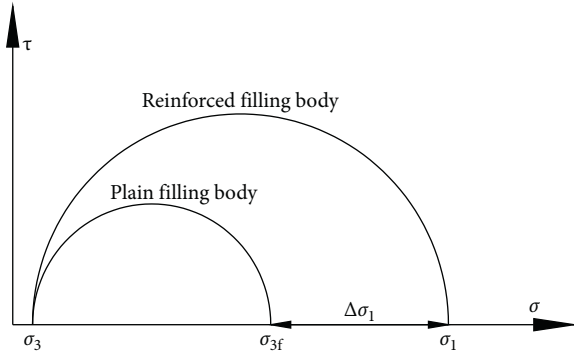
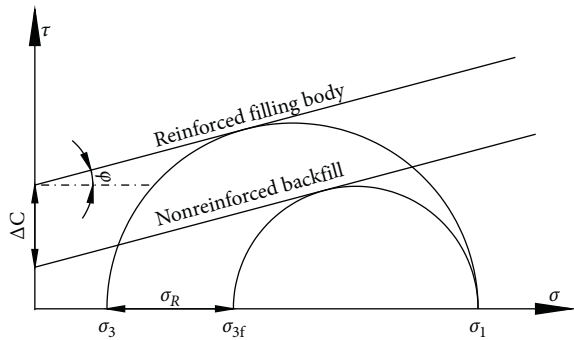Figure 10: Variation of normal stress of backfill under the same side stress condition.

Figure 11: Under the same normal stress condition, the shear strength and lateral stress changes of backfill.

When σ_1 is the maximum principal stress, then $\alpha = 45° + (\varphi/2)$, and

$$\sigma_1 = \sigma_3 \tan^2\left(45° + \frac{\varphi}{2}\right) + \frac{R_t}{\Delta L \cdot \Delta H} \tan^2\left(45° + \frac{\varphi}{2}\right). \qquad (8)$$

Comparing formula (3) and formula (8), it can be found that, under the limit equilibrium condition of the reinforced backfill structure, the linear relationship between the first principal stress and the third principal stress is maintained. Reinforcing does not affect the friction angle of the filling body. Under the condition of the minimum principal stress σ_3, the maximum principal stress σ_1 that can be reached when the backfill fails is increased by a fixed value σ_R compared with the plain backfill, which is the initial stress of the reinforced backfill, as shown in the following equation:

$$\sigma_R = \frac{R_t}{\Delta L \cdot \Delta H} \tan^2\left(45° + \frac{\varphi}{2}\right) - 2c \cdot \tan\left(45° + \frac{\varphi}{2}\right). \qquad (9)$$

The relationship between the shear stress and the normal stress on the fracture surface can be expressed by the following formula:

$$\tau = \sigma_1 \tan\varphi + \frac{R_t}{2\Delta L \cdot \Delta H} \tan\left(45° + \frac{\varphi}{2}\right). \qquad (10)$$

It can be seen from equation (10) that the shear strength of the reinforced backing body is increased by an increment equal to ΔC compared with the shear strength of the unreinforced backing body. This is the cohesive force generated by the reinforced material; that is, the tensile strength generated by the reinforced material corresponds to the molar stress circle of the reinforced and unreinforced filling body, which is the increment of the shear strength line intercept ΔC, as shown in the following equation:

$$\Delta C = \frac{R_t}{2\Delta L \cdot \Delta H} \tan\left(45° + \frac{\varphi}{2}\right) - c. \qquad (11)$$

When the unreinforced plain backfill reaches the limit equilibrium under the action of σ_{3f} and σ_{3f}, the reinforced backfill will not be damaged. After the filling body is reinforced, the maximum principal stress increases from σ_{3f} to σ_1 to reach the ultimate equilibrium state, the maximum principal stress increases, and the resistance of the filling body to damage is significantly enhanced, as shown in Figure 10. Based on the principle of constant internal friction angle and increased cohesive force after the filling body is reinforced, the maximum principal stress remains unchanged. After the filling body is reinforced, the minimum principal stress will decrease σ_R, which strengthens the damage ability of the backfill against lateral pressure, as shown in Figure 11.

5. Conclusions

(1) The reinforcement mechanism of the flexible three-dimensional mesh reinforcement of the filling body is the coupling effect of the reinforcement and the filling body. Through the friction-passive resistance mechanism between the high-strength reinforcement material and the filling body, the insufficient tensile strength of the filling body is compensated and the reinforcement is improved. In terms of strength characteristics, the reinforced filling body improves the cohesion of the backfill without changing the friction angle of the original backfill, so that the backfill obtains higher resistance to external load strength.

(2) The three-dimensional flexible mesh reinforcement of the backfill effectively improves the mechanical properties of the filling body, and the ultimate compressive strength and elastic modulus are improved to a certain extent. At the same time, the backfill has the ability of strain hardening in the later stage of failure. The increased rupture of the filling body maintains greater residual strength, and there is a tendency to continue to grow beyond the ultimate compressive strength.

(3) The reinforcement of the flexible mesh of the backfill changed the failure mode of the filling body, improved the internal stress distribution when the filling body is stressed, eliminated the local stress concentration, avoided the large shear failure of the filling body, and played the role of indirect strengthening of the backfill [21].

Data Availability

Data used to support the findings of this study are available on request to the corresponding author.

Conflicts of Interest

The authors declare that they have no conflicts of interest.

References

[1] D. O'Toole, "The basics of mine backfill," *Engineering and Mining Journal*, vol. 205, no. 12, p. 27, 2004.

[2] Y. Yin, T. Zhao, Y. Zhang et al., "An innovative method for placement of gangue backfilling material in steep underground coal mines," *Minerals*, vol. 9, no. 2, p. 107, 2019.

[3] Z. Wang, F. Jacobs, and M. Ziegler, "Influence of geogrid transverse rib on strength and deformation characteristics of reinforced gravel," *Geotechnical Mechanics*, vol. 38, no. 8, pp. 2234–2240, 2017.

[4] B. Zhou, T. Ling, Z. Zheng, and B. Yang, "Large scale triaxial test of geogrid reinforced soil composite," *Journal of Chongqing Jiaotong University*, vol. 31, no. 4, pp. 792–794, 2012.

[5] Z. He and J. Zou, "Large scale triaxial test analysis of reinforced fine-grained soil sand," *Journal of Railway Science and Engineering*, vol. 16, no. 10, pp. 2451–2458, 2019.

[6] Y. Shi, "Engineering characteristics of geogrid and application of reinforced cushion," Dissertation, Huaqiao University, Quanzhou, China, 2003.

[7] S. Lei, "Study on strength of reinforced soil considering reinforcement damage," *Journal of Three Gorges University*, vol. 32, no. 6, pp. 42–46, 2010.

[8] N. Wang, W. Chen, and D. Zhu, "Analysis of reinforcement effect of geotechnical reinforcement on open pit dump slope," *Coal Mine Safety*, vol. 50, no. 5, pp. 281–284, 2019.

[9] L. Chang, "Construction method and engineering application of reinforced earth retaining wall for high subgrade," *Sichuan Architecture*, vol. 39, no. 2, pp. 315–317, 2019.

[10] W. Liu, "Application of reinforced earth retaining wall in an overseas project," *Energy Saving in Nonferrous Metallurgy*, vol. 35, no. 2, pp. 50–53, 2019.

[11] Y. Hu, "Application of reinforced earth retaining wall in flood control and disaster reduction revetment engineering construction," *Shaanxi Water Conservancy*, vol. 8, pp. 189-190, 2019.

[12] B. Ting, "Engineering backfill fiber as an environmental solution to cost-reduce and improve paste backfill," in *Proceedings of the 2017 International Conference on Mining with Backfill*, Denver, Co, USA, July 2017.

[13] X. Liu, W. Wang, W. Lai, L. Jia, C. Liu, and D. Mo, "Gob Filling method of suspended reinforced filling body," 2019.

[14] Q. Liu, "Study on mechanical properties and reinforcement of filling body with weak interlayer," Dissertation, Changsha Institute of Mining Research, Changsha, China, 2019.

[15] D. Deng, "Study on mechanical properties, damage and stability of filling body in extra large stope of anqing copper mine," 2005.

[16] W. Sun, C. Liu, W. fan, Z. Diao, F. Bo, and X. Li, "Experimental study on mechanical properties of polypropylene fiber high water materials," *Metal Mine*, vol. 1, pp. 53–57, 2018.

[17] G. Ma, Z. Li, X. Yi et al., "Macro and micro tests of fiber reinforced paste filling materials," *Journal of Beijing University of Technology*, vol. 42, no. 3, 2016.

[18] D. Li, Z. Xiong, Y. Wang et al., "Effects of air entraining agent and polypropylene fiber on properties of high water content materials," *China Production Safety Science and Technology*, vol. 12, no. 3, pp. 54–59, 2016.

[19] X. W. Yi, G. W. Ma, and A. Fourie, "Compressive behaviour of fibre-reinforced cemented paste backfill," *Geotextiles & Geomembranes*, vol. 43, no. 3, pp. 207–215, 2015.

[20] X. W. Yi, G. W. Ma, and A. Fourie, "Centrifuge model studies on the stability of fibre-reinforced cemented paste backfill stopes," *Geotextiles and Geomembranes*, vol. 46, no. 4, pp. 396–401, 2018.

Research Article

Mineralogical Characteristics of Phosphate Tailings for Comprehensive Utilization

Song Mao [1,2,3] and Qin Zhang [2,3,4]

¹*College of Resources and Environmental Engineering, Guizhou University, Guiyang, Guizhou 550025, China*
²*National & Local Joint Laboratory of Engineering for Effective Utilization of Regional Mineral Resources from Karst Areas, Guiyang, Guizhou 550025, China*
³*Guizhou Key Laboratory of Comprehensive Utilization of Non-Metallic Mineral Resources, Guiyang, Guizhou 550025, China*
⁴*Guizhou Academy of Science, Guiyang, Guizhou 550001, China*

Correspondence should be addressed to Qin Zhang; zq6736@163.com

The mineralogical characteristics of a phosphate tailing were studied, and the occurrence state, mineral types, and embedded characteristics of phosphorus in the phosphate tailings were ascertained. The results show that the main minerals in the phosphate tailings are collophane. The main gangue minerals are quartz, dolomite, calcite, a small amount of potassium feldspar, plagioclase, chlorite, etc. Monazite was found in phosphate tailings. In addition, the coarse grain size of quartz and feldspar and fine embedded particle size of calcite and dolomite are also the main factors affecting the mineral processing of phosphate tailings. According to the analysis of mineralogical characteristics, the physical and chemical properties of phosphate tailings provided the basis for comprehensive utilization of phosphorus resources.

1. Introduction

A large number of phosphate tailings are produced in the process of phosphate ore dressing, and its output accounts for 20%–30% of the raw ore [1]. Part of the phosphate ore is mainly processed by ore washing, resulting in tailings containing phosphate and clay [2]. Traditionally, most of the phosphate tailings are mainly stored in tailings dams, which occupy a large amount of land with high disposal costs and resulting environmental hazards [3, 4]. With the development of "sustainable mining" [5], backfilling which is composed of mine tailings, cementitious material [6], and processed mine water [7], as a high-density slurry pumped into mined voids from underground mine operations, has increasingly been used. The reuse of tailings in backfilling operation to form an underground support system and a working platform [8] reduces the amount of waste required to be surface-disposed, thus mitigating the potential economic and environmental impacts associated with tailings

disposal [9] and assists with waste management. Because P_2O_5 content in phosphate rock has an important impact on its application in industry and agriculture [10], reducing the phosphorus grade in phosphate tailings also helps to mitigate the amount of wastes for disposal. Therefore, more attention has been paid to the recovery of phosphorus from phosphate tailings [11]. The mineral characteristics of phosphate rock directly influence the mineral processing process [12]; on the other hand, the physical and chemical properties of phosphate tailings depend on the characteristics of phosphate rock and mineral processing process. Through the study of process mineralogy of the ore, we can find out the factors affecting mineral processing and formulate a suitable separation process to achieve the expected mineral processing index [13, 14]. Practice has proved that process mineralogy has guiding significance in mineral processing production, the transformation of technological process, the optimization of mineral processing process design, and the improvement of mineral processing process

[15–17], while the application of automatic mineralogical tools provides more information about ore characteristics, process particle size, etc. [18–20].The recovery of apatite from phosphate tailings can reduce the amount of tailings [21]. It plays a significant role in for the recovery of phosphorus minerals in phosphate tailings. In this paper, the process mineralogy of phosphate tailings was studied by means of chemical multielement analysis, microscopic observation of ground smooth slices, energy spectrum analysis of scanning electron microscope (SEM), and X-ray diffraction (XRD). By finding out the structure, occurrence state, mineral types, and distribution characteristics of phosphate tailings, this study grasps the properties of phosphate tailings, providing a basis for the separation of phosphate tailings, and the physical and chemical properties of phosphate tailings, also providing a guide for further development of backfilling process.

2. Materials and Methods

The sample for this test is a phosphate tailing; the chemical composition and mineral composition of phosphate tailings were analyzed. The mineral structure, embedded properties, the mineral morphology, and element distribution of the main minerals in phosphate tailings were measured by polarizing microscope (Leica DM4500P), scanning electron microscope (Zeiss EVO18), and energy-dispersive spectrometer (Bruker XFLASH6100).

3. Results and Discussion

3.1. Multielement Analysis of Phosphate Tailings. The multielement analysis of phosphate tailings is carried out, and the results are shown in Table 1.

It can be seen from Table 1 that the P_2O_5 content of phosphate tailings is 15.76%, the SiO_2 content is 22.49%, the MgO content is 3.42%, the CaO content is 34.68%, and the content of sesquioxide ($Al_2O_3 + Fe_2O_3$) is 2.28%. In addition, the heavy metal elements such as Pb and Cd in phosphate tailings were analyzed, and their contents were all relatively low.

3.2. Phosphate Tailings Mineral Structure. Under a microscope, the main structures of minerals in phosphate tailings are as follows: Colloidal cryptocrystalline structure: one of the main structures, the colloidal phosphate monomer in the ore is cryptocrystalline; it is difficult to observe the mineral crystal particle size under the microscope, only its aggregate morphology can be observed, and some of them are contaminated with clay minerals to form a colloidal cryptocrystalline structure, as shown in Figure 1(a). Fine sand debris structure: one of the main structures, most of the collophane and quartz in the minerals are sand debris, with good abrasion, round-sub-round, and the particle size (0.06–0.3 mm) is mostly in the fine sand size. The cement is mainly dolomite, mainly porous cementation, as shown in Figure 1(b). Oolitic structure: part of the collophane sand debris has a zoning structure, which is formed by the relative enrichment of inclusions, forming an oolitic structure, as

shown in Figure 1(c). Inclusion structure: one of the main structures in which some collophane in the ore contains pulverulent organic matter, which is difficult to identify under the microscope and constitute poikilitic texture, as shown in Figure 1(d).

Fine-grained structure: one of the secondary structures, some of the dolomite in the ore has a particle size between 0.06 and 0.3 mm and a degree of autotroph, and the particles are distributed in close contact with each other, or between collophane, forming this structure, as shown in Figure 1(e). Micropowder crystal structure: one of the secondary structures, some dolomite and quartz are in the form of micropowder crystals with a particle size of 0.01 mm–0.06 mm, the particles are semiautogenous-heteromorphic, and they are in close mosaic contact with each other, and the aggregate shape is irregular, forming the structure shown in Figure 1(f). Microscopic scalelike structure: one of the rare structures in which clay minerals such as chlorite, sericite, and kaolinite in ores are microscale, distributed between collagenic aggregates or surrounded by collagenic aggregates, forming a microscopic scaly structure, as shown in Figure 1(g). Slab-column structure: one of the rare structures in which plagioclase is scattered in the form of plagioclase in the ore, as shown in Figure 1(h).

3.3. Mineral Composition. Through the study of X-ray diffraction spectrum, combined with light section microscope observation, chemical multielement analysis, and scanning electron microscope energy spectrum analysis, it is found that there are altogether 13 kinds of minerals in the ore, including phosphate, oxide, silicate, carbonate, and natural elements. Among them, phosphate accounts for 45%, oxide accounts for 18.3%, silicate accounts for 8%, carbonate accounts for 28.3%, and natural elements are few. The main useful minerals are collophane; the main gangue minerals are quartz, dolomite, calcite, and a small amount of potassium feldspar, plagioclase, chlorite, etc. The X-ray diffraction spectrum of the sample is shown in Figure 2, and the mineral composition is shown in Table 2.

3.4. Dissemination Characteristics of Main Minerals

3.4.1. Phosphate. The collophane in the phosphate tailings is mostly in the form of sand debris with high roundness, which is mainly cemented by dolomite and calcite; a small part of collophane is poorly ground, showing subangular and irregular granular. Most of the collophane in the phosphate tailings are wrapped with fine-grained organic matter inclusions with particle size less than 0.01 mm, which has a great impact on the flotation of phosphate. The micrograph of embedded characteristics is shown in Figure 3.

In terms of embedded particle size, the particle size of collophane aggregate is mainly concentrated in the range of 0.03–0.5 mm, and the fine particle size of <0.07 mm accounts for 35.8%. The particle size distribution of collophane aggregate is shown in Figure 4.

From the elements detected in the collophane, the dust spots in the collophane should be a mixture of clay minerals

TABLE 1: Results of multielement analysis of phosphate tailings.

Element	P_2O_5	SiO_2	MgO	CaO	TFe_2O_3	CO_2	Organic C	Total C
Content (%)	15.76	22.49	3.42	34.68	0.60	13.00	0.02	3.72
Element	K_2O	Al_2O_3	S	Na_2O	Pb	As	Cd	
Content (%)	0.38	1.68	0.42	0.50	0.0002	0.0006	0.002	
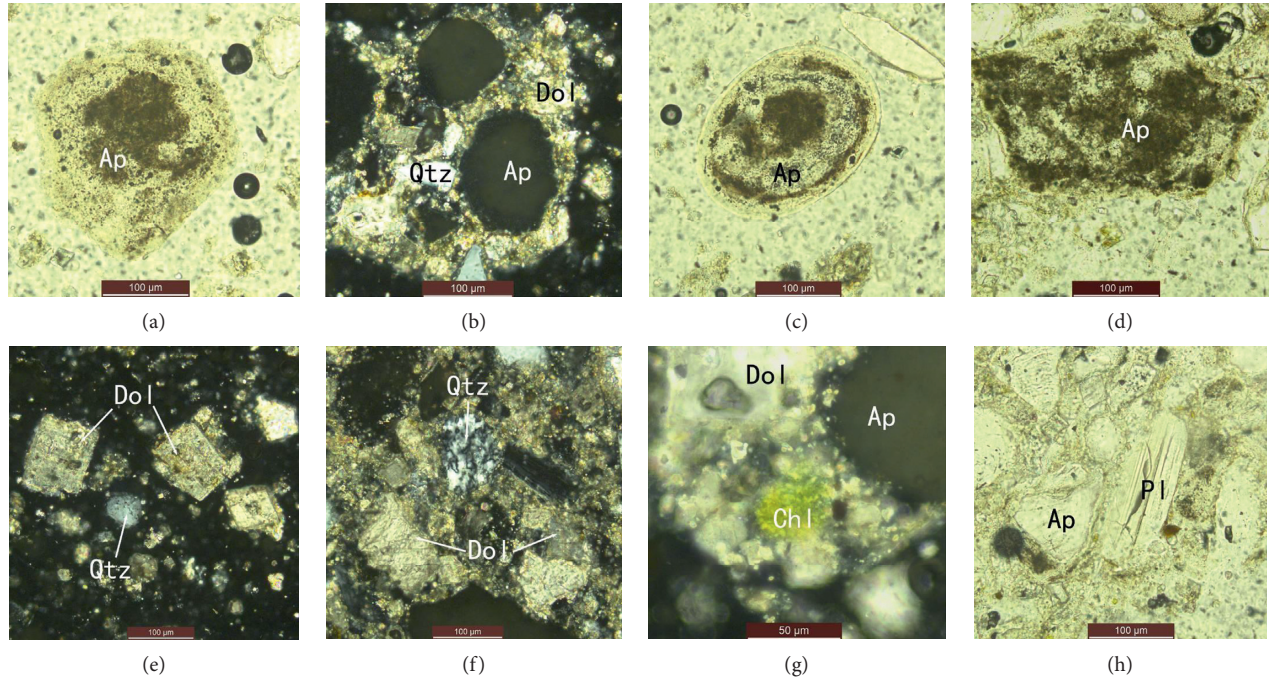
FIGURE 1: Phosphate tailings' mineral structure (TSPL represents transmitted single polarized light, and TCPL represents transmitted crossed polarized light). (a) Colloidal aphanitic collophane (Ap) detritus (TSPL). (b) Fine-grained sand clastic collophane (Ap), quartz (Qtz) (TSLP). (c) Oolitic collophane detritus (TSPL). (d) Dusty substance coated with collophane (Ap) (TSPL). (e) Fine-grained (0.1–0.3 mm) dolomite (Dol) (TSPL). (f) Microcrystalline quartz (Qtz) aggregates (TCPL). (g) Microscopic scaly chlorite (Chl) (TCPL). (h) Allotriomorphic granular plagioclase (PI) (TSPL).

and carbonaceous (possibly organic matter). The backscattered electron diagram and energy spectrum of collophane are shown in Figure 5. The results of energy spectrum analysis are shown in Table 3.

In order to investigate the composition difference of different zones in oolites, the energy spectrum analysis of collophane oolites was carried out. The results show that the main difference of different zones in oolites lies in the different carbonaceous content of inclusions, forming oolitic structure. The electronic image is shown in Figure 6, and the energy spectrum analysis results are shown in Table 4.

Monazite: occasionally seen under electron microscope, connected with quartz, with particle size of 0.02–0.03 mm. The backscattered electron diagram and energy spectrum of monazite are shown in Figure 7.

3.4.2. Oxide. The oxide is mainly quartz, which is one of the main gangue minerals. It is distributed between calcite and dolomite particles in the form of xenomorphic granular and

clastic. A few of them are wrapped in collophane. The psephicity of clastic quartz is poor, which is generally mixed with dolomite and calcite, as shown in Figure 8. The grain size of quartz is between 0.03 and 0.2 mm, and 37.2% is less than 0.07 mm. The particle size distribution of quartz is shown in Figure 9.

No phosphorus element was detected in quartz by SEM energy spectrum analysis. The backscattered electron diagram and energy spectrum of quartz are shown in Figure 10. The results of energy spectrum analysis of quartz are shown in Table 5.

3.4.3. Carbonate. Carbonate minerals mainly exist in the form of dolomite and calcite, both of which are the main gangue minerals. They are semieuhedral to xenomorphic granular, closely connected with each other, and mainly distributed in collophane, quartz, and feldspar clasts, with different particle sizes. In the microcrystalline fine grain size scale, the micrographs are shown in Figure 11. The particle size ranges from 0.01 to 0.5 mm, and 60.9% of them are
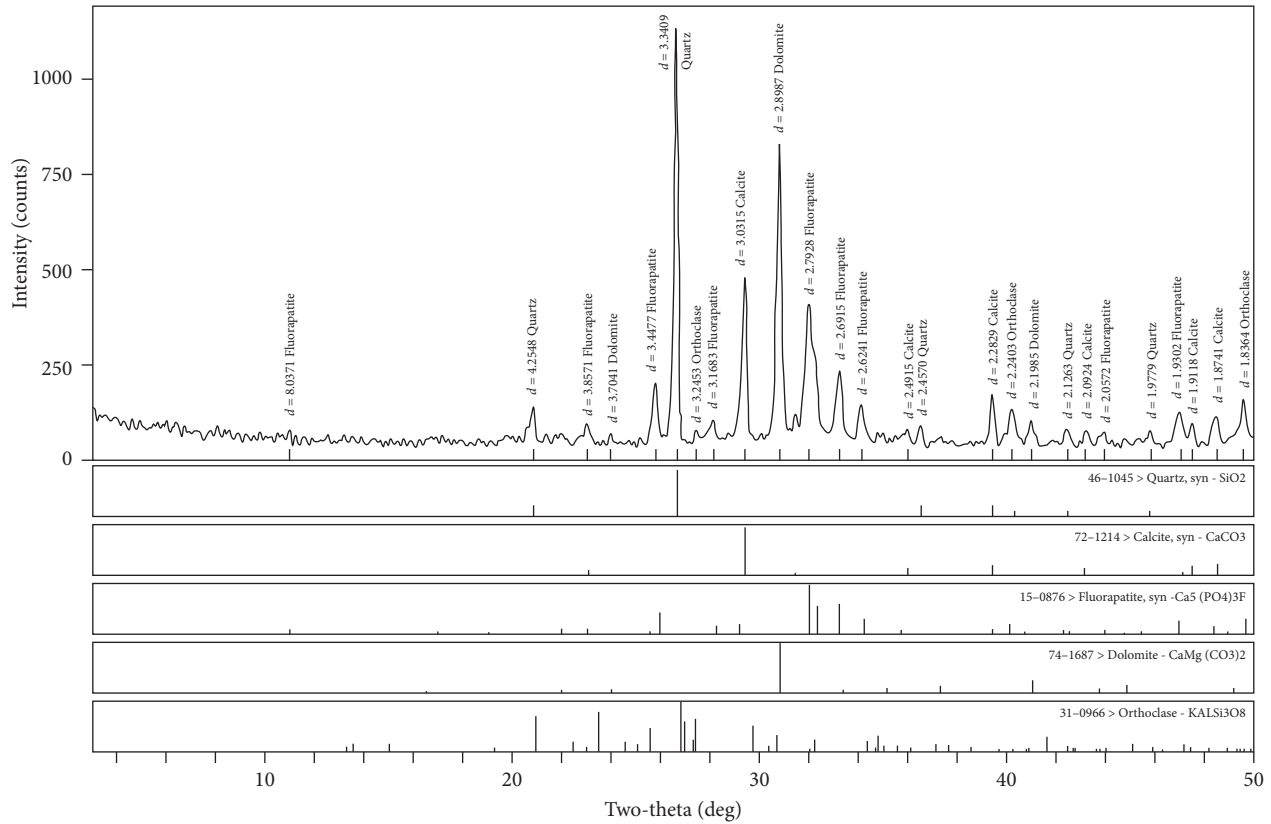
FIGURE 2: X-ray diffraction spectrum of the sample.

TABLE 2: Mineral composition.

Type	Mineral	Molecular formula	Size (mm)	Content (%)
Phosphate	Collophane	$Ca_2Ca_3[PO_4]_3(OH,F)$	<0.004, aggregate 0.03–0.5	45.0
	Monazite	$Ce[PO_4]$	0.02–0.03	Very few
Oxide	Quartz	SiO_2	0.03–0.2	18.3
	Limonite	$FeOOH$	0.04–0.1	Very few
	Anatase/rutile	TiO_2	0.02–0.05	Very few
Silicate	Plagioclase	$Na[AlSi_3O_8]$	0.06–0.2	4
	Potassium feldspar	$K[AlSi_3O_8]$	0.06–0.2	3
	Chlorite	$(Mg, Fe, Al)_3(OH)_6\{(Mg, Fe, Al)_3[(Si, Al)_4O_{10}](OH)_2\}$	<0.05	<1
	Sericite	$K\{Al_2[AlSi_3O_{10}](OH)_2\}$	0.01–0.1	Very few
	Zircon	$ZrSiO_4$	0.01–0.04	Very few
Carbonate	Dolomite	$CaMg[CO_3]_2$	0.01–0.5	16.3
	Calcite	$CaCO_3$	0.01–0.5	12
Natural elements	Carbonaceous	C	<0.01	Very few
Sum	—	—	—	99.6

(a)   (b)   (c)   (d)
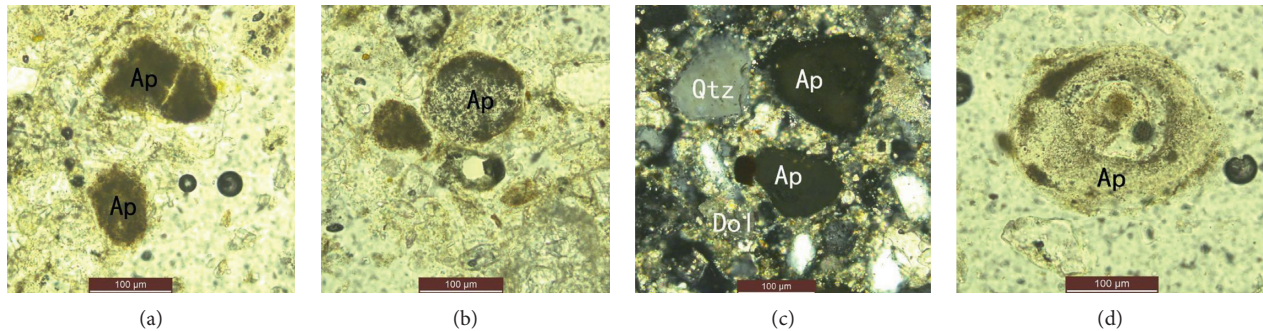
FIGURE 3: Embedded characteristics of phosphate (TSPL represents transmitted single polarized light). (a) Clastic collophane (Ap), TSPL. (b) Clastic collophane (Ap), TSPL. (c) Collophane (Ap) and dolomite (Dol) connected, TSPL. (d) Oolitic collophane (Ap), TSPL.
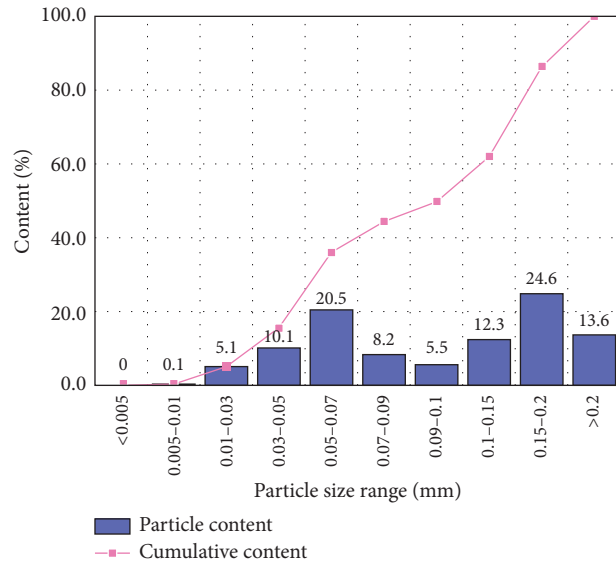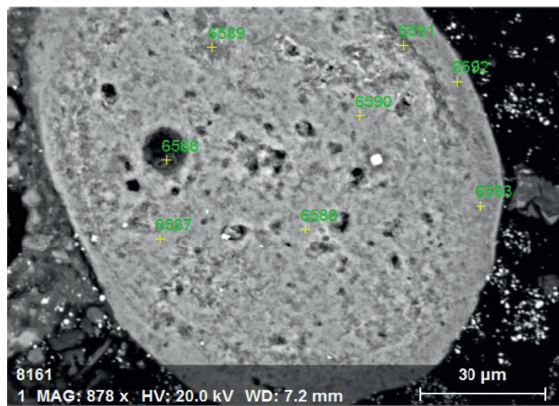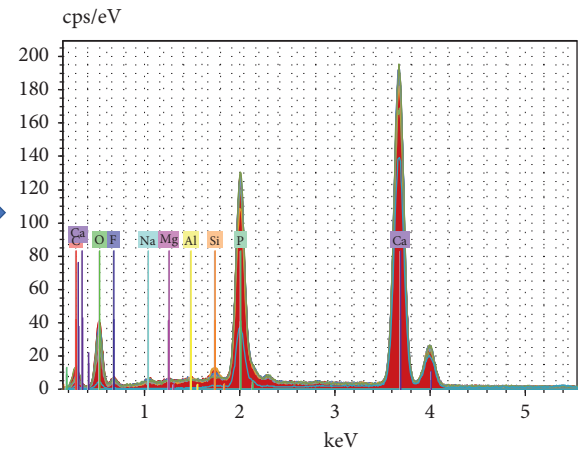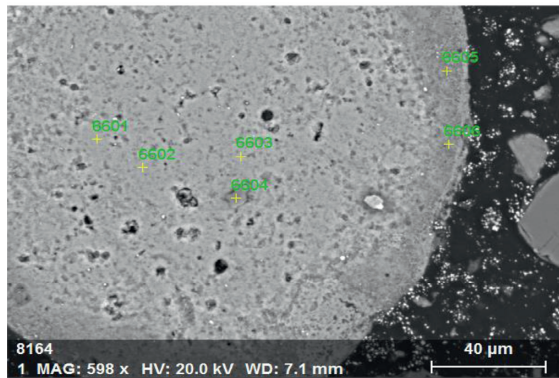
FIGURE 4: Particle size distribution of collophane aggregate.
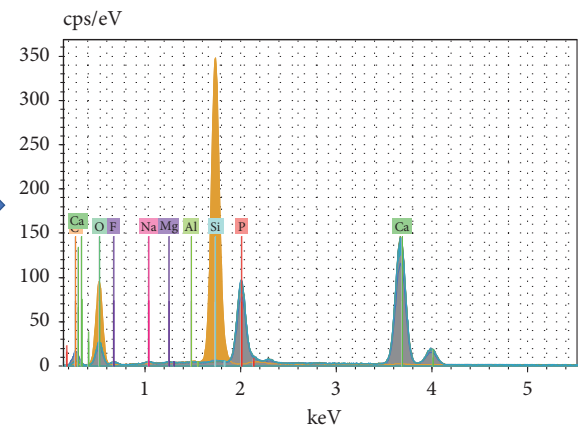

(a)

(b)

(c)

(d)

FIGURE 5: Backscattered electron diagram and energy spectrum of collophane.

TABLE 3: Results of energy spectrum analysis of collophane.

Point	Element (%)								
	C	O	F	Na	Mg	Al	Si	P	Ca
6587	4.90	36.18	4.65	0.44	—	—	—	14.22	39.61
6588	4.05	34.46	4.40	0.42	0.09	0.06	0.25	14.36	41.90
6589	3.87	35.91	4.03	0.34	0.10	0.20	0.76	13.08	41.69
6590	4.87	37.35	4.52	0.55	0.20	0.15	0.37	13.67	38.31
6591	4.00	30.43	3.00	0.17	0.01	0.16	0.42	15.90	45.91
6601	3.72	36.72	4.48	0.72	0.19	—	0.25	13.60	39.32
6602	3.26	36.42	4.72	0.62	0.16	—	—	13.59	41.24
6603	2.38	35.89	4.50	0.64	0.10	—	—	13.85	42.64
Average	3.88	35.42	4.29	0.49	0.11	0.07	0.26	14.03	41.33
Oxide content (%)	—	—	—	Na_2O	MgO	Al_2O_3	SiO_2	P_2O_5	CaO
	—	—	—	0.66	0.18	0.13	0.56	32.15	57.83

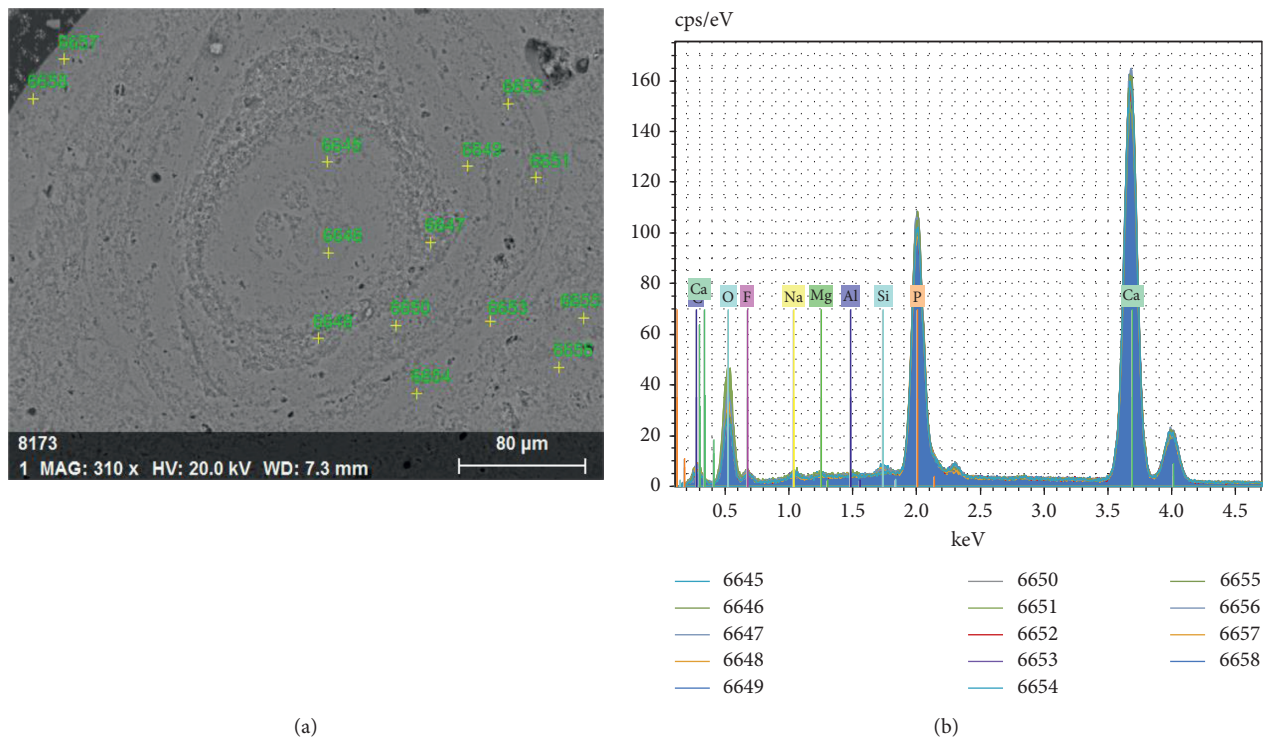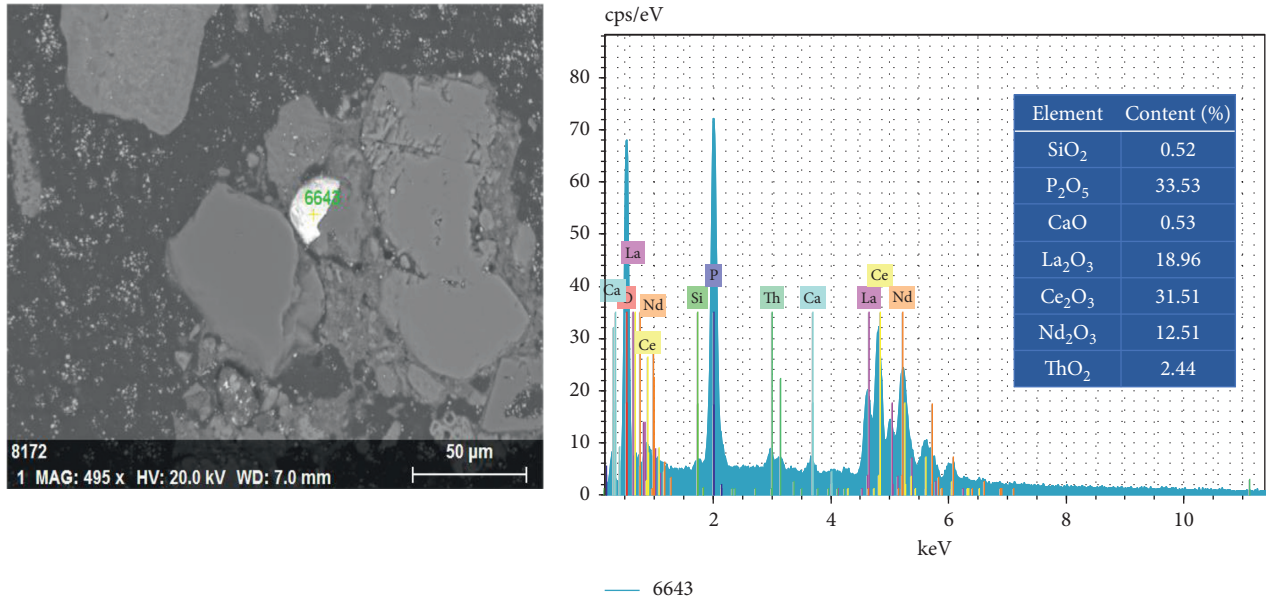(a)   (b)

FIGURE 6: Backscattered electron diagram and energy spectrum of collophane oolite.

TABLE 4: The energy spectrum analysis results.

Point	Element (%)								
	C	O	F	Na	Mg	Al	Si	P	Ca
6645	4.56	34.01	4.20	0.51	0.07	—	—	13.92	42.73
6646	5.18	36.66	4.83	0.55	0.17	—	—	13.40	39.21
6647	4.45	35.71	4.29	0.41	0.14	—	—	13.68	41.33
6648	5.80	38.27	5.34	0.37	0.06	0.00	—	12.47	37.69
6649	5.00	36.96	4.44	0.43	0.05	—	—	13.06	40.05
6650	5.06	36.48	4.72	0.68	0.19	—	—	13.49	39.38
6651	6.68	48.15	—	0.83	0.29	—	—	11.54	32.52
6652	5.38	36.69	4.80	0.65	0.18	—	0.18	13.13	38.98
6653	4.78	36.93	4.90	0.69	0.17	—	0.25	13.17	39.10
6654	5.33	38.46	5.22	0.76	0.31	0.12	0.43	12.74	36.62
6655	3.75	31.80	3.50	0.63	0.24	—	—	14.52	45.55
6656	4.20	34.16	3.77	0.42	—	—	—	14.92	42.53
6657	8.19	36.47	5.04	0.37	0.15	0.07	0.17	13.25	36.30
6658	9.25	32.57	4.27	0.25	—	—	—	14.16	39.49

Element	Content (%)
SiO$_2$	0.52
P$_2$O$_5$	33.53
CaO	0.53
La$_2$O$_3$	18.96
Ce$_2$O$_3$	31.51
Nd$_2$O$_3$	12.51
ThO$_2$	2.44

—— 6643

(a)   (b)

FIGURE 7: Backscattered electron diagram and energy spectrum analysis of monazite.
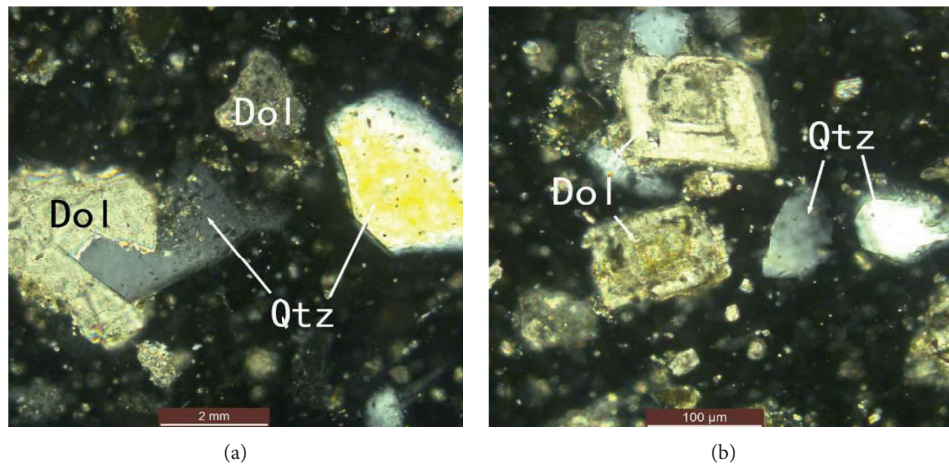
(a)   (b)

FIGURE 8: Embedded characteristics of Quartz (TCPL represents transmitted crossed polarized light). (a) Quartz (Qtz) and dolomite connected, TCPL. (b) Clastic angular quartz (Qtz), TCPL.

smaller than 0.07 mm. The distribution size of dolomite and calcite is shown in Figure 12.

According to the energy spectrum analysis of scanning electron microscope, no phosphorus element is detected in dolomite and calcite, as shown in Table 6. The backscattered electron diagram and energy spectrum image are shown in Figure 13.

3.4.4. Silicate. Plagioclase and potassium feldspar are a small amount of gangue minerals, mainly in clastic form,

distributed between dolomite and calcite in star shape, with poorly rounded, angular, and tabular shape, and the particle size is mainly 0.06–0.2 mm. The micrograph is shown in Figure 14. Chlorite: Microscale, occasionally seen between dolomite particles, particle size <0.05 mm, as shown in the micrograph of Figure 1(g).

3.4.5. Natural Elements. Carbonaceous: it is organic carbon. The monomer is mainly cryptocrystalline and wrapped in collophane. No independent carbonaceous is found. The
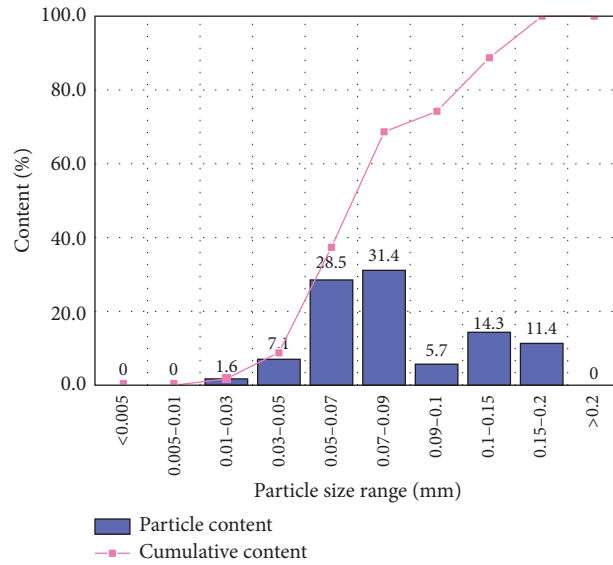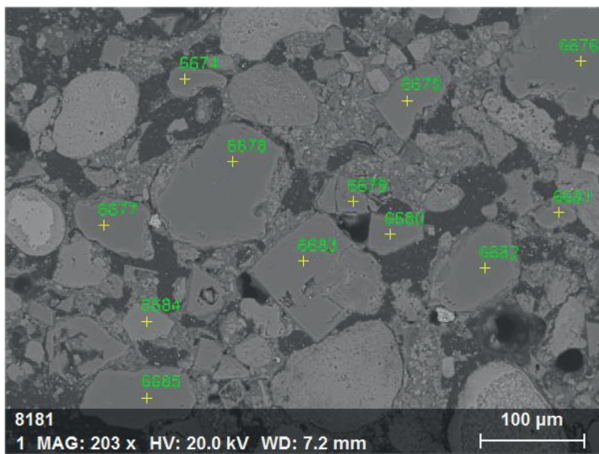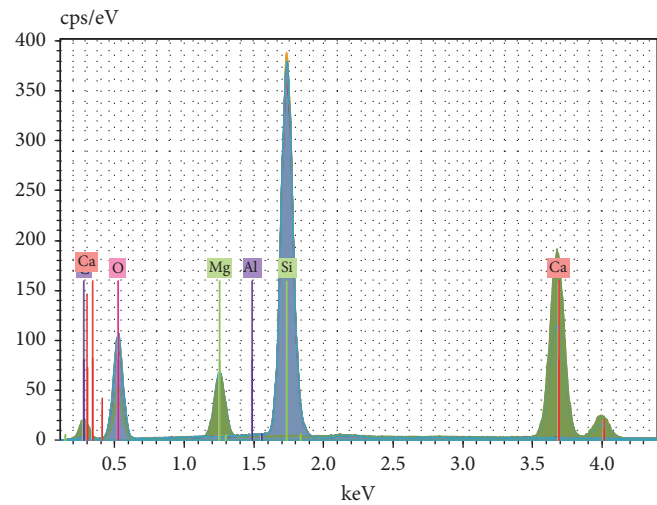
FIGURE 9: Particle size distribution of quartz grain.

(a)

(b)

FIGURE 10: Backscattered electron diagram and energy spectrum of quartz.

particle size is less than 0.02 mm, which mainly affects the concentrate grade of collophane.

3.5. Distribution of Phosphorus. The phosphorus element (P_2O_5) is mainly distributed in collophane as an independent mineral. SiO_2 mainly exists in quartz in the form of independent minerals, a small amount in plagioclase, potassium feldspar, and chlorite, MgO mainly exists in dolomite in the form of independent minerals, and Al_2O_3 mainly exists in plagioclase and potash feldspar in the form of

independent minerals. TFe_2O_3 mainly occurs in chlorite as isomorphism, and a small amount in limonite in the form of independent minerals.

Typical distribution of each element in the ore is shown in Figures 15 and 16. According to the element distribution in Figures 15(b) and 16(b), there are less inclusions in collophane, mainly pulverulent organic matter and clay, and a small amount of fine-grained quartz, which are very difficult to remove in mineral processing. Dolomite and calcite are mainly distributed in the form of cement between the collophane clasts, which are also the main ore associated with the collophane.
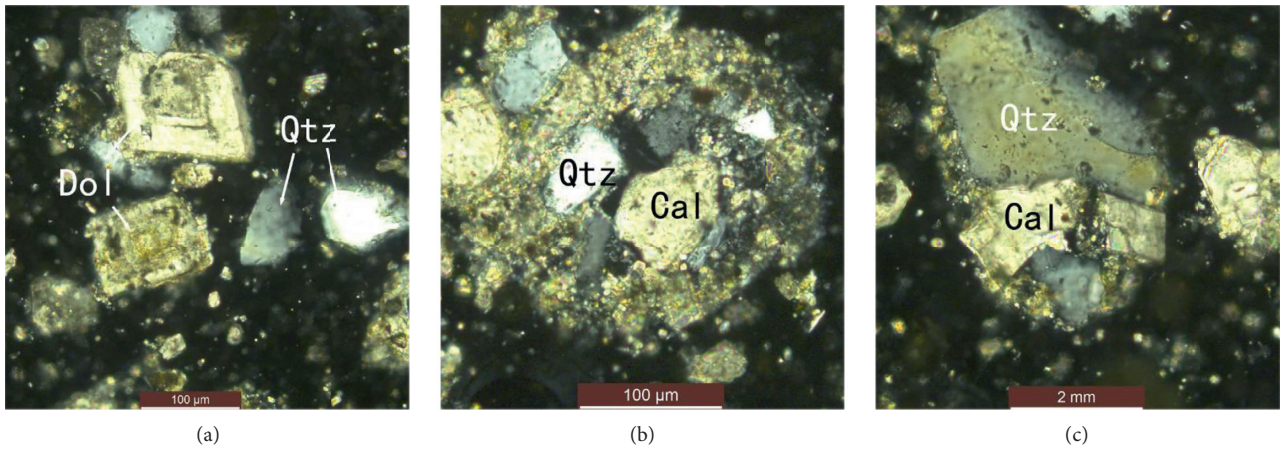
(a)　　　　　(b)　　　　　(c)

FIGURE 11: Embedded characteristics of carbonate minerals (dolomite and calcite) (TCPL represent transmitted crossed polarized light). (a) Euhedral rhombohedral dolomite (Dol), TCPL. (b) Calcite (Cal) and quartz (Qtz) connected, TCPL. (c) Calcite (Cal) and quartz (Qtz) connected, TCPL.
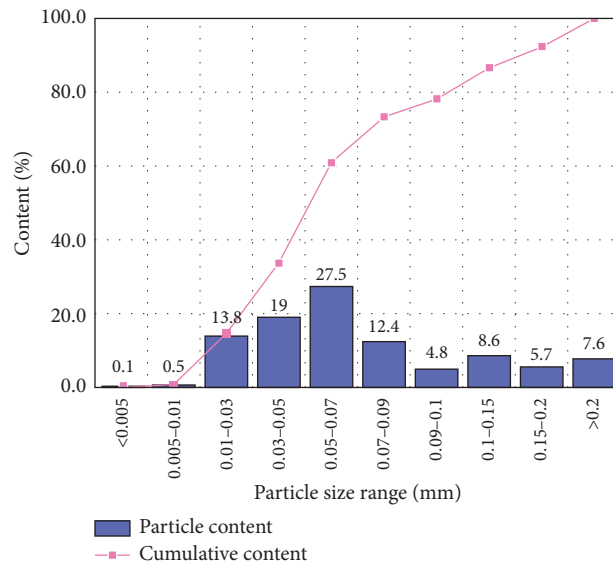

FIGURE 12: Particle size distribution of dolomite and calcite.

TABLE 6: Energy spectrum analysis results of dolomite and calcite.

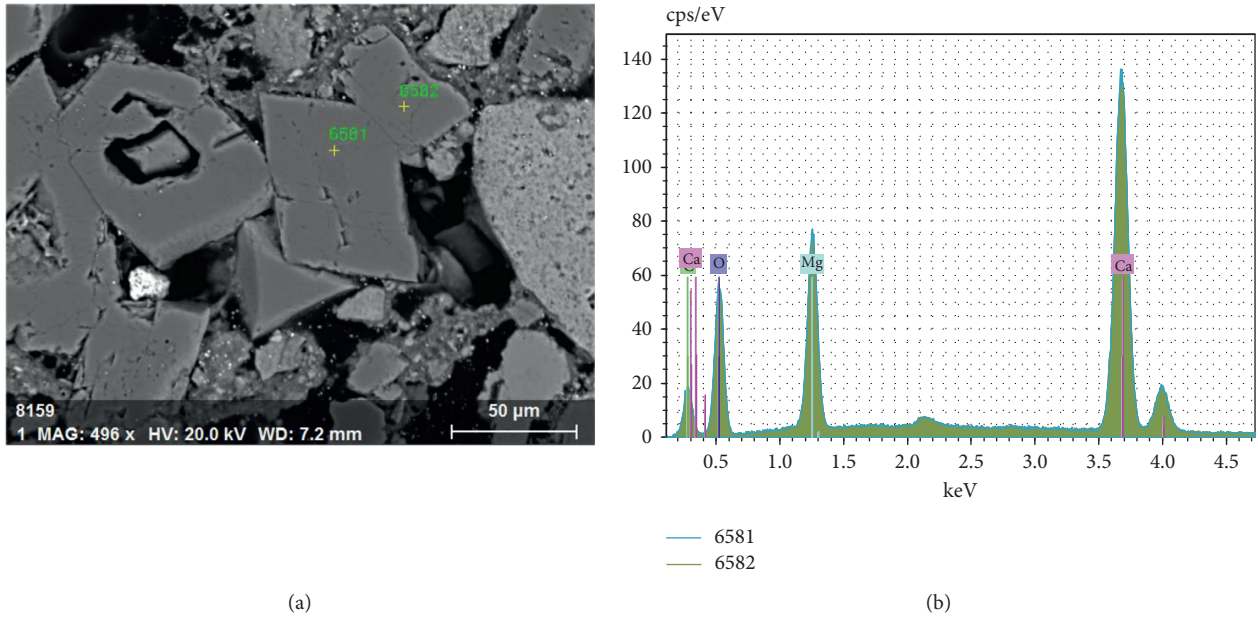| Number	Element (%)				
	C	O	Mg	Ca	Mineral
6581	12.01	49.90	10.71	27.39	Dolomite
6582	11.06	50.13	10.75	28.07	Dolomite
6684	13.04	50.28	0.14	36.54	Calcite

(a)

(b)

Figure 13: Backscattered electron diagram and energy spectrum image of dolomite.
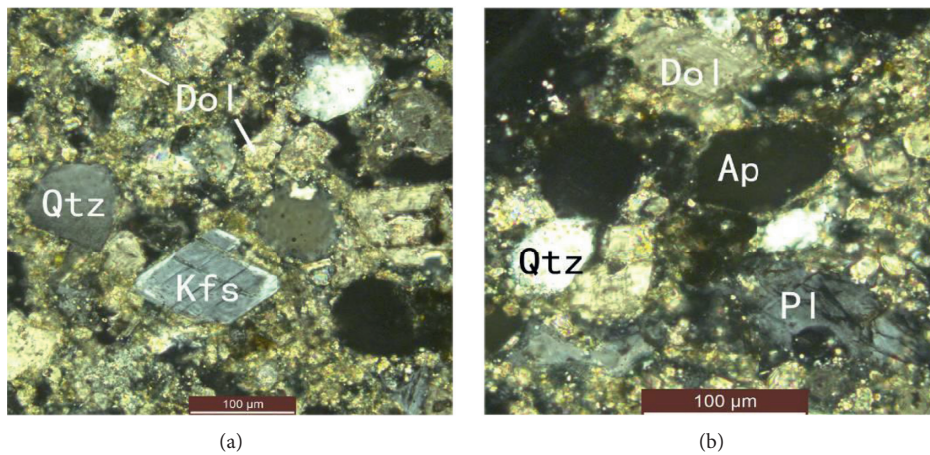

(a)

(b)

Figure 14: Embedded characteristics of silicate minerals (TCPL represents transmitted crossed polarized light). (a) Clastic potash feldspar (Kfs), TCPL. (b) Clastic plagioclase (Pl), TCPL.
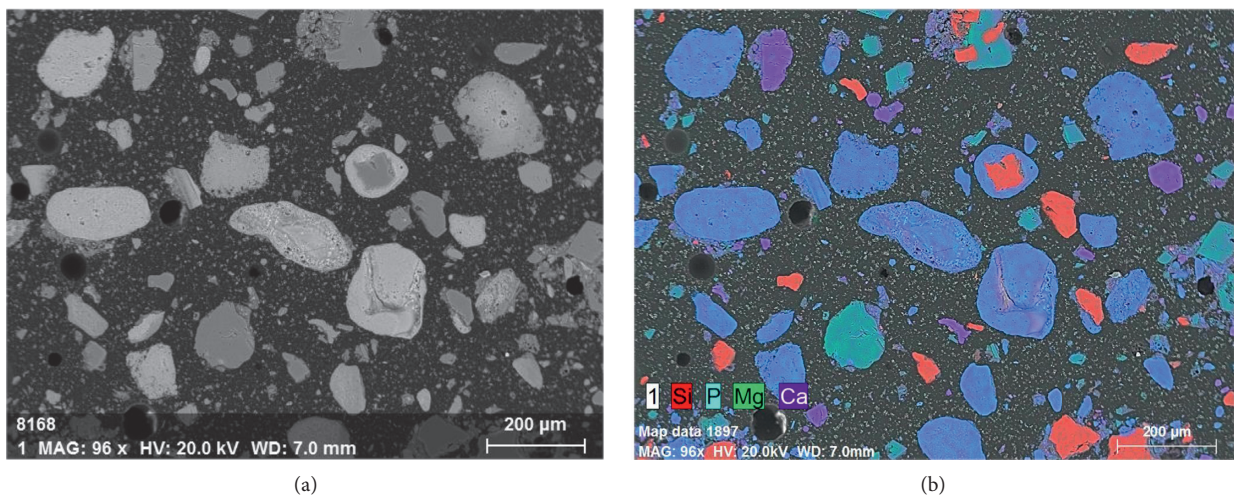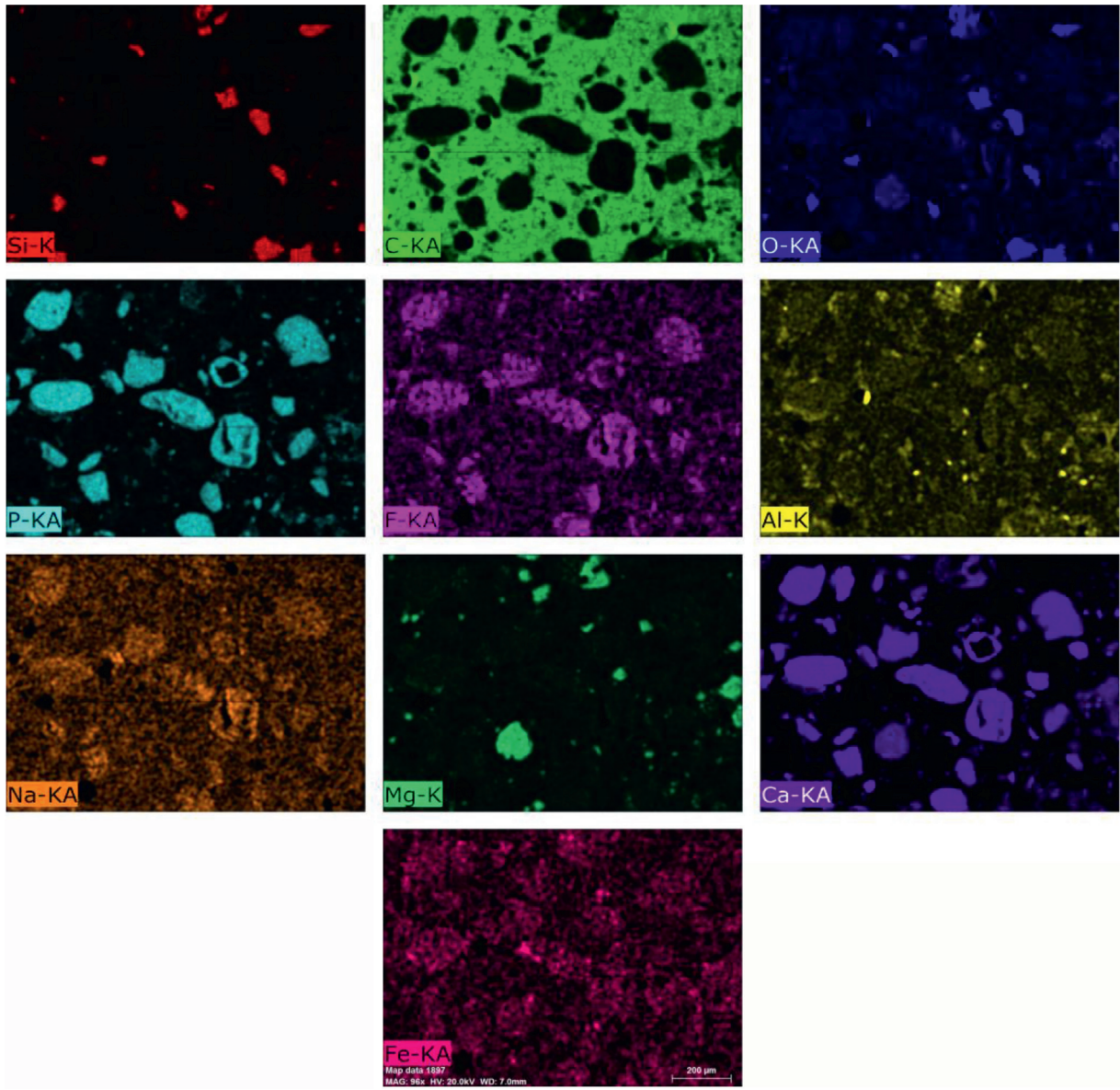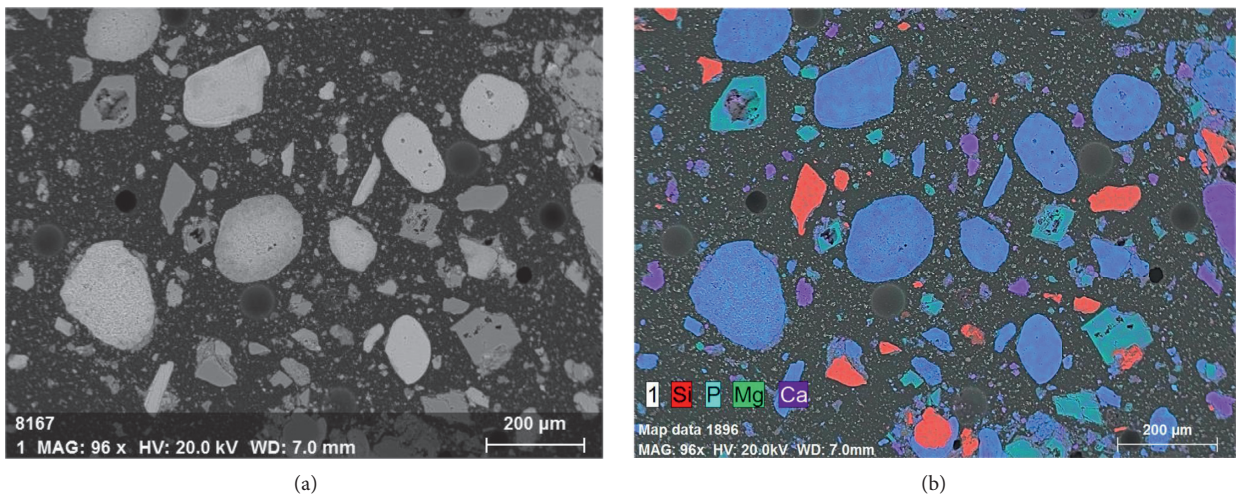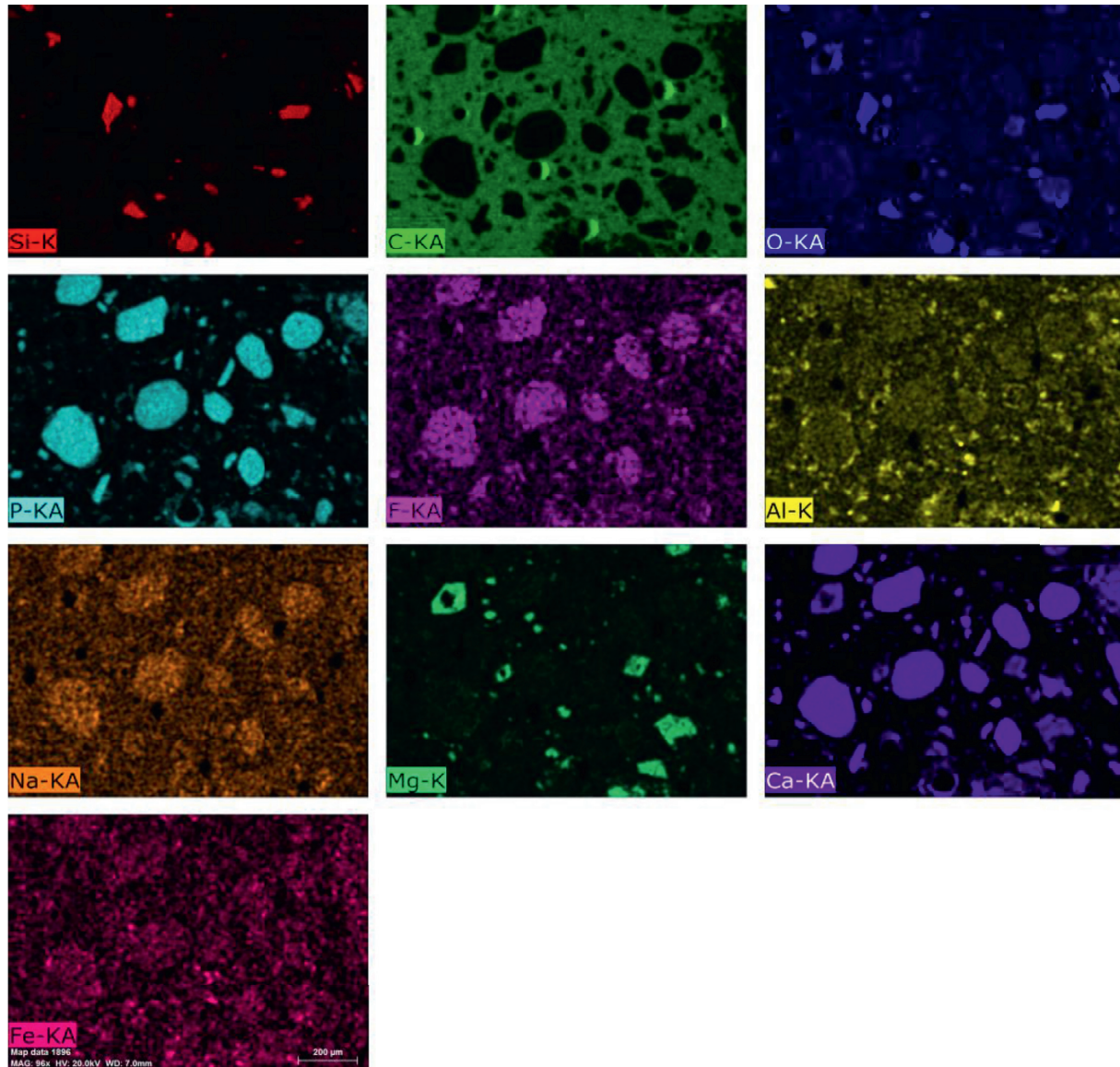

(a)

(b)

Figure 15: Continued.

(c)

FIGURE 15: Backscattered electron diagram and element distribution diagram of collophane, quartz, dolomite, etc. (a) Backscattered electron image. (b) Backscattered element diagram. (c) Regional element distribution map.

(a)

(b)

FIGURE 16: Continued.

(c)

FIGURE 16: Backscattered electron diagram and element distribution diagram of collophane, calcite, and quartz. (a) Backscattered electron image. (b) Backscattered element diagram. (c) Regional element distribution map.

4. Conclusions

There are altogether 13 kinds of minerals in the ore, including phosphate, oxide, silicate, and natural elements, in which phosphate accounts for 45%, oxide accounts for 18.3%, silicate accounts for 8%, carbonate accounts for 28.3%, and natural elements are few; the main ore mineral is collophane, and the main gangue minerals are quartz, dolomite, calcite, a small amount of potassium feldspar, plagioclase, chlorite, etc. The main mineral structures have colloidal aphanitic texture, fine-grained sand chip structure, oolitic structure, and inclusion structure. The combination of mineral aggregates is relatively close, and the way of mutual cementation and association is relatively simple.

P_2O_5 mainly exists in collophane as an independent mineral, MgO as an independent mineral in dolomite, SiO_2 as an independent mineral in quartz, Al_2O_3 in potassium feldspar and plagioclase as an independent mineral, and TFe_2O_3 in chlorite in isomorphic form in the form of independent limonite. The particle size of collophane aggregate is mainly between 0.03 and 0.5 mm. The grain size of quartz is between 0.03 and 0.2 mm; the grain size of dolomite and calcite is between 0.01 and 0.5 mm; some of them are in the range of powder crystal (<0.06 mm), and some belong to fine-grained distribution; the grain size of potassium feldspar and plagioclase is between 0.06 and 0.2 mm. The granularity of quartz and feldspar is coarser, and the granularity of calcite and dolomite is finer.

The phosphate tailings contain relatively high content of Si and Ca and low content of heavy metals such as Cd and Pb, which has little impact on the environment. However, the tailings still have the value of comprehensive utilization because the content of P_2O_5 is 15.76%. Therefore, the phosphorus mineral in tailings can be further recovered by flotation, and then it can be used as filling material. Hence, the effect of phosphorus on the backfilling environment is also reduced. Furthermore, an appropriate filling material ratio can be designed to achieve the appropriate filling strength according to the mineral composition, chemical composition, and particle size distribution of phosphate tailings.

Data Availability

The data used to support the findings of this study are available from the corresponding author upon request.

Conflicts of Interest

The authors declare that they have no conflicts of interest regarding the publication of this paper.

Acknowledgments

References

[1] Q. Chen, Q. Zhang, A. Fourie, and C. Xin, "Utilization of phosphogypsum and phosphate tailings for cemented paste backfill," *Journal of Environmental Management*, vol. 201, pp. 19–27, 2017.

[2] P. Zhang, "Comprehensive recovery and sustainable development of phosphate resources," *Procedia Engineering*, vol. 83, pp. 37–51, 2014.

[3] Y. Chen, Z. Wei, M. Irfan, J. Xu, and Y. Yang, "Laboratory investigation of the relationship between electrical resistivity and geotechnical properties of phosphate tailings," *Measurement*, vol. 126, pp. 289–298, 2018.

[4] K. Zheng, J. Zhou, and M. Gbozee, "Influences of phosphate tailings on hydration and properties of Portland cement," *Construction and Building Materials*, vol. 98, pp. 593–601, 2015.

[5] Y. Zhao, A. Taheri, A. Soltani et al., "Strength development and strain localization behavior of cemented paste backfills using portland cement and fly ash," *Materials*, vol. 12, no. 20, p. 3282, 2019.

[6] Q. Liu, D. Liu, X. Liu, F. Gao, and S. Li, "Research and application of surface paste disposal for clay-sized tailings in tropical rainy climate," *International Journal of Mineral Processing*, vol. 157, pp. 227–235, 2016.

[7] Y. Zhao, A. Taheri, M. Karakus, Z. Chen, and A. Deng, "Effects of water content, water type and temperature on the rheological behaviour of slag–cement and fly ash-cement paste backfill," *International Journal of Mining Science and Technology*, vol. 30, no. 3, pp. 271–278, 2020.

[8] Y. Zhao, A. Soltani, A. Taheri, M. Karakus, and A. Deng, "Application of slag–cement and fly ash for strength development in cemented paste backfills," *Minerals*, vol. 9, no. 1, p. 22, 2019.

[9] D. M. Franks, D. V. Boger, C. M. Côte, and D. R. Mulligan, "Sustainable development principles for the disposal of mining and mineral processing wastes," *Resources Policy*, vol. 36, no. 2, pp. 114–122, 2011.

[10] M. Altiner, "Recovery of apatite from ore slimes using centrifugal heavy liquid separation," *JOM*, vol. 71, no. 9, pp. 3202–3208, 2019.

[11] H. Boujlel, G. Daldoul, H. Tlili et al., "The beneficiation processes of low-grade sedimentary phosphates of Tozeur-Nefta deposit (Gafsa-Metlaoui basin: south of Tunisia)," *Minerals*, vol. 9, no. 1, p. 2, 2019.

[12] A. Z. M. Abouzeid, A. T. Negm, and D. A. Elgillani, "Upgrading of calcareous phosphate ores by flotation: effect of ore characteristics," *International Journal of Mineral Processing*, vol. 90, no. 1-4, pp. 81–89, 2009.

[13] F. Li et al., "Application of process mineralogy study in phosphate beneficiation in Yichang," *Industrial Minerals & Processing*, vol. 43, no. 05, pp. 9–11, 2014.

[14] W. Ling, L. Kaihua, and L. Zhengyao, "Process mineralogy of a gold multi-metal ore in beiya, yunna," *Procedia Environmental Sciences*, vol. 12, pp. 949–956, 2012.

[15] M. Abdollahi, A. Bahrami, M. S. Mirmohammadi, F. Kazemi, A. Danesh, and Y. Ghorbani, "A process mineralogy approach to optimize molybdenite flotation in copper - molybdenum processing plants," *Minerals Engineering*, vol. 157, Article ID 106557, 2020.

[16] X. L. Ye and Y. W. Xiao, "Application of process mineralogy for process optimization in concentrator plant," *Nonferrous Metals (Mineral Processing Section)*, vol. 72, no. 4, pp. 13–33, 2020.

[17] J. Zhong et al., "Experimental study on process mineralogy of a collophanite in Yunnan," *Industrial Minerals & Processing*, vol. 44, no. 03, pp. 4-5, 2015.

[18] Y. Jiao, K.-H. Qiu, P.-C. Zhang, J.-F. Li, W.-T. Zhang, and X.-F. Chen, "Process mineralogy of Dalucao rare earth ore and design of beneficiation process based on AMICS," *Rare Metals*, vol. 39, no. 8, pp. 959–966, 2020.

[19] V. G. Greb, A. Guhl, H. Weigand, B. Schulz, and M. Bertau, "Understanding phosphorus phases in sewage sludge ashes: a wet-process investigation coupled with automated mineralogy analysis," *Minerals Engineering*, vol. 99, pp. 30–39, 2016.

[20] Y. Gu, R. P. Schouwstra, and C. Rule, "The value of automated mineralogy," *Minerals Engineering*, vol. 58, pp. 100–103, 2014.

[21] M. S. Oliveira, R. C. Santana, C. H. Ataíde, and M. A. S. Barrozo, "Recovery of apatite from flotation tailings," *Separation and Purification Technology*, vol. 79, no. 1, pp. 79–84, 2011.

Research Article

Collaborative Mining Sequence Optimization for Multiple Stopes under Intensive Mining

Long Zhang ⓘ,[1] **Jianhua Hu ⓘ,**[2] **Xinzhong Wang,**[1] **Xiuwei Chai,**[3] **and Lei Zhao**[4]

[1]*State Key Laboratory of Hydraulics and Mountain River Engineering, College of Water Resource & Hydropower, Sichuan University, Chengdu 610065, China*
[2]*School of Resources and Safety Engineering, Central South University, Changsha 410083, China*
[3]*School of Resources and Safety Engineering, Wuhan Institute of Technology, Wuhan 430074, China*
[4]*Hubei Sanning Mining Co. Ltd, Yichang 443100, Hubei, China*

Correspondence should be addressed to Jianhua Hu; hujh21@126.com

The optimization of a mining sequence not only reduces stress concentration in surrounding rock but also prevents underground debris flows, significantly improving safety. Firstly, the 870–898 m level of the eastern mining area in the Tiaoshuihe phosphate mine was divided into 25 ore blocks, and six different mining sequences were designed for this area. Then, it was calculated that five ore blocks must be processed simultaneously to reach the annual production output. The distances between the five simultaneously mined ore blocks will inevitably affect the efficiency of the equipment for any scheme. So, a collaborative model considering both the area stability and production capacity was established by combining the distance between the centers of the five ore blocks as an index. Differences in stability, deformation, and plastic zone size between the schemes are compared. The calculation results show that a mining scheme with a convex stepped shape produces the best results. These results provide a general method for entropy-based mining sequence optimization and an optimal solution for the Tiaoshuihe phosphate mine.

1. Introduction

Filling mining is a popular contemporary technique that is increasingly advocated by many governments. Ground pressure in these types of mines will increase considerably as mining continues to deeper depths, so the corresponding requirements for ground pressure control will continue to expand [1, 2]. If measures are only taken after ground pressure triggers surrounding rock damage, production costs will increase and the production efficiency will be reduced. To better compensate for ground pressure, active control must be used instead of passive control. Implementing a reasonable mining sequence is an active ground pressure control method [3].

In 1963, Goodman and Brown put forward the concept of rock engineering excavation steps, which is described as the mining sequence now [4]. In 1972, Zouanalyzed the influence of construction steps on the construction of underground tunnels and proposed the concept of simulated excavation steps for the first time but did not combine finite element calculations and simulations [5]. Liu successfully optimized the mining sequence of the Dongguashan deep well by considering the production capacity, stress, displacement, and plastic zone of the surrounding rock [6]. Kang simulated different mining sequences in the middle level of the Xinli mining area of Sanshandao Gold Mine, obtaining characteristic values of the stress and displacement of rock under different mining steps. This work suggested that it is safe and efficient to mine one panel at the interval of two panels [7]. Based on the time-varying evolution of the mechanical parameters of a rock mass, Hu designed five mining sequence schemes in the deep section of the Gaofeng mine. Using FLAC3D, the spatiotemporal evolutions of rock mass mechanical parameters were simulated under different mining sequences. The results show that case 2 represents the best mining sequence [8].

The Tiaoshuihe phosphate mine is a gently inclined thin ore body with an average thickness of 3.22 m. This mine contains a mining area of approximately 23.42 km² and an estimated reserve of 200 million t [9, 10]. To realize production, it is necessary to plan intensive mining, adjust the mining areas of simultaneous production in one location, and then maximize the utilization rate of personnel and equipment [11]. At present, excavating is mainly concentrated in the 870–898 m level of the eastern mining area. Optimization of the mining sequence in this area is necessary by considering regional stability and productivity objectives [12].

2. Geological Characteristics of Mining Area

Tiaoshuihe phosphate mining area is located in the north margin of Huangling fault area. The strata are inclined to NNE monoclinic structure. The dip angle is generally 4–8°. The attitude of the stratum becomes steep due to the influence of fault structure. There are 6 faults in the mining area, and all faults are normal. Among them, F1 and F4 are NNW trending faults. F3, F5, and F6 are NW trending faults, and F2 is the NNE trending fault. F1 is the eastern natural boundary of the mining area. F5 is the southern natural boundary of the mining area. The F4 fault divides the mining area into two natural blocks, the east and the west. It causes great damage to the continuity of the ore body. The model of ore body is shown in Figure 1.

870–898 m level is the main research area. 870–898 m level belongs to the main industrial phosphate bed, which is stable and widely developed. It is distributed at the bottom of Huji member and occurs in layers. The roof is thin to middle micritic dolomite in the lower submember of Huji member, intercalated with thin layer of gray (weathering color is grayish yellow) micritic mudstone. And the floor is thick bedded siliceous block in the upper submember of Zhangcunping member. The average thickness of 870–898 m level is 4.61 m. The grade of P_2O_5 is 21.22–34.02%, and the average is 27.21%.

3. Model Construction and Scheme Design

3.1. Model Construction. In Figure 2, the ore body was meshed by using a DIMINE-CAD-MIDAS/GTS coupling operation and then imported into the numerical simulation software FLAC3D for calculation. The fractures in the 870–898 m level of the eastern mining area are relatively developed, and the mining sequence is related to the overall stability and mining safety of the area [9]. According to geological occurrence conditions, a three-dimensional ore body model was established, and 25 numbered mining areas were identified. The width of each mining area was 60 m, and the length was 100 m. According to Saint-Venant's principle, an area 3 times greater than the ore body was selected to determine the model boundary [13, 14].

3.2. Scheme Design. Six schemes of mining sequences were designed for optimization. To ensure the comparability of the six schemes, all schemes completely mined and filled the

25 mining areas. Each scheme includes 50 calculation steps to simulate the process of mining and filling. Then, the displacement, stress, and plastic zone results were analyzed.

The six mining sequence schemes are shown in Figure 3. The numbers in the table indicate the mining sequence: scheme 1 mines along the short axis of the mining area, from east to west; scheme 2 mines along the long axis of the mining area, from south to north; scheme 3 mines from southwest to northeast; scheme 4 mines from northeast to southwest; scheme 5 mines northward a convex stepped shape; and scheme 6 mines in a "V" shape.

Numerical simulation of the mining area requires a mathematical model of the rock mechanical properties, which is usually the defined stress-strain relationship [15]. According to a geological investigation at the Tiaoshuihe phosphate mine and laboratory mechanical experimentation, the initial stress is considered to reflect only the self-weight of the rock mass. The Mohr–Coulomb constitutive model is commonly used, as follows [16]:

$$\sigma_1 = \frac{1 + \sin \varphi}{1 - \sin \varphi} \cdot \sigma_3 + \frac{2c \cdot \cos \varphi}{1 - \sin \varphi}, \tag{1}$$

where c is the cohesion in MPa, σ_1 and σ_3 are the principal stresses in MPa, and φ is the internal friction angle, °.

4. Results

Six command flows were compiled according to the mining sequence schemes described above [17]. Combined with the rock mass mechanical parameters in Table 1, the aforementioned three-dimensional ore body grid model was imported into the finite element numerical simulation software, FLAC3D. The maximum displacement, maximum stress, and plastic area volume were obtained after each mining step of each scheme.

4.1. Calculation Results of Six Schemes. The displacement, tensile stress, compressive stress, shear stress, and plastic zone results calculated for six schemes are shown below. The overall trends of the six scheme results were similar, and the displacement results are shown in Figure 4.

Based on the displacement change curve of each step in schemes 1–6 (Figure 4), the maximum displacement is 10.3 cm and occurs in step 19 of scheme 6. In this step, the displacement increases significantly, and the following displacement remains stable. The maximum displacement of the roof does not occur at the current goaf but instead occurs in the roof of the large filling body. Therefore, the displacement of 10.3 cm in the roof of the large filling body will affect the whole project. The displacement of the roof in the 19th step is between 6-7 cm, which is also dangerous. During the actual engineering excavation, the area will be mined block by block. The displacement is expected to be less than 6 cm, so it is necessary to use bolts and anchor mesh for support after excavation.

The plastic tensile failure zone curve under six schemes can be seen in Figure 5. The plastic tensile failure zone changes greatly after each step of mining. The maximum
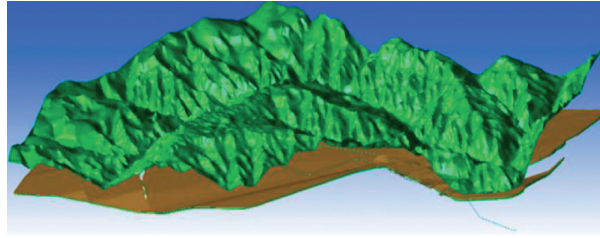
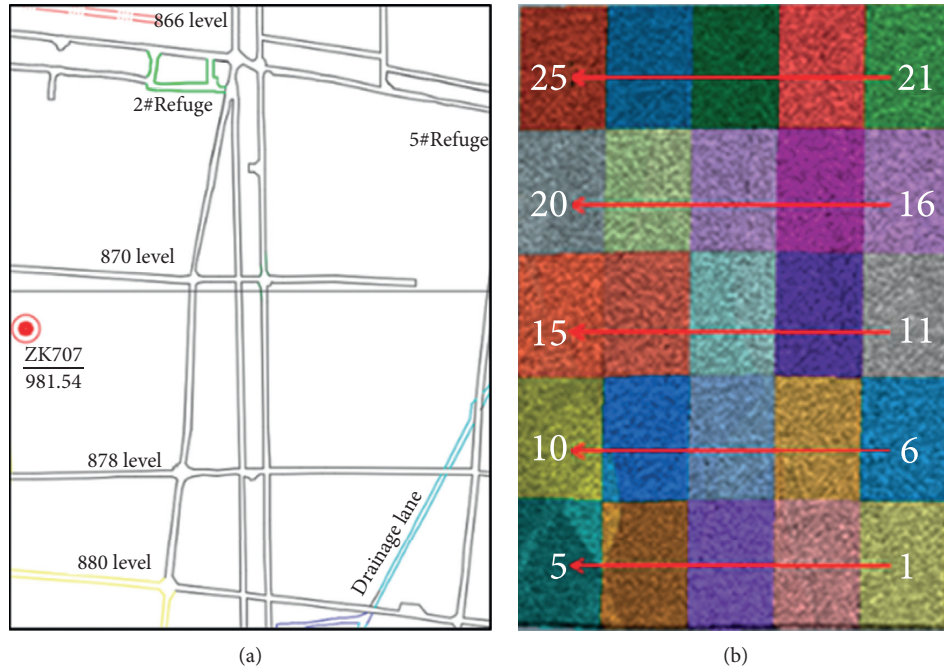FIGURE 1: Geological model of Tiaoshuihe phosphate mine.

| (a) | (b) |

FIGURE 2: Optimization calculation model of mining sequence. (a) Geological map. (b) Block number.

value is found to be $380182\,\mathrm{m}^3$, which arises after step 25 of scheme 4. The interface between the goaf and pillar exhibits high tensile stress, and the plastic tensile failure zone occurs mainly at the backfill. The maximum tensile plastic zone gradually expands with each step of mining for the first five steps and then expands more slowly after subsequent steps.

4.2. Analysis of the Maximum Values of Calculation Results Using Different Schemes. Changes in the displacement, stress, and plastic zone after each step of mining in each scheme are shown below. Table 2 highlights the maximum displacements, stresses, and the final plastic zone total volumes under different schemes. In Table 2, D represents the displacement, TS represents the tensile stress, CS represents the compressive stress, SS represents the shear stress, SF represents plastic shear failure zone volume, TF represents tensile failure zone, TSF represents the total volume of the plastic shear failure zone, and TTF represents the total volume of the plastic tensile failure zone.

Among the six schemes, the displacement of scheme 6 is the largest, while that of scheme 5 is the smallest throughout, with relatively stable displacement in every step. The tensile

stress of scheme 6 is also the greatest, while those of schemes 5 and 2 are greater than those other schemes. Scheme 6 has the greatest compressive and shear stresses, followed by scheme 1. The plastic shear failure zone of scheme 2 is the largest, followed by scheme 4. Scheme 2 produces the largest plastic zone of tensile failure, followed by scheme 3. The total volume of the plastic shear failure zone in scheme 1 is the largest, while that of scheme 6 is the smallest. Scheme 2 produces the largest total volume of the plastic tensile failure zone, while scheme 5 produces the smallest.

The shear stress evolution trend is similar to the compressive stress. The maximum shear stress is 19.98 MPa after step 13, produced at the joint of the long axis side roof, pillar, and filling body.

5. Coordination of Mining Sequence and Production Capacity Target

5.1. Calculation of the Production Capacity of the Tiaoshuihe Phosphate Mine. The current production plan at the Tiaoshuihe phosphate mine is 1 million t/a, and extracted ore is transported and exported by automobiles. Due to the high altitude of Zhangcunping Town, Yichang City, snow

Figure 3: Mining sequence schemes 1–6. (a) Scheme 1. (b) Scheme 2. (c) Scheme 3. (d) Scheme 4. (e) Scheme 5. (f) Scheme 6.

Table 1: Mechanical parameters of the rock mass and backfill.

Rock layer	ρ (g·cm^{-3})	K (GPa)	G (GPa)	Φ (°)	C (MPa)	T (MPa)
Surrounding rock	2.85	35.55	13.94	52.09	3.27	4.57
Phosphate rock layer	3.02	14.22	8.57	60.76	1.05	2.01
Backfill	2.20	2.86	2.61	38	1.40	0.60

covering in winter shuts down transportation and production. Therefore, producing more than 4000 t/d is required to achieve the annual production target.

The ore grade stratification of the mine is relatively apparent. The upper layer is high-grade ore, and the lower layer is low-grade ore. This ore is mined in layers to reduce the mixing rate. Each operation can explore only half of the working face. The footage of one blasting is 2.83 m, and the density of the phosphate rock is 3.021 g/cm^3. The production of one blasting in a single stope is 89.77 t.

Because the mining method of excavating alternate strips is adopted, each ore block can be divided into eight strips. Each ore block can have at most four strips being mined at the same time, so the single production capacity of each ore block is 359.08 t. A two-shift system is used at the Tiaoshuihe phosphate mine, where each shift completes one working procedure of drilling, blasting, and ore drawing and transportation. The daily production capacity of each ore

block is 718.16 t. Therefore, according to the production target of 4000 t/d, at least 5.6 ore blocks need to be mined at the same time to meet the production capacity requirements. However, a small part of the 870–898 m level in the eastern mining area has a good ore grade and does not need to be mined in layers. Therefore, to achieve the annual production, only five ore blocks need to be mined at the same time in this area.

Among the six different mining sequences, there are considerable differences in the distances between the five ore block centers. The discreteness of these five blocks has a significant influence on the cooperative use of equipment and operation cost in the mining process. The center of each group of five ore blocks mined at the same time is taken as the base point, and the sum of the distances from the center of each of the five ore blocks to the base point is called the center distance. Then, the center distance is used to measure the discreteness of five simultaneously mined ore blocks. The
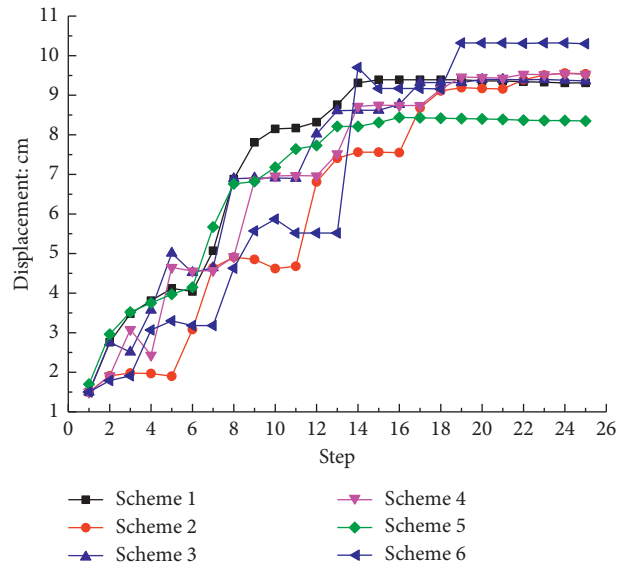
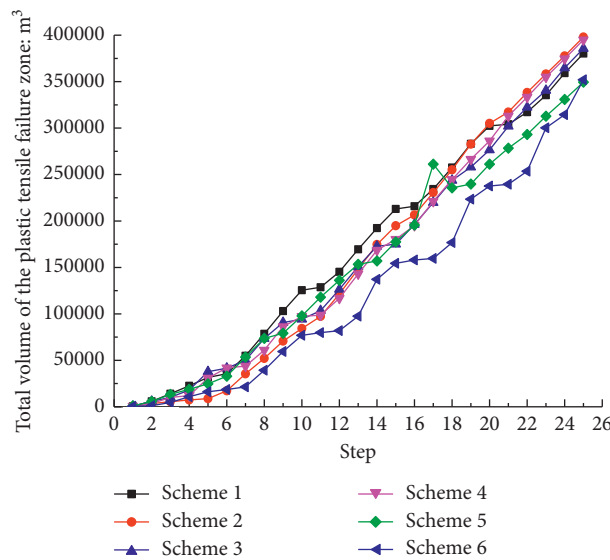FIGURE 4: Displacement curve of schemes 1–6.

FIGURE 5: Plastic tensile failure zone of schemes 1–6.

TABLE 2: Calculation results of the six mining sequence schemes.

Scheme	D (cm)	TS (MPa)	CS (MPa)	SS (MPa)	SF (m³)	TF (m³)	TSF (m³)	TTF (m³)
1	9.39	2.21	52.67	19.98	432578	264.57	10105900	380182
2	9.56	2.24	50.32	18.35	621531	390.88	10024000	397980
3	9.40	2.21	50.44	19.24	459187	375.76	10029400	385725
4	9.55	2.23	50.33	18.26	525976	240.74	10034300	395019
5	8.44	2.25	50.48	18.5	404996	272.14	9786510	349378
6	10.3	2.39	56.71	21.19	473828	175.29	8794870	351962

higher the discreteness, the lower the coordination degree of a given scheme.

Figure 6 shows the center distance calculation for the first group of ore blocks in scheme 1. The distances from the five ore blocks to the base point are 0 m, 60 m, 60 m, 120 m, and 120 m. Therefore, the center distance of the first group in scheme 1 is 360 m. Because the center distances of the five groups in scheme 1 are all 360 m, the sum of the center distances of scheme 1 is 1800 m.
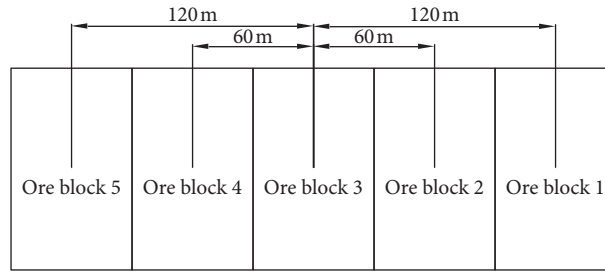
FIGURE 6: Calculating the center distance of the first step in scheme 1.

TABLE 3: Sum of the center distances of the six schemes.

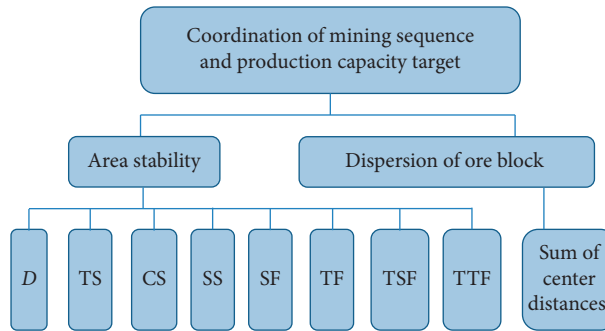| Scheme	1	2	3	4	5	6
Sum of center distance (m)	1800	3000	2497.44	2672.64	2588.17	2588.17

FIGURE 7: Collaborative model of mining sequence and production capacity target.

TABLE 4: Score of the basic elements of the six schemes.

Scheme	D (cm)	T (MPa)	C (MPa)	S (MPa)	SF (m³)	TF (m³)	TSF (m³)	TTF (m³)	Dispersion
1	0.166	0.163	0.169	0.173	0.148	0.154	0.172	0.168	0.119
2	0.169	0.166	0.162	0.159	0.213	0.227	0.171	0.176	0.198
3	0.166	0.163	0.162	0.167	0.157	0.219	0.171	0.171	0.165
4	0.169	0.165	0.162	0.158	0.180	0.140	0.171	0.175	0.176
5	0.149	0.166	0.162	0.160	0.139	0.158	0.167	0.155	0.171
6	0.182	0.177	0.182	0.183	0.162	0.102	0.150	0.156	0.171

TABLE 5: Coordination entropy values of basic elements of six schemes.

Scheme	D (cm)	T (MPa)	C (MPa)	S (MPa)	SF (m³)	TF (m³)	TSF (m³)	TTF (m³)	Dispersion
1	0.298	0.296	0.300	0.304	0.283	0.288	0.303	0.300	0.253
2	0.300	0.298	0.295	0.292	0.329	0.337	0.302	0.306	0.321
3	0.298	0.296	0.295	0.299	0.291	0.333	0.302	0.302	0.297
4	0.300	0.297	0.295	0.292	0.309	0.275	0.302	0.305	0.306
5	0.284	0.298	0.295	0.293	0.274	0.292	0.299	0.289	0.302
6	0.310	0.306	0.310	0.311	0.295	0.233	0.285	0.290	0.302

TABLE 6: Coordination degrees of the basic elements of six schemes.

Scheme	D (cm)	T (MPa)	C (MPa)	S (MPa)	SF (m³)	TF (m³)	TSF (m³)	TTF (m³)	Dispersion
1	0.039	0.034	0.031	0.024	0.141	0.145	0.000	0.021	0.211
2	0.031	0.026	0.049	0.060	0.000	0.000	0.003	0.000	0.000
3	0.038	0.034	0.049	0.039	0.116	0.013	0.003	0.013	0.074
4	0.031	0.028	0.049	0.063	0.062	0.183	0.003	0.003	0.047
5	0.085	0.026	0.049	0.057	0.166	0.135	0.014	0.056	0.059
6	0.000	0.000	0.000	0.000	0.104	0.309	0.061	0.053	0.059

TABLE 7: Coordination degree of six schemes.

Scheme	1	2	3	4	5	6
Coordination degree	0.644	0.169	0.380	0.470	0.646	0.585

The center distance for the other schemes is calculated similarly. The sums of the five groups of center distances for each scheme are shown in Table 3.

5.2. Calculation of Coordination Degree. According to previous calculation indicators, a collaborative model of mining sequence and production capacity target was established [18, 19], as shown in Figure 7.

The collaborative entropy method was used to calculate the coordination degree of various schemes. The value of entropy and the coordination degree of the system are inversely related. So, the larger the coordination entropy, the lower the coordination degree of the system. The smaller the coordination entropy is, the greater the coordination degree of the system is. According to equation (2), the basic elements in the collaboration model were evaluated and scored, and the calculation results are shown in Table 4 [20]:

$$\theta = \frac{A_i}{\sum_{i=1}^{n} A_i}, \quad (i = 1, 2 \ldots, 6), \tag{2}$$

where θ is the score of the basic element and A_i is the value of the basic element.

Entropy value calculations of the basic elements follow equation (3) and are shown in Table 5.

$$H(s) = -\theta \ln \theta, \tag{3}$$

where $H(s)$ is the value of coordination entropy.

Finally, according to equation (4), the coordination degrees of the basic elements of each scheme were calculated [17]:

$$C_i = \frac{1 - H_i}{H_{\max}}, \tag{4}$$

where C_i is the coordination degree of the basic elements.

The calculated values of the coordination degrees of the basic elements are shown in Table 6.

The coordination degree of each scheme can be obtained by summing the coordination degrees of the basic elements. The calculation results are shown in Table 7.

From the results of the coordination entropy method, the highest coordination degree, 0.646, is found in scheme 5. The second highest is calculated from scheme 1, with a value of 0.644. Therefore, the use of a convex stepped shape in scheme 5 is the best mining scheme.

6. Conclusions

An accurate model of the 870–898 m level in the eastern mining area of the Tiaoshuihe phosphate mine was built, and the model grid was divided for mining sequence optimization. Command flows were written according to the six mining sequences. The results of the six schemes were calculated by using the Mohr–Coulomb constitutive model.

The annual production capacity of the mine was also calculated.

A collaborative model of the mining sequence and productivity target was established. Via the coordination entropy method, the final collaborative degree of the six schemes was determined. It was concluded that scheme 5 is the best, while scheme 1 is the second-best. Therefore, it was recommended that the 870–898 m level of the eastern mining area is mined using a convex stepped shape.

The theoretical research result of this study is that the idea of coordination is introduced into the process of mining sequence optimization and filling optimization. The basic parameters are brought into the coordination model by coordination entropy, and the coordination model includes all kinds of factors that affect the stability in the mining process. Economic indicators can also be taken into account in the future.

Data Availability

The data used to support the findings of this study are included within the article.

Conflicts of Interest

The authors declare that they have no conflicts of interest.

References

[1] W. Pytel and B. Pałac-Walko, "Geomechanical safety assessment for transversely isotropic rock mass subjected to deep mining operations," *Canadian Geotechnical Journal*, vol. 52, no. 10, 2015.

[2] R. H. E. M. Koppelaar and H. P. Weikard, "Assessing phosphate rock depletion and phosphorus recycling options," *Global Environmental Change*, vol. 23, no. 6, pp. 1454–1466, 2013.

[3] T. Szwedzicki, "Pre- and post-failure ground behaviour: case studies of surface crown pillar collapse," *International Journal of Rock Mechanics and Mining Sciences*, vol. 36, no. 3, pp. 351–359, 1999.

[4] J. Lu, "Stability analysis of mined-out areas and optimization of residual ore stoping sequence at pumin iron mine," Master's Thesis, Wuhan University of Science and Technology, Wuhan, China, 2012.

[5] Y. Zou, "Study on the layout of deep mining access and optimization of mining sequence in jinchuan no. 2 mining area," Master's Thesis, Central South University, Changsha, China, 2007.

[6] X. Liu, C. Yang, and Z. Luo, "Numerical simulation optimization of mining sequence in deep mining," *Journal of University of South China (Science and Technology)*, vol. 22, no. 4, pp. 15–21, 2008.

[7] P. Kang and X. Li, "Dynamic simulation of reasonable stoping sequence in middle section of panel in sanshandao gold mine," *Mining and Metallurgical Engineering*, vol. 30, no. 3, pp. 8–11, 2010.

[8] Y. Ning and C. Liang, "Study on Optimization of mining sequence of two-step filling mining method," *Mining Technology*, vol. 14, no. 2, pp. 10–12, 2014.

[9] L. Zhang, J.-H. Hu, X.-L. Wang, and L. Zhao, "Optimization of stope structural parameters based on mathews stability graph probability model," *Advances in Civil Engineering*, vol. 2018, Article ID 1754328, 7 pages, 2018.

[10] J. Hu and L. Zhang, "Platform structure for intelligent underground mining system and its construction," *Mining and Metallurgical Engineering*, vol. 38, no. 6, pp. 1–5, 2018.

[11] Z. Yang, W. Li, X. Li, Q. Wang, and J. He, "Assessment of eco-geo-environment quality using multivariate data: a case study in a coal mining area of Western China," *Ecological Indicator*, vol. 12, no. 107, pp. 1–13, Article ID 105651, 2019.

[12] G. Steiner, B. Geissler, I. Watson, and M. C. Mew, "Efficiency developments in phosphate rock mining over the last three decades," *Resources, Conservation and Recycling*, vol. 105, pp. 235–245, 2015.

[13] M. Shabanimashcool and C. C. Li, "Numerical modeling of longwall mining and stability analysis of the gates in a coal mine," *International Journal of Rock Mechanics and Mining Sciences*, vol. 51, pp. 24–34, 2012.

[14] D. J. Reddish, "Numerical and experimental studies on rock presplitting," *Transaction of Nonferrous Metals Society of China (English Edition)*, vol. 8, no. 4, pp. 705–709, 1999.

[15] C. C. Mendoza, *Experimental and numerical behaviour of deep foundations made up by anker alluvial type piles founded in a porous soil of federal district*, PhD Thesis, University of Brasilia, Brasilia, Brazil, 2013.

[16] K. Liu, Y. Xue, and H. Zhou, "Study on 3D nonlinear visco-elastic -plastic creep constitutive model with parameter unsteady of soft rock based on improved Bingham model," *Rock and Soil Mechanics*, vol. 39, no. 11, pp. 4157–4164, 2018.

[17] M. S. P. Wan, J. R. Standing, D. M. Potts, and J. B. Burland, "Pore water pressure and total horizontal stress response to EPBM tunnelling in London Clay," *Géotechnique*, vol. 69, no. 5, pp. 434–457, 2019.

[18] Q. Chen, K. Zhou, D. Gu et al., "Synergetic mining and cavity synergetic utilization," *China Mining Magazine*, vol. 20, no. 12, pp. 77–80, 2011.

[19] H. Haken, A. Wunderlin, and S. Yigitbasi, *An Introduction to Synergetics*, Kluwer Academic Publishers, Amsterdam, Netherlands, 1995.

[20] Q. Chen, "Study on synergism of hidden danger resources mining and goafs treatment," Ph. D's Thesis, Central South University, Changsha, China, 2009.

Research Article

Stability of Coal Pillar and Roof Movement Characteristics in Roadway Backfill Mining

Hai Lin [1,2] **Renshu Yang,** [1,2] **Yongliang Li** [3] **and Shizheng Fang** [1,2]

[1]*School of Civil and Resource Engineering, University of Science and Technology Beijing, Beijing 100083, China*
[2]*Beijing Key Laboratory of Urban Underground Space Engineering, University of Science and Technology Beijing, Beijing 100083, China*
[3]*School of Energy and Mining Engineering, China University of Mining and Technology (Beijing), Beijing 100083, China*

Correspondence should be addressed to Hai Lin; b20200019@xs.ustb.edu.cn

In order to explore the stability of coal pillar and the characteristics of roof movement during the process of roadway backfill mining (RBM), the 301 backfilling test working face of Ordos Chahasu coal mine is taken as the background. Based on the expansive pressure arch theory, the evolution process of the stope expansive pressure arch in RBM is studied; by establishing a mechanical model for the stability of coal pillars, the interactions between the height, width, and the maximum number of branches are obtained. When the width and height of the branch are both 5 m, the optimal number of the branches is obtained. Then, by establishing a mechanical model for the subsidence of the immediate roof, the process of the immediate roof subsidence is divided into three stages, namely, the formation stage of the local pressure arch, the merge stage of the pressure arch, and the expansion stage of the pressure arch. In addition, using the numerical method, the alternate bearing process of coal pillars and filling bodies and the change of the maximum supporting stress are studied, and the evolution of the pressure arch bearing structure above the stope and the staged subsidence characteristics of the roof are analyzed. The on-site test showed that the coal pillar has a good stability during the mining process. The maximum stress of the coal pillar is 16.5 MPa, and the maximum stress of the filling body is 9 MPa. The maximum settlement of the immediate roof is 102 mm, indicating that the roof control effect is good. This research will play an important role on engineering practice.

1. Introduction

The major coal mining region of China has gradually shifted to the western region, and the high-intensity coal mining in the western region has brought a series of social and environmental problems. The traditional caving mining method causes the overlying strata to collapse and develop to the surface, causing surface buildings to settle, soil erosion [1–3], and a large amount of industrial waste, such as gangue, is produced, and the ecological environment continues to deteriorate. In order to reduce the disturbance to the overlying strata and control both the subsidence and deformation of the ground surface, the method of subsidence reduction mining should be adopted [4, 5]. At present, there are mainly two mining systems, partial mining and

filling mining, to control surface subsidence [6]. However, partial mining requires a large number of coal pillars and has a low recovery ratio and a serious waste of resources. The long-term load-bearing strength of coal pillars is gradually weakened, finally causing serious instability and damage [7, 8]. Backfill mining includes longwall backfill mining and roadway backfill mining (RBM). The longwall backfill mining space is small, the mining and backfilling are mutually restricted, and the roof control effect is poor; after the RBM adopts continuous mining and continuous backfilling technology, the mining and backfilling are not carried out in the same branch and do not affect each other. The roof control effect is more prominent [9].

RBM is a support system dominated by backfilling bodies to control the subsidence of the overlying strata

[10, 11]. In the staged mining process, the coal pillar and the filling body bear the load of the overlying strata. The stability of the coal pillar is the key factor that determines the roof movement and the overlying strata structure. Most of the studies focused on the strength of a single coal pillar [12–16], and the stability of the coal pillar group of RBM are ignored. In terms of roof movement and control mechanism, Zhang et al. [17] explored the development mechanism of water-conducting fracture in the overlying rock in RBM; Sun et al. [18] established a mechanical model of the roadway back-filling stope, deduced the stope roof equation and the coal pillar load-bearing formula, and put forward the basis for coal pillar instability; Deng et al. [19] established a mechanical model for the roof movement of extrathick coal seams and proposed the roof instability and fracture conditions; the above studies explored the roof and overlying strata movement mechanism of RBM and promoted the field application of RBM. However, these studies did not consider the influence of RBM coal pillar group stability on roof movement; in fact, as the length of the working face increases, the load on the coal pillars also increases, which intensifies the subsidence of the stope roof. Therefore, it is necessary to consider the influence of the stability of the coal pillars on the roof subsidence to ensure that the roof deformation of the stope is controlled within a reasonable range.

Based on the theory of expansive pressure arch and ultimate strength theory, this paper established a mechanical model of the coal pillar group for RBM, derived the immediate roof subsidence calculation formula of the stope, and proposed the settlement calculation method of the overlying strata, which provides reference for the parameter design of the branch. Through numerical simulation, the load-bearing process of coal pillars and filling body and the characteristics of roof movement in the process of RBM are studied; finally, the on-site test using RBM has been adopted in Chahasu Mine and has achieved good results, hoping to provide a theoretical basis for field applications under the same conditions.

2. Project Overview

2.1. Engineering Background. Chahasu Mine is located in Ordos City, Inner Mongolia, China (Figure 1(a)). The climate in this area is arid, and the surface vegetation is sparse (Figure 1(b)). The annual output of gangue reaches 1 million tons, which is accumulated on the surface, and the ecological environment continues to deteriorate. Therefore, Chahasu Mine has established a RBM test face in the 31st mining area. The backfilling materials are mainly gangue, fly ash, cement, and mine water.

This mining is mainly 3–1 coal; the average thickness of the coal seam is 5 m, the coal seam is nearly horizontal with the inclination angle of 1°~3°, and the average buried depth is 400 m. Assuming that the thickness of each rock strata in the mining area remains unchanged, the typical drilling histogram is shown in Figure 1(c). The immediate roof is

mudstone with 2 m in thickness, the main roof is sandy mudstone with 10 m in thickness, and the immediate bottom is mudstone 12 m in thickness.

2.2. RBM Technology. As shown in Figure 2, the mining and backfilling at the working face are divided into two stages with four phases. First, 5 m wide coal pillars are mined every 15 m and filled, and then, a 5 m coal pillar in the middle of the 15 m coal pillar is mined and filled, this is the first and second phases. In the third and fourth phases, the 15 m coal pillars are mined and backfilled with 5 m coal pillars on the left and right sides, and all the coal pillars of the branches are finally mined. During the mining process, coal pillars are used on both sides of the branches during the first and second phases, which is the first stage of mining. During the third and fourth phases of mining, at least one side is the filling body, which is the second stage of mining. In fact, due to geological conditions and technical reasons, the filling ratio will not reach 100%, and it will take some time for the filling body to reach the design strength. Therefore, before the filling body and the immediate roof are contacted, the load of the overlying strata is mainly borne by the coal pillars, and the stability of the coal pillar determines the control effect of the stope roof.

3. Stability Analysis of Coal Pillars

3.1. The Evolution Process of the Expansive Pressure Arch in Roadway Backfill Mining. As shown in Figure 3, after the branch is excavated, the roof load is transferred to the coal pillars on both sides through the pressure arch, and significant local pressure arches between adjacent coal pillars are generated. With the continuous advancement of the working face, the pressure arches continued to spread outward, superimposed on the coal pillars, and the adjacent pressure arches began to merge, and eventually, an expansive pressure arch composed of high-stress bundles was formed above the stope.

There is a local pressure arch between adjacent coal pillars, and the upper part of the entire stope is an expansive pressure arch. The rock mass outside the arch is compressed, and the rock mass inside the arch is stretched. As the working face excavates, the local stress arch gradually merges, rises, and expands. An enlarged pressure arch is formed. The stability of the overlying strata of the entire stope is determined by the local pressure arch and the expansive pressure arch.

3.2. Coal Pillar Load and Strength. As shown in Figure 4, according to the expansive pressure arch theory [20], after the first stage of mining, the coal pillar in the center of the working face bears the greatest load. Without considering the support conditions, if the bearing capacity of the coal pillar in the center meets the requirements, then all coal pillars in the working face will meet the requirements.
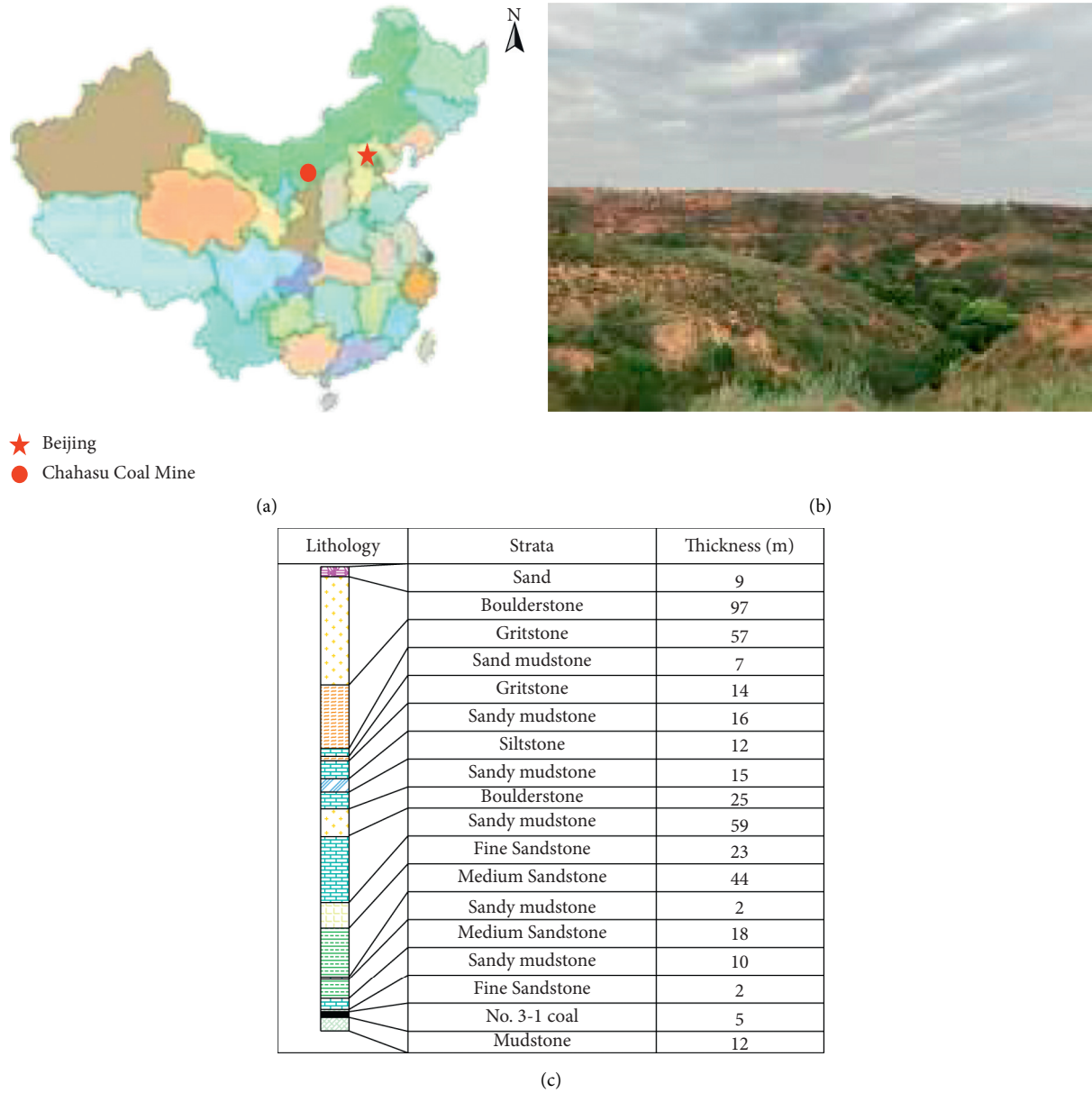
(a)

(b)

Lithology	Strata	Thickness (m)
	Sand	9
	Boulderstone	97
	Gritstone	57
	Sand mudstone	7
	Gritstone	14
	Sandy mudstone	16
	Siltstone	12
	Sandy mudstone	15
	Boulderstone	25
	Sandy mudstone	59
	Fine Sandstone	23
	Medium Sandstone	44
	Sandy mudstone	2
	Medium Sandstone	18
	Sandy mudstone	10
	Fine Sandstone	2
	No. 3-1 coal	5
	Mudstone	12

(c)

FIGURE 1: Chahasu Mine location and drill hole histogram.

3.2.1. Coal Pillar Load. The maximum load of the coal pillar in the working face is as follows[20]:

$$p_{max} = 2b\gamma H, \tag{1}$$

$$H = \frac{W k_s}{2 f_k}, \tag{2}$$

$$W = B + 2h \tan\left(45° - \frac{\varphi}{2}\right), \tag{3}$$

$$B = nb, \tag{4}$$

where H is the height of the expansive pressure arch, m, W is the width of the expansive pressure arch, m, B is the width of the working face, m, n is the number of branches, p_{max} is the maximum load of the coal pillar, MPa, b is the width of the branch, m, γ is the bulk density of the rock formation, kN·m^{-3}, f_k is the general coefficient of the overlying strata, which is generally equal to the 1/10 of the uniaxial compressive strength of the rock, h is the mining height, m, φ is the internal friction angle, °, and k_s is the pressure arch correction coefficient [20] and can be expressed as

$$k_s = \begin{cases} 4.0 \sim 5.0, & f_k \leq 0.8, \text{ unstable rock;} \\ 3.0 \sim 4.0, & 0.8 < f_k \leq 4, \text{ medium rock;} \\ 1.5 \sim 2.0, & 5 < f_k \leq 8, \text{ hard rock.} \end{cases} \tag{5}$$

Then, substituting formulas (3) and (4) into formula (2), the relationship between the height of the expansive pressure arch, the width of the coal pillar, and the number of branches can be written as
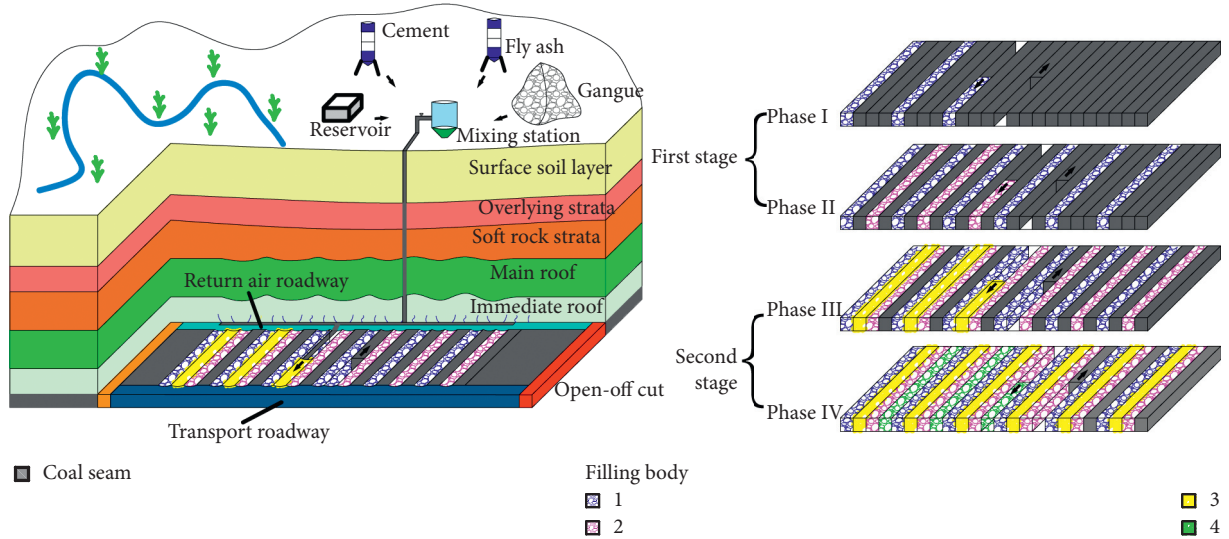
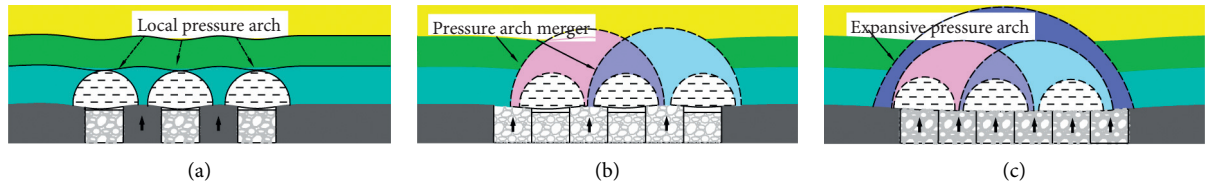FIGURE 2: Working face layout and mining method.

FIGURE 3: The evolution process of the expanding pressure arch in RBM. (a) Local pressure arch. (b) Merging pressure arch. (c) Expansive pressure arch.
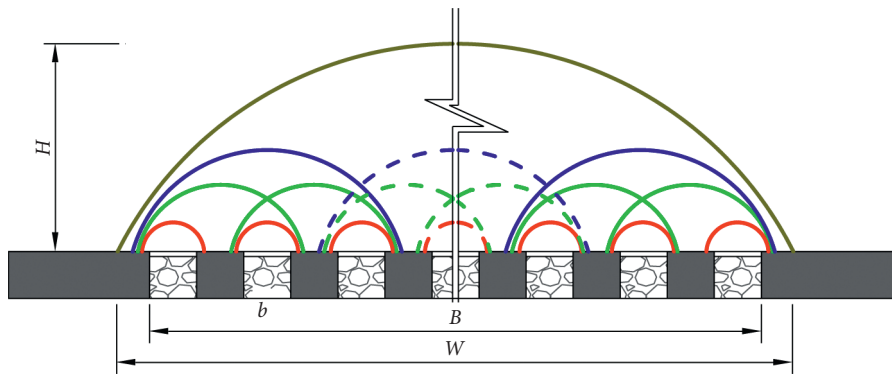

FIGURE 4: Schematic diagram of expansive pressure arch theory.

$$H = \left[nb + 2h \tan\left(45° - \frac{\varphi}{2} \right) \right] \frac{k_s}{2 f_k}. \quad (6)$$

3.2.2. Coal Pillar Strength.

There are many factors that influence the strength of coal pillars, which are not only dependent on the strength of the coal itself but are also related to the size, internal structure, and support strength of the coal pillar. For a long time, many scholars and experts have put forward two coal pillar strength formulas with linear and exponential types based on the field experience and summary [21, 22]. In this paper, without considering the supporting conditions, the exponential formula is used to calculate the strength of coal pillars:

$$\sigma_p = \sigma_m \frac{b^A}{h^B}, \quad (7)$$

where, according to the empirical formula parameters of coal pillar strength proposed by the South African scholar Salamon [20], $\sigma_m = 7.2$ MPa, $A = 0.46$, and $B = 0.66$.

3.3. Stability Analysis of the Coal Pillar.

According to the ultimate strength theory, when the load of the coal pillar reaches the ultimate strength, the bearing capacity of the coal

pillar decreases to zero and begins to lose stability. In RBM, the retention time of the coal pillars will not be too long. When the central coal pillar is in a state of limit equilibrium, formulas (1) and (7) should be combined to determine the maximum number of branches n in the working face to ensure the stability of the coal pillar.

By consulting the geological data of No. 31 mining area of Chahasu Mine, the weighted average of the physical and mechanical parameters of the overlying strata are as follows: the bulk density γ is 25 kN·m^{-3}, the internal friction angle is 35°, the cohesion c is 2 MPa, the general coefficient f_k is 4.6, the lateral pressure coefficient is 1.2, and the pressure arch correction coefficient k_s is 3.625. Assuming the mining height is 3.5 m, 4 m, 4.5 m, and 5 m and the width of the branch is 3.5 m, 4 m, 4.5 m, and 5 m, the strength of the coal pillar and the load curve are obtained, as shown in Figure 5. The integer value at the intersection of the coal pillar load and strength in the curve can determine the maximum number of branches in a mining cycle.

It can be seen from Figure 5 that when the branch width b and the mining height h remain unchanged, the coal pillar load increased approximately linearly with the increase in the number of branches n, and the coal pillar strength remained unchanged; when the number of branches n exceeds the critical value, the coal pillar load increases approximately linearly. The coal pillar load is greater than the strength of the coal pillar, and the coal pillar may begin to lose. The larger the width b of the branch is, the smaller the number n of the branch where the coal pillar reaches the critical strength. In addition, the mining height h has a significant impact on the coal pillar strength. As the mining height h increases, the coal pillar strength begins to decrease, and the critical number of branches n gradually decreases.

In summary, increasing the width of the branch is beneficial to increase the strength of a single coal pillar, reduce the distance of mechanical movement, and improve the mining efficiency. However, the excessive width of the branch limits the number of branches in the working face n, and the coal pillar parameter needs to be optimized according to the on-site conditions; taking the roof conditions and the flexibility of the machinery of the roadheader into account, the mining height is set to 5 m, and the maximum excavation width of the roadheader is 5.5 m. Therefore, the width of the branch is designed to be 5 m, and the maximum number of branches in a mining cycle is 52.

4. Calculation of Roof Subsidence in RBM

4.1. Mechanics Model of Immediate Roof Subsidence.
The RBM technology is completed by filling in different stages. In order to study the influence of the stope roof pressure arch on the movement characteristics of roof subsidence during the staged mining process, the immediate roof is regarded as the beam structure, the coal pillars and the filling body are regarded as elastic foundations, and then, the elastic foundation beam analysis model is established, as shown in Figure 6, where h is the height of the coal seam, b is the width of the branch, k_1 is the elastic coefficient of the coal pillar, and k_2 is the elastic coefficient of the filling body.

According to the description in Section 2, the immediate roof subsidence is mainly divided into three parts. The first part is the subsidence caused by the coal pillar as the main bearing body in the first stage of mining; the second part is the subsidence caused by the first-stage filling body as the main bearing body in the second-stage of mining; when the second-stage filling body reaches a certain strength, all the filling bodies bear the load, and the roof subsidence produced during this period is the third part; the immediate roof settlement d can be expressed as

$$d = d_1 + d_2 + d_3, \tag{8}$$

where d_1 and d_2 are the settlement of the immediate roof during the first and second stages, respectively, and d_3 is the settlement of the roof after all the weight of the overlying strata is transferred to the filling body.

4.2. Immediate Roof Settlement Calculation

4.2.1. Immediate Roof Settlement d_1.
As shown in Figure 7, after the first stage of mining is completed, the overlying strata load is borne by the coal pillar. According to the concept of the yield zone of the coal pillar proposed by AH Wilson [23–26], there is a high-stress core area in the center of the bearing coal pillar due to the constraints, and the supporting capacity of the plastic failure zone on both sides is close to zero, and the width of the plastic failure zone can be expressed as

$$r_p = \frac{h\lambda}{2\tan\varphi}\ln\left(1 + \frac{\sigma\tan\varphi}{c}\right), \tag{9}$$

where r_p is the width of the plastic failure zone, m, σ is the ultimate strength of the coal pillar, MPa, λ is the lateral pressure coefficient of the interface between the plastic failure area and the high-stress core area of the coal pillar, and its value is equal to Poisson's ratio of the coal pillar, and c is the cohesion of the coal pillar, MPa.

Assuming that the width of the high-stress core area is C_l, it can be seen that

$$C_l = b - 2r_p. \tag{10}$$

The average stress acting on the coal pillar σ_z can be written as

$$\sigma_z = \frac{C_l}{b}p_{\max}. \tag{11}$$

After the first stage of mining, the maximum settlement of the immediate roof is

$$d_1 = h\frac{\sigma_z}{E_c} = \frac{hC_l p_{\max}}{bE_c}, \tag{12}$$

where E_c is the Young's modulus of coal, GPa.

4.2.2. Immediate Roof Settlement d_2.
After the first stage of mining, the amount of roof settlement is d_1, and the filling height is h- d_1. In the second-stage mining, the overlying strata load is mainly supported by the first-stage filling body.
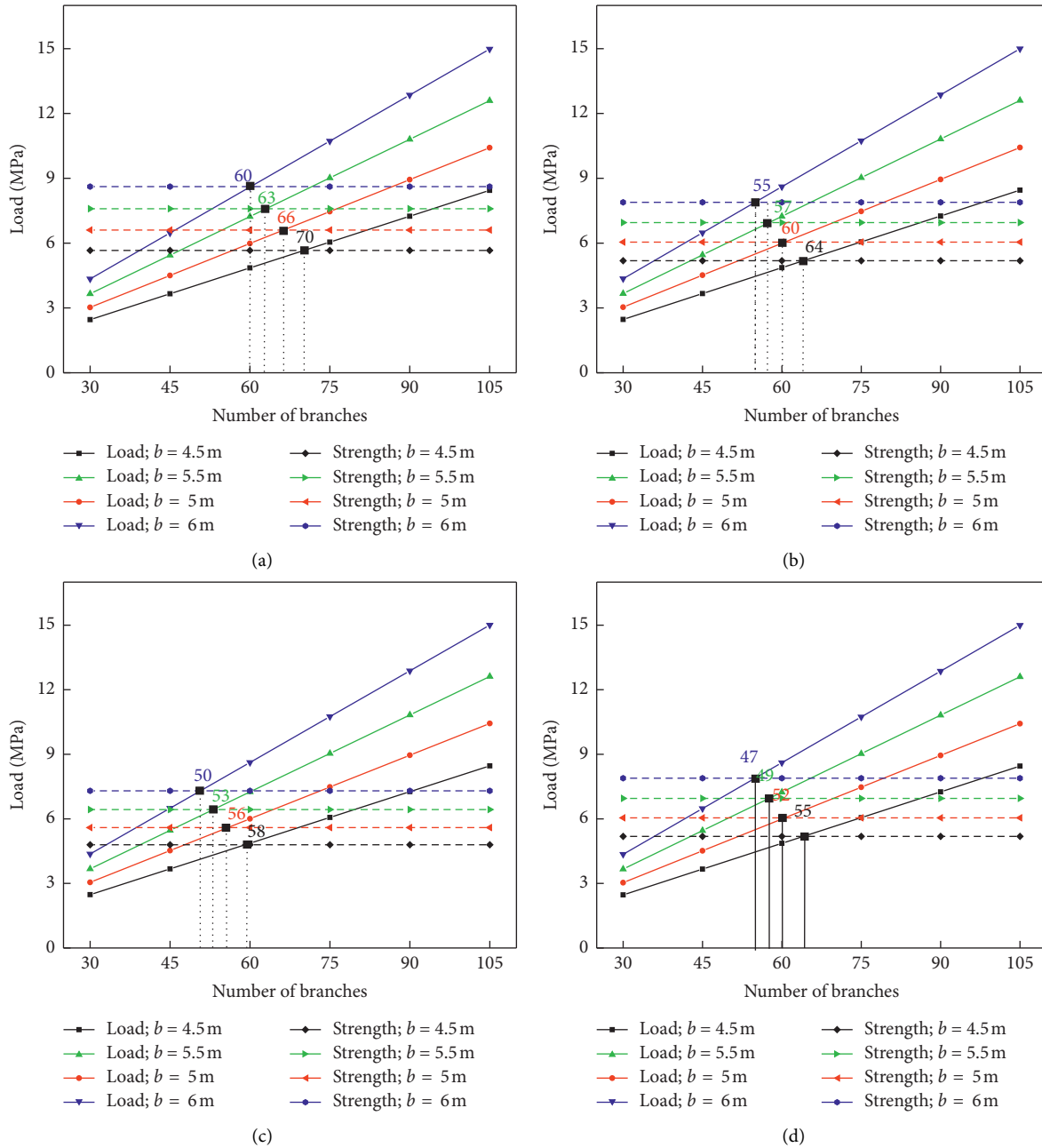
(a)

(b)

(c)

(d)

FIGURE 5: Coal pillar strength and coal pillar load. (a) $h = 3.5$ m. (b) $h = 4$ m. (c) $h = 4.5$ m. (d) $h = 5$ m.

According to equations (1), (9), and (10), the maximum settlement of the immediate roof after the second-stage mining can be calculated as

$$d_2 = (h - d_1)\frac{\sigma_z'}{E_b}, \tag{13}$$

where E_b is the Young's modulus of the filling body, GPa, and σ_z' is the overlying strata load borne by the filling body during the second-stage mining, MPa.

4.2.3. Immediate Roof Settlement d_3. When the coal pillar is replaced by the filling body, the load of the overlying strata in the coal is borne by all filling bodies. According to the elastic foundation assumption [25], the subsidence of any point on the foundation surface is proportional to the pressure on that point, which can be determined as

$$2b\gamma'H' = \frac{E_b b}{h - d_1}(d_2 + d_3) + \frac{E_b b}{h - d_1 - d_2}d_3, \tag{14}$$
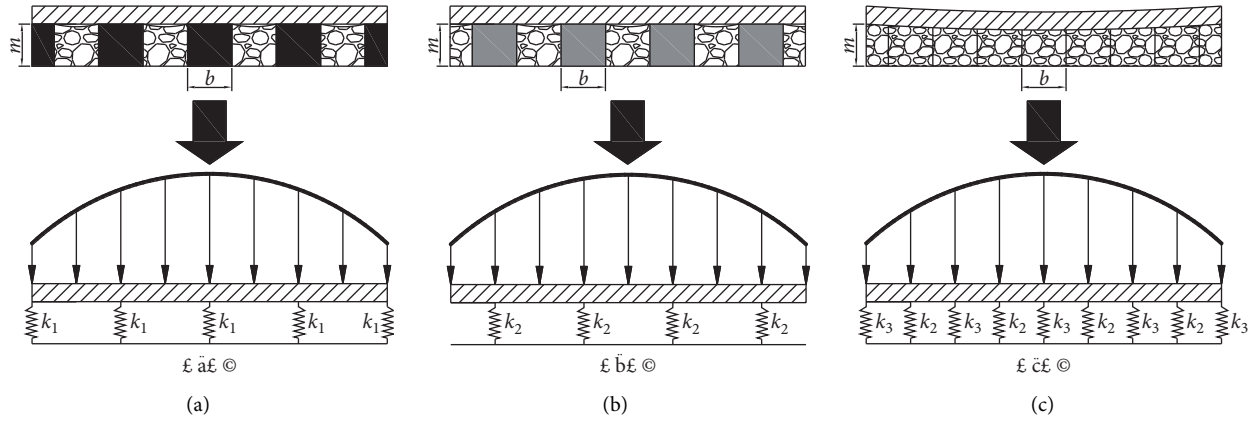
FIGURE 6: Mechanics model of RBM. (a) First stage. (b) Second stage. (c) Third stage.
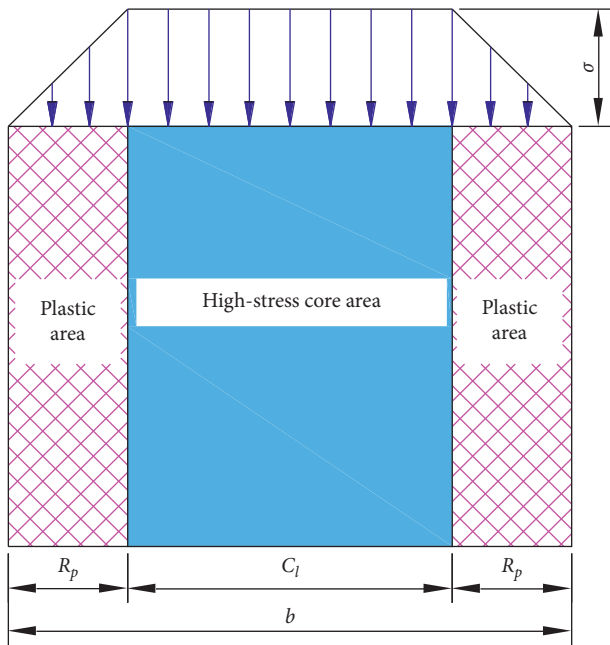
FIGURE 7: Distribution pattern of the load borne by the coal pillar.

where γ' is the average bulk density of the overlying strata, $kN \cdot m^{-3}$, H' is the buried depth of the coal seam, m, and d_3 can be determined according to the following formula:

$$d_3 = \frac{2\gamma'H'(h - d_1) - E_b d_2}{(2h - 2d_1 - d_2)E_b}(h - d_1 - d_2). \quad (15)$$

Then, the maximum settlement of the immediate roof is

$$d = d_1 + (h - d_1)\frac{\sigma'_z}{E_b} + \frac{2\gamma'H'(h - d_1) - E_b d_2}{(2h - 2d_1 - d_2)E_b}(h - d_1 - d_2). \quad (16)$$

According to the conditions of the Chahasu Mine, the elastic modulus E_c of the coal seam is 2.0 GPa, Poisson's ratio μ_c is 0.24, internal friction angle φ is 28°, cohesive force c is 2 MPa, elastic modulus E_b of the filling body is 0.82 GPa, Poisson's ratio μ_b is 0.25, and immediate roof settlement is 117.5 mm.

According to the experimental mechanical parameter test of on-site coal samples and filling bodies, the elastic modulus E_c of the coal seam is 2.0 GPa, Poisson's ratio μ_c is 0.24, internal friction angle φ is 28°, cohesive force c is 2 MPa, elastic modulus E_b of the filling body is 0.82 GPa, and Poisson's ratio μ_b is 0.25, and it can be calculated that the immediate roof settlement is 117.5 mm.

5. Numerical Simulation

5.1. Numerical Model. In order to study the stability of the coal pillar and the roof stress and deformation evolution law of the RBM, taking the engineering geological conditions of Chahasu Mine as the background, a numerical model is established using the FLAC3D, as shown in Figure 8. The size of the model is 240 m × 1 m × 150 m. The constitutive relationship is the Mohr–Coulomb criterion. In order to eliminate boundary effects, 80 m coal pillars are reserved on both sides of the model, and the horizontal displacement around the model and the vertical displacement at the bottom are fixed; the mechanical parameters are shown in Table 1.

After the model is established, the initial balance calculation is carried out. In the first phase, a 5 m coal pillar was excavated, leaving 15 m and backfilled; in the second phase, the middle 5 m of the 15 m coal pillar was excavated and backfilled; the subsequent phases 3 and 4 were excavated and backfilled with 5 m coal pillars on the left and right sides, respectively, and a total of 20 branches were excavated. During the mining and backfilling process, the deformation and stress state of the stope roof are monitored.

5.2. Result Analysis

5.2.1. Analysis of Stress. As shown in Figure 9, during the entire mining process, the coal pillars and filling bodies are alternately loaded, and the vertical stress above the working face is distributed in a pressure arch shape with the mining of the working face. As mining continues to advance, the pressure arches continue to merge, rise, and expand, and the compressive stress of the stope continuously shifts from the side of the working face to the coal wall.
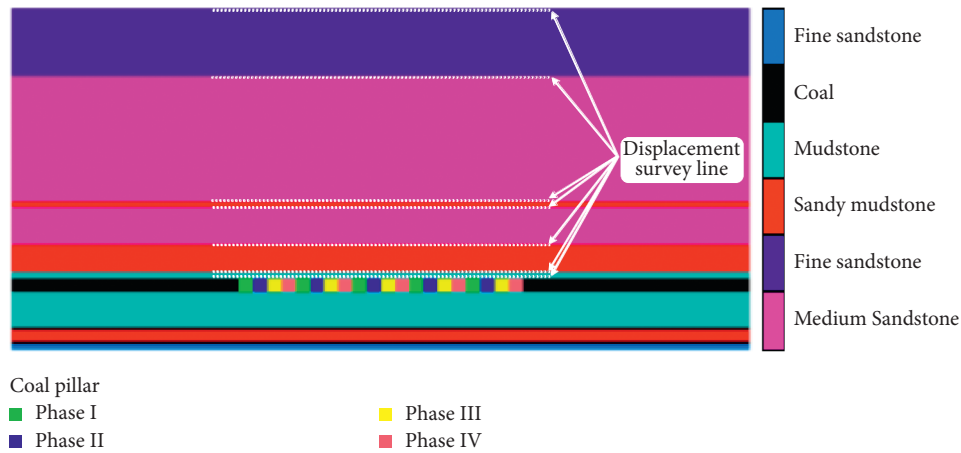
FIGURE 8: RBM calculation model.

TABLE 1: Physical and mechanical parameters of each rock formation.

Lithology	Density (kg·cm³)	Tensile strength (MPa)	Cohesion (MPa)	Internal friction angle (°)	Bulk modulus (GPa)	Shear modulus (GPa)
Fine sandstone	2550	2.5	1.13	30	6.20	4.15
Medium sandstone	2500	2.4	1.12	30	6.17	4.07
Mudstone	2100	0.5	0.22	29	6	5
Coal	1400	1.2	2.0	28	1.94	0.80
Sandy mudstone	2200	0.6	1	28	0.63	0.5
Filling body	1100	1.2	1.3	29	0.9	1.4
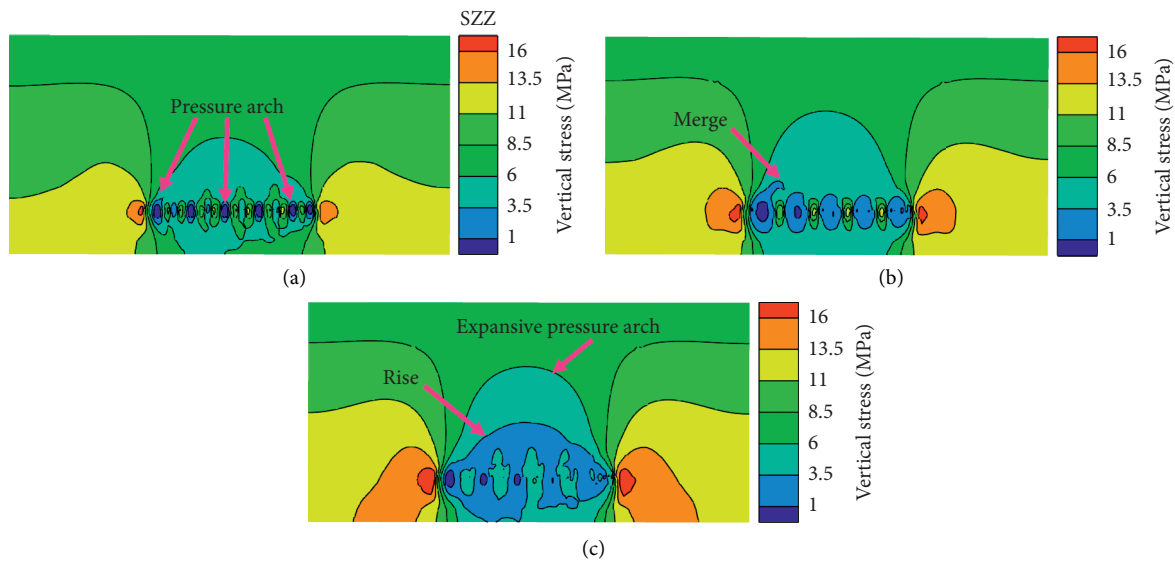
FIGURE 9: Vertical stress. (a) First stage. (b) Second stage. (c) Third stage.

After the first stage mining, the coal pillar is the main bearing body. After the first phases of mining and back-filling, the vertical stress in the central stress core area of the coal pillar is rised to 16 MPa, and the roof above the branch formed a pressure arch distribution. The filling body is not completely compacted, and the compressive stress is 1~3 MPa at this stage; after the second-stage mining, the first-stage filling body is fully in contact with the roof and becomes the main bearing body, and the compressive stress is 7–9 MPa, and the pressure arch above the roof of the branch started to merge and rise, and the second-stage filling body compressive stress is 1~3 MPa; when the second-stage filling body is connected to the roof, the load of the overlying strata is borne by all filling bodies, and finally, a supporting

system dominated by filling bodies is formed to bear the weight of the overlying strata.

5.2.2. Analysis of Roof Subsidence.

5.2.2. Analysis of Roof Subsidence. As shown in Figure 10, the amount of overlying strata subsidence on the working face gradually increases with the staged mining. The immediate roof and main-roof subsidence curves are *w*-shaped with repeatedly upward and downward fluctuations. The rock above the main roof mainly sinks slowly, which can maintain integrity and continuity, and the closer it is to the center of the working face, the greater the amount of the sinking.

After the first stage of mining, the roof is mainly supported by coal pillars. The maximum settlement of the roof above the branch is 114 mm, and the maximum settlement of the main roof is 63.4 mm; in the second stage of the mining, the remaining coal pillars are replaced by the filling bodies, and the first-stage filling body is gradually compacted. At this time, the maximum settlement of the immediate roof is 150.5 mm, and the maximum settlement of the main roof is 136 mm; when the second-stage filling body is connected to the roof, all the filling bodies bear the load of the overlying strata together. The subsidence of the roof continues to increase, and the maximum settlement of the immediate roof is 160 mm. Due to the different degree of compaction and stability, the curve still fluctuates. During the entire mining process, the roof gradually sinks, and the subsidence of the roof is apparently lower than that of caving mining, indicating that the RBM can effectively limit the subsidence and deformation of the overlying strata.

It can be seen from the above results that the numerical results are similar to the theoretical calculation results in Section 4. By adopting the RBM method, the coal pillars and filling bodies can maintain good stability, and the roof subsidence can be controlled within a reasonable range.

6. Engineering Practice

6.1. Main Parameters of the Working Face.

6.1. Main Parameters of the Working Face. The engineering practice site is located at the 301 working face of the 31st mining area in Chahasu Coal Mine, with a branch width of 5 m and a length of 50 m; the filling materials are composed of the coal gangue, cement, fly ash, and mine water, with the weight ratio of 980 : 260 : 350 : 400; the particle size of the gangue after crushing is no more than 15 mm. After 28 days, the strength of the filling body can reach about 9 MPa. Figure 11 shows the actual effect of the roadways after backfilling. Up to now, the 301 face has been fully recovered.

6.2. Application Effect.

6.2. Application Effect. In order to evaluate the effect of RBM, during the mining process, the borehole stress gauge is arranged in the coal pillar and filling body to monitor the stress variation characteristics, and the roof subsidence of the branch is monitored, and the TS-C0601 drilling imaging analyzer is used to monitor the roof of the branch, and the monitoring information mainly includes coal pillar supporting pressure, filling body pressure, roof subsidence, and roof crack development status. Figure 12 shows the sketch diagram of the main monitoring equipment. Figure 13 shows the results of the filling body, coal pillar stress monitoring, and roof subsidence monitoring, respectively. Figure 14 shows the drilling observation results of the filling body, coal pillar, and roof.

From the monitoring data, it can be seen that, in the first stage of the mining process, the coal pillar is the main bearing body; the maximum supporting pressure is 16.5 MPa, and the filling body is not completely compacted; the force changes slowly, and the maximum value is 2.3 MPa. The maximum settlement of the roof is 38 mm; during the second stage of the mining process, the maximum supporting pressure of the coal pillar was 11.5 MPa, and the filling body gradually became the main bearing body, the pressure value increased to 7.1 MPa, and the maximum settlement of the roof was 102 mm. Drilling peeping observation results showed that there are a small number of vertical cracks within 1 m away from the surface of the coal pillar and the filling body, and the deep coal body and the filling body are relatively complete within 1 m, and in the partial separation layers, the vertical cracks are within 2 m away from the surface of the roof. The above roof is relatively complete, and the cracks only developed to the immediate roof.

As shown in Figure 15, during the entire mining process, the filling body was well connected to the roof, and the coal pillars were able to maintain stability, and there was no obvious slabbed spalling phenomenon. A total of about 145,000 tons of coal was mined, and processing gangue was about 260,000 tons, and fly ash was about 90,000 tons. Through adopting RBM technology, both coal pillars and filling bodies can maintain good stability and efficiently constrict the deformation of the stope roof and overlying strata.

7. Discussion

Compared with the longwall backfill mining, the RBM working face layout and mining method are more flexible. The coal mining and filling are carried out in different branches without interfering with each other. The roof is exposed at one time, and the ground deformation is reduced, indicating that the RBM has great potential.

In the process of staged mining, the width of the general branch is between 4.5 and 6 m. If the coal pillar yields and fails under the load of the overlying strata, the pressure of the overlying strata will be borne by the adjacent coal pillars, thus forming an expansive pressure arch. If the width of the coal pillar is wide enough, then a part of the original rock stress area could exist in the middle of the coal pillar. In this case, the number of branches is not limited.

In RBM, coal pillar size, filling rate, filling body strength, and time effect of the filling body will affect the roof control effect. Further consideration should be given to the support strength of the coal pillar, the lateral effect of the filling body on the coal pillar, and the time effect on the strength of coal pillars. Through theoretical analysis, numerical simulation, and on-site test, it is simulated that the roof settlement in the mining area is 117.5 mm, 160 mm, and 102 mm. The results
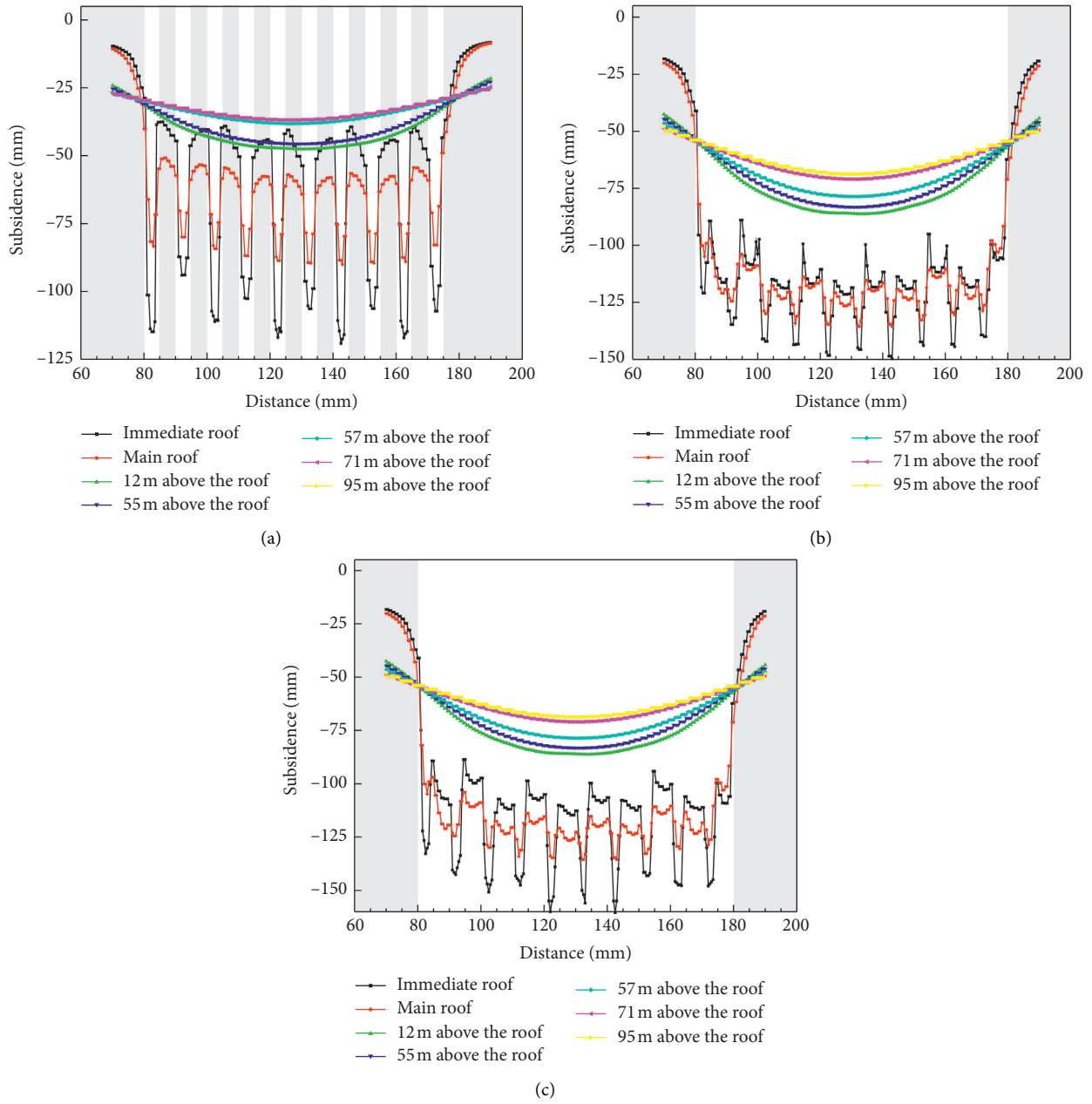
(a)

(b)

(c)

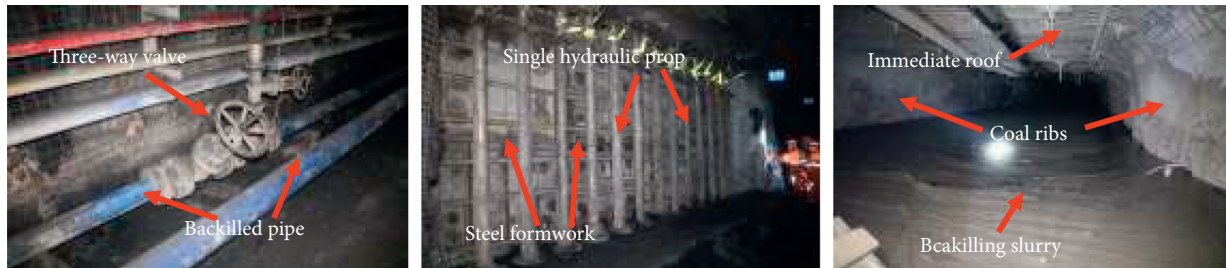FIGURE 10: Roof sinking curve. (a) First stage. (b) Second stage. (c) Third stage.

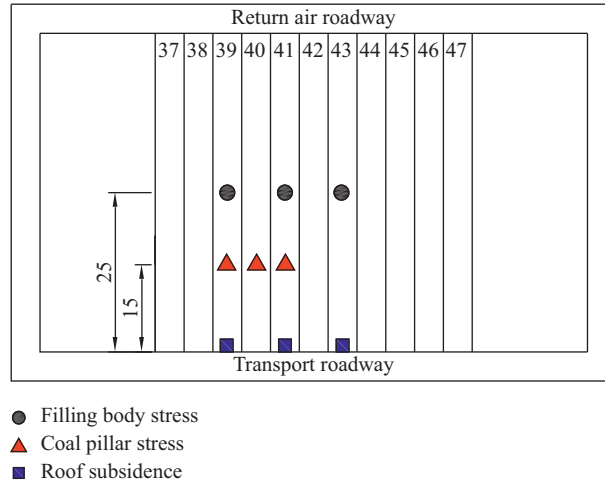FIGURE 11: Photo of the backfilling effect.

FIGURE 12: Schematic diagram of the measuring point layout.
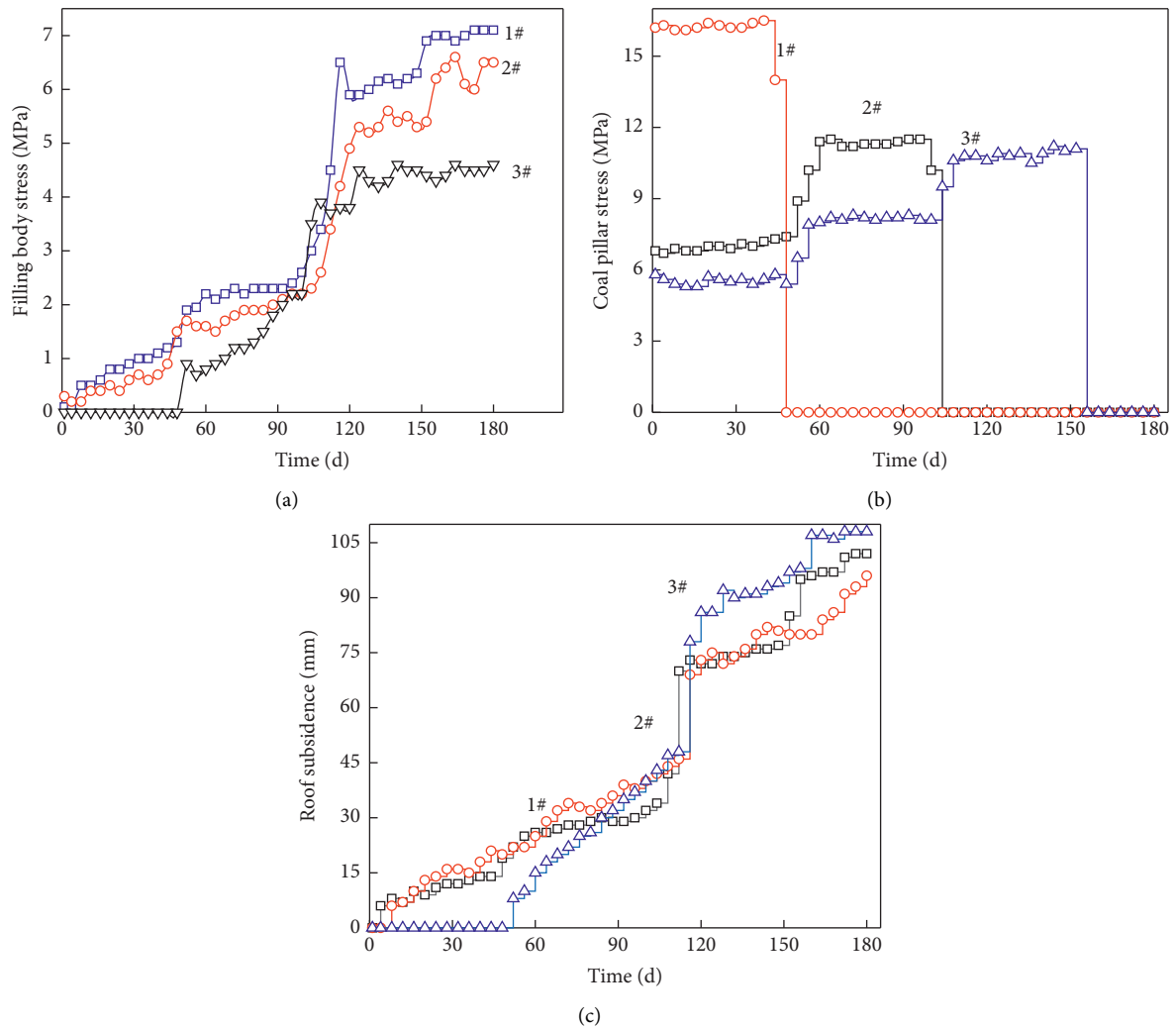

(a)

(b)

(c)

FIGURE 13: Monitoring data. (a) Backfilling body stress. (b) Coal pillar stress. (c) The amount of roof subsidence.

on the site are the smallest, which may be due to the repeated filling of the uncovered area with slurry, thereby increasing the filling rate.

If the RBM technology is adopted in the mining area to deal with coal gangue and the requirements for surface subsidence are not strict, then in the second-stage filling, the
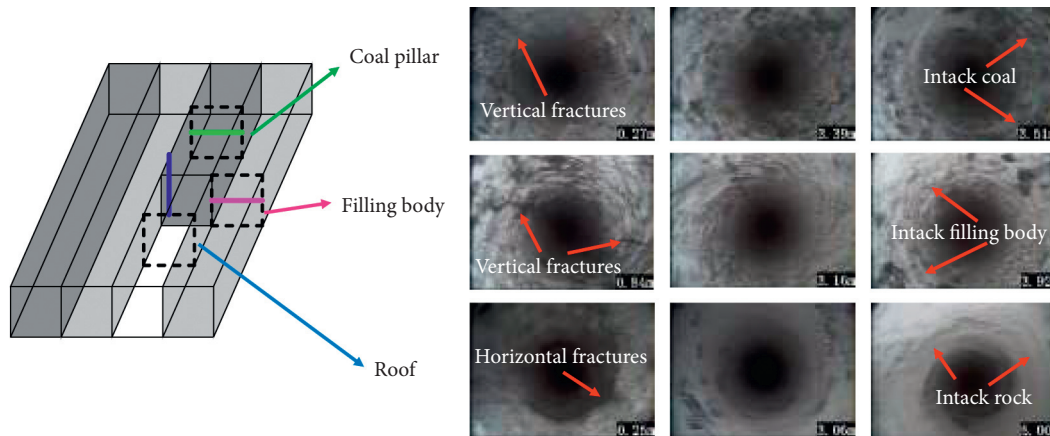
FIGURE 14: Borehole image.
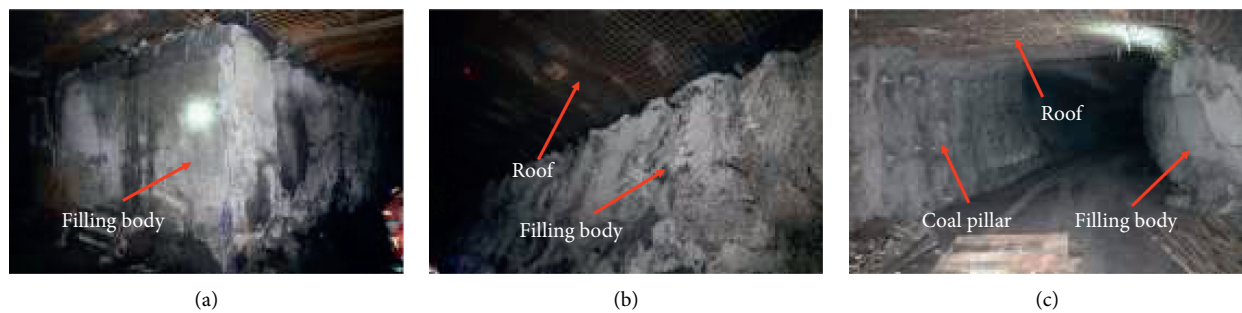
FIGURE 15: Backfilling body. (a) The exposed filling body. (b) The top of the filling body. (c) Coal pillar.

amount of cement can be reduced, the strength of the filling body can be reduced, or the coal gangue can be directly filled to reduce the filling cost.

8. Conclusion

This paper takes the 301 backfill mining test face in Chahasu Coal Mine as the background and explores the influence of the stability of the coal pillar group in RBM on the movement of the stope roof, and the following conclusions are obtained:

(1) Based on the theory of expansive pressure arch, the stability mechanics model of the coal pillar group for RBM is established. When the height and width of the branch are both 5 m, the number of branches does not exceed 52 in one cycle to ensure the stability of the coal pillar.

(2) The pressure arch evolution of the RBM is divided into three stages: the formation of local pressure arches, the merging of pressure arches, and the expansion of pressure arch uplift. The immediate roof subsidence mechanics model is established, and the maximum immediate roof settlement is calculated in stages to 117.5 mm.

(3) Numerical results showed that coal pillars and filling bodies are alternately loaded during the mining process. The peak supporting pressure of coal pillars is 16 MPa, and the maximum pressure of filling bodies is 9 MPa; the sinkage of both the immediate roof and the main roof showed a w-shape. The maximum settlement of the immediate roof is 160 mm, and the overlying strata above the main roof sinks slowly.

(4) Engineering practice showed that the coal pillar is stable in the process of mining. The maximum supporting pressure of the coal pillar is 16.5 MPa, and the maximum pressure of the filling body is 7.1 MPa. The immediate roof of the working face sinks in stages, and the maximum settlement is 102 mm. The filling body has a good control effect on the roof, achieving the purpose of controlling the movement of the overlying strata and processing industrial waste.

Data Availability

The data used to support the findings of this study are included within this article.

Conflicts of Interest

The authors declare that there are no conflicts of interest.

Acknowledgments

References

[1] M. G. Qian, X. X. Miao, and J. L. Xu, "Green mining of coal resources harmonizing with environment," *Journal of China Coal Society*, vol. 32, no. 1, pp. 1–7, 2007.

[2] L. M. Fan, X. D. Ma, Y. H. Li et al., "Geological disasters and control technology in high intensity mining area of western China," *Journal of China Coal Society*, vol. 42, no. 2, pp. 276–285, 2017.

[3] Research Group of National Key Basic Research Program of China (2013CB227900) (Basic Study on Geological Hazard Prevention and Environmental Protection in High Intensity Mining of Western Coal Area), "Theory and method research of geological disaster prevention on high-intensity coal exploitation in the west areas," *Journal of China Coal Society*, vol. 42, no. 2, pp. 267–275, 2017.

[4] X. K. Sun and X. H. Li, "The new technology of waste-filling replacement mining on strip coal pillar," *Journal of China Coal Society*, vol. 3, pp. 259–263, 2008.

[5] G. R. Feng, X. Q. Jia, Y. X. Guo et al., "Study on mixture ratio of gangue-waste concrete cemented paste backfill," *Journal of Mining & Safety Engineering*, vol. 33, no. 6, pp. 1072–1079, 2016.

[6] M. G. Qian, X. X. Miao, and J. L. Xu, "Coal mine green mining technology," *Journal of China University of Mining &Technology*, vol. 4, pp. 5–10, 2003.

[7] F. T. Wang, S. H. Tu, Z. X. Li, H. S. Tu, and F. Chen, "Mutation instability mechanism of the room mining residual pillars in the shallow depth seam," *Journal of Mining & Safety Engineering*, vol. 29, no. 6, pp. 770–775, 2012.

[8] B. An, X. Miao, J. Zhang, F. Ju, and N. Zhou, "Overlying strata movement of recovering standing pillars with solid backfilling by physical simulation," *International Journal of Mining Science and Technology*, vol. 26, no. 2, pp. 301–307, 2016.

[9] B. N. Hu, W. H. Zhang, Q. C. Gao, and P. L. Liu, "Test research on permanent pillar mining with coal refuse backfilling," *Coal Science and Technology*, vol. 11, pp. 46–48, 2006.

[10] B. Q. Wang, S. C. Gu, Q. Fan, and X. B. Li, "Design method of mining room coal pillar in stripe filling mining," *Coal Engineering*, vol. 49, no. 6, pp. 1–5, 2017.

[11] B. Lu, X. G. Zhang, F. Li, B. L. Zhang, and Z. Z. Pang, "Study and application of short-wall gangue cemented backfilling technology," *Journal of China Coal Society*, vol. 42, no. S1, pp. 7–15, 2017.

[12] H. Wang, B. A. Poulsen, B. Shen, S. Xue, and Y. Jiang, "The influence of roadway backfill on the coal pillar strength by numerical investigation," *International Journal of Rock Mechanics and Mining Sciences*, vol. 48, no. 3, pp. 443–450, 2011.

[13] B. F. An, D. D. Wang, J. L. Pang, H. Zhang, and G. L. Cao, "Physical simulation for surrounding rock deformation and bearing capacity of pillars in working face with backfilling mining to recover room mining standing pillars," *Rock and Soil Mechanics*, vol. 46, no. 12, pp. 1–9, 2020.

[14] W. Yu, B. Pan, F. Zhang, S. Yao, and F. Liu, "Deformation characteristics and determination of optimum supporting time of alteration rock mass in deep mine," *KSCE Journal of Civil Engineering*, vol. 23, no. 11, pp. 4921–4932, 2019.

[15] W. J. Yu, G. S. Wu, B. F. An, and P. Wang, "Experimental study on the brittle-ductile response of a heterogeneous soft coal rock mass under multifactor coupling," *Geofluids*, vol. 2019, Article ID 5316149, 15 pages, 2019.

[16] W. J. Yu and K. Li, "Deformation mechanism and control technology of surrounding rock in the deep-buried large-span chamber," *Geofluids*, vol. 2020, Article ID 8881319, 22 pages, 2020.

[17] Y. Zhang, S. G. Cao, X. P. Lai, C. Z. Zhao, and S. Y. Du, "Study on the development mechanism and control of water-conducting fractures in short-wall block backfill mining," *Journal of Mining & Safety Engineering*, vol. 36, no. 6, pp. 1086–1092, 2019.

[18] Q. Sun, J. X. Zhang, W. Yin, N. Zhou, and L. Yang, "Study of stability of surrounding rock and characteristic of overburden strata movement with longwall roadway backfill coal mining," *Journal of China Coal Society*, vol. 42, no. 2, pp. 404–412, 2017.

[19] X. J. Deng, J. X. Zhang, P. Huang, Q. Zhang, and X. F. Hao, "Roof movement characteristics in extra thick coal seam mining with the upward slicing filling technology," *Journal of China Coal Society*, vol. 40, no. 5, pp. 994–1000, 2015.

[20] L. Y. Qin, C. W. Liu, and Y. Q. Fang, "Research on expansive pressure arch theory and rock pillar load about the activity of the covered rock mass in close distance," *Metal Mine*, vol. 12, pp. 20–24, 2007.

[21] J. X. Zhang, X. X. Miao, X. B. Mao, and Z. W. Chen, "Research on waste substitution extraction of strip extraction coal-pillar mining," *Chinese Journal of Rock Mechanics and Engineering*, vol. 26, no. S1, pp. 2687–2693, 2007.

[22] S. J. Chen, J. W. Zhang, D. W. Ying et al., "Mechanism and numerical simulation of filling walls improving performance of coal pillar," *Journal of Mining & Safety Engineering*, vol. 34, no. 2, pp. 268–275, 2017.

[23] W. J. Yu and W. J. Wang, "Strate movement induced by coal-pillar under three circumstances exchanged by gangue backfill and quadratic stability law," *Chinese Journal of Rock Mechanics and Engineering*, vol. 30, no. 1, pp. 105–112, 2011.

[24] A. H. Wilson and J. L. Sun, "Research on determining the size of coal pillar," *Mine Surveying*, vol. 1, pp. 30–42, 1973.

[25] L. X. Wu and J. Z. Wang, "Calculation of yield zone width of coal pillar and analysis of its influencing factors," *Journal of China Coal Society*, vol. 6, pp. 625–631, 1995.

[26] X. X. Miao, F. Ju, Y. L. Huang, and G. L. Guo, "New development and prospect of backfilling mining theory and technology," *Journal of China University of Mining &Technology*, vol. 44, no. 3, pp. 391–399, 2015.

Research Article

A Solution to the Time-Dependent Stress Distribution in Suborbicular Backfilled Stope Interaction with Creeping Rock

Baoxu Yan [ID],[1] **Xingping Lai** [ID],[1] **Hanwen Jia** [ID],[2] **Erol Yilmaz** [ID],[3] **and Chen Hou**[4]

[1]*Energy School, Xi'an University of Science and Technology, Xi'an 710054, China*
[2]*Deep Mining Laboratory, Shandong Gold Group Co., Ltd., Yantai 264000, China*
[3]*Department of Civil Engineering, Geotechnical Division, Recep Tayyip Erdogan University, Fener, Rize TR53100, Turkey*
[4]*Center for Rock Instability and Seismicity Research, School of Resource and Civil Engineering, Northeastern University, Shenyang 110819, China*

Correspondence should be addressed to Hanwen Jia; jiahanwen@sd-gold.com and Erol Yilmaz; erol.yilmaz@erdogan.edu.tr

The creep behavior of deep weak rock masses is important due to an underground opening. Appreciating the nature and source of these deformations requires the knowledge of rock mass and ground support interaction. The theoretical solution of the backfill's internal stresses needs to consider the time-dependent effect. In the present study, the coupling interaction between the creep behavior of the nearby rock material and the internal stresses in the backfilled stope is considered and the interaction characteristics are given analytically. A solution is then proposed regarding the time-dependent stress distribution in suborbicular backfilled stope interaction with creeping rock. Besides, the correctness of the theoretical solution is verified by numerical simulation, while influential parameters such as stope buried depth, lateral pressure coefficient, horizontal stress ratio, creep time of surrounding rock mass, delay time of the backfill, and Young's modulus are thoroughly discussed. Research shows that when the stope buried depth becomes large as well as the rheological effect of the nearby rock materials becomes significant, the stress distribution in the backfill material exceeds its self-weight stress and presents significant time-dependent characteristics. The delayed backfilling weakens the backfill's ground support effect on the nearby rock material. Hence, timely and multipoint simultaneous backfilling is needed for a stope with significant rheological deformation of surrounding rock mass. Lastly, this work will offer useful knowledge while designing the backfill materials for underground mines.

1. Introduction

How to dispose of the mined stope and large number of tailings produced in the mining sector is the current research hotspot [1]. The main aspects of tailings disposal are the use of tailings for construction material [2–4] to absorb carbon dioxide in the atmosphere, to mitigate the greenhouse effect [5], to store tailings on surface disposal areas [6], and prepare them in the cemented fill form to fill the underground mined-out stopes [7]. Among them, the preparation of tailings as cemented mine fill into underground openings is not only beneficial to the environment, regional animal, and plant protection [8] but also can reduce the mining process of ore loss depletion and heavy metal emissions. The mine fill method used can bring significant economic benefits to mines and solve the problem of mining-induced massive surface subsidence, which can be called "One waste management solving two disasters" [9].

However, the backfill mining process also faces new problems, such as how to effectively coordinate the strength requirements with the backfilling cost to achieve maximum economic benefits [10, 11], how to control the barricades destabilization disaster [12, 13], the self-supporting stability of the backfilling mass [14–16], and how to ensure the stability of the backfilling mass as an artificial pillar or sill pillar [17, 18]. The core issue is the interaction mechanism between mine backfilling and the nearby rock materials [19, 20]. The stress distribution within the backfill and its time dependence should not be neglected since there are significant multiphysical field and time effects in the

settlement, drainage, consolidation, strength acquisition, and microstructure evolution of the backfill after it is filled into the mined-out stopes [21].

With the depletion of shallow resources, more and more mines are moving towards deeper mining. The surrounding rock mass under the influence of high temperatures and high stresses at depth will show significant rheological effects [22], which are quite different from the deformations of shallow nearby rock materials; the stress redistribution around the nearby rock material under the influence of mining activities is not instantaneous but rather a gradual development over time [23, 24]. The aging of deformation resulting from this progressive development is likely to occur in weak [25] or jointed rock mass [26, 27] under the effect of high ground stresses. Thus, the effect of the development of deformation on the internal stress distribution of backfilling is not instantaneous but rather a gradual evolution of the nearby rock material under the effects of excavation sequence, large stresses, and temperature conditions [28, 29].

Theoretical analyses can provide a preliminary and rapid estimation of the stress distribution inside the backfill, which is very useful for the initial assessment of filling capacity and options [30, 31]. Until now, numerous works have been undertaken on the internal stress distribution of the backfill, including two- and three-dimensional analytical solutions for the backfilled stope's internal stresses, taking into account the shape and inclination of the stope [19, 32–39] and the saturated conditions of filling [33]. However, the effect of time-dependent deformation of rock on the backfill has been neglected so far. This is usually reasonable in shallow stope or in places where the creep behavior of the nearby rock material is not apparent [40]. However, for deep, high stress and temperature rock mass, many studies show that the rock' creep behavior is significant, and the stress distribution in the backfill will be largely affected by creeping rock mass [18]. This phenomenon is also seen in the field monitoring with regard to the time-dependent stress distribution in the backfill. Unfortunately, no research results regarding analytical solutions have been published to solve the problem of the backfill's time-dependent stress distribution.

In this study, the creep behavior of the mechanism between mine filling and the nearby rock material was analyzed. The theoretical solution of the interaction between the circular roadway and the filling mass was also established while a solution to the time-dependent stress distribution in suborbicular backfilled stope interaction with creeping rock was given. The accuracy of the solution is verified by the numerical simulation. Finally, the geometry and depth of the backfilled stopes and their geo-stress conditions were also analyzed while discussing the changes in the backfill's internal stresses.

2. Interactions between Rock and Backfill

Immediately after the formation of stope, elastic or elastoplastic behavior of the nearby rock material occurs, which is generally considered to be time-independent and can be accomplished in a very short period of time [41]. It generally takes some time for the backfill to fill the stope, depending on the filling capacity and the size of the stope. After the backfill placement into mined-out voids, it needs some time to harden [42]. Thus, it tends to lag behind the elastic or plastic deformation of the surrounding rock material [22]. However, the nearby rock material continues to undergo significant rheological effects due to the stresses in the surrounding rock, and the deformation converges to stope [17]. The deformation is time-sensitive. After filling the stope, the backfill material can be considered as a passive support structure without the ability to generate active support for the nearby rock material. The magnitude of the backfill's ground support is limited by the ability of the nearby rock material to squeeze the backfill. The support reaction force generated by backfilling is passive in nature; only when the nearby rock material deforms and squeezes the backfilling, the backfill will produce some support reaction force on the nearby rock material, and the effect of this support reaction force is affected by the size and nature of the mining space [43]. The support reaction of the backfill on rock will affect the development of creep (time-dependent) deformation of the nearby rock material. Thus, the interaction between mine fill and the nearby rock material has a temporal and spatial coupling effect.

Figure 1 displays the time-dependent interface between creeping rock and filling material. It is considered that the temporal deformation that occurs after the completion of excavation is mainly the creep behavior of the nearby rock material influenced by geo-stress. The expansion and shrinkage deformation can occur when cementitious backfill is affected by drainage, consolidation, and cementation hydration processes, and this process is time-dependent, as confirmed by the results of previous research [44, 45]. Shrinkage of backfill will delay the squeezing pressure from rock mass on the filling mass and thus weaken the supporting effect. The convergent deformation of the nearby rock material into the backfilled openings or stope effected by excavation and ground stresses has a competing effect with the possible shrinkage and expansion deformation of the backfill in terms of interaction forces. In addition, after the backfill is poured into the stope, a hardening process occurs in the backfill, and its strength and stiffness greatly change over time and not evenly distributed throughout the backfilled stope, resulting in differences in the supporting force on the surrounding rock mass. The squeezing force from surrounding mass on the filling mass also changes with the time-dependent creep behavior of the nearby rock material [18], which may result in an interaction time domain and a completely noninteraction time domain as shown in Figure 1.

In this study, we assume that the interaction between mine fill and the nearby rock material conforms to the deformation harmony relation; thus, the interaction force can be set as $q(t)$. Then, we consider the hardening process of the mine backfill, the creep behavior of the nearby rock material, and the shrinkage strain of filling to form a unified spatial-temporal coupling model of the interaction, as shown in Figure 2.

After the excavation, transient elastic stress self-adjustments occur, and the backfill does not contribute to the
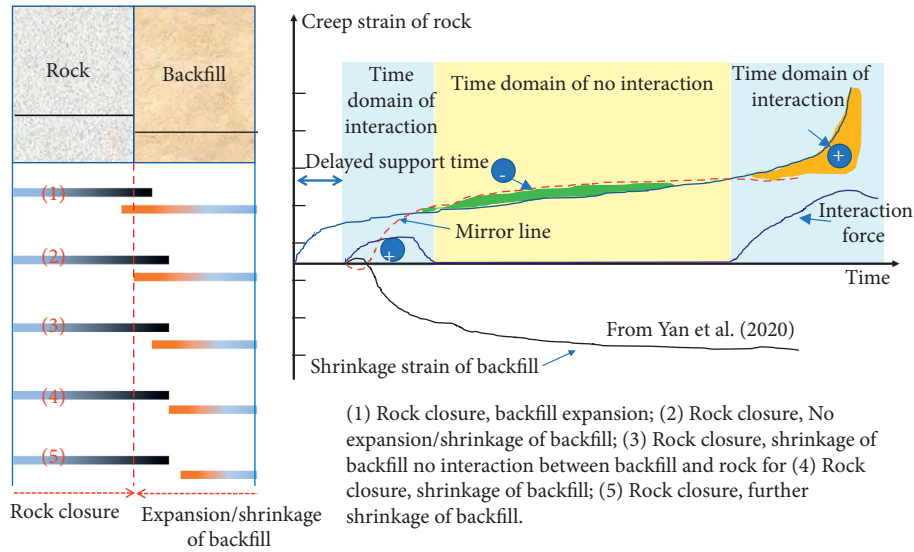
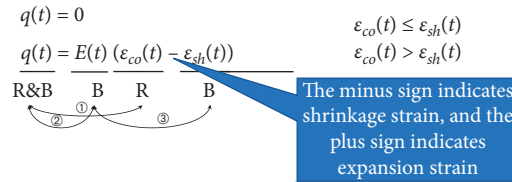FIGURE 1: Diagram of the time-dependent interaction mechanism between backfill and rock.

FIGURE 2: The coupling relationship between backfill stiffness, shrinkage strain, and support force (R is the rock, B is the backfill, $\varepsilon_{co}(t)$ is the creep behavior of the nearby rock material, and $\varepsilon_{sh}(t)$ is the backfill's shrinkage deformation).

transient deformation of that part of the surrounding rock mass but only to the subsequent creep deformation part. Three main interaction processes are as follows:

(1) The large area support of the filling material causes the stress level of the nearby rock material to change, which changes the size and rate of the time-dependent behavior of the nearby rock material. The compression force on backfill produced by the creep behavior of the nearby rock matrices can change the supporting force of backfilling on the rock material, which is a bidirectional coupling process.

(2) The hardening process of the backfill is usually influenced by the cement hydration process, and the changes of elastic modulus and stiffness are time-sensitive and are also governed by water-to-cement (w/c) ratio, concentration, additives, curing conditions, and other factors. The squeezing force exerted on the backfill by the surrounding rock mass puts the backfill under stress curing conditions, which in turn affects the change of elastic modulus and strength.

(3) The changes in the backfill's elastic modulus and stiffness will affect the shrinkage and expansion strain, which can greatly affect the elastic modulus and stiffness performance of backfilling, mainly in the internal structural damage caused by the incongruent deformation.

3. Proposed Analytical Solution

3.1. Viscoelastic Theory Solution

3.1.1. Infinite Round Hole under Weak Support of Backfilling. In this study, it is presumed that the evenly distributed supporting force generated by the backfill on the surrounding rock mass is $q(t)$, and then

$$q(t) = E_b \sqrt{\left(\varepsilon_r^2 + \varepsilon_\theta^2\right)}. \tag{1}$$

At the perimeter of the round hole, $\varepsilon_\theta = 0$ and $q(t) = E_b[\varepsilon_r(t) - \varepsilon_r(0)]$, where $\varepsilon_r(0)$ is the initial strain value at the moment when the rheological behavior of the nearby rock material begins, i.e., the elastic convergence value after the excavation effect. $\varepsilon_r(t)$ is the strain at time 't' of creep of the nearby rock material. The elastic modulus E_b of the backfill is time-dependent and a function of time. Figure 3 demonstrates a theoretical model of the deformation of the backfill with evenly distributed weak support and perimeter rock mass under plane strain conditions affected by the stresses at the remote site.

The expressions of radial stress $\sigma_r[t]$, circumferential stress $\sigma_\theta[t]$, and shear stress $\tau_{r\theta}$ under the influence of backfill support are as follows:

$$
\begin{cases}
\sigma_r[t] = -\dfrac{p+\lambda p}{2}\left(1-\dfrac{a^2}{r^2}\right) + \underbrace{\dfrac{p-\lambda p}{2}\left(1-\dfrac{4a^2}{r^2}+\dfrac{3a^4}{r^4}\right)\cos 2\,\theta}_{\mathbb{A}} - \dfrac{a^2 q(t)}{r^2}, \\[4mm]
\sigma_\theta[t] = -\dfrac{p+\lambda p}{2}\left(1+\dfrac{a^2}{r^2}\right) - \underbrace{\dfrac{p-\lambda p}{2}\left(1+\dfrac{3a^4}{r^4}\right)\cos 2\,\theta}_{\mathbb{B}} + \dfrac{a^2 q(t)}{r^2}, \\[4mm]
\tau_{r\theta} = \underbrace{\dfrac{p-\lambda p}{2}\left(1+\dfrac{2a^2}{r^2}-\dfrac{3a^4}{r^4}\right)\sin 2\,\theta}_{\mathbb{C}}.
\end{cases}
\tag{2}
$$

The Hoek law is expressed by deviator stress and deviator strain, and creep strain is introduced e_c:

$$
e_{\text{total}} = e_e + e_c = \frac{S_{ij}}{2G} + e_c.
\tag{3}
$$

The following empirical formula is used for the creep constitutive equation of surrounding rock mass for its convenience for parameter acquisition and engineering application [46]:

$$
e_{ij} = \frac{3}{2} S_{ij} A \sigma_e [\varepsilon_r(t)]^{m-1} t^n \exp\left(\frac{-\Delta H}{RT}\right).
\tag{4}
$$

Then, the strain expression is as follows:

$$
\begin{cases}
\varepsilon_r(t) = \varepsilon_m + \dfrac{\sigma_r[t]-\sigma_m}{2G} + (\sigma_r[t]-\sigma_m)\dfrac{3}{2}A\sigma_e[t]^{m-1}t^n\exp\left(\dfrac{-\Delta H}{RT}\right), \\[4mm]
\varepsilon_\theta(t) = \varepsilon_m + \dfrac{\sigma_\theta[t]-\sigma_m}{2G} + (\sigma_\theta[t]-\sigma_m)\dfrac{3}{2}A\sigma_e[t]^{m-1}t^n\exp\left(\dfrac{-\Delta H}{RT}\right), \\[4mm]
\varepsilon_z = 0,
\end{cases}
\tag{5}
$$

where $\sigma_z = \mu(\sigma_r + \sigma_\theta)$, mean stress $\sigma_m = ((1+\mu)/3)[\sigma_r + \sigma_\theta]$, mean strain $\varepsilon_m = (\sigma_m/E)(1-2\mu)$, and mean effective stress $\sigma_e[t] = \sqrt{(3/2)[(\sigma_r-\sigma_m)^2 + (\sigma_\theta-\sigma_m)^2 + (\sigma_z-\sigma_m)^2 + 2\tau_{r\theta}^2]}$.

Therefore, under the effect of the interaction between mine filling and the nearby rock material, the radially viscoelastic strain $\varepsilon_r(t)$ and tangentially viscoelastic strain $\varepsilon_\theta(t)$ of the nearby rock material are, respectively, as follows:

$$
\begin{cases}
\varepsilon_r(t) = \varepsilon_m + \left\{\mathbb{A} - \dfrac{a^2 q(t)}{r^2} - \sigma_m\right\}\left[\dfrac{(1+\mu)}{E} + \left(\dfrac{3}{2}A\sigma_e[t]^{m-1}t^n\exp\left(-\dfrac{\Delta H}{RT}\right)\right)\right], \\[4mm]
\varepsilon_\theta(t) = \varepsilon_m + \left\{\mathbb{B} + \dfrac{a^2 q(t)}{r^2} - \sigma_m\right\}\left[\dfrac{(1+\mu)}{E} + \left(\dfrac{3}{2}A\sigma_e[t]^{m-1}t^n\exp\left(-\dfrac{\Delta H}{RT}\right)\right)\right].
\end{cases}
\tag{6}
$$

Equation (6) contains the strain term on left/right sides, and the change of the support force may also have some influence on the mean effective stress σ_e, so it cannot be solved explicitly but can be solved iteratively by MATLAB to obtain $\varepsilon_r(t)$. In fact, for the weak support generated by the backfill, the explicit solution by treating the variation of the effective stress $\sigma_e[t]$ as independent variation of the radial strain $\varepsilon_r(t)$ is almost the same as the implicit solution obtained from the numerical solution as conformed in Figure 4 (see the next section) so that the explicit expression of $\varepsilon_r(t)$ can be used in the subsequent theoretical derivation. The approximation is proved, where the initial elastic strain $\varepsilon_r(0)$ is as follows:
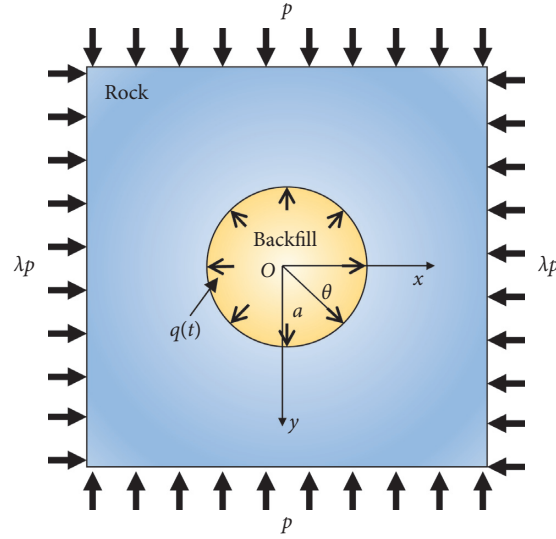
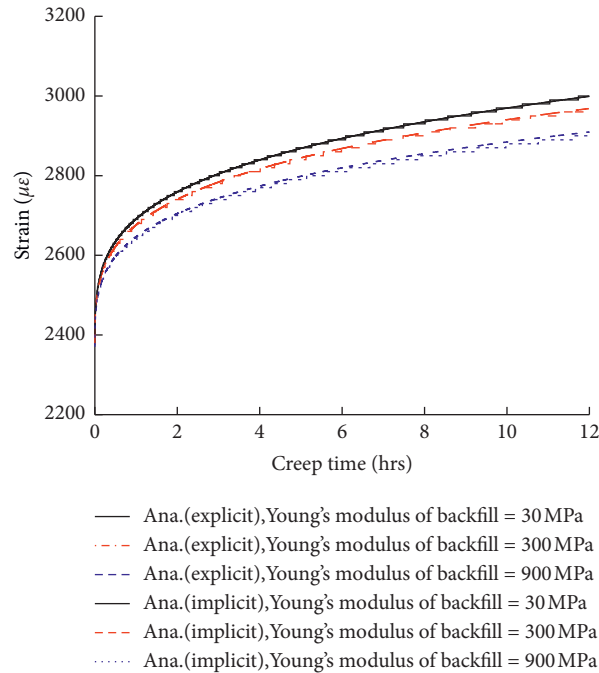FIGURE 3: Schematic of the contact between weak fill support and nearby rock material deformation.

FIGURE 4: Results of coupled implicit solution and uncoupled explicit solution.

$$\varepsilon_r (0) = \varepsilon_m + (\mathbb{A} - \sigma_m) \frac{(1 + \mu)}{E}. \tag{7}$$

3.1.2. Appraisal of Analytical/Numerical Results.

To attest the rationality of the theoretical model in the earlier section, a comparative validation analysis is performed using numerical simulations considering the same boundary conditions and input parameters according to the plane strain problem. To save calculation time, the 1/4 axisymmetric model is selected, as shown in Figure 5. The elastic model is chosen to be the constitutive model of the backfill. A monitoring point is set at P_1 to compare with the theoretical

solution of equation (6). The detailed input factors of the numerical/analytical models are shown in Table 1.

The comparison results are clearly shown in Figures 6 and 7. The change of the elastic modulus of backfill can change the stress distribution of surrounding rock mass. The theoretical solution is consistent with the numerical simulation, which verifies the accuracy of the approach obtained in the earlier section by considering the viscoelastic strain of the nearby rock material under the filling support effect.

In addition, if in hypothesis (6), i.e., $\sigma_e [t] = \sigma_e$, then

$$\mathbb{D} = \frac{(1 + \mu)}{E} + \frac{3}{2} A \sigma_e^{m-1} t^n \exp\left(-\frac{\Delta H}{RT}\right). \tag{8}$$
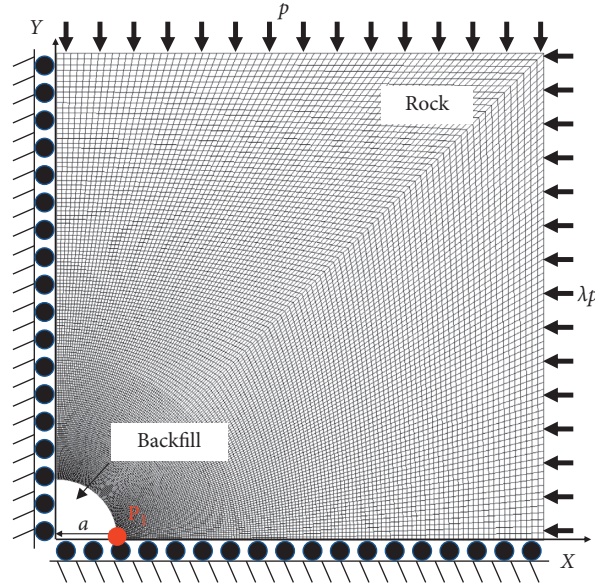
FIGURE 5: Numerical model of creep behavior of nearby rock material under the filling support effect (P1 is the extracted comparison data point).

TABLE 1: Input parameters of the numerical model and analytical model.

Parameters	Analytical results	Numerical results	Unit
Rock material-elastic modulus E_r	8.4	8.4	GPa
Rock material-Poisson ratio ν_r	0.29	0.29	1
Mine backfill-elastic modulus E_b	0, 30, 300, 900	0, 30, 300, 900	MPa
Mine backfill-Poisson's ratio ν_b	0.33	0.33	1
Lateral earth pressure p	10	10	MPa
Lateral earth pressure ratio λ	1	1	1
Radius of circular hole a	3	3	m
Radius of point P_1 position r	3.02608*	3.02608	m

Note. *denotes that it is important to consider the relationship of the difference between the coordinates of the unit stress and the node displacement in the numerical model when comparing with the numerical simulation. Therefore, the r value here should be the coordinates of the center point of the unit in the numerical model since it is at these coordinates that the calculated data can be compared with the theoretical solution.

On the basis of equation (6), $\varepsilon_r(t)$ can be isolated to obtain an explicit approximate expression of the viscoelastic strain of the surrounding rock under the support of the backfill:

$$\varepsilon_r(t) = \frac{\varepsilon_m + \{\mathbb{A} - \sigma_m\}\mathbb{D} + \left(\left(a^2 E_b \varepsilon_{r0}(t=0)\mathbb{D}\right)/r^2\right)}{1 + \left(\left(a^2 E_b \mathbb{D}\right)/r^2\right)}. \tag{9}$$

Figure 4 shows that the coupled implicit solution and the uncoupled explicit solution are essentially the same. For the hypothesis shown above, the explicit solution can be used to examine the impact of mine backfilling on creep behavior of nearby rock material. To a certain extent, the size of backfill stiffness influences the creep behavior of the surrounding rock mass.

3.1.3. Effect of Delay Backfill.

Usually, after excavation, a stope backfilling requires a certain amount of preparation time and cannot be backfilled immediately. To determine the optimal support time for a specific stope and a filling

mass, we need to consider the filling capacity and the condition of the nearby rock material. We need to study the support timing of filling throughout the creep behavior of the nearby rock material. Thus, considering the existence of a delayed support time of t_d for the backfill,

$$q(t) = E_b\left[\varepsilon_r(t) - \varepsilon_r(0) - \varepsilon_{\text{delay}}(t_d)\right], \tag{10}$$

where $\varepsilon_{\text{delay}}(t_d)$ is the amount of creep deformation that occurs in the filler body after the creep deformation of the surrounding rock has gone through t_d. The specific form of $\varepsilon_{\text{delay}}(t_d)$ is as follows:

$$\varepsilon_{delay}(t_d) = (\mathbb{A} - \sigma_m)\frac{3}{2}A\sigma_e[t_d]^{m-1}t_d^n \exp\left(\frac{-\Delta H}{RT}\right). \tag{11}$$

Therefore, the viscoelastic strain of the surrounding rock body when considering the delayed support time of the backfill is solved as follows:
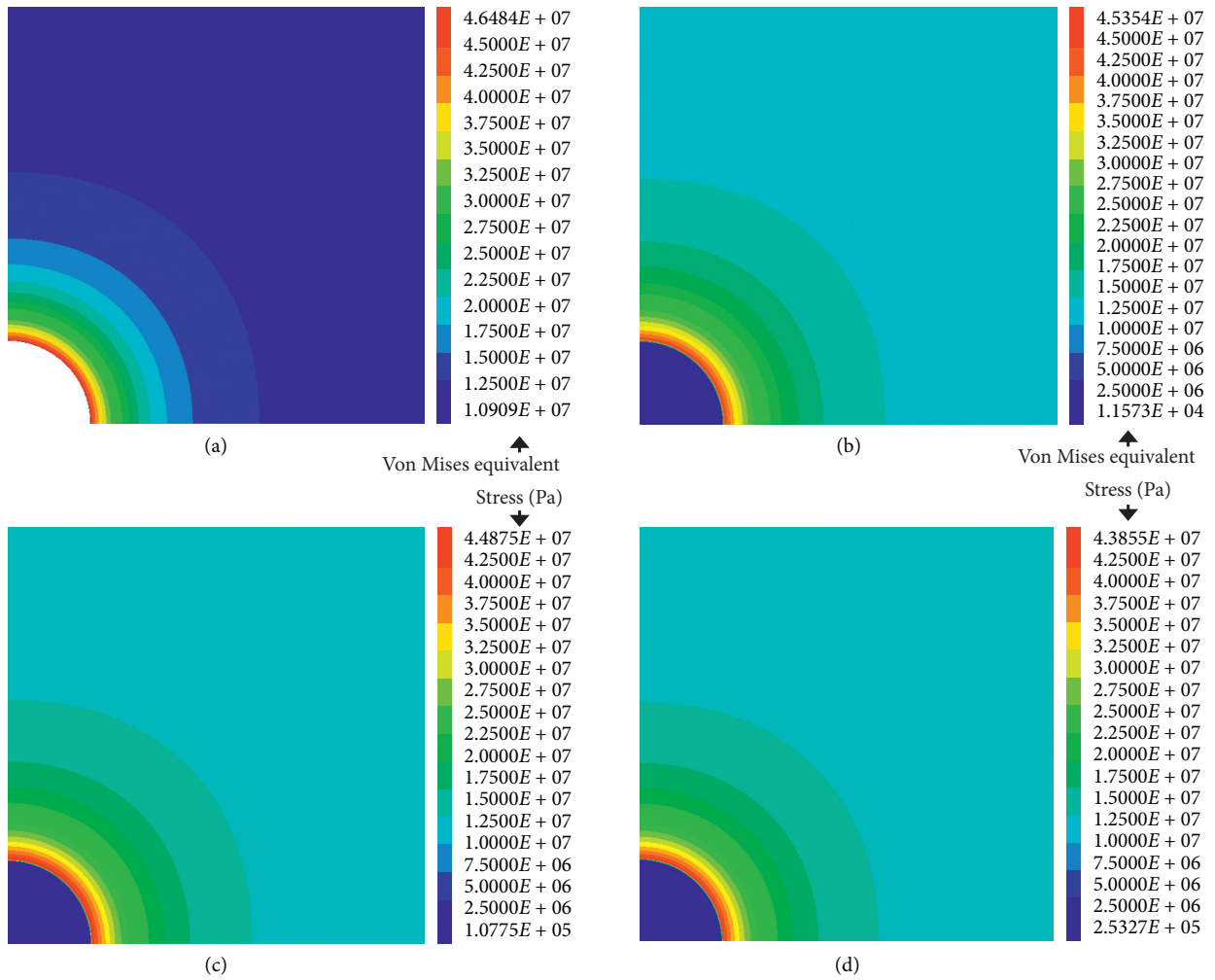
FIGURE 6: Contour of Mises equivalent stress of rock under the influence of different backfill-elastic modulus. (a) Nonbackfill; (b) $(E)_b = 30$ MPa; (c) $(E)_b = 300$ MPa; (d) $(E)_b = 900$ MPa.
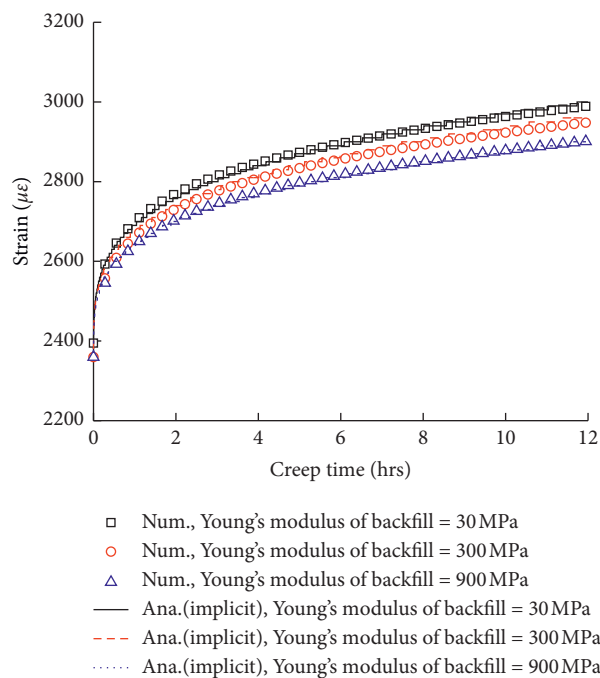

FIGURE 7: Comparison of viscoelastic theoretical solution and numerical simulation of infinite circular hole in backfill support.

$$\begin{cases} \varepsilon_r(t) = \varepsilon_m + \left\{ \mathbb{A} - \dfrac{a^2 E_b \left[\varepsilon_r(t) - \varepsilon_r(0) - \varepsilon_{\text{delay}}(t_d) \right]}{r^2} - \sigma_m \right\} \left[\dfrac{(1+\mu)}{E} + \left(\dfrac{3}{2} A\sigma_e[t]^{m-1} t^n \exp\left(-\dfrac{\Delta H}{RT} \right) \right) \right], \\[4mm] \varepsilon_\theta(t) = \varepsilon_m + \left\{ \mathbb{B} + \dfrac{a^2 E_b \left[\varepsilon_r(t) - \varepsilon_r(0) - \varepsilon_{\text{delay}}(t_d) \right]}{r^2} - \sigma_m \right\} \left[\dfrac{(1+\mu)}{E} + \left(\dfrac{3}{2} A\sigma_e[t]^{m-1} t^n \exp\left(-\dfrac{\Delta H}{RT} \right) \right) \right], \\[4mm] \varepsilon_{r0}(t=0) = \varepsilon_m + \left(\mathbb{A} - \sigma_m \right) \dfrac{(1+\mu)}{E}. \end{cases} \qquad (12)$$

Then, the uncoupled solution of the radial viscoelastic strain $\varepsilon_r(t)$ of the nearby rock material can be integrated as follows:

$$\varepsilon_r(t) = \frac{\varepsilon_m + \{\mathbb{A} - \sigma_m\}\mathbb{D} + \left(\left(a^2 E_b \left(\varepsilon_r(0) + \varepsilon_{\text{delay}}(t_d) \right) \mathbb{D} \right) / r^2 \right)}{1 + \left(\left(a^2 E_b \mathbb{D} \right) / r^2 \right)}. \qquad (13)$$

3.1.4. Effect of Backfills Hardening Process. Regardless of the type of tailings and cement, the strength of backfill will go through a rapid development phase at the beginning and a final stabilization phase (and sometimes a deterioration phase, which is not considered in this study). As shown in Figure 8, the addition of different types of binder ultimately aims to change the rate parameter κ for strength acquisition in the curve, i.e., κ_2 can be considered as the higher rate of backfills strength obtained. The evolution of the backfill strength during the hardening process as a function of curing time is as follows:

$$\begin{cases} \text{UCS}(t) = 0, & t < t_d, \\ \text{UCS}(t) = \text{UCS}_\infty [1 - \exp(-\kappa t)], & t \geq t_d, \end{cases} \qquad (14)$$

where UCS_∞ is the final strength obtained by the backfill and κ is the rate of backfills strength obtained.

Previous research indicated that there exists frequently a certain direct link between strength gaining of cementitious backfill and the modulus of elasticity [47, 48]. This is also conformed by our own laboratory test results for cemented backfill (Figure 9). Thus, it is practical to presume that elastic modulus and strength of backfill during hardening process have the following relation:

$$E(t) = K_{(E/\text{UCS})} \text{UCS}(t), \qquad (15)$$

where $K_{(E/\text{UCS})}$ can be set equal to 218 as shown in Figure 9.

Thus, by presenting equation (15) into (13), the appearance of viscoelastic strain of the nearby rock material under the backfill support effect by considering the hardening process of mine backfilling can be well obtained.

3.2. Analytical Model of Time-Dependent Stress Arching Effect in Backfill. Figure 10 demonstrates that in some cases, the area and volume of the backfilled stope can be assumed to be approximately circular in the vertical direction, and the vertical depth is greater than the width of the cross section. From this, we can use the viscoelastic solution from the plane strain model

obtained in the previous section to analyze the temporal properties of the backfill's stress distribution.

Lateral pressure P is expressed as follows:

$$p = \eta(p_0 + \rho_r g h), \qquad (16)$$

where η is the ratio of horizontal/vertical stress, p_0 is the stress of overlying strata of the backfilled opening or stope, ρ_r is the rock's density, g is the gravitational acceleration, and h is the depth of the backfilled opening or stope.

The p in $\mathbb{A}$ and $\mathbb{B}$ is separated as follows:

$$\begin{cases} \mathbb{A} = -\dfrac{p + \lambda p}{2} \left(1 - \dfrac{a^2}{r^2} \right) + \dfrac{p - \lambda p}{2} \left(1 - \dfrac{4a^2}{r^2} + \dfrac{3a^4}{r^4} \right) \cos 2\theta = p\mathbb{A}', \\[4mm] \mathbb{B} = -\dfrac{p + \lambda p}{2} \left(1 + \dfrac{a^2}{r^2} \right) - \dfrac{p - \lambda p}{2} \left(1 + \dfrac{3a^4}{r^4} \right) \cos 2\theta = p\mathbb{B}'. \end{cases} \qquad (17)$$

The mean strain ε_m and mean stress σ_m can be expressed as follows:

$$\varepsilon_m = p \frac{(1-2\mu)(1+\mu)}{3E} \left[\mathbb{A}' + \mathbb{B}' \right], \qquad (18)$$

$$\sigma_m = p \frac{(1+\mu)}{3} \left[\mathbb{A}' + \mathbb{B}' \right].$$

The instantaneous elastic strain $\varepsilon_r(0)$ formed by initial extraction of the nearby rock material and the creep stress variable $\varepsilon_{\text{delay}}(t_d)$ generated by delayed backfilling of the nearby rock material are as follows:

$$\varepsilon_r(0) = \varepsilon_m + \left(\mathbb{A} - \sigma_m \right) \frac{(1+\mu)}{E}, \qquad (19)$$

$$\varepsilon_{\text{delay}}(t_d) = \left(\sigma_r(t_d) - \sigma_m \right) \frac{3}{2} A\sigma_e^{m-1} t_d^n \exp\left(\frac{-\Delta H}{RT} \right).$$

Consequently, the expression of $\varepsilon_r(t)$ of the radial viscous strain of the nearby rock material can be given as follows:

$$\varepsilon_r(t) = \frac{\varepsilon_m + \{\mathbb{A} - \sigma_m\}\mathbb{D} + \left(\left(a^2 E_b \left(\varepsilon_r(0) + \varepsilon_{\text{delay}}(t_d) \right) \mathbb{D} \right) / r^2 \right)}{1 + \left(\left(a^2 E_b \mathbb{D} \right) / r^2 \right)} = p\mathbb{U}, \qquad (20)$$
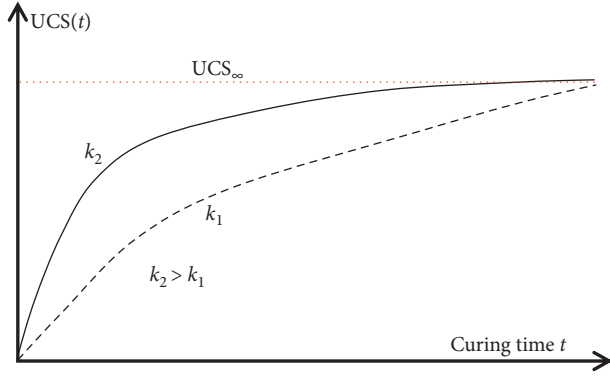
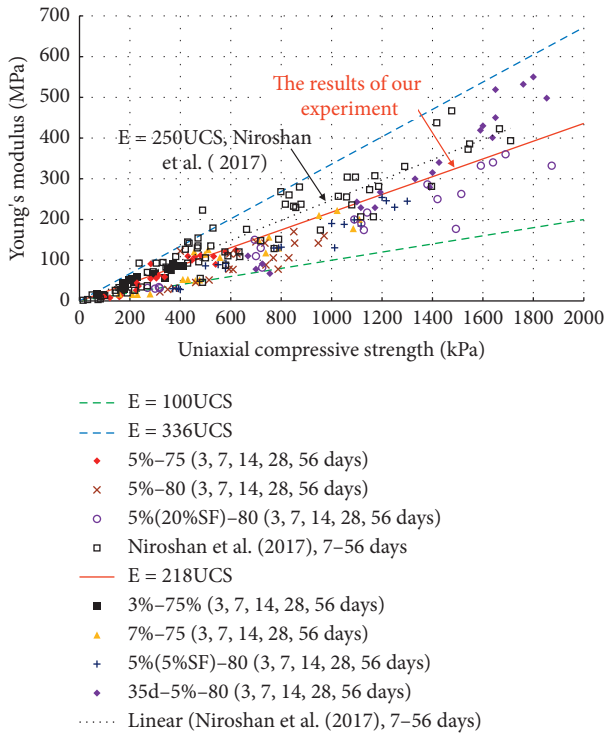FIGURE 8: Curves of relationship between backfills strength and curing age.

FIGURE 9: Plot of the change in the elastic modulus with the strength of cemented mine backfill.

where

$$\mathbb{D} = \frac{(1+\mu)}{E} + \frac{3}{2} A \sigma_e^{m-1} t^n \exp\left(-\frac{\Delta H}{RT}\right),$$

$$\mathbb{U} = \frac{\varepsilon_r(t)}{p}. \tag{21}$$

The expression of strain $\varepsilon_{rc}(t)$ acting on backfilling by the creep behavior of the nearby rock material is given as follows:

$$\varepsilon_{rc}(t) = \mathbb{U}p - \varepsilon_{r0} - \varepsilon_{\text{delay}}(t_d). \tag{22}$$

The gravity on the differential element body is as follows:
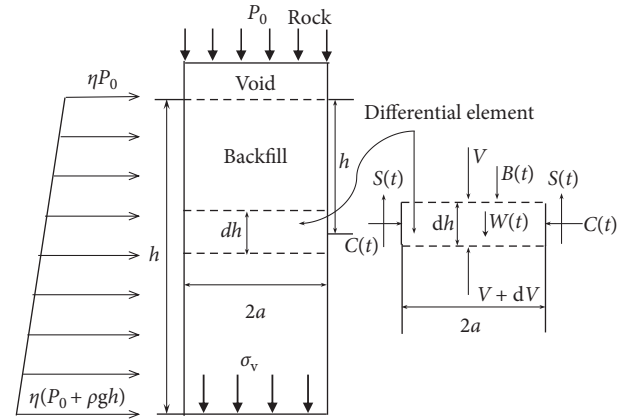
FIGURE 10: Diagram of approximate circular cross section high filling stope backfill force.

$$W = \gamma \pi a^2 dh. \tag{23}$$

When the creep behavior happens in the nearby rock material, the backfill pore structure is compressed tightly when the backfill is squeezed. In addition, backfill drainage produces consolidation effect, which reduces the backfill's porosity, and the backfill's bulk density gradually increases with the development of creep deformation. Thus, there are

$$\gamma = \gamma_0 + \chi E_b \varepsilon_{rc}(t) = \gamma_0 + \chi E_b\big(\mathbb{U}p - \varepsilon_{r0} - \varepsilon_{\text{delay}}(t_d)\big), \quad (\gamma_0 \le \gamma \le \gamma_s). \tag{24}$$

Among them, χ represents the compaction capacity of backfill under confining pressure and is the empirical co-efficient related to the characteristics of backfill materials, γ_0 is the initial backfill density, and γ_s is the tailings bulk density.

Assuming that the horizontal plane of the differential element is subject to the average vertical stress with uniform distribution, the normal pressure C generated by the surrounding rock and the friction force S (without considering the interfacial bonding forces) are, respectively, as follows:

$$C = 2\pi a \sigma_h = 2\pi a \big[K_p \sigma_v + E_b\big(\mathbb{U}p - \varepsilon_{r0} - \varepsilon_{\text{delay}}(t_d)\big)\big],$$

$$S = C \tan \delta dh = 2\pi a \big[K_p \sigma_v - E_b\big(\mathbb{U}p - \varepsilon_{r0} - \varepsilon_{\text{delay}}(t_d)\big)\big] \tan \delta dh. \tag{25}$$

According to Poisson's effect, the differential element is squeezed by the horizontal force from the surrounding rock mass, and it tends to squeeze downward in the vertical direction under the action of gravity. Therefore, the reaction coefficient tends toward the passive condition [49], and the equality in the vertical way can be inferred as follows:

$$V + dV + S = W + V + B, \tag{26}$$

where B refers to the vertical squeezing pressure caused by Poisson's effect in the vertical direction of horizontal squeezing on the differential element body:

$$B = \nu E_b \varepsilon_{rc}(t)dh. \tag{27}$$

Then,

$$d\sigma_v \pi a^2 + 2\pi a \left[K_p \sigma_v - E_b \left(\mathbb{U}p - \varepsilon_{r0} - \varepsilon_{\text{delay}}(t_d) \right) \right] \tan \delta dh$$
$$= \left[\gamma_0 + \chi E_b \left(\mathbb{U}p - \varepsilon_{r0} - \varepsilon_{\text{delay}}(t_d) \right) \right] \pi a^2 dh + v E_b \left(\mathbb{U}p - \varepsilon_{r0} - \varepsilon_{\text{delay}}(t_d) \right) dh, \tag{28}$$

where v is the ratio between horizontal and vertical squeezing pressure caused by the surrounding creeping rock material.

$$\frac{d\sigma_v}{dh} + \frac{2K_o \tan \delta}{a} \sigma_v + \eta \rho_r g E_b \mathbb{U} \left[\frac{-2\tan \delta}{a} - \chi - \frac{v}{\pi a^2} \right] h$$
$$= \left[\gamma_0 + \chi E_b \left(\mathbb{U}\eta p_0 - \varepsilon_{r0} - \varepsilon_{\text{delay}}(t_d) \right) + \frac{v E_b \left(\mathbb{U}\eta p_0 - \varepsilon_{r0} - \varepsilon_{\text{delay}}(t_d) \right)}{\pi a^2} \right] \tag{29}$$
$$+ \frac{2E_b \tan \delta \left(\mathbb{U}\eta p_0 - \varepsilon_{r0} - \varepsilon_{\text{delay}}(t_d) \right)}{a}.$$

The vertical stress σ_v in the backfill is obtained by solving the first-order linear nonuniform differential equations:

(1) when $\delta = 0$ and $\mathscr{B} = 0$, then

$$\sigma_v = \frac{\mathscr{A}}{2} h^2 + \mathscr{C} h + C, \tag{30}$$

where $h = 0$, and then $C = 0$.

(2) when $\delta \neq 0$, then

$$\sigma_v = -\frac{\mathscr{A}h + \mathscr{C}}{\mathscr{B}} - \frac{\mathscr{A}}{\mathscr{B}^2} + \left(\frac{\mathscr{C}}{\mathscr{B}} + \frac{\mathscr{A}}{\mathscr{B}^2} \right) \exp(\mathscr{B}h). \tag{31}$$

Among them, when $h = 0$, $C = (\mathscr{C}/\mathscr{B}) + (\mathscr{A}/\mathscr{B}^2)$,

$$\mathscr{A} = -\eta E_b \rho_r g \mathbb{U} \left[\frac{-2\tan \delta}{a} - \chi - \frac{v}{\pi a^2} \right],$$

$$\mathscr{B} = -\frac{2K_o \tan \delta}{a},$$

$$\mathscr{C} = \begin{bmatrix} \gamma_0 + \chi E_b \left(\mathbb{U}\eta p_0 - \varepsilon_{r0} - \varepsilon_{\text{delay}}(t_d) \right) \\ + \frac{v E_b \left(\mathbb{U}\eta p_0 - \varepsilon_{r0} - \varepsilon_{\text{delay}}(t_d) \right)}{\pi a^2} \end{bmatrix} \tag{32}$$

$$+ \frac{2E_b \tan \delta \left(\mathbb{U}\eta p_0 - \varepsilon_{r0} - \varepsilon_{\text{delay}}(t_d) \right)}{a}.$$

If $\gamma \geq \gamma_s$,

By integration,

$$d\sigma_v \pi a^2 + 2\pi a \left[K_p \sigma_v - E_b \left(\mathbb{U}p - \varepsilon_{r0} \right) \right] \tan \delta dh$$
$$= \gamma_s \pi a^2 dh + v E_b \left(\mathbb{U}\eta (p_0 + \rho_r gh) - \varepsilon_{r0} - \varepsilon_{\text{delay}}(t_d) \right) dh,$$

$$\frac{d\sigma_v}{dh} + \frac{2K_o \tan \delta}{a} \sigma_v + \eta \rho_r g E_b \mathbb{U} \left[\frac{-2\tan \delta}{a} - \frac{v}{\pi a^2} \right] h$$

$$= \left(\gamma_s + \frac{v E_b \left(\mathbb{U}\eta p_0 - \varepsilon_{r0} - \varepsilon_{\text{delay}}(t_d) \right)}{\pi a^2} \right)$$

$$+ \frac{2E_b \tan \delta \left(\mathbb{U}\eta p_0 - \varepsilon_{r0} - \varepsilon_{\text{delay}}(t_d) \right)}{a}, \tag{33}$$

where

$$\mathscr{A} = -\eta E_b \rho_r g \mathbb{U} \left[\frac{-2\tan \delta}{a} - \frac{v}{\pi a^2} \right],$$

$$\mathscr{B} = -\frac{2K_o \tan \delta}{a},$$

$$\mathscr{C} = \left(\gamma_s + \frac{v E_b \left(\mathbb{U}\eta p_0 - \varepsilon_{r0} - \varepsilon_{\text{delay}}(t_d) \right)}{\pi a^2} \right) \tag{34}$$

$$+ \frac{2E_b \tan \delta \left(\mathbb{U}\eta p_0 - \varepsilon_{r0} - \varepsilon_{\text{delay}}(t_d) \right)}{a}.$$

The horizontal stress of backfill σ_h is

$$\sigma_h = K_p \sigma_v + E_b \left(\mathbb{U}p - \varepsilon_{r0} - \varepsilon_{\text{delay}}(t_d) \right), \tag{35}$$

where E_b is positively correlated with the bulk density of backfill as well as the curing age.

4. Verification of the Offered Model

To verify the rationality of the proposed theoretical model, a corresponding numerical model is built for simulating the backfill into the stope influenced by the creep behavior of the nearby rock material and the time-dependent stress distribution in the backfill. As shown in Figure 11, to save calculation time, the axisymmetric model is selected, the width of the backfilled stope is set at 6 m, the height is 45 m, and the void area of the backfilled stope is 0.5 m. The model boundary width is set at 250 m, and the height is set at 500 m in the light of Saint-Venant's principle and the trial calculation results of different mesh sizes. Finally, 151999 tetrahedral elements with a minimum size of 0.25 m were also constructed.

The backfill and surrounding rock mass are modeled as elastic materials. Elastic modulus and Poisson's ratio of rock and backfill can be seen in Table 1. The specific simulation process is as follows: (1) the backfilled stope is selected at a depth of 1000 m, the initial ground stress field conditions are given, the lateral pressure coefficient is set to 2, and the horizontal ground stress ratio is set to 1; (2) excavating the filling stope and solving to equilibrium to complete the elastic equilibrium calculation under the influence of the excavation; and (3) zero the initial displacement field formed by the excavation and perform the solution calculation for the creep or time-dependent deformation of the nearby rock material with and without filling until the target time is set.

To verify the assumption in the established model that the differential elements in the horizontal direction of filling stope approximately meet the plane strain condition, this study calculates the creep deformation without filling after excavation to acquire the vertical strain of the nearby rock material. Figure 12 shows the change of vertical strain along with the height of filling stope in the creep process of adjacent surrounding rock mass. Except that the vertical strain in upper/lower sides of the backfilled stope is not close to 0, all other places meet the requirements of plane strain; that is, the vertical strain is 0.

To verify the validity of the theoretical solution, the simulation process does not take into account the effects of the damage caused by the excavation and the creep deformation process, i.e., the strength of the nearby rock mass is set large. The backfill is not damaged, and the effects of creep deformation of the backfill are not considered. The elastic modulus E_b of backfilling is 300 MPa, and the comparison between the different delay times for the backfill and the different creep deformation times for the nearby rock material is shown in Figures 13(a)–13(c).

The comparison results show that in general the theoretical solution is close to the numerical simulation results, especially the development of vertical stresses in backfill influenced by creeping rock mass. The backfill's horizontal stress is influenced by the extrusion stress in lower sides of the backfilled stope by the bottom corner points, which is different from the mathematical simulation. The stress in the backfill will increase as the creep behavior of the nearby rock material develops, and this increase will become insignificant as the delay time for

filling the mined-out opening or stope increases due to the compression exerted in the backfill by creeping rock material.

5. Sample Application

Researchers have conducted extensive theoretical analyses for underground backfilled stope where the creep behavior effect on the nearby rock material is not considered or is not apparent, and the results confirmed that the stresses in backfill present arching phenomena [50, 51], which is also common in soil foundations [52]. However, when the creep deformation of the surrounding rock mass is considered, the stress distribution changes significantly and the internal stresses exceed the self-weight stresses of backfill. This form of stress distribution is closely related to the stope buried depth, lateral pressure coefficient, Young's modulus of the backfill, creep deformation of the surrounding rock mass, and delayed filling time. Based on this, these influencing parameters are analyzed in this section. Table 2 lists a specific comparison conditions.

Figure 14 demonstrates that the depth of the backfilled stope has a strong impact on its internal stress distribution of backfill. This is primarily reflected in the fact that the deeper the filling stope is, the greater the surrounding rock stress is, and the more likely the surrounding rock mass is to creep deformation under high in situ stress. Consequently, the squeezing pressure of the backfill subjected to the nearby rock deformation is greater. When the buried depth of the filled stope is 500 m, the creep performance of the nearby rock material has a little influence on the backfill's internal stresses.

The backfill's internal stress is close to that obtained when the effect of creeping rock is not considered; that is, the stress in the lower side of the backfilled stope is less important than the self-weight stress value, and the effect of arching is noteworthy. However, when the buried depth of stope is 1000 m and 1500 m, the vertical/horizontal stresses in backfilling surge intentionally, and the squeezing effect of the nearby rock material on the backfill becomes significant. This indicates that when considering the effect of creep property of the nearby rock material on the backfill's internal stress, the depth of the backfill opening or stope cannot be ignored, and there is safety hidden dangers when entering deep mining according to the standard of designing backfill strength according to the distribution of self-weight stress.

Figure 15 demonstrates that the ratio of horizontal/vertical stresses of the nearby rock material has an influence on the backfill's internal stress, which is mainly reflected in that the internal stress of the backfill is more significantly affected by the creep behavior of the nearby rock material as the lateral pressure coefficient increases. When the coefficient of lateral stresses in nearby rock material is 0.5, the horizontal creep deformation of the nearby rock material drops and the squeezing pressure of the nearby rock material on the backfill decreases. At this time, the backfill's internal stresses are less than the self-weight stress. With a lateral pressure coefficient of 2, the horizontal deformation capacity of the nearby rock material rises, and the stress inside the backfill increases significantly. This further indicates that when considering the creep behavior of the nearby rock material, the main reason for
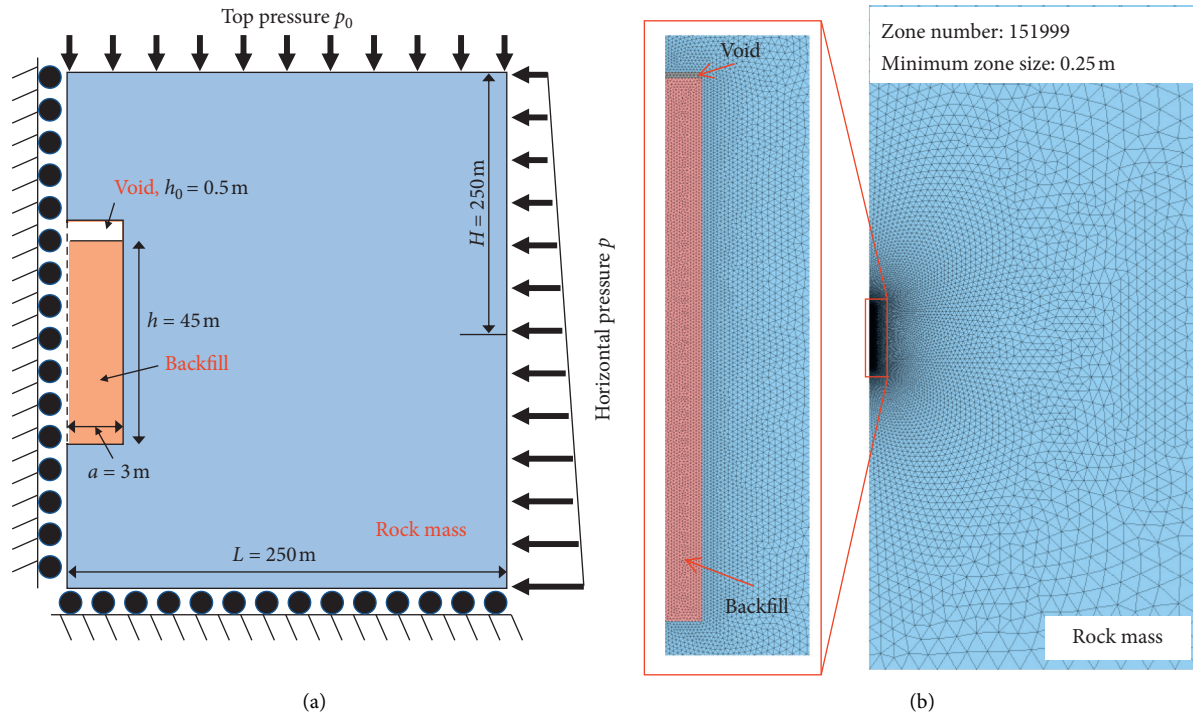
(a)

(b)

FIGURE 11: A schematic view of the numerical model: (a) size/boundary settings and (b) grid model.
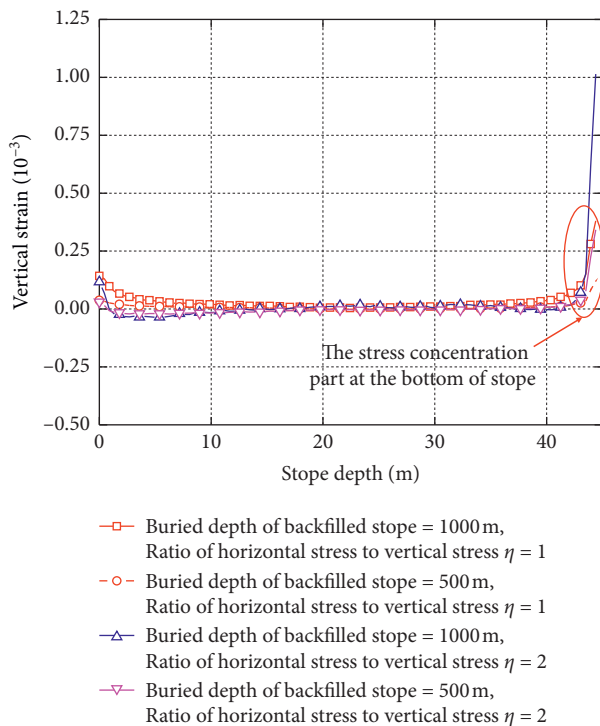

FIGURE 12: Variation of vertical strain of surrounding rock mass in stope area within stope height.

the increase in the internal stress of the backfill is the surge of the horizontal deformation capacity of the nearby rock material and the improvement of the squeezing capacity of the backfill.
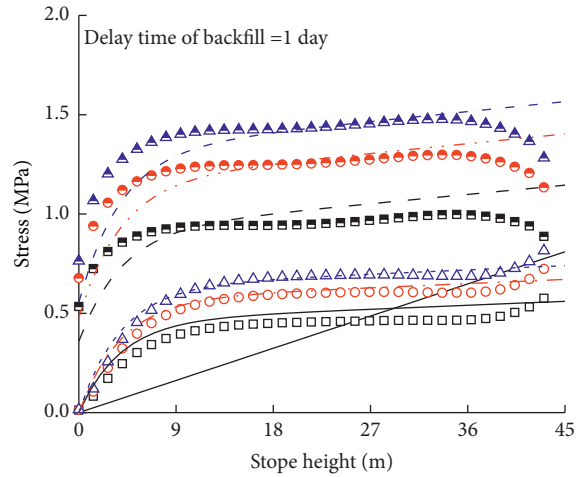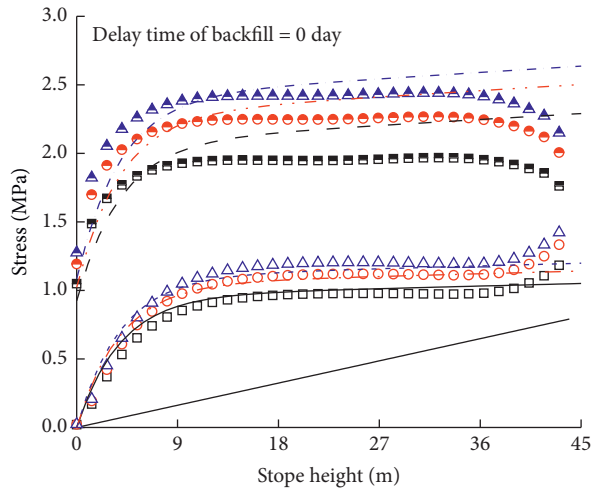
As can be seen from Figure 16, with the increase in backfill's elastic modulus, the vertical and horizontal stresses

in the backfill rise. With the backfill's elastic modulus of 30 MPa, the stress in the backfill is less than the self-weight stress distribution, and the horizontal stress and vertical stress distribution are close to each other.

With the rise in backfill's elastic modulus, difference between horizontal and vertical stresses increases, and both of them gradually exceed their self-weight stress. The supporting reaction force of the nearby rock material also increases with the increase in the creep behavior of the nearby rock material. The two are coupled. It reflects the passive support form of "You are strong, I am strong, you are weak, I am weak" after the backfill is filled into the mined-out opening or stope.

Figure 17 shows that the changes of the ratio between two horizontal stresses also govern the backfill's internal stress influenced by creeping rock. The stresses in backfill decrease with the rise of the ratio of horizontal stress, and the gap between horizontal stress and vertical stress of backfill will shorten. This is because, when the fixed value of horizontal stress in one direction is 0.5 p and when the ratio is 0.5, 1, and 2, the horizontal stress in the other direction is p, 0.5 p, and 0.25 p, respectively. One can see that when the horizontal stress ratio is 0.5, the nearby rock material will be in a stress environment with high confining pressure. Relevant studies show that the creep behavior of the nearby rock material will be enhanced under high confining pressure. Therefore, the horizontal squeezing effect of the nearby rock on the interior of backfilling will increase, leading to the increase in its internal stress.

According to the numerical results of Figure 13, the delay time of backfilling also can affect the internal stress of the backfill. The greater the delay time, the more rock creep
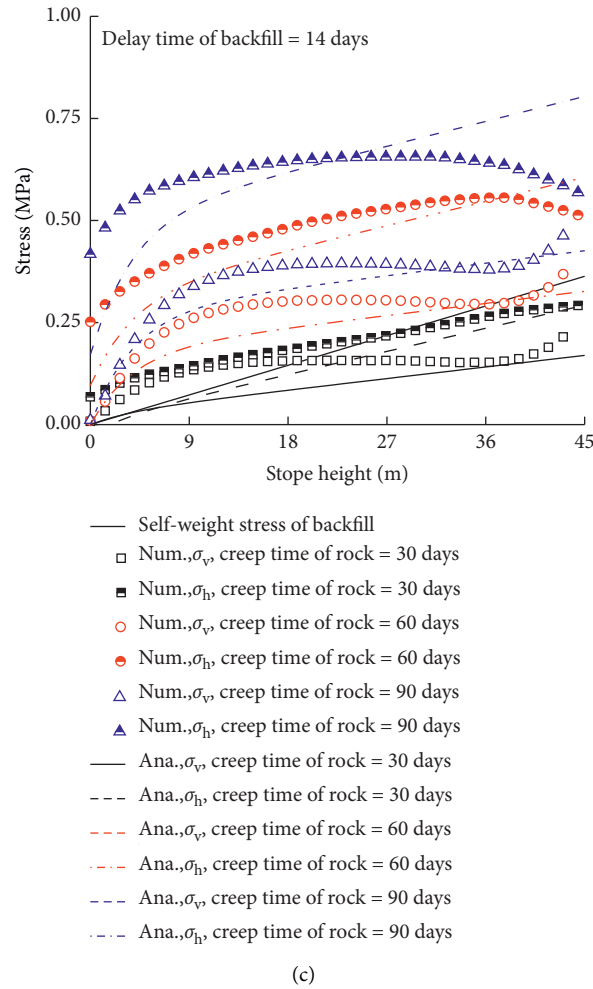
Figure 13: Continued.

(c)

FIGURE 13: Theoretical and numerical results of time-dependent interaction between backfill and surrounding rock mass: (a) stope without delay filling; (b) delayed filling for 1-day; (c) delayed filling for 14-day.

TABLE 2: Analysis of influential factors of rock creep deformation on the stress distribution of backfill.

Factors	Stope depth (m)	Lateral pressure coefficient η	Horizontal stress ratio λ	Creep time of rock mass t (days)	Young's modulus of backfill E_b (MPa)	Delay time of backfill t_d (days)
Stope depth	500	2	1	30	300	1
	1000	2	1	30	300	1
	1500	2	1	30	300	1
Lateral pressure coefficient η	1000	0.5	1	30	300	1
	1000	1	1	30	300	1
	1000	2	1	30	300	1
Horizontal stress ratio λ	1000	2	0.5	30	300	1
	1000	2	1	30	300	1
	1000	2	2	30	300	1
Creep time of surrounding rock mass t	1000	2	1	30	300	1
	1000	2	1	60	300	1
	1000	2	1	90	300	1
Young's modulus of backfill E_b	1000	2	1	30	30	1
	1000	2	1	30	300	1
	1000	2	1	30	900	1
Delay time of backfill t_d	1000	2	1	30	300	0
	1000	2	1	30	300	1
	1000	2	1	30	300	14

Note. Elastic modulus for rock is found to be 8.4 GPa and Poisson's ratio of rock and backfill is 0.29 and 0.33, respectively.
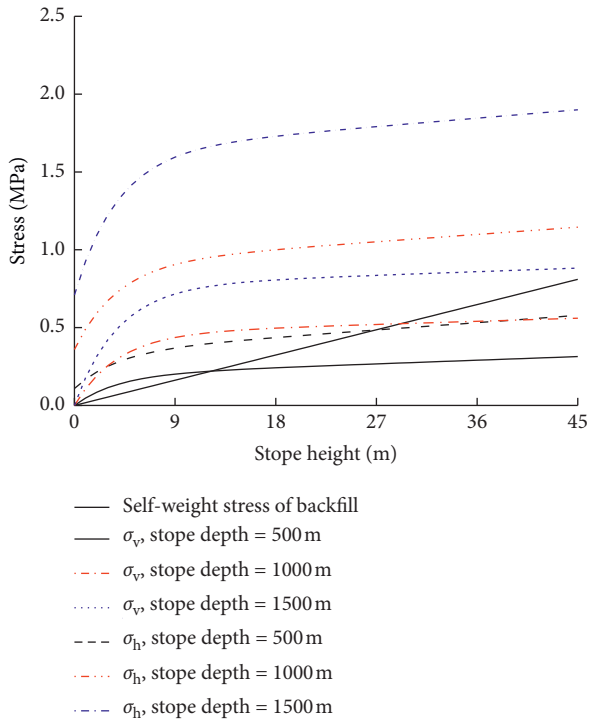
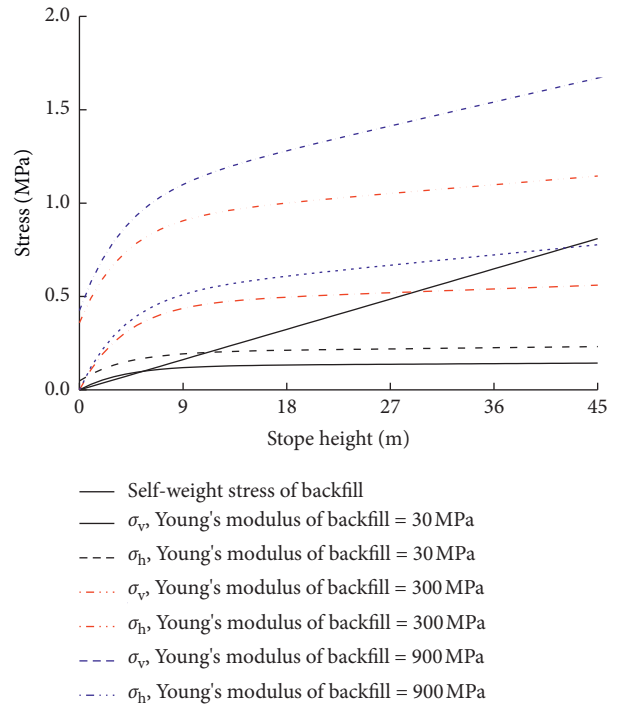FIGURE 14: Stope depth effect on time-dependent stress profile of backfilling.

FIGURE 16: Elastic modulus effect on the time-dependent stress distribution of backfilling.
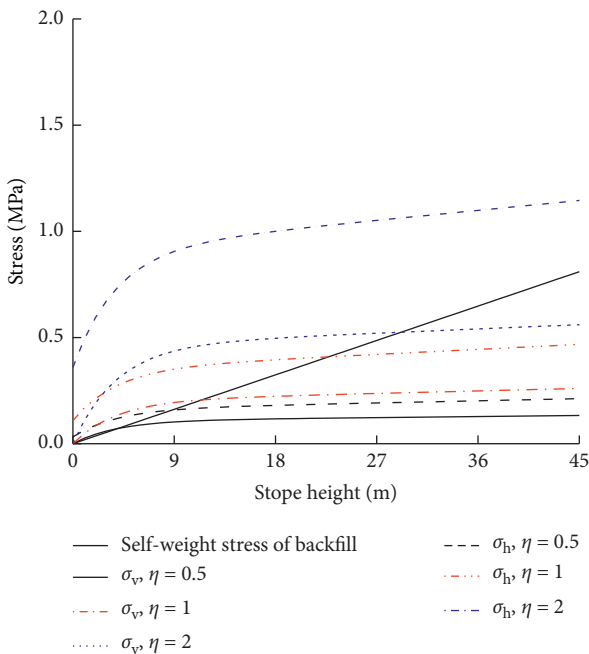

FIGURE 15: Lateral earth pressure effect on time-dependent stress profile of backfilling.
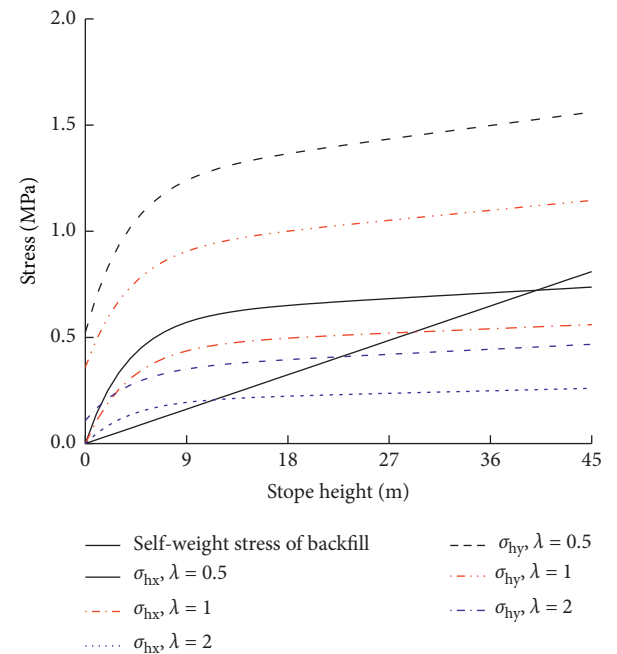

FIGURE 17: Effect of horizontal stress ratio on the time-dependent stress distribution of backfill.

deformation occurs and may then gets back into the stable stage; at this point, the creep deformation rate is relatively small; thus the deformation amount of the nearby rock acting on the backfill is smaller. Thus, the weaker the backfill's stress is under the squeezing capacity of the nearby rock material, the smaller the backfill's internal stress is.

6. Discussion

The contact between mine backfilling and nearby rock material is related to drainage, consolidation, and dynamic disturbance conditions of backfill [10, 20] and is the result of multifield (THMC) and multifactor coupling. The strength

of the surrounding rock mass may be weakening under long-term water erosion influenced by backfill with high water and high permeability, thus increasing the deformation tendency of the surrounding rock mass. This process may further squeeze the backfill and result in increase in the stresses in backfill. However, for the cemented paste backfill, the ability of bleeding and permeability is relatively small, so it is reasonable not to consider the effect of water erosion on strength and deformation of the nearby rock material. Besides, a certain water pond on upper sides of the backfilled stope will be formed in early filling stages with regard to the backfill of high bleeding, which will affect the evolution and development of the backfill's internal strength [32]. The upper sides of the backfilled stope may be also affected by the drying and evaporation effects.

The blasting disturbance near the backfilled stope will lead to further deformation of the nearby rock material, which will surge sharply in a short time, causing a sudden increase in stresses in backfill [53]. It is important for the stability analysis of barricades for this sudden increase in stresses in the backfill. In the early stage of backfilling, when the compressive strength of the backfill is small, dynamic disturbance may cause liquefaction of the backfill [54], resulting in sudden changes in the interaction state between mine backfill and the nearby rock material, and how the hardening process changes after liquefaction of the backfill requires further consideration.

7. Conclusions

In this study, the spatial and temporal coupling effects of the interaction between the hardening process of backfill and the surrounding rock mass are investigated. The present study proposes a corresponding theoretical model and draws the following main conclusions:

(1) The interaction between mine backfill after filling the stope and the nearby rock material shows three main interaction processes: (i) the support action causes the stress level of the nearby rock material to change, which in turn changes the creep behavior of the nearby rock material; (ii) the squeezing force generated by the nearby rock mass puts the backfill under curing stress; and (iii) the change of shrinkage strain in the hardening process of backfilling affects the deformation of the nearby rock material.

(2) The stress distribution of backfill in circular and high filling stope under the effect of time-dependent deformation of rock is solved. The strength and elastic modulus evolution formula which considers the change of curing time, curing stress, and cement content during curing process of backfill are presented.

(3) When the creeping rock mass enters the second creep stage, the controlling effect of backfill over the creep behavior of the nearby rock material is not obvious. For the nearby rock material with minor creep deformation, the stress distribution inside backfill is mainly dependent on the effect of stress arching. When the stope depth is relatively high and the creep effect of rocks is substantial, the stress distribution in backfill is mainly composed of stress arching and squeezing effect, and the squeezing effect makes the stress distribution in backfill exceed its self-weight stress.

(4) After stope excavation, delay backfilling has a major impact on deformation of the nearby rock material in accordance with the monitoring results of Moser et al. [55].

Data Availability

The data used to support the findings of this study are included within the article.

Conflicts of Interest

The authors declare that they have no conflicts of interest regarding the publication of this paper.

Acknowledgments

References

[1] X. Li, D. Wang, C. Li, and Z. Liu, "Numerical simulation of surface subsidence and backfill material movement induced by underground mining," *Advances in Civil Engineering*, vol. 2019, Article ID 2724370, 17 pages, 2019.

[2] I. Ponsot and E. Bernardo, "Self glazed glass ceramic foams from metallurgical slag and recycled glass," *Journal of Cleaner Production*, vol. 59, pp. 245–250, 2013.

[3] A. U. Shettima, M. W. Hussin, Y. Ahmad, and J. Mirza, "Evaluation of iron ore tailings as replacement for fine aggregate in concrete," *Construction and Building Materials*, vol. 120, pp. 72–79, 2016.

[4] A. Rincón, D. Desideri, and E. Bernardo, "Functional glass-ceramic foams from 'inorganic gel casting' and sintering of glass/slag mixtures," *Journal of Cleaner Production*, vol. 187, pp. 250–256, 2018.

[5] S. Bea, S. Wilson, K. Mayer, G. Dipple, I. Power, and P. Gamazo, "Reactive transport modeling of natural carbon sequestration in ultramafic mine tailings," *Vadose Zone Journal*, vol. 11, no. 2, 2012.

[6] T. Deschamps, M. Benzaazoua, B. Bussière, and M. Aubertin, "Laboratory study of surface paste disposal for sulfidic tailings: physical model testing," *Minerals Engineering*, vol. 24, no. 8, pp. 794–806, 2011.

[7] T. Belem and M. Benzaazoua, "Design and application of underground mine paste backfill technology," *Geotechnical and Geological Engineering*, vol. 26, no. 2, pp. 147–174, 2007.

[8] D. Kossoff, W. E. Dubbin, M. Alfredsson, S. J. Edwards, M. G. Macklin, and K. A. Hudson-Edwards, "Mine tailings dams: characteristics, failure, environmental impacts, and remediation," *Applied Geochemistry*, vol. 51, pp. 229–245, 2014.

[9] S. Yin, Y. Shao, A. Wu, H. Wang, X. Liu, and Y. Wang, "A systematic review of paste technology in metal mines for cleaner production in China," *Journal of Cleaner Production*, vol. 247, Article ID 119590, 2020.

[10] Q. Zhou, J.-H. Liu, A.-X. Wu, and H.-J. Wang, "Early-age strength property improvement and stability analysis of unclassified tailing paste backfill materials," *International Journal of Minerals, Metallurgy and Materials*, vol. 27, no. 9, pp. 1191–1202, 2020.

[11] Q. Lei, S. Yannan, and L. Jiangong, "Experimental study on grouting diffusion of gangue solid filling bulk materials," *Journal of Mining and Strata Control Engineering*, vol. 3, no. 2, Article ID 23015, 2021.

[12] E. M. Jaouhar and L. Li, "Effect of drainage and consolidation on the pore water pressures and total stresses within backfilled stopes and on barricades," *Advances in Civil Engineering*, vol. 53, no. 4, 2019.

[13] B. Zhang, J. Xin, L. Liu, L. Guo, and K.-I. Song, "An experimental study on the microstructures of cemented paste backfill during its developing process," *Advances in Civil Engineering*, vol. 2018, pp. 1–10, 2018.

[14] M. Z. Emad, H. Mitri, and C. Kelly, "Dynamic model validation using blast vibration monitoring in mine backfill," *International Journal of Rock Mechanics and Mining Sciences*, vol. 107, pp. 48–54, 2018.

[15] G. Liu, L. Li, X. Yang, and L. Guo, "Stability analyses of vertically exposed cemented backfill: a revisit to Mitchell's physical model tests," *International Journal of Mining Science and Technology*, vol. 26, no. 6, pp. 1135–1144, 2016.

[16] Z. Yang, S. Zhai, Q. Gao, and M. Li, "Stability analysis of large-scale stope using stage subsequent filling mining method in Sijiaying iron mine," *Journal of Rock Mechanics and Geotechnical Engineering*, vol. 7, no. 1, pp. 87–94, 2015.

[17] J. B. Seymour, L. A. Martin, M. J. Raffaldi, S. N. Warren, and L. A. Sandbak, "Long-term stability of a 13.7×30.5-m (45×100-ft) undercut span beneath cemented rockfill at the turquoise ridge mine, nevada," *Rock Mechanics and Rock Engineering*, vol. 52, no. 12, pp. 4907–4923, 2019.

[18] M. J. Raffaldi, J. B. Seymour, J. Richardson, E. Zahl, and M. Board, "Cemented paste backfill geomechanics at a narrow-vein underhand cut-and-fill mine," *Rock Mechanics and Rock Engineering*, vol. 52, no. 12, pp. 4925–4940, 2019.

[19] X. Zhao, A. Fourie, and C.-c. Qi, "An analytical solution for evaluating the safety of an exposed face in a paste backfill stope incorporating the arching phenomenon," *International Journal of Minerals, Metallurgy, and Materials*, vol. 26, no. 10, pp. 1206–1216, 2019.

[20] Y.-Y. Tan, X. Yu, D. Elmo, L.-H. Xu, and W.-D. Song, "Experimental study on dynamic mechanical property of cemented tailings backfill under SHPB impact loading," *International Journal of Minerals, Metallurgy, and Materials*, vol. 26, no. 4, pp. 404–416, 2019.

[21] D. Wu, R.-K. Zhao, C.-W. Xie, and S. Liu, "Effect of curing humidity on performance of cemented paste backfill," *International Journal of Minerals, Metallurgy and Materials*, vol. 27, no. 8, pp. 1046–1053, 2020.

[22] C. Qi and A. Fourie, "Numerical investigation of the stress distribution in backfilled stopes considering creep behaviour of rock mass," *Rock Mechanics and Rock Engineering*, vol. 52, no. 9, pp. 1–19, 2019.

[23] Z. Zhou, Y. Zhao, W. Cao, L. Chen, and J. Zhou, "Dynamic response of pillar workings induced by sudden pillar recovery," *Rock Mechanics and Rock Engineering*, vol. 51, no. 10, pp. 3075–3090, 2018.

[24] Y. Yu, K.-Z. Deng, Y. Luo, S.-E. Chen, and H.-F. Zhuang, "An improved method for long-term stability evaluation of strip mining and pillar design," *International Journal of Rock Mechanics and Mining Sciences*, vol. 107, pp. 25–30, 2018.

[25] E. Maranini and M. Brignoli, "Creep behaviour of a weak rock: experimental characterization," *International Journal of Rock Mechanics and Mining Sciences*, vol. 36, no. 1, pp. 127–138, 1999.

[26] J. Zhao, X.-T. Feng, X. Zhang, and C. Yang, "Brittle and ductile creep behavior of Jinping marble under true triaxial stress," *Engineering Geology*, vol. 258, p. 105157, 2019.

[27] J. Zhao, X.-T. Feng, X. Zhang, C. Yang, and Y. Zhou, "Time-dependent behaviour and modeling of Jinping marble under true triaxial compression," *International Journal of Rock Mechanics and Mining Sciences*, vol. 110, pp. 218–230, 2018.

[28] M. Fahey, M. Helinski, and A. Fourie, "Development of specimen curing procedures that account for the influence of effective stress during curing on the strength of cemented mine backfill," *Geotechnical and Geological Engineering*, vol. 29, no. 5, pp. 709–723, 2011.

[29] M. Helinski, M. Fahey, and A. Fourie, "Behavior of cemented paste backfill in two mine stopes: measurements and modeling," *Journal of Geotechnical and Geoenvironmental Engineering*, vol. 137, no. 2, pp. 171–182, 2011.

[30] A. Hasan, A. Karrech, and B. Chareyre, "Evaluating force distributions within virtual uncemented mine backfill using discrete element method," *International Journal of Geomechanics*, vol. 17, no. 7, Article ID 6016042, 2016.

[31] J. Li, H. Liu, K. Ai, and L. Zhu, "An NMR-based experimental study on the pore structure of the hydration process of mine filling slurry," *Advances in Civil Engineering*, vol. 2018, pp. 1–12, 2018.

[32] P. Yang, L. Li, and M. Aubertin, "A new solution to assess the required strength of mine backfill with a vertical exposure," *International Journal of Geomechanics*, vol. 17, no. 10, 2017.

[33] L. Li and M. Aubertin, "An analytical solution for the nonlinear distribution of effective and total stresses in vertical backfilled stopes," *Geomechanics and Geoengineering*, vol. 5, no. 4, pp. 237–245, 2010.

[34] L. Li, M. Aubertin, and T. Belem, "Formulation of a three dimensional analytical solution to evaluate stresses in backfilled vertical narrow openings," *Canadian Geotechnical Journal*, vol. 42, no. 6, pp. 1705–1717, 2005.

[35] B. Yan, W. Zhu, C. Hou, and K. Guan, "A three-dimensional analytical solution to the arching effect in inclined backfilled stopes," *Geomechanics and Geoengineering*, vol. 14, no. 2, pp. 136–147, 2019.

[36] C. H. Ting, N. Sivakugan, W. Read, and S. K. Shukla, "Analytical expression for vertical stress within an inclined mine stope with non-parallel walls," *Geotechnical and Geological Engineering*, vol. 32, no. 2, pp. 577–586, 2014.

[37] A. Jahanbakhshzadeh, M. Aubertin, and L. Li, "A new analytical solution for the stress state in inclined backfilled mine stopes," *Geotechnical and Geological Engineering*, vol. 35, no. 3, pp. 1–17, 2017.

[38] P. Rajeev, P. R. Sumanasekera, and N. Sivakugan, "Lateral variation of the vertical stress in underground mine stopes filled with granular backfills," *Geotechnical and Geological Engineering*, vol. 34, no. 2, pp. 481–492, 2015.

[39] B. Yan and E. Yilmaz, "Analytical solution for stress distribution in cementitious backfills considering stope inclinations," *Recep Tayyip Erdogan University Journal of Science and Engineering*, vol. 1, no. 2, pp. 26–33, 2020.

[40] E. Yilmaz, "Stope depth effect on field behaviour and performance of cemented paste backfills," *International Journal of Mining, Reclamation and Environment*, vol. 32, no. 4, pp. 273–296, 2018.

[41] N. El Mkadmi, M. Aubertin, and L. Li, "Effect of drainage and sequential filling on the behavior of backfill in mine stopes," *Canadian Geotechnical Journal*, vol. 51, no. 1, pp. 1–15, 2014.

[42] B. D. Thompson, W. F. Bawden, and M. W. Grabinsky, "In situ measurements of cemented paste backfill at the Cayeli Mine," *Canadian Geotechnical Journal*, vol. 49, no. 7, pp. 755–772, 2012.

[43] J. P. Doherty, A. Hasan, G. H. Suazo, and A. Fourie, "Investigation of some controllable factors that impact the stress state in cemented paste backfill," *Canadian Geotechnical Journal*, vol. 52, no. 12, pp. 1901–1912, 2015.

[44] S. Yin, Y. Shao, A. Wu, Z. Wang, and L. Yang, "Assessment of expansion and strength properties of sulfidic cemented paste backfill cored from deep underground stopes," *Construction and Building Materials*, vol. 230, Article ID 116983, 2020.

[45] B. Yan, W. Zhu, C. Hou, Y. Yu, and K. Guan, "Effects of coupled sulphate and temperature on internal strain and strength evolution of cemented paste backfill at early age," *Construction and Building Materials*, vol. 230, Article ID 116937, 2020.

[46] T. Xu, G. Zhou, M. J. Heap, S. Yang, H. Konietzky, and P. Baud, "The modeling of time-dependent deformation and fracturing of brittle rocks under varying confining and pore pressures," *Rock Mechanics and Rock Engineering*, vol. 51, no. 10, pp. 3241–3263, 2018.

[47] N. Niroshan, N. Sivakugan, and R. L. Veenstra, "Laboratory study on strength development in cemented paste backfills," *Journal of Materials in Civil Engineering*, vol. 29, no. 7, Article ID 4017027, 2017.

[48] P. Małkowski, Ł. Ostrowski, and J. Brodny, "Analysis of Young's modulus for Carboniferous sedimentary rocks and its relationship with uniaxial compressive strength using different methods of modulus determination," *Journal of Sustainable Mining*, vol. 17, no. 3, pp. 145–157, 2018.

[49] L. Li, M. Aubertin, R. Simon, B. Bussière, and T. Belem, "Modeling arching effects in narrow backfilled stopes with FLAC," in *Proceedings of the 3rd International Symposium on FLAC & FLAC 3D Numerical Modelling in Geomechanics*, pp. 211–219, Ontario, Canada, October 2003.

[50] P. Rajeev, P. R. Sumanasekera, and N. Sivakugan, "Average vertical stresses in underground mine stopes filled with granular backfills," *Geotechnical and Geological Engineering*, vol. 34, no. 6, pp. 2053–2061, 2016.

[51] L. Li and M. Aubertin, "Limit equilibrium analysis for the design of backfilled stope barricades made of waste rock," *Canadian Geotechnical Journal*, vol. 48, no. 11, pp. 1713–1728, 2011.

[52] R. L. Handy, "The arch in soil arching," *Journal of Geotechnical Engineering*, vol. 111, no. 3, pp. 302–318, 1985.

[53] G. Suazo, A. Fourie, and J. Doherty, "Experimental investigation of propagation and transmission of compressional stress waves in cemented paste backfill," *Journal of Geotechnical and Geoenvironmental Engineering*, vol. 143, no. 3, 2016.

[54] M. Shahsavari, R. Moghaddam, M. Jafari, and M. Grabinsky, "Preliminary investigation of liquefaction potential of cemented paste backfill under dynamic loading using a two-dimensional, time-domain ground response analysis," in *Proceedings of the 12th International Symposium on Mining with Backfill*, Mount Isa, Australia, February 2017.

[55] A. Moser, F. Wallner, H. Wagner, and T. Ladinig, "An experimental study to investigate the interaction of backfill and rock mass," in *Ground Support 2016*, E. Nordlund, Ed., Lulea University of Technology, Luleå, Sweden, 2016.

Research Article

Flocculation Settling Characteristics of Ultra-Fine Iron Tailings with Rich Gypsum

Daiqiang Deng [1,2] **and Guodong Cao** [1]

[1] *College of Civil Engineering and Mechanics, Xiangtan University, Xiangtan 411105, China*
[2] *College of Mining Engineering, Guizhou Institute of Technology, Guiyang, Guizhou 550003, China*

Correspondence should be addressed to Daiqiang Deng; ustbb20070025@126.com and Guodong Cao; gdcao@xtu.edu.cn

Because of the uniqueness of geological mineralization, tailings obtained from Chenchao Iron Mine have low SiO_2 content of only 27.80%. Content of Al_2O_3 and MgO is 13.31% and $CaSO_4$ is 22.09%. The fineness modulus of the ores is large enough for convenient mineral separation, thus resulting in 16.03% $-5\,\mu$m particles and 27.76% $-10\,\mu$m particles in the tailings, respectively. The average particle size is only 69.36 μm; it belongs to the category of very fine tailings. The natural sedimentation of tailings is extremely slow due to the comprehensive effects of their physical and chemical properties. Hence, sedimentation tests using four types of flocculating agents are conducted to accelerate the sedimentation of the tailings of Chenchao Iron Mine. Compared with natural sedimentation, the flocculating sedimentation is considerably quicker. Among the four flocculants, the sedimentation of sample using the special BASF flocculant is the fastest. When the tailings of 1 ton add this flocculant of 20 g, the maximum settling concentration reaches 60.98% after 40 min and its special gravity is 1.577 g/cm^3, thus it fulfills future requirements of filling technologies. As the largest iron mine in the mid-southern region of China, Chenchao Iron Mine must turn to filling mining. This study can provide technological support for goaf management and environment-friendly treatment of solid waste in the Yangtze River basin, which plays important roles in ecological protection.

1. Introduction

Properties of tailings and agents in mineral processing flow sheet are often studied with respect to mine filling. For example, some mines have ultra-fine tailings that are easy to suspend and sediment slowly under natural conditions, thus making the feeding concentration and flow rate difficult to control. Under these circumstances, flocculants should be added to tailings to accelerate sedimentation and reach a high settling concentration in a short time, thus realizing high-concentration filling, which is easy to control [1, 2]. Notably, tailings in some mines have special properties. Except for the small particle size, the mineral composition of tailings is relatively complicated, thus making its sedimentation difficult and influencing the follow-up filling. Special treatment is needed to realize the desired concentration [3, 4].

Natural and flocculation settling experiments have been conducted for the sedimentation of ultra-fine tailings in numerous related studies. Through a contrast experiment of different flocculants and process control, the best flocculant and its application conditions have been determined [5–7]. Regarding flocculation settling experimental method and laws of tailings, Zhou and Zhang [8] conducted natural and flocculation settling experiments of tailings in a measuring cylinder and tested the settling concentration and bulk density of tailing slurry. Moreover, some studies analyzed the sedimentation process of tailings to determine the mechanical mechanism of tailing settling through flocculation settling experiments and provided references for actual application [2, 9, 10]. A sedimentation prediction model for tailings has been established through experimentation, thus providing references for similar studies [11]. Viewed from the microscopic molecular forces of inorganic

and macromolecular flocculants, related studies have explored the flocculation kinetics of aluminum oxide and polyacrylic acid and disclosed the action mechanism of polyacrylate flocculation under different concentrations [12]. As an equipment of tailing concentration, deep-cone thickeners are being used increasingly often recently and have become the first choice in slurry preparation in filling design. Two studies conducted practical analyses of solid concentration distribution and concentration of pasty fluid in deep-cone thickeners, thus providing technological support to the use of high-efficiency thickeners [13, 14]. Other studies analyzed the action mode and application advantages of flocculants, thus providing a direction for the R&D of flocculant products [15, 16].

For the concentration technology of extremely fine particle tailings which has been gradually developed in recent years, combined with the technical problems appearing in the field, new technologies, new equipment, and new materials have been applied to solve the difficult problems in the production. For example, in terms of the settlement and concentration of fine tailing, researchers calculated the size of the efficient thickener with the help of laboratory test results, and it played a good role in the concentration of copper tailing [17]. In terms of paste filling design and application, the relevant researchers summarized the past technological development and put forward views on the future technological trend, which provided a reference for the determination of fine tailings concentration and optimal discharge concentration. In the selection of tailings settlement concentration flocculant, the researchers added super flocculation in the flocculation and settlement process of ultra-fine tailings, optimized the settlement behavior by analyzing the particle size distribution of tailings, and finally achieved a good effect in the paste joint filling process [18–21].

Considering the high gypsum content and slow sedimentation of ultra-fine tailings in Chenchao Iron Mine, natural and flocculant sedimentation experiments of tailings were conducted in this study to provide references for the future mass flow filling system of the mine. As the largest iron mine reserve in the mid-southern region of China, Chenchao Iron Mine is rich in high-quality iron ore reserves. Underground mining will be performed comprehensively after the open pit of the mine is closed to utilize local resources reasonably and sustainably.

Filling mining is essential for the future. Therefore, flocculation settling experiments of tailings should be conducted as they can offer technological parameters for the future introduction of deep-cone thickeners into filling systems. This study not only plays an important role in goaf management and reutilization of solid wastes in the Yangtze River basin but can also protect the local ecological environment and promote harmonious development between mine production and natural ecology.

2. Materials and Methods

2.1. Tailings.
The basic physical properties of the tailings are shown in Table 1. The stacking porosity of the tailings in

Chenchao Iron Mine was 42.6%, which was relatively high. The angle of repose, which is influenced by mineral composition, was 33.73°. Natural slope angle is very important for material transportation in filling engineering. In some other mining enterprises, the natural slope angle of tailings is usually 35~40°. The $CaSO_4$ content of the tailings made them difficult to be stacked high. When stacked high manually, tailings can easily creep downward and scatter due to their small relative internal friction.

The particle size distribution of tailings is shown in Figure 1. It can be seen from Figure 1 that there are many fine particles, of which the content of $-5\,\mu m$ particles and $-20\,\mu m$ particles is 16.03% and 40.46%, respectively. The average particle size is $69.36\,\mu m$. About 10% particles can pass through the sieve of $3.2\,\mu m$ pore, and 60% particles can pass through the sieve of $52\,\mu m$ pore. The high content of fine particles will have a certain negative effect on the settlement of tailings. The fine particles can be suspended in water for a long time, resulting in slow settlement of tailings. Meanwhile, tailings are mostly flaked, and there is a large force between them and water molecules in the settlement process, so the settlement is slow. For tailings of very fine particles, its gravity is very small, so the buoyancy is dominant. It hardly sinks. Moreover, the tiny particles may form colloidal solution; they will attract or repel each other due to electrostatic interaction, so the particles will do chaotic lateral movement in a horizontal direction. The time of particles suspending in the tail slurry will greatly increase which results in slow subsidence.

The chemical composition of the tailings is shown in Figure 2. The tailings had small SiO_2 content of only 27.80%. Al_2O_3 and MgO accounted for 13.31%, and $CaSO_4$ took up 22.09% of the tailings. The content of SiO_2 in tailings is very important for the consolidation, hardening, and permeability of materials in filling engineering. In some other mining enterprises, the content of SiO_2 in tailings is usually about 50–75%. The natural sedimentation of tailings is relatively slow and high settling concentration and bulk density are difficult to reach in a short time due to the comprehensive effects of their special physical and chemical properties.

2.2. Flocculants

   (1) Special BASF flocculant (model no. Pheomax9010) for tailing settling, Germany

   (2) BASF anionic flocculant with high molecular weight (model no. $M^3 42$), Germany

   (3) Anionic flocculant with 12,000,000 MW, Northern Chemistry

   (4) Nonionic flocculant with 12,000,000 MW, Northern Chemistry

2.3. Water.
In the experiments, common tap water at room temperature and pH = 7 was used to prepare the tailing slurry and flocculant solution.

TABLE 1: Physical properties of tailings.

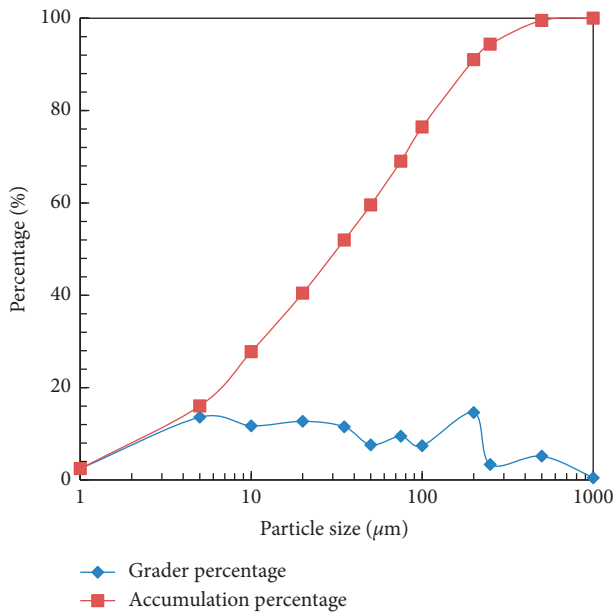| Material	Special gravity	Bulk density (t/m^3)	Dense porosity (%)	Angle of repose (°)
Tailings	2.77	1.590	42.60	33.73

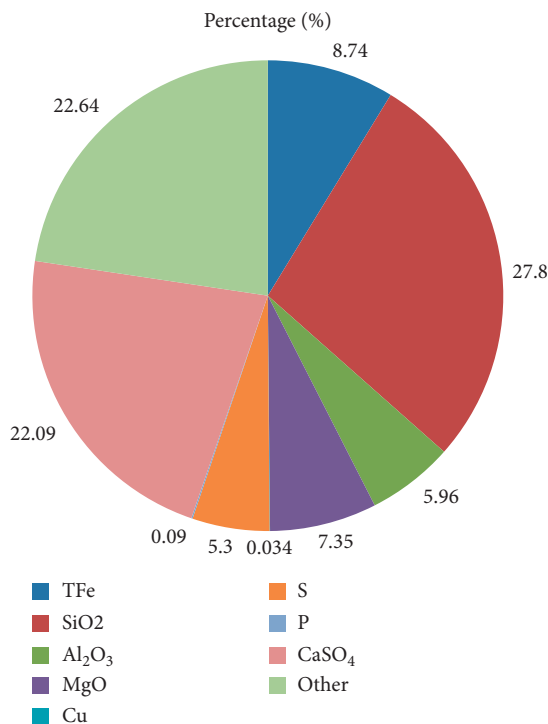FIGURE 1: Particle size distribution curve of tailings.

FIGURE 2: Chemical composition of tailings.

2.4. Preparation of Tailing Slurry and Flocculant Solution. The initial concentration of the tailing slurry was 40%, and the concentration of the flocculant solution was 3‰. The flocculant dosage per ton of the dry tailings was 20 g/t of the flocculants Pheomax9010 BASF and M^{3}42 BASF and 40 g/t of the anionic flocculant with 12,000,000 MW (Northern Chemistry) and the nonionic flocculant with 12,000,000 MW (Northern Chemistry).

2.5. Flocculating Sedimentation Experiment. The particle size, shape, and chemical composition of tailings can influence the settling characteristics of tailing slurry considerably. These parameters determine the stacking state and settling concentration and bulk density of tailings. The tailings in Chenchao Iron Mine are difficult to sediment, except in natural sedimentation experiments. Thus, flocculating sedimentation experiments using four different flocculants were conducted in this study with the aim of recognizing the best flocculant for tailing settling. Changes in supernate volume in a 1000 ml cylinder were recorded; according to the recorded data, the net water growth and variations in settling concentration and bulk density were calculated. The details of the experimental programs are listed in Table 2.

3. Experimental Results

3.1. Natural Sedimentation. The natural sedimentation experiment, which used no flocculants and tested the sedimentation process of tailings under natural conditions, was compared with flocculating sedimentation. The initial concentration of the tailing slurry was 40%. Combined with the technological parameters in the future daily filling production process, the concentration of tailing mortar transported from the dressing plant to the filling slurry preparation station is about 40%, so the preparation concentration of the tailing mortar of this group is 40%.

The variations in the natural sedimentation test parameters of the tailings are shown in Figure 3. In the natural sedimentation experiment, the net water growth climbed up gradually before reaching the maximum of 200 ml at 10 min, declined during the 10–40 min interval, and remained the same after 50 min. The water volume continuously increased rapidly within 0–30 min, increased slowly in the 30–50 min interval, and remained the same after 120 min. The slurry volume decreased rapidly within 0–28 min, decreased continuously at a low speed during the 28–120 min interval, and became stable after 120 min. The total water and slurry volumes followed a linear development law throughout the entire experiment and did not show evident changes.

The variation curves of the settling concentration and bulk density of the tailings under natural conditions are shown in Figure 4. The settling bulk density increased rapidly in the first 30 min, reached 1.484 t/m^3, increased slowly from 1.600 t/m^3 to 1.667 t/m^3 during the 30–120 min interval, and remained the same after 120 min. The settling concentration presented a similar variation law with the settling bulk density, increasing rapidly to 54.35% in the first

TABLE 2: Natural and flocculating sedimentation experiments of tailings.

Experiment no.	Test type	Name of flocculants	Concentration of flocculant solution (‰)	Flocculant dosage per ton of dry tailing (g/t)	Initial concentration of tailing slurry (%)
#1	Natural sedimentation	No flocculant	—	—	40
#2	Flocculating sedimentation	Pheomax9010 BASF	3	20	40
#3	Flocculating sedimentation	M³42 BASF	3	20	40
#4	Flocculating sedimentation	Anionic flocculant with 12,000,000 MW (Northern Chemistry)	3	40	40
#5	Flocculating sedimentation	Nonionic flocculant with 12,000,000 MW (Northern Chemistry)	3	40	40
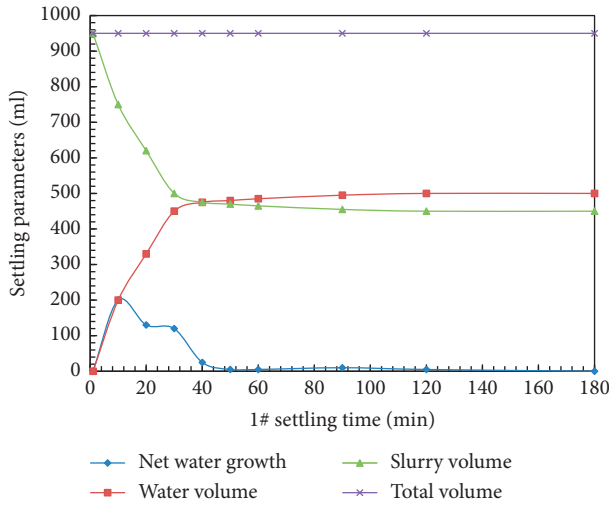
FIGURE 3: Natural sedimentation test parameters of tailings (#1).
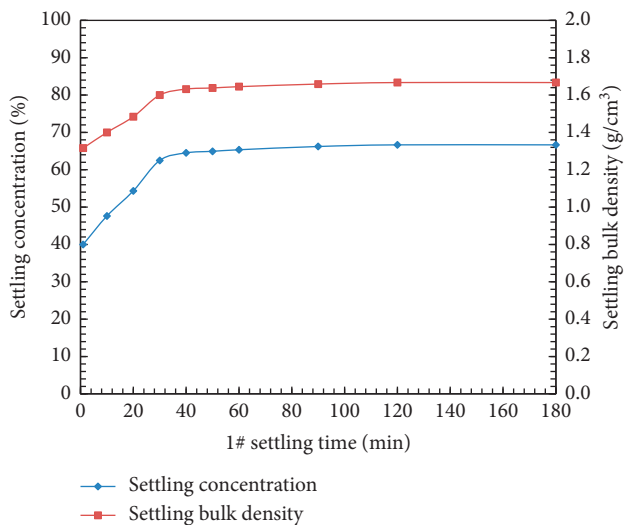
FIGURE 4: Variation curves of natural settling concentration and bulk density (#1).

30 min, climbing up slowly from 62.5% to 66.67% during the 30–40 min interval, and remaining the same after 120 min.

3.2. Flocculating Sedimentation Using Pheomax9010 BASF.

In this experiment, Pheomax9010 BASF at a dosage of 20 g/t was used as the flocculant. The concentration of the flocculant solution was 3‰, and the initial concentration of the tailing slurry was 40%. Combined with the technological parameters in the future daily filling production process, the concentration of tailing mortar transported from the dressing plant to the filling slurry preparation station is about 40%, so the preparation concentration of the tailing mortar of this group is 40%.

The variations in the flocculating sedimentation test parameters of the tailings with Pheomax9010 BASF are shown in Figure 5. The net water growth increased gradually before reaching the maximum of 370 ml at 10 min, began to decrease after 10 min, and remained the same after 20 min. The water volume increased rapidly within 0–10 min, climbed up slowly during the 10–40 min interval, and remained the same after 40 min. The slurry volume decreased rapidly within 0–10 min, decreased continuously at a low speed during the 10–40 min interval, and stabilized after 40 min. The total water and slurry volumes followed a linear development law throughout the entire experiment and did not show evident changes.

The variation curves of the settling concentration and bulk density of the tailings with Pheomax9010 BASF are shown in Figure 6. The settling bulk density increased rapidly and reached 1.517 t/m³ in the first 10 min, increased slowly from 1.517 t/m³ to 1.577 t/m³ only within the 10–40 min interval, and remained the same after 40 min. The settling concentration varied similarly with the settling bulk density, increasing rapidly and reaching 56.82% in the first 10 min, climbing up slowly from 56.82% to 60.98% within the 10–40 min interval, and stabilizing after 40 min.

3.3. Flocculating Sedimentation Using M³42 BASF.

In this experiment, M³42 BASF at a dosage of 20 g/t was used as the flocculant. The concentration of the flocculant solution was
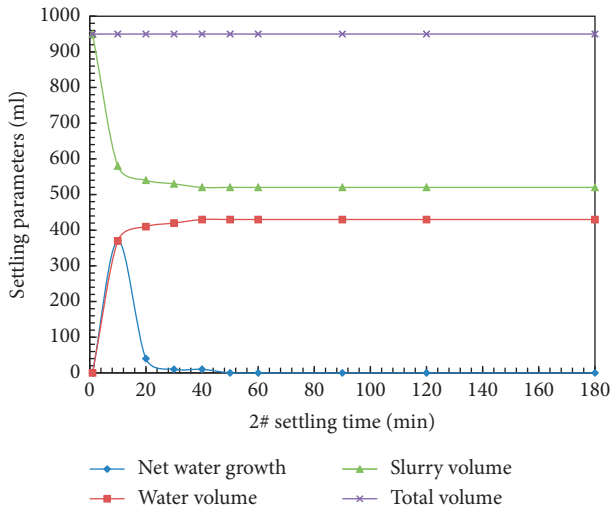
FIGURE 5: Flocculating sedimentation test parameters of tailings (#2).
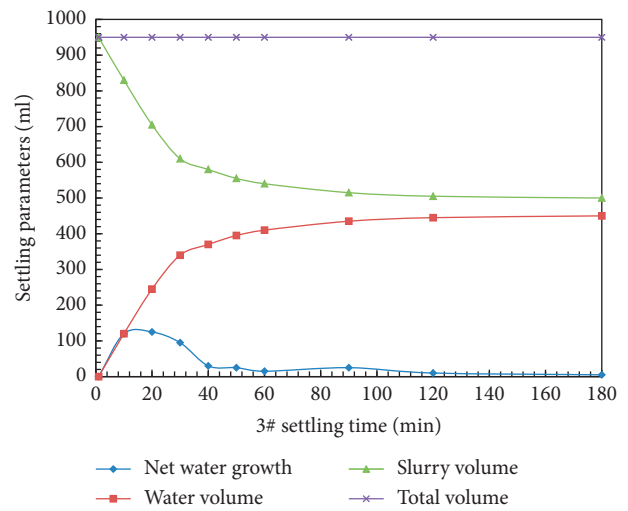

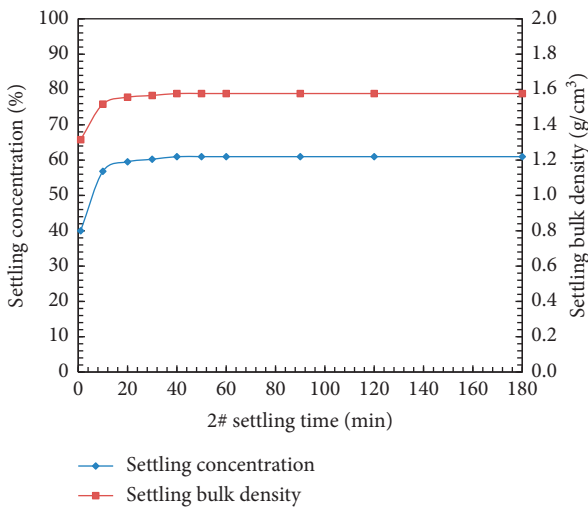FIGURE 7: Flocculating sedimentation test parameters of tailings (#3).

FIGURE 6: Variation curves of flocculation settling concentration and bulk density (#2).
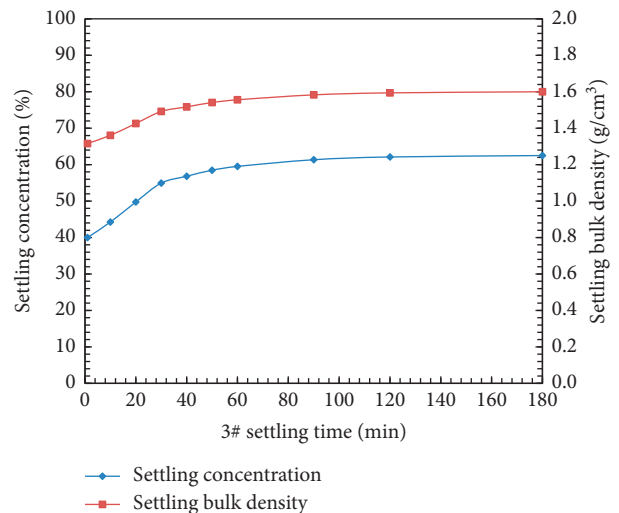

FIGURE 8: Variation curves of flocculation settling concentration and bulk density (#3).

3‰, and the initial concentration of the tailing slurry was 40%.

The variations in the flocculating sedimentation test parameters of the tailings with M³42 BASF are shown in Figure 7. The net water growth increased gradually before reaching the maximum of 125 ml at 20 min, began to decrease after 20 min, and remained the same after 50 min. The water volume continuously increased rapidly within 0–30 min, climbed up slowly during the 30–180 min interval, and remained the same after 180 min. The slurry volume decreased rapidly within 0–30 min, decreased continuously at a low speed during the 30–180 min interval, and stabilized after 180 min. The total water and slurry volumes followed a linear development law throughout the entire experiment and did not show evident changes.

The variation curves of the settling concentration and bulk density of the tailings with M³42 BASF are shown in

Figure 8. The settling bulk density increased gradually and reached 1.492 t/m³ in the first 30 min, climbed up slowly from 1.492 t/m³ to 1.600 t/m³ within the 30–180 min period, and remained the same after 180 min. The settling concentration varied similarly with the settling bulk density, increasing gradually and reaching 54.95% in the first 30 min, climbing up slowly from 54.95% to 62.5% within the 30–180 min interval, and stabilizing after 180 min.

3.4. Flocculating Sedimentation Using Anionic Flocculant with 12,000,000 MW (Northern Chemistry). In this experiment, the anionic flocculant with 12,000,000 MW (Northern Chemistry) at a dosage of 40 g/t was used. The concentration of the flocculant solution was 3‰, and the initial concentration of the tailing slurry was 40%.

Figure 9 shows that in the sedimentation experiment with the anionic flocculant with 12,000,000 MW (Northern Chemistry), the net water growth increased gradually before reaching the maximum of 335 ml at 10 min, began to decrease within the 10–40 min interval, and remained the same after 50 min. The water volume increased rapidly within 0–10 min, climbed up slowly during the 10–60 min interval, and remained the same after 60 min. The slurry volume decreased rapidly within 0–10 min, decreased continuously at a low speed during the 10–60 min interval, and stabilized after 60 min. The total water and slurry volumes followed a linear development law throughout the entire experiment and did not show evident changes.

Figure 10 shows that in the sedimentation experiment with the anionic flocculant with 12,000,000 MW (Northern Chemistry), the settling bulk density increased gradually and reached $1.488 \, t/m^3$ in the first 10 min, climbed up slowly from $1.488 \, t/m^3$ to $1.600 \, t/m^3$ within the 10–60 min interval, and remained the same after 60 min. The settling concentration varied similarly with the settling bulk density, increasing rapidly and reaching 54.64% in the first 10 min, increasing continuously from 54.64% to 62.5% at a low speed within the 10–60 min interval, and stabilizing after 60 min.

3.5. Flocculating Sedimentation Using Nonionic Flocculant with 12,000,000 MW (Northern Chemistry).

In this experiment, the nonionic flocculant with 12,000,000 MW (Northern Chemistry) at a dosage of 40 g/t was used. The concentration of the flocculant solution was 3‰, and the initial concentration of the tailing slurry was 40%.

The variations in the flocculating sedimentation test parameters of the tailings with the nonionic flocculant with 12,000,000 MW (Northern Chemistry) are shown in Figure 11. The net water growth increased gradually before reaching the maximum of 170 ml at 20 min, began to decrease during the 20–120 min interval, and remained the same after 120 min. The water volume increased rapidly during the 0–20 min interval, climbed up slowly during the 20–120 min period, and remained the same after 120 min. The slurry volume decreased continuously within 0–20 min, reached a turning point during the 20–120 min interval, and stabilized after 120 min. The total water and slurry volumes followed a linear development law throughout the entire experiment and did not show evident changes.

The variation curves of the settling concentration and bulk density of the tailings with the nonionic flocculant with 12,000,000 MW (Northern Chemistry) are shown in Figure 12. The settling bulk density increased gradually and reached $1.531 \, t/m^3$ in the first 30 min, climbed up from $1.531 \, t/m^3$ to $1.625 \, t/m^3$ at a low speed within the 30–120 min interval, and remained the same after 120 min. The settling concentration varied similarly with the settling bulk density, increasing gradually and reaching 57.8% in the first 30 min, climbing up from 57.8% to 64.1% at a low speed within the 30–120 min interval, and stabilizing after 120 min.

3.6. Analysis of Natural and Flocculating Sedimentation Experimental Results.

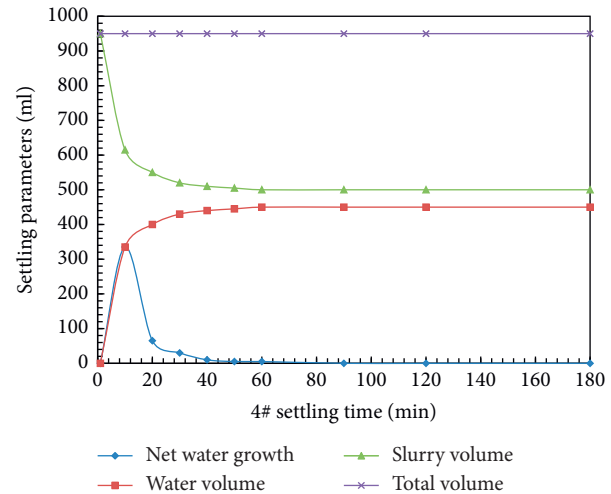The times for reaching the final settling,

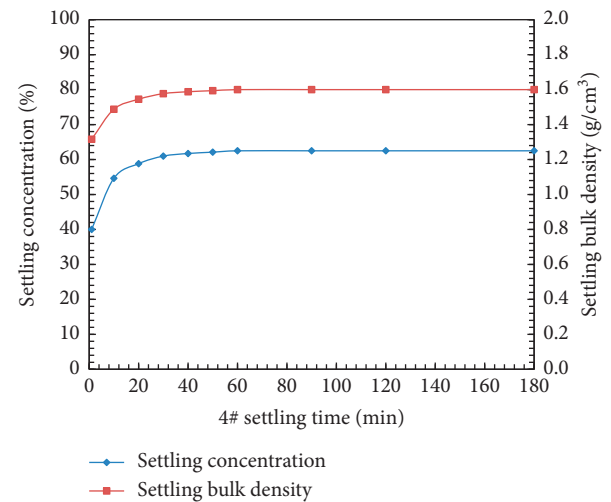FIGURE 9: Flocculating sedimentation test parameters of tailings (#4).

FIGURE 10: Variation curves of flocculation settling concentration and bulk density (#4).

maximum settling concentration, and maximum settling bulk density of the five experiments were analyzed. The flocculants were ranked on the basis of the required final settling concentration of 55% (Table 3). To show an intuitive representation of the difference between the natural and flocculating sedimentation of the tailings, data of the natural sedimentation experiment (#1) and those of the four flocculating sedimentation experiments (#2–5) at different time periods were summarized and integrated in the same plane coordinates. The settling concentration and bulk density at 30, 60, 90, and 120 min, as well as test images at these time periods , are shown in Figures 13–16, respectively. The volume of the cylinders shown in the images is 1000 ml. Five cylinders were placed in a line and represented the following (from left to right): natural sedimentation (#1), flocculating sedimentation using Pheomax9010 BASF (#2), flocculating sedimentation using M³42 BASF (#3), flocculating
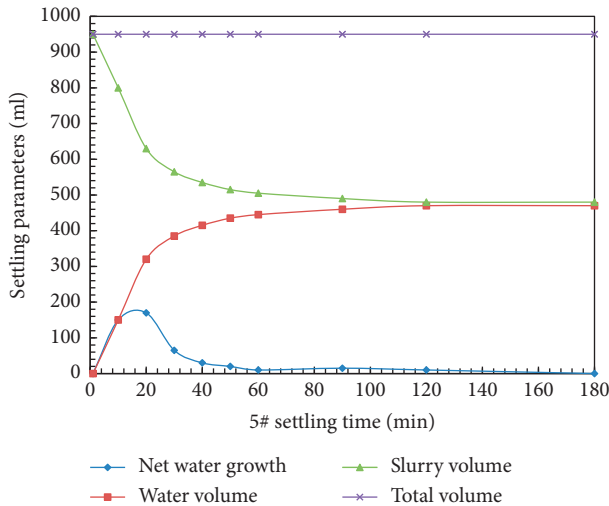
FIGURE 11: Flocculating sedimentation test parameters of tailings (#5).
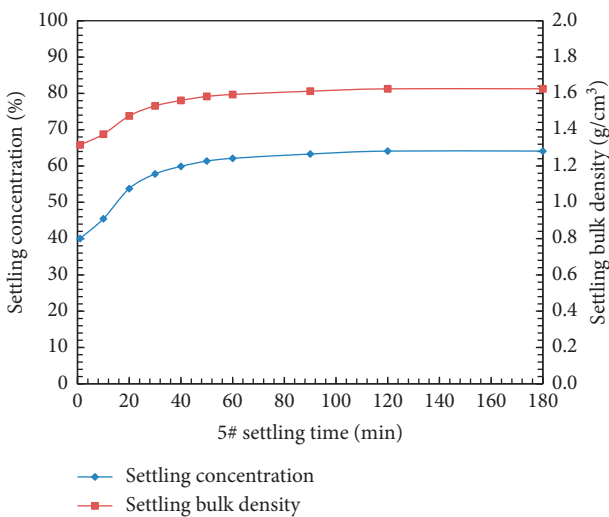

FIGURE 12: Variation curves of flocculation settling concentration and bulk density (#5).

sedimentation using anionic flocculant with 12,000,000 MW (Northern Chemistry) (#4), and flocculating sedimentation using nonionic flocculant with 12,000,000 MW (Northern Chemistry) (#5).

As shown in Table 3 and Figures 13–16, 120 min was needed in test #1 to reach the maximum settling concentration in Chenchao Iron Mine. The maximum settling concentration was 66.67%, and the maximum bulk density was 1.667 g/cm^3. Meanwhile, only 40 min was needed in test #2 to reach the maximum settling concentration of 60.98%, and the maximum bulk density was 1.577 g/cm^3. In test #3, the maximum settling concentration of 62.5% was reached at 180 min, and the maximum bulk density was 1.600 g/cm^3. In test #4, 60 min was needed to reach the maximum settling concentration of 62.5%, and the maximum bulk density was 1.600 g/cm^3. In test #5, the maximum settling concentration

of 64.1% was reached at 120 min, and the maximum bulk density was 1.625 g/cm^3.

The comparison of the four flocculating sedimentation experimental results shows that different flocculants cause tailings to show different settling characteristics. Pheomax9010 BASF (20 g/t) achieved the highest settling speed, followed by the anionic flocculant with 12,000,000 MW (Northern Chemistry) (40 g/t), nonionic flocculant with 12,000,000 MW (Northern Chemistry) (40 g/t), and M^{3}42 BASF (20 g/t). The sequence of final settling concentration from large to small is natural sedimentation (66.67%), nonionic flocculant with 12,000,000 MW (Northern Chemistry) (64.18%), anionic flocculant with 12,000,000 MW (Northern Chemistry) (62.5%), M^{3}42 BASF (62.53%), and Pheomax9010 BASF (61.12%). The future filling technique only requires a settling concentration of tailings of at least 55% hence, the flocculant that can reach 55% settling concentration in the shortest time is the best. The experimental results show that using Pheomax9010 BASF, the settling concentration of the tailing slurry could reach 55% in 40 min, thus indicating that Pheomax9010 BASF is the optimal flocculant material for tailing settling in Chenchao Iron Mine. The anionic flocculant with 12,000,000 MW (Northern Chemistry), could lead to a 55% settling concentration in 60 min, is the second best.

In summary, although natural sedimentation took a long time to reach the final settling state, the settling concentration and bulk density in this setting were relatively high and accompanied with tight tailing stacking structures. The supernate was light grey during the settling process, was not clear in the beginning, and became transparent in the final settling state. The natural sedimentation images show that the slurry volume under natural sedimentation was the highest in the beginning but became the lowest in the end, thus resulting in high settling concentration and bulk density. Under natural conditions, 120 min was needed to reach the final settling state. The final settling concentration was 66.67%, and the final settling bulk density was 1.667 t/m^3.

The comparison of the flocculating experiments shows that the tailing slurry has high sedimentation speed. The supernate can become transparent in a short time and was most transparent when Pheomax9010 BASF was used. Furthermore, the final settling state and the best settling performance were achieved in the shortest time when this flocculant was used. The images show that the tailings became relatively fluffy at their final settling. The slurry volumes in all flocculating experiments were higher than that under natural sedimentation, thus resulting in relatively smaller settling concentration and bulk density. Pheomax9010 BASF achieved the smallest settling concentration and bulk density, reaching the final settling state in only 40 min. The final settling concentration was 60.98%, and the final settling bulk density was 1.577 t/m^3. These parameters can meet settling requirements. The required ≥55% settling concentration meant that the key to evaluating the performances of the flocculating materials was the time. Therefore, Pheomax9010 BASF is the best flocculant for Chenchao Iron Mine.

TABLE 3: Statistics on parameters at final settling.

Test no.	Time for reaching the final settling (min)	Maximum settling concentration (%)	Maximum settling bulk density (t/m^3)	Order of flocculants
#1	120	66.67	1.667	Standard
#2	40	60.98	1.577	1
#3	180	62.50	1.600	3
#4	60	62.50	1.600	2
#5	120	64.10	1.625	4
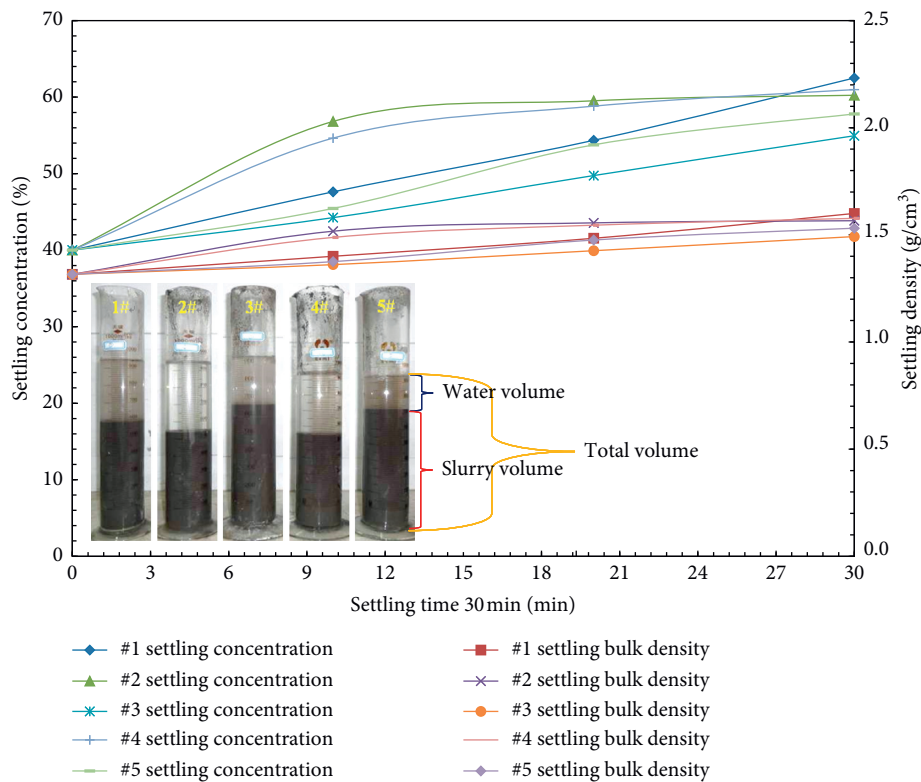
FIGURE 13: Curves of settling concentration and bulk density (30 min).

4. Discussion

The settling performance of tailings often influences the tailing filling system considerably. With slow sedimentation of tailings, preparing high-concentration filling slurry and meeting the required physical properties, such as strength of fill, are difficult. The sedimentation of tailings is often influenced by their properties. An appropriate amount of flocculant is often needed for tailings with special properties and slow settling. Jiao et al. determined the best flocculant through flocculating sedimentation experiment of tailings. Consequently, the tailing slurry reached the desired concentration and the prepared strength of fill could meet mining requirements [22, 23]. Wang and Li et al. achieved high-concentration filling slurry by combining a high-efficiency deep-cone thickener and flocculant. The entire thickening system had stable working conditions and good performance [24, 25].

To provide references for future filling system design and environment-friendly treatment of abundant solid waste, the optimal flocculant was chosen by the current study

considering the difficult settling of ultra-fine iron tailings with rich gypsum. Tailing slurry in the future filling system for Chenchao Iron Mine will be prepared with a deep-cone thickener. Hence, related studies that combine properties of tailings shall be conducted. In mines with tailing filling, sedimentation properties of tailings are important in technique connection, working efficiency, and comprehensive effect of enterprises. Filling techniques with tight technique connection, few errors, and high efficiency are important in enterprise development and competition. Therefore, a method that allows for the quickest settling of tailings should be developed to provide technological references for increasing the preparation efficiency of filling slurry.

A large area in the Yangtze River basin in China has ore mines. Solid wastes from mining production are stacked in the surface tailing pond and migrate outside through natural factors, such as wind and rain, thus causing potential risks to surrounding land, rivers, and underground water. Hence, effective measures should be adopted to avoid surrounding environmental pollution by heavy metals and other harmful elements in solid waste. As an ultra-large mine in the Wuhan
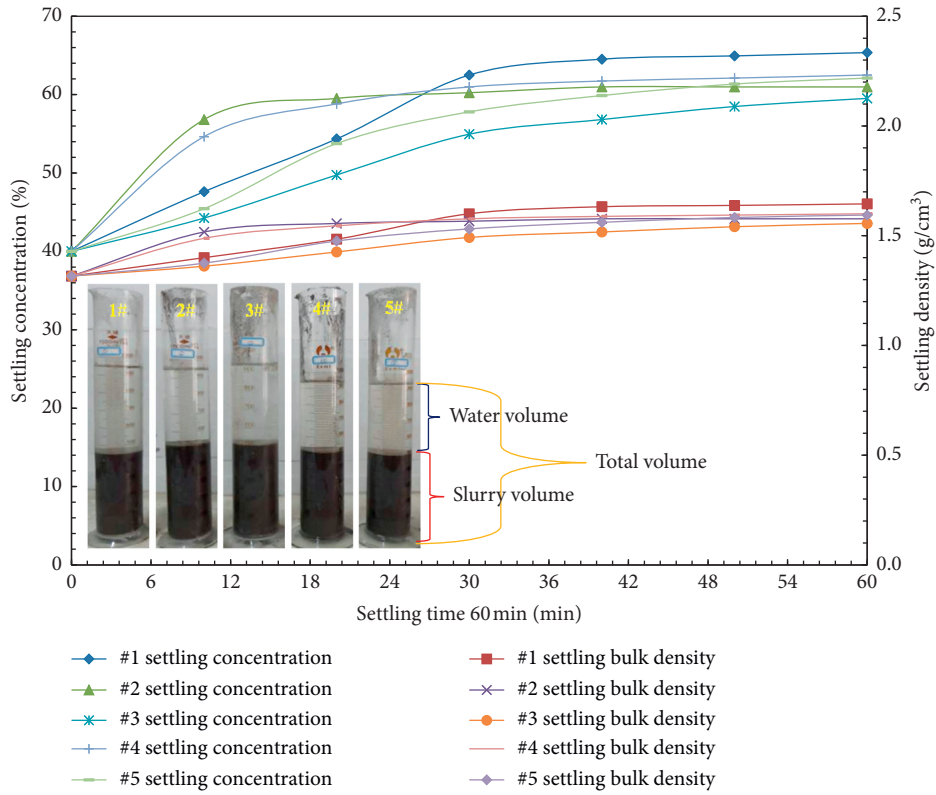
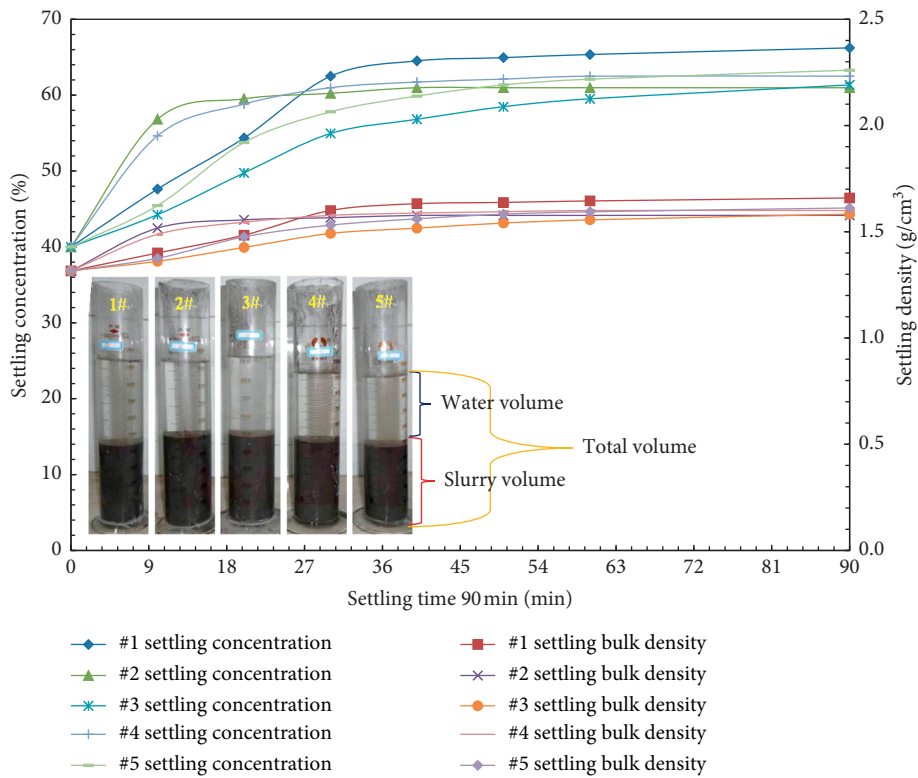FIGURE 14: Curves of settling concentration and bulk density (60 min).

FIGURE 15: Curves of settling concentration and bulk density (90 min).
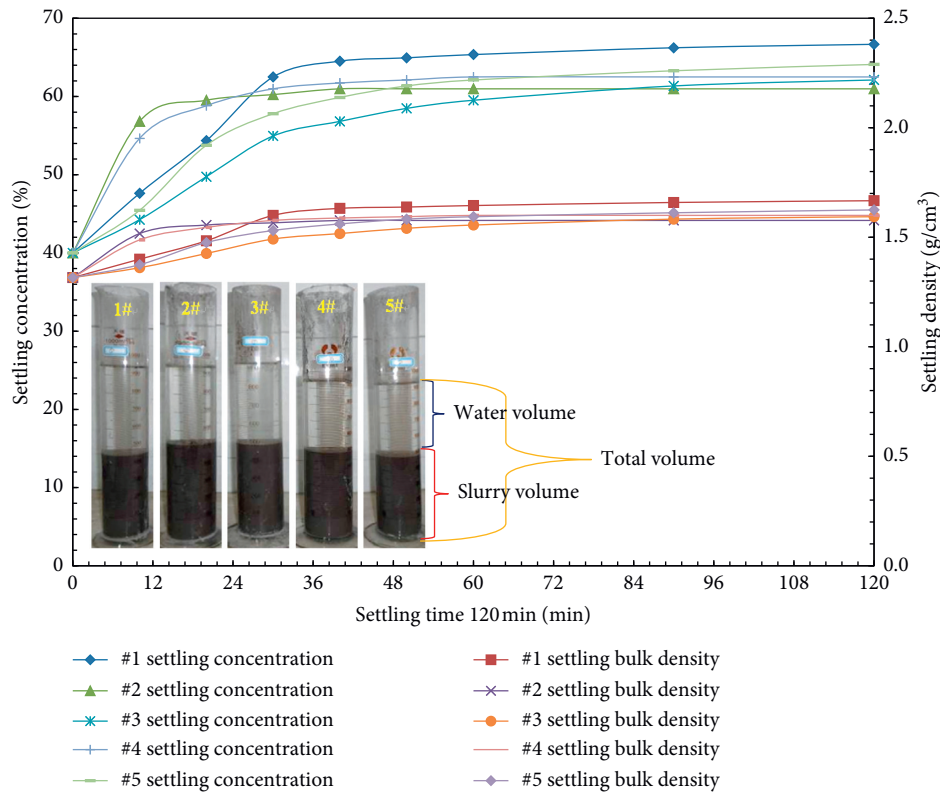
Figure 16: Curves of settling concentration and bulk density (120 min).

economic circle and along the Yangtze River basin, Chenchao Iron Mine has a long exploitation history. The water and land resources in the Yangtze River basin should thus be protected through the proper disposal of solid waste. Meanwhile, goaf filling engineering is used for the reutilization of solid wastes; hence, studying the sedimentation properties of tailings can provide early technological parameters for filling engineering. Consequently, discussing the flocculating sedimentation performances of ultra-fine iron tailings with rich gypsum is important as it aims to protect the ecological environment in the Yangtze River basin.

5. Conclusions

(1) In Chenchao Iron Mine, about 2711 m^3 goaf volume arises every day. However, the existing conventional flow filling system can only fill 750 m^3 and make selective filling to goaf. The tailing dosage is 745 t/d. The dosage of tailings for comprehensive filling exploitation in the future will increase dramatically to 2692 t/d; thereby, it considerably reduces the stacking amount of tailings in the surface tailing pond. The service life of the tailing pond will thus be prolonged, and tailing emission and disposal cost will be reduced dramatically.

(2) Tailings of Chenchao Iron Mine contain some gypsum and a small number of quartz, which have strong sandiness and easily sink. Moreover, the tailings have a low natural settling rate due to the ultra-fine size of particles, which make the final dense settling state difficult to reach in a short time without a flocculant. A contrast analysis between the natural and flocculating sedimentation of tailings was conducted on the basis of the properties of the tailings in Chenchao Iron Mine. The Pheomax9010 BASF was the most effective. Compared to other flocculants, it can decrease 80 mins to achieve the same settling concentration and settling bulk density.

(3) As shown in the flocculating sedimentation images, the supernate of experiment was the clearest at 30 min and the sedimentation of tailings was the quickest without the suspending particles. Even the ultra-fine particles sedimented with large ones. The settling concentration of the tailings in experiment was not the highest at 40 min but still meets the concentration limit of 55%. Therefore, Pheomax9010 BASF is recommended as the flocculating sedimentation of tailings in the future.

(4) In the future study of tailings materials, they can be classified according to the detailed grading of granular material; the tailings with special particle size distribution are divided to the size of the corresponding category. Combined with the specific use of tailings materials, mesoscopic and microscopic analysis is conducted to investigate the relationship of particle shape and the settling velocity and to obtain the analytical expression of the granular

material sedimentation process to the analysis of the related laws and prediction.

(5) As the largest iron mine reserve in the mid-southern region of China, it has a long history of exploitation. The long-term caving exploitation has accumulated great goaf space, and surfaces in some regions have collapsed, thus serious risks exist. Chenchao Iron Mine is the main mine for Wuhan Steel Inc. For goaf management and environment-friendly treatment of solid wastes, Chenchao Iron Mine will gradually use filling mining pattern. This study is a preliminary exploration that provides basic parameters for its future filling system design. The results of this study will be used to guide the goaf management and environment-friendly treatment of solid wastes in the Yangtze River basin.

Data Availability

The data used to support the findings of this study are available from the corresponding author upon request.

Conflicts of Interest

The authors declare no conflicts of interest concerning the publication of this paper.

Authors' Contributions

Daiqiang Deng wrote the main text of the manuscript. Guodong Cao collected and analyzed the data. All authors reviewed and commented on the manuscript.

Acknowledgments

References

[1] Y.-n. Yuan, L.-y. Chai, Z.-h. Yang, Y.-p. Laio, X.-h. Deng, and S.-j. Zhang, "Application of polymeric aluminum salts in remediation of soil contaminated by Pb, Cd, Cu, and Zn," *Journal of Central South University*, vol. 20, no. 6, pp. 1638–1644, 2013.

[2] N. N. DengLiao, J. S. Laskowski, and F. Concha, "The use of ultra-flocculation in optimization of the experimental flocculation procedures," *Physicochemical Problems of Mineral Processing*, vol. 1, no. 47, pp. 5–16, 2011.

[3] F. H. Wang and D. B. Chen, "Study and application of the technology of slime pulp flocculation and thickening in a vertical sand bin," *Metal Mine*, vol. 283, no. 1, pp. 21–24, 2000.

[4] X. z. Shi, H. y. Hu, X. h. Du, M. L. Ling, and H. Y. Wang, "Experimental study on flocculating sedimentation of tailings slurry in a vertical sand tank," *Mining and Metallurgical Engineering*, vol. 30, no. 3, pp. 1–3, 2010.

[5] X. m. Wang, J. x. Liu, Q. s. Chen, C. c. Xiao, and X. h. Wan, "Optimal flocculating sedimentation parameters of unclassified tailings," *Science&Technology Review*, vol. 32, no. 17, pp. 23–28, 2014.

[6] Z.-n. Li, L.-j. Guo, W.-y. Xu, and C. x. Shi, "Experimental study on flocculation sedimentation of fine tailings," *China Mining Magazine*, vol. 23, no. S2, pp. 215–218, 2014.

[7] H. Wang, J. Yang, Q. An, and C. b. Han, "Expeirimental study on sedimentation of ultra-fine unclassified tailings," *Mining Engineering*, vol. 9, no. 5, pp. 27–29, 2011.

[8] X. l. Zhou and W. b. Zhang, "Methods for settlement experiment of slurry in the measuring cylinder," *Nonferrous Metals Mieral Processing Section*, vol. 5, pp. 30–32, 2005.

[9] J. j. Wang, W. y. Xu, and L. j. Guo, "Study on flocculation sedimentation rules of full tailings," *China Mining Magazine*, vol. 21, no. 6, pp. 92–94, 2012.

[10] H. z. Jiao, H. j. Wang, A. x. Wang, X. w. Ji, Q. w. Yan, and X. Li, "Rule and mechanism of flocculation sedimentation of unclassified tailings," *Journal of University of Science and Technology Beijing*, vol. 32, no. 6, pp. 702–707, 2010.

[11] Q. l. Zhang, Q. s. Chen, X. m. Wang, and C. c. Xiao, "Study on GA-SVM optimal prediction model on flocculating sedimentation parameter of unclassified tailings," *Journal of Safety Science and Technology*, vol. 10, no. 5, pp. 24–30, 2014.

[12] K. K. Das and P. Somasundaran, "A kinetic investigation of the flocculation of alumina with polyacrylic acid," *Journal of Colloid and Interface Science*, vol. 271, no. 1, pp. 102–109, 2004.

[13] H. Jiao, A. Wu, H. Wang, S. Zhong, R. Ruan, and S. Yin, "The solids concentration distribution in the deep cone thickener: a pilot scale test," *Korean Journal of Chemical Engineering*, vol. 30, no. 2, pp. 262–268, 2013.

[14] D. Tao and B. K. Parekh, "Pilot-Scale demonstration of deep cone paste thickening process for phosphatic clay/sand disposal," *Separation Science and Technology*, vol. 45, no. 10, pp. 1418–1425, 2010.

[15] P. D. ZhangZhao, S. A. Rothenberg, I. H. Heitner et al., "Development of new Bayer process flocculants," *Essential Readings in Light Metals: Alumina and Bauxite*, vol. 1, pp. 431–435, 1991.

[16] L. Botha and J. B. P. Soares, "The influence of tailings composition on flocculation," *The Canadian Journal of Chemical Engineering*, vol. 93, no. 9, pp. 1514–1523, 2015.

[17] C. Shi, L. Guo, and C. Yang, "Application of high-efficient thickener size estimation method in copper tailings thickening," *Nonferrous Metals Engineering*, vol. 7, no. 5, pp. 86–91, 2017.

[18] C. Qi and A. Fourie, "Cemented paste backfill for mineral tailings management: review and future perspectives," *Minerals Engineering*, vol. 144, no. C, Article ID 106025, 2019.

[19] C. Yang, L. Guo, G. Hou, and Z. Li, "Determination method of the best discharge concentration for fine tailing paste," *Metal Mine*, vol. 491, no. 5, pp. 29–32, 2017.

[20] A. Wu, Z. Ruan, J. Wang, S. Ying, and C. Ai, "Optimizing the flocculation behavior of ultrafine tailings by ultra-flocculation," *Chinese Journal of Engineering*, vol. 41, no. 8, pp. 981–986, 2019.

[21] H.-y. Cheng, S.-c. Wu, X.-q. Zhang, and A.-x. Wu, "Effect of particle gradation characteristics on yield stress of cemented paste backfill," *International Journal of Minerals, Metallurgy and Materials*, vol. 27, no. 1, pp. 10–17, 2020.

[22] H. z. Jiao, A. x. Wu, H. j. Wang, X. h. Liu, S. k. Yang, and Y. t. Xiao, "Experiment study on the flocculation settlement characteristic of unclassified tailings," *Journal of University of Science and Technology Beijing*, vol. 33, no. 12, pp. 1437–1441, 2011.

[23] H.-j. Wang, Q.-r. Cheng, A.-x. Wu, Y.-g. Zhai, and X.-p. Zhang, "Study on the thickening properties of unclassified tailings and its application to thickener design," *Journal of University of Science and Technology Beijing*, vol. 33, no. 6, pp. 676–681, 2011.

[24] Y. Wang, A.-x. Wu, H.-j. Wang, S.-z. Liu, and B. Zhou, "Influence mechanism of flocculant dosage on tailings thickening," *Journal of University of Science and Technology Beijing*, vol. 35, no. 11, pp. 1419–1423, 2013.

[25] H. Li, H.-j. Wang, A.-x. Wu, H.-z. Jiao, and X.-h. Liu, "Pressure rake analysis of deep cone thickeners based on tailings'settlement and rheological characteristics," *Journal of University of Science and Technology Beijing*, vol. 35, no. 12, pp. 1553–1558, 2013.

Research Article

Research on Optimization of a Solid Filling Mining Face Layout Based on a Combined Clamped Beam Model

Zhi-Yong Fu [iD],[1] **Xu-Fei Gong** [iD],[1] **Peng-Fei Zhang** [iD],[1] and **Cun-Wen Wang** [iD][2]

[1]*College of Energy and Mining Engineering, Shandong University of Science and Technology, Qingdao 266590, China*
[2]*Shandong Energy Group Co., Ltd., Jinan 250014, China*

Correspondence should be addressed to Xu-Fei Gong; gong_xufei@126.com and Peng-Fei Zhang; 122787742@qq.com

Optimizing the mining scheme is an essential work for improving recovery efficiency of filling mining. An optimization equation of mining face width under a gangue mining condition is derived firstly. Then, analysis of the optimization equation of the mining face width is carried out based on the measure data of the F5001 mining face in the Tangshan Coal Mine. At last, the reasonable mining face width is determined combined with numerical simulation. Results show that mining face width and roof subsidence increase with the increase of unit weight and mining depth, but decrease with the increase of the elastic modulus of roof. The maximum width of the mining face is 105 m in Tangshan Coal Mine. When the mining width increases from 66 to 105 m, the increasing percentage of roof subsidence is 15–18%. Roof subsidence is controlled less than 30% of the mining height. The variation range of the maximum roof subsidence is small, which means the mining face width can be designed reasonably through the proposed equation.

1. Introduction

It has been acknowledged that the traditional mining technology can lead to serious surface subsidence, damage, and deformation of upper buildings and ecological environment problems. It also causes deformation of the rocks around the working face and leads to extensive needs of support measures such as large deformation bolt [1]. Fortunately, the development of solid filling mining technology gives a solution for this issue [2–5]. Different from the traditional mining method, filling mining uses waste gangue to fill the goaf to control the deformation and movement of the overburden strata [6, 7]. Thus, the surface subsidence and the damage of upper buildings can be mitigated. For the solid filling mining technology, choosing a reasonable mining face width is one of the most essential issues. A reasonable mining face width can not only reduce the cost but also mitigate the ground pressure and control the surface subsidence.

At present, scholars have carried out lots of works in the area of filling mining technology. Wang et al. [8] used similar material simulation and on-site borehole detection to study the overburden failure of solid compacted mining. Xu et al.

[9] established a mechanical model for analyzing the relationship between the compressive modulus of the filling body and the development height of the rock beam. Yu et al. [10] analyzed the support mechanism of the filling body based on rock mechanics, control principles of the roadway, and other related theories. Liu et al. [11] studied the working performance of hydraulic support with field monitoring, numerical simulation, and theoretical analysis. Zhang et al. [12] analyzed the relationship between support of filling mining and the surrounding rock. Zhao et al. and Zhao et al. [13, 14] used numerical simulation and theoretical analysis to study the evolution of the abutment pressure distribution and its influence on the coal damage. Deng et al. [15] studied the roof movement characteristics under filling mining condition by establishing the elastic foundation beam model. Gong [16] studied the layout optimization of a fully mechanized mining face under specimen geological conditions.

Because the roof is supported by the filling body, the size of the mining face can be further optimized, and the filling of the mining face can be reasonably improved to reduce the cost per ton of coal. At present, there is little research on

determining the size of the mining face under the filling and mining conditions. In this paper, we first propose the optimization equation of mining face parameters for a solid filling mining condition based on the combined beam model. Then, practical calculations are performed based on the data of the F5001 mining face in the Tangshan Coal Mine, China. At last, the reasonable mining face width is determined combined with numerical simulation.

2. Clamped Beam Model of Goal-Roof Combination

2.1. Basic Assumptions and Equations. Considering the geometry characteristics and engineering practice, we introduce four hypotheses of material mechanics:

(1) Plane hypothesis: the cross section of the beam still keeps planar after deformation

(2) No normal stress hypothesis of longitudinal fiber: there is no interacted normal stress among longitudinal fibers

(3) Liner elastic hypothesis

(4) Homogeneous beam hypothesis: the beam consists of homogeneous material

The overburden pressure is simplified as a uniform load. Assuming that the coal seam suffers from elastic-plastic deformation, there are two cases, one neglecting the lateral deformation of the coal seam and the other not. Then, the deformation of the coal seam in the thickness direction is analyzed. In the theoretical study of the roof deformation law, the roof is simplified as an elastic combined clamped beam.

The simplified coal seam and roof and the calculation model are given in Figure 1.

The dominant failure mode of the roof is shear failure. Thus, the roof can be simplified as a combined clamped beam, where only elastic deformation is considered. Assuming that the roof is rigid and suffers from no deformation, the clamped beam model is given in Figure 2.

The relevant variable is defined as

$$w = \frac{\gamma L^4}{32E \cdot H^2},\tag{1}$$

where w is the vertical deflection of the roof, m; H is the thickness of the roof, m; L is the equivalent elastic beam span of the roof, m; E is the equivalent elastic modulus, MPa; and γ is the unit weight, kN/m^3.

2.2. Maximum Deflection Equation of the Clamped Beam. In the combined clamped beam model, a section of the clamped beam is assumed as square. The simplified section of the roof is given in Figure 3.

The calculation equation of this square section is as follows:
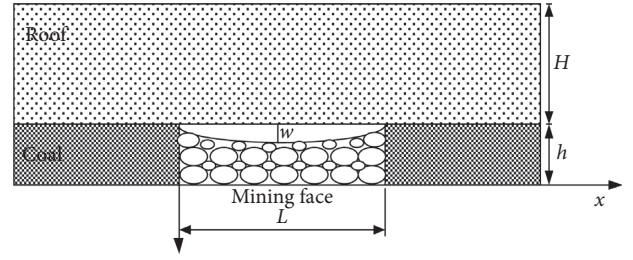
$$I_z = \frac{H^4}{12}.\tag{2}$$

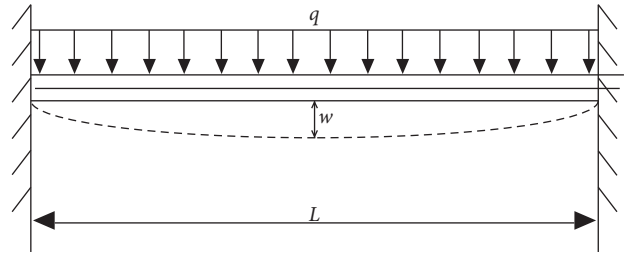Figure 1: Sketch of the calculation model.

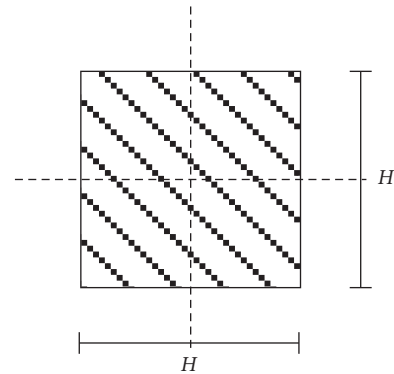Figure 2: Sketch of the clamped beam model.

Figure 3: Sketch of the square section of the clamped beam.

The overburden rock masses of the mining face are stratified based on their physical and mechanical properties. The H in Figure 4 is layered and combined to calculate its equivalent section moment of inertia. According to the combined beam theory, the H in equation (2) is stratified as well. After the section is stratified, the equivalent equation of the inertia moment is as follows:

$$I^* = \left\{ e^L + e^{(\beta^2 - 1)} \left(384/5 (0.5\alpha L)^4 \right) \left[(1/\cosh \cdot (\alpha L/4)) + \left((\alpha L)^2/32 \right) - 1 \right] \right\} I,\tag{3}$$

where I^* is the equivalent inertia moment, m^4; I is the conventional inertia moment, m^4; α is the elastic modulus ratio of roofs in the combined beam; β, generally larger than 1, is the ratio of I^* and I; and L is the span of the combined beam, m.

According to the equivalent inertia moment, the maximum deflection of the combined beam can be calculated with
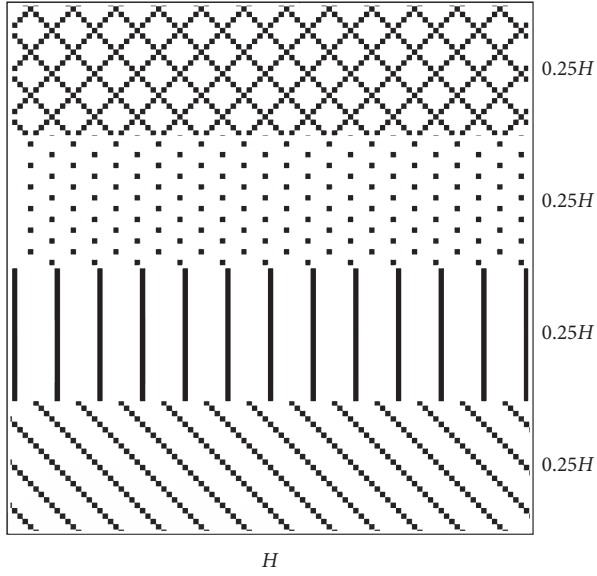
FIGURE 4: Sketch of the equivalent section.

$$w = \frac{q \cdot L^4}{384E \cdot I^*} = \frac{\gamma \cdot D \cdot L^4}{32E \cdot H^3}, \quad (4)$$

where D is the buried depth of the mining face, m.

2.3. Optimization Equation of the Mining Face. A model for obtaining the relationship between the mining face width and the tensile strength of the roof is established, which can prove a theoretical basis for the reasonable design of mining face width. Assuming that the span of a failure beam is L, the height H and the width $b = H$. The beam is under uniform load q, and the neutral layer is located in the middle of the longitudinal section, as shown in Figure 5.

Taking $x > 0$ as the research section, the bending moment of the rock beam is calculated with the following equation:

$$M = \frac{q}{2}\left(\frac{L}{2} - x\right). \quad (5)$$

The tensile strength of the rock beam in the x-direction is

$$\sigma_x = \frac{M \cdot y}{I_z}, \quad (6)$$

where I_z is the inertia moment of section in the neutral axis.

According to equations (2) and (5), the optimization equation of the mining face can be obtained:

$$L = \frac{\sigma_x H^4}{3\gamma q} + 2x. \quad (7)$$

The ultimate tensile strength of the goaf roof is taken as the criterion for designing the mining face width. Then, the parameter optimization of the mining face is established. According to the model of combined clamped beam, when x is 0 and y is $H/2$, the tensile strength of the roof reaches the maximum. Then, the constrain condition of roof fracture is
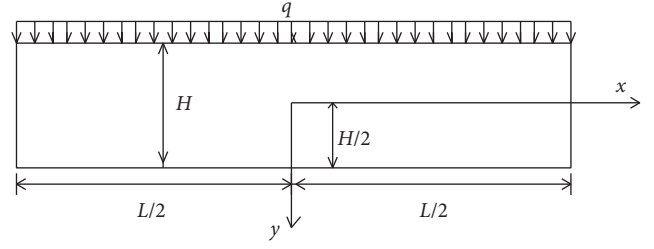

FIGURE 5: Model of the combined clamped beam.

$$L \le \frac{2H^3 [\sigma_x]}{3\gamma D}. \quad (8)$$

3. Analysis of Influencing Factors

According to equation (4), calculating the maximum deflection involves a few parameters, i.e., mining face width L, roof subsidence w, roof thickness H, buried depth D, unit weight γ, and elastic modulus E. Elastic modulus is obtained with laboratory tests. Roof subsidence and roof thickness are obtained through field observation and theoretical analysis. Unit weight, buried depth, and elastic modulus vary greatly in different engineering conditions. Thus, the F5001 mining face of the Tangshan Coal Mine is taken as the engineering background in this paper. Then, the influences of different factors on the relationship between maximum deflection and mining face width in different conditions are analyzed using the theoretical equation.

3.1. Engineering Condition. The F5001 mining face of the Tangshan Coal Mine is in the No. 5 coal seam. The thickness varies from 1.5 to 2.3 m with an average of 2.2 m. The dip angle varies from 4 to 11° with an average of 7°. The buried depth varies from 588 to 712 m with an average of 650 m. The length is 639.5 m in the advancing direction and 66 m in the inclined direction. An integrated mechanized mining method is used. The goaf is filled with waste gaugue, and the mining-filling ration is 1 : 1.36. The designed filling rate is 95% (the density of coal is 1400 kg/m³, and the density of vermiculite is 1080 kg/m³). The field borehole detection and laboratory tests show that the lithology of the roof and floor varies slightly. As shown in Figure 6, it mainly includes mudstone and sandstone. The average elastic modulus of the roof is 14 GPa.

3.2. Parameter Determination. According to equation (4), the amount of roof subsidence and the thickness of the roof can be obtained with field measurement and theoretical calculation. The roof displacement sensor in the goaf is arranged to monitor the subsidence of the roof, and the fracture of the overburden is arranged along the axial direction of the drain. The TV monitors the damage of the roof.
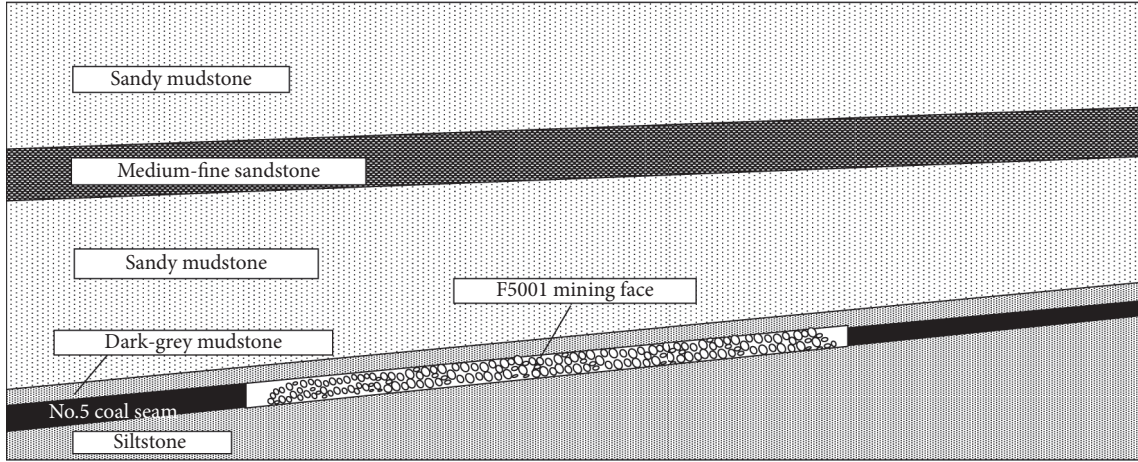
Figure 6: Sketch of the lithology of the roof and floor.

3.2.1. Calculation of Roof Subsidence. The maximum roof subsidence can be obtained through field monitoring. The calculation equation is

$$H_z = h_c + h_q + w_1, \qquad (9)$$

where H_z is the maximum roof subsidence of roof, m; h_c is the roof subsidence before prop installation, m; h_q is the roof subsidence from prop installation to sensor installation, and m; w_1 is the roof subsidence monitored by the sensor, m.

Due to mining height and face width, there is some amount of subsidence before gangue filling, which is referred to as a roof subsidence h_c before filling. During the filling process, easy mobility of gaugue, large filling height, etc. can lead to insufficient filling height.

The monitoring results of roof subsidence before filling are given/shown in Figure 7. The roof subsidence in the goaf is given in Figure 8. When the monitoring value keeps steady, it is 0.221 m, which means w_1 is 0.221 m. Before prop installation, the roof subsidence is 0.201 m. According to the relationship between stopping distance and roof subsidence, h_q is 0.116 m. Then, H_z is 0.538 m.

3.2.2. Determination of Roof Thickness. According to the borehole detection, the roof separation is shown in Figure 9, and the drawing of separation distribution is illustrated in Figure 10. Within the borehole depth of 12.169–12.881 m, the roof experiences obvious separation. Thus, the average roof thickness is 12.5 m.

3.3. Analysis of Influencing Factors. According to field monitoring results, it can be obtained that H is 12.5 m, E is 14 GPa, γ is 25 kN/m^3, and D is 650 m. Taking these parameters into equations (3) and (4), the relationship between mining face width and deflection can be obtained:

$$w = 0.45 \cdot e^{0.003L} + 15 \times 10^{-5} \cdot e^{0.05L}. \qquad (10)$$

In order to analyze the influences of different parameters on the relationship between mining face width and reflection, three analysis schemes are designed:

Scheme I (E) is 14 GPa, (H) is 650 (m), and γ is 20 kN/m^3, 23 kN/m^3, and 25 kN/m^3.

Scheme II (E) is 14 GPa, γ is 25 kN/m^3, and (H) is 600 m, 650 m, and 700 m.

Scheme III (H) is 650 (m), γ is 25 kN/m^3, and (E) is 8 GPa, 11 GPa, and 14 GPa.

According to the analysis schemes, mining face width L varies from 20 to 150 m. Influences of different factors on the mining face width are illustrated in Figures 11–13. When the mining face width face is 66 m, roof subsidence w is 0.529 m based on equation (10), which is very close to the field monitoring result 0.538 m.

(1) The mining face width increases with the unit weight. When the maximum roof subsidence is 0.53 m, the mining face width increases from 66 to 78 m as the unit weight increases from 20 to 25 kN/m^3. If the mining face width is 66 m, the roof subsidence increases from 0.51 to 0.53 m as the unit weight increases from 20 to 25 kN/m^3.

(2) When the roof subsidence is steady, the mining face width increases with the buried depth. When the roof subsidence is 0.53 m, the mining face width increases from 66 to 81 m as the buried depth increases from 600 to 700 m. If the mining face width is 66 m, the roof subsidence increases from 0.51 to 0.53 m.

(3) When the roof subsidence is steady, the mining face width decreases with increase in the elastic modulus of roof. When the roof subsidence is 0.58 mm, the mining face width increases from 66 to 90 m as the elastic modulus increases from 8 to 14 GPa. If the mining width is 66 m, the roof subsidence decreases from 0.58 to 0.53 m.

4. Application of Numerical Simulation

In order to optimize the mining scheme, equation (8) is used to determine the reasonable mining face width. Then,
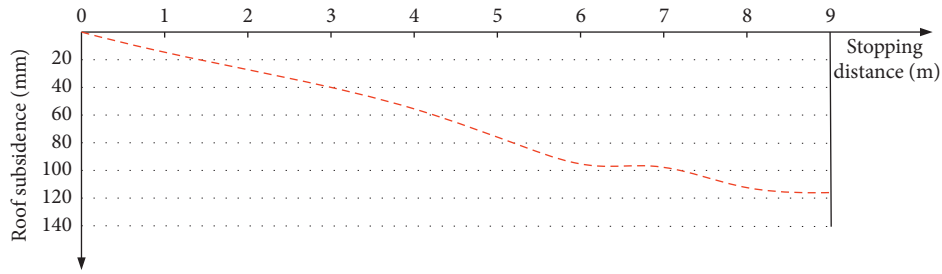
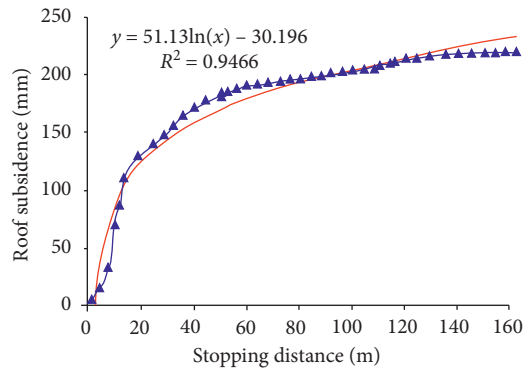FIGURE 7: Roof subsidence before filling.

FIGURE 8: Roof subsidence in the goaf.

FIGURE 9: Separation of the roof. (a) No. 1 borehole-separation (b) No. 2 borehole-separation.

FLAC^{3D} software is applied to check/testify the calculation result.

4.1. Determination of Reasonable Mining Face Width.

In order to determine the maximum mining face width, σ_x should be the limiting value. According to the properties of overburden strata, the limiting tensile strength is 4.72 MPa, i.e. σ_x is 4.72 MPa. Then, the related mining face width is 126.3 m based on equation (8).

When the mining face width is 120 m, the roof subsidence is in the range of 0.5–0.8 m. When the mining face width is larger than 126 m, the tensile strength of the roof reaches the maximum value 4.72 MPa. The corresponding roof subsidence is 0.83 m, which accounts for 37.8% of

mining height. Then, considering the safety coefficient 1.2, the reasonable mining face width is 105 m.

4.2. Numerical Model Construction.

FLAC^{3D} is used for simulating the mining process of F5001 mining face. The actual mining face width is 66 m, and the calculating reasonable width is 105 m. Thus, three conditions are designed, including 66 m, 86 m, and 105 m. According to the engineering condition, a numerical model ($x \times y \times z = 136\,m \times 196\,m \times 52\,m$) is established, as shown in Figure 14. The strata from top to down include sandy mudstone, medium-fine sandstone, sandy mudstone, mudstone, No. 5 coal seam, siltstone, find sandstone, and
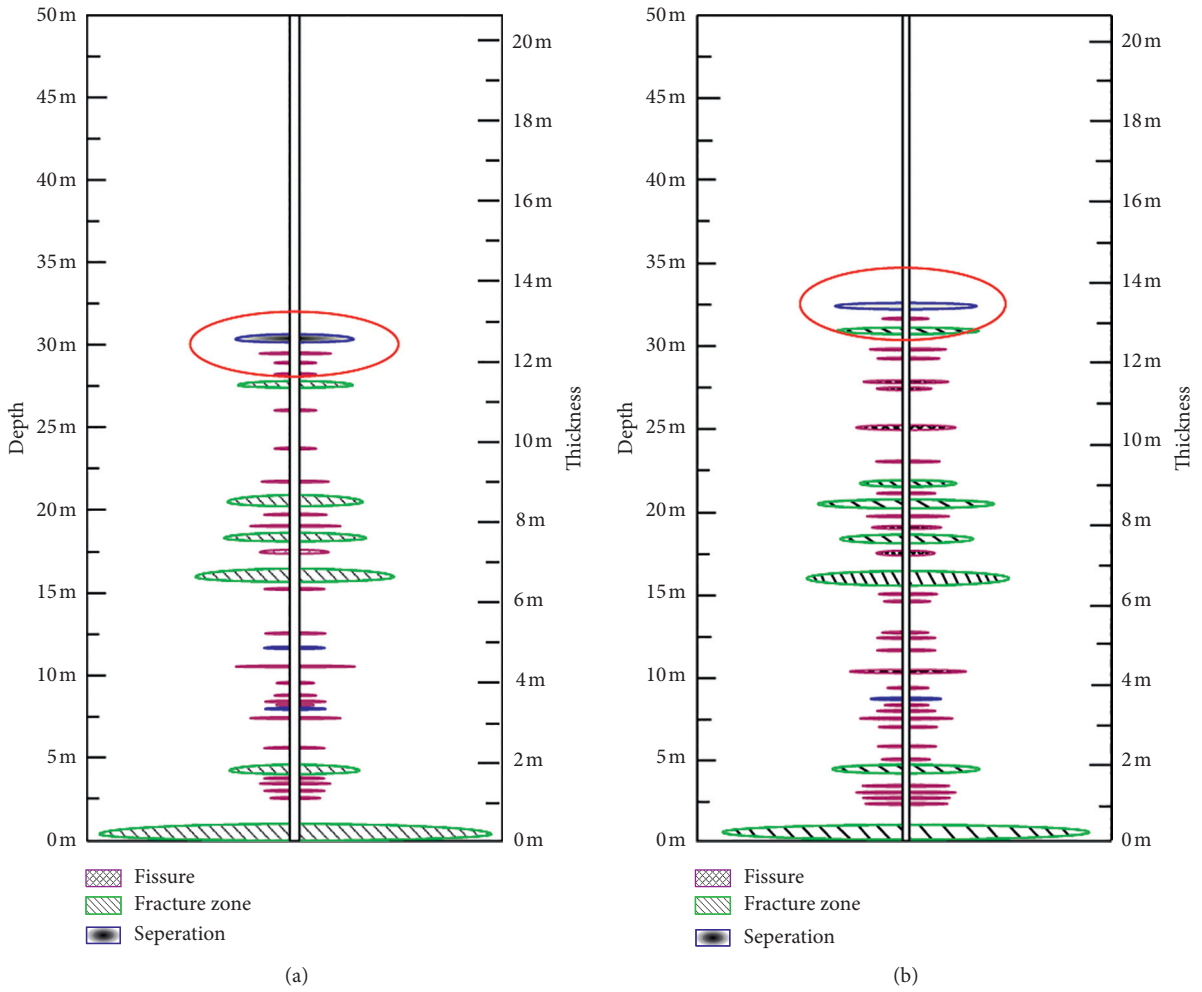
Fissure
Fracture zone
Seperation

(a)

Fissure
Fracture zone
Seperation

(b)

FIGURE 10: Drawing of separation distribution. (a) No. 1 borehole (b) No. 2 borehole.

$\gamma = 20 \, kN/m^3$
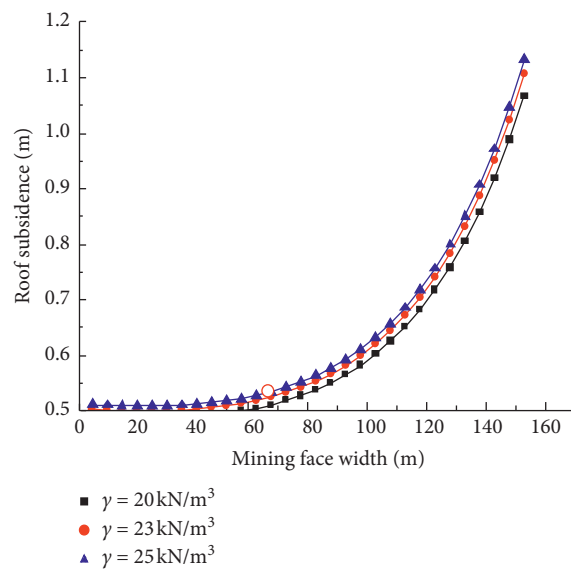$\gamma = 23 \, kN/m^3$
$\gamma = 25 \, kN/m^3$

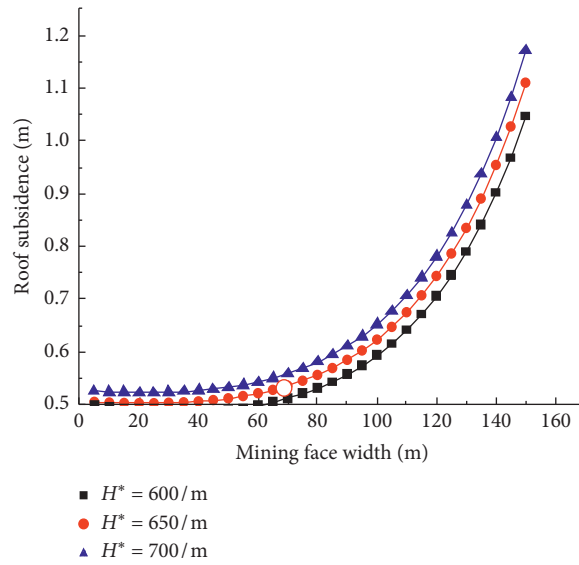FIGURE 11: Relationship between mining face width and unit weight.

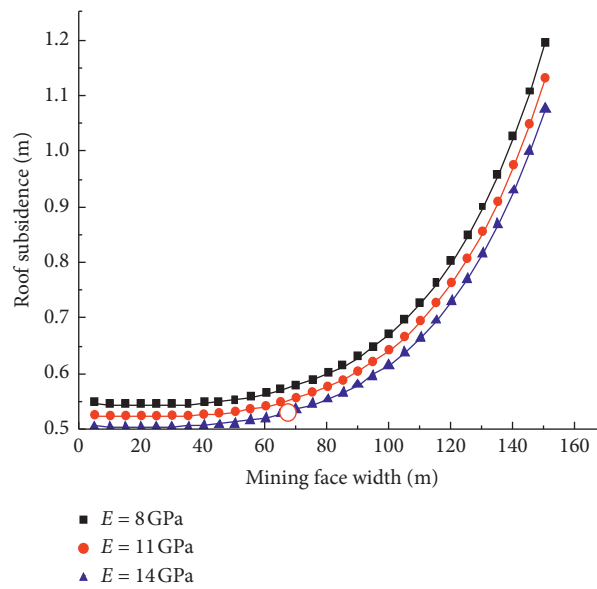FIGURE 12: Relationship between mining face width and buried depth.

FIGURE 13: Relationship between mining face width and elastic modulus of the roof.
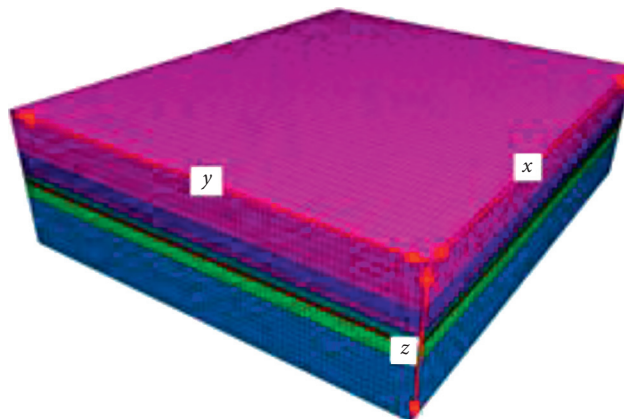

FIGURE 14: Numerical model.

TABLE 1: Physical mechanical parameters of strata.

| Lithology	Thickness (m)	Density (kg·m³)	Bulk modulus (GPa)	Shear modulus (GPa)	Internal friction (°)	Cohesion (MPa)	Tensile strength (MPa)
Sandy mudstone	20.5	2300	1.6	0.9	36	9.5	8
Medium-fine sandstone	7.4	2650	3.31	1.71	41	18.5	14
Sandy mudstone	2.0	2300	1.6	0.9	36	9.5	8
Mudstone	1.3	2300	1.82	0.91	38	9	8
No. 5 coal seam	2.2	1340	1.14	0.45	26	3	1.4
Siltstone	1.4	2650	4.35	2.0	44	13	10
Fine sandstone	5.2	2650	3.31	1.71	41	18.5	14
Mudstone	20.0	2300	1.82	0.91	38	9	8
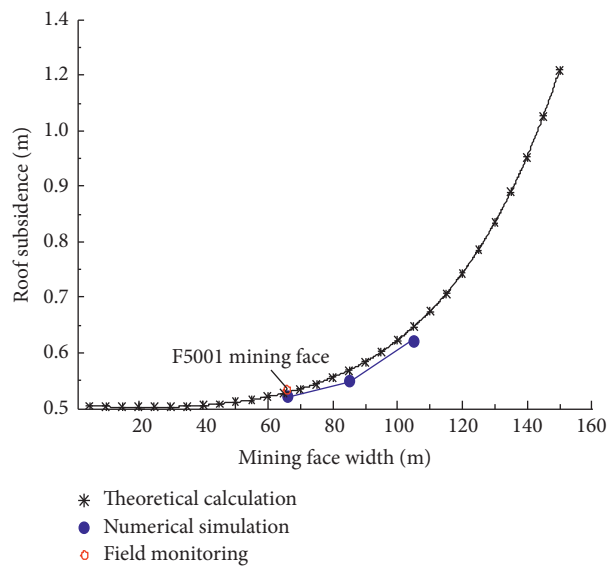
FIGURE 15: Relationship between mining face width and roof subsidence.
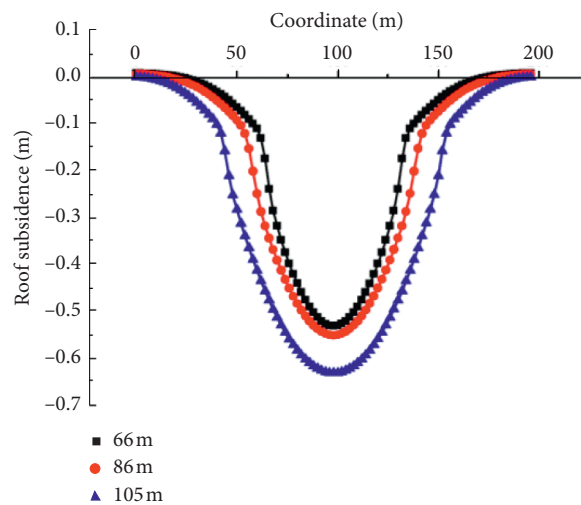

FIGURE 16: Subsidence curves with different mining face widths.

mudstone. The Mohr–coulomb model is chosen. The physical mechanical parameters are listed in Table 1.

4.3. Analysis of Numerical Simulation Results. The Roof subsidence monitoring line is arranged in the middle of the mining face. The monitoring results are given in Figures 15–16. Additionally, theoretical calculation results are also plotted for comparison.

(1) The relationship between the mining face width and the roof subsidence can be obtained with equation (10). The numerical results show that the maximum roof subsidence is 0.524 m, 0.549 m, and 0.623 m, respectively. The corresponding theoretical values are 0.529 m, 0.559 m, and 0.647 m, respectively. The differences between numerical simulation and theoretical calculation are small.

(2) When the mining face width increases from 66 to 105 m, the maximum roof subsidence obtained by numerical simulation and theoretical calculation increase from 0.529 to 0.647 m and from 0.524 to 0.623 m, respectively. The corresponding increasing percentages are 18% and 15%, respectively. Generally, the maximum roof subsidence is only 0.647 m, accounting for 29% of the mining height. Thus, it can be concluded that when the mining face width increases to 105 m, it is also reasonable.

5. Conclusions

Based on the combined clamped beam model, the roof subsidence and fracture constraint conditions used for solid filling mining are deduced. When the mining width of the F5001 mining face is 66 m, the calculated maximum deflection of roof is very close to the field monitoring result, indicating that equation (10) is valid.

The relationship between the maximum deflection and the mining face width is obtained under different factors, i.e., unit weight, buried depth, and elastic modulus of the roof. Theoretical analysis reveals that both the maximum deflection and the mining face width increase as the unit weight or buried depth increases, but the elastic modulus of the roof decreases. When designing the sizes of mining face, these factors must be considered.

The mining face width in the Tangshan Coal Mine can be designed by the optimization equation. Combined with the field monitoring data, when the mining face width is 126 m, the roof reaches the limiting tensile strength. The engineering safety coefficient is 1.2, and the maximum mining face width is 105 m.

When the mining width increases from 66 to 105 m, theoretical calculations show that the maximum roof subsidence increases from 0.524 to 0.623 m, whose corresponding increasing percentage is 18% while numerical simulation results show that the roof subsidence increases from 0.524 to 0.623 m. The roof subsidence is controlled less than 30% of the mining height. Generally, when the mining width increases, the roof subsidence varies slightly under filling mining condition.

Data Availability

The data used to support the findings of this study are included within the article.

Conflicts of Interest

The authors declare that they have no conflicts of interest.

Acknowledgments

References

[1] T. -B. Zhaon, M. -L. Xing, W. -Y. Guo, C. -W. Wang, and B. Wang, "Anchoring effect and energy-absorbing support mechanism of large deformation bolt," *Journal of Central South University*, vol. 28, no. 2, pp. 572–581, 2021.

[2] K. Cheng, B. G. Yang, B. G. Zhang et al., "Present situation and development direction of filling mining technology in coal mines in China," *Coal Technology*, vol. 37, no. 03, pp. 73–76, 2018.

[3] G. W. Liu and C. J. Yan, "Analysis of surface subsidence law of solid filling mining under buildings," *Safety in Coal Mines*, vol. 02, pp. 214–218, 2019.

[4] M. Li, J. X. Zhang, and Y. L. Huang, "Research on compression ratio design based on compaction properties of solid backfill materials," *Journal of China Coal Society*, vol. 34, no. 6, pp. 1110–1115, 2017.

[5] C. D. Sun, D. S. Zhang, and X. F. Wang, "Study and application of overlying strata control technology in bag type backfill longwall mining with super high-water content material," *Journal of China Coal Society*, vol. 40, no. 6, pp. 1313–1319, 2015.

[6] Z. M. Huang, *Study on the Macro-Micro Mechanical Properties of Gangue Backfilling Body and Relationship between Support and Surrounding Rock in Comprehensive Mechanized Filling Mining*, China University of Mining and Technology, Beijing, China, 2016.

[7] Q. Zhang, J. Zhang, Y. Huang, and F. Ju, "Backfilling technology and strata behaviors in fully mechanized coal mining working face," *International Journal of Mining Science and Technology*, vol. 22, no. 2, pp. 151–157, 2012.

[8] L. Wang, X. N. Zang, and G. L. Guo, "Research on surface subsidence prediction model of coal mining with solid compacted backfilling," *Rock and Soil Mechanics*, vol. 35, no. 7, pp. 1973–1978, 2014.

[9] P. Xu, Y. J. Zhou, and M. X. Zhang, "Fracture development of overlying strata by backfill mining under thick alluvium and thin bedrock," *Journal of Mining and Safety Engineering*, vol. 32, no. 4, pp. 617–622, 2015.

[10] W. J. Yu, T. Feng, and W. J. Wang, "Coordination support systems in mining with filling and mechainical behavior," *Chinese Journal of Rock Mechanics and Engineering*, vol. 31, pp. 2803–2813, 2012.

[11] X. M. Liu, T. B. Zhao, and M. Q. Wang, "Analysis of working characteristics and roof control of backfilling hyaraulic

support," *Journal of Shandong University of Science and Technology (Natural Science)*, vol. 36, no. 2, pp. 42–47, 2017.

[12] Z. N. Zhang, X. X. Miao, and X. R. Ge, "Testing study on compaction breakage of loose rock blocks," *Chinese Journal of Rock Mechanics and Engineering*, vol. 24, no. 3, pp. 451–455, 2005.

[13] T. B. Zhao, H. H. Zhang, and Y. J. Chen, "Evolution of abutment pressure distribution and impact on coal-rock damage," *Journal of Liaoning Technical University (Natural Science)*, vol. 29, no. 3, pp. 420–423, 2010.

[14] T. B. Zhao, W. Y. Guo, and Y. L. Tan, "Mechanics mechanism of rock burst caused by mining in the variable region of coal thickness," *Journal of China Coal Society*, vol. 41, no. 7, pp. 1659–1666, 2016.

[15] X. J. Deng, J. X. Zhang, and P. Huang, "Roof movement characteristics in extra thick coal seam mining with the upward slicing filling technology," *Journal of China Coal Society*, vol. 40, no. 5, pp. 994–1000, 2015.

[16] P. L. Gong, *Surrounding Rock Control Theory and Application Study of the Coal Face with Greater Mining Height*, Taiyuan University of Technology, Taiyuan, China, 2006.

Research Article

The Potential to Replace Cement with Nano-Calcium Carbonate and Natural Pozzolans in Cemented Mine Backfill

Mohammed Hefni [iD] and Maaz A. Ali [iD]

Mining Engineering Department, King Abdulaziz University, Jeddah 21589, Saudi Arabia

Correspondence should be addressed to Mohammed Hefni; mhefni@kau.edu.sa

The effectiveness of mine backfilling depends on the properties of its constituents. The high cost of cement, which is commonly used as a binder in mine backfill, has led researchers to seek alternatives to partially replace it with other binders. This study investigated the potential to use nano-calcium carbonate (NCC) and natural pozzolans (zeolite and pumice) along with Portland cement (PC) in mine backfill. Two types of experimental samples were prepared: (1) gold tailings and silica sand to investigate the effect of NCC and (2) nickel tailings to investigate the effect of natural pozzolans. The unconfined compressive strength (UCS) was measured for samples cured for up to 56 days. Moreover, selected samples were subject to mercury intrusion porosimetry to investigate microstructural properties. Results show that addition of NCC did not improve the UCS of backfill prepared with gold tailings and cured for 28 days, whereas a dosage of 1% NCC in backfill samples prepared with silica sand improved UCS by 20%, suggesting that the gold tailings negatively affected strength development. Natural pozzolans, in particular, 20% zeolite, had 24% higher UCS after 56 days of curing compared to samples prepared with PC and thus have the potential to partially replace cement in mine backfill.

1. Introduction

Mine backfilling is the practice of filling underground voids created during ore extraction in underground mining operations to (1) provide stability for the underground working environment [1], (2) reduce negative environmental impacts from tailings' storage on the surface [2–4], and (3) maximize extracted ore volumes, such as in room and pillar mining [5, 6]. Three common mine backfill materials are rock fill (RF), hydraulic fill (HF), and paste fill (PF) [1, 7–9]. To make RF, waste rocks from the surface or underground are crushed (typically to 16 mm) and possibly cemented, depending on the required strength [10–12]. By decreasing waste rock piles on the surface, adverse environmental impacts and rock subsidence are avoided [11–14]. However, to ensure backfilling efficiency, binder consumption is high [15]. HF is produced during the classification of mill tailings using hydrocyclones: coarse, dense (>70 wt.% solids) underflow is obtained [16–19]. The high water content of HF facilitates transport through pipelines directly into stopes [19, 20]. According to

Adiansyah et al. [21], drainage is the most critical factor in designing HF because ineffective drainage can pose a risk to workers if porous barriers are not used, and piping and liquefaction problems are common. PF consists of mill tailings with 15% of the material <20 μm in size and solid concentrations of 70–85 wt.% [15, 22, 23]. The high solids and low water content can cause issues for transport through pipelines and necessitate addition of a superplasticizer to enhance flowability [24, 25].

Mine tailings are waste products from ore concentration in mineral processing plants [26]. Their chemical and physical properties must be considered during backfill design because they can affect backfill mechanical properties [27]. For instance, tailings that contain sulfide minerals are prone to sulfate attack, which can decrease the unconfined compressive strength (UCS) over the long term due to ettringite formation [28]. Thus, binders that are compatible with the tailings are added to backfill at low concentrations to enhance UCS and other mechanical properties [29]. Cement is typically the main binder, but it is expensive. Therefore, alternative binders are required [30].

Recent advances in nanotechnology have presented the opportunity to use nanomaterials as supplementary cementitious materials [31]. The fine particles act as nuclei for cement to accelerate hydration and improve UCS at early stages [32]. Nano-silica, carbon nanotube, and nano-calcium carbonate (NCC) have been shown to increase cement base material strength [33–35]. For example, adding NCC to cement and silica fume accelerated the pozzolanic reaction at an early age and compensated for the low initial strength [36, 37].

Supplementary cementitious materials such as natural (e.g., volcanic pumice and zeolite) and artificial pozzolans (e.g., fly ash) could partially replace cement to prevent sulfate attack [38, 39]. Pozzolanic materials in mine backfill can reduce binder costs by more than 15% on an annual basis [30, 40–42]. At concentrations ranging from 10 to 30%, natural pozzolans improved concrete mechanical properties, permeability, durability, and transport properties [43–46]. Volcanic pumice properties vary by source and location due to different ash formation conditions, mineral components, and grain size characteristics [47–49]. Addition of zeolite enhanced the mechanical properties, durability, and performance of concrete [50–53]. Many industrial wastes also have pozzolanic properties [54]. For example, clay pozzolans, produced through calcination at temperatures ranging from 700 to 900°C [2, 55], are inexpensive, have low CO_2 emissions compared to cement, and improve backfill mechanical properties [56, 57]. Addition of 10% clay pozzolans to mine backfill produced maximum UCS and an annual savings of >7% [2, 58].

The application of NCC and natural pozzolans has primarily focused on concrete production: possible effects on backfill mechanical properties have not yet been widely investigated. Therefore, this paper investigates partial replacement of cement by NCC, pumice, or zeolite in cemented mine backfill. To investigate the effect of NCC, backfill samples were prepared with gold tailings and a superplasticizer to aid nanoparticle dispersion: various dosages of NCC were compared with reference samples containing only Portland cement (PC). To investigate the effect of natural pozzolans, backfill samples were prepared with nickel tailings and various dosages of pumice and zeolite were compared against reference samples containing PC only or a combination of PC and fly ash. Samples were subject to UCS tests after up to 56 days of curing and selected samples were subjected to mercury intrusion porosimetry to investigate microstructural properties.

2. Methods

2.1. Materials.
Tailings from gold and nickel mines and silica sand were used to make experimental backfill samples (Table 1). The particle size distribution (PSD) of these materials is shown in Figure 1.

The chemical composition of Type 10 PC with a specific gravity of 3.15, pumice (provided by Hess Pumice Company) with a specific gravity of 2.35, zeolite (provided by Bear River Zeolite), and fly ash are shown in Table 2. The chemical and physical properties of the NCC (provided by US Research Nanomaterials, Inc.) are shown in Table 3.

TABLE 1: Mineralogy and physical properties of silica sand and two types of tailings (% by weight).

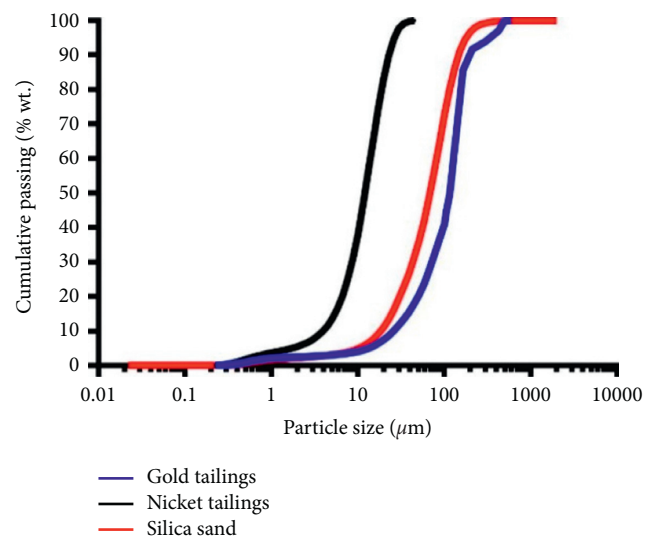| Characteristic	Gold tailings	Nickel tailings	Silica sand
Mineralogy (wt.%)			
SiO_2	49.02	77.28	—
Al_2O_3	17.68	11.09	—
Fe_2O_3	9.15	2.13	—
SO_3	7.29	—	—
CaO	6.52	2.22	—
MgO	3.79	1.14	—
K_2O	2.70	2.19	—
TiO_2	0.64	0.27	—
Physical properties			
Specific gravity	2.89	2.80	2.69
D10 (μm)	35.22	3.54	20.14
D30 (μm)	75.37	82.05	48.03
D50 (μm)	97.72	9.92	75.60
D60 (μm)	105.78	170.55	88.65
D90 (μm)	200.09	189.66	185.95
Cu (D60/D10)	3.003	48.177	4.407
Cc (D30^2/(D10 × D60))	1.52	11.15	1.29

FIGURE 1: Particle size distribution of gold and nickel tailings and silica sand.

NCC is characterized by high energy and surface area; thus, surface reactions occur, and particles are prone to adhere on direct contact via magnetic, electrostatic, and Van der Waals forces [37]. To aid NCC dispersion, a superplasticizer (sodium dodecyl sulfate, Thermo Scientific Company) was used, with the chemical and physical properties listed in Table 4.

Tap water (pH 7.5) was used to prepare experimental backfill samples. Compounds in mixing water can influence the mechanical properties of backfill and cement hydration [59]. For instance, dissolved calcium and magnesium enhance cement hydration, whereas salty brine decreases binder workability [60].

TABLE 2: Chemical composition of Portland cement and supplementary cementitious materials (wt.%).

Material	CaO	Al_2O_3	SiO_2	MgO	Fe_2O_3	TiO_2	Na_2O	K_2O	SO_3
Portland cement	61.14	4.6	19.38	3.35	2.02	—	2.03	0.71	2.28
Pumice	0.8	13.5	76.2	0.05	1.1	0.2	1.6	1.8	—
Zeolite	5.6	3.5	70.3	—	3.05	—	4.7	3.8	0.03
Fly ash	5.02	20	41.22	1.4	23.84	—	0.81	1.5	1.94

TABLE 3: Chemical and physical properties of nano-calcium carbonate.

Appearance	$CaCO_3$ (%)	HCl insoluble (%)	Particle size (nm)	Fe (%)	Mn (%)
White powder	≥98	≤0.1	20–50	≤0.08	≤0.006

TABLE 4: Chemical and physical properties of the sodium dodecyl sulfate superplasticizer.

Appearance	Concentration (%)	Density (g/cm^3)	pH	Boiling point (°C)
Liquid	73–79	1.08	5–7	78

2.2. Experimental Design. Backfill samples containing NCC were prepared with 7 wt.% (by weight of dry materials) PC as a binder and 78% solids' concentration using gold tailings (Table 5). Mixtures of PC and 1, 3, and 5% NCC (by dry weight of PC, equation (1)) were initially dry mixed to break up agglomerated nanoparticles that were visible to the naked eye. Dried tailings were then added, and water was gradually added to the mixture to make a paste. Finally, super-plasticizer was added (by dry weight of NCC, equation (2)). Samples were poured into 5.08×10.16 cm cylindrical molds and cured for 7, 14, and 28 days at 25 ± 2°C and 90 ± 2% relative humidity:

$$M_{\text{NCC}} = D_{\text{NCC}} \times M_{\text{PC}}, \quad (1)$$

$$M_{\text{SP}} = D_{\text{SP}} \times M_{\text{NCC}}, \quad (2)$$

where M_{NCC} is the mass of NCC (g), D_{NCC} is the dosage of NCC (%), M_{PC} is the mass of PC (g), M_{SP} is the mass of superplasticizer (g), and D_{SP} is the dosage of the super-plasticizer (%).

Backfill samples containing 10 and 20% pumice, zeolite, or fly ash were prepared using nickel tailings and PC with a solid concentration of 80% (Table 6; equations (3) and (4)). Samples were cured for 7, 14, 28, and 56 days at 25 ± 2°C and 90 ± 2% relative humidity:

$$D_{\text{PC}} = \frac{M_{\text{PC}}}{M_{\text{PC}} + M_{\text{T}}}, \quad (3)$$

$$M_{\text{POZ}} = R \times M_{\text{PC}}, \quad (4)$$

where D_{PC} is the dosage of PC (%), M_{T} is the mass of tailings (g), M_{POZ} is the mass of pozzolans (g), and R is the per-centage of PC replaced by pumice, zeolite, or fly ash (%).

2.3. Unconfined Compressive Strength. On each curing date, the UCS of triplicate cured backfill samples was measured on a Wykeham Farrance 100 kN loading machine with a 50 kN load cell after ASTM D2166/D2166M-16 [61] (Figure 2). UCS values are reported as means.

2.4. Mercury Intrusion Porosimetry. Mercury intrusion porosimetry (MIP after ASTM D4404-18 [62]) was used to describe the pore structure of select backfill samples made with 20% pumice, zeolite, and fly ash after 56 days of curing (Table 6). The macrosize and volume distribution of pores inside materials are commonly measured using MIP, which is a well-known technique, although it has adverse environmental effects.

3. Results and Discussion

3.1. NCC Backfill Samples. The mean UCS of backfill samples increased with curing time at all NCC dosages and was consistently higher in reference samples than those made with 1% NCC and 10–100% superplasticizer (Figure 3), 3% NCC and 10–80% superplasticizer (Figure 4), or 5% NCC and 10–30% superplasticizer (Figure 5). Thus, the maximum UCS was observed for reference samples on day 28 (~0.80 MPa). The differences between treatment and reference sample means became more pronounced with NCC content, such that, on day 28, the UCS of the 30% super-plasticizer sample was 5% (Figure 3), 25% (Figure 4), and 36% (Figure 5) lower for the 1, 3, and 5% NCC samples, respectively. At 1 and 5% NCC, addition of superplasticizer had a negative effect on UCS on each curing date (Figures 3 and 5), but at 3% NCC, it had a positive effect on UCS (Figure 4).

Figure 6 shows the samples with the maximum UCS on each curing day for 1, 3, and 5% NCC. Relative to the reference sample, increasing NCC from 1 to 5% decreased the UCS of backfill samples by 24–56% on day 7, 3–32% on day 14, and 5–30% on day 28.

Since adding NCC did not improve the UCS of backfill samples, the gold tailings were replaced with a more neutral material to see if the loss of strength was due to an interaction between the tailings and the NCC. Samples prepared with silica sand augmented with 7% PC or 7% PC + 1% NCC were tested for UCS. The UCS increased with curing time as above (Figure 7). Addition of 1% NCC increased the UCS from 0.71 to 0.82 MPa by day 7, did not affect UCS on day 14, and by day 28, increased the UCS

TABLE 5: Mixing design for all backfill samples containing nano-calcium carbonate.

Mixture ID	Portland cement (%)	Nano-calcium carbonate (%)	Superplasticizer (%)
Reference	7	0	0
1NCC	7	1	0
1NCC10SP	7	1	10
1NCC20SP	7	1	20
1NCC30SP	7	1	30
1NCC40SP	7	1	40
1NCC50SP	7	1	50
1NCC100SP	7	1	100
3NCC	7	3	0
3NCC30SP	7	3	30
3NCC40SP	7	3	40
3NCC50SP	7	3	50
3NCC60SP	7	3	60
3NCC80SP	7	3	80
5NCC10SP	7	5	10
5NCC20SP	7	5	20
5NCC30SP	7	5	30

TABLE 6: Mixing design for all backfill samples containing natural pozzolans.

Mixture ID	Tailings (kg)	Portland cement (g)	Tap water (g)	Pumice (g)	Zeolite (g)	Fly ash (g)
Reference	2.5	131.6	657.9	0	0	0
FA10	2.5	118.4	657.9	0	0	13.2
FA20	2.5	105.3	657.9	0	0	26.3
PU10	2.5	118.4	657.9	13.2	0	0
PU20	2.5	105.3	657.9	26.3	0	0
ZE10	2.5	118.4	657.9	0	13.2	0
ZE20	2.5	105.3	657.9	0	26.3	0

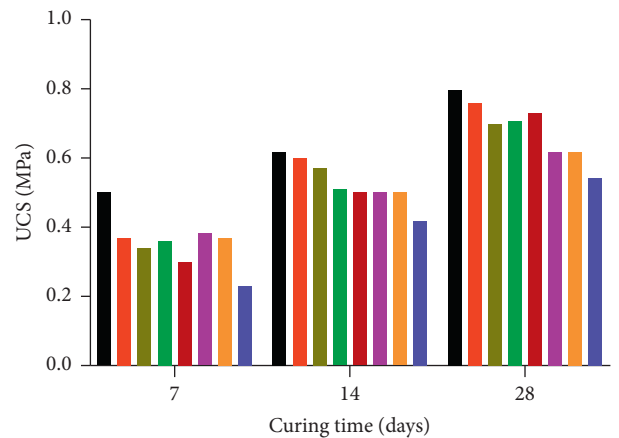FIGURE 2: Experimental setup for unconfined compressive strength tests.

FIGURE 3: Mean unconfined compressive strength (UCS) for triplicate backfill samples prepared with 1% nano-calcium carbonate (NCC) and 0–100% superplasticizer (SP). See Table 5, for mixture designs.

from 1.0 to 1.2 MPa. Silica sand had a higher PSD than gold tailings (Figure 1), which might contribute to the effectiveness of NCC. Previous studies have shown that NCC increased the UCS of concrete mixtures. Concrete has larger and relatively neutral in-earth components compared to backfill tailings. It is believed that physical (PSD) and chemical (components) differences contribute to NCC efficiency early in UCS development.

3.2. Natural Pozzolan Backfill Samples. As with the NCC experiments, the UCS increased with curing time from 7 to 56 days (Figure 8), whereas reference samples had the highest UCS on day 14, and backfill samples prepared with

20% zeolite or 10% fly ash after 56 days of curing had the highest UCS (0.66 MPa), 24% higher than the reference UCS on that day.

The porosity and pore size distribution of samples containing 20% pumice, zeolite, and fly ash are shown in Figures 9 and 10, respectively. Samples containing 20% fly
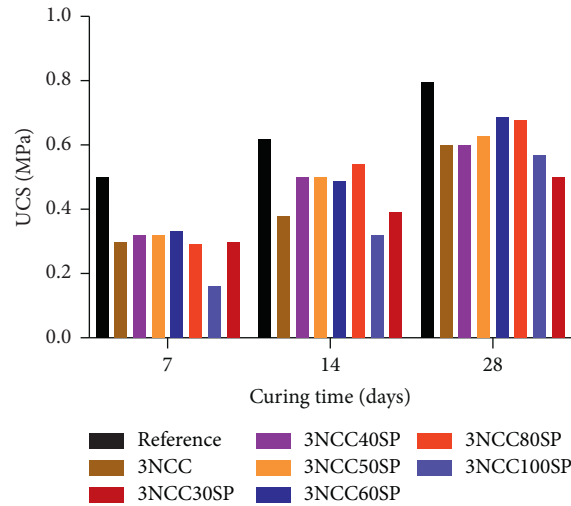
FIGURE 4: Mean unconfined compressive strength (UCS) for triplicate backfill samples prepared with 3% nano-calcium carbonate (NCC) and 0–100% superplasticizer (SP). See Table 5, for mixture designs.
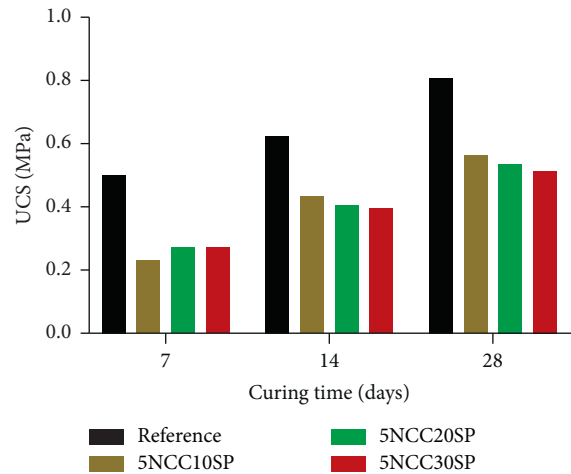

FIGURE 5: Mean unconfined compressive strength (UCS) for triplicate backfill samples prepared with 5% nano-calcium carbonate (NCC) and 0–30% superplasticizer (SP). See Table 5, for mixture designs.
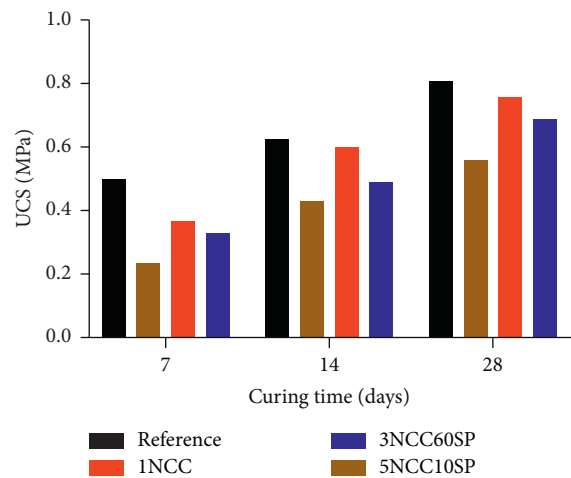

FIGURE 6: Maximum unconfined compressive strength (UCS) for backfill samples prepared with 0 (reference), 1, 3, and 5% nano-calcium carbonate (NCC) and 0, 10, and 60% superplasticizer (SP). See Table 5, for mixture designs.
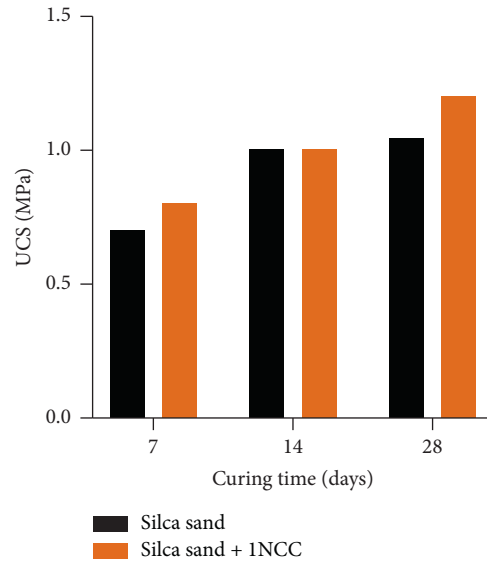
FIGURE 7: Mean unconfined compressive strength (UCS) of triplicate backfill samples prepared with silica sand without and with 1% nano-calcium carbonate (NCC). See Table 5, for the NCC mixture design.
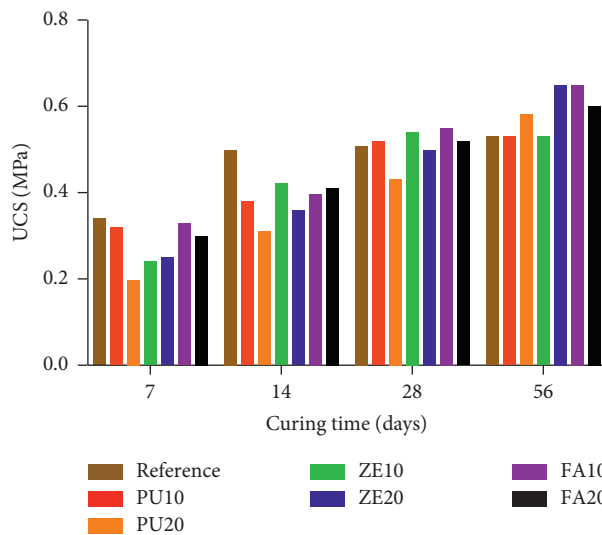

FIGURE 8: Mean unconfined compressive strength (UCS) for backfill samples prepared without (reference) and with 10 and 20% fly ash (FA), pumice (PU), and zeolite (ZE). See Table 6, for mixture designs.

ash had higher porosity (~33%) compared to samples containing natural pozzolans (~31%). This could explain the lower UCS value obtained for samples containing fly ash after 56 days of curing (Figure 8). Samples containing fly ash and natural pozzolans had similar range of pore size (~0.006–10 μm), as shown in Figure 10. Adding 20% natural pozzolans decreased the number of pores, especially in the range of 0.01–0.02 μm (Figure 10).
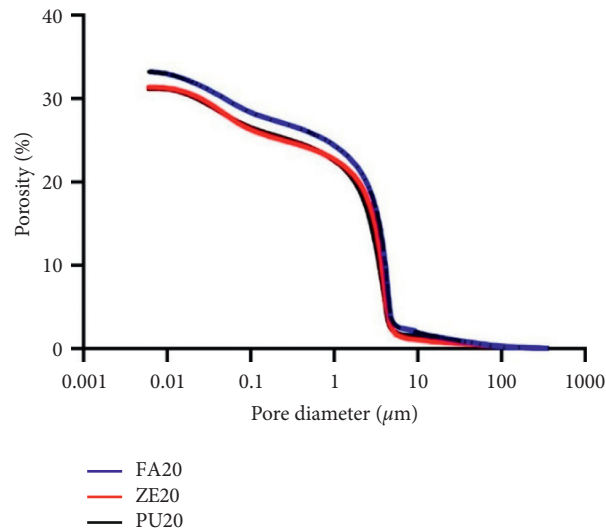
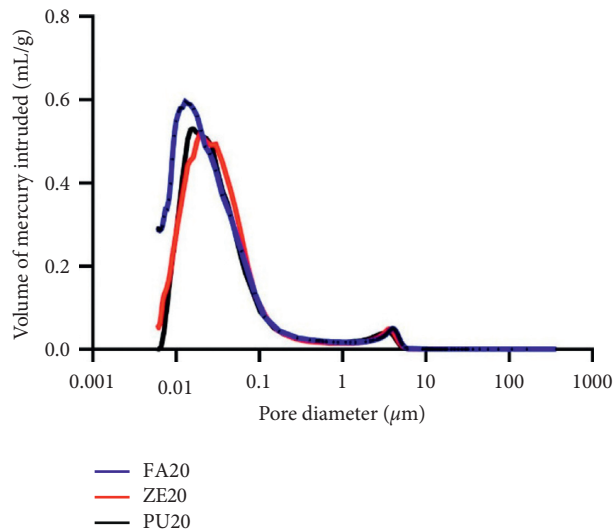FIGURE 9: Cumulative porosity of natural pozzolans samples.

FIGURE 10: The volume of mercury intruded in natural pozzolans samples.

4. Conclusions

This study investigated the potential replacement of cement by NCC and natural pozzolans in cemented mine backfill. Key conclusions are summarized as follows:

(i) Addition of NCC did not improve UCS relative to reference samples prepared with PC and gold tailings

(ii) 1% NCC without superplasticizer yielded the highest UCS among the experimental samples

(iii) Samples containing silica sand instead of gold tailings improved UCC, suggesting that the gold tailings had a negative effect on strength development

(iv) Addition of superplasticizer to NCC samples did not improve the UCS

(v) Natural pozzolans may have some potential to partially replace cement in mine backfill

(vi) Addition of 20% zeolite or 10% fly ash improved UCS the most on day 56 (24%) relative to the reference sample

(vii) Samples prepared with 20% natural pozzolans had a similar pore size distribution (~ 0.006–$100\,\mu$m) and porosity

(viii) Additional studies are required to examine the effect of particle size and chemistry on the UCS of backfill samples prepared with NCC

Data Availability

The data used to support the findings of the study are available within the article.

Conflicts of Interest

The authors declare no conflicts of interest.

References

[1] M. Sheshpari, "A review of underground mine backfilling methods with emphasis on cemented paste backfill," *Electronic Journal of Geotechnical Engineering*, vol. 20, no. 13, pp. 5183–5208, 2015.

[2] S. N. Eshun, S. S. R. Gidigasu, and S. K. Y. Gawu, "The effect of clay pozzolana-cement-composite on the strength development of a hydraulic backfill," *Ghana Mining Journal*, vol. 18, no. 1, pp. 32–38, 2018.

[3] Y. Yao, Z. Cui, and R. Wu, "Development and challenges on mining backfill technology," *Journal of Materials Science Research*, vol. 1, no. 4, 2012.

[4] T. Belem and M. Benzaazoua, "Design and application of underground mine paste backfill technology," *Geotechnical and Geological Engineering*, vol. 26, pp. 147–174, 2008.

[5] E. Yilmaz, B. Ercikdi, A. Kesimal, M. Yumlu, and K. Karaoglu, "The application of high density paste backfill at an underground mine," in *Proceedings of the 5th International Scientific Conference of Modern Management of Mine Producing*, Geology and Environmental Protection, Varna, Bulgaria, June 2005.

[6] B. S. Choudhary, "Paste filling—an overview to improve the quality of filling material," *Journal of Mines, Metals and Fuels*, 2015.

[7] M. Z. Emad, H. Mitri, and C. Kelly, "State-of-the-art review of backfill practices for sublevel stoping system," *International Journal of Mining, Reclamation and Environment*, vol. 29, no. 6, pp. 544–556, 2015.

[8] M. Bloss, "An operational perspective of mine backfill," in *Proceedings of the Eleventh International Symposium on Mining with Backfill*, May 2014.

[9] M. Hefni and F. Hassani, "Experimental development of a novel mine backfill material: foam mine fill," *Minerals*, vol. 10, no. 6, p. 564, 2020.

[10] N. J. F. Koupouli, T. Belem, P. Rivard, and H. Effenguet, "Direct shear tests on cemented paste backfill-rock wall and cemented paste backfill-backfill interfaces," *Journal of Rock Mechanics and Geotechnical Engineering*, vol. 8, no. 4, pp. 472–479, 2016.

[11] W. Sun, H. Wang, and K. Hou, "Control of waste rock-tailings paste backfill for active mining subsidence areas," *Journal of Cleaner Production*, vol. 171, pp. 567–579, 2018.

[12] D. M. Franks, D. V. Boger, C. M. Côte, and D. R. Mulligan, "Sustainable development principles for the disposal of mining and mineral processing wastes," *Resources Policy*, vol. 36, no. 2, pp. 114–122, 2011.

[13] L. J. Guo, K. P. Zhou, X. C. Yang, G. S. Liu, and W. Y. Xu, "An experimental study on the mechanical properties of cemented rock-tailings fill," *Advanced Materials Research*, vol. 941–944, pp. 2611–2619, 2014.

[14] J. C. Wilson, S. Benbow, and R. Metcalfe, "Reactive transport modelling of a cement backfill for radioactive waste disposal," *Cement and Concrete Research*, vol. 111, pp. 81–93, 2018.

[15] G. Swan and R. Brummer, "Backfill design for deep, underhand drift-and-fill mining," in *Proceedings of the Seventh International Symposium on Mining with Backfill MINEFILL 2001*, Seattle, WA, USA, 2001.

[16] N. Sivakugan, R. Veenstra, and N. Naguleswaran, "Underground mine backfilling in Australia using paste fills and hydraulic fills," *International Journal of Geosynthetics and Ground Engineering*, vol. 1, no. 2, 2015.

[17] M. Fahey, M. Helinski, and A. Fourie, "Some aspects of the mechanics of arching in backfilled stopes," *Canadian Geotechnical Journal*, vol. 46, no. 11, p. 1322, 2009.

[18] M. Fall, M. Benzaazoua, and E. G. Saa, "Mix proportioning of underground cemented tailings backfill," *Tunnelling and Underground Space Technology*, vol. 23, no. 1, pp. 80–90, 2008.

[19] L. Li, "Generalized solution for mining backfill design," *International Journal of Geomechanics*, vol. 14, no. 3, 2014.

[20] L. Li and M. Aubertin, "An improved method to assess the required strength of cemented backfill in underground stopes with an open face," *International Journal of Mining Science and Technology*, vol. 24, no. 4, pp. 549–558, 2014.

[21] J. S. Adiansyah, M. Rosano, S. Vink, and G. Keir, "A framework for a sustainable approach to mine tailings management: disposal strategies," *Journal of Cleaner Production*, vol. 108, pp. 1050–1062, 2015.

[22] G. Blight, "Mine waste: a brief overview of origins, quantities, and methods of storage," in *Waste*, 2011, ISBN 9780123814753.

[23] J. Alcott, D. Dallaire, and T. Belem, "Pastefill optimisation at hecla québec's casa berardi mine," in *Proceedings of the 53rd U.S. Rock Mechanics/Geomechanics Symposium*, American Rock Mechanics Association, New York, NY, USA, June 2019.

[24] G. Chancellor and J. Gonzalez, "Implementation of pastefill at the barrick goldstrike mine," in *Proceedings of the 2015 SME Annual Conference and Expo and CMA 117th National Western Mining Conference—Mining: Navigating the Global Waters*, Denver, CO, USA, February 2015.

[25] M. J. Raffaldi, J. B. Seymour, J. Richardson, E. Zahl, and M. Board, "Cemented paste backfill geomechanics at a narrow-vein underhand cut-and-fill mine," *Rock Mechanics and Rock Engineering*, vol. 52, no. 12, pp. 4925–4940, 2019.

[26] E. Yilmaz and M. Fall, *Paste Tailings Management*, Springer, Cham, Switzerland, 2017, ISBN 9783319396828.

[27] N. Sivakugan, R. M. Rankine, K. J. Rankine, and K. S. Rankine, "Geotechnical considerations in mine backfilling in Australia," *Journal of Cleaner Production*, vol. 14, no. 12-13, pp. 1168–1175, 2006.

[28] N. Niroshan, N. Sivakugan, and R. Veenstra, "Effects of Different Binders on the Strength and Stiffness of Paste Fills," in *Proceedings of the Fourth Geo-China International Conference*, July 2016.

[29] A. Kesimal, E. Yilmaz, B. Ercikdi, I. Alp, and H. Deveci, "Effect of properties of tailings and binder on the short-and long-term strength and stability of cemented paste backfill," *Materials Letters*, vol. 59, no. 28, pp. 3703–3709, 2005.

[30] B. Ercikdi, F. Cihangir, A. Kesimal, H. Deveci, and İ. Alp, "Effect of natural pozzolans as mineral admixture on the performance of cemented-paste backfill of sulphide-rich tailings," *Waste Management & Research*, vol. 28, no. 5, p. 430, 2010.

[31] S. Parveen, S. Rana, and R. Fangueiro, "A review on nanomaterial dispersion, microstructure, and mechanical properties of carbon nanotube and nanofiber reinforced

cementitious composites," *Journal of Nanomaterials*, vol. 2013, Article ID 710175, 2013.

[32] S. Parveen, S. Rana, R. Fangueiro, and M. C. Paiva, "Microstructure and mechanical properties of carbon nanotube reinforced cementitious composites developed using a novel dispersion technique," *Cement and Concrete Research*, vol. 73, pp. 215–227, 2015.

[33] T. Sato and J. J. Beaudoin, "Effect of nano-$CaCO_3$ on hydration of cement containing supplementary cementitious materials," *Advances in Cement Research*, vol. 23, no. 1, pp. 33–43, 2011.

[34] S. Chuah, Z. Pan, J. G. Sanjayan, C. M. Wang, and W. H. Duan, "Nano reinforced cement and concrete composites and new perspective from graphene oxide," *Construction and Building Materials*, vol. 73, pp. 113–124, 2014.

[35] L. P. Singh, S. R. Karade, S. K. Bhattacharyya, M. M. Yousuf, and S. Ahalawat, "Beneficial role of nanosilica in cement based materials - a review," *Construction and Building Materials*, vol. 47, pp. 1069–1077, 2013.

[36] F. U. A. Shaikh and S. W. M. Supit, "Mechanical and durability properties of high volume fly ash (HVFA) concrete containing calcium carbonate ($CaCO_3$) nanoparticles," *Construction and Building Materials*, vol. 70, pp. 309–321, 2014.

[37] S. Kawashima, J.-W. T. Seo, D. Corr, M. C. Hersam, and S. P. Shah, "Dispersion of $CaCO_3$ nanoparticles by sonication and surfactant treatment for application in fly ash-cement systems," *Materials and Structures*, vol. 47, no. 6, pp. 1011–1023, 2014.

[38] A. Kesimal, E. Yilmaz, and B. Ercikdi, "Evaluation of paste backfill mixtures consisting of sulphide-rich mill tailings and varying cement contents," *Cement and Concrete Research*, vol. 34, no. 10, pp. 1817–1822, 2004.

[39] T. Raghavendra, Y. H. Siddanagouda, F. Jawad, C. Y. Adarsha, and B. C. Udayashankar, "Performance of ternary binder blend containing cement, waste gypsum wall boards and blast furnace slag in CLSM," *Procedia Engineering*, vol. 145, pp. 104–111, 2016.

[40] B. Ercikdi, F. Cihangir, A. Kesimal, H. Deveci, and I. Alp, "The effect of natural pozzolan properties on the strength and stability of paste backfill," *Earth Sciences*, vol. 29, pp. 25–35, 2008.

[41] O. Peyronnard and M. Benzaazoua, "Alternative by-product based binders for cemented mine backfill: recipes optimisation using Taguchi method," *Minerals Engineering*, vol. 29, pp. 28–38, 2012.

[42] A. Sargeant, E. De Souza, and J. F. Archibald, "The use of glass as Pozzolan in Backfill binder recipes," in *Proceedings of the 42nd U.S. Rock Mechanics Symposium*, San Francisco, CA, USA, June 2008.

[43] A. M. Zeyad, B. A. Tayeh, and M. O. Yusuf, "Strength and transport characteristics of volcanic pumice powder based high strength concrete," *Construction and Building Materials*, vol. 216, pp. 314–324, 2019.

[44] A. M. Zeyad, A. H. Khan, and B. A. Tayeh, "Durability and strength characteristics of high-strength concrete incorporated with volcanic pumice powder and polypropylene fibers," *Journal of Materials Research and Technology*, vol. 9, no. 1, p. 806, 2020.

[45] L. Yu, H. Ou, and S. Zhou, "Application of high performance concrete with compound admixtures of fly ash and perlite powder in pavement of highway," *Advanced Materials Research*, vol. 413, 2012.

[46] K. M. A. Hossain, S. Ahmed, and M. Lachemi, "Lightweight concrete incorporating pumice based blended cement and aggregate: mechanical and durability characteristics," *Construction and Building Materials*, vol. 25, no. 3, p. 1186, 2011.

[47] B. Y. Pekmezci and S. Akyüz, "Optimum usage of a natural pozzolan for the maximum compressive strength of concrete," *Cement and Concrete Research*, vol. 34, no. 12, p. 2175, 2004.

[48] A. Çolak, "Characteristics of pastes from a Portland cement containing different amounts of natural pozzolan," *Cement and Concrete Research*, vol. 33, pp. 585–593, 2003.

[49] P. N. Lemougna, K. t. Wang, Q. Tang et al., "Review on the use of volcanic ashes for engineering applications," *Resources Conservation and Recycling*, vol. 137, pp. 177–190, 2018.

[50] E. Vejmelková, T. Kulovaná, M. Ondráček, and R. Černý, "Application of natural zeolite as supplementary cementitious material in concrete production," in *Proceedings of the CESB 2013 PRAGUE—Central Europe towards Sustainable Building 2013*, Sustainable Building and Refurbishment for Next Generations, Prague, Czech Republic, June 2013.

[51] Y. T. Tran, J. Lee, P. Kumar, K. H. Kim, and S. S. Lee, "Natural zeolite and its application in concrete composite production," *Composites Part B: Engineering*.vol. 165, pp. 354–364, 2019.

[52] D. Jana, "A new look to an old pozzolan: clinoptilolite-a promising pozzolan in concrete," in *Proceedings of the International Cement Microscopy Association—29th International Conference on Cement Microscopy*, PQ, Canada, May 2007.

[53] K. Narasimhulu, R. Gettu, and K. G. Babu, "Beneficiation of natural zeolite through flash calcination for its use as a mineral admixture in concrete," *Journal of Materials in Civil Engineering*, vol. 26, no. 1, pp. 24–33, 2014.

[54] G. Külekçi, B. Erçikdi, and Ş. Aliyazicioğlu, "Effect of waste brick as mineral admixture on the mechanical performance of cemented paste backfill," in *Proceedings of the IOP Conference Series Earth and Environmental Science*, Prague, Czech Republic, September 2016.

[55] F. Cihangir and Y. Akyol, "Mechanical, hydrological and microstructural assessment of the durability of cemented paste backfill containing alkali-activated slag," *International Journal of Mining, Reclamation and Environment*, vol. 32, no. 2, pp. 123–143, 2018.

[56] L. Dembovska, D. Bajare, I. Pundiene, and L. Vitola, "Effect of pozzolanic additives on the strength development of high performance concrete," *Procedia Engineering*, vol. 172, pp. 202–210, 2017.

[57] N. Beuntner and K. C. Thienel, "Properties of calcined lias delta clay-technological effects, physical characteristics and reactivity in cement," *RILEM Bookseries*, vol. 10, pp. 43–50, 2015.

[58] M. Bediako, A. A. Adjaottor, and S. K. Y. Gawu, "Selected mechanical properties of mortar used for masonry incorporating artificial pozzolana," in *Proccedings of the Modern Methods and Advances in Structural Engineering and Construction*, Zurich, Switzerland, June 2011.

[59] J. S. Mahlaba, E. P. Kearsley, R. A. Kruger, and P. C. Pretorius, "Evaluation of workability and strength development of fly ash pastes prepared with industrial brines rich in and Cl^- to expand brine utilisation," *Minerals Engineering*, vol. 24, no. 10, p. 1077, 2011.

[60] A. Wu, Y. Wang, H. Wang, S. Yin, and X. Miao, "Coupled effects of cement type and water quality on the properties of cemented paste backfill," *International Journal of Mineral Processing*, vol. 143, p. 65, 2015.

[61] *ASTM D2166/D2166M-16 Standard Test Method for Unconfined Compressive Strength of Cohesive Soil*, ASTM International, West Conshohocken, PA, USA, 2016.

[62] *ASTM D4404-18 Standard Test Method for Determination of Pore Volume and Pore Volume Distribution of Soil and Rock by Mercury Intrusion Porosimetry*, ASTM International, West Conshohocken, PA, USA, 2018.

Research Article

Influence of Binder Types and Temperatures on the Mechanical Properties and Microstructure of Cemented Paste Backfill

Zhaowen Du [ID],[1,2] **Shaojie Chen** [ID],[1,2] **Sheng Wang**,[1,2] **Rui Liu**,[1,2] **Dehao Yao**,[1,2] **and Hani S. Mitri**[3]

[1]*College of Energy and Mining Engineering, Shandong University of Science and Technology, Qingdao 266590, China*
[2]*State Key Laboratory Breeding Base for Mining Disaster Prevention and Control,*
 Shandong University of Science and Technology, Qingdao 266590, China
[3]*Department of Mining and Materials Engineering, McGill University, Montreal, Canada*

Correspondence should be addressed to Shaojie Chen; csjwyb@163.com

In order to study the influence of burial depth or fire on the core area of cemented paste backfill (CPB), the experiment of CPB with different types of binder and temperature was carried out. Three types of binders, red mud (RM), Portland cement (PC), and slag cement (SC), are used and tested at 20°C, 40°C, 60°C, and 80°C. The macroperformance and microstructural evolution of CPB are analyzed using slump, uniaxial compressive strength (UCS), X-ray diffraction, and scanning electron microscopy (SEM). The results show that the coupled effects of binder type and temperature have a significant impact on the macroscopic performance and microstructural evolution of CPB. The CPB slump prepared with three types of binder meets the production requirement of the mine. Regardless of curing temperature and curing time, the uniaxial compressive strength of CPB samples with PC and SC is much higher than that of CPB samples with red mud. When cured for 12 hours, the uniaxial compressive strength of CPB samples containing PC and SC increases first, then decreases, and finally increases again with the increase of temperature. However, with the increase of temperature, the uniaxial compressive strength of CPB samples containing RM only increases first and then decreases. When the curing temperature is less than 40°C, the main reason for the increase in UCS was attributed to the fact that the temperature increase accelerates the hydration reaction and improves the density of the sample. When the curing temperature is 60°C, the main reason for the decrease in UCS is the formation of the expansive ettringite (AFt) which destroys the internal spatial structure of the sample. When the curing temperature is 80°C, the UCS increases again due to the fact that such high temperature can destroy the crystal structure of AFt and harden the hydration product C-S-H gel.

1. Introduction

Cemented paste backfill (CPB) is an environmentally friendly filling material that has attracted increasing attention and has been extensively used by mining operations [1–3]. CPB is essentially made from solid granular waste produced by operations such as milling and coal separation. The benefits of CPB are many including better underground mine stability, control of surface subsidence, and enhanced ore recovery. By using CPB, it is possible to mine under surface infrastructure such as buildings and railways and mine under water [4–6]. CPB used in coal mines is mainly made of binder, fly ash, and coal gangue; its solid content is in the range of 70% to 85%.

As one of the components of CPB, binder mainly plays the role of cementation. When the binder is in contact with water, it will undergo hydration reaction and generate hydration products to provide strength for CPB. The cost of binder for coal mines accounts for 90% of the total cost of CPB filling materials (for example, the Xinhe Coal Mine in the Shandong Province in China). Portland cement (PC) has been traditionally used as a binder in proportions that commonly range from 2% to 7% by total weight [7, 8]. However, different types of binders have different prices and cementitious effects. Therefore, it is of great significance to study the influence of different types of binders on the performance of CPB. With the depletion of shallow coal

resources in China, the depth of coal mining is increasing every year, and the geothermal problem is becoming increasingly serious. During the process of paste backfill in the mine, the posterior part of the working face is in a completely closed state with poor ventilation. Combined with the influences of rock temperature, air compression and expansion, hydration reaction, and heat generation, the temperature behind the working face can be significantly hot. Therefore, it is necessary to conduct experimental research on the thermal stability of CPB.

In recent decades, many scholars have conducted extensive research on the factors influencing the performance of CPB. Wu et al. [9] investigated the effects of three types of binders on CPB, and the results showed that these types of binders had a significant impact on the coagulation performance and compressive strength. Ercikdi et al. [10] investigated the effects of OPC, PCC, and SRC, on the mechanical properties and microstructure of CPB. The results showed that the mechanical properties of CPB were closely related to sulphide-rich tailings. Sun et al. [11] studied the influences of different silica fume proportions as binders on CPB properties, and the results showed that the UCS of CPB samples are largest when the silica fume proportion is 5%. Xu et al. [12] studied the effect of the type of binder on UCS. The results showed that the slag cement (SC) has more advantages than PC and SC with 5 wt % NaOH. Yilmaz et al. [13] studied the effect of curing time and content of different types of binders on the characteristics of CPB samples based on the use of an improved experimental apparatus. The results showed that the effects of different binder types on the mechanical properties of CPB mainly depend on the different consolidation behaviors of different binder types.

Previous studies showed that the type of binder has a significant effect on the performance of CPB. However, there are a few studies on the effect of ambient temperature as an influencing factor on the performance of CPB. In addition, some studies only investigated the effect of a single factor on CPB performance [14, 15]. There are no studies on the coupled effects of binder type and temperature on strength development and microstructural evolution of CPB.

Therefore, this study investigates the coupled effects of binder type and temperature on strength development and microstructural evolution of CPB. The purpose of this experimental research is to examine (a) whether the CPB containing three types of binder can meet the engineering requirements of paste slump, (b) the influence of binder type and temperature on UCS properties, and (c) the microstructural evolution of CPB.

2. Materials and Methods

2.1. Materials

2.1.1. Binders. Three types of binders were used in this experiment. These binders are red mud (RM), PC, and SC, as shown in Figure 1. The RM used in this experiment was produced by the Bayer process at the Haitao Aluminum Mine in Henan Province, with a density of 3.01 g/cm^3 and a

specific surface area of 0.48 m^2/g. The PC and SC binders were produced by the Yishui Cement Plant in the Shandong Province. Their densities are 3.07 g/cm^3 and 3.1 g/cm^3, respectively, and their specific surface areas are 0.36 m^2/g and 0.39 m^2/g, respectively. Their main chemical compositions are shown in Table 1.

2.1.2. Fly Ash. The fly ash used in the experiment is grade II fly ash from the Huangdao Power Plant in the Qingdao city in the Shandong Province, with a density of 2.15 g/cm^3 and a specific surface area of 0.98 m^2/g. And its appearance is light gray. Its main chemical composition is shown in Table 2.

2.1.3. Coal Gangue. The gangue selected in this experiment comes from solid waste produced in the process of roadway excavation, coal mining, and separation in the Daizhuang Coal Mine at the Zibo Mining Group in the Shandong Province. Its particle size is less than 25 mm. Its chemical properties and particle size are shown in Tables 3 and 4.

2.2. Mixing Procedure and Mix Proportions. Samples used for the experiment are mainly made of RM, PC, SC, fly ash, and gangue. Considering the composition of CPB at Daizhuang Coal Mine of Zibo Mining Bureau of Shandong Province, the Bureau pointed out that when the mix ratio of the binder to fly ash and gangue is 1 : 4:6, the product performance was optimal [16, 17]. In the same way, three types of binders were chosen for the synthesis of samples subject to constant proportion conditions. First, the filling material was mixed and stirred according to the designed proportion. The stirred CPB was then injected into cubic molds of 70.7 mm × 70.7 mm × 70.7 mm. Once shaken and tamped, CPB samples are then placed in constant temperature and humidity chamber to cure for 28 days. After 28 days, the samples were cured at 40°C, 60°C, and 80°C, for 4, 8, and 12 hours, respectively.

2.3. Testing Methods

2.3.1. Slump Measurement. Slump is a comprehensive index used to evaluate the transportation performance of CPB in pipeline [18, 19]. In this work, the CPB slump test was conducted in accordance with the American Society for Testing and Materials (ASTM) standard C143 [20]. The upper and lower diameters of the slump cone are 100 mm and 200 mm, respectively, and the height is 300 mm. The CPB is poured into the cone, and a shaker is used to ensure complete filling. Once the cone is filled, excess material is removed. The cone is slowly lifted during a 5–10 second period, and the height of the sample is measured.

2.3.2. Testing of Mechanical Properties. The UCS is frequently tested to evaluate the mechanical performance of CPB. UCS tests are relatively inexpensive and can be easily incorporated into routine quality control programs in mines [21, 22]. In the current laboratory investigation, the UCS values of CPB were determined with a Shimazu AG-X250 electric hydraulic pressure-testing machine. The test
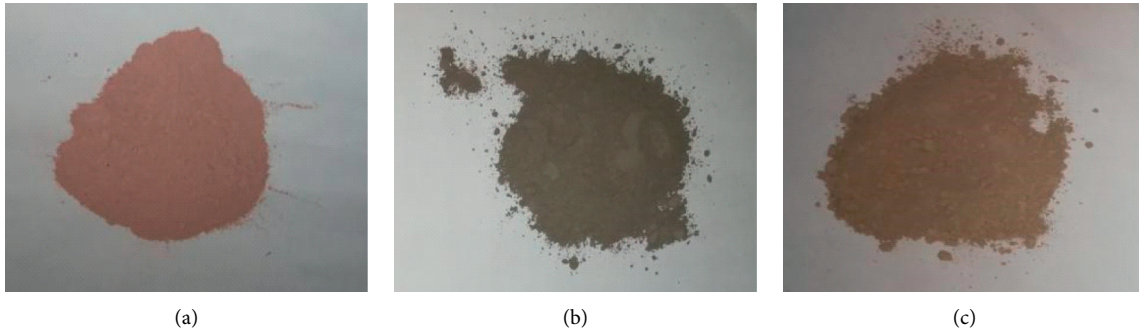
FIGURE 1: Three types of binders: (a) red mud, (b) Portland cement, and (c) slag cement.

TABLE 1: Main chemical constituents of binders (in % weight).

Binder	CaO	SiO$_2$	Al$_2$O$_3$	Fe$_2$O$_3$	MgO
Red mud	11.29	46.05	30.54	6.13	0.67
Portland cement	52.41	29.13	10.38	1.26	5.31
Slag cement	25.28	7.86	3.51	52.62	4.02

TABLE 2: Main chemical constituents of fly ash.

Element unit	SiO$_2$	Al$_2$O$_3$	Fe$_2$O$_3$	CaO	MgO	Burning loss
Weight (%)	53.94	30.91	2.38	6.53	0.92	6.34

TABLE 3: Main chemical composition of gangue.

Element unit	CaO	Fe$_2$O$_3$	Al$_2$O$_3$	SiO$_2$	MgO	K$_2$O
Weight (%)	2.36	4.3	18.9	59.1	1.41	1.89

TABLE 4: Grain size grading of gangue.

Particle size (mm)	+10	10-6	6-3	3-1.5	1.5-0	Total
Weight (kg)	5.26	4.12	3.98	2.36	4.34	20.06
Productive rate (%)	26.22	20.54	19.84	11.76	21.64	100.00
Accumulated on sieve (%)	26.22	46.76	66.60	78.36	100.00	—

machine is driven by a servo-controlled motor and loaded with a double screw structure. The test machine can perform a wide variety of mechanical property tests. The precision is ±0.1%, the crosshead stroke measurement resolution is 0.0104 μm, and the effective test width is 595 mm. The speed is 0.01 mm/s in displacement control mode.

2.3.3. X-Ray Diffraction (XRD) Experiment. XRD was used to analyze the selected samples to identify characteristic crystalline substances generated by hydration of CPB. The XRD analyses were performed with a Rigaku Ultima IV X-ray diffraction device (radiation, $2\theta = 5$–$80°$) with an operating voltage of 40 kV, an emission current of 40 mA, and a step size of 0.02.

First, the sample is poured into a mortar and ground into powder. Then, the powder sample is poured into the glass slot and put into the XRD diffractometer. Finally, we set the starting angle to 5°, the ending angle to 60°, and the scanning speed to 8° per minute.

2.3.4. Scanning Electron Microscopy (SEM) Experiment. To observe the morphology and structure of the hydration products of CPB more intuitively, an APREO electron microscope (FEI, USA) was used for high- and low-vacuum scanning. Its high-vacuum resolution is 0.8 nm at 15 kV and 0.8 nm at 1 kV/0.8 nm at 1 kV, and its low-vacuum resolution is 0.9 nm at 500 V.

Prior to SEM observations, samples were soaked in anhydrous ethanol to prevent hydration. Then, the sample is processed into a block with a diameter of 10 mm and a height of 5 mm and sprayed with conductive metal. Then, the gold-sprayed sample was placed on the scanning electron

microscope (SEM) internal platform, and the sample was sealed and evacuated. Finally, the samples were scanned in different multiples.

3. Results

3.1. Effect of Binder Type on Slump Performance. Three slump tests were conducted for each type of CPB, and the difference between the test results was less than 5%. The slump test configuration is shown in Figure 2. The average slump test results are reported in Table 5.

3.2. Coupled Effect of Binder Type and Temperature on the UCS

3.2.1. Four-Hour Curing Process. Figure 3 shows the UCS test results for different binder CPB types (RM, PC, and SC) after curing for 4 hours at 20°C, 40°C, 60°C, and 80°C. As can be seen, regardless of the curing temperature, the UCS values of CPB samples contained PC and SC are much higher than those of the CPB that contained RM. On the other hand, regardless of the type of binder, higher curing temperature leads to increase in CPB strength, with the exception of the RM samples at 80°C, which gave a UCS value 0.09 MPa, the lowest strength.

3.2.2. Eight-Hour Curing Process. Figure 4 shows the UCS test results for different types of binder after curing for 8 hours at different curing temperatures. As shown in Figure 4, the UCS of the RM and PC samples exhibited the same trends; that is, the UCS increased to a peak at 60°C and then decreased at 80°C curing temperature. When the curing temperature was 60°C, the UCS of these two types of samples reached the maximum values of 0.21 MPa and 1.32 MPa, respectively. Compared with the curing temperature of 20°C, the UCS of the samples cured at 60°C, respectively, increased by 29% and 31%. The UCS values of the samples containing SC after curing at 20°C, 40°C, and 60°C for 8 hours exhibited minor differences, ranging from 1.69 to 1.77 MPa. However, when the curing temperature is 80°C, the UCS of SC samples is the highest at 2.25 MPa. Compared with the curing temperature of 20°C, the UCS of SC sample increased by 33%.

3.2.3. Twelve-Hour Curing Process. Figure 5 shows the results of UCS tests for different types of binder after curing for 12 hours at 20°C, 40°C, 60°C, and 80°C. As shown in Figure 5, the UCS values of the samples that contain three types of binder after curing for 12 hours at the four curing temperatures exhibit large differences. Like the results of curing after 4 and 8 hours, the UCS values of the CPB samples that contained PC and SC are much higher than those of the RM samples. When the temperature is 80°C, the UCS value of the SC sample is 31.5 times that of the RM sample. At the same time, it can be observed that the SC sample shows an increasing trend followed by a decrease and a final increase at 80°C. The UCS values of the SC samples cured at 20°C and 40°C for 12 hours are 1.69 MPa and 1.72 MPa, respectively. However, it is worth noting that when the curing

temperature is 60°C, the UCS value of the SC sample is lowest at 1.39 MPa. In addition, the maximum UCS value of the sample at the curing temperature of 80°C is 2.52 MPa. As the temperature increases, the UCS values of the PC samples increase from 1.01 MPa to 1.28 MPa, then decrease from 1.28 MPa to 1.13 MPa, and finally increase to 1.71 MPa. At the same curing time, the UCS values of all sample types at 40°C, 60°C, and 80°C are higher than those at 20°C, with increases of 26.7%, 11.9%, and 69.3%, respectively. The UCS values of RM samples increase first and then decrease with higher temperature. The UCS values range from 0.08 to 0.21 MPa.

3.3. XRD Results. The abovementioned test results have shown that the type of binder, curing temperature, and curing time have significant influence on CPB. Furthermore, a curing time of 12 hours deems more representative than 4 and 8 hours. As can be observed from the UCS results after 12 hours of curing time, some samples showed an increase then a decrease in strength and finally exhibited increase at 80oC. To better understand the influence of these factors, the phases of CPB samples after 12 hours of curing time were analyzed by XRD.

Figure 6 shows the XRD patterns of hydration products of CPB with different types of binder after curing at 20°C for 12 hours. As can be seen, the strongest diffraction is silica (SiO_2). The appearance of silica's diffraction peak indicates that the sample still contains numerous silica particles that do not participate in the hydration reaction. The diffraction peaks of silica in PC and SC samples are relatively weak. This indicates that more silica has participated in the hydration reaction to produce more hydration products. At the same time, the diffraction peaks of C-S-H, C-A-H, gypsum, and AFt can also be observed. The appearance of these diffraction peaks indicates that the hydration reaction occurred in the sample during the curing period and corresponding hydration products were generated. It is easy to observe that the diffraction peak of hydration products generated by the PC and SC samples is more (in number) and stronger (in intensity) than those of the RM sample. This indicates that C3S and C3A in the samples containing PC and SC participate in the hydration reaction and produce more C-S-H and calcium aluminate hydrate (C-A-H). However, the sample that yielded the largest number of peaks with the highest C-S-H and AFt diffraction peak intensities is the SC sample.

Figure 7 shows the XRD pattern of hydration products of CPB with different types of binder after curing at 40°C for 12 hours. It can be observed from Figure 7 that the diffraction peaks of silica, gypsum, C-S-H, and AFt still appear after the three types of CPBs are cured at 40°C for 12 hours. However, compared with Figure 6, the diffraction peaks of the hydration products of each sample are significantly enhanced, and the diffraction peak of silica is significantly decreased. The results show that the secondary hydration occurs at 40°C and more crystal forms of hydration products are generated. Moreover, the hydration products of the PC and SC samples (Figures 7(b) and 7(c)) are more than those of the RM sample (Figure 7(a)).
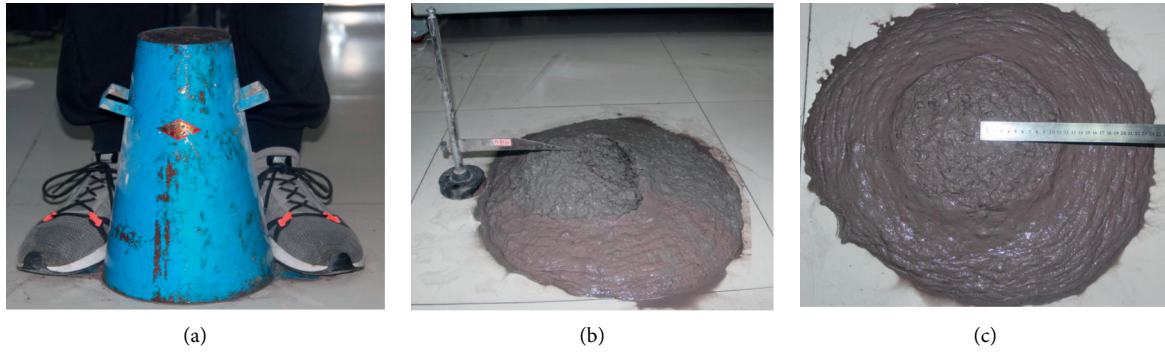
(a)   (b)   (c)

Figure 2: Slump test configuration.

Table 5: CPB slump test results.

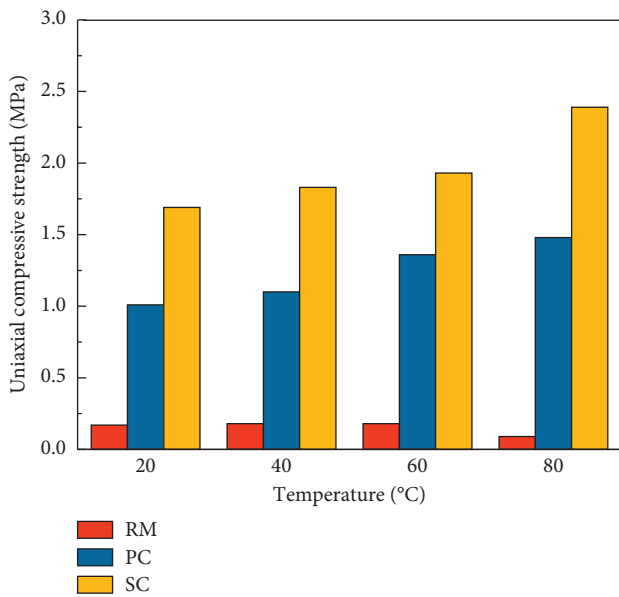| Binder	Red mud (RM)	Portland cement (PC)	Slag cement (SC)
Slump	22.45 cm	22.55 cm	25.45 cm

Figure 3: Effect of binder type and temperature on the UCS of CPB after curing for 4 hours.

Figure 4: Effect of binder type and temperature on the UCS of CPB after curing for 8 hours.

Figure 8 shows the XRD pattern of hydration products of CPB with different types of binders after curing at 60°C for 12 hours. It can be observed from Figure 8 that the peak diffraction intensity is still associated with silica. In addition to silica, the diffraction peaks of C-S-H, C-A-H, and AFt are also relatively high. At the same time, it is obvious from Figures 8(b) and 7(c) that there are more hydration products, especially AFt. Compared with Figure 7, the XRD peaks of gypsum in Figures 8(b) and 8(c) are weaker, indicating that more gypsum is involved in the secondary hydration reaction to produce more AFt.

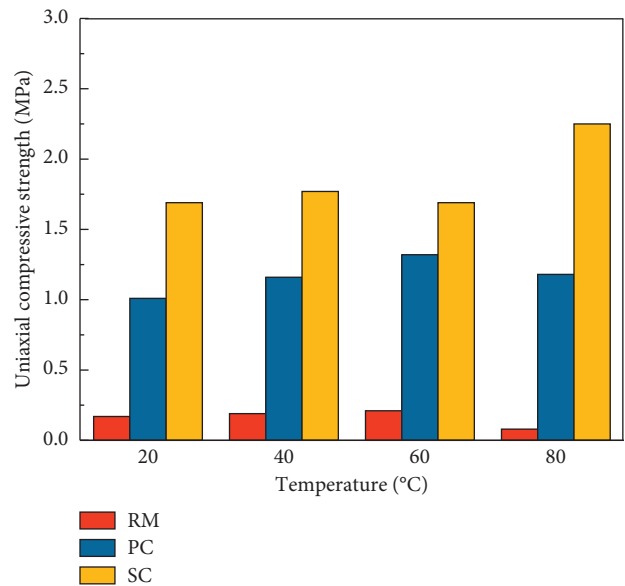Figure 9 shows the XRD patterns of hydration products of CPB with different types of binder after curing at 80°C for 12 hours. It can be observed from Figure 9 that the number of hydration products and the diffraction peak strength of the SC sample are larger than those of the PC sample. In turn, the numbers and intensities of PC peaks are larger than those of the RM sample. Figure 9(a) shows that the diffraction peak of the hydration products of the RM samples is weak, indicating that the hydration products are relatively small at 80°C. Figures 9(b) and 9(c) show that the PC and SC samples produce more C-S-H gel after curing at 80°C for 12 hours. However, the AFt diffraction peaks become weaker.

3.4. SEM Results. To observe the internal microstructure of the three types of binder samples more closely, SEM tests were conducted on CPB samples that were cured for 12 hours.

Figure 10 shows the SEM images at a magnification of 5000 times. The SEM test results show that the microstructure of the three types of binder is different. Figure 10(a) shows that the RM sample has a single internal
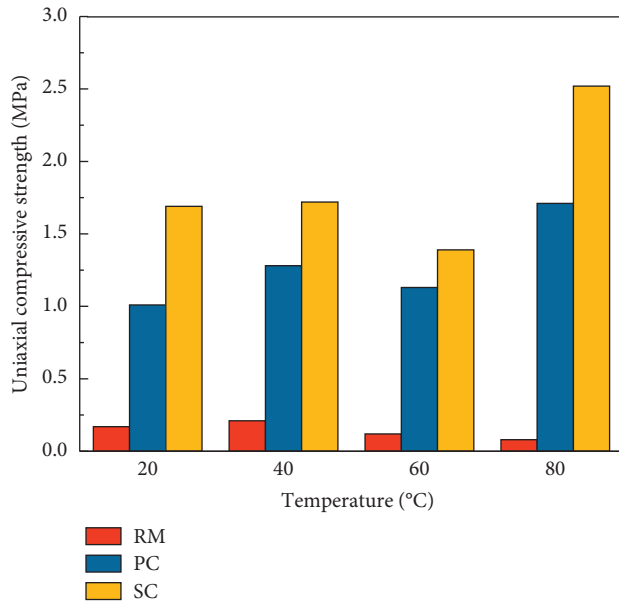
FIGURE 5: Effect of binder type and temperature on the UCS of CPB after curing for 12 hours.
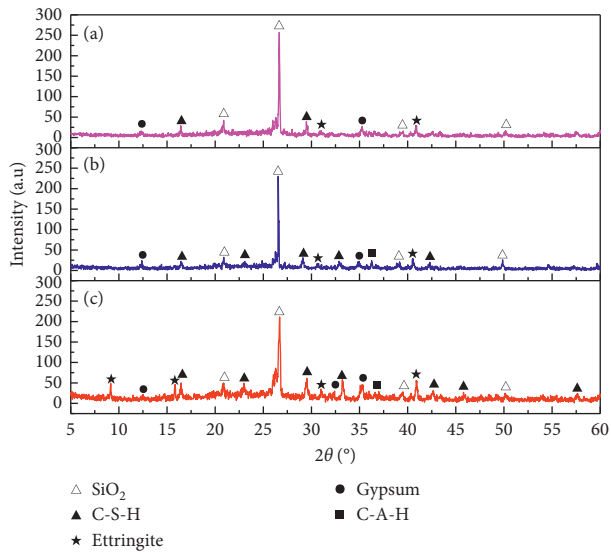

FIGURE 7: XRD patterns for CPB samples after curing at 40°C for 12 hours: (a) RM, (b) PC, and (c) SC.

FIGURE 6: XRD patterns of CPB samples after curing at 20°C for 12 hours: (a) red mud (RM), (b) Portland cement (PC), and (c) slag cement (SC).

FIGURE 8: XRD patterns for CPB samples after curing at 60°C for 12 hours: (a) RM, (b) PC, and (c) SC.

structure, mainly spherical fly ash. There are also a few C-S-H gel. However, the internal structure of the PC and SC samples is more complex. Figure 10(b) displays the SEM image of the PC sample. As can be observed, there is cotton-like C-S-H gel and acicular Aft. The C-S-H gel and AFt are interlaced in the middle of the raw material. Figure 10(c) shows the SEM image of the SC sample. Overall, there are some smaller voids in the SC sample. However, outside the voids, hydration products, such as C-S-H gel, acicular, and rod-shaped AFt, are observed between the particles of the
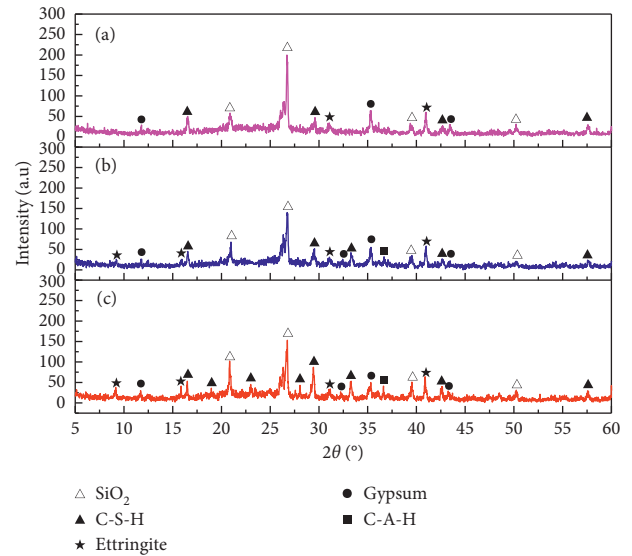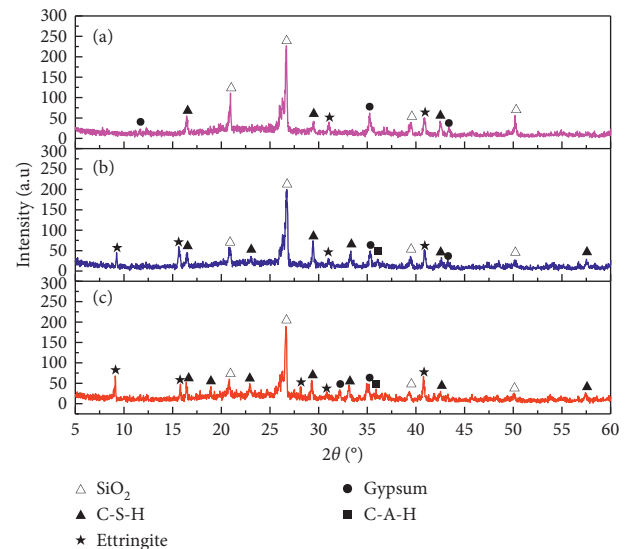
sample. These hydration products are tightly surrounded by the raw material particles.

Figure 11 shows the SEM image magnified 5000 times after the samples of the three types of binders were cured at 60°C for 12 hours. Compared with Figure 10(a), the hydration products (C-S-H gel) between the particles in Figure 11(a) are increased considerably. However, it is worth noting that the PC sample in Figure 11(b) has a relatively dense internal structure with virtually no gaps. It is obvious that the hydration products are compact and evenly distributed, and the spaces between the material particles are filled in a large number of hydration products. A thick rod-like substance (AFt) is formed near and in the middle of the
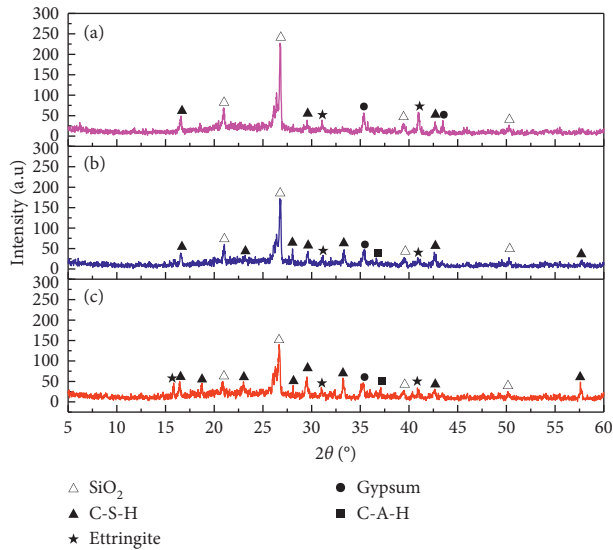
Figure 9: XRD patterns of CPB samples after curing at 80°C for 12 hours: (a) RM, (b) PC, and (c) SC.

C-S-H gel. This thick rod-like AFt breaks the C-S-H gel and is mixed tightly in the C-S-H gel. The results show that the crystal of AFt is relatively coarse and large, and there is not enough space in the sample. Figure 11(c) shows the internal structure of the sample that contains SC. It can be observed from the figure that some voids still exist inside the test piece. However, there are still cotton-like C-S-H gel and rod-like AFt crystals between the raw materials.

Figure 12 shows the SEM images magnified 5000 times after the samples of the three types of binders were cured at 80°C for 12 hours. At 80°C, the hydration products can hardly be observed in the RM sample. However, it is worth noting that most of the AFt in Figures 12(b) and 12(c) has obvious damaged powdery states. In addition, in Figures 12(b) and 12(c), more cotton-like C-S-H gel has coatings with raw material particles.

4. Discussion

The slump test serves as a macro index for evaluating the rheological properties of CPB and is more easily obtained in practice. It can be clearly seen from the results in Table 5 that the slump test results of the three types of binders are not significantly different and range from 22.45 cm to 25.45 cm. The results of slump test show that the CPB prepared by these three binders can meet the requirements of mine engineering fluidity [23].

Figures 3–5 show that the effect of curing temperature on the CPB strength is strongly dependent on the binder type. It is shown that the UCS values of the PC and SC samples are much higher than those of the samples that contain RM mainly because of the cementing performance of the binders in the samples. PC and SC can provide CPB with more raw materials for hydration reactions, such as C3S, C2S, and C3A. The hydration products generated by the hydration reactions of these binders promote the filling materials to bond together, reduce the porosity in CPB, and improve the

overall UCS values of the samples [24–31]. At the same time, it can be inferred that the PC sample is more sensitive to temperature than the SC sample.

However, regardless of the curing time, the RM sample shows a trend of first increasing and then decreasing as temperature increases. Specifically, the RM sample RM yielded the lowest strength at 80°C. The main reason for this phenomenon is the poor heat resistance of the RM sample. High temperatures are likely to hinder or destroy hydration products, thus resulting in lower UCS values. The most fundamental reason is attributed to the fact that the RM sample cannot continually provide raw materials for hydration reaction. This view is fully supported by the XRD and SEM images shown above.

Curing temperature also plays a decisive role in the UCS responses of the samples. When the samples are cured for 12 hours, the UCS values at 40°C are greater than those at 20°C. The increase of UCS can be explained as the rate of temperature increase accelerates the dissolution of the clinker phase, thus accelerating the hydration process of the binder. Accordingly, hydration products (AFt and C-S-H gel) increase as a function of temperature. The formation of these hydration products is conducive to the increase of the CPB strength. C-S-H is the main binding phase of hardened cement. The content of C-S-H gel and AFt increases as a function of the curing temperature. With the increase of curing temperature, the precipitation of hydration products increases, thus resulting in the refinement of the void structure. As a result, the sample has a denser microstructure and a finer pore distribution that improves the strength of CPB.

It is interesting to infer (based on In Figure 5) that the UCS of PC and SC samples decreases considerably in an environment at 60°C. This is mainly attributed to the fact that the curing temperature of 60°C promotes the formation of more AFt. The AFt generation is considerably larger than the space-bearing capacity of the pores inside the sample. This has led to the expansion of the sample and the decrease of UCS. In addition, AFt itself possesses specific expansibility, and the expansion pressure leads to the decrease of the UCS [32, 33]. AFt can break the flocculent structure of C-S-H and reduce the integrity of C-S-H gel. The XRD pattern in Figure 8 and the SEM image in Figure 11 prove this assertion. However, the production of C-S-H gel also increases as a function of temperature. However, the overall strength of the sample decreases. The results show that AFt production, C-S-H bonding force, and the internal space of the sample have a competitive relationship at specific temperatures.

It is worth noting that the UCS values of the samples that contained PC and SC after curing at 80°C for 12 hours increase to 1.71 MPa and 2.52 MPa, respectively. This is mainly attributed to the fact that the curing temperature of 80°C prompted the PC and SC samples to produce more hydration products (C-S-H gel) that are favorable to the strengths of the samples. The XRD diffraction pattern and SEM images confirm this view. It is not difficult to discern from the XRD spectra that the diffraction peak of C-S-H gel increases after curing for 12 hours at 80°C, while the
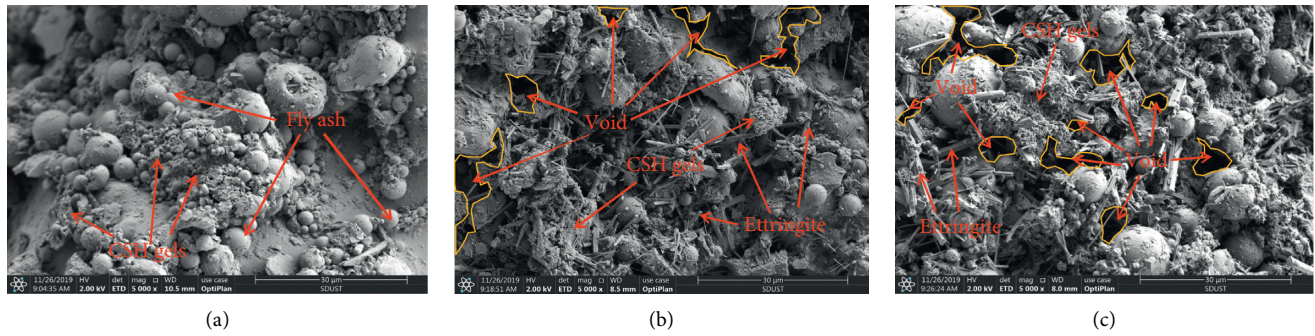
FIGURE 10: Scanning electron microscopy (SEM) images of different samples cured at 40°C for 12 hours: (a) RM, (b) PC, and (c) SC.
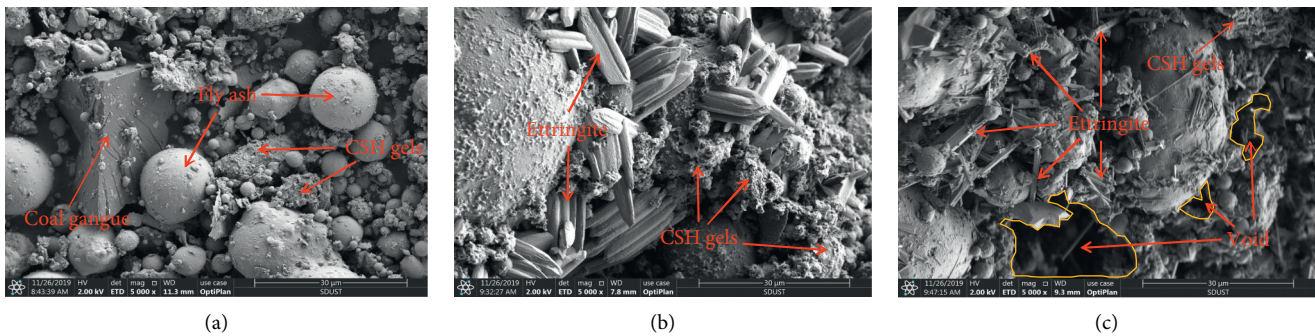

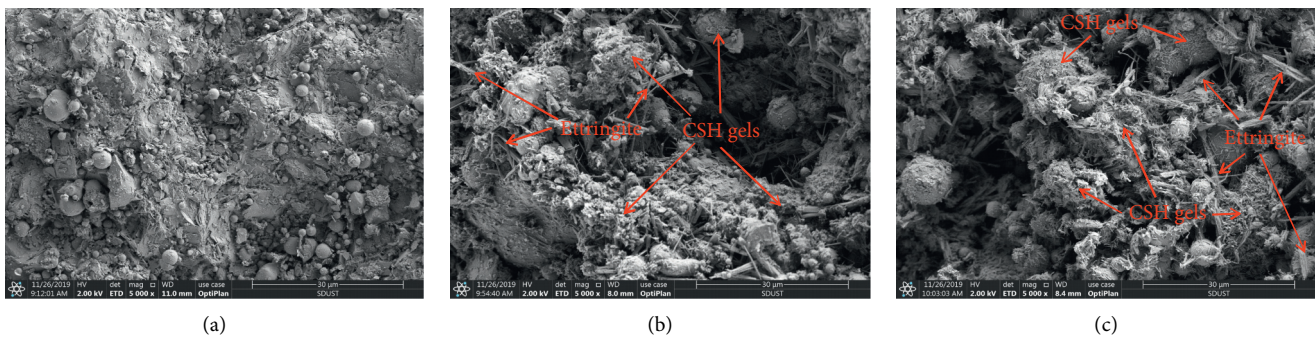FIGURE 11: SEM images of CPB samples cured at 60°C for 12 hours: (a) RM, (b) PC, and (c) SC.

FIGURE 12: SEM images of different samples cured at 80°C for 12 h: (a) RM, (b) PC, and (c) SC.

diffraction peak of AFt decreases. SEM images show that the samples show obvious powdery damage after being cured for 12 hours at 80°C. This is mainly because 80°C has exceeded the limit temperature of AFt. In other words, the structure of AFt was destroyed at 80°C [34].

The change of the UCS of the sample was closely related to the internal space of the sample, the volume of the crystal, the heat resistance of the crystal, and the hydration raw material provided by the binder. In other words, the UCS of the sample is an index that is affected by many factors. The coupled effect of binder type and temperature on UCS shows that PC and SC binders and temperatures (20°C, 40°C, and 80°C) seem to have positive effects. This discovery is of great significance for mining efficiency and improvement of backfill support. The stability variation of the CPB strength is

particularly important for the design of mine filling. This is obviously related to the economic benefits of the mine, and the risk of failure can be reduced by mastering the matching point pair of stability.

In addition, we only studied the effect of medium and low temperature on the stability of CPB. When the underground fire occurs, the CPB will be affected by high temperature. It is a new idea to study the stability of CPB near high temperature heat source.

5. Conclusions

The purpose of the study is to evaluate the effect of binder type and temperature on the microstructural evolution and macroscopic strength development of CPB. The results

provide some new evidence that can contribute to the understanding of the hardening process of CPB with different binder types, namely, RM, PC, and SC, at different temperatures (20°C, 40°C, 60°C, and 80°C). The following conclusions can be drawn from this work:

(1) It is demonstrated that temperature strongly affects the performance of CPB. The UCS values of the SC sample are greater than those of the PC sample; the latter in turn is greater than the RM sample. The UCS of samples mainly depends on whether the binder could provide more raw materials for hydration products. SC and PC can provide an increased number of hydration raw materials (C3A, C3S) for the sample and can produce more hydration products, such as C-S-H gel and AFt. These hydration products fill the inner space structure of the sample and thus improve the compactness and UCS of the sample.

(2) It is found that temperature has positive and negative effects on the UCS of samples. When the samples that contain SC and PC are cured at different temperatures for 12 hours, the UCS of the samples will increase at the beginning, then decrease, and finally increase as a function of temperature. When the curing temperature is ≤40°C, the UCS of the sample is positively related to the temperature mainly because the increase of temperature can accelerate the hydration process of the binder. When the curing temperature is 60°C, the UCS values of the samples decrease. The main reason is attributed to the fact that this temperature promotes the formation of more expansive AFt that has a larger bearing capacity than that of the internal space of the samples. When the curing temperature is 80°C, the strengths of the samples that contain PC and SC increase again. The main reason is that the increased temperature damages the structure of AFt and promotes the hardening of the C-S-H gel. In addition, the UCS of the sample is closely related to the internal space of the sample, the volume of hydration products, the influence of temperature on the hydration products, and the hydration raw materials provided by the binder.

Data Availability

The data used to support the findings of this study are available from the corresponding author upon request.

Conflicts of Interest

The authors declare that there are no conflicts of interest regarding the publication of this paper.

Acknowledgments

References

[1] W. Li and M. Fall, "Sulphate effect on the early age strength and self-desiccation of cemented paste backfill," *Construction and Building Materials*, vol. 106, pp. 296–304, 2016.

[2] L. Liu, Z. Fang, M. Wang, C. Qi, Y. Zhao, and C. Huan, "Experimental and numerical study on rheological properties of ice-containing cement paste backfill slurry," *Powder Technology*, vol. 370, pp. 206–214, 2020.

[3] C. Qi and A. Fourie, "Cemented paste backfill for mineral tailings management: review and future perspectives," *Minerals Engineering*, vol. 144, Article ID 106025, 2019.

[4] L. Liu, J. Xin, C. Huan, C. Qi, W. Zhou, and K.-I. Song, "Pore and strength characteristics of cemented paste backfill using sulphide tailings: effect of sulphur content," *Construction and Building Materials*, vol. 237, Article ID 117452, 2020.

[5] Q. Sun, S. Tian, Q. Sun et al., "Preparation and microstructure of fly ash geopolymer paste backfill material," *Journal of Cleaner Production*, vol. 225, pp. 376–390, 2019.

[6] W. Xu, M. Tian, and Q. Li, "Time-dependent rheological properties and mechanical performance of fresh cemented tailings backfill containing flocculants," *Minerals Engineering*, vol. 145, Article ID 106064, 2020.

[7] S. Chen, Z. Du, Z. Zhang, D. Yin, F. Feng, and J. Ma, "Effects of red mud additions on gangue-cemented paste backfill properties," *Powder Technology*, vol. 367, pp. 833–840, 2020.

[8] M. Fall and M. Pokharel, "Coupled effects of sulphate and temperature on the strength development of cemented tailings backfills: Portland cement-paste backfill," *Cement and Concrete Composites*, vol. 32, no. 10, pp. 819–828, 2010.

[9] A. Wu, Y. Wang, H. Wang, S. Yin, and X. Miao, "Coupled effects of cement type and water quality on the properties of cemented paste backfill," *International Journal of Mineral Processing*, vol. 143, pp. 65–71, 2015.

[10] B. Ercikdi, A. Kesimal, F. Cihangir, H. Deveci, and İ. Alp, "Cemented paste backfill of sulphide-rich tailings: importance of binder type and dosage," *Cement and Concrete Composites*, vol. 31, no. 4, pp. 268–274, 2009.

[11] Q. Sun, T. Li, and B. Liang, "Preparation of a new type of cemented paste backfill with an alkali-activated silica fume and slag composite binder," *Materials*, vol. 13, no. 2, p. 372, 2020.

[12] W. Xu, P. Cao, and M. Tian, "Strength development and microstructure evolution of cemented tailings backfill containing different binder types and contents," *Minerals*, vol. 8, no. 4, p. 167, 2018.

[13] E. Yilmaz, T. Belem, B. Bussière, M. Mbonimpa, and M. Benzaazoua, "Curing time effect on consolidation behaviour of cemented paste backfill containing different cement types and contents," *Construction and Building Materials*, vol. 75, pp. 99–111, 2015.

[14] K. Fang and M. Fall, "Effects of curing temperature on shear behaviour of cemented paste backfill-rock interface," *International Journal of Rock Mechanics and Mining Sciences*, vol. 112, pp. 184–192, 2018.

[15] W. Xu, Q. Li, and B. Liu, "Coupled effect of curing temperature and age on compressive behavior, microstructure and ultrasonic properties of cemented tailings backfill,"

Construction and Building Materials, vol. 237, Article ID 117738, 2020.

[16] S. Chen, Z. Du, Z. Zhang, H. Zhang, Z. Xia, and F. Feng, "Effects of chloride on the early mechanical properties and microstructure of gangue-cemented paste backfill," *Construction and Building Materials*, vol. 235, Article ID 117504, 2020.

[17] X. G. Zhang, J. Lin, J. X. Liu et al., "Investigation of hydraulic-mechanical properties of paste backfill containing coal gangue-fly ash and its application in an underground coal mine," *Energies*, vol. 10, pp. 1–19, 2017.

[18] W. Mu, L. Li, T. Yang, G. Yu, and Y. Han, "Numerical investigation on a grouting mechanism with slurry-rock coupling and shear displacement in a single rough fracture," *Bulletin of Engineering Geology and the Environment*, vol. 78, no. 8, p. 6159, 2019.

[19] O. H. Wallevik and J. E. Wallevik, "Rheology as a tool in concrete science: the use of rheographs and workability boxes," *Cement and Concrete Research*, vol. 41, no. 12, pp. 1279–1288, 2011.

[20] ASTM C 143, *Standard Test Method for Slump of Hydraulic Cement Concrete*, ASTM International, West Conshohocken, PA, USA, 2008.

[21] W. Xu, M. Han, and P. Li, "Influence of freeze-thaw cycles on mechanical responses of cemented paste tailings in surface storage," *International Journal of Mining, Reclamation and Environment*, vol. 34, no. 5, pp. 326–342, 2020.

[22] J. Zhao, L. Yin, and W. Guo, "Stress-seepage coupling of cataclastic rock masses based on digital image technologies," *Rock Mechanics and Rock Engineering*, vol. 51, no. 8, pp. 2355–2372, 2018.

[23] Y. Guo, P. Wang, G. Feng, T. Qi, G. Liu, and A. Ren, "Performance of coal gangue-based cemented backfill material modified by water-reducing agents," *Advances in Materials Science and Engineering*, vol. 2020, Article ID 2302895, 11 pages, 2020.

[24] P. Ghoddousi and L. Adelzade Saadabadi, "Study on hydration products by electrical resistivity for self-compacting concrete with silica fume and metakaolin," *Construction and Building Materials*, vol. 154, pp. 219–228, 2017.

[25] T. Johanna, C. Andrzej, and P. Vesa, "Effects of mineral powders on hydration process and hydration products in normal strength concrete," *Construction and Building Materials*, vol. 72, pp. 7–14, 2014.

[26] X. Lu, S. Wang, Z. Ye, C. Li, and X. Cheng, "Study on the hydration product of ettringite in cement paste with ethanoldiisopropanolamine," *Journal of Thermal Analysis and Calorimetry*, vol. 139, no. 2, pp. 1007–1016, 2020.

[27] X. B. Min, D. G. Liu, L. Y. Chai et al., "Comparison of arsenic immobilization properties among calcium silicate hydrate, ettringite, and Friedel's salt in a slag-based binder," *Environmental Progress & Sustainable Energy*, vol. 38, pp. 422–428, 2019.

[28] C. Qi, Q. Chen, A. Fourie, J. Zhao, and Q. Zhang, "Pressure drop in pipe flow of cemented paste backfill: experimental and modeling study," *Powder Technology*, vol. 333, pp. 9–18, 2018.

[29] N. Yoobanpot, P. Jamsawang, K. Krairan, P. Jongpradist, and S. Likitlersuang, "Laboratory investigation of the properties of cement fly ash gravel for use as a column-supported embankment," *Construction and Building Materials*, vol. 257, Article ID 119493, 2020.

[30] J. Zhao, X. Zhang, N. Jiang, L. Yin, and W. Guo, "Porosity zoning characteristics of fault floor under fluid-solid coupling," *Bulletin of Engineering Geology and the Environment*, vol. 79, no. 5, pp. 2529–2541, 2020.

[31] J. Zhao, J. Chen, X. Zhang, J. Ning, and Y. Zhang, "Distribution characteristics of floor pore water pressure based on similarity simulation experiments," *Bulletin of Engineering Geology and the Environment*, vol. 79, no. 9, p. 4805, 2020.

[32] X. Qiao and J. Chen, "Correlation of propagation rate of corrosive crack in concrete under sulfate attack and growth rate of delayed ettringite," *Engineering Fracture Mechanics*, vol. 209, pp. 333–343, 2019.

[33] J. Yu, J. Qian, J. Tang, Z. Ji, and Y. Fan, "Effect of ettringite seed crystals on the properties of calcium sulphoaluminate cement," *Construction and Building Materials*, vol. 207, pp. 249–257, 2019.

[34] F. Han, Y. Zhou, and Z. Zhang, "Effect of gypsum on the properties of composite binder containing high-volume slag and iron tailing powder," *Construction and Building Materials*, vol. 252, Article ID 119023, 2020.